

AD-605186

ASD-TDR-63-554

AD-605186

VOLUME II

SUMMARY OF LAMINAR BOUNDARY  
LAYER CONTROL RESEARCH

TECHNICAL DOCUMENTARY REPORT ASD-TDR-63-554

Prepared under Contract No. AF33(616)-7564  
by Northrop Noroir, A Division of  
Northrop Corporation, Hawthorne, California  
Author: Boundary Layer Research Section

REPRODUCED BY  
NATIONAL TECHNICAL  
INFORMATION SERVICE  
U. S. DEPARTMENT OF COMMERCE  
SPRINGFIELD, VA. 22151

44

## **DISCLAIMER NOTICE**

**THIS DOCUMENT IS BEST QUALITY PRACTICABLE. THE COPY FURNISHED TO DTIC CONTAINED A SIGNIFICANT NUMBER OF PAGES WHICH DO NOT REPRODUCE LEGIBLY.**

## SUMMARY OF LAMINAR BOUNDARY LAYER CONTROL RESEARCH

## VOLUME II



## A GOVERNMENT RESEARCH REPORT

## U.S. DEPARTMENT OF COMMERCE

Luther H. Hodges, Secretary

## OFFICE OF TECHNICAL SERVICES

Donald A. Schon, Director

distributes this and thousands of similar reports in the interest of science, industry, and the public—for which research and new products mean better health, better living, and a stronger economy.

## HOW TO GET OTHER REPORTS

The Office of Technical Services is the Nation's clearinghouse for reports of research supported by the Army, Navy, Air Force, Atomic Energy Commission, and other Government agencies.

*Abstracts* of new reports available are published twice a month in U. S. GOVERNMENT RESEARCH REPORTS (\$15 a year domestic).

*Selected Reports* of particular interest to small business are described monthly in TECHNICAL REPORTS NEWSLETTER (\$1 a year domestic).

*Translations* of foreign technical material are also available from the Office of Technical Services and other sources. These are listed or abstracted semimonthly in TECHNICAL TRANSLATIONS (\$12 a year domestic).

The above periodicals may be ordered from Superintendent of Documents, U. S. Government Printing Office, Washington, D. C., 20402, or through a U. S. Department of Commerce Field Office.

*Inquiries* about the availability of reports and translations on any particular subject may be directed to Office of Technical Services, U. S. Department of Commerce, Washington, D. C., 20230, or to any Commerce field office.

Reports and translations are published by the Office of Technical Services for use by the public. Thus, you may use the know-how or reprint the information therein except that where patent questions appear to be involved the usual preliminary search is advised, and where copyrighted material is used permission should be obtained for its further publication.

These documents are reprinted by OTS from the best available copy.

ASD-TDR-63-554

S U M M A R Y   O F   L A M I N A R   B O U N D A R Y  
L A Y E R   C O N T R O L   R E S E A R C H

TECHNICAL DOCUMENTARY REPORT ASD-TDR-63-554

March 1964

Air Force Flight Dynamics Laboratory  
Aeronautical Systems Division  
Air Force Systems Command  
Wright-Patterson Air Force Base, Ohio

Project No. 1366, Task No. 136612

Prepared under Contract No. AF33(616)-7564  
by Northrop Norair, A Division of  
Northrop Corporation, Hawthorne, California  
Author: Boundary Layer Research Section



**SECTION II PART 2**  
**EXPERIMENTAL AERODYNAMIC INVESTIGATIONS**  
**AT SUPERSONIC SPEEDS**

CHAPTER A. INVESTIGATION OF A LAMINAR FLAT PLATE WITH SUCTION THROUGH MANY FINE SLOTS WITH AND WITHOUT WEAK INCIDENT SHOCK WAVES

a. LOW DRAG BOUNDARY LAYER SUCTION EXPERIMENTS ON A FLAT PLATE AT MACH NUMBERS 2.5, 3.0 AND 3.5

E. E. Groth

(A) Acknowledgements

The work reported herein was accomplished under the direction of Dr. W. Pfenninger, Director of the Norair Boundary Layer Research Group. The model was designed by C. G. Stall and built by the Boundary Layer Laboratory. J. Wada and R. N. Worth participated in the design work and the wind tunnel tests. Most of the design calculations and data reduction, all boundary layer calculations on the IBM 7090, and the final plots of the report were done by J. D. Ryan.

The project engineers, J. H. Jones and S. R. Pate, and the personnel of Tunnel A of ARO, Inc., AEDC, deserve special acknowledgement for their efforts in executing the tests and the basic data reduction.

(B) Summary

Low drag boundary layer suction experiments on a 41-inch long flat plate were conducted at the 40- by 40-inch continuous supersonic Tunnel A of the Arnold Engineering Development Center at Tullahoma, Tennessee. The model was equipped with 76 closely spaced, fine slots arranged in eight suction chambers. Full length laminar flow was obtained at  $M = 2.5, 3.0$  and  $3.5$  up to the highest possible tunnel pressures, resulting in length Reynolds numbers of  $21.8 \times 10^6$ ,  $25.7 \times 10^6$  and  $21.4 \times 10^6$ , respectively. The measured drag coefficients (sum of wake and suction drag) were of the order of 26 to 43 percent of the turbulent friction drag at the same Reynolds and Mach numbers.

The results of calculations of the laminar boundary layer development along the plate at typical suction distributions are compared with the test data.

(C) Notation

$b_k$	average span of slots in $k^{\text{th}}$ chamber	
$c$	reference chord length, location of boundary layer rake ( $c = 40.23$ inches)	
$C_{D_s}$	suction drag coefficient	} referred to freestream dynamic pressure, unit span, and reference chord
$C_{D_t}$	total drag coefficient	
$C_{D_w}$	wake drag coefficient	
$C_f$	friction drag coefficient	

(C) Notation (Continued)

$$C_{W_k} = \frac{W_k}{\rho_{\infty} g U_{\infty} b_k c} = \text{suction weight flow coefficient}$$

M Mach number

p static pressure

q dynamic pressure

R Reynolds number

$$R_c = \frac{U_{\infty} c}{\nu_{\infty}} = \text{reference Reynolds number}$$

T temperature

u velocity inside boundary layer

U potential flow velocity

$W_k$  suction weight flow through  $k^{\text{th}}$  chamber

x coordinate along plate

y coordinate perpendicular to plate

$\delta^*$  boundary layer displacement thickness

$\theta$  boundary layer momentum thickness

$\mu$  viscosity

$\nu$  kinematic viscosity

$\rho$  density

Subscripts

b suction box

c chordwise station c

k running parameter,  $k = 1, \dots, 8$

n measuring nozzle

s suction chamber inside model

w wall condition

(C) Notation (Continued)

x            chordwise station x  
o            stagnation  
 $\infty$           freestream

(D) Introduction

Earlier boundary layer suction experiments on a two-dimensional surface at supersonic speeds were conducted in 1957 on a 20-inch chord 5-percent thick biconvex wing at Mach numbers 2.23 and 2.77 and at a length Reynolds number of  $12.5 \times 10^6$  (Reference 98). The present program extends these results to higher Mach and Reynolds numbers and to an airfoil section which does not produce a favorable pressure gradient along its chord.

(E) Description of the Model

The flat plate suction model had a chord of 41 inches and a span of 40 inches. The leading edge thickness was .007 inch; the bevel angle increased from 11.5 degrees over the forward 1.3 inches to 15.8 degrees between stations 1.3 and 9.4 inches, resulting in a total thickness of the model of 2.50 inches.

Suction was applied through 76 slots located between chordwise stations 2.0 and 39.9 inches. The slot width increased from .004 inch in front to .005 inch in the rear, the slot spacing from 0.42 inch in front to 0.55 inch in the rear. The span of the first slot was 14.6 inches. Allowing a wedge angle of 8.3 degrees for the spread of turbulent disturbances from the end points of the slots reduced the slot span to a value of 3.61 inches for the last slot. The slots were cut through a .020-inch thick upper skin which was bonded together with a thicker lower skin. The latter contained rows of .20-inch deep holes placed .25 inch apart and varying in diameter from .042 to .062 inch. The sucked air was collected in eight suction chambers and ducted from there through tubes of 0.93 inch i.d. through the tunnel wall to eight metering boxes, where the suction quantities could be adjusted manually and measured through calibrated nozzles. The sucked air was removed through a 12-inch diameter pipe of a pressure of .05 to .10 psia, provided by ARO, Inc.

The model was instrumented to measure surface pressures, suction chamber pressures and temperatures, metering box pressures and temperatures and metering nozzle pressures. A rake of ten total head probes was mounted at the rear of the model; it could be moved between stations 23.5 and 40.5 inches to measure the boundary layer profile at various chordwise stations. The drive mechanism for the rake was provided by ARO, Inc.

A list of the pertinent slot dimensions is presented in Table I. A sketch and photographs of the model are shown in Figures 1 to 5.

## (F) Measurements and Data Reduction

The tests were conducted at AEDC Tunnel A of the von Karman Gas Dynamics Facility of ARO, Inc., Tullahoma, Tennessee, with J. H. Jones and S. R. Pate as project engineer (Reference 99). At a given Mach number and tunnel pressure the suction quantities through the eight chambers were varied and the changes of the boundary layer profile at the rake location observed. The pressure and temperature data were recorded for typical cases.

The equations for the data reduction are the same ones used in the previous supersonic suction experiments and are summarized as follows (most of the symbols are defined in the Notation).

The suction coefficient for the  $k^{\text{th}}$  chamber is determined by

$$C_{Wk} = \frac{W_k}{\rho_{\infty} g U_{\infty} b_k c} = \alpha_k \frac{M_{nk} (1 + .2 M_{\infty}^2)^3 \frac{\pi}{4} d_k^2 p_{bk} \sqrt{\frac{T_o}{T_{bk}}}}{M_{\infty} (1 + .2 M_{nk}^2)^3 b_k c p_o}$$

where  $M_{nk}$  is the Mach number inside the metering nozzle of diameter  $d_k$  and defined by the suction box pressure  $p_{bk}$  and the nozzle pressure  $p_{nk}$

$$M_{nk}^2 = 5 \left[ \left( \frac{p_{bk}}{p_{nk}} \right) \cdot .286 - 1 \right]$$

$b_k$  is the average span of the slots in the  $k^{\text{th}}$  chamber; the values are listed in Table I. The reference chord length is identical with the rake location; in most cases  $c = 40.23$  inches.

The suction drag coefficient per unit span is given by

$$C_{Ds} = \frac{D_s}{q_{\infty} c} = \sum C_{Wk} \left( 1 + \frac{M_{sk}^2 T_{sk}}{M_{\infty}^2 T_o} \right)$$

where  $M_{sk}^2$  is determined by the pressure in the suction chamber,  $p_{sk}$ ,

$$M_{sk}^2 = 5 \left[ \left( \frac{p_o}{p_{sk}} \right) \cdot .286 - 1 \right]$$

the wake drag coefficient per unit span is evaluated from the formula

$$C_{Dw} = \frac{D_w}{q_{\infty} c} = \frac{2 \theta}{c} \left( \frac{U_c}{U_o} \right)^{H+2-M^2}$$

(F) Measurements and Data Reduction (Continued)

where  $\theta_c$  is the momentum thickness at the rake location

$$\theta_c = \int_0^{\delta} \frac{\rho}{\rho_c} \frac{u}{U_c} \left(1 - \frac{u}{U_c}\right) dy$$

and (Reference 123)

$$H + 2 - M^2 = 3.145 - .26 M_c^2 - .30 M_\infty^2$$

Although the flat plate has constant static pressure along its surface, small local changes occur due to the shock waves from the individual slots, resulting in values of  $U_c \neq U_\infty$ . The total drag is defined as the sum of wake and suction drag,

$$C_{D_t} = C_{D_w} + C_{D_s}.$$

(G) Results of the Drag and Suction Measurements

The basic test results are presented in Figures 6 to 9 where the wake, suction and total drag coefficients are plotted versus total suction coefficient for  $M = 2.0$  and  $2.5$  and the Reynolds numbers investigated. Each total drag curve has a minimum at a certain suction coefficient. These minimum total drag and optimum suction coefficients are plotted in Figures 10 and 11 for the two Mach numbers,  $3.0$  and  $3.5$ . Included are the theoretical values of a laminar and turbulent plate. The laminar value was taken from the boundary layer calculation for an insulated wall at a stagnation temperature of  $100^\circ\text{F}$ . The turbulent curve follows van Driest's theory (Eqs 11-29 and Figure F-111 of Reference 100).

Full laminar flow was maintained at  $M = 3.0$  and  $3.5$  up to the maximum tunnel pressures available, resulting in maximum length Reynolds numbers of  $25.7 \times 10^5$  at  $M = 3.0$  and  $21.4 \times 10^6$  at  $M = 3.5$ . The following minimum drag and optimum suction coefficients were obtained at the highest Reynolds numbers:

$$M_\infty = 3.0, R_c = 25.7 \times 10^6, C_{D_t} = 4.50 \times 10^{-4}, C_{W_t} = 2.10 \times 10^{-4}$$

$$M_\infty = 3.5, R_c = 21.4 \times 10^6, C_{D_t} = 5.65 \times 10^{-4}, C_{W_t} = 2.70 \times 10^{-4}$$

The test points in Figures 10 and 11 indicate that no increase in suction quantities was observed at the high Reynolds numbers due to increased external disturbances at the higher tunnel pressures so that higher length Reynolds numbers with full laminar flow could have been provided if higher tunnel pressures had been available. The measured minimum total drag coefficients of the suction plate are between  $1.60$  and  $1.77$  times the laminar plate friction coefficients and between  $0.37$  and  $0.28$  times the turbulent plate friction

(G) Results of the Drag and Suction Measurements (Continued)

coefficients at  $M = 3.0$ ; the corresponding data at  $M = 3.5$  are  $C_{Dt} \sim 2.05 \times C_{f_{lam}}$  and  $C_{Dt} \sim 0.40 \times C_{f_{turb}}$ .

The slightly higher drag coefficients at  $M = 3.5$  are partially caused by the higher suction requirements at the higher Mach number. A plot of  $(C_{Wt} \sqrt{R_c})_{opt}$  versus  $R_c$  is shown in Figure 12. About 25 percent higher suction coefficients are required at  $M = 3.5$  than at  $M = 3.0$ . Typical experimental suction distributions are presented in Figure 13. The low suction coefficient through chamber 7 at  $M = 3.0$  was caused accidentally by a blockage of the suction tube inside the model. Slightly higher suction in the adjacent chambers compensated for the loss in chamber 7. The continuous suction inflow velocity coefficient  $\frac{\rho_w v_o}{\rho_\infty U_\infty} \sqrt{R_c}$  for equivalent area suction is related to the suction coefficient  $C_{Wk}$  for  $k^{th}$  chamber by the equation

$$C_{Wk} = \frac{\rho_w v_o}{\rho_\infty U_\infty} \frac{\Delta k}{c}$$

where  $\Delta k$  is the chordwise length of the  $k^{th}$  suction chamber. Typical values for  $\frac{\rho_w v_o}{\rho_\infty U_\infty} \sqrt{R_c}$  are of the order of 1.5, or

$$\frac{\rho_w v_o}{\rho_\infty U_\infty} \sim .003$$

for Reynolds numbers between 20 and  $25 \times 10^6$ . Because of  $\frac{\rho_w}{\rho_\infty} \sim .3$  and  $U_\infty \sim 2000$  ft/s at  $M_\infty = 3.0$  to 3.5, the continuous inflow velocity  $v_o$  is about 2 ft/s.

(H) Discussion of Test Results and Comparison with Theory

The test results will be discussed in connection with theoretical data obtained from a calculation of the laminar boundary layer development for an insulated flat plate at a stagnation temperature of 100°F and for suction distributions similar to the experimental ones. The method of computation originates from Reference 45. Two suction distributions with total coefficients  $C_{Wt} \times \sqrt{R_c} = 1.160$  and 1.328 were selected. They are plotted in Figure 14 as

$\frac{\rho_w v_o}{\rho_\infty U_\infty} \sqrt{R_c}$  vs  $x$ . Included in this figure is the development of the Reynolds number based on the local momentum thickness of the boundary layer plotted in

(H) Discussion of Test Results and Comparison with Theory  
(Continued)

the form  $\frac{R_0}{\sqrt{R_c}}$  vs  $x$  for the two suction distributions. The calculations were performed for both suction distributions at  $M = 3.0$  and  $3.5$ . The variation of  $R_0$  with Mach number is so small that the plotted curves are valid for both Mach numbers. For a flat plate the wake drag is related to  $R_0$  by the formula

$$C_{Dw} \sqrt{R_c} = 2 \left( \frac{R_0}{\sqrt{R_c}} \right)_{x=c}$$

The variation of  $C_{Dw} \sqrt{R_c}$  with the suction coefficient  $C_{Wt} \sqrt{R_c}$  is plotted in Figure 15; the theoretical curve fairs into the value  $C_{Dw} \sqrt{R_c} = 1.27$  at  $C_{Wt} = 0$ . This curve can be compared with experimental data in the following way: wake drag coefficients  $C_{Dw}$  and total suction coefficients  $C_{Wt}$  at a given Reynolds number  $R_c$  are taken from the curves in Figures 6 to 9, and each point selected produces a test point  $(C_{Dw} \sqrt{R_c}, C_{Wt} \sqrt{R_c})$  in Figure 15. The points included in Figure 15 were taken at the optimum suction coefficient  $(C_{Wt})_{opt}$  for the five Reynolds numbers tested at  $M = 3.0$  and the three Reynolds numbers at  $M = 3.5$ . Since the boundary layer velocity profile at the trailing edge for the case of optimum suction is usually slightly distorted toward a turbulent shape, additional points for  $M = 3.0$  and a total suction coefficient which is 30 percent higher than optimum suction are also included in Figure 15. The test points fall into a band limited by the lines 1.45 and 1.75 times the theoretical curve; the experimental data at  $M = 3.0$  are about 50 percent higher than the theoretical values, those at  $M = 3.5$  about 75 percent higher; no difference was observed between the data for  $(C_{Wt})_{opt}$  and  $1.3 (C_{Wt})_{opt}$ .

A possible explanation for this high wake drag may be found from one additional test point which was obtained by moving the rake to the end of the seventh suction chamber, station  $x = 31.4$ . If  $x = 31.4$  is introduced as the new chord length and all suction and drag coefficients are made nondimensional by this new value, one point occurs in Figure 15 which is only 14 percent higher than the theoretical value. This single point is also included in Figure 6. Additional test points at chordwise stations ahead of the trailing edge were not obtained because of a failure of the rake drive mechanism and time limitations in the later part of the program. If this test point is correct, it suggests the possibility that the high experimental wake drag coefficients are caused by a spanwise contamination of the laminar boundary layer from the adjacent turbulent sections. The last slot of chamber 8 had a span of 3.6 inches compared with 6.2 inches for the last slot of chamber 7. Since the turbulent boundary layer has a thickness of the order of one inch, it is possible that it interferes with the laminar layer (which is only about 0.1 inch high), and this interaction would be more



(H) Discussion of Test Results and Comparison with Theory  
(Continued)

severe at  $c = 40.2$  than at  $x = 31.4$ . An increase of the suction area on the model was not possible because of the limited volume inside the model and the requirement to remove the sucked air at acceptable pressure losses.

Since the one test point at station  $x = 31.4$  was obtained at a total suction coefficient which seems to be close to optimum suction, the total drag must be close to the minimum drag. Therefore, the total drag coefficient  $C_{D_t} = 4.98 \times 10^{-4}$  at  $R_c = 14.0 \times 10^6$  can be compared with the minimum drag coefficients at  $M = 3.0$  measured at  $c = 40.23$  inches, as shown in Figure 16. Comparison with the laminar and turbulent plate friction coefficients results in  $C_{D_t} = 1.45 (C_f)_{\text{lam}} = .28 (C_f)_{\text{turb}}$ . These values are considerably better than those measured at  $c = 40.2$  inches.

A comparison of the theoretical and experimental velocity profiles is shown for the following conditions:

Figure 17  $M_\infty = 3.0$ ,  $R_c = 25.7 \times 10^6$ ,  $c = 40.23$  inches;

Figure 18  $M_\infty = 3.5$ ,  $R_c = 21.4 \times 10^6$ ,  $c = 40.23$  inches;

Figure 19  $M_\infty = 3.0$ ,  $R_c = 18.0 \times 10^6$ ,  $c = 40.23$  inches;

Figure 20  $M_\infty = 3.0$ ,  $R_x = 14.0 \times 10^6$ ,  $x = 31.40$  inches.

The experimental velocity profiles are thicker than the theoretical by about the same ratio as the experimental wake drag coefficients are higher than their theoretical values.

(I) Effect of Leading Edge Bluntness on Wake Drag

Another reason for the discrepancy between the theoretical and experimental wake drag data consists in the fact that a theoretical flat plate has an infinitely thin leading edge while the experimental plate had a finite nose thickness ( $t = .007$  inch) and the lower surface was inclined by  $11.5$  degrees, causing a certain amount of unsymmetry between the top and bottom surfaces. The effect of a blunt leading edge on the transition of a laminar boundary layer and its momentum loss has been discussed frequently (e.g., Reference 101 & 102). The detached shock wave from the leading edge causes a considerable total head loss for the streamlines next to the surface and produces a momentum loss even in the absence of a viscous layer. The order of magnitude of this effect can be estimated by the following analysis.

It will be assumed that the plate has the shape of a half cylinder followed by a flat surface of constant thickness equal to the diameter  $t$  of the cylinder. The bevel angle will be neglected. The detached shock wave for a circular cylinder was computed in Reference 103 for  $M = 3.0$ . The stand-off distance of the shock is equal to  $\Delta = .355 t$ . Since the shock wave will gradually reduce to the Mach wave for  $M = 3.0$ , the shape of the shock is approximated by

(I) Effect of Leading Edge Bluntness on Wake Drag (Continued)

a hyperbola (also used in Reference 102) of the equation

$$\frac{y}{t} = 5.06 \sqrt{(1 + .070 \frac{x}{t})^2 - 1}$$

The shape of the model and shock wave are shown in Figure 21.

The local slope  $\sigma$  of the shock wave permits the calculation of the total head loss through the shock wave as a function of  $M \sin \sigma$ ,

$$K = \frac{p_{t2}}{p_{t1}}$$

where  $p_{t2}$  is the total head aft of the shock,  $p_{t1} = p_o$  = total head ahead of the shock. The variation of  $\sigma$  and  $K$  along the height  $y/t$  are plotted in Figure 22. The momentum loss of the air through the shock wave can be computed, following a similar procedure described in Reference 104. The static pressure  $p_2$  aft of the shock changes adiabatically till it finally reaches the undisturbed value  $p_o$ . The Mach number at infinity aft of the shock,  $M_3$ , is defined by

$$1 + .2 M_3^2 = \left(\frac{p_{t2}}{p_o}\right)^{\frac{\gamma-1}{\gamma}} = \left(\frac{K p_o}{p_o}\right)^{\frac{\gamma-1}{\gamma}} = (1 + .2 M_o^2)^{\frac{\gamma-1}{\gamma}} K^{\frac{\gamma-1}{\gamma}}$$

The temperature at infinity is

$$T_3 = \frac{T_o}{1 + .2 M_3^2} = \frac{T_o}{1 + .2 M_o^2} K^{-\frac{\gamma-1}{\gamma}} = T_o \cdot K^{-\frac{\gamma-1}{\gamma}}$$

since the total temperature remains constant through the shock. The velocity  $U_3$  at infinity is given by

$$\frac{U_3^2}{U_1^2} = \frac{.2 M_3^2 T_3}{.2 M_o^2 T_o} = \frac{(1 + .2 M_o^2)^{\frac{\gamma-1}{\gamma}} K^{\frac{\gamma-1}{\gamma}} - 1}{.2 M_o^2} K^{-\frac{\gamma-1}{\gamma}}$$

$$\frac{U_3^2}{U_1^2} = 1 - \frac{1}{.2 M_o^2} \left( K^{-\frac{\gamma-1}{\gamma}} - 1 \right).$$

(I) Effect of Leading Edge Bluntness on Wake Drag (Continued)

The momentum loss of the air within an element of height  $d \frac{y}{t}$  is equal to

$$\rho_{\infty} U_{\infty}^2 \left(1 - \frac{U_3}{U_{\infty}}\right) d \frac{y}{t}$$

and the momentum loss between the height  $y = 0$  and  $y = h$  is proportional to the integral

$$I \left(\frac{h}{t}\right) = \int_0^{h/t} \left(1 - \frac{U_3}{U_{\infty}}\right) d \frac{y}{t}$$

The corresponding drag coefficient referred to freestream dynamic pressure and chord length  $c$  is equal to

$$C_D(h) = 2 \frac{t}{c} I \left(\frac{h}{t}\right).$$

The functions  $1 - \frac{U_3}{U_{\infty}}$  and  $I \left(\frac{h}{t}\right)$  are plotted vs  $\frac{h}{t}$  in Figure 23.

The validity of this approach can be verified by checking some of the test results of Reference 101, which contains measurements of the laminar boundary layer on a flat plate with different leading edge thicknesses at Mach number  $M = 3.05$  and a chordwise station  $x = 1.75$  inches,  $R_x = 0.74 \times 10^6$ . The measured wake drag coefficient,  $C_{D_w}(t)$ , for a given leading edge thickness  $t$  should include, according to the above analysis, a contribution

$$\Delta C_D = 2 \frac{t}{x} I_{\max} = .368 \frac{t}{x}$$

where  $I_{\max} = .184$  is the asymptotic value of  $I \left(\frac{h}{t}\right)$  shown in Figure 23. Therefore,

$$C_{D_w}(t=0) = C_{D_w}(t) - \Delta C_D = C_{D_w}(t) - \frac{.368 t}{x}$$

should be the wake drag coefficient extrapolated to zero leading edge thickness. The measured data, shown in Figure 7 of Reference 101, and the present corrections are listed below:

(I) Effect of Leading Edge Bluntness on Wake Drag (Continued)

Leading edge thickness, $t$ , $10^{-3}$ in.	0.3	5.7	11.7
Measured wake drag coefficient, $C_{D_w}(t)$	.0018	.0029	.0042
Drag correction, $\Delta C_D = \frac{.368 t}{1.75}$	.0001	.0012	.0024
Drag coefficient at $t = 0$ , $C_{D_w}(0) = C_{D_w}(t) - \Delta C_D$	.0017	.0017	.0018

The extrapolated value of  $C_{D_w}(t=0) = .0017$  is slightly higher than the theoretical value at the same Mach and Reynolds numbers,  $[C_{D_w}(t=0)]_{\text{theor}} = .0014$

The contributions of the shock momentum loss in the wake drag of a suction plate can now be estimated. The total amount of sucked air represents a height  $h_s$  of freestream air given by

$$h_s = C_{w_t} c.$$

The height  $h_{b_0}$  of freestream air corresponding to the mass flow through the boundary layer at the rake location is equal to

$$h_{b_0} = \delta - \delta^*$$

where  $\delta$  is the total thickness of the boundary layer and  $\delta^*$  the displacement thickness. Therefore, the momentum loss from the shock wave between the heights  $h_s$  and  $h_s + h_{b_0}$  is included in the wake drag analysis, or

$$C_{D_{\text{shock}}} = C_D (h_s + h_{b_0}) - C_D (h_s)$$

The numerical values for a few test points at  $M = 3.0$  are listed in the table shown on the following page.

The momentum loss due to the detached shock wave, which is included in the wake drag evaluation of the measured boundary layer profile, amounts to about 10 percent of the wake drag coefficient for the examples selected. This amount is rather low since a large portion of the air with the high momentum is sucked into the plate.

(I) Effect of Leading Edge Bluntness on Wake Drag (Continued)

<u>Chord</u>	<u>40.23</u>	<u>40.23</u>	<u>40.23</u>	<u>31.4</u>
$10^{-6} R_c$	25.69	18.21	12.96	14.04
$10^4 C_{Wt}$	2.374	2.184	2.580	2.280
$h_s$ (in)	.00955	.00878	.01038	.0072
$\delta$ (in)	.060	.080	.090	.060
$\delta^*$ (in)	.027	.040	.044	.025
$h_{b\delta}$ (in)	.033	.040	.046	.035
$10^4 C_D (h_s)$	.416	.393	.438	.437
$10^4 C_D (h_s + h_{b\delta})$	.637	.638	.639	.812
$10^4 C_{D_{shock}}$	.221	.245	.201	.375
$10^4 C_{D_w}$	2.101	2.740	3.718	2.582
$100 \frac{C_{D_{shock}}}{C_{D_{wake}}}$	10.52	8.94	5.41	14.52

The chordwise development of  $h_s(x)$  and  $h_{b\delta}(x)$  is plotted in Figure 24 for the case of the first example listed in the above table.  $h_s(x)$  results from the measured suction distribution;  $h_{b\delta}(x)$  was developed from a theoretical boundary layer calculation under conditions similar to the test case. Since the streamlines entering the outer edge of the boundary layer at any chordwise station  $x$  have a distance  $h_s(x) + h_{b\delta}(x)$  from the centerline ahead of the shock, the actual total head loss  $\frac{P_{t2}}{P_{t1}}$  can be plotted vs  $x$  by combining Figures 22 and 24. The result is shown in Figure 25-1, which also includes the local Mach number as a function of  $\frac{P_{t2}}{P_{t1}}$ . The Mach number at the outer edge of the boundary layer decreases from the freestream value 3.0 near the trailing edge of the model to a value of 2.3 near the leading edge. This large variation along the chord and the velocity gradient of the external flow perpendicular to the flow direction make it quite obvious that the simple superposition of the effects of the flat plate boundary layer and the detached shock wave as described above can only be considered as a first approximation to the problem.

(J) Conclusions

Boundary layer suction experiments on a flat plate with 76 suction slots provided the following results:

- (1) Full chord laminar flow was obtained up to the maximum tunnel pressures at Mach numbers 3.0 and 3.5, resulting in maximum length Reynolds numbers of  $25.7 \times 10^6$  at  $M = 3.0$  and  $21.4 \times 10^6$  at  $M = 3.5$ .

(J) Conclusions (Continued)

(2) The total suction weight flow coefficients required were between 2 and  $3 \times 10^{-4}$ .

(3) The measured minimum drag coefficients were between 28 and 43 percent of the friction coefficients of a turbulent plate.

(4) Comparison of the measured data with the results of theoretical boundary layer calculations shows that the measured boundary layer thicknesses and wake drag coefficients are about 40 to 80 percent larger than the theoretical data computed for the same total suction coefficients.

(5) Two reasons for this discrepancy are discussed:

- (a) the possibility of a spanwise contamination of the laminar boundary layer in the center portion of the plate from the adjacent turbulent areas;
- (b) the effect of the detached shock wave from the blunt leading edge of the plate which is not included in the theoretical analysis.

(K) Addendum--Additional Low Drag Boundary Layer Suction Experiments on a Flat Plate at Mach Numbers 2.5, 3.0, and 3.5

The flat plate suction model which was tested during July 1961, at the AEDC Tunnel A was installed again in April 1962 for shock interaction measurements (Section II, Part 2, Chapter A-b). A few drag measurements were conducted before the shock generator was installed, they provided the following results:

(1) In order to check the repeatability of the experimental data, a few points were recorded at similar conditions as in the original program. The drag coefficients agreed with the corresponding old data within a few percent (see the first four test points in Table II).

(2) Drag and suction measurements were conducted at  $M = 2.5$  and several Reynolds numbers. The wake, suction and total drag coefficients are plotted vs total suction coefficient in Figure 25-2 the resulting minimum total drag and optimum total suction coefficients are included in Figure 25-5. Laminar flow was maintained up to the maximum tunnel pressure corresponding to a length Reynolds number of  $21.8 \times 10^6$ . The minimum total drag coefficient was about 26 percent of the friction coefficient of a turbulent plate at Reynolds numbers around  $20 \times 10^6$ .

(3) More data were collected with the rake in further forward positions,  $x_{\text{rake}} = 31.4$  inches at the end of suction chamber 7 and  $x_{\text{rake}} = 23.7$  inches at the end of suction chamber 6. One test point was mentioned on first

(K) Addendum--Additional Low-Drag Boundary Layer Suction Experiments on a Flat Plate at Mach Numbers 2.5, 3.0, and 3.5 (Continued)

page of Section H which had a considerably lower wake drag than was measured at the most aft position of  $x_{\text{rake}} = 40.2$  inches at the end of suction chamber

8. Since the spanwise extent of the slotted area decreased toward the trailing edge of the model, the possibility of a spanwise contamination of the laminar region from the adjacent turbulent portions of the model was discussed as a possible reason in part (H) above. The additional experimental evidence presented in Figures 25-3 and 25-5 confirms the above observation. The reduction in  $C_{Dw}$  at  $M = 3.0$  and  $R_x \sim 14 \times 10^6$  is of the order of more than 25 per-

cent when the rake is located at  $x = 23.7$  and  $31.4$  inches instead of  $x_{\text{rake}} = 40.2$  inches. The minimum total drag coefficient at  $M = 3.0$  and  $R_x = 14 \times 10^6$  is reduced from  $6.15 \times 10^{-4}$  at  $x_{\text{rake}} = 40.2$  inches to  $5.10 \times 10^{-4}$  at  $x_{\text{rake}} = 31.4$  inches at a simultaneous reduction of the optimum total suction coefficient from  $2.4 \times 10^{-4}$  to  $2.2 \times 10^{-4}$ .

The effect was less pronounced at  $M = 3.5$ . Figure 25-4 shows that the breakdown of the laminar flow was delayed to lower suction quantities at the more forward rake position. The reduction of the minimum total drag coefficient was about 3 percent, of the optimum total suction coefficient about 6 percent.

(4) All performance measurements on the flat plate suction model are summarized in Figure 25-5. The minimum total drag and optimum total suction coefficients are plotted vs length Reynolds number at Mach numbers 2.5, 3.0 and 3.5 and compared with the friction coefficients of a laminar and turbulent plate. The drag reduction by means of boundary layer suction through many fine slots is of the following order of magnitude: the total drag coefficients of the suction model at length Reynolds numbers around  $20 \times 10^6$  and Mach numbers 2.5, 3.0 and 3.5 are 26.0, 29.5 and 38.5 percent of the friction coefficients of a turbulent plate, respectively.

b. BOUNDARY LAYER SUCTION EXPERIMENTS ON A SLOTTED FLAT PLATE MODEL WITH INTERFERING SHOCK WAVES

E. E. Groth

(A) Summary

The interaction of an impinging shock wave with the laminar boundary layer was investigated at the AEDC Tunnel A on a 41-inch chord flat plate suction model by mounting a plate (shock generator) vertically on the suction model. The shock wave intersected the suction slots in the rear half of the model under an acute angle. The flat plate model and its suction system were the same ones which were used previously for shock-free low-drag measurements.

Laminar flow was maintained aft of the shock wave up to certain intensities depending on Mach and Reynolds number. The increases in suction quantities and total drag as function of the shock intensity were measured at Mach numbers between 2.5 and 3.5 and Reynolds numbers up to  $26 \times 10^6$ .

(B) Notation

$b_k$	average span of slots in $k^{\text{th}}$ chamber	
$c$	reference chord length, most rearward location of boundary layer rake ( $c = 40.23$ inches)	
$C_{Ds}$	suction drag coefficient	} referred to freestream dynamic pressure, unit span and reference chord
$C_{Dt}$	total drag coefficient	
$C_{Dw}$	wake drag coefficient	
$C_f$	friction drag coefficient	
$C_{wk}$	$= \frac{W_k}{\rho_{\infty} g U_{\infty} b_k c}$	= suction weight flow coefficient of $k^{\text{th}}$ suction chamber
$C_{wt}$	$= \sum C_{wk}$	= total suction coefficient
$M$	Mach number	
$p$	static pressure	
$q$	dynamic pressure	



(B) Notation (Continued)

R	Reynolds number
$R_c$	$= \frac{U_\infty c}{\nu_\infty}$ = reference Reynolds number
u	velocity inside boundary layer
U	potential flow velocity
$W_k$	suction weight flow through $k^{th}$ chamber
x	coordinate along plate
y	coordinate perpendicular to plate
$\mu$	viscosity
$\nu$	$= \frac{\mu}{\rho}$ kinematic viscosity
$\rho$	density

Subscripts

c	chordwise station c
k	running parameter, $k = 1, \dots, 8$
x	chordwise station x
o	stagnation
$\infty$	freestream
1	condition ahead of shock wave
2	condition aft of shock wave

(C) Introduction

Laminar flow and low drag coefficients were obtained at supersonic speeds and high length Reynolds numbers by means of boundary layer suction. The experiments conducted thus far (e.g., Chapter A-a of this section) were restricted to surfaces which were free of impinging shock waves. On an actual airplane cruising at supersonic speeds, shock waves originating from the fuselage or nacelles can intersect the wing. Therefore, the problem has to be investigated whether laminar flow can be maintained in the presence of interfering shock waves.

(C) Introduction (Continued)

The two-dimensional problem of the interaction of an oblique shock wave with a laminar boundary layer has been investigated frequently. A summary of the experimental and theoretical results is included in Reference 19. At a certain pressure ratio, the shock wave causes separation of the laminar boundary layer near the impingement point, but the boundary layer remains laminar. At higher pressure ratios, the boundary layer becomes turbulent after re-attachment. One experimental study has been conducted in the presence of boundary layer suction through fine slots (Reference 18, also described in Reference 19). Boundary layer suction delays the beginning of separation to higher shock intensities, reduces the size of the separation area, and delays the beginning of turbulent re-attachment to stronger shocks. The results of these tests can briefly be summarized as follows (page 1204 of Reference 19). The tests were conducted on a flat plate model at  $M = 2.0$ , the Reynolds number at the impingement point was  $0.5 \times 10^6$ , and the following pressure ratios were measured through the shock:

	No Suction	With Suction
Beginning of boundary layer separation	1.20	1.62
Beginning of turbulent re-attachment	1.45	1.66

The first boundary layer suction experiments involving a three-dimensional shock wave interaction are described in the following report.

(D) Description of the Test Configuration and Objective of the Test Program

The present shock interaction experiments were conducted on the flat plate suction model which had been used previously for low drag and suction measurements at AEDC Tunnel A (Chapter A-a of this section). The impinging shock wave was provided by a small flat plate (shock generator) mounted vertically on the model. A sketch of the configuration is shown in Figure 26, photographs of the model installation in the wind tunnel are presented in Figures 27 and 28. The angle of attack of the shock generator was adjustable from outside while the tunnel was in operation. The location and size of the shock generator were determined by the requirements that the movable boundary layer rake in its most forward position had to be ahead of the shock wave and constant flow conditions had to exist to the rear end of the suction area.

The shock wave intersected the suction slots under an angle, the last four suction chambers were affected by this interference and, therefore, had non-uniform inflow (Figure 29). Since the suction quantities are proportional to the pressure difference between external surface and suction chamber, more air was sucked through the portion of the slots aft of the shock wave than ahead of it.

One alternative configuration was investigated for the following reason: since the shock generator was mounted outside the suction area, it was actually standing in turbulent air. The shock wave near the model surface was, therefore, passing through the thick turbulent boundary layer before it reached the laminar flow inside the suction area. In order to investigate the

(D) Description of the Test Configuration and Objective of the Test Program (Continued)

the possibility, whether the test results were affected by this discontinuity in the path of the shock wave, the shock generator was mounted inside the suction area at a fixed angle of  $\alpha = 1.88^\circ$ . The exact locations of the shock generator and shock waves at several Mach numbers are shown in Figures 30 and 31 for the two configurations selected.

The present test setup was selected to provide experimental evidence on the following questions: (1) how much increase in suction quantities is required and what are the drag penalties in order to maintain laminar flow through weak shock waves; (2) what are the maximum shock intensities which can be tolerated without losing laminar flow. The tests were conducted at Mach numbers between 2.5 and 3.5 and length Reynolds numbers up to  $25 \times 10^6$ . It is important to emphasize that the suction system was the same as had been used for the shock-free drag measurements and had not been modified for the particular conditions of the present program.

(E) Presentation of Test Results

The tests were conducted at AEDC Tunnel A in April 1962 with S. R. Pate as project engineer (Reference 106). The tests with the adjustable shock generator were conducted in the following way. Laminar flow was established at a given Mach and Reynolds number with the shock generator at zero degree and the rake in its most rearward position ( $x = 40.2$  inches) by means of moderate suction (slightly higher than optimum suction). Then the shock generator was turned to a small angle of attack. If laminar flow was lost, suction was increased to re-establish laminar flow. Finally, a shock generator angle was obtained where laminar flow could not be provided anymore in spite of high suction.

With the shock generator mounted in the fixed position inside the suction area, laminar flow was established ahead of the shock wave (station  $x = 23.7$  inches) and then the rake moved aft. When laminar flow was lost, suction was increased. Because of the large number of parameters involved, it was not possible to record several suction distributions for each configuration in order to determine the minimum total drag and optimum total suction coefficients. It was tried during the tests that each suction distribution adjusted was close to its optimum.

The shock intensity was determined in two ways. Since the shock generator deflection was known, the pressure rise could be established from the theoretical shock relations (Figure 32). A few static pressure orifices in the rear half of the model provided immediately the measured pressure rise. If  $p_1$  is the static pressure on the model ahead of the shock wave,  $p_2$  the value aft of it, and  $p_\infty$  the static pressure of the undisturbed freestream, then the accuracy of the pressure measurements can be seen from the following table.

(E) Presentation of Test Results (Continued)

	$M_\infty$	2.489	2.989	3.50
Adjustable shock generator mounted outside suction area	$\frac{p_1}{p_\infty}$	$\begin{cases} 1.016 \pm .020 \\ 1.009 \pm .009 \end{cases}$	$\begin{cases} 1.039 \pm .015 \\ 1.003 \pm .013 \end{cases}$	$1.015 \pm .010$
Fixed shock generator mounted inside suction area	$\frac{p_1}{p_\infty}$	$1.046 \pm .020$	$\begin{cases} 1.088 \pm .030 \\ 1.059 \pm .020 \\ 1.028 \pm .010 \end{cases}$	$1.008 \pm .010$
Both shock generator installations	$\left(\frac{p_2}{p_1}\right)_{\text{exp}} - \left(\frac{p_2}{p_1}\right)_{\text{theor}}$	-.01	+.02	-.01

The different readings of  $p_1/p_\infty$  in the table were established during different runs of the tunnel. The higher pressure ratios of  $p_1/p_\infty$  (ahead of the shock wave) with the shock generator installed inside the suction area at  $M = 2.5$  and  $3.0$  cannot be explained. The difference between the theoretical and experimental values of the pressure ratio through the shock might have been caused by small zero-shifts of the shock generator.

The drag and suction coefficients are reduced in the usual form. They are referred to undistributed freestream conditions and the chordwise distance of the rake,  $x_{\text{rake}}$ . The total drag is defined as the sum of rake and suction drag,

$$C_{D_t} = C_{D_w} + C_{D_s}$$

The test results are presented as curves of  $C_{D_t}$  and  $C_{w_t}$  vs shock intensity,  $p_2/p_1$ , for fixed Mach and Reynolds numbers and the rake in its most rearward position,  $x_{\text{rake}} = 40.2$  inches (Figures 33 to 38). The test points represent the data obtained with the adjustable shock generator mounted outside the suction area and include the one test point of the fixed shock generator installed inside the suction area. The values at  $p_2/p_1 = 1.00$  are the minimum total drag and optimum total suction coefficients obtained in shock-free laminar flow (Chapter A-a of this section). Figures 39 to 42 present plots of  $C_{D_t}$  and  $C_{w_t}$  vs chordwise distance,  $x_{\text{rake}}/c$ , for given Mach and Reynolds numbers. The data for the fixed shock generator at  $\alpha = 1.88^\circ$  are compared with those for the adjustable shock generator at an angle  $\alpha = 2.0^\circ$ . The location where the shock wave intersected the center of the suction area (rake location) is marked on the graphs. The curves ahead of the shock location were faired into the values of the minimum drag and optimum suction coefficients of the shock free tests.

(F) Discussion of Test Results

The test data presented in Figures 33 to 38 show an increase of the total drag and suction coefficients with increasing shock intensity. The effects of Mach and Reynolds numbers on these data can be observed by plotting

(F) Discussion of Test Results (Continued)

the drag rise,  $\frac{C_{D_t}}{(C_{D_t})_{\min}}$ , and the suction increase,  $\frac{C_{W_t}}{(C_{W_t})_{\text{opt}}}$ , versus shock

intensity,  $p_2/p_1$ , for the Mach numbers 2.5 and 3.0 and the different Reynolds numbers (Figure 43). At both Mach numbers, an increase in Reynolds number caused higher drag increases at approximately the same suction quantities, only at  $M = 3.0$  the two high Reynolds number tests provided nearly identical results. The test results at  $M = 3.0$  were more favorable than at  $M = 2.5$ , laminar flow was maintained at higher shock intensities and lower drag and suction penalties at  $M = 3.0$  than at  $M = 2.5$ . Typical numerical values are as follows: at  $M = 2.5$

and  $R = 19.9 \times 10^6$ , an increase in suction of 60 percent and in drag of 25 percent was required to maintain laminar flow behind a shock wave of a pressure ratio  $p_2/p_1 = 1.08$ , corresponding to a two-dimensional corner angle of  $\alpha = 1.15^\circ$ .

At  $M = 3.0$  and  $R = 19.0$  or  $26.4 \times 10^6$ , an increase in suction of 40 percent and in drag of 20 percent was required in the presence of a shock wave of pressure ratio 1.13, or two-dimensional corner angle of  $\alpha = 1.60^\circ$ . At  $M = 3.0$ ,

$R = 11.0 \times 10^6$  and the same pressure ratio and suction increase, the drag penalty was only 10 percent. The test data at  $M = 3.5$  (Figure 38) were not included in this analysis since not enough air could be sucked through the model at this Mach number; the maximum suction quantities available were only 15 percent higher than the optimum suction coefficients in shock-free flow.

The higher suction requirements and drag penalties at  $M = 2.5$  are caused, to a certain extent, by the present test configuration. Figure 30 shows that the shock wave at  $M = 2.5$  is about 3.5 inches ahead of the shock at  $M = 3.0$ , so that a larger portion of the suction area is exposed to the shock disturbance at  $M = 2.5$  than at  $M = 3.0$ . If the comparison between the two Mach numbers is conducted at the same chordwise distance from the shock intersection, then the data at  $M = 3.0$  and  $x/c = 1.00$  have to be compared with those at  $M = 2.5$  and  $x/c = 0.91$ . Figures 39 and 40 show a considerable reduction of the drag and suction coefficients at the more forward station.

The shock generator installed inside the suction area produced higher drag coefficients than the one installed outside the slotted area (Figures 33 to 38). If expressed in shock intensities, the same drag coefficients were measured at slightly lower shock intensities; the difference in  $p_2/p_1$  was approximately of the order 0.02. Figures 39 to 42 also show consistently higher drag data for the shock generator inside the suction area at about the same total suction coefficients as for the shock generator mounted outside.

The four test points at  $M = 3.0$ ,  $R_x = 26.4 \times 10^6$ ,  $x = 40.2$  inches (Figure 37) which were recorded at the shock generator angles  $\alpha = 0, 1.0, 1.5$  and  $2.0^\circ$  were selected to show the change in the chordwise variation of the suction distribution with increasing shock intensity. The local suction inflow coefficients

$$f_o^* = \frac{\rho_w v_o}{\rho_\infty U_\infty} \sqrt{R_x}$$

#### (F) Discussion of Test Results (Continued)

(Figure 44) in the area of the shock impingement and immediately ahead of it (chambers 4 to 7) were increased up to a factor 2 at the higher shock generator angles, while the front portion of the model remained nearly unchanged. The maximum values of  $f_o^*$  in the last three chambers were the highest values which could be provided with the present suction arrangement.

The measured boundary layer velocity profiles at station 40.2 for these four test conditions are plotted in Figure 45. Thin laminar profiles were measured at  $\alpha = 0$  and  $1^\circ$ , the profile at  $\alpha = 1.5^\circ$  is still as thin as the laminar ones, the increase of the velocity near the wall indicates beginning transition, the profile at  $\alpha = 2^\circ$  is fully turbulent.

#### (G) Conclusions

A shock generator was installed vertically on a 41-inch chord flat plate suction model which was used previously for low-drag and suction measurements in shock-free flow. The shock wave intersected the suction slots in the rear half of the model. Laminar flow was maintained over the whole chord length of the model at increased suction and drag coefficients for certain shock intensities depending on Mach and Reynolds number.

At  $M = 3.0$  and length Reynolds numbers of  $19$  and  $26 \times 10^6$ , laminar flow was maintained through a shock wave of pressure ratio 1.13 (flow deflection angle  $\alpha = 1.6^\circ$ ) by increasing the suction by 40 percent beyond the optimum suction coefficient in shock free flow which resulted in an increase of the total drag coefficient by 20 percent beyond its minimum value. The same shock wave at  $R = 11 \times 10^6$  caused only a 10 percent drag rise.

At  $M = 2.5$  and  $R = 20 \times 10^6$ , full chord laminar flow was maintained at a shock intensity of  $p_2/p_1 = 1.08$  (deflection angle  $1.15^\circ$ ) by increasing suction by 60 percent which provided a 25 percent increase of the total drag.

These results were obtained with the slot arrangement designed for shock-free flow. It is expected that an increase of the local suction quantities in the immediate vicinity of the location of the shock wave would produce more favorable results.

CHAPTER B. LOW DRAG BOUNDARY LAYER SUCTION EXPERIMENTS AT SUPERSONIC SPEEDS  
ON AN OGIVE CYLINDER WITH 29 CLOSELY SPACED SLOTS

E. E. Groth

(A) Acknowledgement

The work reported herein was accomplished under the direction of Dr. W. Pfenninger, Director of the Norair Boundary Layer Research Group. The model was designed by S. Smith and built by W. Wilkinson. J. Ryan participated in the design calculations and the wind tunnel tests, and he deserves credit for most of the data analysis, all calculations on the IBM 7090 machine, and the final plots for the report.

Special acknowledgement goes to W. Strike and the personnel of Tunnel E-1 at ARO, Inc., for their continuous effort in executing the tests and the basic data reductions.

(B) Summary

Low drag boundary layer suction experiments on an ogive cylinder were conducted at the Arnold Engineering Development Center supersonic Tunnel E-1 at Tullahoma, Tennessee, at Mach numbers 2.5, 3.0 and 3.5. The model had the same external dimensions as the one tested in 1958, but was equipped with an improved suction system. A larger number of closely spaced slots approached continuous suction to a better degree, and larger suction tubes permitted higher suction coefficients. Full laminar flow and drag coefficients were measured up to Reynolds numbers  $R_L \sim 15 \times 10^6$  at  $M = 2.5$ ,  $R_L \sim 12 \times 10^6$  at  $M = 3.0$  and  $R_L \sim 7 \times 10^6$  at  $M = 3.5$ .

The boundary layer development along the body was computed for several experimental suction and surface pressure distributions and the results were compared with the test data.

(C) Notation

- x coordinate along model axis
- x' arc length along model surface
- L = 18.8 inches; length of model, location of boundary layer rake
- y coordinate perpendicular to model axis
- r radius of model
- M Mach number
- U potential flow velocity
- u velocity inside boundary layer

(C) Notation (Continued)

p static pressure

$\rho$  density

T temperature

$\mu$  viscosity

$\nu$  kinematic viscosity

R Reynolds number

W suction weight flow (lb/s)

$C_W = \frac{W}{\rho_{\infty} g U_{\infty} A} = \text{suction weight flow coefficient}$

A wetted surface area ( $A = 144.0 \text{ in}^2$  for  $L = 18.8$  inches)

$C_{DW}$  wake drag coefficient

$C_{DS}$  suction drag coefficient

$C_{Dt}$  total drag coefficient

$C_f$  friction drag coefficient

} referred to freestream dynamic pressure and wetted surface

$\theta$  momentum thickness

$\delta^*$  displacement thickness

$H = \frac{\delta^*}{\theta} = \text{boundary layer form parameter}$

h height of roughness particle

Subscripts

o stagnation

$\infty$  freestream

L station  $x = L$

T Transition

w wall condition

l outer edge of boundary layer



(C) Notation (Continued)

- h height of roughness particle
- s suction chamber inside model
- b suction box
- n measuring nozzle
- k running parameter;  $k = 1, 2, 3, 4$

Other symbols are defined in the body of the report.

(D) Introduction

The low drag boundary layer suction experiments on an ogive cylinder which were conducted in 1958 at the Arnold Engineering Development Center Tunnel E-1 at ARO, Inc., Tullahoma, Tennessee, resulted in full length laminar flow over a rather limited range of length Reynolds numbers at Mach numbers 2.5, 3.0 and 3.5 (Reference 123). In order to investigate the effect of an improved suction system on the test results, a new model of the same geometric dimensions but equipped with more slots and larger suction tubes was built and tested in the same wind tunnel during February and March 1961.

(E) Description of the Model

The model was a 20-caliber ogive cylinder with a maximum diameter of 3.25 inches; the length of the ogive was 14.443 inches. It was built and mounted in the wind tunnel in the same way as described in Reference 123 for the old model tested in 1958. The only difference between the two models consisted in the suction system. Continuous suction was approached more efficiently on the new model by reducing the distance between consecutive slots. The new model had a total of twenty-nine slots located between stations 4.5 and 18.5 inches at a constant spacing of 0.5 inch and arranged in four suction chambers, compared to only twelve slots between stations 5.0 and 18.0 at spacings varying between 1.4 and 1.0 inches for the old model. By eliminating unnecessary instrumentation lines, it was possible to increase the diameter of the suction tubes which removed the sucked air from the suction chambers so that the pressure loss of the sucked air was reduced and larger quantities could be sucked. The new model had tube diameters of 0.75 inch to station 29.5 inches and 1.00 inch aft of station 31.0 compared to diameters of 0.50 and 0.75 inch, respectively, for the old model.

The suction air from the four chambers was ducted to four suction boxes outside the tunnel where the suction quantities were adjusted manually and measured through calibrated nozzles.

A total head rake of seven probes was mounted aft of the last slot to measure the boundary velocity profile from which the wake drag was evaluated.

(E) Description of the Model (Continued)

A sketch of the model and a photograph of the model mounted in the wind tunnel are shown in Figures 46 and 47. Some of the slot dimensions are listed in Table III.

(F) Measurements and Data Reduction

The tests were conducted at the AEDC Tunnel E-1 of the von Karman Gas Dynamics Facility of ARO, Inc., Tullahoma, Tennessee, with W. T. Strike as project engineer. The tunnel could be operated continuously over long periods of time (about ten minutes at  $M \approx 2.5$  and about one hour at  $M \approx 3.5$ ) by removing the tunnel air from the vacuum sphere during the tunnel operation. Because of these long running times, it was possible to cover a wide range of suction distributions at a given Reynolds and Mach number and to adjust the distributions according to the observed status of the boundary layer at the rake location.

The measured pressures and temperatures were recorded on tape from which nondimensional coefficients were computed on an automatic computing machine. Shadowgraph pictures were taken during most of the tests.

The equations for the data reduction which were described in detail in Reference 123 are summarized as follows (most of the symbols are defined in the Notation section).

The suction coefficient for the  $k^{\text{th}}$  chamber is determined by

$$C_{Wk} = \frac{W_k}{\rho_{\infty} g U_{\infty} A} = \alpha_k \frac{M_{nk} (1 + .2 M_{\infty}^2)^3 \frac{\pi}{4} d_k^2 p_{bk} \sqrt{\frac{T_o}{T_{bk}}}}{M_{\infty} (1 + .2 M_{nk}^2)^3 A p_o}$$

where  $M_{nk}$  is the Mach number inside the metering nozzle of diameter  $d_k$  and defined by the suction box pressure  $p_{bk}$  and nozzle pressure  $p_{nk}$

$$M_{nk} = \sqrt{5 \left[ \left( \frac{p_{bk}}{p_{nk}} \right)^{.286} - 1 \right]};$$

$A = 144 \text{ in}^2$  is the total wetted area of the model up to station 18.8 inches;  $\alpha_k$  is a nozzle calibration factor depending on the nozzle Reynolds number.

The suction drag coefficient is given by

$$C_{Ds} = \frac{D_s}{q_{\infty} A} = \sum_{k=1}^4 C_{Wk} \left( 1 + \frac{M_{sk}^2 T_{sk}}{M_{\infty}^2 T_{\infty}} \right)$$

where  $M_{sk}^2$  is determined by the pressure in the suction chamber  $p_{sk}$ ,

$$M_{sk}^2 = 5 \left[ \left( \frac{p_{\infty}}{p_{sk}} \right)^{.286} - 1 \right]$$

(F) Measurements and Data Reduction (Continued)

The boundary layer velocity profile at the rake location is computed from the measured total head pressures under the assumption of constant static pressure and total temperature in the boundary layer and zero heat transfer between flow and surface.\* The wake drag is given by

$$C_{D_w} = \frac{2 \pi d_L}{A} \theta_L \left( \frac{U_L}{U_\infty} \right)^{H+2-M^2}$$

where the momentum thickness at the rake location is

$$\theta_L = \int_0^\delta \frac{\rho u}{\rho_L U_L} \left( 1 - \frac{u}{U_L} \right) \left( 1 + \frac{y}{r_L} \right) dy$$

and

$$H+2-M^2 = 3.145 - .28 M_L^2 - .30 M_\infty^2$$

The total drag is defined as the sum of wake and suction drag:

$$C_{D_t} = C_{D_w} + C_{D_s}$$

(G) Results of the Drag and Suction Measurements

(1) Test Results of the Present Model

The results of the drag and suction measurements are presented in Figures 48 to 53. The variation of wake, suction, and total drag with total suction coefficient for given Reynolds numbers is shown in Figures 48, 50 and 52 for the three Mach numbers, 2.5, 3.0 and 3.5. The optimum suction quantities and minimum total drag coefficients are plotted versus Reynolds number in Figures 49, 51 and 53 for the three Mach numbers. Included in these figures are the drag coefficients of the nonsuction configuration with the slots sealed and the friction coefficients of the laminar and turbulent plate. Typical boundary layer velocity profiles at the rake location are shown in Figure 54 for  $M = 3.5$ ,  $R_L = 4.85 \times 10^6$  and several suction coefficients.

The measurements  $M = 2.5$  showed that low drag coefficients could be maintained for length Reynolds numbers of the order of  $15 \times 10^6$ . Increased suction quantities were required for Reynolds numbers

\*The error introduced by the assumption of constant total temperature was checked for one of the numerical examples reported in Chapter (I). The exact momentum thickness or wake drag coefficient was found to be smaller by 0.5 percent than the corresponding approximate value. The assumption of constant static pressure will be discussed in Chapter (H).

(G) Results of the Drag and Suction Measurements (Continued)

between  $15$  and  $17 \times 10^6$  to keep the boundary layer laminar over the whole body in spite of the increasing level of external disturbances. Full laminar flow could not be maintained beyond  $R_L = 17 \times 10^6$  although ample suction air was available. Apparently, at these high numbers, which correspond to unit Reynolds numbers of more than  $10 \times 10^6$  per foot, model roughness and tunnel noise became critical. Shadowgraph pictures showed that minor roughness spots caused by sandblasting effects on the tunnel air caused premature transition on one side of the model while the other side remained unaffected. The already high level of tunnel noise was amplified occasionally by oscillations of the shock wave at the end of the test section.

At  $M = 3.0$ , full laminar flow and low drag coefficients were maintained until  $R_L \sim 12 \times 10^6$ . A thin laminar profile was observed once at  $R_L = 12.8 \times 10^6$ , but the sudden increase in tunnel noise due to vibrations of the opening valve of the tunnel caused an immediate transition to turbulent flow before the data were recorded. For unit Reynolds numbers beyond  $8 \times 10^6$  per foot the external disturbances were too large to keep the boundary layer laminar in spite of high suction quantities available.

The tests at  $M = 3.5$  provided laminar flow over the whole model up to length Reynolds numbers of the order of  $7 \times 10^6$ . The measurements at  $R_L = 7.8 \times 10^6$  indicated that transition moved forward because of insufficient suction. Since the model was designed for a Mach number of 3.0, the slot widths and holes underneath the slots were too narrow for the relatively large volumes of low density suction air at the higher Mach numbers. An extrapolation of the curve  $(C_{Wt})_{opt}$  versus  $R_L$  in Figure 53 shows that a total suction coefficient of  $\sim 2.3 \times 10^{-4}$  would be required at  $R_L = 7.8 \times 10^6$ , but the largest amount available was only  $1.9 \times 10^{-4}$ .

The minimum total drag and optimum suction coefficients from Figures 49, 51 and 53 are combined in Figure 55 to present a clearer picture of the variation of the coefficients with Mach number. The lowest drag coefficients and corresponding Reynolds numbers are compared in the following table with the laminar and turbulent friction coefficients at the same Mach and Reynolds numbers.

Freestream Mach Number	Length Reynolds Number	Total Drag Coefficient	Friction Coefficients of	
			Laminar Plate	Turbulent Plate
$M_\infty$	$10^{-6} R_L$	$10^4 C_{Dt}$	$10^4 C_f$	$10^4 C_f$
2.5	14	4.9	3.3	19.9
3.0	11	5.6	3.7	18.3
3.5	7	7.6	4.5	17.6

The drag of the suction body is 1.5 times the friction drag of a laminar plate at  $M = 2.5$  and 3.0, and 1.7 times greater at  $M = 3.5$ . The turbulent friction drag is 4.0 times larger at  $M = 2.5$ , 3.3 times larger at  $M = 3.0$

and 2.3 times larger at  $M = 3.5$  than the drag of the suction body. The reduction of the ratio of the turbulent plate drag to the drag of the suction body with increasing Mach number is due to the reduction of the turbulent friction drag with Mach number.

The suction quantities required to provide the minimum drag coefficients are included in Figure 55. They show a steep rise with Mach number at a given length Reynolds number. One reason for this variation with Mach number is the forward shift of transition without suction with increasing Mach numbers. Figures 56, 57 and 58 present all the information available about boundary layer transition. The test points are marked where the boundary layer stayed laminar to the rake station either without or with suction. The highest test points from the previous measurements (Reference 123) are included for comparison. Shadowgraph pictures of the area between stations 6.5 and 14.8 inches were taken for most of the test points. As an example, transition occurred at a unit Reynolds number of  $0.5 \times 10^6$  per inch at the following stations:

$M_\infty$	$x_T$ (in.)	$R_T = \frac{U_\infty x_T^*}{\nu_\infty}$
2.5	12.8	$6.4 \times 10^6$
3.0	9.8	$4.9 \times 10^6$
3.5	8.6	$4.3 \times 10^6$

The optimum suction coefficients of Figure 55 and the natural transition Reynolds numbers without suction of Figures 56, 57 and 58 are replotted in Figure 59 versus length Reynolds number, from which Figure 60 is derived. Figure 60 presents the suction quantities required for maintaining laminar flow to station 18.8 inches at minimum total drag as a function of the location of natural transition without suction (station  $x_T$ ). The  $x_T$  scale is plotted backward so that the abscissa represents the chordwise distance by which the range of laminar flow has to be extended. In this presentation the curves for  $M = 2.5$  and  $3.0$  nearly coincide, which can be interpreted in the form that the increase in suction requirements between  $M = 2.5$  and  $3.0$  is caused by the change in natural boundary layer transition between these Mach numbers. But this effect is not sufficient to explain the further increase in suction at  $M = 3.5$ , where about 40 percent more suction is required than for  $M = 2.5$  and  $3.0$ . Figure 60 also emphasizes the steep increase of suction because of excessive external disturbances. This occurs for  $M = 2.5$  and  $3.0$  at Reynolds numbers which provide boundary layer transition without suction at  $x_T \sim 9$  inches.

## (2) Effect of the Different Suction Systems of the Old and New Models on the Test Results

The difference in the suction systems of the two models consisted of two items: (1) continuous suction was approached to a better

\*The local unit Reynolds number,  $U_1/\nu_1$ , deviates from the freestream value,  $U_\infty/\nu_\infty$ , by less than  $\pm 5$  percent between stations  $x = 10$  and  $19$  inches for the three Mach numbers.

(G) Results of the Drag and Suction Measurements (Continued)

degree on the new model (slot spacing 0.5 inch) than on the old one (slot spacing 1.4 to 1.0 inches); (2) the maximum suction quantities which could be sucked through the model were larger on the new one because of larger cross sections of the suction tubes.

The effects of these differences in the suction system on the test results are presented in the following table:

Freestream Mach Number	Maximum Total Suction Coefficient, $10^4 C_{Wt}$ , Available		Maximum Length Reynolds Number with Full Laminar Flow, $10^{-6} R_L^*$	
	Old Model	New Model	Old Model	New Model
$M_\infty$				
2.5	1.6	4.2	10.6	15.3
3.0	1.2	3.1	7.0	11.5
3.5	.8	2.0	4.7	6.3

The improvement in maximum length Reynolds number at  $M = 3.5$  is caused primarily by the increase in total suction quantities. The Reynolds number level at this Mach number appears too low for external disturbances to become critical so that slot spacing is not yet important. A comparison between corresponding test points from the two models shows good agreement:

( $M_\infty = 3.5$ )	$10^{-6} R_L$	$10^4 C_{Wt}$	$10^4 C_{Ds}$	$10^4 C_{Dw}$	$10^4 C_{Dt}$
Old Model	4.44	.771	.92	7.35	8.27
New Model	4.82	.832	.89	7.18	8.07

The slightly larger slot widths and hole sizes on the new model are responsible for the reduction in suction drag.

A different situation exists for  $M_\infty = 3.0$ . At  $R_L = 6.8 \times 10^6$  the old model had just enough suction to approach minimum drag; the high wake drag at  $R_L = 8.0 \times 10^6$  indicated that transition had moved forward. The present tests show that the same suction quantities are sufficient to maintain full laminar flow at this Reynolds number so that the improvement is probably due to the narrower slot spacings. The extension of the laminar range beyond  $R_L = 8 \times 10^6$  is primarily due to the higher suction quantities available. A comparison of corresponding old and new points is shown on the following page.

\*Defined at the length Reynolds number where total drag coefficient exceeds the nonsuction laminar flow value by 15 percent (same definition as in Reference 123).

(G) Results of the Drag and Suction Measurements (Continued)

$(M_\infty = 3.0)$	$10^{-6} R_L$	$10^4 C_{Wt}$	$10^4 C_{Ds}$	$10^4 C_{Dw}$	$10^4 C_{Dt}$
Old Model	{ 6.83 7.98	1.232 1.205	1.51 1.51	5.34 7.39	6.85 8.90
New Model	7.71	1.227	1.32	5.13	6.45

The favorable effect of the narrower slot spacing is even more pronounced at  $M = 2.5$ , where higher suction at a lower Reynolds number produced a higher wake drag on the old model than the lower suction at a higher Reynolds number on the new model, as is shown in the following comparison:

$(M_\infty = 2.5)$	$10^{-6} R_L$	$10^4 C_{Wt}$	$10^4 C_{Ds}$	$10^4 C_{Dw}$	$10^4 C_{Dt}$
Old Model	12.10	1.584	2.13	4.90	7.03
New Model	13.24	1.335	1.39	3.83	5.22

With the total suction available for the old model, laminar flow could have been maintained up to  $R_L \sim 13 \times 10^6$  if a better approach to continuous suction had been provided. The increase in Reynolds number range beyond this value required higher total suction coefficients.

The requirement of the narrow slot spacing for producing high length Reynolds numbers with full laminar flow might be partly due to the high level of external disturbances of this wind tunnel. According to a communication by the author with Mr. C. J. Schueler of ARO, Inc., transition measurements on a hollow cylinder provided about 25 percent higher transition Reynolds numbers in the continuous Tunnel A than in Tunnel E-1. He also mentioned that sound measurements in the stilling chamber of Tunnel E-1 had indicated a high noise level caused by the high speed jet flow from the control valve. The total sound power output was of the order of 2000 watts/ft<sup>2</sup>, corresponding to pressure fluctuations of the order of 9 lb/ft<sup>2</sup> or 147 db. This high sound level at unit Reynolds numbers of the order of  $10 \times 10^6$  per foot represents really severe test conditions for maintaining laminar flow.

(H) Flow Field Near Last Slot

The total head readings of the boundary layer rake provide some information about the flow field and the shock wave originating at the last slot. A typical plot of the variation of the total pressure,  $p_{rake}$  (uncorrected for the pressure loss due to the shock wave from the probe tip), perpendicular to the model surface is shown in Figure 61 for  $M = 2.5$ ,  $R_L = 15.8 \times 10^6$ , station 18.81 inches. The outer edge of the boundary layer is reached at the maximum value of  $p_{rake}$ . This value  $(p_{rake}/p_o)_{max}$  determines a Mach number  $M_{ref}$  by means of the standard charts for normal shocks. It is assumed that the static pressure defined by  $M_{ref}$  is constant throughout the

(H) Flow Field Near Last Slot (Continued)

boundary layer. The variation of  $p_{\text{rake}}/p_o$  outside the boundary layer is interpreted as a variation of the local Mach number in the potential flow. The Mach number distribution corresponding to  $p_{\text{rake}}/p_o$  is also included in Figure 61. Under the assumption of constant static pressure (or local Mach numbers) along Mach lines, the Mach number variation along the y axis can be plotted along the chordwise distance x. The discontinuity of  $p_{\text{rake}}/p_o$  between the heights 0.12 and 0.13 inch is caused by the shock wave from the last slot (located at station 18.5). A possible interference between the shock waves from the slot and the pressure probes is neglected. Since the local Mach number at station 18.25 is known from the static pressure orifice, the variation of the local Mach number along the outer edge of the boundary layer can be plotted between station 18.25 and the rake bottom as is shown for three examples in Figures 62, 63 and 64. Figure 62 was developed from the data presented in Figure 61. The reduction of the local Mach number variation due to a reduction in suction quantities is shown in Figure 63. The suction coefficient at the last slot is approximately one-seventh of the value for the fourth suction chamber. Figure 64 presents the data obtained at two rake locations under identical test conditions. The rake was moved aft for the tests at  $M_\infty = 3.5$  to eliminate the interference with the shock wave from the last slot.

The few test points available restrict the accuracy of the curves. The actual thickness of the boundary layer depends on the way the curve is faired through the few rake total head readings, and the exact height of the probes above the surface is not known with sufficient accuracy. The shock lines at the bottom of Figures 62 to 64 were developed in such a way that the chordwise location of the steep decrease of the local Mach number coincides with the point where the shock wave penetrates the outer edge of the boundary layer. The direction of the shock wave was assumed to be slightly steeper than the local Mach line. The shock waves plotted in Figures 63 and 64 can be extrapolated to the slot, but the shock at  $M = 2.5$  (Figure 62) apparently is displaced by about 0.02 inch.

The three example cases are in qualitative agreement with the results of a detailed flow field survey reported in Reference 107, where it was discussed that the assumption of a constant static pressure inside the boundary layer might not be accurate enough in regions where noticeable chordwise gradients of the external static pressure occur within distances equal to a few boundary layer thicknesses. The rather steep change of the local Mach number near the outer edge of the boundary layer ( $M = 2.502$  at chordwise station 18.81 or  $y = .032$  inch above the surface and  $M = 2.523$  at station 18.77 or  $y = 0.50$  inch, as shown in Figures 61 and 62) might represent a typical case where a variation of the static pressure inside the boundary layer has to be considered.

The evaluation of the boundary layer velocity profile at the rake location was set up originally in the form that the surface pressure at station 18.25 was used for determining the reference Mach number. The above examples show that the shock wave from the last slot can change the actual value of the reference Mach number at the rake location so much that the accuracy of the drag evaluation would be affected. All wake drag coefficients published in this report have been evaluated with the correct value of the referenced Mach number at the rake location.



# (I) Comparison of Experimental Results with Theory

The development of the laminar boundary layer over the ogive cylinder was computed on the IBM 7090 machine by means of an exact theory (Reference 45) for the following three cases:

$M_\infty$	$10^{-6} R_L$	$10^4 C_{Wt}$	$10^4 C_{Ds}$	$10^4 C_{Dw}$	$10^4 C_{Dt}$
2.5	13.24	1.335	1.389	3.832	5.221
3.0	11.36	1.642	1.811	3.844	5.655
3.5	4.85	1.454	1.667	6.143	7.810

The calculation was performed under the following conditions: the measured freestream reference values and measured surface pressure distributions were used; the model surface was assumed to be at adiabatic wall

temperature,  $(\frac{\partial T}{\partial y})_y = 0$ , without heat conduction or radiation.

A continuous suction distribution was developed in such a way that the integrated values per chamber were equal to the measured suction coefficients. The distributions within a chamber were estimated from the measured pressure drop through the skin and the known slot and hole dimensions. Discontinuities in the slopes were admitted since they had no noticeable effect on the accuracy of the integration. An analytical expression for this continuous suction distribution is the quantity  $dC_W/dx$  defined by

$$\frac{dC_W}{dx} = \frac{\rho_w v_o}{\rho_\infty U_\infty} \frac{2\pi r}{A}$$

where  $v_o$  is the local inflow velocity and  $r$  the body radius at station  $x$ .

$\frac{dC_W}{dx}$  has the dimension  $(\text{inch})^{-1}$ . Since the slot spacing is 0.5 inch, the term

$$C_W = \frac{1}{2} \frac{dC_W}{dx}$$

represents approximately the suction coefficient for a single slot.

The surface pressure and suction distributions for the three examples are shown in Figures 65, 66 and 67. Since the boundary layer is computed along the arc length,  $x'$ , of the body, the data are plotted versus  $x'$  instead of the chord length  $x$  along the axis. In the cylindrical section,  $x' = x + 0.12$  (in.).

The Reynolds number based on momentum thickness,  $R_\theta = \frac{\theta U_1}{\nu_1}$ ,

divided by the square root of the length Reynolds number is plotted versus  $x'$

in Figure 68 for the three examples. The variation of  $\frac{R_\theta}{\sqrt{R_L}}$  versus  $x'$  can be

(I) Comparison of Experimental Results with Theory (Continued)

related to the local suction distribution in the sense that high suction produces rather small increases of  $R_\theta$  and vice versa. The value of  $R_\theta$  at the rear end of the body and the wake drag coefficient  $C_{Dw}$  can be compared with the experimental values evaluated from the measured rake profile. The results are listed in the following table:

$M_\infty$	Rake Location $x'$ (In.)	$\left(\frac{R_\theta}{\sqrt{R_L}}\right)_{\text{theor}}$	$(R_\theta)_{\text{theor}}$	$(10^4 C_{Dw})_{\text{theor}}$	$(R_\theta)_{\text{exp}}$	$(10^4 C_{Dw})_{\text{exp}}$
2.5	18.93	.3953	1448	2.928	1840	3.832
3.0	18.93	.4043	1362	3.268	1602	3.844
3.5	19.21	.4357	959	5.252	1170	6.143

The experimental  $R_\theta$  values and wake drag coefficients are about 22 percent higher than the corresponding theoretical data.

The boundary layer velocity profiles at the rake location are compared in Figure 69. The theoretical and experimental values of the total boundary layer thickness are listed below (because of the asymptotic behavior of the boundary layer the value of  $\delta$  is defined as the height for  $u/U = .99$ ).

$M_\infty$	$\delta_{\text{theor}}$	$\delta_{\text{exp}}$
2.5	.026	.032
3.0	.033	.040
3.5	.064	.066

The experiments provide higher velocities near the wall and lower velocities near the outer edge than the theory predicts. The experimental boundary layer thickness is about 22 percent thicker than the theoretical one at  $M = 2.5$  and  $3.0$ ; good agreement exists at  $M_\infty = 3.5$ .

The discrepancy between theory and experiment is rather high and cannot be explained without a more refined analysis. The assumption of continuous suction for the theoretical calculation instead of suction through individual slots might be a severe simplification in supersonic flow, since it neglects the variation of the external pressure field caused by the shock waves from the individual suction slots. As a consequence, the assumption of constant static pressure through the boundary layer may no longer be justified. Also, the external disturbances in the wind tunnel, particularly the noise field, might contribute to a deformation of the laminar boundary layer profile and require higher suction quantities to maintain its stability.\*

\*Oscillations in the laminar boundary layer can be amplified rapidly when certain frequencies of the external disturbances coincide with critical frequencies of the laminar boundary layer, as was shown in Reference 96.

(I) Comparison of Experimental Results with Theory (Continued)

The computed wall temperatures and recovery factors,

$$r = \frac{T_w - T_1}{T_0 - T_1} = \frac{\frac{T_w}{T_1} - 1}{.2 M_1^2}$$

are plotted in Figures 70a, 70b and 70c for the three cases. The theoretical wall temperature varies by less than  $\pm 5^\circ\text{F}$ , which indicates that the assumption of an insulated body for the boundary layer calculations is sufficiently accurate. The recovery factor grows from its value  $r \sim .86$  in the front part of the model (no suction) to  $r \sim .90$  near the rear end of the model. It is also known from other calculations that the recovery factor in laminar flow in the presence of suction can exceed the value of .90.

The computed velocity and temperature profiles permit a calculation of the height of the portion of the boundary layer which is sucked into a slot. The results of this calculation for one slot near the middle of each chamber are presented in the following table, together with the slot width of the model.

Station $x'$ (in.)	Thickness of Sucked Layer (in.)			Slot Width of Model (in.)
	$M = 2.5$	$M = 3.0$	$M = 3.5$	
6.0	.0016	.0021	.0026	.0035
10.0	.0013	.0022	.0030	.0040
13.1	.0016	.0025	.0043	.0070
16.0	.0025	.0025	.0049	.0070

The increase of the thickness of the sucked layer with increasing Mach number is quite pronounced. The actual slot widths have to be larger than the thickness of the sucked layer in supersonic wind tunnel experiments because of the large pressure losses of the low density air which might lead to early choking. There is no apparent danger of local separation effects inside the slots since the slot Reynolds numbers ( $R_s$ ) based on slot width and mean inflow velocity are extremely low, e.g.,  $R_s = 16$  to  $51$  at  $M = 2.5$ ,  $R_s = 12$  to  $40$  at  $M = 3.0$  and  $R_s = 7$  to  $9$  at  $M = 3.5$  for the above example cases. These values of  $R_s$  can be changed to other length Reynolds numbers by multiplying them with the ratio of the square root of the length Reynolds numbers ( $\frac{R_s}{\sqrt{R_L}}$  independent of  $R_L$ ).

(J) Effects of Surface Roughness

One single roughness particle, a .093-inch diameter disc of .0035-inch height, was placed at station 2.00 inches of the model and tested at  $M = 3.0$ . The shadowgraph pictures of the nonsuction configuration show that transition moved from  $x_T = 14$  inches to  $x_T = 12$  inches at  $R_L = 6.3 \times 10^6$ ,

(J) Effects of Surface Roughness (Continued)

but the boundary layer stayed laminar with suction (also, see Figure 57). At  $R_L = 7.6 \times 10^6$ , transition without suction moved from  $x_T = 12$  inches to  $x_T = 7.5$  inches due to roughness; with suction laminar flow could not be maintained; transition with roughness was at  $x_T = 9.0$  inches.

The boundary layer calculations permit the computation of the following roughness parameters: the roughness Reynolds number, defined as

$$R_h = \frac{h u(h)}{v(h)}$$

where velocity and kinematic viscosity are taken at the height  $h$  of the roughness particle; the ratio of the height of the particle to the displacement thickness  $\delta^*$ ; and the Mach number  $M_h$  at the height of the particle. The following table lists these values for the above test conditions at  $M_\infty = 3.0$  and  $h = .0035$ . Also included is the ratio of transition Reynolds number with roughness to its value without roughness for the nonsuction case.

$10^{-6}R_L$	$R_h$	$\frac{h}{\delta^*}$	$M_h$	$\frac{R_t}{R_{t0}}$
6.3	163	.57	.82	.85
7.6	232	.63	.90	.62
11.3	464	.76	1.13	- -

Reference 108 presents an evaluation of available roughness measurements in supersonic tunnels by plotting  $\sqrt{R_{h_{cr}}}$  versus  $M_h$  where the critical height,  $h_{cr}$ , is defined as the particle height which causes transition at a length Reynolds number which is 5 percent less than its value without roughness. Figure 18 of Reference 108 gives  $\sqrt{R_{h_{cr}}} \sim 16$  to 19 for  $M_h = .8$  to .9, compared with the value of about 12 for the nonsuction tests and of the wind tunnels and the different methods of computing the boundary layer profiles might explain the discrepancy. The increase in allowable roughness height in the front portion of the body ahead of the suction area due to suction is rather small.

Estimates of allowable roughness height can be obtained from the theoretical layer development by plotting the quantities  $M_h$  and

$\frac{R_h}{\sqrt{R_L}}$  versus  $\frac{h}{L} \sqrt{R_L}$ . In this form, all data are independent of length Reynolds

number. Since it was expected that model roughness might have become critical at the high unit Reynolds numbers at  $M = 2.5$ , the above roughness parameters are plotted at stations  $x = 1.0, 2.0$  and  $5.0$  inches in Figure 71. Assuming a value  $\sqrt{R_{h_{cr}}} = 13$  and  $R_L = 18 \times 10^6$  gives the following maximum roughness heights for the ogive cylinder body for the tests in Tunnel E-1:

(J) Effects of Surface Roughness (Continued)

<u>Station x (in.)</u>	<u>Critical Roughness Height (in.)</u>
1.0	.0011
2.0	.0014
5.0	.0017

Surface contamination of that order of magnitude must have occurred since laminar flow was lost occasionally at high Reynolds numbers and regained after the model had been polished.

Another possible roughness spot was station  $x = 1$  inch, where the nose cone of the model was attached to the remainder of the body. The above roughness analysis requires that the step at this joint has to be considerably less than .0011 inch, a condition which was hard to maintain during the tests since the nose cones had to be exchanged occasionally. It should be emphasized that these severe roughness requirements are caused by the fact that the tests were conducted at unit Reynolds numbers of the order of  $10 \times 10^6$  per foot.

(K) Conclusions

The boundary layer suction experiments on the ogive cylinder provided the following results:

(1) Low drag coefficients and full laminar flow were maintained at high length Reynolds numbers at Mach numbers 2.5, 3.0 and 3.5. Total drag coefficients of  $5.0 \times 10^{-4}$  were measured at  $R_L = 15 \times 10^6$  and  $M = 2.5$ ;  $C_{D_t} = 5.6 \times 10^{-4}$  at  $R_L = 11 \times 10^6$  and  $M = 3.0$ ;  $C_{D_t} = 7.6 \times 10^{-4}$  at  $R_L = 7 \times 10^6$  and  $M = 3.5$ . The total suction coefficients at these Reynolds and Mach numbers were close to  $2.0 \times 10^{-4}$ .

(2) At a given Reynolds number, the suction coefficients increased with Mach number. This effect could only partly be explained by the forward shift of transition without suction with increasing Mach number.

(3) Laminar flow was lost beyond  $17 \times 10^6$  at  $M = 2.5$  and  $13 \times 10^6$  at  $M = 3.0$  in spite of high suction due to the combined effects of external disturbances such as tunnel noise and turbulence as well as model roughness.

(4) A theoretical analysis of the boundary layer development along the body provided wake drag coefficients which are between 18 and 27 percent lower than the measured values and boundary layer velocity profiles, which are between 3 and 21 percent thinner than the measured ones. The largest discrepancies occurred at the high Reynolds number at  $M = 2.5$ , indicating an influence of the external disturbances on the test results.

## CHAPTER C. INVESTIGATIONS OF SWEEPED WINGS WITH SUPERSONIC LEADING EDGES

### a. LOW DRAG BOUNDARY LAYER SUCTION EXPERIMENTS ON A 36° SWEEP WING AT MACH NUMBERS 2.5, 3.0 AND 3.5

E. E. Groth

#### (A) Summary

A 36° swept suction wing of 3-percent-thick biconvex section was tested at AEDC Tunnel A at Mach numbers between 2.5 and 3.5. Laminar flow and low drag coefficients were maintained up to the highest tunnel pressures, resulting in length Reynolds numbers of 17, 25 and 20 x 10<sup>6</sup> at Mach numbers 2.5, 3.0 and 3.5, respectively.

The computation of the laminar boundary layer development along the wing chord for typical test conditions provided numerical values of crossflow Reynolds numbers with full laminar flow.

Two separate tests were conducted. The first model with the original -- relatively narrow -- slots was successful at M = 2.5 and in the Reynolds number range up to R = 13 x 10<sup>6</sup> at M = 3.0. The second model, with wider slots, provided satisfactory data at M = 3.0 and 3.5 at further increased chord Reynolds numbers. Both models were rather sensitive to the local suction quantities.

#### (B) Notation

b	wing span, measured perpendicular to flow direction	
$b_k$	spanwise extent of $k^{\text{th}}$ suction chamber, perpendicular to flow direction	
$b'$	wing span, measured parallel to leading edge	
c	wing chord, measured parallel to flow direction (c = 39.0 inches)	
$c'$	wing chord, measured perpendicular to leading edge ( $c' = 31.5$ inches)	
$C_{D_s}$	suction drag coefficient	} Referred to freestream dynamic pressure, unit span and reference length in flow direction
$C_{D_t}$	total drag coefficient	
$C_{D_w}$	wake drag coefficient	
$C_f$	friction drag coefficient	
$C_{W_k}$	$= \frac{W_k}{\rho_{\infty} g Q_{\infty} b_k c} = \text{suction weight flow coefficient through } k^{\text{th}} \text{ chamber}$	

(B) Notation (continued)

$C_{W_t}$	$= \sum_k C_{W_k}$ = total suction coefficient
M	Mach number
p	static pressure
R	Reynolds number
$R^{(1)}$	$= \frac{Q_\infty}{\nu_\infty}$ = reference unit Reynolds number (per inch)
U	potential flow velocity perpendicular to leading edge
V	$= V_\infty$ = potential flow velocity parallel to leading edge
Q	$= \sqrt{U^2 + V^2}$ = resultant potential flow velocity
u	velocity component inside boundary layer perpendicular to leading edge
$W_k$	suction weight flow through $k^{th}$ chamber (lb/s)
x	coordinate in flow direction
$x'$	coordinate perpendicular to leading edge
$y'$	coordinate parallel to leading edge
z	coordinate perpendicular to wing surface
$\nu$	kinematic viscosity
$\rho$	density
$\theta$	sweep angle
$\delta$	boundary layer thickness

Subscripts

x	chordwise station x
k	running parameter, $k = 1 \dots 8$
$\infty$	freestream
l	outer edge of boundary layer

Other symbols are defined in the body of the report. Coordinates and velocity components are shown in Figure 75.

### (C) Introduction

Laminar flow and low drag coefficients were maintained on straight two-dimensional wings by means of boundary layer suction at Mach numbers between 2.5 and 3.5 and at length Reynolds numbers up to  $26 \times 10^6$ . The next step in the development toward a three-dimensional supersonic suction wing is the investigation of the effects of crossflow on the stability of the laminar boundary layer in supersonic flow. For this purpose, a two-dimensional wing swept ahead of the Mach cone was built and tested at AEDC Tunnel A. The first experiments were conducted in March 1962; the tests were repeated with a modified suction arrangement in October 1962.

### (D) Description of the Model and Purpose of the Tests

The model selected for the boundary layer suction measurements was a two-dimensional wing of  $36^\circ$  sweep; the chord length in flow direction was  $c = 39.0$  inches and perpendicular to the leading edge was  $c' = 31.5$  inches. The model spanned the tunnel,  $b = 40$  inches. The biconvex airfoil section was 3-percent thick perpendicular to the leading edge or 2.43-percent thick in flow direction. Suction was applied to an area which was not disturbed by any shock waves for Mach numbers  $M \geq 3.0$ . The shock lines from the intersection of the model leading edge with the tunnel side walls intersected the last suction chamber at  $M = 2.5$ . The reflection of the leading edge shock wave from the tunnel walls at  $M = 2.5$  barely missed the rear end of the suction area. A sketch and photograph of the model are shown in Figures 72 and 73; the location of the shock lines relative to the suction area is presented in Figure 74.

The original suction system consisted of 66 slots arranged in eight suction chambers. The slots were 0.42 to 0.45 inch apart (measured perpendicular to the slots) and between 0.005 and 0.014 inch wide; the first slot was 1.6 inches aft of the leading edge ( $\perp$  l.e.). Since the first test indicated that this arrangement provided insufficient suction quantities at the higher Mach and Reynolds numbers, the model was modified by increasing the slot widths and adding two slots in front. The first slot of the modified model was 0.76 inch aft of the leading edge (measured  $\perp$  l.e.). Table IV contains a list of the pertinent dimensions of the two suction arrangements. The slots near the leading edge of the model were about 19 inches long (measured parallel to the leading edge); their length reduced to about five inches near the trailing edge. The ducting and metering of the suction air was done in the same way as in previous tests (Section II, Part 2, Chapter A-a and A-b).

The boundary layer rake was located in the middle of the suction area and could be moved from its most rearward position at the end of the last suction chamber ( $x_{\text{rake}} = 37.8$  inches) to the end of suction chamber 7 ( $x_{\text{rake}} = 32.8$  inches) and to its most forward position at the end of suction chamber 6 ( $x_{\text{rake}} = 27.7$  inches).

The purpose of the tests was to establish laminar flow at supersonic speeds and high length Reynolds numbers by means of boundary layer suction in the presence of strong boundary layer crossflow. Suction requirements had to be established as functions of Mach and Reynolds numbers. Theoretical analyses of the laminar boundary layer development at the experimental pressure and suction distributions had the purpose of providing numerical data of crossflow Reynolds numbers at which laminar flow could be maintained. In order to develop



(D) Description of the Model and Purpose of the Tests (continued)

strong crossflow effects along the whole wing chord, a two-dimensional swept wing model was selected. The sweep angle was low enough to provide supersonic leading edge flow at all Mach numbers under consideration.

(E) Drag and Suction Measurements

The experiments were conducted in AEDC Tunnel A; S. R. Pate of ARO, Inc., was project engineer (References 106 & 109). The first tests took place in March 1962, the second tests with the modified suction system in October 1962. Preliminary results of both tests were reported in References 110 and 111.

The suction and drag coefficients of a two-dimensional swept wing are defined in Part (H) of this report, which also includes a derivation of the wake drag in compressible flow. The coordinates and velocity components used are shown in Figure 75.

Plots of wake, suction and total drag coefficients vs total suction coefficient are presented in Figures 76 to 82 for Mach numbers  $M = 2.5$ ,  $3.0$  and  $3.5$  and for three rake locations (end of suction chambers 6, 7 and 8). The test points from the two tests are marked differently to demonstrate the different behavior of the model with the two suction arrangements.

The first tests provided laminar flow at  $M = 2.5$  up to the highest possible tunnel pressures; the flow over the last few inches was disturbed, probably by the reflected shock from the leading edge. No laminar flow could be obtained at  $x = 37.8$  inches for unit Reynolds numbers  $R^{(1)} > 0.42 \times 10^6$  per inch, but the flow remained laminar at  $x = 32.8$  inches up to the highest value of  $R^{(1)} = 0.54 \times 10^6$  per inch. The tests at  $M = 2.5$  with the first suction system were conducted at low total suction coefficients. It was observed during these tests that suction in chambers 2, 3 and 4 had to be kept at low values (less than one-half of the suction quantities sucked through chamber 1) in order to maintain laminar flow. Apparently, some disturbance of unknown nature caused instability of the laminar boundary layer at higher suction quantities. A possible reason for such a behavior may be found in the fact that the bonding of the outer skin was not as uniform as on the other suction models; a portion of the outer skin was loose in the front portion of the model and was fastened to the inner structure by a few rivets. In spite of the limitation in the adjustment of the suction distribution, a sufficient number of test points was recorded in the range of the minimum total drag.

The tests with the first suction system at  $M = 3.0$  were restricted to length Reynolds numbers below  $R_x \sim 13 \times 10^6$ . Reduced suction was again required in the third and fourth suction chambers. The maximum suction quantities available in the first two chambers were not sufficient to obtain laminar flow at higher Reynolds numbers. No laminar flow was observed with the first model at  $M = 3.5$ .

The modified suction system provided laminar flow and low drag coefficients at rather uniform suction distributions at  $M = 3.5$  up to the highest possible Reynolds numbers. Suction could be reduced considerably in the rear half of the model without a drag penalty. The curves at  $R = 19.7 \times 10^6$  in

#### (E) Drag and Suction Measurements (continued)

Figure 81 show that the total drag still decreased for total suction coefficients  $C_{W_t} < 3 \times 10^{-4}$ . Although the boundary layer velocity profiles looked rather unstable, they remained thin enough so that the reduction in suction drag was larger than the increase in wake drag.

Full laminar flow up to the maximum Reynolds number was also observed with the modified suction system at  $M = 3.0$  and  $2.5$ . The measurements at low Reynolds numbers agree with the data obtained during the first tests (Figures 76 and 79a). With increasing Reynolds numbers it became necessary to maintain high suction quantities in the front half of the model, resulting in rather high total suction coefficients and, therefore, total drag coefficients.

The minimum total drag and optimum total suction coefficients are presented in Figures 83 to 85 for the three Mach numbers. The optimum data at  $M = 2.5$  and at the low Reynolds numbers at  $M = 3.0$  were observed in the first tests; the high Reynolds number points at  $M = 3.0$  and all values at  $M = 3.5$  resulted from the second tests. The minimum total drag coefficients near the trailing edge ( $x_{\text{rake}} = 37.8$  inches  $= 0.97$  c) were slightly lower than two times the friction coefficient of a laminar plate at  $M = 2.5$  and  $3.5$  and approximately  $2.4 C_{f_{\text{lam plate}}}$  at  $M = 3.0$  and Reynolds numbers beyond  $13 \times 10^6$ . The optimum total suction coefficients were near  $2.5 \times 10^{-4}$  at  $M = 2.5$ , near  $3.0 \times 10^{-4}$  at  $M = 3.5$  and above  $4.0 \times 10^{-4}$  at  $M = 3.0$ . Lower drag and suction coefficients were observed at stations ahead of the trailing edge.

The variation of  $(C_{D_t})_{\min}$  and  $(C_{W_t})_{\min}$  with Mach and Reynolds numbers is not as uniform as was observed on the flat plate model (Section II, Part 2, Chapter A). The data indicate a rather high degree of sensitivity toward the suction system. Apparently, it is not possible to use one suction arrangement for the whole Mach and Reynolds number range which was covered in this test program. A further discussion of the test results will be presented in the following section in connection with theoretical developments of the laminar boundary layer at typical test conditions.

#### (F) Comparison of Test Results with Theory

Calculations of the development of the laminar boundary layer over the  $36^\circ$  swept wing of 3-percent-thick biconvex section were conducted by means of the method of Reference 45 at Mach numbers  $2.5$ ,  $3.0$  and  $3.5$  and suction distributions which were close to experimental cases. The potential flow pressure distribution was determined by means of second-order theory. The suction distribution is defined by an equivalent continuous inflow coefficient

$$f_{O^*} = \frac{\rho_w v_o}{\rho_\infty Q_\infty} \sqrt{R_c}$$

which is related to the individual suction coefficient  $C_{W_k}$  by the equation

$$C_{W_k} \sqrt{R_c} = \frac{\Delta k}{c} f_{O^*}$$

(F) Comparison of Test Results with Theory (continued)

where  $\Delta_k$  is the length of the  $k^{\text{th}}$  suction chamber; uniform suction is assumed through each chamber. Parameters for estimating the stability of the boundary layer are the Reynolds numbers  $R_{\delta_{ss}}$  based on the momentum thickness  $\delta_{ss}$  in the direction of the local streamline and the crossflow Reynolds number  $R_{0.1}$  based on maximum crossflow velocity and a boundary layer thickness defined as the height where the crossflow velocity is one-tenth of its maximum value. The theory provides both Reynolds numbers divided by  $\sqrt{R_c}$ .

Theoretical drag coefficients were computed in the same manner as they were evaluated from the wind tunnel tests. The detailed expressions are presented in Part (I) of this report. Numerical values of the chord Reynolds number  $R_c$  were selected so that the theoretical data could be compared with the experimental results.

Boundary layer calculations were conducted for the following cases:

$M_\infty$	$C_{W_t} \sqrt{R_c}$	Suction Distribution Selected from	Drag Comparison at $10^{-6} R_c$	Figure Numbers
2.5	1.222	First tests	11.1, 16.6, 19.8	86a, b, c, d
2.5	2.013	Second tests	13.5, 21.0	87a, b, c
3.0	1.840	First tests	13.0	88a, b
3.0	1.982	Second tests	25.5	89a, b
3.5	1.698	First tests	20.2	90a, b

The suction distribution in Figure 86a at  $M = 2.5$  is typical of the first tests -- high suction in the first chamber, low suction in chambers 2, 3 and 4. The effect of this non-uniform distribution on the developments of  $R_{\delta_{ss}}$  and  $R_{0.1}$  is quite insignificant, which confirms the conclusion discussed in the previous section that some disturbance must have existed in the front part of the model which caused boundary layer instability at higher suction quantities. The agreement between theoretical and experimental drag data (Figures 86b, c, d) is satisfactory, except for the higher values of  $C_{D_w}$  near the trailing edge which were probably caused by shock interference. Figures 86b, c, d include numerical values for the crossflow Reynolds number; they exceeded the value of 250 in the rear portion of the wing. The streamwise component of the boundary layer was rather stable.  $R_{\delta_{ss}}/\sqrt{R_c} \sim 0.3$  for  $x/c > 0.6$ , so that  $R_{\delta_{ss}} \sim 1350$  at  $R_c \sim 20 \times 10^6$ .

The second calculation at  $M = 2.5$  was conducted at a suction distribution typical for the second tests (Figure 87a). The agreement of the experimental drag coefficients with the theoretical values is good at  $R_c = 13.5 \times 10^6$  (Figure 87b); the experimental values of  $C_{D_w}$  are 40 to 50 percent higher than the theoretical data at  $R_c = 21.0 \times 10^6$  (Figure 87c). Crossflow Reynolds numbers with laminar flow stayed below 200.

(F) Comparison of Test Results with Theory (continued)

The nearly constant suction distribution at  $M = 3.0$  (Figure 88a) agreed with the experimental data presented in Figure 88b, except that suction was lower by nearly 20 percent in the third and fourth suction chambers. The experimental wake drag coefficient at  $R_c = 13.0 \times 10^6$  increased rapidly over the last 10 percent of chord. The maximum crossflow Reynolds number with laminar flow was of the order of 130.

The second suction distribution at  $M = 3.0$  (Figure 89a) was typical for the second tests -- high suction in front, low in the rear. At  $R_c = 25.5 \times 10^6$ , it produced crossflow Reynolds numbers which increased from  $R_{0.1} = 140$  at  $x/c = 0.7$  to  $R_{0.1} = 280$  at  $x/c = 1.0$ . The measured wake drag coefficients were 30 to 50 percent higher than the theoretical values. The experimental and theoretical boundary layer velocity profiles for this case are shown in Figure 91. The two profiles agree at  $x = 32.8$  inches except for a small thickening near the outer edge ( $u/U > 0.95$ ); the experimental profile at  $x = 37.8$  inches deviates more from the theoretical profile at velocity ratios  $u/U > 0.8$ .

At  $M = 3.5$ , the experimental values of  $C_{Dw}$  were about 50 percent higher than the theoretical values (Figure 90b). The crossflow Reynolds number increased from  $R_{0.1} = 190$  at  $x/c = 0.7$  to  $R_{0.1} = 315$  at  $x/c = 1.0$ . The streamwise boundary layer component is quite stable,  $R_{\delta_{ss}} = 1200$  at  $x/c = 1.0$  and  $R_c = 20.2 \times 10^6$ .

The high wake drag coefficients at  $M = 3.0$  and  $3.5$  and  $R_c \geq 20 \times 10^6$  (Figures 89b and 90b) occurred at crossflow Reynolds numbers near 300. This might lead to the conclusion that the crossflow stability limit was exceeded by a large margin. Since Figures 86b to d showed good agreement between theory and experiment up to  $R_{0.1} \sim 250$ , this value should be considered as an upper limit of the crossflow Reynolds number near the trailing edge of the wing.

For a few cases, the thickness of the sucked layer was computed and compared with the actual slot width. At  $M = 3.5$  the slot widths were about 2.2 to 2.5 times larger than the thicknesses of the sucked layer. Apparently, with the low values for the slot flow Reynolds number,\* no disturbances developed at the slot inlets which affected the stability of the boundary layer flow. The high suction quantities in the front half of the model which were required to maintain laminar flow at  $M = 2.5$  and  $3.0$  (typical suction distributions are included in Figures 87a and 89a) resulted in a ratio of slot width to thickness of the sucked layer of the order of 3.0. It is possible that at lower suction quantities, the discrepancy between slot width and thickness of the sucked

\*The slot flow Reynolds number,  $R_s$ , is defined by the slot width, the average inflow velocity into the slot and the wall density and viscosity. Its value at  $M = 3.5$  was always below 50. Flow separation effects are not expected to become serious before  $R_s$  exceeds a value of  $\sim 120$ .

(F) Comparison of Test Results with Theory (continued)

layer might have been so large that the separation of the sucked air at the slot entrance caused major disturbances to the boundary layer flow. The assumption that the flow did not attach to the slot walls is confirmed by the fact that considerably higher pressure losses through the skin were measured than was computed under the assumption that the sucked air filled the slots uniformly.

The slots of the modified suction arrangement were built so wide in order to reduce the pressure losses through the skin and to provide adequate suction quantities, especially for the tests at  $M = 3.5$ . Probably, these slot widths were too wide for tests at optimum suction distributions and the lower Mach numbers where smaller volumes of air have to be sucked through the slots.

(G) Determination of Suction and Drag Coefficients of Untapered Swept Wings in Compressible Flow

The suction and drag coefficients of an untapered swept wing shall be referred to quantities measured in flow direction, such as undisturbed velocity  $Q_\infty$  and chord length  $c$  (Figure 75). The local suction coefficient of the  $k^{\text{th}}$  chamber, which is located between the chordwise stations  $x'_k$  and  $x'_{k+1}$  and has an average span  $b'_k$  (measured perpendicular and parallel to the leading edge) is defined by

$$C_{W_k} = \frac{W_k}{\rho_\infty Q_\infty c b_k} = \frac{1}{b'_k} \int_{x'_k}^{x'_{k+1}} \frac{\rho_w v_o}{\rho_\infty Q_\infty} b'_k \frac{dx'}{c'}$$

where  $v_o$  is the continuous inflow velocity through the skin,  $\rho_w$  = wall density,  $b_k c = b'_k c'$ . The total suction coefficient per unit span is equal to

$$C_{W_t} = \sum_k C_{W_k} = \int_0^1 \frac{\rho_w v_o}{\rho_\infty Q_\infty} d \frac{x}{c}$$

The suction drag coefficient of the  $k^{\text{th}}$  chamber is defined as

$$C_{D_{s_k}} = \frac{2 D_{s_k}}{\rho_\infty Q_\infty^2 b_k c} = C_{W_k} \left( 1 + \frac{M_{s_k}^2 T_{s_k}}{M_\infty^2 T_\infty} \right)$$

where  $M_{s_k}^2$  is defined by the static pressure  $p_{s_k}$  inside the  $k^{\text{th}}$  suction chamber:

$$M_{s_k}^2 = 5 \left[ \left( \frac{p_\infty}{p_{s_k}} \right)^{.286} - 1 \right]$$

(G) Determination of Suction and Drag Coefficients of  
Untapered Swept Wings in Compressible Flow (continued)

It is assumed that the air from the  $k^{\text{th}}$  chamber is compressed to ambient pressure  $p_\infty$  and accelerated to freestream velocity  $Q_\infty$ . The total suction drag coefficient is given by

$$C_{Ds} = \sum_k C_{Ds_k}$$

The wake drag  $D_w$  is defined as the momentum loss of the external air. Its value for a two-dimensional swept wing in incompressible flow has been derived in Reference 69. The same procedure can be applied to compressible flow. The momentum loss of the air in a spanwise section of width  $b'$  (see Figure 75) is determined by

$$D_w = \int_0^{b'} dy' \int_0^\infty \rho u [(U_\infty - u) \cos\theta + (V_\infty - v) \sin\theta] dz,$$

where the integrations have to be carried out far enough downstream of the wing. The wake drag coefficient  $C_{Dw}$  is equal to

$$\begin{aligned} C_{Dw} &= \frac{2 D_w}{\rho_\infty Q_\infty^2 b' c'} = \frac{2}{b' c'} \int_0^{b'} dy' \int_0^\infty \frac{\rho u}{\rho_\infty Q_\infty} \left( \frac{U_\infty - u}{Q_\infty} \cos\theta + \frac{V_\infty - v}{Q_\infty} \sin\theta \right) dz \\ &= \frac{2}{c'} \left[ \int_0^\delta \frac{\rho u}{\rho_\infty U_\infty} \left( 1 - \frac{u}{U_\infty} \right) \cos^3\theta \, dz + \int_0^\delta \frac{\rho u}{\rho_\infty U_\infty} \left( 1 - \frac{v}{V_\infty} \right) \cos\theta \sin^2\theta \, dz \right] \quad (1) \\ &= \frac{2}{c} \left[ \int_0^\xi \frac{\rho u}{\rho_x U_x} \left( 1 - \frac{u}{U_x} \right) \cos^2\theta \, dz + \int_0^\delta \frac{\rho u}{\rho_x U_x} \left( 1 - \frac{v}{V_x} \right) \sin^2\theta \, dz \right] \end{aligned}$$

(Note that  $b' = b/\cos\theta$ ,  $c' = c \cos\theta$ ,  $b'c' = bc$ .)

The following displacement and momentum thicknesses can be defined on a swept wing (the subscript 1 refers to the conditions at the outer edge of the boundary layer):

$$\begin{aligned} \delta_u &= \int_0^\xi \left( 1 - \frac{\rho u}{\rho_1 U} \right) dz, & \delta_v &= \int_0^\xi \left( 1 - \frac{\rho v}{\rho_1 V} \right) dz \\ \delta_{uu} &= \int_0^\xi \frac{\rho u}{\rho_1 U} \left( 1 - \frac{u}{U} \right) dz, & \delta_{vv} &= \int_0^\xi \frac{\rho u}{\rho_1 U} \left( 1 - \frac{v}{V} \right) dz. \end{aligned}$$

(G) Determination of Suction and Drag Coefficients of  
Untapered Swept Wings in Compressible Flow (continued)

Then Equation (1) can be written as

$$C_{D_w} = \frac{2}{c} [(\delta_{uu})_{\infty} \cos^2 \theta + (\delta_{vu})_{\infty} \sin^2 \theta] \quad (2)$$

The subscript  $\infty$  has been added to indicate that the values of the momentum thicknesses have to be evaluated infinitely far downstream.

The relations between the momentum thickness at infinity and at the trailing edge of the wing can be obtained in the usual way from the momentum equations of a swept wing in compressible flow, which can be written (Reference 112) in the form

$$\frac{d}{dx} (\rho_1 U^2 \delta_{uu}) + \rho_1 U \delta_u \frac{dU}{dx} = 0$$

$$\frac{d}{dx} (\rho_1 U V \delta_{vu}) = 0$$

since there is no friction aft of the trailing edge. Integrating these equations between the trailing edge and infinity results in

$$(\delta_{uu})_{\infty} = (\delta_{uu})_{te} \overline{\left( \frac{U_{te}}{U_{\infty}} \right)^{H_u + 2 - \frac{U^2}{Q^2} M^2}} \quad (3)$$

$$(\delta_{vu})_{\infty} = \frac{(\rho_1 U)_{te}}{\rho_{\infty} U_{\infty}} (\delta_{vu})_{te} \quad (4)$$

Use has been made of the relations

$$\frac{1}{\rho_1} \frac{d\rho_1}{dx} = - \frac{M^2}{Q^2} U \frac{dU}{dx}, \text{ and } H_u = \frac{\delta_u}{\delta_{uu}}.$$

The bar on top of the exponent in Equation (3) means the average value of the expression between the trailing edge and infinity,  $Q^2 = U^2 + V^2$ ,  $V = V_{\infty} = \text{const}$ ,  $M = Q/a$ . Introducing Equations (3) and (4) into (2) leads to

$$C_{D_w} = \frac{2}{c} \left\{ (\delta_{uu})_{te} \overline{\left( \frac{U_{te}}{U_{\infty}} \right)^{H_u + 2 - \frac{U^2}{a^2}}} \cos^2 \theta + \frac{\rho_{te} U_{te}}{\rho_{\infty} U_{\infty}} (\delta_{vu})_{te} \sin^2 \theta \right\} \quad (5)$$

(G) Determination of Suction and Drag Coefficients of  
Untapered Swept Wings in Compressible Flow (continued)

This expression can be simplified by utilizing the fact that the potential flow velocity at the trailing edge is only a few percent higher than the freestream velocity, so that only the first-order terms of

$$\eta = \frac{Q_{te}}{Q_{\infty}} - 1$$

have to be considered. This leads to the following approximate relations:

from  $U_{te}^2 = Q_{te}^2 - Q_{\infty}^2 \sin^2 \theta$  follows

$$\left(\frac{U_{te}}{U_{\infty}}\right)^2 = \frac{1}{\cos^2 \theta} \left(\frac{Q_{te}}{Q_{\infty}}\right)^2 - \frac{\sin^2 \theta}{\cos^2 \theta} = \frac{1 + 2\eta - \sin^2 \theta}{\cos^2 \theta} = 1 + \frac{2\eta}{\cos^2 \theta}$$

$$\frac{U_{te}}{U_{\infty}} = 1 + \frac{\eta}{\cos^2 \theta} \quad (6a)$$

The density ratio at the trailing edge is defined by

$$\frac{\rho_{te}}{\rho_{\infty}} = \left[ 1 - \frac{\gamma-1}{2} M_{\infty}^2 \left( \left( \frac{Q_{te}}{Q_{\infty}} \right)^2 - 1 \right) \right]^{\frac{1}{\gamma-1}} \approx 1 - \frac{M_{\infty}^2}{2} \left( \left( \frac{Q_{te}}{Q_{\infty}} \right)^2 - 1 \right)$$

$$\frac{\rho_{te}}{\rho_{\infty}} = 1 - M_{\infty}^2 \eta \quad (6b)$$

The Mach number ratio at the trailing edge is related to the velocity ratio in the form

$$\frac{Q_{te}}{Q_{\infty}} = \frac{M_{te}}{M_{\infty}} \sqrt{\frac{1 + .2M_{\infty}^2}{1 + .2M_{te}^2}}$$

$$\text{or } \left(\frac{M_{te}}{M_{\infty}}\right)^2 = \frac{\left(\frac{Q_{te}}{Q_{\infty}}\right)^2}{1 - .2M_{\infty}^2 \left(\left(\frac{Q_{te}}{Q_{\infty}}\right)^2 - 1\right)} \approx \frac{1 + 2\eta}{1 - .4M_{\infty}^2 \eta} \approx 1 + 2\eta (1 + .2M_{\infty}^2)$$

$$\frac{M_{te}}{M_{\infty}} = 1 + (1 + .2M_{\infty}^2) \eta \quad (6c)$$

Equations (6a) and (6c) can be used to determine



(G) Determination of Suction and Drag Coefficients of  
Untapered Swept Wings in Compressible Flow (continued)

$$\begin{aligned} \frac{U_{te}}{a_{te}} &= \frac{U_{te}}{U_{\infty}} \frac{Q_{te}}{a_{te}} \frac{Q_{\infty} \cos \theta}{Q_{te}} \approx \frac{\left(1 + \frac{\eta}{\cos^2 \theta}\right) M_{\infty} \left[1 + \eta \left(1 + .2 M_{\infty}^2\right)\right] \cos \theta}{1 + \eta} \\ &= M_{\infty} \cos \theta \left[1 + \eta \left(\frac{1}{\cos^2 \theta} + 1 + .2 M_{\infty}^2 - 1\right)\right] \\ \frac{U_{te}}{a_{te}} &= M_{\infty} \cos \theta \left(1 + \frac{1 + .2 M_{\infty}^2 \cos^2 \theta}{\cos^2 \theta} \eta\right) \end{aligned} \quad (6d)$$

Later in the derivation the following quantities will be used:

$$\left(\frac{v}{U}\right)_{te} = \frac{U_{\infty} \tan \theta}{U_{te}} = \frac{\tan \theta}{1 + \frac{\eta}{\cos^2 \theta}} = \tan \theta \left(1 - \frac{\eta}{\cos^2 \theta}\right) \quad (6e)$$

$$\left(\frac{v^2 - Q^2 \sin^2 \theta}{U^2}\right)_{te} = \frac{Q_{\infty}^2 \sin^2 \theta \left(1 - \left(\frac{Q_{te}}{Q_{\infty}}\right)^2\right)}{\left(\frac{U_{te}}{U_{\infty}}\right)^2 Q_{\infty}^2 \cos^2 \theta} = -2\eta \tan^2 \theta \quad (6f)$$

Evaluation of the exponent of  $U_{te}/U_{\infty}$  in Equation (3) requires an estimate for the expression  $H_u = \delta_u/\delta_{uu}$ . On a straight wing (Reference 123) it is assumed that the flow becomes turbulent aft of the last suction slot so that the value of  $H$  is taken as that of a flat plate at the local Mach number  $M$ . In case of a swept wing, the additional assumption is made that the  $u$  and  $v$  components of the boundary layer are similar,  $u/U = v/V$ ; this was confirmed with sufficient accuracy by laminar boundary layer calculations on thin swept wings with supersonic leading edges up to  $50^\circ$  sweep. Since the compressibility correction for the displacement and momentum thickness depend only on the density, which is a function of the resultant velocity, the resultant Mach number and not the component in chordwise direction has to be taken for estimates of  $\delta_u$  and  $\delta_{uu}$ .<sup>\*</sup> Therefore, the same expressions can be used for  $H_u$  which were developed in Reference 123:

$$(H_u)_{te} = 1.29 + 0.44 M_{te}^2, \quad (H_u)_{\infty} = 1.00 + 0.40 M_{\infty}^2.$$

Introducing the first-order terms of Equations (6a) through (6f) result in

$$H_u + 2 - \frac{U^2}{a^2} = \frac{1}{2} (H_u)_{te} + \frac{1}{2} (H_u)_{\infty} + 2 - \frac{1}{2} \left(\frac{U^2}{a^2}\right)_{te} - \frac{1}{2} \left(\frac{U^2}{a^2}\right)_{\infty}$$

<sup>\*</sup>This formulation was suggested by J. Goldsmith, Norair Boundary Layer Research Section.

(G) Determination of Suction and Drag Coefficients of Untapered Swept Wings in Compressible Flow (continued)

$$\begin{aligned}
 &= \frac{1}{2} \left\{ 1.29 + .44 M_\infty^2 [1 + 2\eta (1 + .2 M_\infty^2)] \right\} + \frac{1}{2} (1 + .4 M_\infty^2) + 2 \\
 &- \frac{1}{2} M_\infty^2 \cos^2 \theta \left[ 1 + \frac{2\eta}{\cos^2 \theta} (1 + .2 M_\infty^2 \cos^2 \theta) \right] - \frac{1}{2} M_\infty^2 \cos^2 \theta \\
 &= 3.145 - .58 M_\infty^2 \cos^2 \theta + .42 M_\infty^2 \sin^2 \theta + ( ) \eta
 \end{aligned}$$

$$\left( \frac{U_{te}}{U_\infty} \right)^{H_u + 2 - \frac{U^2}{a^2}} = 1 + (3.145 - .58 M_\infty^2 \cos^2 \theta + .42 M_\infty^2 \sin^2 \theta) \frac{\eta}{\cos^2 \theta}$$

$$\frac{\rho_{te} U_{te}}{\rho_\infty U_\infty} = 1 + \left( \frac{1}{\cos^2 \theta} - M_\infty^2 \right) \eta$$

Introducing these expressions into Equation (5) provides

$$\begin{aligned}
 C_{D_w} = \frac{2}{c} \left\{ (\delta_{uu})_{te} \cos^2 \theta + (\delta_{vu})_{te} \sin^2 \theta \right. \\
 + \eta [ (3.145 - .58 M_\infty^2 \cos^2 \theta + .42 M_\infty^2 \sin^2 \theta) (\delta_{uu})_{te} \\
 \left. + (1 - M_\infty^2 \cos^2 \theta) (\delta_{vu})_{te} \tan^2 \theta \right\} \quad (7)
 \end{aligned}$$

This expression has to be modified since  $\delta_{uu}$  and  $\delta_{vu}$  cannot be measured directly. The streamlines at the outer edge of the boundary layer and their normals are introduced now as new coordinates and the local boundary layer velocity components  $u$  and  $v$  are transformed to  $s$  and  $n$  (see Figure 75) by means of the relations

$$s = \frac{U}{Q} u + \frac{V}{Q} v, \quad n = -\frac{V}{Q} u + \frac{U}{Q} v$$

The boundary layer thicknesses in these new directions are defined as follows (see Reference 45; note that the present notation is different from that of Reference 45):

(G) Determination of Suction and Drag Coefficients of  
Untapered Swept Wings in Compressible Flow (continued)

$$\delta_s = \int_0^{\delta} \left(1 - \frac{\rho s}{\rho_1 Q}\right) dz$$

$$\delta_n = \int_0^{\delta} \frac{\rho n}{\rho_1 Q} dz$$

$$\delta_{ss} = \int_0^{\delta} \frac{\rho s}{\rho_1 Q} \left(1 - \frac{s}{Q}\right) dz$$

$$\delta_{ns} = \int_0^{\delta} \frac{\rho ns}{\rho_1 Q^2} dz$$

$$\delta_{nn} = \int_0^{\delta} \frac{\rho n^2}{\rho_1 Q^2} dz$$

The following relations exist between the different boundary layer thicknesses:

$$\delta_{uu} = \delta_{ss} + \frac{V}{U} (\delta_{ns} - \delta_n) + \frac{V}{U} \delta_{ns} - \frac{V^2}{U^2} \delta_{nn} \quad (8a)$$

$$\delta_{vu} = \delta_{ss} + \frac{V}{U} (\delta_{ns} - \delta_n) - \frac{U}{V} \delta_{ns} + \delta_{nn} \quad (8b)$$

$$\begin{aligned} \delta_{uu} \cos^2 \theta + \delta_{vu} \sin^2 \theta = \delta_{ss} + \frac{V}{U} (\delta_{ns} - \delta_n) \\ - \frac{V^2 - Q^2 \sin^2 \theta}{U^2} (\delta_{nn} - \frac{U}{V} \delta_{ns}) \end{aligned} \quad (8c)$$

The theoretical boundary layer calculations on the present configuration at Mach numbers between 2.5 and 3.5 showed the following orders of magnitude:

$$\delta_{ns} - \delta_n < 0.02 \delta_{ss} \quad \delta_{nn} < 0.001 \delta_{ss} \quad \delta_{ns} < 0.06 \delta_{ss} \quad (8d)$$

Since the factor of  $(\delta_{nn} - \frac{U}{V} \delta_{ns})$  in Equation (8c) is small -- of the order of  $\eta$  (see Equation 6d) -- Equation (8c) can be approximated by

$$(\delta_{uu})_{te} \cos^2 \theta + (\delta_{vu})_{te} \sin^2 \theta \approx \delta_{ss}$$

$(\delta_{uu})_{te}$  and  $(\delta_{uv})_{te}$  occur separately in Equation (7) as factors of  $\eta$ . Introducing the approximate values of Equation (8d) into (8a) and (8b) shows that  $(\delta_{uu})_{te}$  and  $(\delta_{uv})_{te}$  deviate from  $\delta_{ss}$  by small quantities. In first-order approximation therefore  $(\delta_{uu})_{te} \sim (\delta_{ss})_{te} \eta$  and

$$C_{D_w} = \frac{2 \delta_{ss}}{c} [1 + (3.145 + \tan^2 \theta - 0.58 M_\infty^2) \eta] \quad (9)$$

(G) Determination of Suction and Drag Coefficients of  
Untapered Swept Wings in Compressible Flow (continued)

where

$$\eta = \frac{Q_{te}}{Q_{\infty}} - 1.$$

Since the streamline direction at the trailing edge deviates from the freestream direction only by a few degrees (the angle is proportional to  $\eta$ ), the boundary layer rake in flow direction determines the value of  $\delta_{ss}$  with sufficient accuracy.

Since the measured streamwise boundary layer velocity profiles near the wing trailing edge of the model deviated from the theoretical ones by a certain amount, as was discussed in Part (F), it is possible that the order of magnitude of the crossflow boundary layer quantities  $\delta_n$ ,  $\delta_{ns}$ ,  $\delta_{nn}$  is different from the theoretical estimates mentioned above. But it is expected that they remain small enough so that the accuracy of Equation (9) is not affected.

(H) Evaluation of Wake, Suction and Total Drag Coefficients at  
an Arbitrary Chordwise Station from Theoretical Boundary  
Layer Calculations

The boundary layer calculations were conducted at a certain total suction coefficient, defined by

$$C_{W_t} \sqrt{R_c} = \int_0^1 f_0^* d \frac{x}{c}$$

At an arbitrary station  $x < c$ :

$$C_{W_t}(x) = \frac{W_t(x)}{\rho_{\infty} Q_{\infty} g x} = \frac{1}{x/c \sqrt{R_c}} \int_0^{x/c} f_0^* d \frac{x}{c}$$

The wake drag coefficient is defined by

$$C_{D_w}(x) = \frac{2D_w(x)}{\rho_{\infty} Q_{\infty}^2 x} = \frac{2\delta_{ss}(x)}{x} \left[ 1 + \left( \frac{Q(x)}{Q_{\infty}} - 1 \right) f(M_{\infty}, \theta) \right]$$

$$f(M_{\infty}, \theta) = 3.145 + \tan^2 \theta - 0.58 M_{\infty}^2$$

The boundary layer integration program (Reference 45) provides  $\delta_{ss}^*(x) = \frac{\delta_{ss}(x)}{c} \sqrt{R_c}$ ; therefore

(H) Evaluation of Wake, Suction and Total Drag Coefficients at an Arbitrary Chordwise Station from Theoretical Boundary Layer Calculations (continued)

$$C_{D_w}(x) = \frac{2\delta_{ss}^*}{x/c \sqrt{R_c}} \left[ 1 + \left( \frac{Q(x)}{Q_\infty} - 1 \right) f(M_\infty, \theta) \right]$$

The suction drag coefficient  $C_{D_s}$  is proportional to  $C_{W_t}$ . An average factor was evaluated from the present tests. The curves of  $C_{D_s}$  vs  $C_{W_t}$  in Figures 76 to 82 can be approximated by

$$C_{D_s}(x) = C_{W_t}(x) [1 + 100 M_\infty C_{W_t}(x)].$$

Finally,

$$C_{D_t}(x) = C_{D_w}(x) + C_{D_s}(x)$$

The local crossflow Reynolds number  $R_{0.1}$  is obtained from the value  $R_{0.1}/\sqrt{R_c}$ , which is tabulated in the boundary layer integration program.

(I) Conclusion

Low drag boundary layer suction experiments on a  $36^\circ$  swept wing of 3-percent biconvex cross section (perpendicular to the leading edge) provided the following results:

(1) Laminar flow was maintained up to the highest possible Reynolds numbers:  $R = 17 \times 10^6$  at  $M = 2.5$ ,  $R = .25 \times 10^6$  at  $M = 3.0$ , and  $R = 20 \times 10^6$  at  $M = 3.5$ .

(2) The minimum total drag coefficients measured near the trailing edge of the wing ( $x = .97 c$ ) were close to twice the friction coefficient of a flat plate at  $M = 2.5$  and  $3.5$  and about 2.4 times  $C_{f_{lam \text{ plate}}}$  at  $M = 3.0$ .

(3) Optimum total suction coefficients were below  $3.0 \times 10^{-4}$  at  $M = 2.5$ , near  $4.0 \times 10^{-4}$  at  $M = 3.0$  and near  $3.0 \times 10^{-4}$  at  $M = 3.5$ .

(4) The theoretical laminar boundary layer development at typical suction distributions provided crossflow Reynolds numbers near the trailing edge up to 250 with laminar flow and values up to around 300 with low total drag coefficients.

(I) Conclusion (continued)

(5) The model was sensitive to suction. Two surfaces with different slot widths were tested. The narrow slots (first tests) provided better results at  $M = 2.5$ ; the wider slots (second tests) were better at  $M = 3.5$ .

b. BOUNDARY LAYER TRANSITION MEASUREMENTS ON SWEEP WINGS AT SUPERSONIC SPEEDS

E. E. Groth

(A) Summary

Boundary layer transition measurements were conducted in AEDC Tunnel E-1 on two-dimensional swept wings of 24, 36 and 50° sweep at Mach numbers between 2.5 and 5.0. Two models were built; one had a 3-percent-thick biconvex section, and the other section was a combination of a straight wedge with a biconvex section. The test results showed a strong dependence on the leading edge bluntness. The measured reduction of transition length Reynolds number due to sweep was of the same order as obtained on blunt flat plate models from earlier NASA measurements. The effect of the two different airfoil sections on transition was negligible.

(B) Notation

c	wing chord in flow direction, $c = \frac{9.45}{\cos \Lambda}$ (in.)
x	lengthwise coordinate measured in flow direction
$x_T$	distance to transition
Q	local resultant potential flow velocity
$Q_\infty$	freestream velocity
$\theta$	momentum thickness in streamline direction
$R_\infty^{(1)}$	$= Q_\infty / \nu_\infty$ , unit Reynolds number
$R_T$	$= x_T R_\infty^{(1)}$ , transition Reynolds number
$R_\theta$	$= \theta Q / \nu$ , momentum thickness Reynolds number
$R_{0.1}$	$= n_{\max} \delta_{0.1} / \nu$ , crossflow Reynolds number
$n_{\max}$	maximum crossflow velocity
$\delta_{0.1}$	height in boundary layer where crossflow velocity $n = 0.1 n_{\max}$
$\Lambda$	sweep angle

(C) Introduction

The available information on boundary layer transition on swept wings at supersonic speeds is rather small. A few tests conducted on flat swept surfaces (References 113 & 114) showed a reduction of the transition Reynolds

(C) Introduction (continued)

number with increasing sweep angle. A theoretical analysis (References 114 and 115) confirmed this trend by computing the local flow conditions aft of the detached shock wave which develops ahead of the blunt leading edge of a swept wing. An additional reduction of the transition Reynolds numbers on swept wings seemed to be caused by the boundary layer crossflow at the blunt leading edge. Since any curved airfoil section on a swept wing causes additional crossflow components along the whole wing chord, a wind tunnel program was conducted at AEDC Tunnel E-1 for the purpose of investigating the effect of two different airfoil sections on boundary layer transition at various sweep angles and Mach numbers.

(D) Description of the Model and Its Instrumentation

Since the original purpose of the tests was to provide boundary layer transition data for the 36° swept suction wing (Chapter C-a above), the model had the same cross section as this suction wing. The upper surface was a 3-percent-thick biconvex section; the lower surface was flat with an 11.84° bevel angle at the leading edge (both values measured perpendicular to the leading edge). The sides of the model were cut off in such a way that the model could be rotated about its central mounting sting to any sweep angle between 24 and 50°.

In order to investigate the effect of crossflow on boundary layer transition, a second model of the same planform and a modified airfoil section was built. The second model had a straight wedge section over the first 17 percent chord, followed by a biconvex section of slightly larger curvature to match the total thickness ratio of the first model. The actual coordinates of the two sections are defined by the following equations:

Biconvex Section

$$y = 0.06 x (1 - x)$$

Modified Section

$$y = 0.045 x$$

$$0 \leq x \leq 0.16667$$

$$y = 0.0675 [x(1 - x) - 0.02778]$$

$$0.16667 \leq x \leq 0.83333$$

$$y = 0.045 (1 - x)$$

$$0.83333 \leq x \leq 1.00$$

The coordinates  $x$  and  $y$  are made nondimensional by the chord length ( $c = 9.45$  inches, measured perpendicular to the leading edge).

Since the bottom surface had a steeper slope than the upper side near the leading edge, it was considered possible that the unsymmetric flow field near the leading edge at zero degree angle of attack might affect the boundary layer development on the test surface. Arrangements were therefore made to test both models at angles of attack at which the pressures on the top and bottom surfaces were equal near the leading edge. This angle was  $\alpha = -4.20^\circ$  for the biconvex section and  $-4.63^\circ$  for the modified one, both angles measured perpendicular to the leading edge.

Transition was measured with a movable total head probe. For the observation of possible spanwise effects, three probe heads were mounted on a holding fixture and moved simultaneously along the wing. The position of the probe heads was adjustable in chord and spanwise directions. Pressure transducers were located inside the housings close to the probe tips so that the time



(D) Description of the Model and Its Instrumentation (continued)

lag of the pressure readings could be neglected. Reference pressures for the transducers could be provided by a total head probe outside the boundary layer or by some outside source, such as tunnel freestream static pressure or vacuum. Since the moving mechanism for the probes was located in a fixed position in the center of the tunnel, the individual probe heads had to be built in such a way that they could follow the curved wing surface at both angles of attack. The probes were held against the surface by a magnet. The heads were movable around a pivot point, and the height above the surface was self-adjusted by a shaft mounted in ballbearings. The moving mechanism was available from previous, similar tests conducted by ARO, Inc. (Reference 116).

The model was equipped with three rows of static pressure orifices for checking the surface pressure distribution. A surface spray suitable for blowdown tunnel operation was developed at ARO and used as an alternate method for detecting transition.

Two sketches of the model, its instrumentation and its mounting in the tunnel are presented in Figures 92 and 93, two photographs in Figures 94 and 95. The shapes of the biconvex and modified airfoil sections are compared in Figure 96; the selected spanwise stations for the three probe heads at the three sweep angles of 24, 36 and 50° are shown in Figure 97.

(E) Results of the Transition Measurements

A complete description of the tests, the recording and evaluation of the transition traces from the pitot probes and the test results are presented by S. R. Pate, project engineer at ARO, Inc., in Reference 91. Since the report was not available in time to be included in this place, some of the test results are submitted and discussed in this chapter.

Figures 98 to 100 present the transition Reynolds numbers  $R_T$  vs freestream unit Reynolds number  $R_\infty^{(1)}$  per inch for the three sweep angles of 24, 36 and 50° and Mach numbers 3.0 and 4.0 and the two airfoil sections.  $R_T$  is defined by

$$R_T = x_T R_\infty^{(1)} = \frac{x_T Q_\infty}{\nu_\infty}$$

where  $x_T$  and  $Q_\infty$  are measured in flow direction. Station  $x_T$  is defined as the beginning of transition, i.e., the point where the chordwise trace of the total pressure near the surface starts to deviate from its trend in laminar flow (for details see Reference 91). The local Reynolds number at station  $x_T$  was not much different from the freestream or 50 percent chord value at  $\alpha = 0^\circ$ ; the largest discrepancy occurred at the stagnation point where  $R_{\text{stagn}}^{(1)}$  was less than 10 percent larger than  $R_\infty^{(1)}$  for the sweep angles and Mach numbers under consideration.

All measurements show a spanwise variation of transition; the upstream portion of the swept wing had larger transition lengths than the downstream portion. The increase of transition Reynolds number with  $R_\infty^{(1)}$  is linear in log-log scale, except for a few data at 50° sweep. The exponent  $n$  in

(E) Results of the Transition Measurements (continued)

$$R_T \sim [R_\infty^{(1)}]^n$$

varied with the test condition; it is plotted versus sweep angle in Figure 101 for the three cases presented in Figures 98 to 100. At  $\Lambda = 24$  and  $36^\circ$ , the values of  $n$  scattered around the value of 0.5, which occurred frequently at flat plate measurements;  $n$  was considerably lower at  $\Lambda = 50^\circ$ .

The variation of  $R_T$  with Mach number (Figures 98 and 99) was small; slightly lower values were recorded at  $M = 4.0$  than at 3.0. Reference 116 shows nearly constant  $R_T$  values on a hollow cylinder in this Mach range. The modification of the airfoil section (Figures 98 and 100) had practically no effect on transition at  $M = 3.0$ .

The effect of sweep is shown in Figures 102 to 104, where  $R_T$  is plotted versus  $\Lambda$  for the three cases of Figures 98 to 100 at two values of the unit Reynolds number,  $R_\infty^{(1)} = 0.3$  and  $0.6 \times 10^6$ . Included for comparison are the results of Reference 114 where  $\frac{(R_T)_\Lambda}{(R_T)_{\Lambda=0}}$  was plotted versus  $\Lambda$  for a swept plate with

a leading edge thickness of  $b = 0.005$  inch. The values of  $R_T$  for zero sweep were selected so that the curves from Reference 114 matched the present test results obtained with probe number 1. The variation of  $R_T$  with sweep angle of the present test program agrees rather well with the measurements of Reference 114.

The exact values of the leading edge thicknesses of the present models were checked by ARO personnel and the following values were obtained:

<u>Near Probe</u>	<u>Biconvex Model</u>	<u>Modified Section</u>
1	0.0060	0.0065
2	0.0070	0.0070
3	0.0080	0.0075-0.0080

The spanwise variation of  $R_T$  measured in the present test program can be explained by this spanwise increase in leading edge thickness,  $b$ . The increase of  $b$  has two consequences: (1)  $(R_T)_{\Lambda=0}$  increases with sweep (e.g., References 114 & 116), although it might be negligible at  $R_b = bR_\infty^{(1)} \sim 3000$  and the rather large bevel angles (Figure 24, Page 66 of Reference 116); (2) the ratio  $\frac{(R_T)_\Lambda}{(R_T)_{\Lambda=0}}$  decreases with increasing  $b$ , as shown in Reference 114. According

to this reference,  $R_T$  is reduced at  $M = 3.0$  by about 5 percent at  $\Lambda = 24^\circ$ , by 24 percent at  $\Lambda = 36^\circ$  and by 33 percent at  $\Lambda = 50^\circ$ , when the leading edge thickness is increased from the value 0.005 to 0.007 inch. The present test points of Figures 102 to 104 agree with these reductions fairly well.

(E) Results of the Transition Measurements (continued)

The present tests seem to prove that boundary layer transition on a swept wing with supersonic leading edge is primarily determined by the bluntness of the leading edge. The crossflow which develops at the rounded nose has a stronger influence on transition than the crossflow resulting from the pressure distribution over the airfoil section.

This fact seems to be in agreement with the results of theoretical laminar boundary layer calculations which were conducted at  $M = 3.0$ ,  $\Lambda = 24, 36$  and  $50^\circ$  for wings with infinitely sharp leading edges. The basic results of the calculation, the crossflow Reynolds number  $R_{0.1}$  and the streamwise momentum thickness Reynolds number  $R_\theta$ , both divided by  $\sqrt{R_c}$  where  $c$  is the reference chord length in flow direction, are plotted in Figure 105 for the three sweep angles. Introducing the chord length of the present tests

$$c = \frac{9.45}{\cos \Lambda} \text{ (in.)}$$

results in crossflow and momentum thickness Reynolds numbers which are plotted versus unit Reynolds number  $R_\infty^{(1)}$  per inch in Figures 106 to 108 for the three sweep angles. The test results from probe 1 (Figure 98) are included, too. It follows from these curves that the experimental transition locations occurred at the following values of  $R_{0.1}$  and  $R_\theta$ :

$\Lambda$ (deg)	$R_{0.1}$	$R_\theta$
24	160-140	800-1100
36	140-120	700-1000
50	120-80	650-800

The first values of  $R_{0.1}$  and  $R_\theta$  occur at low unit Reynolds numbers [ $R_\infty^{(1)} \sim 0.3 \times 10^6$ ], the second values at  $R_\infty^{(1)} \sim 0.8 \times 10^6$ . The values of  $R_{0.1}$  and  $R_\theta$  for  $\Lambda = 24^\circ$  might be high enough to cause transition; at  $\Lambda = 36^\circ$  and  $\Lambda = 50^\circ$  the additional crossflow contribution from the blunt leading edge seems to be necessary to cause transition.

(F) Conclusions

Boundary layer transition measurements on swept wings at supersonic speeds provided the following results:

(1) The transition Reynolds number  $R_T = x_T R_\infty^{(1)}$ , where  $x_T$  and  $R_\infty^{(1)}$  are determined in freestream direction, is reduced with increasing sweep angle. The amount of the reduction depends primarily on the bluntness of the leading edge. The effect of the airfoil section is of secondary order.

(2) The transition Reynolds number increases with unit Reynolds number; the amount of the increase becomes smaller with increasing sweep angle.

(F) Conclusions (continued)

(3) The variation of  $R_T$  with Mach number is small.

(4) Theoretical boundary layer calculations on models with infinitely sharp leading edges provide crossflow Reynolds numbers and momentum thickness Reynolds numbers at the measured transition stations which seem to be too small for causing transition. This confirms the predominance of the leading edge thickness on transition.

## CHAPTER D. INVESTIGATION OF LAMINAR FLOW CONTROL AIRFOILS SWEPT BEHIND THE MACH ANGLE

### a. LOW DRAG BOUNDARY LAYER SUCTION EXPERIMENTS ON A 72° SWEPT WING MODEL AT MACH NUMBER 2.0 AND 2.25

J. Goldsmith

#### (A) Summary

An investigation was made to determine the effectiveness of combining the advantages of laminar suction with sweepback in excess of the Mach angle for the purpose of obtaining low drags on supersonic airfoils. This initial investigation was limited to that portion of a wing over which the flow could be considered two-dimensional in nature, i.e., the region where the flow field was similar to that of an infinite swept airfoil. Calculation of the drags for such an airfoil indicated encouragingly low drags and a wind tunnel model simulating a long swept airfoil was designed for Mach 2.0 and tested at Mach 2.0 and 2.25 in order to confirm the results of the calculations. Although the measured total drags were somewhat higher than the calculated values, they were respectably low ( $C_{D_t} < 1.4 \times 10^{-3}$  at  $C_L \cong 0.068$ ) for upper wing surface only, and it is clear that laminar flow is possible for supersonic wings swept behind the Mach cone. The approximate lift coefficient of 0.068 was determined from measured pressures on the upper surface and an estimated lower surface pressure distribution. Its value was less than predicted, but there is no indication that it could not be increased to a  $C_L = 0.09$  or better by increasing the angle of attack or design camber of the airfoil. Calculations indicated that the airfoil would be supercritical (supersonic velocity component perpendicular to the leading edge) at Mach 2.25, but because the lift coefficient was lower than predicted the measured flow was everywhere subcritical at this higher Mach Number, and the measured total drag coefficients ( $C_{D_t} < 1.6 \times 10^{-3}$ ) indicated laminar flow.

#### (B) Notation

a	velocity of sound
c	wing chord measured parallel to flow direction (c = 33 in.)
c'	wing chord measured perpendicular to leading edge (c' = 10 in.)
d	suction metering hole diameter
$C_D$	drag coefficient
$C_{D_s}$	equivalent suction drag coefficient
$C_{D_t}$	total drag coefficient
$C_{D_w}$	wake drag coefficient
$C_L$	lift coefficient
$C'_L$	lift coefficient based on flow perpendicular to leading edge

$C_W$	suction mass flow coefficient
$e$	exponent for use in wake drag correction (defined in Part M)
$f_o^*$	$= \frac{\rho_w f}{\rho_\infty Q_\infty} \sqrt{R_c}$
$f$	suction velocity at airfoil surface for (equivalent) continuous suction
$F_1$	chordwise momentum thickness factor (defined in Part M)
$F_2$	spanwise momentum thickness factor (defined in Part M)
$H_u$	boundary layer shape factor for the $u$ component profile $H_u = \delta_u / \delta_{uu}$
$k_L$	limit constant for empirical wake crossflow correction
$k_0$	constant for empirical wake correction that determines slope at $\delta_{ss}^* / K_s = 0$
$k_s$	factor to make wake correction independant of $(V/U)_{te}$
$M$	Mach number
$n$	boundary layer velocity component perpendicular to potential flow direction
$n_{max}$	maximum boundary layer crossflow velocity
$P$	pressure
$\Delta P$	pressure decrement with respect to $P_\infty$ ( $\Delta P = P_\infty - P$ )
$q$	resultant boundary layer velocity
$q_\infty$	dynamic pressure at infinity ( $q_\infty = \rho_\infty Q^2 / 2$ )
$Q$	resultant potential flow velocity
$R_c$	airfoil Reynolds number ( $R_c = Q_\infty c / \nu$ )
$R_{0.1}$	crossflow Reynolds number ( $R_{0.1} = n_{max} z_{0.1} / \nu_1$ )
$s$	boundary layer velocity component in streamwise direction (parallel to $Q$ )
$s'$	perpendicular distance along airfoil surface from airfoil leading edge
$u$	boundary layer velocity component perpendicular to leading edge
$\Delta U$	velocity increment relative to freestream velocity ( $\Delta U = U - U_\infty$ )

$V$	potential flow velocity component parallel to leading edge ( $V = V_\infty$ )
$v$	boundary layer velocity component parallel to leading edge
$w$	slot width
$x$	chordwise distance in streamwise direction
$x'$	chordwise distance perpendicular to leading edge
$y$	spanwise coordinate perpendicular to streamwise direction
$y'$	spanwise coordinate parallel to leading edge
$z$	distance perpendicular to airfoil surface or vertical coordinate
$z_{0.1}$	boundary layer height to point where $n = 0.1 n_{\max}$ (largest distance)
$\alpha$	angle of attack
$\alpha'$	angle of attack for flow component perpendicular to the leading edge
$\gamma$	metering hole spacing
$\delta_n$	$= \int_0^{\delta} \frac{\rho n}{\rho_1 Q} dz$
$\delta_{nn}$	$= \int_0^{\delta} \frac{\rho n^2}{\rho_1 Q^2} dz$
$\delta_{ns}$	$= \int_0^{\delta} \frac{\rho n s}{\rho_1 Q^2} dz$
$\delta_{ss}$	$= \int_0^{\delta} \frac{\rho s}{\rho_1 Q} \left(1 - \frac{s}{Q}\right) dz$
$\delta_{ss}^*$	$= \frac{\delta_{ss}}{sC} \sqrt{R_C}$
$\delta_{uu}$	$= \int_0^{\delta} \frac{\rho u}{\rho_1 U} \left(1 - \frac{u}{U}\right) dz$
$\delta_{vu}$	$= \int_0^{\delta} \frac{\rho u}{\rho_1 U} \left(1 - \frac{v}{V}\right) dz$
$\delta_{vu}^*$	$= \frac{\delta_{vu}}{C} \sqrt{R_C}$
$\theta$	sweep angle ( $\theta = \cos^{-1} 0.3 \approx 72.5^\circ$ )
$\rho$	density
$\nu$	kinematic viscosity

### Subscripts

a	corresponding stagnation condition for isentropic compression
c	corrected for crossflow in wake
i	incompressible
n	based on n component of velocity
r	based on resultant local velocity
s	based on s component of velocity
u	uncorrected for crossflow in wake <u>or</u> based on u-component of velocity
v	based on v component of velocity
$\infty$	freestream conditions at infinity
l	outer edge of the boundary layer
te	trailing edge of airfoil
w	at wall or airfoil surface

### (C) Introduction

Although the application of laminar flow control (or, briefly, LFC) at supersonic speeds is still in its infancy, sufficient work has been done to show that significant reductions in skin friction are clearly possible. It is well known, however, that the proportion of friction drag to total drag is generally lower at supersonic velocity than at subsonic velocity. The overall drag improvement obtained by reduction of skin friction as a single improvement is necessarily lower, therefore, in supersonic flows. There is an associate advantage, however, which makes the application of suction particularly attractive at supersonic speeds; namely, the wing area can be increased by a considerable factor without appreciably increasing the zero lift drag of the complete airplane. This can result in a lower wing loading, greater wing span, or an airfoil with lower percent thickness (for a given span) or a combination of all three. In such cases the increase in wing area can result in reduced wave drag due to lift or thickness.

If sweep in excess of the Mach angle is incorporated in the design of a supersonic wing, the zero lift wave drag can be completely eliminated along the portion of the span where the flow may be considered of a two-dimensional nature. The advantages of sweep as a single element for drag reduction must be viewed with caution, however, since the aspect ratio is necessarily low for highly swept wings, and the reduced wave drag may be offset by increases in induced drag unless the wing loading is correspondingly reduced. Stated in another way, the span must remain essentially constant for constant induced drag so that the lower aspect ratio associated with high sweep angles leads to a larger wing area if the induced drag is to remain the same. This required increase in wetted area makes the application of laminar flow control especially profitable for highly swept wings.



(C) Introduction (continued)

The drag reductions due to sweep also depend on the thrust due to so-called "leading edge suction." In practice, it is not always easy to achieve this leading edge suction on highly swept wings, primarily because of separation near the leading edge. The application of laminar flow control to highly swept wings requires heavy suction in the leading edge region. This suction, combined with a typical laminar flow pressure distribution, might reasonably be expected to prevent any tendency toward leading edge separation.

The combination of high sweep angles and LFC, therefore, is expected to be doubly potent as a means of reducing the drag at supersonic speeds. In addition, the conversion of energy to shock waves is theoretically reduced so that this design combination could very well be a partial solution to the very important problem of sonic boom.

This report describes an investigation of laminar flow control for airfoils swept behind the Mach cone. This initial investigation was concerned primarily with the basic characteristics of infinite swept airfoils which have all isobars parallel to the leading and trailing edges of the airfoil. The infinite swept wing bears the same relation to an actual finite swept wing as the two-dimensional airfoil does to a finite straight wing. It represents a limiting condition which the performance of the finite wing may approach but never quite reaches due to root and tip effects. The finite wing and associated three-dimensional effects are to be covered in a future investigation, but in the present program it was desired to avoid the three-dimensional difficulties that occur at the ends of a swept wing panel and to concentrate on determining the basic characteristics of an infinite laminar suction airfoil swept in excess of the Mach angle.

The investigation began with a brief study of the requirements of the suction airfoil swept behind the Mach cone. This study was primarily for the purpose of determining the probable desired sweep angles, lift coefficients, and other airfoil characteristics. Since the airfoil requirements were unusual, a special airfoil shape was developed for use on highly swept wings. The drag was then estimated for such an airfoil, assuming continuous laminar suction was applied, and the results were found to compare favorably to those of a straight biconvex suction airfoil when allowance was made for the fact that the swept airfoil had no wave drag. Finally, a wind tunnel model was designed, built and tested to verify the possibility of obtaining low drags. The infinite two-dimensional flow characteristics of the airfoil model were simulated by mounting a finite length wing on a plate which was contoured in such a manner that its pressure field duplicated the pressure field generated by a forward extension of the airfoil section. Additional description of the model is given in the succeeding sections.

(D) Sweep Characteristics - Requirements for Shockless Flow

For finite span airfoils which have sufficient sweep so that none of the flow components exceed sonic velocity in the plane perpendicular to the isobars, it is possible to derive certain relations which are nearly exact. These relations are subject only to the degree of approximation encountered in the derivation of the well-known supersonic flow equations or in tables such as given in reference 117. The relations for infinite swept wings are quite simple because the component of velocity along the span is constant, and velocity and

(D) Sweep Characteristics - Requirements for Shockless Flow  
(continued)

pressure changes occur only in the chordwise direction. In addition, if the chordwise component of velocity remains subsonic, shocks will not form even though the resultant of the spanwise and chordwise components is supersonic. The charts in Figures 109, 110, and 111 show the limits for shockless flow for infinite span swept wings at various freestream Mach numbers. The points in these figures represent the condition where the chordwise component of velocity is exactly equal to the local velocity of sound. The distinction between the Mach number of the airstream at infinity ( $M_\infty$ ) and the local resultant Mach number ( $M_r$ ) should be carefully noted. The results are plotted with  $M_r$  as the independent variable since this is the parameter from which the remaining variables are most easily determined. The subscript "a" refers to adiabatic (also isentropic) stagnation conditions.

Two things, in particular, should be noted from inspection of these charts. The first is that there are limiting values for local Mach number ( $M_r$ ) and pressure decrement ratio ( $\Delta P/P_\infty$ ) for shockless flow at each freestream Mach number. This limit, of course, corresponds to the case of ninety degrees of sweep. The second is that the slope of the pressure decrement ratio curves is less for high Mach numbers than for low Mach numbers; consequently, at higher Mach numbers a greater increment in sweep angle (in excess of the Mach angle) is required to compensate for a fixed increment in pressure due to airfoil thickness or lift changes. The lift of the airfoil is limited, therefore, if full advantage of the sweep effects is to be taken. It is because of this limitation that the wing loadings for airplanes employing highly swept wings will necessarily be low. This of course, makes LFC especially advantageous.

It is recognized that it may be more economical sometimes to permit slightly supersonic chordwise components of velocity at the higher speeds, but the calculation of the limitations becomes considerably more complicated under these circumstances. Also, LFC has a better chance of working in a shockless airstream. The design procedure, therefore, was to use the calculated critical velocity as given in the figures as the design criterion.

(E) Compressibility Corrections

The design of an airfoil shape for highly swept wings and the calculation of the airstream boundaries which simulate an infinite extension of a finite length wing depend upon the calculation of a two-dimensional potential flow field about the airfoil section taken in the chordwise direction (perpendicular to the isobars on the swept airfoil). These calculations are easily performed with the aid of currently available automatic computer programs for the case of incompressible flow (Reference 118). The component of freestream velocity perpendicular to the isobars for wings swept past the Mach cone would be expected to correspond to a two-dimensional Mach number ( $M_{u_\infty}$ ) in the category of 0.5 to 0.8. Such values exceed the range in which the flow may be considered incompressible, and an appropriate compressibility correction must be chosen from the various theoretical or empirical corrections available. The constant spanwise component of velocity can be completely ignored in this correction, so that the correction proceeds on the basis of the velocities and Mach numbers as observed in the plane that is perpendicular to the leading and trailing edges of the wing.

(E) Compressibility Corrections (continued)

Some of the well-known compressibility corrections at  $M_{u_\infty} = 0.6$  are shown in Figure 112, together with a modified Göthert correction which will be described shortly. It is seen that the variation of the  $\Delta U/U_\infty$  for the various methods becomes considerable as the compressible velocity approaches the velocity of sound. The correction at this point is used to determine the maximum permissible incompressible velocity ratio ( $U/U_\infty$ ) that is permitted in the airfoil design. Since it is very desirable to have subcritical flow (two-dimensional component) on a laminar flow wing, the Spreiter and Alksne correction (reference 119) was employed to determine the maximum incompressible velocity ratio for the subject airfoil.

For the calculation of the outer field near the airfoil, however, other factors come into play, so that it is not convenient to use the Spreiter and Alksne correction for this purpose. The chosen compressibility correction must meet certain requirements if it is to be incorporated in the currently available computer programs for calculation of the flow field past an airfoil:

- (1) The accuracy of the velocity correction must be acceptable throughout the complete velocity range from zero to nearly sonic velocity (corrected value).
- (2) There must be a unique solution of the correction corresponding to any incompressible velocity -- even those that correspond to supersonic compressible velocities.
- (3) The correction must account for changes in velocity and streamline pattern in the outer field as well as local velocity on the airfoil surface.

The compressibility correction of Spreiter and Alksne (Reference 119) has three drawbacks which eliminate it as the proper choice for this program:

- (1) the correction becomes indeterminate for certain values of  $\Delta U_1/U_\infty$  due to an infinite slope for the correction curve.
- (2) the correction does not account for the change of slope of the streamlines; and
- (3) zero incompressible velocity does not give zero compressible velocity (although Spreiter's correction is closer than others in this respect).

The well-known Karman-Tsien correction eliminates the first objection given above, but the other two objections are still present. The Göthert compressibility correction (Reference 120) accounts for the changes in slope of the streamlines, but otherwise is nothing more than an extension of the very simple linear correction of Prandtl. The changes in slope of the streamlines is made consistent with the velocity and lift changes by first transforming the airfoil to a new airfoil with vertical coordinates and angle of attack multiplied by the factor  $\sqrt{1 - M_{u_\infty}^2}$ . The streamlines and velocities are determined for this thinner airfoil, and the resulting flow field is then transformed back to the original

#### (E) Compressibility Corrections (continued)

airfoil configuration. In this second transformation the velocity increments as determined for the thin airfoil are increased by the factor  $1/(1 - M_{u\infty}^2)$  or  $1/\sqrt{1 - M_{u\infty}^2}$  more than the straight Prandtl correction. This accounts for the use of the factor  $\sqrt{1 - M_{u\infty}^2}$  in the abscissa when the Göthert correction is compared with other methods.

In order to meet the three correction requirements cited previously the Göthert correction was chosen as a basic correction and an adjustment function was added to the correction resulting in a modified Göthert correction. The choice of the Göthert correction came about chiefly because it accounts for streamline slopes as well as velocities. The adjustment function is shown in Figure 113. It is a parabolic function with  $M_{u\infty}^2/(1 - M_{u\infty}^2)$  assigned as the proportionality constant so that the total modified correction passes through -1.0, -1.0 (Figure 113); i.e., so that zero incompressible velocity results in zero compressible velocity. This adjustment results in improved accuracy near the stagnation points and avoids the occurrence of negative velocities which would cause difficulty in the computer programs. The adjustment is negligible when  $\Delta U/U_i = 0$  and this is clearly desirable since the modified correction is accurate for small increments. In the region of large positive values of  $\Delta U/U_i$  the modified Göthert correction is more accurate than the unmodified version since it tends to give results more closely in agreement with the more accurate Spreiter-Alksne or Karman-Tsien corrections. Comparison is shown with the former of these.

#### (F) Airfoil Characteristics

It is well known that the characteristics of a swept airfoil are such that the airfoil responds to the component of velocity that is perpendicular to the leading and trailing edges of the airfoil. Also, the cross sectional shape of the airfoil taken in the corresponding perpendicular plane is the shape that is significant. The design of the airfoil shape may be treated, therefore, as though the flow field were two-dimensional, having a freestream velocity equal to  $U_\infty$ . Due to the high sweep angles needed at supersonic velocity, however, the airfoil requirements are found to be unusual when compared to an unswept airfoil. In addition, the application of laminar flow control results in added restrictions and since the well-known conventional airfoil shapes do not meet these requirements or restrictions, an airfoil shape was developed to satisfy the special requirements of the highly swept LFC airfoil.

The development of this special airfoil shape was done by trial and error, utilizing the calculation procedure described in Reference 118. This calculation is a modified version of Theodorsen's airfoil calculation given in Reference 80. The resulting airfoil shape and its incompressible velocity distributions at various incompressible lift coefficients are shown in Figure 114. The angle between the airfoil surfaces at the trailing edge is seen to be relatively large. This feature provided adequate internal volume in this region at full-scale dimensions so that suction ducts could be installed. The second special feature is that concave curvature was eliminated except for a small region on the airfoil undersurface near the trailing edge. This feature is helpful in stabilizing the laminar boundary layer. The airfoil section is 10% thick in the two-dimensional plane. This is relatively thick for a high speed airfoil, but has the advantage of adequate internal volume for suction ducts. Added thickness also results in an increased range of lift coefficients for which

#### (F) Airfoil Characteristics (continued)

there are no undesirable peak velocities at the nose of the airfoil. For the velocity distributions shown in the figure, the incompressible two-dimensional lift coefficients vary from 0.52 to 0.88 based on flow components perpendicular to the airfoil leading and trailing edges. The corresponding two-dimensional compressible lift coefficients and three-dimensional swept airfoil lift coefficients (Mach 2.0 and 72.5° sweep) are given in Table V. This table gives several values, depending upon the compressibility correction that is adopted. The range of lift coefficients is seen to be equal to the mean lift coefficient  $\pm 28\%$ . This should allow for an adequate range of flight conditions for which no large peak velocities occur. The peak at the nose of the undersurface at  $C'_{L} = 0.52$  in Figure 114 is expected to be about the maximum for which laminar flow can be maintained with reasonable suction.

It should also be noted that the flat top velocity distribution extends well aft so that a large lift coefficient can be attained without exceeding the critical velocity on the upper surface at the maximum angle of attack. The critical value of  $U/U_{\infty}$  may be determined from Figure 109 by dividing  $a/a_a$  at  $M_r$  by  $U_{\infty}/a_a$  at the same  $M_r$ . For the design point of  $M_{\infty} = 2.0$  and  $\theta = 72.5^\circ$  the critical velocity ratio is 1.575. The incompressible equivalent of this value is a function of the compressibility correction at  $M_{u\infty} = 0.6$  (see Figure 112), but as mentioned in the previous section, compressibility corrections are notoriously poor at the critical velocity and an incompressible equivalent of the critical velocity equal to 1.35 was adopted for the test point. This value corresponds approximately to the correction given by Spreiter and Alksne in Reference 119 with allowance for a slight margin of error. Its value was chosen to determine the critical velocity, not necessarily because it was thought to be most accurate, but rather because it was largest and, therefore, safest to use. On the other hand, the Karman-Tsien correction was employed to estimate the compressible velocity distribution for the boundary layer calculations. This correction represents a good average of the available correction schemes and was felt, therefore, to give a reasonably reliable correction for the velocities.

#### (G) Calculation of the Boundary Layer Development and Suction Requirements

The development of the boundary layer was calculated for the upper surface of the airfoil described in the previous section for several continuous suction distributions at an angle of attack of 0.15 degrees. The Mach number based on the perpendicular component of velocity ( $M_{u\infty}$ ) was assumed to be 0.6 for the calculations. The corresponding sweep angles are approximately 72.5° at  $M_{\infty} = 2.0$  and 78.25° at  $M_{\infty} = 3.0$ . The results were used to estimate drag coefficients and the corresponding limiting Reynolds numbers. These calculations employed an IBM 7090 program which is based on a computation procedure originally developed by Raetz (Reference 45). The suction distributions were determined by trial and error and were adjusted so that the crossflow Reynolds number  $Re_{0.1}$  did not exceed about 120 over the forward 70 percent of the airfoil, nor 300 to 400 in the last 30 percent of the airfoil except that rapid growth to higher values was permitted at the trailing edge. These limiting conditions were based on the results of subsonic experiments on swept suction wings as described in Reference 9. The resulting suction distributions were typical of swept wings with subsonic type pressure distributions requiring high suction near the leading and trailing edges of the airfoil, where the crossflow pressure gradients are large, and low suction in the midchord region, where the pressure is nearly constant. The results of some of these calculations are shown in Figures 115 to 118 and Table VI. The calculated suction requirements were rather high compared to straight or slightly swept airfoils. The reason, of course, is due to the high sweep angle.

(G) Calculation of the Boundary Layer Development and Suction Requirements (continued)

In addition, it was estimated that because of increased skin friction about 20 percent increase in suction would be required when suction through finite slots was substituted for continuous suction. On the other hand, the calculated wake drags are relatively small, and the theoretical wave drag is zero for the two-dimensional swept airfoil. The low values of these latter items should help to compensate for the increased equivalent suction drag. Despite the high suction drag, there is no question that the calculated drags were considerably less than those of a turbulent airfoil so that it was desired to obtain experimental verification of the results of the calculations. The experimental verification was done at the lower Mach number (2.0) because this choice resulted in a simpler model and the chances for success for these first experiments were greater. The principles involved could be proved equally as well at Mach 2.0 as at Mach 3.0.

(H) Outer Field Flow

In order to obtain basic experimental data on infinite swept LFC airfoils, a method of simulating such an airfoil had to be worked out. Because the chord Reynolds number was important, and also because reasonably large chords were necessary in order to install the suction system, the minimum chord of the model was limited. Since the size of wind tunnels was limited, it was impossible to test even finite airfoils with spans that were large compared to this minimum chord. For this reason the infinite extension of the span had to be simulated. One way of doing this was to mount the airfoil on a surface with contours that follow the same paths as the streamlines past an infinite swept wing. In this way the surface generated pressure waves identical to those that would be generated by the missing portions of the airfoil. It might be noted that a similar contouring of a fuselage at the wing root would extend the region of parallel isobars in the wing to the fuselage wall.

The coordinates of the contoured plate were calculated by adding the component of freestream velocity parallel to the leading edge to the velocities for a two-dimensional airfoil. This produced the spanwise slopes for the swept airfoil streamlines, and integration of these slopes produced the desired streamline paths.

The two-dimensional outer field was calculated for the airfoil described earlier at the mean test angle of attack, and resulting streamlines are shown in Figure 119. This flow field was machine-calculated by a program which extends the theory of airfoils to the outer field (Reference 118). Compressible effects were taken into account by calculating the streamlines and velocities for a thinner airfoil at a reduced angle of attack as is the practice for applying the Göthert compressibility correction. Then, the resulting flow pattern was transformed to the desired airfoil dimension and the modified Göthert correction (Figure 113) was applied to the velocity increments. When the spanwise component of the freestream resultant velocity was added vectorially, the three dimensional streamlines followed a crossflow pattern which depended only on the sweep and the two-dimensional field. The paths for several of these calculated streamlines is shown in Figure 120. The failure of the upper and lower streamlines to meet at the trailing edge in this figure is due to the circulation, which corresponds to the lift of the airfoil. In addition, air

#### (H) Outer Field Flow (continued)

passing near an airfoil tends to dwell near the stagnation regions. This occurrence, combined with the fact that the path is longer for the surface streamlines, results in greater spanwise flow for the surface streamlines. This latter point is brought out more vividly in Figure 121, where a portion of the required wall contours as viewed in the downstream direction is shown for the region near the leading edge of the airfoil. It is seen that only the streamlines passing very near the airfoil are subject to the excessive dwell that results in extra spanwise shift.

Wall contouring should theoretically extend to infinity. Limitation of contouring to a finite area, however, has an effect somewhat like limiting the span of a swept wing to something less than infinite, but the flow past the center of a long-span wing is very nearly identical to that past an infinite wing. Limitation of the contouring region is therefore not only a practical limitation, but thoroughly acceptable providing the limits are not cut so short as to simulate a wing span that is too short.

#### (I) Comments Concerning The Wind Tunnel Model

One of the significant characteristics of a swept wing is that the flow over the upper surface bends toward the perpendicular chordwise direction to such a degree that only a small portion of the span is contaminated by a turbulent wedge originating at the intersection of the wing leading edge with a fuselage or contoured surface. This characteristic is very helpful toward reducing the required spanwise extent of the LFC region on the upper surface of an experimental model. The extent of a satisfactory laminar region is shown in the upper sketch in Figure 122, and it is seen that the span of the airfoil need not be excessive.

On the other hand, the streamlines on the undersurface bend toward the leading edge. This is shown by lower sketch in Figure 122, and it is seen that an excessively large span is required in order to maintain laminar flow to the trailing edge. It is clear, therefore, that experiments on the lower surface of a highly swept suction model require a much higher aspect ratio. The compromise in model scale required to obtain this aspect ratio makes tests on the lower surface impractical for the selected sweep angle. This does not necessarily mean that such a sweep angle is excessive for an airplane, however, because the turbulent wedge does not occur if extensive laminar flow can be continued past the wing and fuselage juncture. In fact, the contamination wedge on the lower surface of the highly swept wing is a powerful argument in favor of the development of a laminar juncture. With the current state of the art, however, we shall be content with the calculated results for the lower surface. A rough check on the calculations is at hand, however, since experiments performed for the upper surface can be compared with calculations for the upper surface, and a similar order of accuracy should be applicable for the lower surface.

From Figure 122 (upper surface) it is seen that although the required span of an airfoil model is relatively short, the streamwise length is necessarily large. In addition, some additional length must be provided for wall contouring which simulates an extension of the airfoil. One can obtain an idea of how much contouring is required in the following manner. Consider that the contour plate extends ahead of the airfoil only as far as the point "p" in Figure 123. Then a

(I) Comments Concerning the Wind Tunnel Model (continued)

bow wave will emanate from point "p" since the flow will be at freestream velocity ahead of this point. The dashed lines show a three-dimensional wing which would also produce a bow wave through point "p", and it can be concluded that the termination of the contour plate at "p" very roughly stimulates an airfoil which changes abruptly at point "n", as does the dashed portion of the airfoil. The change in direction of the dashed lines at "n" is symbolic only and not necessarily realistic. For the case shown (Figure 123) the vertex of the simulated wing is more than four chordlengths (chord measured perpendicular to the leading and trailing edges) away from the contoured wall so that the flow past the wall may be considered reasonably close to two-dimensional, although not exactly. The location of point "p" was considered a satisfactory contour limit for the subject test model from a practical point of view (the test results, however, indicated some loss of lift probably occurred as a result of this termination). The point "p" is 50 percent chord upstream of the leading edge.

With these considerations in mind, a wind tunnel model was designed and built for testing in Tunnel A at AEDC. The dimensions of the test section of this tunnel is 40 inches square; and by choosing a configuration in which the wing was mounted on the contour plate and the plate supported by the wind tunnel walls slightly below the tunnel centerline (Figure 124), it was possible to arrive at a simulated model chord of 10 inches measured perpendicular to the leading edge. The term "simulated model chord" is used because the actual model chord extended downstream of the simulated trailing edge as shown in Figure 125 in order to obtain internal ducts for suction in this small size model. The upper surface of this trailing edge extension was contoured to match the stagnation streamline flow for the airfoil at the mean test lift coefficient so that it would have minimum influence at the design lift coefficient on the pressure distribution at outboard stations. The original airfoil contour was carried sufficiently far aft on the lower surface so that the pressures on the upper test surface were unaffected by the modified airfoil shape. The support plate for the wing was also contoured to streamline flow up to a similar aft position for the undersurface and all the way to the end of the airfoil extension on the upper side of the airfoil. Figure 126 shows the support plate with the skin removed and illustrates the general shape of this contouring.

The test area on the upper surface of the airfoil is similar to that given in Figure 122 and is indicated by the location of the slots as shown in Figure 127. In general, the ends of the slots lie along curves which follow the edges of contamination regions caused by turbulence originating at the ends of the first slot. Details of the slot design are given in Part (J) below. Suction could be controlled independently in each of seven separate suction regions, as shown in Figures 125 & 128. Other details of the model are shown in Figures 129 through 132. The chord in the streamwise direction was 33 inches for this model; the Reynolds number capability of the wind tunnel based on this chord at  $M = 2.0$  was about 25 to 26 million, which was quite adequate. As pointed out in the next section, however, this limit could not be reached due to limits in the model dimensions.



## (J) The Suction Slots

Experience with laminar suction through finite size slots has indicated that success in maintaining laminar flow is most likely to occur when certain design limitations are observed. One of these limitations is that the slot width should not exceed the height of the sucked layer by more than 20%. A general design rule has been to design the slot width equal to the height of the layer of air removed by that slot at the highest test Reynolds number. Secondly, the outer edge of the sucked layer should not extend too far up into the boundary layer; i.e., one should not depart too greatly from the condition which approximates continuous suction. A fair rule is that the suction layer height should not exceed the momentum thickness. At high Mach numbers there has also been an indication that the Mach number at the top of the sucked layer should not exceed about 0.60, but test data confirming this rule are limited at the present time. These last items result in a maximum permissible slot spacing. In addition, the slot Reynolds number is generally limited to about 120, but on supersonic models this has never been a problem since the densities in the sucked layer are so low. When these slot design "rules" are observed, it is usually possible to achieve laminar flow at the design Reynolds number. When they are not observed, experience has shown that laminar flow is usually possible if adequate suction can be applied, but only at some value of Reynolds number less than the design value.

For scaled-down models, one must also be concerned with dynamic similarity of the model to the full-scale airplane or airplane component. This simply means scaling down all full-scale dimensions, and testing at approximately the same chord Reynolds number. This scaling down is extremely difficult for small LFC models because of the machining limits for the models. Slots, for instance, could not be reliably made narrower than about 0.0035 inch at the time the model was constructed. Also, in regions of strong pressure gradients the slot spacing becomes small even at full scale, and reduces to a few thousandths of an inch for a 10-inch chord model. Prior to construction of the 72.5° swept wing model the closest slot spacing was 0.25 inch. For this model this dimension was reduced to 0.080 inch, or 0.27 inch in the streamline direction (see Figure 25), and slots as narrow as 0.003 to 0.0035 inch (made with an 0.003 inch saw) were employed. When these minimum dimensions were considered together with the rules cited above and checked against calculations of the boundary layer development, it became quite apparent that the Reynolds number for laminar flow would be limited by the model dimensions. Indications from conservative application of the "rules" was that 4 million Reynolds number was assured, and by stretching to the limits of the "rules" there was a possibility of 10 million. The slots were designed, therefore, on the basis that 10 million was possible.

The slot design rules discussed above were known to be effective for unswept or slightly swept slots, and it was assumed that they would also be applicable for highly swept slots. The same rules were used, therefore, to determine the slot widths and spacing for the 72.5° swept wing model. Departure from the usual procedure was required, however, for the calculation of the losses through the highly swept slots. An efficient application of laminar suction required metering of the suction through successive slots along the chord since the difference in internal and external pressure varied along the chord length. This metering was accomplished by installing holes between the suction slot chamber and the main suction chamber (see Figure 125) of such dimensions that the total suction losses for the desired airflow matched the internal and external pressure differential. Then, the hole selection

(J) The Suction Slots (continued)

required a knowledge of the slot losses. It has been conventional to assume the slots were two-dimensional laminar flow channels, and for such a channel the losses may be calculated (Reference 123). For the highly swept model, however, the spanwise flow was expected to have considerable influence on the slot losses; consequently, adjustments had to be made for this spanwise flow. The calculation of the slot losses was done by the method described in Chapter D, Section b, which takes the spanwise flow into consideration.

The resulting slot and hole dimensions are given in Table VII.

(K) Instrumentation of Model

Pressure taps were installed along three rows in the upper surface of the airfoil, located as shown in Figure 128 and Table VIII. There were originally thirteen pressure taps installed for each row although a number of them developed leaks or plugging before the model and tests were completed, as indicated in the table. The loss of some of these pressure taps is attributed to the difficulty of installing them satisfactorily in the cramped space of a suction model of such small dimensions. The plugging of the midspan pressure taps prior to the final experiments at  $0.75^\circ$  angle of attack was deliberate in order to achieve maximum test Reynolds number.

In addition, static pressure taps were installed in each of the seven suction chambers, and the stagnation temperatures were also measured in three of these chambers in order to supply the required information for the calculation of the equivalent suction drags for the model. The mass flow of air from each suction chamber was measured in separate flow measuring nozzles outside the tunnel. The stagnation temperature and the total (stagnation) and dynamic pressures were recorded for each nozzle so that the mass flow could be calculated.

All of the foregoing instrumentation has been "standard" for supersonic laminar flow models and was similar to (if not actually the same as) that used for the  $36^\circ$  swept wing experiments described in Section II, Part 2, Chapter C-a of this report. The measurement of the wake of the  $72.5^\circ$  swept airfoil, however, presented a different problem than for previous experiments. It has been customary to obtain many boundary layer profile readings in the wake. This has been accomplished in the past by judicious spanwise spacing of the total head tubes in the wake rake and has been successful because the boundary layer thickness was relatively large. For airfoils swept behind the Mach cone the situation does not permit a similar approach. In the first place, the boundary layer was expected to be extremely thin, for the calculations indicated momentum thicknesses of the order of 0.001 inch and total boundary layer thicknesses of perhaps 20 times this figure, or 0.020 inch. A dimension of 0.012 inch was about the closest to the surface that a total head measurement could be made with practical instrumentation; consequently, one could not be expected to obtain accurate profile shapes for wakes of these dimensions. But since the wake drag was calculated to be only a small portion of the total drag, it was felt that an approximate profile shape would be adequate and resulting errors would not appreciably limit the accuracy of the total drag. In view of these considerations, the wake rake shown in Figure 133 was built for the experiments. The first total head tube was located as near to the surface as practical and the remaining tubes were spaced vertically so that the bow waves of each tube would not interfere

(K) Instrumentation of Model (continued)

with the remaining tubes. The spanwise displacement could not be used on this model in order to reduce the vertical spacing because of the high sweep angle of the wing and the slots. When this sweep is in excess of the Mach angle, a spanwise displacement of the wake rake tubes either results in measurements which cross slots or else results in stagger to such an extent that many tubes are measuring the losses through the shock waves of others. For this reason the simple vertical rake was adopted. Initially, it was felt that the rake would only be used to determine whether or not laminar flow occurred and that the laminar boundary layer shape would be approximated. During the tests, however, the model developed boundary layers considerably larger than those predicted. Fortunately, the wake rake proved to be adequate for the measurement of these larger boundary layers.

(L) Experimental Measurements and Data Reduction

Tests were conducted in January 1963 at AEDC Tunnel A of the von Karman Gas Dynamics Facility of ARO, Inc., Tullahoma, Tennessee. S. R. Pate and J. S. Deitering of ARO were project engineers for these tests at this facility.

Tests consisted of observation of the wake profile to determine how it varied as the suction was adjusted in each of the separate suction chambers. The pressure and temperature data were recorded for several profiles varying from a thin laminar profile with strong suction to a thick laminar or possibly even turbulent profile for weak or zero suction. This process was repeated for several Reynolds numbers at each of three angles of attack at Mach 2.0. A limited number of runs were also made at Mach 2.25. Most of the data reduction was completed at the Tunnel A facility. The method was comparable to that of the data reduction for the supersonic flat plate and the  $36^\circ$  swept wing except for the correction to the wake drag for crossflow and for the variation of momentum deficit between the trailing edge and the freestream at infinity. These latter corrections were omitted in the ARO report (Reference 122) because the method of correction had not been worked out at the time the tests were conducted. Since the correction is always in the direction of reduced drag, the drags quoted in Reference 122 are necessarily pessimistic. The nature of the crossflow correction is given in the appendix, and this correction was applied to the results quoted here.

(1) Results of the Experiments

The results conducted at Mach 2.0 will be considered first. The results of the measurements of the drag components are shown as a function of the suction coefficient in Figures 134 through 136. The trend of these results was typical of those for laminar flow airfoils except that the equivalent suction drag was higher than usual due to the large suction rates required for laminar stability in a flow field having exceptionally strong crossflow pressure gradients. The exceptional pressure gradients, of course, were a direct result of the high sweep angle, which had to exceed the Mach angle for this type wing. These high suction requirements were predicted from calculations made in the early part of the investigation. The resulting relatively high suction drags were offset somewhat by the corresponding low wake drags since the wakes were very small at

(1) Results of the Experiments (continued)

high suction quantities (although not as small as the boundary layer calculations indicated). It might be well to point out at this time that a practical application of the sweep concept to an airplane would result in the use of a tapered swept wing in which the sweep angle at the trailing edge would be reduced somewhat at Mach 2.0. This local reduction of sweep would help to reduce the crossflow and consequently the suction requirements and equivalent suction drag for the trailing edge region. On the other hand the wake drag would increase somewhat because of the reduced suction, so that the overall tendency would be toward an equalization of the wake and suction drags.

The measured wake drags for the constant chord model (Figures 134-136) are based on wake measurements after they were corrected for crossflow. The crossflow correction employed was empirical, and the method of correction and basis for the method are described in Part (M). Briefly, the correction was required because the wake rake indicated a momentum deficit based on  $\delta_{ss}$ , which is the momentum thickness based on only one component of the flow. The use of  $\delta_{ss}$  correctly accounted for the velocity decrement in the wake, but the mass flow rate (by which the velocity decrement should have been multiplied to obtain momentum deficit) required modification due to the crossflow component. The modification was considerable at high sweep angles and was always in the direction of reduced mass flow. The reason for the modification can be seen in another way by inspecting Figure 137, in which a control volume is shown for a unit span length of a swept airfoil. Wake rake readings indicate that the mass flow rate out of the control volume is proportional to the streamwise velocity component, but it is seen that the crossflow component is in such a direction as to give flow back into the control volume and this results in a net reduction of the mass flow rate. This reduction of mass flow rate for a given streamwise velocity decrement can result in reductions of the momentum deficit and corresponding wake drags at 72.5° of sweep by as much as 60 percent, as shown in Part (M). The wake drag correction, although based on calculated results, is of necessity an empirical correction. Every effort was made to be conservative in applying this correction, as explained in the appendix (Part (M)), but the accuracy of the correction could be considered open to question. For this reason both the corrected results and those based on wake drags determined from  $\delta_{ss}$  are given as a function of Reynolds number in Figures 138 to 140 (part a of each figure is for corrected and part b for uncorrected data). The plotted points are the minimum measured total drags at each Reynolds number. Although only the wake drag was corrected, the suction drags also differ for parts a and b of each figure because the "optimum" suction coefficient at each Reynolds number changes with variation of the wake drag. The large magnitude of the wake correction is apparent from these figures, but comparison with the changes in the calculated drags due to crossflow corrections (given in Table IX) indicates that these large wake corrections are not unrealistic. The total drag coefficients for the model at 9 million Reynolds number were respectably low and, by comparison with the drag curves for the flat plates it may be seen that the flow was clearly laminar. The drag rise at Reynolds numbers greater than 9 million was a limitation due to the small scale of the model and is discussed fully in Part (J) above. It should not be considered a limiting Reynolds number for larger scale applications.

Figures 141 and 142 show typical variations of the measured average suction intensities as a function of the chordwise location. The distributions are typical of those for swept wings having subsonic type pressure distributions and the shapes agree reasonably well with the calculated suction distributions (Figures 116 or 141b). Comparison of the measured and calculated values

(1) Results of the Experiments (continued)

of the suction coefficient and the various drag components are given in Table X for  $\alpha = 0.15$ . It is seen that the measured  $C_{D_s}$  is less than the calculated one. This is due primarily because of a pessimistic estimate of  $P_g/P_\infty$  for the calculated suction drag (Table VI). The measured value of this pressure ratio averaged about 0.74 as opposed to the value of 0.648 given in the table. The measured wake drag coefficients are considerably larger than the calculated ones. This is a typical result for laminar flow experiments since drag calculations have always assumed continuous suction; but suction was accomplished through finite slots. The discrepancy in the wake drag is especially large for this model at 8-9 million Reynolds number, because at this Reynolds number the limits of efficient slot design have been exceeded as explained in Section (J). Typical wake profiles for the optimum suction conditions are shown in Figure 143. Although thicker than predicted, these profiles were still thin, Figure 143 also shows a typical variation of the profiles with change in suction.

Pressures were recorded for all runs on the upper surface of the airfoil at the three chordwise stations shown in Figure 128. Precise interpretation of the pressure measurements is difficult because the scatter that occurred at any given  $\alpha$  was large. Only a small portion of the scatter could be attributed to instrumentation although the measured pressures were of the order of only 1.0 psia. A greater portion of the scatter was a direct result of changes in the suction distribution. Figure 144 indicates the order of magnitude of the variation of some of the pressures with the suction coefficient. It is difficult to determine whether this trend of changes was due to the proximity of the slots, which had a local sink effect, or to the changes in boundary layer displacement thickness, which effectively changed the airfoil contour. Reducing the suction to zero was of no help because the airfoil, which was designed for suction, was then subjected to extreme crossflow (bordering, perhaps, on separation) in the region of the steep pressure rise near the trailing edge. By comparing the pressure distributions at a given constant suction coefficient (a moderate value of  $0.9 \times 10^{-4}$  was chosen for the reported results), the influence of suction can be minimized and some interesting trends can be observed.

Figure 145 shows a comparison of the measured pressure distributions at the three spanwise stations. It is seen that the pressure distribution was essentially two-dimensional in nature, although some local departures are seen to have occurred. Figure 146 shows the variation of pressure with angle of attack. For comparison, the dashed curve shows the calculated potential flow pressures corresponding to 0.15 angle of attack. It can be immediately observed that the variation with angle of attack was slight and that the design lift coefficient was not quite achieved. In Figure 147 the equivalent two-dimensional velocity distribution (corresponding to the measured midspan pressures) is shown in comparison with the potential flow calculations for  $\alpha' = -0.625^\circ$  and  $\alpha' = 1.50^\circ$  (modified G6thert compressibility correction). Although the latter angle corresponds to the angle for which the measurements were made, the plotted velocity distribution corresponds more nearly to that of the calculations for the former angle. Calculation of the lift coefficient for the measured velocities assuming undersurface velocities corresponding to  $\alpha' = -0.625$  and  $\alpha' = 1.5^\circ$  results in respective values of  $C'_L$  equal to 0.755 and 0.863. The potential flow value of  $C'_L$  at  $1.5^\circ$  as shown in Figure 147 is 1.011 so that only about 75% to 85% of the calculated lift was developed during the tests. The small change in pressure distribution with change in angle of attack would indicate that the influence of the contour plate combined with the fixed

(1) Results of the Experiments (continued)

trailing edge stagnation streamline had an overwhelming effect on the velocity distribution of the airfoil test panel. This is not an extraordinary result, considering the relative sizes of the contour plate and the airfoil. Although it was recognized that the variation of lift with angle of attack would be somewhat unrealistic, it was not realized that the effect of the fixed plate and trailing edge extension contours would be so overpowering. In view of the strong influence of the contour plate, it is also understandable that the lifts did not quite meet expectation, for the contour plate was limited in extent, by the size of the test section. The tunnel walls also acted as reflection planes at the ends of the contour plate. This resulted in simulation of an image of the contour plate and would tend to reduce the lift somewhat. Finally, no influence of the boundary layer was taken into account in designing the contoured plate or trailing edge extension. This boundary layer certainly had an influence on the flow field and might account for some of the loss in lift.

The discrepancies between the calculated and measured flow were not so large, however, that the experiments could not be considered successful. The pressure distributions were of the subsonic type with no apparent leading edge separation and a strong pressure rise near the trailing edge. The corresponding lift coefficient was still of considerable magnitude and the measured pressures corresponded everywhere to subcritical conditions. In addition, a small change in pressure distribution did result from the angle of attack changes -- enough, in fact, so that it was noticeably easier to establish laminar flow at the higher angles during the test program. Finally, and most important, the measured drags were low, and there was nothing in results of the experiments that would indicate that these drags would not remain low at higher (still subcritical) lift coefficients.

The results of the few experiments made at  $M_\infty \approx 2.25$  are given in Figures 148 & 149. The data are sparse because during the tests the wake readings indicated a very peculiar profile shape that seemed to be unresponsive to changes in suction quantity or suction distribution. Typical measured profiles at  $M_\infty = 2.25$  are shown in Figure 150 and may be compared with the profile for  $M_\infty = 2.0$  shown in Figure 143. The reason for the peculiar wake is not understood, but it was impossible to determine during the tests whether or not the flow was laminar or if changes in suction were advantageous. In order not to jeopardize the completion of the test program, only a limited number of test points were recorded, but they are probably not optimum conditions.

In spite of the strange wake profiles the drags were respectably low (Figure 149), although not as low as at Mach 2.0. A typical pressure distribution is shown in Figure 151, and the pressures, although very close to critical at some points, are seen to have been subcritical even though potential flow calculations indicated critical flow at this Mach number for the design lift coefficient. This development is not surprising, however, since the design lift coefficient was not achieved, as discussed previously. Little else can be said concerning the Mach 2.25 experiments except, perhaps, that it is clear that low drags can be maintained for velocity distributions very close to the critical values.

(M) Appendix -- Description of the Empirical Correction for the Wake Drag

The momentum thickness ( $\delta_{ss}$ ) as measured in the wind tunnel does not take the crossflow effects into account, and although these effects are small for slight or moderate sweep angles, they become rather large at high sweep angles. The crossflow component must be considered because it modifies the mass flow rate on which the momentum deficit should be based. In the section describing the  $36^\circ$  swept wing experiment (Section II, Part 2, Chapter C-a) it is shown that the wake drag for swept wings may be found from

$$C_{D_w} = \frac{2}{c} \left\{ (\delta_{uu})_{te} \frac{(U_{te})^e}{U_\infty} \cos^2 \theta + \frac{\rho_{te} U_{te}}{\rho_\infty U_\infty} (\delta_{vu})_{te} \sin^2 \theta \right\} \quad (1)$$

where  $e = H_u + 2 - (UM/Q)^2$  (2)

$$\delta_{uu} = \delta_{ss} + \frac{V}{U} (\delta_{ns} - \delta_n) + \frac{V}{U} \delta_{ns} - \left( \frac{V}{U} \right)^2 \delta_{nn} \quad (3)$$

$$\delta_{vu} = \delta_{ss} + \frac{V}{U} (\delta_{ns} - \delta_n) - \frac{U}{V} \delta_{ns} + \delta_{nn} \quad (4)$$

$$H_u = \delta_u / \delta_{uu}$$

For simplification these will be rewritten as follows:

$$\frac{\delta_{uu}}{\delta_{ss}} = 1 - \frac{V}{U} \left( \frac{\delta_n - \delta_{ns}}{\delta_{ss}} \right) + \left( \frac{V}{U} \right)^2 \left( \frac{\frac{U}{V} \delta_{ns} - \delta_{nn}}{\delta_{ss}} \right) \quad (5)$$

$$= 1 - F_1 + (V/U)^2 F_2 \quad (6)$$

$$\frac{\delta_{vu}}{\delta_{ss}} = 1 - \frac{V}{U} \left( \frac{\delta_n - \delta_{ns}}{\delta_{ss}} \right) - \left( \frac{U}{V} \frac{\delta_{ns} - \delta_{nn}}{\delta_{ss}} \right) \quad (7)$$

$$= 1 - F_1 - F_2 \quad (8)$$

The problem of determining the wake drag now reduces to that of determining  $F_1$  and  $F_2$  at the airfoil trailing edge. Since  $F_1$  and  $F_2$  depend upon the values of  $\delta_n$ ,  $\delta_{ns}$ , and  $\delta_{nn}$  and since, during the experiments, there was no way of measuring these boundary layer thicknesses, an empirical correction has been adopted in which these thicknesses may be determined from  $\delta_{ss}^* = \delta_{ss} \sqrt{R_c/c}$ . This correction is based on the results of the computations of the boundary layer development which were described previously and which included calculation of all the boundary layer thicknesses.

In Figure 152,  $F_1 + F_2$  is plotted as a function of  $\delta_{ss}^*$  and it is seen that the sum can be approximated by straight lines whose slope

(M) Appendix -- Description of the Empirical Correction for the Wake Drag (continued)

depends on the ratio  $V/U$ . Then the data are represented roughly by

$$F_1 + F_2 = \delta_{ss}^*/k_s \quad (9)$$

and  $k_s$  is given as a function of  $(V/U)^2$  in Figure 153. These relations suggest that if the ratio  $\delta_{ss}^*/k_s$  is used as the independent variable, one obtains a unique relation in which  $F_1 + F_2$  varies linearly with  $\delta_{ss}^*/k_s$  with a slope of 1.0.

Inspection of Equation (8), however, indicates that  $F_1 + F_2$  probably has a maximum less than 1.0, for if it did not,  $\delta_{vu}$  would become negative and would indicate reverse flow on the wing. This reasoning suggests that the data are better represented by an equation of the form

$$F_1 + F_2 = \frac{k_L (\delta_{ss}^*/k_s)}{\sqrt{k_0^2 + (\delta_{ss}^*/k_s)^2}} \quad (10)$$

which is the first derivative of a hyperbola. This equation has a limit of  $k_L$  and a slope through zero equal to  $k_L/k_0$ . One could perhaps argue that  $k_L$  should be 1.0 since this is the limit for which no reverse flow occurs, but such a limit leads to data corrections that almost eliminate the spanwise component of drag. Mathematically, the limit for reverse flow is 1.0, but this leads to a rectangular profile for the  $u$  component of velocity and such a profile will not even be approached. It is possible to determine a more realistic limit by analyzing the vectors in the boundary layer. Figure 154 shows the loci of the ends of calculated vectors for a profile in which  $\delta_{ss}^*/k_s = 0.46$ . The dashed line in the same figure represents the loci of vectors for an estimated maximum crossflow, and these latter loci were assumed to represent maximum crossflow conditions for a variety of  $s$  component profiles. It was then possible to calculate corresponding values  $\delta_{vu}^*/\delta_{ss}^* = \delta_{vu}/\delta_{ss}$ . This ratio was found to average about 0.23. Then the estimated maximum for  $F_1 + F_2$  is given by

$$(F_1 + F_2)_{\max} = k_L \approx 1.0 - 0.23 = 0.77 \quad (11)$$

This indicates a possibility of at least a 77 percent reduction in the spanwise component of drag, if the estimated maximum crossflow is correct.

The reasoning above gives an idea of the possible magnitude of the wake correction, which always results in a reduction of this drag component. When dealing with unknowns, however, it is wise to be conservative; and, in view of this, a value of  $k_L$  of only 0.629 was chosen. This value was felt to be the minimum value that could be selected that would result in a reasonable representation of the computed information. The corresponding value of  $k_0$  which best represented the data was 0.600. Figure 155 shows the computed data in comparison to the empirical curve proposed for the wake corrections.



(M) Appendix -- Description of the Empirical Correction for the Wake Drag (continued)

In order to evaluate  $\delta_{uu}$  it is necessary to determine  $F_1$  and  $F_2$  separately. Since  $F_2$  is the smaller value, it will be determined first. A plot of  $F_2$  vs  $\delta_{ss}^*/k_s$  is shown in Figure 156 and, like the sum  $F_1 + F_2$ , the data for  $F_2$  are approximated by a straight line when  $\delta_{ss}^*/k_s$  is small. Although the scatter is much greater than for the sum  $F_1 + F_2$ , the value of  $F_2$  is smaller so that the scatter is less significant.  $F_2$  also has an approximate upper limit which can be determined in a simple manner by evaluating the maximum for  $(V/U)^2 F_2$ .

$$\begin{aligned} \left(\frac{V}{U}\right)^2 F_2 &= \frac{1}{\delta_{ss}} \left[ \frac{V}{U} \delta_{ns} - \left(\frac{V}{U}\right)^2 \delta_{nn} \right] \\ &= \frac{1}{\delta_{ss}} \left[ \int_0^{\infty} \frac{V}{U} \frac{ns}{Q^2} \frac{\rho}{\rho_1} dz - \int_0^{\infty} \left(\frac{V}{U}\right)^2 \frac{n^2}{Q^2} \frac{\rho}{\rho_1} dz \right] \\ &= \frac{1}{\delta_{ss}} \left[ \int_0^{\infty} \frac{V}{U} \frac{n}{Q} \left( \frac{s}{Q} - \frac{V}{U} \frac{n}{Q} \right) \frac{\rho}{\rho_1} dz \right] \end{aligned} \quad (12)$$

The maximum value of this latter integral has been determined for several calculated  $s$  profile shapes, assuming two conditions: (1) that  $n$  has the maximum possible value corresponding to  $U = 0$  (except where it would result in  $v$  exceeding  $V$ ) and (2) that  $n$  has a value corresponding to the loci of vector terminal points represented by the dashed line in Figure 154. The two cases gave about the same maximum values of  $F_2$  and the average of both cases for several profiles was about 0.198. Since a large value of  $F_2$  results in a small wake correction, this estimated limit was adopted as computed without further adjustment. The resulting empirical equation for  $F_2$  is

$$F_2 = \frac{0.198 \delta_{ss}^*/k_s}{\sqrt{0.360 + (\delta_{ss}^*/k_s)^2}} \quad (13)$$

The data and this empirical curve are shown in Figure 156.  $F_1$  is determined by simply taking the difference between  $(F_1 + F_2)$  and  $F_2$ . The final empirical correction factors used for the wake correction are summarized in Figure 157, and  $k_s$  is given in Figure 153. The added subscript "c" is employed with  $C_{Dw}$  to denote that the empirical crossflow correction has been used to determine this drag component.

(M) Appendix -- Description of the Empirical Correction for the Wake Drag (continued)

Table IX shows a comparison of the correct calculated wake drag coefficients corrected by equation (1) with the results using the empirical correction given by equations (8), (10), (13). The results of the boundary layer calculations for the conditions shown in Figures 115, 116, 117 were used for this comparison. It is seen that the final wake drags as determined from the empirical correction are a bit pessimistic. This is a direct result of selecting constants in the empirical correction so as to obtain a conservative reduction of the drag.

b. CALCULATION OF COMPRESSIBLE FLOW LOSSES THROUGH SWEEP SUCTION SLOTS

J. Goldsmith

(A) Summary

Results of laminar flow experiments performed on a supersonic 36° swept wing model indicated that it might be desirable to consider the influence of the spanwise component of velocity when calculating the losses through swept slots. If the spanwise component of velocity is of importance at 36 degrees of sweep, it certainly is logical that it would be more influential at higher sweep angles. Since a model with a sweep angle of 72 degrees was being designed, an analysis was made to determine the influence of sweep on slot losses. The conclusions derived from this analysis are presented in this report, together with the description of a workable procedure for calculating the compressible flow losses through swept slots.

(B) Notation

Dimensional Variables

$a'$	velocity of sound
$A$	area of metering hole
$c$	chord measured in freestream direction
$C^*$	constants; used with various subscripts
$C_p$	Specific heat at constant pressure
$f'$	local suction velocity for continuous suction
$f'_s$	equivalent "local" suction velocity for finite slots
$F_b$	portion of buoyancy force compensating for friction force due to the slot walls (in the $u$ direction)
$F_u$	friction force opposing the $u$ component of velocity
$F_v$	friction force opposing the $v$ component of velocity
$H'$	average local total head pressure for the suction layer
$I$	denotes integral; defined where used
$l$	chord measured perpendicular to the leading edge
$l'$	surface distance from stagnation point measured perpendicular to the leading edge

(B) Notation (Continued)

$m_q$	rate of q-component momentum flow per unit slot span
$m_r$	suction mass flow rate per unit slot span
$m_u$	rate of u-component momentum flow per unit span
$m_{u2}$	kinetic energy flow rate based on the u-component of velocity
$m_{u2i}$	$m_{u2}$ at slot inlet
$m_v$	rate of v-component momentum flow per unit slot span
$m_{v2}$	kinetic energy flow rate based on the v-component of velocity
$n'$	velocity component in the boundary layer perpendicular to $Q'$
$P'$	local static pressure
$q'$	resultant velocity in the boundary layer or suction system
$Q'$	resultant potential flow velocity
$r'$	gas constant
$r_f$	slot inlet recovery factor
$s'$	velocity component in boundary layer parallel to $Q'$
$t^*$	time
$t'$	temperature in the boundary layer or suction system
$T'$	potential flow temperature
$\bar{u}$	mean velocity across a slot (incompressible)
$u'$	perpendicular velocity component in the boundary layer or suction system
$U'$	perpendicular component of the potential flow velocity
$v'$	spanwise component of the boundary layer or suction system velocity
$V'$	spanwise component of the potential flow velocity
$w$	slot width (see also nondimensional $w$ )

(B) Notation (Continued)

$w_x$	effective slot width at station $x$
$w^*$	critical effective slot width or suction layer height
$w'$	general velocity; component not specified
$W_b$	buoyancy work per unit mass due to motion along pressure gradient
$W_f$	work per unit mass due to friction
$x'$	perpendicular distance from inlet of slots or holes
$x'_s$	flow distance through slots in the local streamwise direction
$y'$	distance along the span of the airfoil or slot
$z'$	distance measured from wall through the boundary layer
$\gamma$	hole spacing in spanwise direction
$\Delta'$	slot spacing in feet (measured in perpendicular direction)
$\Delta''$	slot spacing in inches (measured in perpendicular direction)
$\mu$	absolute viscosity of the fluid
$\nu$	kinematic viscosity of the fluid
$\rho$	density of the fluid

Nondimensional Quantities

$b$	$= 0.218 C_{ue} w_i / w_e$
$B$	$= 1 + M_o^2 / 5$
$C$	$= K / t_a = 0.2 (w' / a'_s)^2$
$d$	$= 1 - 2z' / w$
$f$	$= \xi^* R^{1/2} f' \rho / (U' \rho_o) = \xi^* R^{1/2} f' T / (U' t)$
$f_o^*$	$= R_c^{1/2} f' \rho / (\rho_o Q_o')$
$g$	$= 1 + h/2$

(B) Notation (Continued)

$$h = 4\Delta\sigma_e/w_i$$

$$H = H'/\rho_o Q_o'$$

$$J = M^2/5$$

$$k_f = f'_s/f'$$

$$k_{mv} = m_v/m_r v'_x$$

$$K = q^2 Q^2/7$$

$$m_h = m_r/\rho_{ah} a_a^A$$

$$M = w'/a'$$

$$n = n'/Q' \text{ (also exponent for polytropic process)}$$

$$N = \rho/\rho_o T$$

$$P = P'/\rho_o Q_o'$$

$$q = q'/Q'$$

$$r_f = (H_{ul}-P)/(H_{ur}-P)$$

$$R = U' \ell / v_\delta$$

$$R_c = Q' c / v_o$$

$$s = s'/Q'$$

$$t = r' t' / (Q_o')^2$$

$$T = r' T' / (Q_o')^2$$

$$u = u'/Q'$$

$$U = U'/Q'$$

$$U^* = U'/Q_o'$$

$$v = v'/Q'$$

$$V = V'/Q'$$

$$w = w'/Q'$$

$$z = R^{1/2} (\xi^* \rho_\delta \ell)^{-1} \int_0^{z'} \rho \, dz'$$

$$z^* = z' R^{1/2} / c'$$

(B) Notation (Continued)

$$\sigma = 4x' \mu_w / w_1 m_r$$

$$\sigma_h = \pi x_3' \mu_{st} / \gamma m_r$$

$$\tau_h = \sigma_h m_h$$

$\xi$  = nondimensional coordinate for principal flow direction (see paragraph (I) "Appendix--Nondimensional Variables...")

$\xi^*$  = singularity factor (see paragraph (I) "Appendix--Nondimensional Variables...")

Subscripts

- o freestream value or coefficient subscript
- 1 local value on surface of airfoil or coefficient subscript
- 2 exit of suction slot or coefficient subscript
- 3 exit of suction metering hole or coefficient subscript
- 4 coefficient subscript
- 5 coefficient subscript
- a stagnation value for suction air
- d station d
- e station e; end of inlet length in a slot (compressible flow)
- h denotes hole
- i station i; slot inlet
- $\ell$  station  $\ell$ ; used to calculate kinetic energy losses in suction layer
- m mean or average value
- q denotes value based on resultant velocity (see also  $m_q$ )
- r reference station r (see also  $m_r$ )
- s denotes outer edge of suction layer, local stream direction, or slot
- st freestream stagnation condition

(B) Notation (Continued)

- u denotes value based on the u component of velocity (see also  $m_u$ )
- v denotes value based on the v component of velocity (see also  $m_v$ )
- w denotes wall of slot or wing surface
- x general station through a slot, usually on the center streamline
- $\delta$  denotes at the outer edge of the boundary layer

(C) Introduction

It has been conventional to calculate the suction losses through a slot for incompressible laminar flow models by assuming that the slot is a two-dimensional laminar flow channel (reference 73). This procedure has proved to be very satisfactory for the design of low-speed models. The initial experiments on supersonic suction models (reference 98) indicated that the incompressible laminar flow channel calculations were inadequate for supersonic models, since the incompressible calculation does not account for the density changes through the slot. Thereafter, slot losses for supersonic models were calculated at Norair by means of an approximate method derived by Groth (Appendix II of reference 123).

The use of Groth's approximate method seemed to result in adequate suction systems for subsequent unswept models. For a  $36^\circ$  swept supersonic model, however, the suction losses appeared to differ somewhat from the calculated values, and this led to the belief that the spanwise flow that inevitably occurs in swept slots may have a significant effect on the slot losses. Since future experiments include sweeps as high as 72 degrees, an analysis of the influence of spanwise flow on slot losses was made and the results are reported herein.

Also, in the past it has been conventional to disregard the dynamic energy (kinetic energy) in the suction layer air. This has been a reasonable procedure for straight or slightly swept wings since the suction flow rates and dynamic energy are low for such wings. For highly swept wings, however, the suction layer thicknesses are necessarily relatively large compared to the boundary layer thickness. This is a direct result of the requirement that the crossflow profiles be limited (for laminar stability) to a given maximum Reynolds number. On a highly swept wing at high speed the limiting crossflow Reynolds number will be excessive unless the boundary layer is maintained relatively thin by means of strong suction. When the suction layer thickness is large compared to the boundary layer thickness (as in the case of strong suction), the dynamic energy of the sucked layer cannot be ignored. In fact, if the spanwise component of this dynamic energy could be considered negligible, there would be no need to be concerned about the spanwise flow



(C) Introduction (Continued)

within the slot. The influence of the suction layer energy on the slot losses is included, therefore, in the analysis of the swept slot losses.

(D) A Qualitative Look at the Influence of Spanwise Flow in a Slot

Just as there are no spanwise pressure gradients on an infinite swept wing, it is also assumed that there are no spanwise pressure gradients for a long swept slot. Then all velocity changes for the spanwise flow are functions only of the skin friction and are independent of pressure gradients. The chordwise flow, on the other hand, may be treated very nearly the same as strictly two-dimensional flow; that is, the relation between the perpendicular component of the friction forces, the pressure gradients and the chordwise velocity changes are somewhat similar to those for slots without spanwise flow. Also, the continuity equation is valid for this component of the flow. The spanwise flow does have one influence on the chordwise flow, however, and this is because the dissipation of spanwise flow results in a temperature rise which in turn influences the density of the chordwise flow. For this reason, and only this reason, the spanwise flow component may influence the slot losses. To put this another way, the perpendicular component of flow for a swept slot may be considered to be strictly two-dimensional flow with heat transfer. In this case the quantity of heat transferred is a function of the spanwise flow dissipation.

An important parameter for two-dimensional channel loss calculations has always been  $\sigma = 4x'v/\bar{u}w^2$  and, for compressible flow, is more conveniently written in the form

$$\sigma = 4x'\mu_w/\dot{m}_r \quad (1)$$

where:

$x'$  = length of channel (slot skin thickness)

$\mu_w$  = viscosity coefficient at wall

$\dot{m}_r$  = mass flow rate/unit slot span

$w$  = channel (slot) width.

When a slot is swept, the spanwise component results in the air taking a longer path ( $x'$ ) along the slot walls in a diagonal direction, and one might wonder whether or not this would modify the value of  $\sigma$ . The answer is that  $\sigma$  does not change since the term  $\dot{m}_r$  (mass flow rate/unit length normal to flow direction) changes in proportion to the path length (parallel to the flow direction). One can conclude, therefore, that  $\sigma$  is independent of spanwise flow due to sweep and may be defined by Eq. (1) whether the slot is perpendicular to or swept relative to the freestream direction. For compressible flow the pressure drop through a slot is a unique function of  $\sigma$ , and when the flow is two-dimensional and compressible, the flow is then a unique function of  $\sigma$  and inlet Mach number. For the swept slot we have an additional correction due to density

(D) A Qualitative Look at the Influence of Spanwise Flow in a Slot (Continued)

changes caused by conversion of the spanwise kinetic energy to internal energy. The amount of energy converted is a function of spanwise kinetic energy at the inlet and of  $\sigma$  so that the pressure drop is still primarily a function of  $\sigma$ .

The problem of calculating losses for swept slots, therefore, seems to narrow down to calculation of the spanwise energy that is converted to heat, and to treat the slot as though it were a two-dimensional slot in which this heat is transferred to the two-dimensional flow. The overall flow for both velocity components combined is still adiabatic relative to its surroundings (assuming insulated walls). When the perpendicular flow is treated as an isolated two-dimensional flow, however, the influence of the spanwise flow on the density must be treated as a heat addend.

(E) Outline of Calculation

The proposed method for calculation of the slot losses for a swept slot is somewhat involved, but basically it can be said to follow the procedure below.

(1) The boundary layer profiles are plotted for the region of the suction layer, and the spanwise and perpendicular velocity distributions are approximated by a uniformly varying velocity, i.e., a triangular-shaped profile. Also, the temperature variation is approximated by a straight line resulting in a trapezoidal-shaped profile. These profiles are determined for the nondimensional form of the variables employed in reference 45 since the z-coordinate (distance perpendicular to the surface) incorporates a density factor that simplifies the analysis. These nondimensional quantities are included in the output of the Norair boundary layer calculation program.

(2) The momentum, kinetic energy, and thermal energy are then determined for each streamline in the simulated suction layer, and the overall averages are found by weighing the specific values by the local mass flow rate in the perpendicular direction. It is in this process that the use of the nondimensional variables excels over the use of the dimensional ones.

(3) The losses in the total pressure (based on the perpendicular component) are estimated as the air flows into the slot entrance, and the slot entry conditions are then determined on the assumption that the velocity distribution is uniform at the slot entrance. This latter assumption is consistent with the assumption that a slot can be treated as a two-dimensional channel.

(4) The losses and other flow characteristics are then calculated at the end of the inlet length (station e, Fig. 159) where the boundary layer for the perpendicular flow just fills the slot. The profile at station e is assumed parabolic in shape, and calculations

(D) A Qualitative Look at the Influence of Spanwise Flow in a Slot (Continued)

are accomplished by employing one-dimensional relations along the center streamline. The growth of the perpendicular component of the boundary layer in this inlet length causes a contraction of this center streamline due to the increased boundary layer displacement thickness. The spanwise component of flow has only a small influence on this displacement thickness until the boundary layer for this latter component fills the slot. In paragraph (M) it is shown that the entry length for the spanwise component of flow is slightly shorter than the entry length for the perpendicular component. For the region between the two entry lengths a small heat transfer to the perpendicular component of flow must be considered due to spanwise velocity dissipation.

(5) The calculation is completed by assuming a one-dimensional polytropic process for the center streamline from station 1 to station 2 at the slot exit. In this region both the spanwise and perpendicular profiles are assumed parabolic in shape. The magnitude of the spanwise component of velocity decreases logarithmically due to the friction forces. This results in a temperature rise and correspondingly lower density. Accordingly, the chordwise velocity must (in order to satisfy continuity) gradually increase. It is only through this reduction of the air density that the spanwise component of flow has any influence on the losses in this region.

(F) Calculation Procedure

The calculation procedure employs not only the usual nondimensional quantities but also the more unusual nondimensional quantities incorporated in the Norair boundary layer calculation program. These latter quantities are described briefly in paragraph (I) and in more detail in reference 45. The reader should familiarize himself with these quantities before proceeding. Derivation of most of the relations dealing specifically with swept slot losses are given in the remainder of the paragraph appendices, and the reader may wish to refer to these frequently. A copy of reference 117 or a similar set of tables would also be helpful in following the calculation procedure.

Constants

Constants here refer to items which are constant for a given configuration, scale, freestream Mach number and wing Reynolds number. Beginning, then, with the following knowns,

$$M_o, T_{st}', U_o'/V_o', R_c, l, \mu_{st} \quad (2)$$

one may calculate (see Fig. 159 for locations of stations denoted by subscripts):

$$B = 1 + 0.2M_o^2 \quad (3)$$

$$T_o' = T_{st}'/B \quad (4)$$

(F) Calculation Procedure (Continued)

$$a'_0 = \sqrt{2402.4 T'_0} \quad (5')$$

$$Q'_0 = M'_0 a'_0 \quad (6)$$

$$\mu_0 = \mu_{st} (T'_{st} + 198.6) / [(T'_0 + 198.6) B^{3/2}] \quad (7)$$

(Sutherland's formula)

$$c = \ell / (U'_0 / V'_0) \quad (8)$$

$$\rho_0 = R_c \mu_0 / (Q'_0 c) \quad (9)$$

$$\rho_{st} = \rho_0 B^{5/2} \quad (10)$$

$$T_{st} = r' T'_{st} / Q'_0 \quad (11)$$

$$T_0 = T_{st} / B \quad (12)$$

Frequently used combinations of constants are given below:

$$C_1^* = 12.0c / \sqrt{R_c} \quad (13)$$

$$C_4^* = \rho'_0 Q'_0 \quad (14)$$

$$C_2^* = C_4 \ell / \sqrt{R_c} \quad (15)$$

The following factors may or may not be constant, depending whether or not the factor  $k_f$  is constant. This factor is set equal to the estimated ratio of equivalent finite slot suction to the continuous suction intensity used in the boundary layer calculation.

$$C_0^* = k_f / 6\ell \quad (16)$$

$$C_3^* = k_f / (12 \sqrt{R_c}) \quad (17)$$

Variables Tabulated in the Norair Boundary Layer Calculation Program

At a specific slot location the results of the boundary layer calculation provide values for the following variables:

$$\xi^*, f, f_0^*, t_w, \sqrt{R/R_c}, T, P, U^*, U, V, n, s, z, z^*, t$$

where these variables are described briefly in the Notation or in paragraph (I), or in complete detail in reference 45.

Selected Variables

The slot configuration must be selected in order to complete the calculation of the losses. The items of concern are listed below.

(F) Calculation Procedure (Continued)

w or  $w_i$  - the slot width

$x_2$  - the slot skin thickness

$\Delta''$  - the slot spacing in inches (measured in direction perpendicular to the slot length)

The Suction Layer Characteristics

The suction layer characteristics are calculated for triangular-shaped profiles which approximate the real profiles. The real u and v profiles may be determined from the following relations [see Eq. (106) and (107)]:

$$u = sU - nV \quad (18)$$

$$v = sV + nU \quad (19)$$

The simplest procedure is to plot  $sU$  and  $nV$  versus  $z$  and to subtract graphically to obtain the  $u$  profile. Then the hyperbola representing a constant value for the product  $u_s z_s$  is plotted on the same axes (Fig. 160). The value of this product is given by:

$$u_s z_s = -C \Delta'' f U / \xi^*{}^2 \quad [\text{see Eq. (116)}] \quad (20)$$

A straight line is then drawn from the origin to the hyperbola in such a manner that the straight line approximates the real  $u$  component of the profile as nearly as possible. In particular, the line is chosen so that the value of  $z_s$  is identical for the triangular and the real profiles. The method of doing this is described in paragraph (J). The temperature profile and the variation of  $z^*$  are also plotted versus  $z$ . The temperature variation is then simulated by a straight line passing through  $t_w$  at  $z = 0$  (see Fig. 160). Then at  $z_s$  one can read

$$t_s, z_s^*, s_s U, n_s V$$

Once these items are determined, it is possible to calculate the remaining unknowns at the outer edge of the suction layer.

$$v_s = s_s U (V/U) + n_s V (U/V) \quad (21)$$

$$q_s = \sqrt{v_s^2 + u_s^2} \quad (22)$$

$$\Delta t = t_s - t_w \quad (23)$$

$$z_s' = C_1 z_s^* \quad (24)$$

The significant average one-dimensional characteristics are derived in paragraph (J) and are summarized below:

$$t_1 = t_w + 2\Delta t/3 \quad (25)$$

(F) Calculation Procedure (Continued)

$$k_1 = q^2 Q^2 / 14 \quad (26)$$

$$t_a = t_1 + K_1 \quad (27)$$

$$\mu'_a = \mu'_{st} (t_a / t_{st})^{0.76} \quad (\text{reference 117}) \quad (28)$$

$$m_r = -C_3^* C_4^* f_o^* \Delta'' \quad (29)$$

The next major step is to determine the characteristics at station  $i$  at the slot inlet where the velocity is assumed uniform. To accomplish this the slot entry losses must be estimated. For this purpose a three-step process is assumed with the two intermediate stations  $r$  and  $l$  representing the boundaries between the steps (see Fig. 159). The work chart for the flow into the slot is shown in Fig. 164. The characteristics of such a chart are described in paragraph (L) and inspection of this chart may be helpful in visualizing the calculation of the losses upstream of the slot entrance.

It is customary to assume that the velocity distribution is uniform across the slot at the slot inlet. Then, between stations  $l$  and  $r$  the mixing losses, which occur as a result of conversion from a triangular profile to a rectangular one, are calculated. For this step the momentum flow rate ( $m_q$ ), the total nondimensional temperature ( $t_a$ ), and the pressure coefficient ( $P$ ) are assumed constant. From equation (128) it is noted that the unit momentum is given by

$$m_q / m_r = 2q'_s / 3 = q'_r \quad (30)$$

This must equal  $q'_r$  because the unit momentum (which is constant between stations  $l$  and  $r$ ) is equal to the velocity when the velocity is uniform. Then for station  $r$

$$K_r = K_1 (q_r / q_1)^2 = 8K_1 / 9 \quad (31)$$

$$t_r = t_a - K_r \quad (32)$$

$$z'_r = m_r / \rho_r u'_r = m_r t_r / P u_r Q C_4^* \quad (33)$$

$$K_{ur} = K_r (u_s / q_s)^2 \quad (34)$$

$$J_{ur} = K_{ur} / t_r \quad (35)$$

$$M_{ur} = \sqrt{5J_{ur}} \quad (36)$$

$$H_{ur} / P = (1 + J_{ur})^{3.5} \quad (37)$$

$$(u_r / a_{av})^2 = M_{ur}^2 / (1 + J_{ur}) \quad (38)$$

$$w^* / z'_r = 1.728 M_{ur} / (1 + J_{ur}) \quad (39)$$

$$t_{vr} = t_r + K_{ur} \quad (40)$$

(F) Calculation Procedure (Continued)

$$K_{vr} = K_r - K_{ur} \quad (41)$$

From stations  $r$  to  $\ell$  the slot entry and turning losses are established by a recovery factor  $r_f$  which may be defined as follows:

$$r_f = (H_{u\ell} - P)/(H_{ur} - P) \quad (42)$$

Then, after  $r_f$  has been selected (by experience or as suggested in the Discussion), one may calculate a new total pressure for station  $\ell$ .

$$H_{u\ell}/P = 1 + [(H_{ur}/P) - 1] r_f \quad (43)$$

It should be noted that the total pressure  $H_u$  is altered by the assumed loss and that this  $H_u$  is the pressure resulting from complete isentropic diffusion of only the  $u$ -component of velocity. The spanwise component of velocity  $v_r$  is assumed unaltered between stations  $r$  and  $\ell$  so that  $t_{vr} = t_{v\ell}$ . Also, by assumption,  $P_\ell = P$  and one may then calculate the characteristics at station  $\ell$  as follows:

$$t_{vr}/t_a = (H_{u\ell}/P)^{2/7} \quad (44)$$

$$M_{u\ell} = \sqrt{5(t_{vr}/t_\ell) - 5} \quad (45)$$

$$(u_\ell/a_{v\ell})^2 = M_{u\ell}^2/(t_{vr}/t_\ell) \quad (46)$$

$$u_\ell/u_r = \sqrt{(u_\ell/a_v)^2/(u_r/a_{vr})^2} \quad (47)$$

$$\rho_\ell/\rho_r = (t_{vr}/t_\ell)/(t_{vr}/t_r) \quad (48)$$

$$z'_r/z'_i = (\rho_\ell/\rho_r)(u_\ell/u_r) \quad (49)$$

$$w^*/z'_\ell = 1.728M_{u\ell}/(t_{vr}/t_\ell) \quad (50)$$

$$z'_\ell/w_i = (z'_r/w_i)/(z'_r/z'_\ell) \quad (51)$$

$$K_{u\ell} = K_{ur}(u_\ell/u_r)^2 \quad (52)$$

An isentropic flow is assumed from station  $\ell$  to station  $i$  with no change in the spanwise flow. Then

$$H_{ui} = H_{u\ell} \quad (53)$$

$$w^*/w_i = (w^*/z'_\ell)(z'_\ell/w_i) \quad (54)$$

$M_{ui}$  can be obtained from the relation given below or from tables or charts. A method of solving this equation on digital computers is given in the Discussion.

$$1.728M_{ui}/(1 + 0.2M_{ui}^2)^3 = w^*/w_i \quad (55)$$

(F) Calculation Procedure (Continued)

$$(u_1/a_{v1})^2 = M_{u1}^2 / (1 + 0.2M_{u1}^2) \quad (56)$$

$$K_{ui} = K_{u\ell} (u_1/a_{v1})^2 / (u_\ell/a_{v\ell})^2 \quad (57)$$

$$(v_1/u_1)^2 = K_{vr}/K_{ui} \quad (58)$$

The next step is the calculation of the losses at the end of inlet length of the slot. For a two-dimensional slot such a calculation would be straightforward since the characteristics of the flow can be calculated along the center streamline which follows an isentropic flow path by definition of the inlet length. As explained in paragraph (O), however, the boundary layer for a spanwise flow in a slot fills the slot at a point upstream of the two-dimensional inlet length. Downstream of this point the center streamline flow cannot be considered isentropic if the slot is swept. To facilitate the computation the flow between stations i and e is considered to take place in two steps (Fig. 159). The first step, from i to the pseudo station d, is assumed to be isentropic. Then, from stations d to e, a constant pressure energy conversion is assumed to take place which very nearly corrects for any error due to the assumption of isentropic flow.

In paragraph (O) it is pointed out that the calculation is not easily performed from stations i to e, but that it is readily made from e to i. The results of a series of these reverse calculations are shown in Fig. 161 together with an empirical equation which simulates the data quite nicely. Either the chart or the equation can be used to determine the ratio  $(u_e/u_i)^2$  once the initial conditions  $(v_1/u_1)^2$  and  $w^*/w_1$  are established. The choice of paths (isentropic from i to d and constant pressure from d to e) results in the following relations:

$$v_d = v_\ell = v_i \quad (59)$$

$$u_e = u_d \quad (60)$$

$$a_{vi} = a_{vd} \quad (61)$$

$$P_e = P_d \quad (62)$$

$$H_{ud} = H_{ui} \quad (63)$$

$$C_{vd} = K_{vr}/t_a \quad (64)$$

$$C_{ui} = K_{ui}/t_a \quad (65)$$

$$C_{ue} = C_{ud} = C_{ui}(u_e/u_i)^2 \quad (66)$$

$$C_d = C_{ud} + C_{vd} \quad (67)$$

$$t_d/t_a = 1 - C_d \quad (68)$$

$$J_{ud} = C_{ue}/(t_d/t_a) \quad (69)$$



(F) Calculation Procedure (Continued)

$$M_{ud} = \sqrt{5J_{ud}} \quad (70)$$

$$H_{ui}/P_e = H_{ui}/P_d = (1 + J_{ud})^{3.5} \quad (71)$$

$$C_{ve} = C_{vd}/1.12 \quad (\text{see Eq. 234}) \quad (72)$$

$$C_e = C_{ve} + C_{ue} \quad (73)$$

$$t_e/t_a = 1 - C_e \quad (74)$$

$$J_{ue} = C_{ue}/(t_e/t_a) \quad (75)$$

$$w_e/w_i = (1 - C_e)(0.66667 + 0.45714C_e + 0.36939C_e^2 + 0.31810C_e^3) \quad (76)$$

$$(v_e/u_e)^2 = C_{ve}/C_{ue} \quad (77)$$

Losses are now calculated for the final segment between the end of the inlet length and the slot exit. Note that  $\sigma_e$  is assumed to be 0.12, as discussed in paragraph (M).

$$\sigma = 4\mu_a x'_2/w_i m_r \quad (78)$$

$$\Delta\sigma = \sigma - 0.120 \quad (79)$$

$$(v_2/v_e)^2 = e^{-5\Delta\sigma} \quad (80)$$

$$\Delta(v/u_e)^2 = (v_e/u_e)^2 [(v_e/v_2)^2 - 1] \quad (81)$$

$$h = 4\Delta\sigma w_e/w_i \quad (82)$$

$$g = (2\Delta\sigma w_e/w_i) + 1 \quad (83)$$

$$b = 0.218C_{ue}w_i/w_e \quad (84)$$

These variables are then used to determine the value of  $P_2/P_e$  by some iterative process such as the one described in paragraph (L). Finally, the pressure ratio at the slot exit can be calculated:

$$P_2/P = (P_2/P_e) (H_{ul}/P)/(H_{ui}/P_e) \quad (85)$$

(G) Calculation of Metering Hole Dimensions

The suction air passing through slots is generally metered by holes located just downstream of slot chambers in the suction system. The losses through these holes are unaffected by the sweep of a slot so that conventional means may be used to calculate these hole losses. Since the calculation of the losses through a swept slot is unconventional, however, the reader may find that the relations given in the succeeding text are useful for continuing with the hole loss calculations.

(G) Calculation of Metering Hole Dimensions (Continued)

Generally, it is desired to obtain a certain suction mass flow rate for a given increment of pressure ratio ( $P_3/P$ ) through the slots and holes combined. If station 3 represents the conditions at the hole exit, we may write for the pressure ratio across the holes

$$P_3/P_2 = (P_3/P)/(P_2/P). \quad (86)$$

A second parameter which may be calculated immediately is

$$\sigma_h = \pi \frac{x_3}{\gamma} \frac{\mu_{st}}{m_r} \quad (87)$$

where  $x_3$  is the hole skin thickness and  $\gamma$  is the hole spacing along the span.  $x_3$  and  $\gamma$  are in the same units.

Then from Fig. 162 one may obtain graphically the value of  $m_h$  which corresponds to the given values of  $\sigma_h$  and  $P_3/P_2$ . This chart was constructed from the results of hole losses which were determined by the method proposed in reference 123. The parameter  $m_h$  is a mass flow ratio and is defined as follows:

$$m_h = \gamma m_r / \rho_a h a_a A \quad (88)$$

where  $A$  = the area of the hole. Then

$$A = \gamma m_r / \rho_a h a_a m_h = \gamma m_r \sqrt{t_a} / [P(P_2/P) \rho_o Q_o m_h \sqrt{1.4}] \quad (89)$$

whence one can find the hole area corresponding to the required mass flow and pressure drop.

(H) Discussion

The proposed method for calculating the losses through a swept slot is rather lengthy in comparison to the usual methods employed to calculate unswept slot losses. There must be justification, therefore, for including the influence of sweep. Although experience with swept slots is limited, calculations have been made for some slots swept at an angle of 72.5 degrees. Results of such calculations for a swept slot are given in Table XII for two different recovery factors. For the high suction quantities required for this sweep angle it is clear that the recovery of the dynamic energy in the suction layer can be quite significant. As seen from the table the swept slot method of calculation was also used to calculate the losses for a nearly straight slot (swept less than one degree). An additional calculation for an unswept slot was made using the method of Groth (reference 123). It is seen that the results for the two unswept slots compare favorably with each other. Also, the significance of the spanwise component of flow (compare the swept and unswept slot calculations for  $r_f = 0.0001$ ) is seen to be of sufficient magnitude (22 percent increase in losses for the example) so that it cannot be neglected. This is true even when the slot losses are rather small, as

#### (H) Discussion (Continued)

in the example. As the slot velocity increases, the effect of the spanwise flow becomes more significant and might even lead to choking. It seems worthwhile, therefore, to consider the effect of spanwise flow even though the calculation is then somewhat more lengthy.

For the 72.5-degree slot the major portion of the calculations was performed on an automatic computer. Experience with this program is limited, but, for the calculations made to date, the program has proved to be quite satisfactory. The iterative process for determining the ratio  $P_2/P_e$  as described in paragraph (L) converged rapidly. Another iterative process was used to determine the value of  $M_{ui}$  from the ratio  $w_i/w^*$ . This process also converged rapidly and was programmed as follows:

$$(1) \text{ Set } M_1 = 0.5787w^*/w_i \quad (90)$$

$$(2) \text{ Set } M_2 = M_1 \quad (91)$$

$$(3) \text{ Calculate } M_{ui} = M_1(1 + 0.2M_2) \quad (92)$$

$$(4) \text{ Set } M_2 = M_{ui} \quad (93)$$

Then steps 3 and 4 are repeated about five times. Convergence will occur for values of  $M_{ui} < 0.65$ , and  $M_{ui}$  should not exceed this value or choking of the slot is probable.

The program is also set up on the assumption that  $\Delta\sigma$  will be positive. Generally,  $\Delta\sigma$  will be positive, but it should be noted that adjustments must be made if  $\Delta\sigma$  should become negative. Such adjustments have not been considered in developing the calculation program since the problem has not arisen in any of the calculations made in the past.

A means for selecting a realistic value for  $r_f$  has not been established, and much experience will be required to be able to select accurate values for this factor. In most slot loss calculation methods, including the one presented by Groth in reference 123,  $r_f$  is assumed equal to zero. In the past this had been a good assumption. For large suction intensities, such as may be employed on highly swept wings, a portion of the kinetic energy in the suction layer is undoubtedly recoverable, and the choice of  $r_f$  becomes important. Until additional information is available it is suggested that  $r_f$  be set equal to 1.0 as a first try. If the resulting value of  $z_h'/w_i \geq 1.0$ , the results may be considered acceptable. If, however, the calculated value of  $z_h'/w_i < 1.0$ , then the recovery factor should be progressively reduced until the value of  $z_h'/w_i$  equals unity. The assumption employed here is that the entry losses for a contracting flow are negligible, whereas losses are high when the suction layer is forced to diffuse as it flows into the slot. In order to reduce disturbances in the laminar layer on the wing surface, however, slot widths should be chosen so that diffusion of the suction layer is minimized. Often, however, a compromise must be made (particularly on small supersonic test models), either because the losses in

#### (H) Discussion (Continued)

narrow slots become excessive or because there is a minimum size slot that can be machined with present techniques. When such a compromise must be made, the selection of  $r_f$  may be done as suggested previously.

It has already been noted above that  $M_{u1}$  should not exceed 0.65. Experience with supersonic straight or moderately swept suction models has indicated that, perhaps, the Mach number at the outer edge of the suction layer also has a limitation of about 0.65. For swept slots it is assumed that this Mach number limitation applies only to the perpendicular component of velocity. The spanwise velocity may have no limit, just as it has no limit for infinitely long swept wings with a subcritical perpendicular component of velocity. The conditions are identical for the two cases in that there are no pressure gradients in the spanwise direction. The only Mach number of significance for a swept wing is due to the perpendicular component of velocity, and a similar assumption is made for the swept slot. It should be pointed out, however, that even though no physical limit is recognized for the spanwise Mach number, the accuracy of the calculation program depends on certain simplifications such as the limitation of the number of terms used in the various equations of paragraph (K). Some sacrifice of accuracy must be expected, therefore, when the spanwise flow causes resultant Mach numbers well in excess of 1.0.

#### (I) Appendix--Nondimensional Variables Employed in Calculation of Swept Slots

The calculation of the slot losses generally utilizes the results of a boundary layer calculation. At Norair most laminar flow boundary layer calculations incorporate the method set forth by Raetz (reference 45) so that it is convenient to employ many of the nondimensional working variables used in this method. These variables are given below, together with some additional quantities used to calculate the slot losses. It will be noted that when a quantity is used in both the nondimensional and the dimensional versions, the nondimensional symbol is usually denoted by an unprimed English alphabetic symbol and the dimensional version of the same variable may be denoted by either the same symbol after it has been primed or by a Greek letter. Also, in general, capital letters are used to denote potential flow values and lower case letters to denote values within the boundary layer. Ratios of dimensional and nondimensional quantities are often identical.

#### The Temperature and Kinetic Energy Relations

The energy equation may be written

$$C_p t'_a = C_p t' + (q')^2/2 \quad (94)$$

and, dividing by  $C_p \frac{(Q'_0)^2}{r'}$ , one obtains

$$\frac{r' t'_a}{Q'^2_0} = \frac{r' t'}{(Q'_0)^2} + \frac{r' (q')^2}{2 C_p (Q'_0)^2} = \frac{r' t'}{(Q'_0)^2} + \frac{1}{7} \left| \frac{q'}{Q'_0} \right|^2 \left| \frac{Q'_0}{Q'_0} \right|^2 \quad (95)$$

(I) Appendix--Nondimensional Variables Employed in Calculation of Swept Slots

or

$$t_a = t + q^2 Q^2 / 7 = t + K \quad (\text{by definition of the unprimed quantities}). \quad (96)$$

Dividing now by  $t_a$

$$\begin{aligned} 1 &= t/t_a + K/t_a = t/t_a + C = t/t_a + 0.2(q'/a'_a)^2 \\ &= t'/t'_a + (q')^2 / 2C_p t'_a \end{aligned} \quad (97)$$

or, dividing by  $t$ ,

$$t_a/t = 1 + J = 1 + K/t = 1 + M^2/5 = 1/(1-C) \quad (98)$$

Equations (94), (95), (96), (97), and (98) may also be written with  $u$  or  $v$  substituted for  $q$  and the additional subscripts  $u$  or  $v$  respectively added to all the remaining variables except  $r'$ ,  $C_p$ ,  $Q'_o$  and  $Q$ . Then, for example,

$$t_{au} = t_u + u^2 Q^2 / 7 = t_u + K_u, \text{ etc.}$$

Consistent with these variables are the pressure and density relations

$$P = P' / [\rho_o (Q'_o)^2] = \rho_\delta T / \rho_o = \rho t / \rho_o \quad (99)$$

$$\rho_\delta / \rho_o = P/T \quad \text{or} \quad \rho / \rho_o = P/t \quad (100)$$

Nondimensional Boundary Layer Coordinate

The variable representing distance through the boundary layer incorporates a density correction that transforms the actual distance to its equivalent incompressible distance.\*

$$z = \left( R^{1/2} / \xi^* \right) \int_0^{z'} (\rho / \rho_\delta) (dz' / \ell) = \left( R^{1/2} / \xi^* \right) \int_0^{z'} (T' / t') (dz' / \ell) \quad (101)$$

---

\*For those not familiar with reference 45, the principal coordinate (in the  $U$  direction) is  $\xi$ , which is so selected that  $dx'/d\xi$  is exactly proportional to  $\xi$  at  $\xi = 0$  and nearly proportional to  $\xi$  near the point  $\xi = 0$ .  $\xi^*$  then is exactly equal to  $\xi$  near  $\xi = 0$  and may be any convenient function of the coordinates elsewhere. If a method other than that of reference 45 is used to calculate the boundary layer,  $\xi^*$  may be considered equal to  $\xi$  and  $\xi$  may be set equal to  $\sqrt{z'/\ell}$  where  $\ell'$  is the distance along the surface from the stagnation point measured in the perpendicular direction.

(I) Appendix--Nondimensional Variables Employed in Calculation of Swept Slots (Continued)

The Suction Variables

Two of the suction parameters used in the boundary layer calculation are also employed in the calculation of slot losses:

$$f = \xi * R^{1/2} \rho_w f' / (\rho_\delta U') \quad (102)$$

$$f_\delta^* = (\rho / \rho_o) (f' / Q_o') \sqrt{R_c} \quad (103)$$

The Velocity Components

The nondimensional velocity components of interest for the slot losses are those perpendicular to the slot  $U$ ,  $u$  and those parallel to the slot length  $V$ ,  $v$ . The capitals denote the value at the outer edge of the boundary layer, and the lower case letters denote the area within the boundary layer. The corresponding resultant nondimensional velocities are 1.0 and  $q$ . If primed quantities denote dimensional values, then the nondimensional values given above are defined as follows:

$$\begin{aligned} U &= U' / Q' & u &= u' / Q' \\ V &= V' / Q' & v &= v' / Q' \\ 1.0 &= Q' / Q' & q &= q' / Q' \\ Q &= Q' / Q_o' & U^* &= U' / Q_o' \end{aligned} \quad (104)$$

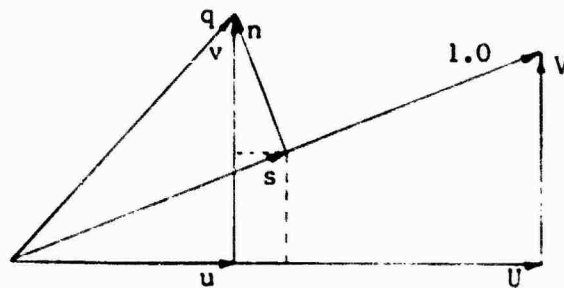
The printed output of the Norair boundary layer calculation, however, is generally given in terms of  $s$  and  $n$ , the local streamwise and normal components, respectively. If  $Q'$  is the reference local potential velocity,

$$s = s' / Q' \quad n = n' / Q' \quad (105)$$

The components are converted to  $v$  and  $u$  as follows:

$$u = sU - nV \quad (106)$$

$$v = nU + sV \quad (107)$$



(J) Appendix--Characteristics of a Triangular Profile

In the calculation of the swept slot losses the velocity distribution in the suction layer is assumed to be triangular. Also, the temperature profile is assumed trapezoidal. The constants for these approximate profiles are determined by plotting the actual profile components in nondimensional form and then approximating these profiles by straight lines within the suction layers.

The components in which one is interested are  $u$  and  $v$ , and these may be determined from the calculated streamwise and normal components as follows:

$$u = sU - nV \quad (108)$$

$$v = sV + nU \quad (109)$$

To determine the constants for the approximate triangular profiles,  $sU$  and  $nV$  are plotted as functions of  $z$ . The graphical difference is equal to  $u$  and this is also plotted as a function of  $z$ . In order to determine the thickness of the suction layer it is necessary to calculate the mass flow rate per unit span along the slot length.

$$m_r = -\rho_w k_f f' \Delta' = -\rho_\delta k_f f \Delta' U' / \xi^* \sqrt{R} \quad (110)$$

where  $\Delta' =$  slot spacing in the perpendicular direction

$k_f =$  ratio of average suction velocity required for finite slots to simulate the calculated continuous suction velocity.

The mass flow rate may also be written in terms of the nondimensional quantities for a triangular profile.

$$m_r = \int_0^{z'_s} \rho u' dz' \quad (111)$$

$$u' = uQ' = u_s Q' z / z_s \quad (112)$$

$$\rho dz' = \xi^* \ell \rho_\delta R^{-1/2} dz \quad (\text{by definition of } z) \quad (113)$$

$$\rho u' dz' = \xi^* \ell \rho_\delta u_s Q' z dz / (z_s \sqrt{R}) \quad (114)$$

$$m_r = (\xi^* \ell / \sqrt{R}) \rho_\delta Q' u_s z_s \int_0^1 (z/z_s) d(z/z_s) \quad (115)$$

The integral is equal to 0.5. Substituting equation (110) for  $m_r$  and solving for  $u_s z_s$ , one obtains

$$u_s z_s = -2k_f f U \Delta' / (\ell \xi^{*2}) \quad (116)$$

Fig. 160 shows the relation between the boundary layer profile and the curve  $u_s$  versus  $z_s$ . Of course, the latter is a hyperbola and represents

(J) Appendix--Characteristics of a Triangular Profile (Continued)

the loci of points at the outer edge of a triangular profile that would give the desired suction. The triangular profile that simulates the real profile is given by a straight line passing through the origin and terminating on the hyperbola. The slope of this line is chosen in such a manner that it approximates the actual profile as closely as possible; in particular, the height of the suction layer  $z_s$  should be the same for the real and triangular profiles. The values of  $z_s$  and  $u_s$  at the selected terminal point are the values which are sought. The corresponding spanwise component  $v_s$  is determined from the interpolated values of  $s_s U$  and  $n_s V$  at the height  $z_s$ .

$$v_s = n_s V(U/V) + s_s U(V/U) \quad (117)$$

The resultant velocity at the outer edge of the boundary layer is given by

$$q_s = \sqrt{u_s^2 + v_s^2} \quad (118)$$

Then, the three triangular velocity variations are given by

$$u = u_s(z/z_s) \quad v = v_s(z/z_s) \quad q = q_s(z/z_s) \quad (119)$$

The temperature profile is approximated by a straight line passing through the point  $t_w$  and matching the real profile as closely as possible. The minimum value ( $t_s$ ) is read for the height  $z_s$ , and the local boundary layer temperature is then given by

$$t = t_w + (t_s - t_w)z/z_s \quad (120)$$

or

$$t'/t_w' = t/t_w = 1 + (\Delta t/t_w)z/z_s \quad (121)$$

In addition, it is necessary to determine  $z^*$ . This may be done by plotting  $z^*$  as a function of  $z$  and interpolating at  $z_s$ . The value of  $z^*$  is also tabulated as part of the output of the Norair boundary layer calculation program. If this program is not used,  $z^*$  may be calculated from the definitions of  $z^*$  and  $z$ .

The momentum flow rate ( $m_u$ ) for the perpendicular triangular profile in the suction layer is given by

$$m_u = \int_0^{z_s'} \rho (u')^2 dz' = \xi^* L \rho_0 Q' u_s^2 z_s R^{-1/2} \int_0^1 (z/z_s)^2 d(z/z_s) \quad (122)$$

and the integral is equal to one-third. Then the momentum per unit mass, which will also be called the unit momentum, becomes

$$m_u/m_r = 2u_s Q'/3 = 2u_s'/3 \quad (123)$$



(J) Appendix--Characteristics of a Triangular Profile (Continued)

In like manner the kinetic energy flow ( $m_{u2}$ ) per unit mass can be calculated

$$m_{u2}/m_r = (0.5/m_r) \int_0^{z'_s} \rho (u')^2 dz' = u_s^2 (Q')^2 / 4 = (u'_s)^2 / 4 \quad (124)$$

The unit momentum and energy flow rates for the v and q directions are determined in the same way, bearing in mind that they are always referenced to the mass flow rate in the perpendicular (u) direction. In this manner one obtains (for the triangular profile):

$$m_v = \int_0^{z'_s} \rho u' dz = \xi^* \ell \rho_\delta Q' u_s v_s z_s R^{-1/2} \int_0^1 (z/z_s)^2 d(z/z_s) \quad (125)$$

$$m_v/m_r = 2v_s Q' / 3 = 2v'_s / 3 \quad (126)$$

$$m_{v2}/m_r = v_s^2 (Q')^2 / 4 = (v'_s)^2 / 4 \quad (127)$$

$$m_q/m_r = 2q_s Q' / 3 = 2q'_s / 3 \quad (128)$$

$$m_{q2}/m_r = q_s^2 (Q')^2 / 4 = (q'_s)^2 / 4 \quad (129)$$

The thermal energy flow rate ( $m_t$ ) is determined from

$$m_t = C_p \int_0^{z'_s} t' \rho u' dz' \quad (138)$$

$$= C_p t'_w \rho_\delta Q' \xi^* \ell u_s z_s R^{-1/2} \int_0^1 [1 + (\Delta t/t_w)] (z/z_s) d(z/z_s) \quad (139)$$

$$\int_0^1 = 0.5 + \Delta t / 3t_w \quad (140)$$

$$m_t/m_r = C_p t'_w (1 + 2\Delta t / 3t_w) \quad (141)$$

and the total energy per unit mass is

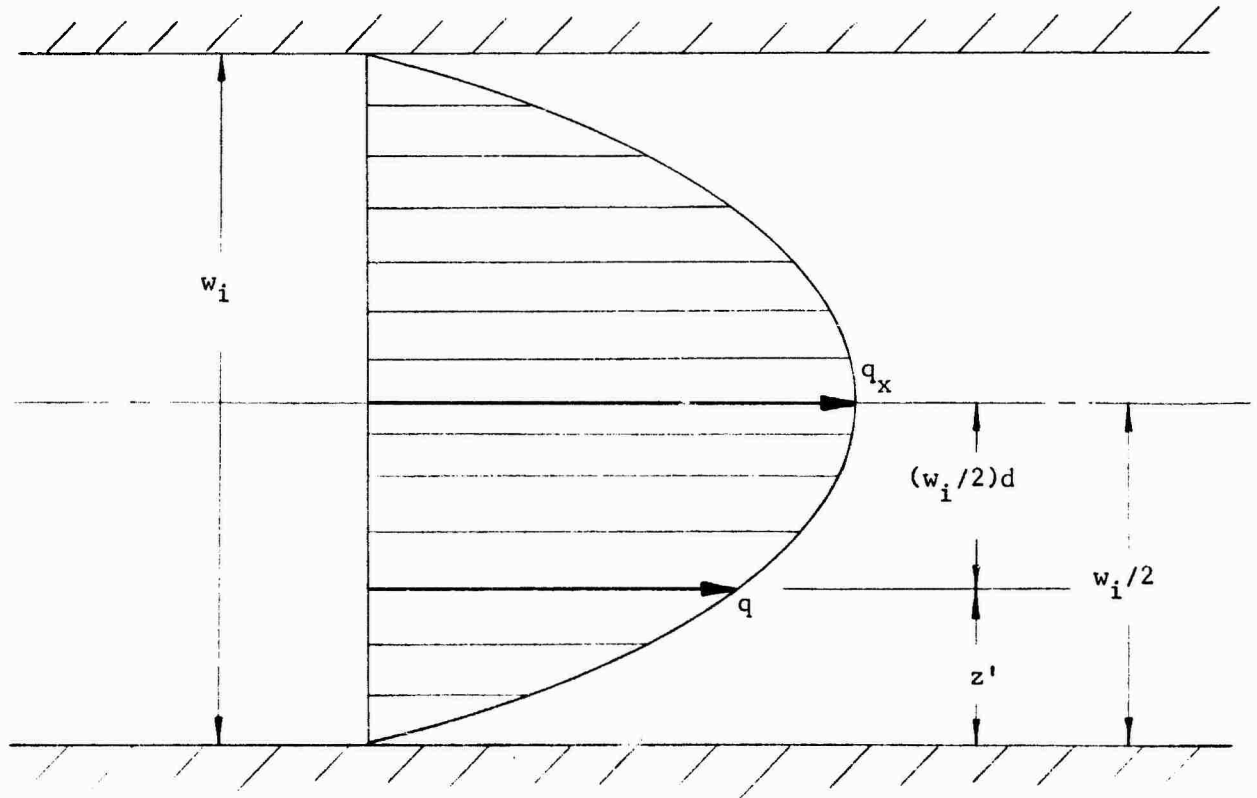
$$C_p t'_a = C_p t'_w (1 + 2\Delta t / 3t_w) + (q')^2 / 4 \quad (142)$$

Dividing the energy terms by the factor  $C_p (Q'_o)^2 / r'$  in order to obtain the nondimensional form [see paragraph (I)]:

$$t_a = t_w (1 + 2\Delta t / 3t_w) + q_s^2 Q^2 / 14 \quad (143)$$

(K) Appendix--Relations for a Compressible Parabolic Profile  
with Constant Total Temperature

The Velocity Distribution



$$d = [(w_i/2) - z'] / (w_i/2) = 1 - 2z'/w_i \quad (144)$$

$$q = q_x(1 - d^2) \quad (145)$$

where the subscript x denotes the centerline value at station x

$$u = u_x(1 - d^2) \quad (146)$$

$$v = v_x(1 - d^2) \quad (147)$$

(K) Appendix--Relations for a Compressible Parabolic Profile  
with Constant Total Temperature (Continued)

The Pressure Distribution

In conventional manner, the pressure distribution is assumed constant across the channel or slot.

The Temperature Distribution

The nondimensional energy equation has been shown to be [paragraph (I)]:

$$t_a = t_x + q_x Q^2 / 7 \quad (148)$$

Dividing this equation by  $t_x$ , transposing, remembering  $q_x Q^2 / 7 t_a = C_x$  and  $t_a / t_x = 1 / (1 - C_x)$

$$t' / t'_x = t / t_x = [1 - q_x Q^2 (1 - d^2)^2 / 7 t_a] t_a / t_x \quad (149)$$

$$= [1 - C_x (1 - d^2)^2] t_a / t_x \quad (150)$$

$$= [1 - C_x (1 - d^2)^2] / (1 - C_x) \quad (151)$$

The Density Distribution

Since the pressure is constant through the boundary layer, the density is inversely proportional to the temperature.

$$\rho' / \rho'_x = \rho / \rho_x = t_x / t = (1 - C_x) / [1 - C_x (1 - d^2)^2] \quad (152)$$

But this expression is awkward when it is used as a multiplier for the integrations below, and a more convenient relation results when the density ratio is expanded in a series.

$$\begin{aligned} \rho / \rho_x = (1 - C_x) [1 + C_x (1 - d^2)^2 + C_x^2 (1 - d^2)^4 \\ + C_x^3 (1 - d^2)^6 + \dots] \end{aligned} \quad (153)$$

These first four terms are adequate when the flow is less than sonic.

The Mass Flow Rate

The mass flow rate that is of interest is the one in the chordwise or perpendicular direction and is measured per unit slot span.

$$m_r = 2 \int_0^{w_i/2} \rho u' d(w_i d/2) = \rho_x u'_x w_i \int_0^1 (\rho / \rho_x) (u / u_x) d(d) \quad (154)$$

$$\begin{aligned} = \rho_x u'_x w_i (1 - C_x) \int_0^1 [(1 - d^2) + C_x (1 - d^2)^3 \\ + C_x^2 (1 - d^2)^5 + C_x^3 (1 - d^2)^7] d(d) \end{aligned} \quad (155)$$

(K) Appendix--Relations for a Compressible Parabolic Profile with Constant Total Temperature (Continued)

$$m_r = \rho_x u_x' w_i (1 - C_x) [0.6667 + 0.45714 C_x + 0.36939 C_x^2 + 0.31810 C_x^3] \quad (156)$$

$$= \rho_x u_x' w_i (w_x/w_i) \quad (157)$$

The term  $w_x$  is equal to  $w_i$  less the two displacement thicknesses; i.e., it is equal to the effective width of the slot. The effective width ratio  $w_x/w_i$  is plotted as a function of  $C_x$  in Fig. 163. It will be noted that the ratio  $w_x/w_i$  is closely represented by the relation

$$w_x/w_i \cong 0.6667 - 0.218 C_x. \quad (158)$$

Flow Rate of Spanwise Momentum

The spanwise momentum is based on the spanwise velocity as indicated by its name, but the mass flow rate that is of interest is in the perpendicular direction and is based on the  $u$  component of velocity.

$$m_v = \int_0^1 v' dm_r = \rho_x u_x' v_x' \int_0^1 (\rho/\rho_x) (u/u_x) (v/v_x) d(w_i d/2) \quad (159)$$

$$= \rho_x u_x' v_x' w_i (1 - C_x) \int_0^1 [(1 - d^2)^2 + (1 - d^2)^4 C_x + \dots] d(d) \quad (160)$$

The integral is given by

$$\int_0^1 = 0.53333 + 0.40635 C_x + 0.34093 C_x^2 + 0.29919 C_x^3 \quad (161)$$

and the unit spanwise momentum becomes

$$\begin{aligned} m_v/m_r &= v_x' k_{mv} \\ &= v_x' (0.53333 + 0.40635 C_x + \dots) / (0.66667 + 0.45714 C_x + \dots) \end{aligned} \quad (162)$$

The momentum factor  $k_{mv}$  is plotted in Fig. 163 as a function of  $C_x$ . Inspection of the figure indicates that the variation is small and that it can be considered nearly constant as given below

$$K_{mv} \cong 0.80. \quad (163)$$

(L) Appendix--Slot Losses Downstream of the Perpendicular Inlet Length

Pressure Drop Along Slot Centerline

As derived in paragraph (N),  $d^2F_v/dy'dx' = 8\mu_w(v'_x/w_i)$ . In a similar manner, we can show that

$$d^2F_u/dy'dx' = -8\mu_w u'_x/w_i \quad (164)$$

where  $u'_x$  is the local centerline velocity and  $w_i$  is the slot width, and this is exactly equal to the portion of the buoyancy force which compensates for the friction force, namely:

$$d^2F_b/dy'dx' = w_i dP'/dx'. \quad (165)$$

Equating the friction force to this portion of the buoyancy force

$$-8\mu_w u'_x/w_i = w_i dP'/dx' \quad (166)$$

or

$$dP' = -(8\mu_w u'_x/w_i^2) dx' \quad (166)$$

This can be shown to be equivalent to the incompressible case in which we know that  $u'_x = \text{constant}$  and  $2\Delta P'/\rho(u'_x)^2 = 6\Delta\sigma$ . This is done by dividing both sides of equation (166) by  $\rho(u'_i)^2/2$  where  $u'_i$  is the velocity at the slot inlet.

$$d[2P'/\rho(u'_i)^2] = -[16\mu_w u'_x/\rho(u'_i)^2 w_i^2] dx' \quad (167)$$

Since  $u'_i = 2u'_x/3$  (incompressible flow),  $\sigma = 4\mu_w x'/m_r w_i$ , and  $m_r = \rho_i u'_i w_i$ , this becomes, after integration,

$$2\Delta P'/\rho(u'_i)^2 = -6\Delta\sigma \quad \text{Q.E.D.} \quad (168)$$

Returning to the compressible case, one may multiply and divide equation (166) by the mass flow rate  $m_r$ .

$$dP' = -(2m_r u'_x/w_i) d\sigma \quad (169)$$

It is possible to reduce this problem to a one-dimensional one by considering the velocity and density of only the center streamline, i.e., by restricting the calculation to the centerline flow. When this is done, one may write

$$m_r = \rho_x u'_x w_x \quad (170)$$

where  $w_x$  is the effective slot width at station  $x$  [see paragraph (K)].

$$-dP'_x = 2\rho_x (u'_x)^2 (w_x/w_i) d\sigma \quad (171)$$

(L) Appendix--Slot Losses Downstream of the Perpendicular Inlet Length (Continued)

Evaluation of the Work Terms per Unit Mass

Dividing equation (171) by  $\rho_x$  and integrating, one obtains the portion of the buoyancy work per unit mass (work due to motion of a finite volume along a pressure gradient) that compensates for the friction work.

$$\begin{aligned} -\int_1 (1/\rho_x) (dP'_x/dx') dx' &= -\int_1 (1/\rho_x) dP'_x \\ &= 4 \int_{\sigma_e}^{\sigma_2} (w_x/w_i) [(u'_x)^2/2] d\sigma \end{aligned} \quad (172)$$

In order to evaluate the righthand integral easily, it is assumed that  $w_x/w_i$  is substantially constant at its initial value,  $w_e/w_i$ . This is a reasonable assumption downstream of the inlet length. The kinetic energy term  $(u'_x)^2/2$  is assumed to vary linearly with  $\sigma$ . Then, if  $\Delta(u')^2/2$  is the total change in  $(u'_x)^2/2$  between stations e and 2, we may write

$$(u'_x)^2/2 = (u'_e)^2/2 + (\sigma - \sigma_e) \Delta(u'_x)^2/2\Delta\sigma$$

Then, the work per unit mass for the center streamline is given by

$$-\int_1 (1/\rho_x) (dP'_x) = (w_e/w_i) \Delta\sigma [2(u'_e)^2 + \Delta(u')^2] \quad (173)$$

where

$$\Delta\sigma = \sigma_2 - \sigma_e$$

and the tag "1" on the integral sign denotes the portion buoyancy work which offsets friction work downstream of the inlet length. The increment in kinetic energy along the center streamline is primarily a result of the change in density, which will decrease due to conversion of spanwise kinetic energy into heat for all streamlines including the center streamline. Although the resultant centerline flow is considered adiabatic in regard to heat exchange across streamlines, this same flow cannot be considered adiabatic when the perpendicular components of the flow are considered alone. These perpendicular components can be treated separately only when the spanwise velocity dissipation is included as a heat addend. The effect of this heat appears as a density reduction so that the chordwise velocity must increase in order to satisfy continuity. An additional buoyancy force is necessary to produce the required acceleration, and the corresponding additional buoyancy work is

$$\int_{\gamma} (1/\rho_x) dP'_x = -\Delta(u')^2/2 = [(u'_e)^2 - (u'_2)^2]/2 \quad (174)$$

where the tag " $\gamma$ " denotes an isentropic portion of work due to buoyancy

(L) Appendix--Slot Losses Downstream of the Perpendicular Inlet Length (Continued)

combined with motion. Then the total buoyancy work is the sum of equations (173) and (174). When these terms are nondimensionalized by dividing by  $(u')^2/2$ , one obtains

$$\begin{aligned} I &= -[2/(u_e')^2] \left[ \int_1 (1/\rho_x) dP_x' + \int_Y (1/\rho_x) dP_x' \right] \\ &= 4\Delta\sigma(w_e/w_i) + [2\Delta\sigma(w_e/w_i) + 1] \Delta(u/u_e)^2 \\ &= h + g\Delta(u/u_e)^2 \end{aligned} \quad (175)$$

In addition to buoyancy work there is a piston or expansion work which is denoted

$$\int P_x' d(1/\rho_x)$$

The Work Chart

The relation between the different portions of work is shown in Fig. 165, where the buoyancy work (due to pressure gradient) is plotted versus the piston work (due to expansion or contraction).

In the figure isothermic lines have a slope of -1.0 and each such line corresponds to a unique temperature. Also, since the total temperature is assumed constant, these isothermic lines represent constant values of resultant kinetic energy per unit mass  $[(q')^2/2]$  which can be determined from the energy equation (94), and increments in kinetic energy are given by

$$\begin{aligned} \Delta(q')^2/2 &= C_p \Delta t' = 3.5R\Delta t' \\ &= 3.5 \left[ \int P_x' d(1/\rho_x) \right]_{\text{constant pressure}} \end{aligned} \quad (176)$$

Since there is no spanwise pressure gradient, there is no buoyancy work associated with the reduction of spanwise kinetic energy. The work that is associated with the spanwise kinetic energy loss, therefore, must be expansion work of the type  $\int_0^o P_x' d(1/\rho_x)$ , and this appears as a horizontal line in the Work Chart (Fig. 165). The tag "o" on the integral denotes the slope of the path on the diagram. This work is real in that it is the work performed by each unit of mass on the surrounding air. It is not useful work, however, since there are no moving boundaries.

There is no velocity change connected with the  $\int_1 (1/\rho_x) dP_x'$  term so that this portion of the process is isothermic and, therefore, has a slope of -1.

(L) Appendix--Slot Losses Downstream of the Perpendicular Inlet Length (Continued)

The work terms which bring about the change in chordwise velocity have a slope of  $-\gamma$  since this process is isentropic; that is, all pressure work in this process is converted to change in kinetic energy. The choice of integral tags "1" and " $\gamma$ " now becomes apparent, since they represent the negative of the slopes of the paths on the work diagram.

The Polytropic Process

Then, the work increments and velocity changes between any two points on the Work Chart are easily found, but such a diagram tells one nothing of the pressure and density changes at such points, for these latter variables will have values depending on the paths taken between the two points. For the purpose of our present calculation a polytropic path will be assumed between the end of the inlet length (station e) and the slot exit (station 2). For such a polytropic process one may write

$$P_e \rho_e^{-n} = P_2 \rho_2^{-n} \quad (177)$$

where  $n$  is the negative of the slope of the straight line connecting the two stations in Fig. 165. Also, for a polytropic process, the buoyancy work is given by

$$-\int \frac{dP'_x}{\rho_x} = \frac{n}{n-1} \frac{P'_e}{\rho_e} \left[ 1 - \left( \frac{\rho_2}{\rho_e} \right)^{n-1} \right] \quad (178)$$

The omission of a subscript for the integral here denotes that that total value is considered. This equation can be nondimensionalized by dividing by the kinetic energy at the end of the inlet length,  $(u'_e)^2/2$ . Also, noting that

$$\frac{2P'_e}{(u'_e)^2 \rho_e} = \frac{2r'_e t'_e}{(u'_e)^2} = \frac{2C_p t'_e}{3.5(u'_e)^2} = \frac{1}{3.5J_{ue}} \quad (179)$$

one obtains

$$I = - \frac{2}{(u'_e)^2} \int \frac{dP'_x}{\rho_x} = \frac{n}{(n-1)3.5J_{ue}} \left[ 1 - \left( \frac{\rho_2}{\rho_e} \right)^{n-1} \right] \quad (180)$$

Inspection of Fig. 165 shows that the negative of the slope of the polytropic path is given by

$$n = \frac{-\int dP'_x / \rho_x}{\int P'_x d(1/\rho_x)} \quad (181)$$

When it is noted that the isothermal designated  $t'_e$  in Fig. 165 has a slope of  $-1.0$ , it is seen that one may substitute  $-\int dP'_x / \rho_x + \Delta(q')^2/7$  for  $\int P'_x d(1/\rho_x)$ . Dividing top and bottom by  $(u'_e)^2/2$  gives



(L) Appendix--Slot Losses Downstream of the Perpendicular Inlet Length (Continued)

$$n = \frac{I}{I - \frac{2}{7} \Delta \left( \frac{q}{u_e} \right)}^2 \text{ where } \Delta \left( \frac{q}{u_e} \right)^2 = \Delta \left( \frac{q'}{u_e'} \right)^2 \quad (182)$$

$$\frac{n}{n-1} = \frac{1}{1 - \frac{1}{n} \frac{2}{7} \Delta \left( \frac{q}{u_e} \right)}^2 \quad (183)$$

Next, from equations (180) and (183), one may derive

$$\rho_e / \rho_2 = [1 - J_{ue} \Delta(q/u_e)^2]^{1/(1-n)} \quad (184)$$

where:

$$\Delta(q/u_e)^2 = \Delta(v/u_e)^2 + \Delta(u/u_e)^2 \quad (185)$$

Also,

$$(u_2/u_e)^2 = 1 + \Delta(u/u_e)^2 \quad (186)$$

and from the approximate expression for  $w_x/w_i$  [equation (158)]

$$\begin{aligned} w_2/w_i &= w_e/w_i + \Delta w/w_i \\ &= w_e/w_i + (0.66667 - 0.218C_2) - (0.66667 - 0.218C_e) \quad (187) \\ &= w_e/w_i - 0.218(C_2 - C_e) = w_e/w_i - 0.218\Delta q^2/(2C_p t_a) \end{aligned}$$

and

$$\begin{aligned} w_2/w_e &= 1 - 0.218\Delta(q')^2 w_i / (2C_p t_a' w_e) \\ &= 1 - b\Delta(q/u_e)^2 \end{aligned}$$

where

$$b = 0.218 w_i (u_e')^2 / (2C_p t_a' w_e) = 0.218 C_{ue} (w_i/w_e) \quad (189)$$

Continuity provides a final equation

$$\rho_2 u_2 w_2 / (\rho_e u_e w_e) = \rho_2 w_2 \sqrt{1 + \Delta(u/u_e)^2} / (\rho_e w_e) = 1.0 \quad (190)$$

Squaring and solving for  $\Delta(u/u_e)^2$  results in

$$\Delta(u/u_e)^2 = [(\rho_e / \rho_2)^2 / (w_2/w_e)^2] - 1 \quad (191)$$

(L) Appendix--Slot Losses Downstream of the Perpendicular Inlet Length (Continued)

Summary of Knowns

At station e (end of the chordwise inlet length) one knows, or assumes, the following variables:

$$\sigma_e = 0.12 \text{ [equation (211)]}$$

$$\Delta\sigma = \sigma_2 - \sigma_e \quad (192)$$

$$\left. \begin{aligned} h &= 4(w_e/w_i)\Delta\sigma \\ g &= 2(w_e/w_i)\Delta\sigma + 1 \end{aligned} \right\} \text{ equation (175)}$$

$$J_{ue} = M_{ue}^2/5 \text{ [equation (98)]}$$

$$C_{ue} = (u_e/a_a)^2/5 \text{ [equation (97)]}$$

$$b = 0.218C_{ue}w_i/w_e \text{ [equation (189)]}$$

$$\Delta(v/v_e)^2 = e^{-5.0\Delta\sigma} - 1 \text{ [equation (228)]}$$

$$\Delta(v/u_e)^2 = \Delta(v/v_e)^2 (v_e/u_e)^2 \quad (193)$$

Working Equations

$$\Delta(q/u_e)^2 = \Delta(v/u_e)^2 + \Delta(u/u_e)^2 \quad (194)$$

$$I = h + g\Delta(u/u_e)^2 \quad (195)$$

$$n = I/[I - (2/7)\Delta(q/u_e)^2] \quad (196)$$

$$\rho_e/\rho_2 = [1 - J_{ue}\Delta(q/u_e)^2]^{1/(1-n)} \quad (197)$$

$$\Delta(u/u_e)^2 = \left[ (\rho_e/\rho_2) / [1 - b\Delta(q/u_e)^2] \right]^2 - 1 \quad (198)$$

These simultaneous equations are solved easily for large sweep angles by first assigning a value of  $\Delta(u/u_e)^2$  and then calculating  $\Delta q^2/u_e^2$ ,  $n$ ,  $\rho_e/\rho_2$ , and  $\Delta(u/u_e)^2$  in that order. Then a recalculation is performed using the new value of  $\Delta(u/u_e)^2$ . Convergence occurs rapidly for large sweep angles even if zero is initially assigned to the value of  $\Delta(u/u_e)^2$ . Convergence has not been checked for other sweep angles so that a different procedure may be necessary if the sweep angle is changed.

Once the density ratio is established, the pressure ratio is easily found from the polytropic relation:

$$P_2/P_e = P'_2/P'_e = (\rho_e/\rho_2)^{-n} \quad (199)$$

(M) Appendix--Calculation of the Inlet Length for Zero Pressure Gradient

The inlet length of a slot is defined as the length of the slot required before the boundary layer extends completely across the slot. In the two-dimensional slot with no spanwise velocity component there is a negative pressure gradient along the flow direction which is directly related to the centerline velocity. This gradient tends to accelerate the boundary layer air and, therefore, to extend the inlet length. The spanwise component of velocity which results when the slot is swept is not aided by spanwise pressure gradients so that the inlet length is shorter than it would be with a favorable pressure gradient. This inlet length is estimated below from known incompressible characteristics (see reference 73).

For any station along the inlet length the kinetic energy flow rate for incompressible flow is given by the summation of the energy flow rates in the two boundary layers plus that in the isentropic core. In the boundary layers

$$m_{u2\delta} = \rho(u_x')^3 \delta \int_0^1 (1 - d^2)^3 d(d) = (16/35) \rho(u_x')^3 \delta \quad (200)$$

where  $\delta$  = boundary layer thickness and  $d = 1 - 2z'/w_i$ .

In the isentropic core

$$m_{u2c} = 0.5 \rho(u_x')^3 (w_i - 2\delta) \quad (201)$$

And the total kinetic energy flow rate is

$$m_{u2x} = 0.5 \rho(u_x')^3 w_i [1 - (19/35)(2\delta/w_i)] \quad (202)$$

The mass flow rate  $m_r$  is equal to  $\rho u_i w_i$  so that the unit energy flow rate is

$$m_{u2x}/m_r = 0.5(u_x'/u_i)^2 (u_x'/u_i) [1 - (19/35)(2\delta/w_i)] \quad (203)$$

The displacement thickness of the boundary layer is  $\delta/3$  for a parabolic profile. Also, the center streamline is isentropic in the inlet length so that one may write

$$u_x'/u_i = w_i/w_e = w_i/(w_i - 2\delta/3) \quad (204)$$

or

$$2\delta/w_i = 3(1 - u_i/u_x) \quad (205)$$

Substituting this value in equation (203), one obtains

$$\begin{aligned} m_{u2x}/m_r &= 0.5(u_x'/u_i)^2 (u_x'/u_i) [1 - 1.62857(1 - u_i/u_x)] \\ &= 0.5(u_x')^2 [1 + 0.62857(1 - u_x'/u_i)] \end{aligned} \quad (206)$$

(M) Appendix--Calculation of the Inlet Length for Zero Pressure Gradient (Continued)

This is the total unit energy flow rate. One can subtract the portion of the energy change due to the buoyancy work and obtain the friction work. The unit buoyancy work to any station is  $(u_x^i)^2/2$  and when this quantity is subtracted from equation (207) the friction work is seen to be

$$W_f = -0.62857(1 - u_x/u_i)(u_x^i)^2/2 \quad (207)$$

or

$$2W_f/(u_i^i)^2 = -0.62857(1 - u_x/u_i)(u_x/u_i)^2 \quad (208)$$

The velocity ratios in the equation above can be represented approximately by the expressions given below. These empirical representations were obtained by plotting the information given in reference 73 on log-log graph paper and approximating the curves with straight lines. The expression obtained for the velocity ratio may also be used to obtain the corresponding inlet length since it may be solved for  $u_x/u_i = 1.5$  which is the value at the end of the inlet length.

$$u_x/u_i = 1 + 1.28\sigma^{0.4435} \quad (209)$$

$$(u_x/u_i)^2 = 1 + 3.6084\sigma^{0.5} \quad (210)$$

$$\sigma_e = 0.12 \text{ (when } u_x/u_i = 1.5) \quad (211)$$

Then approximately

$$2W_f/(u_i^i)^2 = -0.62857(1 + 3.6084\sigma^{0.5})(1.28\sigma^{0.4435}) \quad (212)$$

and the differential with respect to  $\sigma$  is

$$d[2W_f/(u_i^i)^2]d\sigma = -2.7392\sigma^{-0.0565} - 0.35683\sigma^{-0.5565} \quad (213)$$

It is now desired to find a similar differential that can be used for the spanwise flow, but such a differential should be based on the local velocity and a modified value of  $\sigma$ , namely  $\sigma_u$ , which is defined as  $4\mu_w x / \rho u_x^i w_i^2$ . Note that this is based on the local rather than the inlet velocity. Then

$$d\sigma_u = (u_x/u_i)d\sigma \quad (214)$$

$$d[2W_f/(u^i)^2]/d\sigma_u = (u_i/u_x)d[2W_f/(u_i^i)^2]/d\sigma \quad (215)$$

$$= -(2.7392\sigma^{-0.0565} + 0.35683\sigma^{-0.5565})/(1 + 1.28\sigma^{0.4435})$$

This differential may now be averaged over the inlet length by integrating with respect to  $\sigma$  and dividing by 0.12 (the inlet length  $\sigma$ ). This has

(M) Appendix--Calculation of the Inlet Length for Zero Pressure Gradient (Continued)

been done graphically and the average value was found to be -4.335. It is assumed that a similar average value is appropriate for the spanwise flow. Then

$$\left\{ d[2W_f/(v'_x)^2]/d\sigma_v \right\}_m = -4.335 \quad (216)$$

where  $v'_x = v'_i = \text{constant}$ , and the subscript m denotes the average value in the inlet length.

The unit kinetic energy lost in the inlet length (for the spanwise flow) equals the spanwise friction work and is given by

$$\Delta W_f = -4.335 \Delta \sigma_v (v'_i)^2 / 2 = 0.3143 (v'_i)^2 / 2 \quad (217)$$

where the second equality is simply the energy deficit in the parabolic profile. Solving for  $\Delta \sigma_v$  one obtains

$$\Delta \sigma_v = 0.726 \quad (218)$$

But the reference parameter used in the calculation of the slot losses is  $\sigma$ , which is based on the perpendicular component of flow. It is desirable, therefore, to determine the value of  $\Delta \sigma_v$  in terms of  $\sigma$ . This may be done as follows:

$$\frac{d\sigma}{d\sigma_v} = \frac{4\mu_w dx' \rho v'_i w_i^2}{\rho u'_i w_i^2 4\mu_w dy'} = \frac{v'_i dx'}{u'_i dy'} = \frac{v'_i u'_x}{u'_i v'_i} = \frac{u'_x}{u'_i} = \frac{u_x}{u_i} \quad (219)$$

Substituting equation (209) for  $u_x/u_i$  and integrating

$$\sigma_d = \int_0^{\Delta \sigma_v} d\sigma_v = \int_0^{\sigma_d} [1/(1 + 1.28\sigma^{0.4435})] d\sigma \cong 0.0974 \quad (220)$$

The integration was carried out graphically. It is seen, then, that for incompressible flow  $\Delta \sigma_v$  will occur when  $\sigma_d = 0.0974$ . It is clear that the spanwise boundary layer fills the slot upstream of the point where the chordwise boundary layer fills the slot; i.e., the spanwise inlet length is indeed shorter than the chordwise inlet length (based on the perpendicular distance from the inlet).

For compressible flow these values of  $\sigma$  at the end of the inlet lengths would probably increase because of the reduction of density and consequent additional acceleration of the perpendicular component of velocity. Then the inlet length would be different for each inlet Mach number and the problem of calculating the losses becomes very complicated. It is convenient, therefore, to assume that the inlet lengths do not vary with Mach number and to use the incompressible values calculated above. This assumption is justified because the friction forces change slowly near the end of the inlet length and are essentially the same as the

(M) Appendix--Calculation of the Inlet Length for Zero Pressure Gradient (Continued)

friction forces just downstream of the inlet length. Then a large change in the value assumed for the inlet length causes only a small change in the calculated losses for the slot. Since the inlet length is not critical, and since considerable simplification results when constant values are assumed, the incompressible values calculated may be assumed to be applicable for all Mach numbers in the calculation of the compressible flow losses for swept slots.

(N) Appendix--Reduction of Spanwise Velocity Downstream of the Inlet Length

Since there is no pressure gradient for the spanwise component of velocity, the reduction of velocity is directly related to the skin friction. Then, from the definition of  $\mu$ , one may write for a slot

$$d^2 F_V / dy' dx' = -2\mu_w (dv' / dz')_w \quad (221)$$

where the factor 2 results from the fact that there are two walls. For the assumed parabolic velocity distribution with maximum centerline velocity  $v'_x$  the slope at the wall is

$$(dv' / dz')_w = 4v'_x / w_i \quad (222)$$

The rate of change of momentum per unit slot span for boundary layers extending to the slot centerlines may be shown to be

$$d^2 m_V / dt^* dy' = m_r k_{mv} dv'_x / dx' \quad [\text{see paragraph (K)}] \quad (223)$$

where

$m_r$  = mass flow rate in the perpendicular direction

$k_{mv}$  = ratio of average momentum velocity to  $v'$

$x'$  = distance through slot (perpendicular direction)

$t^*$  = time

Equating the rate of change of momentum to the friction force per unit area

$$-8\mu_w v'_x / w_i = m_r k_{mv} dv'_x / dx' \quad (224)$$

or

$$-(8\mu_w / k_{mv} m_r w_i) dx' = (1/v'_x) dv'_x \quad (225)$$

and, after integrating between the end of the inlet (station e) and the slot exit (station 2), one obtains

(N) Appendix--Reduction of Spanwise Velocity Downstream of the Inlet Length (Continued)

$$\ln(v_2'/v_e') = -8\mu_w \Delta x / k_{mv} m_r w_i = -2\Delta\sigma / k_{mv} \quad (226)$$

where  $\Delta\sigma$  is the difference between the exit and inlet length  $\sigma$ 's. The momentum factor  $k_{mv}$  is given in paragraph (K) where it is noted that it is approximately equal to 0.80. With this approximation

$$\ln(v_e'/v_2') = 2.5\Delta\sigma \quad (227)$$

or

$$(v_2/v_e)^2 = (v_2'/v_e')^2 = e^{-5\Delta\sigma} = 1 + \Delta(v/v_e)^2 \quad (228)$$

(O) Appendix--Calculation of Losses in the Inlet Length for Perpendicular Flow

The inlet length of a slot (two-dimensional channel) is defined as the distance along the flow direction which is required before the boundary layer extends from wall to wall. For the extent of this length the center streamline flow is isentropic for two-dimensional flow. For a swept slot the inlet length will be defined in a similar manner; namely, the perpendicular distance between the slot inlet and the loci of points where the boundary layer for the component of velocity under consideration just begins to extend from wall to wall. For such swept slots, however, the inlet length for the spanwise component of velocity is shorter than the inlet length for the perpendicular component of velocity (see paragraph (M)). Downstream of the inlet length for the spanwise flow, therefore, some of the kinetic energy of the center streamline is converted to heat so that the center streamline flow is no longer isentropic downstream of this point. The energy conversion is small along this difference in inlet lengths, however, so that it is convenient to perform the calculation in two parts consisting of an isentropic step from station i to station d followed by a heat addition at constant pressure from station d to e (Figs. 159 & 165). Only a negligible error is introduced by this procedure because of the small heat addend.

It has been shown in paragraph (M) that the effective channel width for a parabolic profile (such as at station e) is a function of the kinetic energy due to the resultant velocity. On the other hand, the perpendicular component of velocity at e is a function of the effective channel width ratio. This interrelation makes a forward solution of the problem difficult. However, it is relatively simple to assume final values of  $C_e$  and  $(v_e/u_e)^2$  and then to work forward to determine what combination of inlet variables result in the assumed end of inlet variables. The procedure begins by assuming  $C_e$  and calculating the effective channel width ratio from Equations (156) and (157).

$$w_e/w_i = (1-C_e)(0.66667 + 0.45714C_e + 0.36939C_e^2 + 0.31810C_e^3) \quad (229)$$

Then  $(v_e/u_e)^2$  is assumed, and the remaining variables at station e are found.

(0) Appendix--Calculation of Losses in the Inlet Length for Perpendicular Flow (Continued)

$$t_e/t_a = 1 - C_e \quad (230)$$

$$u_e^2/2C_p t_a = C_{ue} = C_e/[1 + (v_e/u_e)^2] \quad (231)$$

$$C_{ve} = C_e/[1 + (u_e/v_e)^2] = C_{ue}(v_e/u_e)^2 \quad (232)$$

In paragraph (M) the value of  $\sigma$  at the end of the inlet length for spanwise flow is shown to be 0.0974 [equation (220)] whereas the  $\sigma$  at the inlet length for the perpendicular flow is 0.120 [equation (211)]. The difference, then, is  $\Delta\sigma = 0.0226$ . Then by virtue of equation (228), the corresponding kinetic energy ratio is

$$(v_d/v_e) = e^{5.0\Delta\sigma} \cong 1.12 \quad (233)$$

so that

$$C_{vd} = 1.12C_{ve} \quad (234)$$

Since the path from e to d is at constant pressure, there can be no change in  $u$  for the center streamline (friction is eliminated for this streamline since the boundary layer thickness for the  $u$  component does not yet reach the centerline of the slot).

$$C_{ud} = C_{ue} \quad (235)$$

$$C_d = C_{ue} + C_{vd} \quad (236)$$

$$t_d/t_a = 1 - C_d \quad (237)$$

$$\rho_e w_e / \rho_d w_d = 1.0 \quad (238)$$

and at constant pressure

$$w_d/w_e = \rho_e/\rho_d = (t_d/t_a)/(t_e/t_a) \quad (239)$$

$$J_{ud} = C_{ud}/(t_d/t_a) \quad (240)$$

$$M_{ud} = \sqrt{5.0J_{ud}} \quad (241)$$

$$w^*/w_d = 1.728M_{ud}/(1 + 0.2M_{ud}^2)^{3.0} \quad (242)$$

$$(u_d/a_{vd})^2 = M_{ud}^2/(1 + J_{ud}) \quad (243)$$

$$\begin{aligned} w^*/w_i &= (w^*/w_d)(w_d/w_e)(w_e/w_i) \\ &= 1.728M_{ui}/(1 + 0.2M_{ui}^2)^{3.0} \end{aligned} \quad (244)$$

from which  $M_{ui}$  may be determined as well as  $w^*/w_i$ . Then,

$$(u_i/a_{vi})^2 = M_{ui}^2/(1 + 0.2M_{ui}^2) \quad (245)$$



(0) Appendix--Calculation of Losses in the Inlet Length for Perpendicular Flow (Continued)

and since  $a_{vi} = a_{vd}$ ,  $u_e = u_d$ , and  $v_i = v_d$

$$(u_d/u_i)^2 = (u_e/u_i)^2 = (w_d/a_{av})^2 / (u_i/a_{av})^2 \quad (246)$$

$$(v_i/u_i)^2 = (v_d/u_d)^2 (u_d/u_i)^2 = (C_{vd}/C_{ue})(u_e/u_i)^2 \quad (247)$$

Thus, one may arrive at the initial conditions  $w^*/w_i$  and  $(v_i/u_i)^2$  that result in a velocity ratio of  $(u_e/u_i)^2$ . A series of such calculations has been completed and after some crossplotting and interpolation the results shown in Fig. 161 were obtained. The data points represent the results obtained from graphical interpolation of the calculated results. The lines which approximate the data points are given by the empirical equation in the figure. It is seen that these lines very closely represent the calculated values of  $(u_e^2/u_i^2)$ .

## CHAPTER E. PRESSURE DROP IN LAMINAR FLOW TUBES WITH COMPRESSIBLE FLOW

W. Pfenninger

K. H. Rogers

### (A) Summary

The pressure drop for laminar flow in a circular tube of 0.244-inch inside diameter and 11.3-foot length was measured for several inlet Mach numbers  $M_0$  at different reservoir pressures  $p_k$ . The pressure ratio  $p/p_k$  is presented versus the nondimensional tube length  $x/RR_R$  for various inlet Mach numbers. With increasing values of  $M_0$  and  $x/RR_R$  the density and static pressures decreased rapidly until choking occurred at the downstream end of the test tube at pressure ratios  $p/p_k \approx 0.20$  to  $0.25$ . These pressure ratios at choking are considerably lower than for one-dimensional potential flow in a tube. Boundary layer measurements at the downstream end of the test tube for choked conditions showed supersonic flow in the center and subsonic flow toward the wall of the tube with an average Mach number of approximately one.

The highest length Reynolds number with full length laminar flow was  $\bar{U}_0 x_E / \nu_0 = 26.1 \times 10^6$  at  $M_0 = 0.430$ .

### (B) Notation

$x$	tube length measured from the fictitious inlet where the boundary layer thickness is zero
$p$	absolute static pressure
$R$	tube radius
$\nu_0$	kinematic viscosity at tube inlet
$M_0$	Mach number at tube inlet
$U$	potential flow velocity
$\bar{U}_0$	mean velocity at tube inlet
$R_{\eta}$	$= \frac{\bar{U}_0 R}{\nu_0}$ = tube Reynolds number at tube inlet with zero boundary layer thickness

### Indices

$o$	fictitious tube inlet where the boundary layer thickness is zero
$k$	inlet reservoir, with the air at rest
$5$	station of first static pressure orifice in test tube
$E$	end of test tube

### (C) Introduction

In supersonic low drag suction airplanes and suction models for wind tunnel investigations the pressure drop through the components of the suction ducting system can be a relatively large percentage of the absolute pressure. The flow through the components of the suction ducting system (suction slots and holes, ducts, etc.) must then be treated as compressible, and the question then arises as to the pressure drop through the suction slots, holes and ducts for compressible flow.

In order to provide data for the compressible laminar pressure drop in suction holes, the pressure distribution for compressible laminar flow was measured along the inside of a circular tube of 0.244-inch inside diameter and 11.3-foot length at various inlet Mach numbers  $M_0$  and several absolute pressures  $p_k$  in the inlet reservoir.

### (D) Experimental Setup

The experimental setup, consisting of a large inlet tube of 4-inch inside diameter with seven damping screens (0.0035-inch wire diameter, 120 mesh size) followed by a long inlet nozzle and the test tube of 0.244-inch inside diameter and 11.3-foot length, is shown in Figure 166. The inlet tube was connected to a high-pressure dry air supply. The air was removed by means of a pump located downstream of the exit reservoir (Figure 166). The flow rate through the tube and the absolute pressure at the inlet downstream of the screens could be varied over a wide range.

The static pressure in the inlet nozzle and in the test tube was measured by means of 0.020-inch diameter static pressure orifices connected to a bank of mercury U-tube manometers. The wall temperature was measured by means of thermocouples.

Full length laminar flow was maintained at  $p_k = 0.8$  atmosphere up to an inlet Mach number  $M_0 = 0.430$ , corresponding to a tube length Reynolds

number for laminar flow  $\frac{\bar{U}_0 \cdot X_E}{\nu_0} = 26.1 \times 10^6$ . The highest reservoir pressure

$p_k$  with full length laminar flow for a short time was 1.0 atmosphere. Transition occurred, however, before pressure data could be taken.

The pressure ratio  $p/p_k$  ( $p_k$  = absolute static pressure with the flow at rest) was evaluated at various stations along the tube for different Mach numbers at the beginning of the test tube and for several reservoir static pressures  $p_k$  ( $p_k = 0.1$  to 0.8 atmosphere). The mean velocity  $\bar{U}_0$  at the fictitious inlet of the test tube, where the boundary layer thickness is zero, was determined from the pressure drop across the inlet nozzle and from a nozzle calibration obtained during previous experiments in a 2-inch inside diameter tube with a geometrically similar inlet nozzle shape. Compressibility corrections were applied to the nozzle calibration curves of Figure 167, which show, for various Reynolds numbers  $R_R$  and Mach number  $M_0$ , the ratio  $U_5/\bar{U}_0$  of

(E) Measurements, Evaluation and Experimental Results (Continued)

the potential flow velocity  $U_5$  at the first static pressure orifice (number 5) in the test tube to the mean velocity  $\bar{U}_0$  at the tube inlet, where the boundary layer thickness is zero. Figure 168 shows the distance  $x_5$  from the first static pressure orifice (number 5) in the test tube to the fictitious tube inlet of zero boundary layer thickness for various Reynolds numbers  $RR_R = \frac{\bar{U}_0 R}{\nu_0}$  (index zero refers to condition at tube inlet with zero boundary layer thickness).

According to theory, for a given inlet Mach number  $M_0$ , the pressure ratio  $p/p_k$  is a function of the nondimensional tube length  $x/RR_R$ .

In Figures 169-172 and Table XII the pressure ratio  $p/p_k$  is plotted versus the nondimensional tube length  $\frac{x \cdot \nu_0}{\bar{U}_0 R^2} = \frac{x}{RR_R}$  for various inlet Mach numbers

$M_0$  and for different values of the absolute reservoir pressure  $p_k$  with the air at rest.

At the lower inlet Mach numbers  $M_0$  and for smaller values of  $x/RR_R$  the density variation along the tube is relatively small and compressibility effects do not appreciably affect the pressure drop in the tube. At higher values of  $M_0$  and  $x/RR_R$ , however, the density and static pressure  $p$  decreases rapidly in downstream direction until choking occurs at the downstream end of the test tube. At larger nondimensional tube lengths choking was observed at pressure ratios  $p/p_k \approx 0.2$ . At smaller values  $x/RR_R \approx 0.04$  to  $0.05$  the pressure ratio at choking was  $p/p_k \approx 0.25$  (Figures 173 and 174).

The values of  $x/RR_R$  at choking increase considerably with decreasing inlet Mach numbers  $M_0$  (Figures 173 and 174).

The observed pressure ratios at choking are considerably lower than for the case of one-dimensional potential flow in a tube. Boundary layer measurements at the downstream end of the test tube for choked conditions showed supersonic flow in the center and subsonic flow toward the wall of the tube. The average Mach number at the tube exit was then approximately  $\bar{M} \approx 1$ . Under such conditions the higher Mach number in the center of the tube requires a considerably lower pressure for choking than for the case of one-dimensional potential flow in a tube.

LIST OF TABLES FOR SECTION II, Part 2

<u>Table No.</u>	<u>Table Title</u>	<u>Page</u>
I	SLOT DIMENSIONS AND RAKE HEIGHTS OF 41" CHORD FLAT PLATE SUCTION MODEL.....	552
II	MEASURED SUCTION AND DRAG COEFFICIENTS OF 41" FLAT PLATE SUCTION MODEL.....	553
III	SLOT LOCATIONS AND WIDTHS OF OGIVE CYLINDER SUCTION MODEL.....	554
IV	SUCTION SYSTEM OF ORIGINAL AND MODIFIED 36° SWEEP SUCTION MODEL.....	555
V	COMPRESSIBLE LIFT COEFFICIENTS FOR 72.5° SWEEP WING.....	556
VI	CALCULATED DRAG COEFFICIENTS FOR 72.5° SWEEP WING.....	557
VII	METERING HOLE & SLOT VARIABLES FOR 72.5° SWEEP WING.....	558
VIII	STATIC PORT LOCATIONS AND NOTES FOR 72.5° SWEEP WING.....	560
IX	COMPARISON OF ACTUAL AND EMPIRICAL WAKE DRAG CORRECTIONS FOR 72.5° SWEEP WING.....	561
X	COMPARISON OF CALCULATED AND MEASURED DRAG COMPONENTS OF $\alpha = 0.5$ , 72.5° SWEEP WING.....	562
XI	COMPARISON OF SLOT LOSSES CALCULATED FOR DIFFERENT SWEEP ANGLES AND ASSIGNED VALUES OF $r_f$ .....	563
XII	PRESSURE DROP IN LAMINAR FLOW TUBE WITH COMPRESSIBLE FLOW.....	564

TABLE I

SLOT DIMENSIONS AND RAKE HEIGHTS OF 41" CHORD FLAT PLATE SUCTION MODEL

Slot Dimensions

<u>Suction Chamber</u>	<u>Location of First Slot (in)</u>	<u>Location of Last Slot (in)</u>	<u>Number of Slots</u>	<u>Slot Spacing (in)</u>	<u>Slot Width (in)</u>	<u>Average Slot Span (in)</u>
1	2.00	3.68	5	.42	.0040	14.36
2	4.11	6.26	6	.43	.0045	13.68
3	6.70	9.40	7	.45	.0050	12.84
4	9.90	13.40	8	.50	.0050	11.80
5	13.90	17.90	9	.50	.0050	10.57
6	18.40	23.40	11	.50	.0050	9.12
7	23.95	31.10	14	.55	.0050	7.20
8	31.65	39.90	16	.55	.0050	4.80

Rake Heights

(Average values during period of testing)

1	.014 in
2	.036 in
3	.053 in
4	.067 in
5	.090 in
6	.113 in
7	.150 in
8	.183 in
9	.226 in
10	.300 in

TABLE II

MEASURED SUCTION AND DRAG COEFFICIENTS OF 41" FLAT PLATE SUCTION MODEL

M	$x_{\text{rake}}$ (in)	$10^{-6} R_x$	$10^4 C_{Wt}$	$10^4 C_{Ds}$	$10^4 C_{Dw}$	$10^4 C_{Dt}$
3.0	40.19	13.40	2.897	3.152	3.279	6.431
		19.17	2.191	2.283	3.093	5.376
		26.48	2.176	2.286	2.316	4.602
3.5	40.23	21.91	2.572	2.850	3.033	5.883
2.5	40.16	14.18	2.465	2.528	3.025	5.553
		14.08	2.916	3.019	2.894	5.913
		14.08	3.778	4.049	2.571	6.620
		19.32	1.867	1.923	2.941	4.864
		19.34	2.083	2.148	2.625	4.773
		19.31	2.978	3.159	2.093	5.252
		19.27	3.527	3.831	2.119	5.950
		19.23	4.060	4.583	2.119	6.702
		21.83	2.052	2.121	2.734	4.855
		21.73	2.569	2.682	2.165	4.847
		13.64	2.558	2.817	2.519	5.336
		14.42	2.397	2.540	2.688	5.228
		14.53	2.839	3.100	2.460	5.560
		14.10	2.590	2.862	3.944	6.806
		14.10	2.754	3.068	3.820	6.888
		14.09	3.329	4.011	2.990	7.001
3.5	31.38	16.87	2.367	2.609	3.697	6.306
		16.85	2.597	2.878	3.144	6.022
		16.92	3.331	4.027	2.865	6.892
		16.88	3.367	4.063	2.352	6.415

TABLE III

SLOT LOCATIONS AND WIDTHS OF OGIVE CYLINDER SUCTION MODEL

<u>Chamber</u>	<u>Slot Location (in.)</u>	<u>Slot Width (in.)</u>
1	4.5	.0035
	5.0	
	5.5	
	6.0	
	6.5	
	7.0	
	7.5	
	8.0	.0035
2	8.5	.0040
	9.0	
	9.5	
	10.0	.0040
	10.5	.0045
	11.0	.0045
	11.5	.0050
3	12.0	.0060
	12.5	.0065
	13.0	.0070
	13.5	.0070
	14.0	
	14.5	
	15.0	
4	15.5	.0070
	16.0	
	16.5	
	17.0	
	17.5	
	18.0	
	18.5	.0070



TABLE IV

SUCTION SYSTEM OF ORIGINAL AND MODIFIED 36° SWEEP SUCTION MODEL

<u>Suction Chamber</u>	<u>Number of Slots per Chamber</u>	<u>Slot Spacing (in.)</u>	<u>Location of</u>		<u>Slot Width (in.)</u>
			<u>First Slot</u>	<u>Last Slot</u>	
			<u>x (in.)</u>		
<u>Original Model (First Tests)</u>					
1	6	0.42	1.60	3.70	0.005
2	7	0.42	4.12	6.64	0.006
3	8	0.44	7.07	10.15	0.006
4	9	0.44	10.59	14.11	0.007
5	9	0.45	14.55	18.15	0.007-0.008
6	9	0.45	18.60	22.20	0.008-0.009
7	9	0.45	22.65	26.25	0.009-0.011
8	9	0.45	26.70	30.30	0.012-0.014
<u>Modified Model (Second Tests)</u>					
1	7	0.42	0.76	3.28	0.005-0.008
2	8	0.42	3.70	6.64	0.008
3	8	0.44	7.07	10.15	0.009
4	9	0.44	10.59	14.11	0.009
5	9	0.45	14.55	18.15	0.009-0.010
6	9	0.45	18.60	22.20	0.010-0.011
7	9	0.45	22.65	26.25	0.011-0.012
8	9	0.45	26.70	30.30	0.012-0.014

TABLE V

COMPRESSIBLE LIFT COEFFICIENTS FOR 72.5° SWEPT WING

$\alpha'$	-1.0	-0.5	0.0	0.5	1.0	1.5	2.0	2.5
$\alpha$	-0.30	-0.15	0.0	0.15	0.30	0.45	0.60	0.75
$C_L'$ incompressible	0.52	0.58	0.64	0.70	0.76	0.82	0.88	0.94
$C_L'$ } Modified $C_L$ } Göthert correction	0.67	0.74	0.82	0.90	0.97	1.05	1.12	1.19
	0.060	0.067	0.074	0.081	0.88	0.95	0.101	0.107
$C_L'$ } Karman-Tsien $C_L$ } correction	0.69	0.77	0.85	0.94	1.02	1.10	1.19	1.29
	0.062	0.069	0.077	0.085	0.092	0.099	0.107	0.116
$C_L'$ } Spreiter-Alksne $C_L$ } correction	0.72	0.81	0.90	0.99	1.08	1.18	1.27	1.36
	0.065	0.073	0.081	0.089	0.097	0.106	0.104	0.122

TABLE VI

## CALCULATED DRAG COEFFICIENTS FOR 72.5° SWEEP WING

M	2.0	2.0	2.0	3.0
$R \times 10^{-6}$	4.0	10.0	30.0	30.0
$P/P_a$ (minimum)	0.08648	→		0.01936
$q_\infty/P_a$	0.3605	→		0.1414
$0.01 q_\infty/P_a$ (assumed loss)	0.00365	→		0.00141
$P_s/P_a$ (average suction pressure)	0.08283	→		0.01795
$P_\infty/P_a$	0.1278	→		0.02722
$P_s/P_\infty$	0.648	→		0.659
$T_\infty/T_a \approx T_\infty/T_{as}$	0.5556	→		0.3571
$\bar{f}_0^*$	2.19	2.86	3.82	4.706
$\sum C_{wh} \times 10^4 = \bar{f}_0^* / \sqrt{R_c}$	11.0	9.05	6.97	8.60
$2 \delta_{ss}/t \times 10^4 = C_{D_{wu}} \times 10^4$	1.840	0.806	0.299	0.217
$C_{D_{wc}} \times 10^4$	0.983	0.545	0.233	0.180
$C_{D_s} \times 10^4$	14.25	11.7	9.02	10.30
$C_{D_t} \times 10^4$	15.23	12.24	9.25	10.48

TABLE VII

## METERING HOLE &amp; SLOT VARIABLES FOR 72.5° SWEEP WING

Suction Chamber No.	Slot Number	S/C°	Slot Width $W_1 \sim$ in.	Hole Spacing $\gamma \sim$ in.	Hole Dia. $d \sim$ in.
1	1	0.024	0.003	0.250	0.0350
1	2	0.048			0.0420
1	3	0.072			0.0465
2	4	0.096			0.0320
2	5	0.120			0.0330
2	6	0.144			0.0310
2	7	0.168			0.0292
3	8	0.192			0.0292
3	9	0.216			0.0292
3	10	0.240			0.0292
3	11	0.264			0.0202
3	12	0.288			0.0310
3	13	0.312			0.0310
4	14	0.336			0.0310
4	15	0.368			0.0330
4	16	0.400			0.0330
4	17	0.432			0.0330
4	18	0.464			0.0350
4	19	0.496			0.0350
4	20	0.528			0.0350
4	21	0.556			0.0330
4	22	0.580			0.0330
4	23	0.600			0.0350
5	24	0.615			0.0310
5	25	0.629			0.0310
5	26	0.640			0.0310
5	27	0.648	0.003		0.0350
5	28	0.656	0.004		0.0292
5	29	0.664			0.0310
5	30	0.672			0.0320
5	31	0.680			0.0330
5	32	0.688			0.0350
5	33	0.696			0.0360
5	34	0.704			0.0370
5	35	0.712			0.0360
5	36	0.720			0.0350
5	37	0.728			0.0330
5	38	0.736			0.0320
5	39	0.744			0.0320
5	40	0.752	0.004	0.250	0.0310

**TABLE VII**  
**METERING HOLE & SLOT VARIABLES FOR 72.5° SWEEP WING**  
**(continued)**

Suction Chamber No.	Slot Number	S'/C'	Slot Width $W_s \sim \text{in.}$	Hole Spacing $\gamma \sim \text{in.}$	Hole Dia. $d \sim \text{in.}$
5	41	0.760	0.003	0.250	0.0310
5	42	0.768	<u>0.003</u>	0.125	0.0310
5	43	0.776	↑	0.125	0.0280
5	44	0.784		<u>0.250</u>	0.0350
5	45	0.792		↑	0.0330
5	46	0.800			0.0320
5	47	0.808			0.0310
5	48	0.816			0.0292
5	49	0.824			0.0292
5	50	0.832			0.0280
6	51	0.840			0.0330
6	52	0.848			0.0320
6	53	0.856			0.0310
6	54	0.864			0.0292
6	55	0.872			0.0292
6	56	0.880			0.0280
6	57	0.888			0.0280
6	58	0.896			0.0260
6	59	0.904			0.0260
6	60	0.912			0.0250
6	61	0.920			0.0250
6	62	0.928			0.0250
6	63	0.936			0.0250
6	64	0.944			0.0250
7	65	0.952			0.0330
7	66	0.960			0.0320
7	67	0.968			0.0310
7	68	0.976			0.0292
7	69	0.984			0.0292
7	70	0.992			0.0280
7	71	1.000	↓	↓	0.0280
7	72	1.008			0.0260
7	73	1.016			0.0260
7	74	1.024			0.0250
7	75	1.032	<u>0.003</u>	<u>0.250</u>	0.0250

TABLE VIII

STATIC PORT LOCATIONS AND NOTES FOR 72.5° SWEPT WING

Chordwise Location		References Numbers and Notes (See Fig. 128 for Spanwise Location)		
X/C	Surface	Root	Midspan	Tip
0.002	lower	1	21 <sup>Δ</sup>	41
0.002	upper	2	22 <sup>Δ</sup>	42
0.008	"	3	23 <sup>Δ</sup>	43
0.025	"	4	24*	44
0.046	"	5	25 <sup>Δ</sup>	45*
0.090	"	6*	26 <sup>Δ</sup>	46
0.210	"	7	27 <sup>Δ</sup>	47
0.395	"	8	28 <sup>Δ</sup>	48
0.603	"	9*	29 <sup>Δ</sup>	49*
0.728	"	10	30 <sup>Δ</sup>	50
0.853	"	11*	31 <sup>Δ</sup>	51
0.952	"	12*	32	2*
0.998	"	13	33*	53

\*Not used because of plugged or leaky tubes

<sup>Δ</sup>Deliberately sealed at  $\alpha = 0.75^\circ$

TABLE IX

COMPARISON OF ACTUAL AND EMPIRICAL WAKE DRAG CORRECTIONS  
FOR 72.5° SWEEP WING

$C_{D_{w_u}} = \frac{2 \delta_{ss}}{C}$	$.1840 \times 10^{-3}$	$.806 \times 10^{-3}$	$.0299 \times 10^{-3}$
$C_{D_w}$ (Actual Corrected $C_{D_w}$ from calculations of boundary layer)	$.0983 \times 10^{-3}$	$.0545 \times 10^{-3}$	$.0233 \times 10^{-3}$
$C_{D_{w_c}}$ (Empirical Correction)	$.1304 \times 10^{-3}$	$.0652 \times 10^{-3}$	$.0261 \times 10^{-3}$

TABLE X

COMPARISON OF CALCULATED AND MEASURED DRAG COMPONENTS OF  
72.5° SWEEP WING

$\alpha = 0.15$	Measured		Calculated
$R_c \times 10^{-6}$	8.85	8.80	10.0
$C_W \times 10^3$	0.997	0.884	0.905
$C_{D_s} \times 10^3$	1.158	1.014	1.170
$2\delta_{ss}/C \times 10^3$	0.335	0.654	0.081
$C_{D_{wc}} \times 10^3$	0.189	0.342	0.055
$C_{D_t} \times 10^3$	1.347	1.356	1.225



TABLE XI  
COMPARISON OF SLOT LOSSES CALCULATED FOR  
DIFFERENT SWEEP ANGLES AND ASSIGNED VALUES OF  $r_f$

VARIABLE	SWEEP $\cong 0.0^\circ$		SWEEP = $72.5^\circ$	
	GROTH'S METHOD*	SWEPT SLOT METHOD	SWEPT SLOT METHOD	
$\Delta''$ - inches	0.08	0.08	0.08	0.08
$w_i$ - inches	0.0035	0.0035	0.0035	0.0035
$r_f$	0.0000	0.0001	<u>0.0001</u>	<u>1.0000</u>
$\mu_a \times 10^6$	0.3604	0.3604	0.3930	0.3930
$\sigma_2$	0.5369	0.5369	0.5855	0.5855
$R_c \times 10^{-6}$	10.0	10.0	10.0	10.0
$f_o^*$	5.4897	5.4897	5.4897	5.4897
$P_2/P$	0.9450	0.9473	0.9354	0.9568
$\Delta P/P = (P - P_2)/P$	0.0550	0.0527	0.0646	0.0432

\*In the application of Groth's method a simplification is frequently made in which it is assumed that  $u_b/u_a = T_b/T_a$ . The more accurate relation given in reference 117,  $u_b/u_a = (T_b/T_a)^{0.76}$ , was used in the calculation above to be more consistent with the assumptions used for the swept slot method.

TABLE XII

PRESSURE DROP IN LAMINAR FLOW TUBE WITH COMPRESSIBLE FLOW $p/p_k$  vs  $x/RR_R$ 

$M_0$	$p_0/p_k$	$R_R$	$p_k$ (at.)	$M_0$	$p_0/p_k$	$R_R$	$p_k$ (at.)
0.101	0.9928	848	0.1	0.1336	0.9876	1875	0.2

$x/RR_R$	$p/p_k$	$x/RR_R$	$p/p_k$
0.0091	0.989	0.0043	0.984
0.0167	0.988	0.00775	0.982
0.0456	0.984	0.0208	0.977
0.0747	0.977	0.0341	0.973
0.1040	0.972	0.0472	0.969
0.1325	0.968	0.0603	0.966
0.1710	0.962	0.7770	0.961
0.2100	0.959	0.0952	0.958
0.2480	0.953	0.1128	0.953
0.2870	0.950	0.1301	0.949
0.3250	0.943	0.1476	0.946
0.3830	0.934	0.1738	0.940
0.4420	0.925	0.2000	0.934
0.4990	0.920	0.2260	0.929
0.5510	0.911	0.2520	0.923
0.6720	0.895	0.3045	0.913
0.7900	0.878	0.3570	0.899
0.9030	0.862	0.4100	0.889
1.0200	0.842	0.4620	0.869
1.1350	0.823	0.5150	0.863
1.2530	0.803	0.5670	0.847
1.3400	0.790	0.6060	0.838

TABLE XII (continued)

<u>M<sub>O</sub></u>	<u>P<sub>O</sub>/P<sub>k</sub></u>	<u>R<sub>R</sub></u>	<u>P<sub>k</sub></u> <u>(at.)</u>	<u>M<sub>O</sub></u>	<u>P<sub>O</sub>/P<sub>k</sub></u>	<u>R<sub>R</sub></u>	<u>P<sub>k</sub></u> <u>(at.)</u>
0.139	0.9866	3910	0.4	0.143	0.9858	978	0.1

<u>x/RR<sub>R</sub></u>	<u>P/P<sub>k</sub></u>	<u>x/RR<sub>R</sub></u>	<u>P/P<sub>k</sub></u>
0.00211	0.9829	0.0081	0.980
0.00376	0.9816	0.0146	0.977
0.01005	0.9773	0.0398	0.968
0.0164	0.9757	0.0652	0.963
0.0227	0.9721	0.0903	0.954
0.0290	0.9704	0.1153	0.949
0.0373	0.9675	0.1487	0.940
0.0457	0.9648	0.1824	0.932
0.0540	0.9625	0.2155	0.924
0.0625	0.9606	0.2495	0.915
0.0709	0.9580	0.2830	0.908
0.0835	0.9547	0.3330	0.895
0.960	0.9517	0.3835	0.880
0.1085	0.9484	0.4330	0.869
0.1210	0.9451	0.4830	0.854
0.1462	0.9399	0.5840	0.828
0.1712	0.9336	0.6850	0.796
0.1968	0.9267	0.7860	0.766
0.2220	0.9215	0.8880	0.733
0.2470	0.9149	0.9870	0.700
0.2720	0.9083	1.0880	0.664
0.2910	0.9034	1.1620	0.637

TABLE XII (continued)

<u>M<sub>O</sub></u>	<u>P<sub>O</sub>/P<sub>k</sub></u>	<u>R<sub>R</sub></u>	<u>P<sub>k</sub></u> <u>(at.)</u>	<u>M<sub>O</sub></u>	<u>P<sub>O</sub>/P<sub>k</sub></u>	<u>R<sub>R</sub></u>	<u>P<sub>k</sub></u> <u>(at.)</u>
0.197	0.9733	2750	0.2	0.202	0.9719	1370	0.1

<u>x/RRR</u>	<u>p/p<sub>k</sub></u>	<u>x/RRR</u>	<u>p/p<sub>k</sub></u>
0.00295	0.965	0.0059	0.9617
0.0053	0.963	0.0106	0.9564
0.0143	0.953	0.0285	0.9419
0.0232	0.946	0.0466	0.9287
0.0322	0.940	0.0645	0.9194
0.0411	0.935	0.0825	0.9089
0.0529	0.927	0.1063	0.8956
0.0648	0.920	0.1302	0.8824
0.0767	0.913	0.1540	0.8692
0.0887	0.907	0.1780	0.8573
0.1007	0.901	0.2020	0.8441
0.1184	0.892	0.2380	0.8243
0.1362	0.880	0.2735	0.8045
0.1539	0.872	0.3090	0.7847
0.1717	0.861	0.3450	0.7635
0.2076	0.844	0.4170	0.7213
0.2430	0.824	0.4880	0.6711
0.2795	0.804	0.5610	0.6196
0.3150	0.784	0.6330	0.5601
0.3405	0.761	0.7040	0.4848
0.3860	0.738	0.7760	0.3923
0.4130	0.721	0.8300	0.2559

TABLE XII (continued)

<u>M<sub>O</sub></u>	<u>P<sub>O</sub>/P<sub>k</sub></u>	<u>R<sub>R</sub></u>	<u>P<sub>k</sub></u> <u>(at.)</u>	<u>M<sub>O</sub></u>	<u>P<sub>O</sub>/P<sub>k</sub></u>	<u>R<sub>R</sub></u>	<u>P<sub>k</sub></u> <u>(at.)</u>
0.206	0.9708	8620	0.6	0.212	0.9691	1765	0.1

<u>x/RR<sub>R</sub></u>	<u>P/P<sub>k</sub></u>	<u>x/RR<sub>R</sub></u>	<u>P/P<sub>k</sub></u>
0.00097	0.9647	0.0046	0.9580
0.00172	0.9625	0.0082	0.9541
0.00456	0.9575	0.0221	0.9409
0.00745	0.9535	0.0362	0.9291
0.01030	0.9498	0.0501	0.9173
0.01313	0.9467	0.0640	0.9055
0.01692	0.9428	0.0825	0.8924
0.02075	0.9390	0.1010	0.8793
0.02455	0.9360	0.1197	0.8661
0.02836	0.9329	0.1380	0.8530
0.0322	0.9294	0.1567	0.8399
0.0379	0.9252	0.1847	0.8202
0.0436	0.9206	0.222	0.7979
0.0492	0.9165	0.240	0.7756
0.0549	0.9125	0.268	0.7507
0.0664	0.9051	0.324	0.7034
0.0778	0.8970	0.379	0.6535
0.0894	0.8893	0.435	0.5984
0.1008	0.8814	0.491	0.5302
0.1120	0.8731	0.547	0.4501
0.1234	0.8662	0.603	0.3412
0.1320	0.8610	0.644	0.1798

TABLE XII (continued)

$\underline{M_o}$	$\underline{P_o/P_k}$	$\underline{R_R}$	$\underline{P_k}$ (at.)	$\underline{M_o}$	$\underline{P_o/P_k}$	$\underline{R_R}$	$\underline{P_k}$ (at.)
0.225	0.9652	12,520	0.8	0.233	0.9629	3220	0.2

$\underline{x/RR_R}$	$\underline{p/p_k}$	$\underline{x/RR_R}$	$\underline{p/p_k}$
0.00068	0.9589	0.00266	0.945
0.00120	0.9571	0.00457	0.941
0.00315	0.9519	0.0122	0.927
0.00515	0.9477	0.0199	0.917
0.00708	0.9442	0.0276	0.909
0.00903	0.9413	0.0352	0.901
0.01163	0.9376	0.04535	0.890
0.01427	0.9342	0.0555	0.881
0.01688	0.9310	0.0657	0.872
0.01950	0.9282	0.0760	0.862
0.02215	0.9252	0.0863	0.853
0.02604	0.9212	0.1014	0.839
0.02997	0.9173	0.1167	0.825
0.03380	0.9130	0.1318	0.811
0.03775	0.9093	0.1470	0.797
0.0456	0.9015	0.1778	0.782
0.0534	0.8948	0.2080	0.741
0.0613	0.8877	0.2390	0.710
0.0692	0.8803	0.2695	0.674
0.0770	0.8736	0.3000	0.640
0.08485	0.8670	0.3305	0.599
0.0907	0.8617	0.3540	0.573

TABLE XII (continued)

$\underline{M_o}$	$\underline{P_o/P_k}$	$\underline{R_R}$	$\underline{P_k}$ (at.)	$\underline{M_o}$	$\underline{P_o/P_k}$	$\underline{R_R}$	$\underline{P_k}$ (at.)
0.2375	0.9615	6560	0.4	0.283	0.9459	11,630	0.6

$\underline{x/RR_R}$	$\underline{p/p_k}$	$\underline{x/RR_R}$	$\underline{p/p_k}$
0.00128	0.9526	0.00072	0.9355
0.00226	0.9500	0.00128	0.9324
0.00600	0.9420	0.00338	0.9236
0.00976	0.9351	0.00553	0.9168
0.0135	0.9299	0.00726	0.9109
0.0172	0.9243	0.00975	0.9061
0.0223	0.9183	0.01253	0.8990
0.0273	0.9131	0.01538	0.8933
0.0323	0.9071	0.01817	0.8876
0.0372	0.9009	0.02100	0.8823
0.0421	0.8959	0.02380	0.8769
0.0497	0.8887	0.02805	0.8694
0.0572	0.8811	0.0323	0.8624
0.0646	0.8749	0.03645	0.8556
0.0721	0.8673	0.04065	0.8472
0.0872	0.8535	0.0491	0.8338
0.1020	0.8393	0.0576	0.8202
0.1172	0.8255	0.0661	0.8071
0.1320	0.8113	0.0745	0.7937
0.1470	0.7975	0.0830	0.7801
0.1620	0.7824	0.0915	0.7671
0.1732	0.7712	0.0978	0.7564

TABLE XII (continued)

$\underline{M_o}$	$\underline{P_o/P_k}$	$\underline{R_R}$	$\underline{P_k}$ $\underline{(at.)}$	$\underline{M_o}$	$\underline{P_o/P_k}$	$\underline{R_R}$	$\underline{P_k}$ $\underline{(at.)}$
0.316	0.9331	9000	0.4	0.3275	0.9287	17,880	0.8

$\underline{x/RR_R}$	$\underline{p/p_k}$	$\underline{x/RR_R}$	$\underline{p/p_k}$
0.00093	0.9190	0.00049	0.9164
0.00165	0.9151	0.00085	0.9125
0.00437	0.9019	0.00222	0.9026
0.00713	0.8917	0.00361	0.8951
0.00985	0.8825	0.00498	0.8890
0.01257	0.8752	0.00635	0.8831
0.01621	0.8647	0.00818	0.8758
0.01987	0.8548	0.01002	0.8693
0.02350	0.8456	0.01183	0.8632
0.02715	0.8374	0.01368	0.8587
0.0308	0.8292	0.01552	0.8512
0.0363	0.8167	0.01826	0.8431
0.0417	0.8035	0.02100	0.8353
0.0471	0.7920	0.02375	0.8275
0.0525	0.7788	0.0265	0.8197
0.0635	0.7538	0.0320	0.8050
0.0744	0.7288	0.03745	0.7900
0.0855	0.7031	0.0431	0.7756
0.0963	0.6758	0.0485	0.7610
0.1073	0.6484	0.0540	0.7464
0.1180	0.6162	0.0595	0.7316
0.1263	0.5918	0.0637	0.7207



TABLE XII (continued)

$M_0$	$P_0/P_k$	$R_R$	$P_k$ (at.)	$M_0$	$P_0/P_k$	$R_R$	$P_k$ (at.)
0.3445	0.9212	13,930	0.6	0.355	0.9166	9600	0.4

$x/RRR$	$p/p_k$	$x/RRR$	$p/p_k$
0.00061	0.9081	0.00088	0.897
0.00107	0.9019	0.00155	0.890
0.00283	0.8896	0.00410	0.877
0.00461	0.8798	0.00669	0.863
0.00637	0.8714	0.00924	0.851
0.00813	0.8644	0.01179	0.839
0.01048	0.8548	0.01520	0.828
0.01283	0.8466	0.01860	0.815
0.01517	0.8381	0.02200	0.806
0.01755	0.8300	0.02544	0.793
0.01987	0.8227	0.02884	0.782
0.0234	0.8118	0.0340	0.766
0.02695	0.8010	0.03905	0.749
0.0304	0.7900	0.0441	0.733
0.0339	0.7791	0.0492	0.714
0.0410	0.7576	0.0595	0.680
0.0480	0.7361	0.0697	0.642
0.0552	0.7146	0.0801	0.602
0.0622	0.6922	0.0903	0.553
0.0693	0.6696	0.1004	0.497
0.0763	0.6459	0.1107	0.418
0.0815	0.6264	0.1183	0.234

TABLE XII (continued)

$\underline{M_O}$	$\underline{P_O/P_k}$	$\underline{R_R}$	$\underline{P_k}$ (at.)	$\underline{M_O}$	$\underline{P_O/P_k}$	$\underline{R_R}$	$\underline{P_k}$ (at.)
0.364	0.9125	19,750	0.8	0.396	0.8975	15,800	0.6

$\underline{x/RR_R}$	$\underline{p/p_k}$	$\underline{x/RR_R}$	$\underline{p/p_k}$
0.00044	0.89981	0.00055	0.883
0.00077	0.89504	0.00096	0.875
0.00201	0.88369	0.00251	0.859
0.00327	0.87481	0.00408	0.845
0.00451	0.86708	0.00563	0.835
0.00576	0.85984	0.00718	0.825
0.00740	0.85145	0.00924	0.812
0.00907	0.84356	0.01135	0.800
0.01072	0.83632	0.01340	0.788
0.01239	0.82875	0.01545	0.779
0.01405	0.82163	0.01753	0.768
0.01653	0.81197	0.02065	0.753
0.01903	0.80243	0.02375	0.737
0.02150	0.79273	0.02680	0.721
0.02400	0.78318	0.02990	0.704
0.0290	0.76443	0.03615	0.670
0.03395	0.74601	0.0424	0.635
0.0390	0.72742	0.0486	0.598
0.0439	0.70916	0.0548	0.555
0.048	0.68958	0.0610	0.503
0.0539	0.66952	0.0673	0.429
0.0576	0.65455	0.0718	0.240

TABLE XII (continued)

<u>M<sub>0</sub></u>	<u>P<sub>0</sub>/P<sub>k</sub></u>	<u>R<sub>R</sub></u>	<u>P<sub>k</sub></u> <u>(at.)</u>	<u>M<sub>0</sub></u>	<u>P<sub>0</sub>/P<sub>k</sub></u>	<u>R<sub>R</sub></u>	<u>P<sub>k</sub></u> <u>(at.)</u>
0.408	0.8917	21,800	0.8	0.419	0.8862	20,300	0.73

<u>x/RR<sub>R</sub></u>	<u>P/P<sub>k</sub></u>	<u>x/RR<sub>R</sub></u>	<u>P/P<sub>k</sub></u>
0.00040	0.877	0.00043	0.8712
0.00070	0.872	0.00075	0.8645
0.00182	0.859	0.00195	0.8487
0.00296	0.845	0.00318	0.8362
0.00409	0.837	0.00439	0.8258
0.00521	0.828	0.00559	0.8161
0.00671	0.818	0.00720	0.8041
0.00821	0.807	0.00883	0.7933
0.00970	0.797	0.01043	0.7820
0.01122	0.788	0.01204	0.7714
0.01272	0.778	0.01367	0.7610
0.01497	0.767	0.01607	0.7457
0.01722	0.753	0.01850	0.7299
0.01946	0.742	0.02090	0.7152
0.02170	0.727	0.02330	0.6991
0.02620	0.703	0.02815	0.6671
0.03075	0.675	0.03300	0.6331
0.03525	0.648	0.03785	0.5968
0.0398	0.618	0.0427	0.5548
0.0443	0.587	0.0475	0.5044
0.0488	0.552	0.0524	0.4339
0.0522	0.522	0.0560	0.2324

TABLE XII (continued)

<u>M<sub>0</sub></u>	<u>P<sub>0</sub>/P<sub>k</sub></u>	<u>R<sub>R</sub></u>	<u>P<sub>k</sub></u> <u>(at.)</u>
0.430	0.8807	23,000	0.8

<u>x/RR<sub>R</sub></u>	<u>p/P<sub>k</sub></u>
0.00038	0.868
0.00066	0.860
0.00173	0.843
0.00282	0.833
0.00390	0.820
0.00496	0.810
0.00639	0.800
0.00783	0.789
0.00925	0.778
0.01070	0.768
0.01211	0.758
0.01427	0.743
0.01640	0.727
0.01853	0.712
0.02068	0.685
0.02500	0.664
0.02930	0.631
0.03360	0.595
0.03790	0.555
0.04220	0.505
0.0464	0.436
0.0497	0.257

# LIST OF FIGURES FOR SECTION II, PART 2

<u>Figure No.</u>	<u>Figure Title</u>	<u>Page</u>
1	FLAT PLATE SUCTION MODEL AEDC TUNNEL A .....	588
2	INSIDE OF MODEL, BOTTOM PLATE REMOVED .....	589
3	MODEL AND RAKE INSTALLED IN TUNNEL A, ONE TUNNEL WALL REMOVED .....	590
4	TUNNEL WINDOWS ON OPERATING SIDE .....	591
5	SUCTION EQUIPMENT ON NON-OPERATING SIDE OF TUNNEL .....	592
6	WAKE, SUCTION AND TOTAL DRAG COEFFICIENTS VS SUCTION COEFFICIENT $M = 3.0$ , $R_c = 8.0$ and $13.0 \times 10^6$ .....	593
7	WAKE, SUCTION AND TOTAL DRAG COEFFICIENTS VS SUCTION COEFFICIENT $M = 3.0$ , $R_c = 18.0$ and $22.2 \times 10^6$ .....	594
8	WAKE, SUCTION AND TOTAL DRAG COEFFICIENTS VS SUCTION COEFFICIENT $M = 3.0$ , $R_c = 25.7 \times 10^6$ .....	595
9	WAKE, SUCTION AND TOTAL DRAG COEFFICIENTS VS SUCTION COEFFICIENT $M = 3.5$ , $R_c = 13.8$ , $17.6$ and $21.4 \times 10^6$ .....	596
10	MINIMUM TOTAL DRAG AND OPTIMUM SUCTION COEFFICIENTS VS REYNOLDS NUMBER, $M = 3.0$ .....	597
11	MINIMUM TOTAL DRAG AND OPTIMUM SUCTION COEFFICIENTS VS REYNOLDS NUMBER, $M = 3.5$ .....	598
12	OPTIMUM SUCTION COEFFICIENT VS REYNOLDS NUMBER FOR $M = 3.0$ and $3.5$ .....	599
13	EXPERIMENTAL SUCTION DISTRIBUTIONS FOR $M_n = 3.0$ , $R_c = 25.8 \times 10^6$ AND FOR $M_n = 3.5$ , $R_c = 21.7 \times 10^6$ .....	600
14	SUCTION DISTRIBUTIONS AND MOMENTUM THICKNESS REYNOLDS NUMBERS FOR THEORETICAL BOUNDARY LAYER CALCULATIONS $\frac{\rho_w v_o}{\rho_m U_m} \sqrt{R_c}$ and $\frac{R_n}{\sqrt{R_c}}$ vs $x$	601

LIST OF FIGURES FOR SECTION II, PART 2 (Continued)

<u>Figure No.</u>	<u>Figure Title</u>	<u>Page</u>
15	COMPARISON OF THEORETICAL AND EXPERIMENTAL WAKE DRAG COEFFICIENTS $C_{Dw} \sqrt{R_c}$ VS $C_{wt} \sqrt{R_c}$ .....	602
16	COMPARISON OF TOTAL DRAG COEFFICIENT MEASURED AT STATION $x = 31.4$ INCHES MINIMUM TOTAL DRAG COEFFICIENTS MEASURED AT $c = 40.23$ INCHES FOR $M_\infty = 3.0$ .....	603
17	COMPARISON OF THEORETICAL AND EXPERIMENTAL BOUNDARY LAYER VELOCITY PROFILES $M = 3.0$ , $R_c = 25.7 \times 10^6$ , $c = 40.23$ INCHES .....	604
18	COMPARISON OF THEORETICAL AND EXPERIMENTAL BOUNDARY LAYER VELOCITY PROFILES $M = 3.5$ , $R_c = 21.4 \times 10^6$ , $c = 40.40$ INCHES .....	605
19	COMPARISON OF THEORETICAL AND EXPERIMENTAL BOUNDARY LAYER VELOCITY PROFILES $M = 3.0$ , $R_c = 18.0 \times 10^6$ , $c = 40.23$ INCHES .....	606
20	COMPARISON OF THEORETICAL AND EXPERIMENTAL BOUNDARY LAYER VELOCITY PROFILES $M = 3.0$ , $R_x = 14.0 \times 10^6$ , $x = 31.4$ INCHES .....	607
21	BLUNT PLATE AND APPROXIMATE SHOCK WAVE FOR $M = 3.0$ .....	608
22	SLOPE OF SHOCK WAVE AND TOTAL HEAD LOSS VS HEIGHT $\frac{y}{t}$ .....	609
23	VELOCITY RATIO $1 - \frac{U_3}{U_\infty}$ AND MOMENTUM LOSS  FUNCTION $I \left( \frac{h}{t} \right)$ VS $\frac{h}{t}$ .....	610
24	CHORDWISE "SUCTION HEIGHT" $h_s (x)$ AND BOUNDARY LAYER MASS FLOW HEIGHT $h_{bf}$ VS $x/c$ FOR $M_\infty = 3.0$ , $C_{wt} = 2.374 \times 10^{-4}$ , $R_c = 25.7 \times 10^6$ .....	611
25-1	MACH NUMBER AND TOTAL HEAD DISTRIBUTION AT OUTER EDGE OF BOUNDARY LAYER FOR $M_\infty = 3.0$ , $C_{wt} = 2.374 \times 10^{-4}$ , $R_c = 25.7 \times 10^6$ .....	612

LIST OF FIGURES FOR SECTION II, PART 2 (Continued)

<u>Figure No.</u>	<u>Figure Title</u>	<u>Page</u>
25-2	WAKE, SUCTION AND TOTAL DRAG COEFFICIENTS VS TOTAL SUCTION COEFFICIENT $M = 2.5$ , $x_{rake} = 40.2$ in. ....	613
25-3	WAKE, SUCTION, AND TOTAL DRAG COEFFICIENTS VS TOTAL SUCTION COEFFICIENT $M = 3.0$ .....	614
25-4	WAKE, SUCTION, AND TOTAL DRAG COEFFICIENTS VS TOTAL SUCTION COEFFICIENT $M = 3.5$ .....	615
25-5	MINIMUM TOTAL DRAG AND OPTIMUM TOTAL SUCTION COEFFICIENTS ON FLAT PLATE SUCTION MODEL .....	616
26	SHOCK GENERATOR MOUNTED ON FLAT PLATE SUCTION MODEL .....	617
27	INSTALLATION OF THE FLAT PLATE SUCTION MODEL IN WIND TUNNEL .....	618
28	INSTALLATION OF THE FLAT PLATE SUCTION MODEL IN WIND TUNNEL .....	619
29	INFLUENCE OF SHOCK WAVE ON PRESSURE FIELD IN SLOTTED AREA .....	620
30	LOCATION OF SUCTION CHAMBERS AND SHOCK WAVES FOR SHOCK GENERATOR MOUNTED OUTSIDE SUCTION AREA .....	621
31	LOCATION OF SUCTION CHAMBERS AND SHOCK WAVES FOR SHOCK GENERATOR MOUNTED INSIDE SUCTION AREA .....	622
32	THEORETICAL PRESSURE RISE $\frac{P_2}{P_1}$ VS SHOCK GENERATOR ANGLE $\gamma$ .....	623
33	TOTAL DRAG AND SUCTION COEFFICIENTS VS SHOCK INTENSITY $M = 2.5$ , $R_x = 14.2 \times 10^6$ , ( $x_{rake} = 40.2$ in.) .....	624
34	TOTAL DRAG AND SUCTION COEFFICIENTS VS SHOCK INTENSITY $M = 2.5$ , $R_x = 19.9 \times 10^6$ , ( $x_{rake} = 40.2$ in.) .....	625
35	TOTAL DRAG AND SUCTION COEFFICIENTS VS SHOCK INTENSITY $M = 3.0$ , $R_x = 11.0 \times 10^6$ , ( $x_{rake} = 40.2$ in.) .....	626

LIST OF FIGURES FOR SECTION II, PART 2 (Continued)

<u>Figure No.</u>	<u>Figure Title</u>	<u>Page</u>
36	TOTAL DRAG AND SUCTION COEFFICIENTS VS SHOCK INTENSITY $M = 3.0$ , $R_x = 19.0 \times 10^6$ , ( $x_{rake} = 40.2$ in.) .....	627
37	TOTAL DRAG AND SUCTION COEFFICIENTS VS SHOCK INTENSITY $M = 3.0$ , $R_x = 26.4 \times 10^6$ , ( $x_{rake} = 40.2$ in.) .....	628
38	TOTAL DRAG AND SUCTION COEFFICIENTS VS SHOCK INTENSITY $M = 3.5$ , $R_x = 21.6 \times 10^6$ , ( $x_{rake} = 40.2$ in.) .....	629
39	TOTAL DRAG AND SUCTION COEFFICIENTS VS CHORDWISE DISTANCE, $x_{rake}$ , $M = 2.5$ , $R_c = 14.4 \times 10^6$ , ( $c = 40.2$ in.) .....	630
40	TOTAL DRAG AND SUCTION COEFFICIENTS VS CHORDWISE DISTANCE, $x_{rake}$ , $M = 2.5$ , $R_c = 19.9 \times 10^6$ , ( $c = 40.2$ in.) .....	631
41	TOTAL DRAG AND SUCTION COEFFICIENTS VS CHORDWISE DISTANCE, $x_{rake}$ , $M = 3.0$ , $R_c = 19.0 \times 10^6$ , ( $c = 40.2$ in.) .....	632
42	TOTAL DRAG AND SUCTION COEFFICIENTS VS CHORDWISE DISTANCE, $x_{rake}$ , $M = 3.0$ , $R_c = 26.4 \times 10^6$ , ( $c = 40.2$ in.) .....	633
43	INCREASE IN TOTAL DRAG AND SUCTION COEFFICIENTS VS SHOCK INTENSITY .....	634
44	SUCTION DISTRIBUTIONS AT DIFFERENT SHOCK INTENSITIES, $M = 3.0$ , $R_x = 26.4 \times 10^6$ , $x = 40.2$ in. ....	635
45	BOUNDARY LAYER VELOCITY PROFILES AT DIFFERENT SHOCK INTENSITIES, $M = 3.0$ , $R_x = 26.4 \times 10^6$ , $x_{rake} = 40.2$ in. ....	636



LIST OF FIGURES FOR SECTION II, PART 2 (Continued)

<u>Figure No.</u>	<u>Figure Title</u>	<u>Page</u>
46	SKETCH OF SUCTION MODEL.....	637
47	PHOTOGRAPH OF MODEL MOUNTED IN TUNNEL E-1.....	638
48	WAKE, SUCTION AND TOTAL DRAG COEFFICIENTS VS SUCTION QUANTITIES AT $M_\infty = 2.5$ .....	639
49	MINIMUM TOTAL DRAG AND OPTIMUM TOTAL SUCTION COEFFICIENTS VS LENGTH REYNOLDS NUMBER AT $M_\infty = 2.5$ .....	640
50	WAKE, SUCTION AND TOTAL DRAG COEFFICIENTS VS SUCTION QUANTITIES AT $M_\infty = 3.0$ .....	641
51	MINIMUM TOTAL DRAG AND OPTIMUM TOTAL SUCTION COEFFICIENTS VS LENGTH REYNOLDS NUMBER AT $M_\infty = 3.0$ .....	642
52	WAKE, SUCTION AND TOTAL DRAG COEFFICIENTS VS SUCTION QUANTITIES AT $M_\infty = 3.5$ .....	643
53	MINIMUM TOTAL DRAG AND OPTIMUM TOTAL SUCTION COEFFICIENTS VS LENGTH REYNOLDS NUMBER AT $M_\infty = 3.5$ .....	644
54	MEASURED BOUNDARY LAYER VELOCITY PROFILES AT $M_\infty = 3.5$ AND $R_L = 4.85 \times 10^6$ FOR VARIOUS SUCTION QUANTITIES, STATION L = 19.09 INCHES.....	645
55	VARIATION OF MINIMUM TOTAL DRAG AND OPTIMUM SUCTION COEFFICIENTS WITH REYNOLDS NUMBER FOR $M_\infty = 2.5, 3.0, \text{ and } 3.5$ .....	646
56	TRANSITION REYNOLDS NUMBER VS FREESTREAM UNIT REYNOLDS NUMBER AT $M_\infty = 2.5$ .....	647
57	TRANSITION REYNOLDS NUMBER VS FREESTREAM UNIT REYNOLDS NUMBER AT $M_\infty = 3.0$ .....	648
58	TRANSITION REYNOLDS NUMBER VS FREESTREAM UNIT REYNOLDS NUMBER AT $M_\infty = 3.5$ .....	649
59	OPTIMUM TOTAL SUCTION COEFFICIENT AND NATURAL TRANSITION REYNOLDS NUMBER VS REFERENCE LENGTH REYNOLDS NUMBER.....	650
60	OPTIMUM TOTAL SUCTION COEFFICIENT VS LOCATION OF TRANSITION WITHOUT SUCTION.....	651
61	RAKE TOTAL HEAD AND CORRESPONDING MACH NUMBER DISTRIBUTION PERPENDICULAR TO MODEL SURFACE AT RAKE LOCATION, STATION 18.81, for $M_\infty = 2.5, R_L = 15.8 \times 10^6$ .....	652

LIST OF FIGURES FOR SECTION II, PART 2 (Continued)

<u>Figure No.</u>	<u>Figure Title</u>	<u>Page</u>
62	EFFECT OF THE SHOCK WAVE FROM THE LAST SLOT (STATION 18.50) ON THE LOCAL POTENTIAL FLOW FIELD, $M_\infty = 2.5$ , $R_L = 15.8 \times 10^6$ ..	653
63	EFFECT OF THE SHOCK WAVE FROM THE LAST SLOT (STATION 18.50) ON THE LOCAL POTENTIAL FLOW FIELD, $M_\infty = 3.0$ , $R_L = 7.6 \times 10^6$ ...	654
64	EFFECT OF THE SHOCK WAVE FROM THE LAST SLOT (STATION 18.50) ON THE LOCAL POTENTIAL FLOW FIELD, $M_\infty = 3.5$ , $R_L = 5.8 \times 10^6$ .....	655
65	EXPERIMENTAL SURFACE PRESSURE AND SUCTION DISTRIBUTION $M_\infty = 2.5$ , $R_L = 13.24 \times 10^6$ .....	656
66	EXPERIMENTAL SURFACE PRESSURE AND SUCTION DISTRIBUTION $M_\infty = 3.0$ , $R_L = 11.32 \times 10^6$ .....	657
67	EXPERIMENTAL SURFACE PRESSURE AND SUCTION DISTRIBUTION $M_\infty = 3.5$ , $R_L = 4.85 \times 10^6$ .....	658
68	THEORETICAL VARIATION OF THE REYNOLDS NUMBER BASED ON MOMENTUM THICKNESS ALONG THE MODEL AXIS.....	659
69	THEORETICAL AND EXPERIMENTAL BOUNDARY LAYER VELOCITY PROFILES AT THE RAKE LOCATION.....	660
70a	THEORETICAL WALL TEMPERATURES AND TEMPERATURE RECOVERY FACTORS ALONG BODY AXIS.....	661
70b	THEORETICAL WALL TEMPERATURES AND TEMPERATURE RECOVERY FACTORS ALONG BODY AXIS.....	662
70c	THEORETICAL WALL TEMPERATURES AND TEMPERATURE RECOVERY FACTORS ALONG BODY AXIS.....	663
71	ROUGHNESS REYNOLDS NUMBER, $R_h$ , AND MACH NUMBER AT HEIGHT OF ROUGHNESS PARTICLE, $M_h$ , VS HEIGHT $h$ AT $M_\infty = 2.5$ AND SEVERAL CHORDWISE STATIONS.....	664
72	SKETCH OF $36^\circ$ SWEEPED SUCTION MODEL INSTALLATION AT AEDC TUNNEL A.....	665
73	PHOTOGRAPH OF $36^\circ$ SWEEPED WING SUCTION MODEL.....	666
74	SHOCK LINES AND SUCTION AREA ON $36^\circ$ SWEEPED WING MODEL.....	667
75	SWEEPED WING COORDINATES AND VELOCITY COMPONENTS.....	668
76	WAKE SUCTION AND TOTAL DRAG COEFFICIENTS VS TOTAL SUCTION COEFFICIENT $M = 2.5$ , $X_{rake} = 37.8$ .....	669

# LIST OF FIGURES FOR SECTION II, PART 2 (Continued)

<u>Figure No.</u>	<u>Figure Title</u>	<u>Page</u>
77	WAKE, SUCTION AND TOTAL DRAG COEFFICIENTS VS TOTAL SUCTION COEFFICIENT $M = 2.5$ , $X_{rake} = 32.8$ in. ....	670
78	WAKE, SUCTION AND TOTAL DRAG COEFFICIENTS VS TOTAL SUCTION COEFFICIENTS $M = 2.5$ , $X_{rake} = 27.7$ in. ....	671
79a	WAKE, SUCTION AND TOTAL DRAG COEFFICIENTS VS TOTAL SUCTION COEFFICIENTS $M = 3.0$ , $X_{rake} = 37.8$ in. ....	672
79b	WAKE, SUCTION AND TOTAL DRAG COEFFICIENTS VS TOTAL SUCTION COEFFICIENTS $M = 3.0$ , $X_{rake} = 37.8$ in. ....	673
80	WAKE, SUCTION AND TOTAL DRAG COEFFICIENTS VS TOTAL SUCTION COEFFICIENTS $M = 3.0$ , $X_{rake} = 27.7$ and $32.8$ in. ....	674
81	WAKE, SUCTION AND TOTAL DRAG COEFFICIENTS VS TOTAL SUCTION COEFFICIENTS $M = 3.5$ , $X_{rake} = 37.8$ in. ....	675
82	WAKE, SUCTION, AND TOTAL DRAG COEFFICIENTS VS TOTAL SUCTION COEFFICIENT $M = 3.5$ , $X_{rake} = 32.8$ and $27.7$ in. ....	676
83	MINIMUM TOTAL DRAG AND OPTIMUM TOTAL SUCTION COEFFICIENTS VS LENGTH REYNOLDS NUMBERS $M = 2.5$ .....	677
84	MINIMUM TOTAL DRAG AND OPTIMUM TOTAL SUCTION COEFFICIENTS VS LENGTH REYNOLDS NUMBER $M = 3.0$ .....	678
85	TOTAL MINIMUM DRAG AND OPTIMUM SUCTION COEFFICIENTS VS LENGTH REYNOLDS NUMBER $M = 3.5$ .....	679
86a	BOUNDARY LAYER CALCULATION, $M = 2.5$ , $C_{wt} \sqrt{R_c} = 1.222$ .....	680
86b	THEORETICAL AND EXPERIMENTAL DRAG COEFFICIENTS AND CROSSFLOW REYNOLDS NO. $M = 2.5$ , $C_{wt} \sqrt{R_c} = 1.222$ , $R_c = 11.1 \times 10^6$ .....	681
86c	THEORETICAL AND EXPERIMENTAL DRAG COEFFICIENTS, AND CROSSFLOW REYNOLDS NUMBERS $M = 2.5$ , $C_{wt} \sqrt{R_c} = 1.222$ , $R_c = 16.6 \times 10^6$ ... ..	682
86d	THEORETICAL AND EXPERIMENTAL DRAG COEFFICIENTS, AND CROSSFLOW REYNOLDS NO. $M = 2.5$ , $C_{wt} \sqrt{R_c} = 1.222$ , $R_c = 19.8 \times 10^6$ .....	683
87a	BOUNDARY LAYER CALCULATION, $M = 2.5$ , $C_{wt} \sqrt{R_c} = 2.013$ .....	684
87b	THEORETICAL AND EXPERIMENTAL DRAG COEFFICIENTS AND CROSSFLOW REYNOLDS NO. $M = 2.5$ , $C_{wt} \sqrt{R_c} = 2.013$ , $R_c = 13.5 \times 10^6$ .....	685
87c	THEORETICAL AND EXPERIMENTAL DRAG COEFFICIENTS, AND CROSSFLOW REYNOLDS NUMBERS $M = 2.5$ , $C_{wt} \sqrt{R_c} = 2.013$ , $R_c = 21.0 \times 10^6$ ... ..	686

LIST OF FIGURES FOR SECTION II, PART 2 (Continued)

<u>Figure No.</u>	<u>Figure Title</u>	<u>Page</u>
88a	BOUNDARY LAYER CALCULATION, $M = 3.0$ , $C_{w_t} \sqrt{R_c} = 1.840$ .....	687
88b	THEORETICAL AND EXPERIMENTAL DRAG COEFFICIENTS, AND CROSSFLOW REYNOLDS NUMBERS, $M = 3.0$ , $C_{w_t} \sqrt{R_c} = 1.840$ , $R_c = 13.0 \times 10^6$ ....	688
89a	BOUNDARY LAYER CALCULATION, $M = 3.0$ , $C_{w_t} \sqrt{R_c} = 1.982$ .....	689
89b	THEORETICAL AND EXPERIMENTAL DRAG COEFFICIENTS, AND CROSSFLOW REYNOLDS NUMBERS $M = 3.0$ , $C_{w_t} \sqrt{R_c} = 1.982$ , $R_c = 25.5 \times 10^6$ ....	690
90a	BOUNDARY LAYER CALCULATION, $M = 3.5$ , $C_{w_t} \sqrt{R_c} = 1.698$ .....	691
90b	THEORETICAL AND EXPERIMENTAL DRAG COEFFICIENTS, AND CROSSFLOW REYNOLDS NUMBERS $M = 3.5$ , $C_{w_t} \sqrt{R_c} = 1.698$ , $R_c = 20.2 \times 10^6$ ....	692
91	THEORETICAL AND EXPERIMENTAL BOUNDARY LAYER VELOCITY PROFILES $M = 3.0$ , $R_c = 25.5 \times 10^6$ .....	693
92	SKETCH OF MODEL AT $36^\circ$ SWEEP AND TRANSITION PROBING MECHANISM.	694
93	SKETCH OF MODEL MOUNTING.....	695
94	PHOTOGRAPH OF MODEL AND TRANSITION PROBING MECHANISM.....	696
95	PHOTOGRAPH OF MODEL INSTALLED IN TUNNEL E-1.....	697
96	BICONVEX AND MODIFIED AIRFOIL SECTIONS.....	698
97	SPANWISE LOCATIONS OF TOTAL HEAD PROBES FOR THE THREE SWEEP ANGLES.....	699
98	TRANSITION VS UNIT REYNOLDS NUMBER, BICONVEX WING, $M = 3.0$ ....	700
99	TRANSITION VS UNIT REYNOLDS NUMBER, BICONVEX WING, $M = 4.0$ ....	701
100	TRANSITION VS UNIT REYNOLDS NUMBER, MODIFIED WING, $M = 3.0$ ....	702
101	EXPONENT $n$ OF POWER LAW, $R_T \sim [R_{\infty}^{(1)}]^n$ VS SWEEP ANGLE.....	703
102	VARIATION OF TRANSITION WITH SWEEP, BICONVEX WING, $M = 3.0$ ....	704
103	VARIATION OF TRANSITION WITH SWEEP, BICONVEX WING, $M = 4.0$ ....	705
104	VARIATION OF TRANSITION WITH SWEEP, MODIFIED WING, $M = 3.0$ ....	706
105	RESULTS FROM THEORETICAL BOUNDARY LAYER CALCULATION ON $3\%$ BICONVEX WING AT $M = 3.0$ .....	707

LIST OF FIGURES FOR SECTION II, PART 2 (Continued)

<u>Figure No.</u>	<u>Figure Title</u>	<u>Page</u>
106	CROSSFLOW AND MOMENTUM THICKNESS REYNOLDS NUMBER AT TRANSITION, BICONVEX WING, $M = 3.0$ , $\Lambda = 24^\circ$ .....	708
107	CROSSFLOW AND MOMENTUM THICKNESS REYNOLDS NUMBER AT TRANSITION BICONVEX WING, $M = 3.0$ , $\Lambda = 36^\circ$ .....	709
108	CROSSFLOW AND MOMENTUM THICKNESS REYNOLDS NUMBER AT TRANSITION BICONVEX WING, $M = 3.0$ , $\Lambda = 50^\circ$ .....	710
109	VELOCITY COMPONENT RATIOS CORRESPONDING TO $M_u = 1.0$ .....	711
110	RELATION BETWEEN FREESTREAM OR RESULTANT MACH AND SWEEP ANGLE FOR $M_u = 1.0$ .....	713
111	LIMITING PRESSURE RATIO INCREMENTS FOR $M_u = 1.0$ .....	714
112	COMPARISON OF COMPRESSIBILITY CORRECTIONS AT $M_{u\infty} = 0.6$ .....	715
113	MODIFICATION OF THE GÖTHERT CORRECTION AT $M_{u\infty} = 0.6$ .....	716
114	LFC AIRFOIL AND TWO DIMENSIONAL INCOMPRESSIBLE VELOCITY DISTRIBUTION.....	717
115	COMPUTED BOUNDARY LAYER PARAMETERS AT $M_\infty = 2.0$ FOR LOW SUCTION - CRITICAL CHORD REYNOLDS NUMBER $\approx 4 \times 10^6$ .....	718
116	COMPUTED BOUNDARY LAYER PARAMETERS AT $M_\infty = 2.0$ AND MEDIUM SUCTION-CRITICAL CHORD REYNOLDS NUMBER $\approx 10 \times 10^6$ .....	719
117	COMPUTED BOUNDARY LAYER PARAMETERS AT $M_\infty = 2.0$ AND HIGH SUCTION-CRITICAL CHORD REYNOLDS NUMBER $\approx 30 \times 10^6$ .....	720
118	COMPUTED BOUNDARY LAYER PARAMETERS AT $M_\infty = 3.0$ -CRITICAL CHORD REYNOLDS NUMBER $\approx 30 \times 10^6$ .....	721
119	TWO DIMENSIONAL FLOW FIELD FOR LFC AIRFOIL.....	722
120	PATH OF STREAMLINES WHICH DEFINE SHAPE OF CONTOURED PLATE.....	723
121	FLOW FIELD NEAR LEADING EDGE ILLUSTRATING EXCESSIVE SPANWISE FLOW NEAR AIRFOIL SURFACE.....	724
122	LAMINAR & TURBULENT (SHADED) REGIONS AT $M_\infty = 2.0$ .....	725
123	EFFECT OF LIMITING CONTOURED WALL TO FINITE DIMENSIONS.....	726
124	INSTALLATION OF MODEL IN 40 x 40 INCH WIND TUNNEL--(RIGHT HAND DOOR REMOVED).....	727

LIST OF FIGURES FOR SECTION II, PART 2 (Continued)

<u>Figure No.</u>	<u>Figure Title</u>	<u>Page</u>
125	CROSS SECTION OF THE AIRFOIL SHOWING SUCTION CHAMBERS AND TRAILING EDGE EXTENSION.....	728
126	STREAMWISE VIEW OF CONTOURED SUPPORT PLATE (SKIN REMOVED) FOR AIRFOIL SHOWING SHAPE OF CONTOUR LINES.....	729
127	PLAN VIEW OF SIMULATED AIRFOIL SHOWING LOCATION OF SUCTION SLOTS.....	730
128	PLAN VIEW OF SUCTION CHAMBERS AND LOCATION OF PRESSURE ORIFICES.....	731
129	PLAN VIEW AND SECTIONS OF CONTOUR PLATE.....	732
130	MODEL INSTALLED IN TUNNEL A - NOTE RAKE LOCATION NEAR TIP OF AIRFOIL TRAILING EDGE.....	733
131a	BOTTOM VIEW OF MODEL AIRFOIL (LOWER SKIN REMOVED).....	734
131b	DETAILS OF CONTOUR PLATE WITH SKINS REMOVED.....	735
132	CLOSE UP OF SLOTS NEAR AIRFOIL TRAILING EDGE.....	736
133	DETAILS OF WAKE RAKE.....	737
134a	VARIATION OF DRAG COMPONENTS WITH SUCTION COEFFICIENT $M_{\infty} \sim 1.99$ , $R_c \sim 7.3 \times 10^6$ , $\alpha = 0.15^\circ$ .....	738
134b	VARIATION OF DRAG COMPONENTS WITH SUCTION COEFFICIENT $M_{\infty} \sim 1.99$ , $R_c \sim 8.8 \times 10^6$ , $\alpha = 0.15^\circ$ .....	739
134c	VARIATION OF DRAG COMPONENTS WITH SUCTION COEFFICIENT $M_{\infty} \sim 1.99$ , $R_c \sim 11.0 \times 10^6$ , $\alpha = 0.15^\circ$ .....	740
135a	VARIATION OF DRAG COMPONENTS WITH SUCTION COEFFICIENTS $M_{\infty} \sim 1.99$ , $R_c \sim 3.7 \times 10^6$ , $\alpha = 0.45^\circ$ .....	741
135b	VARIATION OF DRAG COMPONENTS WITH SUCTION COEFFICIENT $M_{\infty} \sim 1.99$ , $R_c \sim 5.3 \times 10^6$ , $\alpha = 0.45^\circ$ .....	742
135c	VARIATION OF DRAG COMPONENTS WITH SUCTION COEFFICIENT $M_{\infty} \sim 1.99$ , $R_c \sim 7.5 \times 10^6$ , $\alpha = 0.45^\circ$ .....	743
135d	VARIATION OF DRAG COMPONENTS WITH SUCTION COEFFICIENT $M_{\infty} \sim 1.99$ , $R_c \sim 9.1 \times 10^6$ , $\alpha = 0.15^\circ$ .....	744
135e	VARIATION OF DRAG COMPONENTS WITH SUCTION COEFFICIENT $M_{\infty} \sim 1.99$ , $R_c \sim 10.8 \times 10^6$ , $\alpha = 0.45^\circ$ .....	745

LIST OF FIGURES FOR SECTION II, PART 2 (Continued)

<u>Figure No.</u>	<u>Figure Title</u>	<u>Page</u>
136a	VARIATION OF DRAG COMPONENTS WITH SUCTION COEFFICIENT $M_\infty \approx 1.99$ , $R_c \approx 3.5 \times 10^6$ , $\alpha = 0.75^\circ$ .....	746
136b	VARIATION OF DRAG COMPONENTS WITH SUCTION COEFFICIENT $M_\infty \approx 1.99$ , $R_c \approx 7.1 \times 10^6$ , $\alpha = 0.75^\circ$ .....	747
136c	VARIATION OF DRAG COMPONENTS WITH SUCTION COEFFICIENT $M_\infty \approx 1.99$ , $R_c \approx 9.2 \times 10^6$ , $\alpha = 0.75^\circ$ .....	748
136d	VARIATION OF DRAG COMPONENTS WITH SUCTION COEFFICIENT $M_\infty \approx 1.99$ , $R_c \approx 10.7 \times 10^6$ , $\alpha = 0.75^\circ$ .....	749
136e	VARIATION OF DRAG COMPONENTS WITH SUCTION COEFFICIENTS $M_\infty \approx 1.99$ , $R_c \approx 14.2 \times 10^6$ , $\alpha = 0.75^\circ$ .....	750
137	REDUCTION OF WAKE MOMENTUM DEFICIT DUE TO CROSSFLOW VELOCITY IN THE WAKE.....	751
138a	VARIATION OF CORRECTED OPTIMUM DRAG COEFFICIENTS WITH REYNOLDS NUMBER $M_\infty \approx 1.99$ , $\alpha = 0.15^\circ$ .....	752
138b	VARIATION OF UNCORRECTED OPTIMUM DRAG COEFFICIENTS WITH REYNOLDS NUMBER $M_\infty \approx 1.99$ , $\alpha = 0.15^\circ$ .....	753
139a	VARIATION OF CORRECTED OPTIMUM DRAG COEFFICIENTS WITH REYNOLDS NUMBER $M_\infty \approx 1.99$ , $\alpha = 0.45^\circ$ .....	754
139b	VARIATION OF UNCORRECTED OPTIMUM DRAG COEFFICIENT WITH REYNOLDS NUMBER $M_\infty \approx 1.99$ , $\alpha = 0.45^\circ$ .....	755
140a	VARIATION OF CORRECTED OPTIMUM DRAG COEFFICIENTS WITH REYNOLDS NUMBER $M_\infty \approx 1.99$ , $\alpha = 0.75^\circ$ .....	756
140b	VARIATION OF UNCORRECTED OPTIMUM DRAG COEFFICIENTS WITH REYNOLDS NUMBER $M_\infty \approx 1.99$ , $\alpha = 0.75^\circ$ .....	757
141a	TYPICAL SUCTION DISTRIBUTIONS FOR OPTIMUM SUCTION - $M_\infty \approx 1.99$ .	758
141b	COMPARISON OF CALCULATED AND MEASURED SUCTION DISTRIBUTIONS $M_\infty \approx 1.99$ , $\alpha = 0.15^\circ$ .....	759
142	TYPICAL SUCTION DISTRIBUTIONS FOR $M_\infty \approx 2.25$ .....	760
143	TYPICAL MEASURED PROFILES AT $M_\infty = 2.0$ .....	761
144	TYPICAL VARIATION OF SURFACE PRESSURE RATIO WITH TOTAL SUCTION $M_\infty \approx 1.99$ .....	762
145	COMPARISON OF SURFACE PRESSURES AT THREE SPANWISE STATIONS $M_\infty \approx 1.99$ .....	763

LIST OF FIGURES FOR SECTION II, PART 2 (Continued)

<u>Figure No.</u>	<u>Figure Title</u>	<u>Page</u>
146	COMPARISON OF SURFACE PRESSURES AT THREE ANGLES OF ATTACK $M_\infty \cong 1.99$ .....	764
147	COMPARISON OF MEASURED TWO DIMENSIONAL VELOCITY DISTRIBUTION WITH CALCULATED DISTRIBUTION.....	765
148	VARIATION OF DRAG COMPONENTS WITH SUCTION COEFFICIENT $M_\infty \cong 2.25$ .....	766
149a	A VARIATION OF CORRECTED DRAG COEFFICIENTS WITH REYNOLDS NUMBER $M_\infty \cong 2.25$ .....	767
149b	VARIATION OF UNCORRECTED DRAG COEFFICIENTS WITH REYNOLDS NUMBER $M_\infty \cong 2.25$ .....	768
150	TYPICAL MEASURED WAKE PROFILES AT $M_\alpha = 2.25$ .....	769
151	PRESSURE DISTRIBUTION AT $\alpha = 0.45$ AND $M_\infty = 2.28$ .....	770
152	VARIATION OF $F_1 + F_2$ WITH $\delta_{ss}^*$ .....	771
153	VARIATION OF $k_s$ WITH $(V/U)_{te}^2$ .....	772
154	LOCI OF RESULTANT VECTOR TERMINATION POINTS IN THE BOUNDARY LAYER.....	773
155	SIMULATION OF $(F_1 + F_2)$ BY EMPIRICAL EQUATION.....	774
156	SIMULATION OF $F_2$ BY EMPIRICAL EQUATION.....	775
157	SUMMARY OF EMPIRICAL CROSSFLOW CORRECTION FACTORS.....	776
158	EXTERNAL REFERENCE STATIONS FOR LOSS CALCULATIONS THROUGH SWEPT SLOTS.....	777
159	LOCAL AND INTERNAL REFERENCE STATIONS FOR LOSS CALCULATIONS THROUGH SLOTS.....	778
160	SIMULATION OF SUCTION LAYER PROFILE.....	779
161	VELOCITY RATIO FOR THE INLET LENGTH OF SWEPT SLOTS.....	780
162	COMPRESSIBLE FLOW LOSSES THROUGH HOLES.....	781
163	APPROXIMATIONS FOR $w_x/w_i$ AND $k_{mv}$ .....	782
164	WORK CHART FOR FLOW OUTSIDE SLOT.....	783



LIST OF FIGURES FOR SECTION II, PART 2 (Continued)

<u>Figure No.</u>	<u>Figure Title</u>	<u>Page</u>
165	WORK CHART FOR FLOW INSIDE SLOT.....	784
166	SKETCH - COMPRESSIBLE FLOW TUBE.....	785
167	POTENTIAL FLOW VELOCITY RATIO $\frac{U_5}{U_9}$ AT ORIFICE NO. 5 VS REYNOLDS NUMBER $R_R$ .....	786
168	DISTANCE $X_5$ OF ORIFICE NO. 5 FROM FICTITIOUS TUBE INLET VS REYNOLDS NUMBER $R_R$ .....	787
169	PRESSURE RATIO $P/P_k$ VS NON-DIMENSIONAL TUBE LENGTH $\frac{X}{R R_R}$ FOR VARIOUS INLET MACH NUMBER $M_O$ .....	788
170	PRESSURE RATIO $P/P_k$ VS NON-DIMENSIONAL TUBE LENGTH $\frac{X}{R R_R}$ FOR VARIOUS INLET MACH NUMBER $M_O$ .....	789
171	PRESSURE RATIO $P/P_k$ VS NON-DIMENSIONAL TUBE LENGTH $\frac{X}{R R_R}$ FOR VARIOUS INLET MACH NUMBER $M_O$ .....	790
172	PRESSURE RATIO $P/P_k$ VS NON-DIMENSIONAL TUBE LENGTH $\frac{X}{R R_R}$ FOR VARIOUS INLET MACH NUMBER $M_O$ .....	791
173	CRITICAL VALUES OF PRESSURE RATIO $P/P_k$ , TUBE LENGTH $\frac{X}{R R_R}$ AND MACH NUMBER $M_O$ AT CHOKING CONDITION.....	792
174	CRITICAL VALUES OF PRESSURE RATIO $P/P_k$ , TUBE LENGTH $\frac{X}{R R_R}$ AND MACH NUMBER $M_O$ AT CHOKING CONDITION.....	793

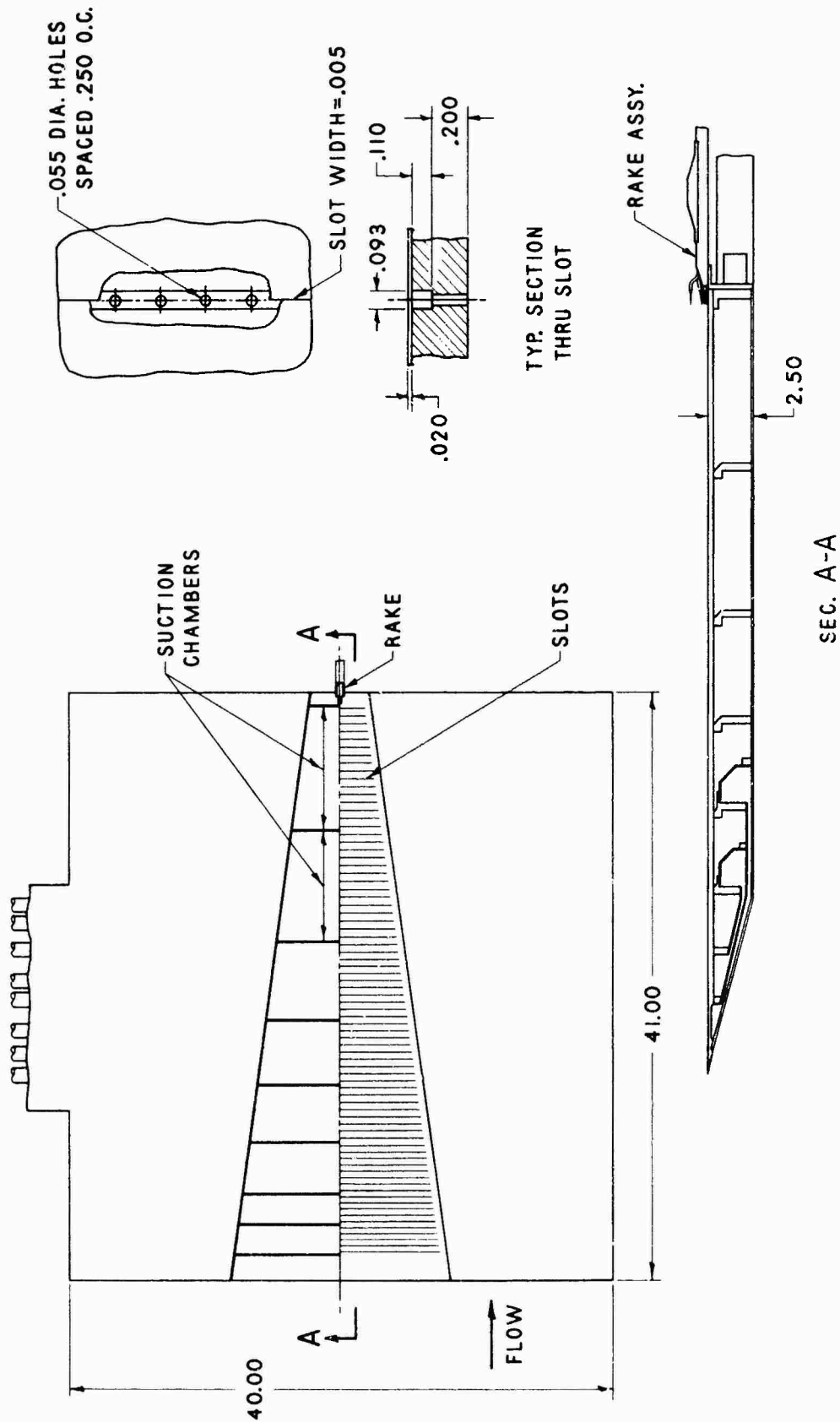


FIGURE 1 FLAT PLATE SUCTION MODEL AEDC TUNNEL A



FIGURE 2 INSIDE OF MODEL, BOTTOM PLATE REMOVED



FIGURE 3 MODEL AND RAKE INSTALLED IN TUNNEL A, ONE TUNNEL WALL REMOVED

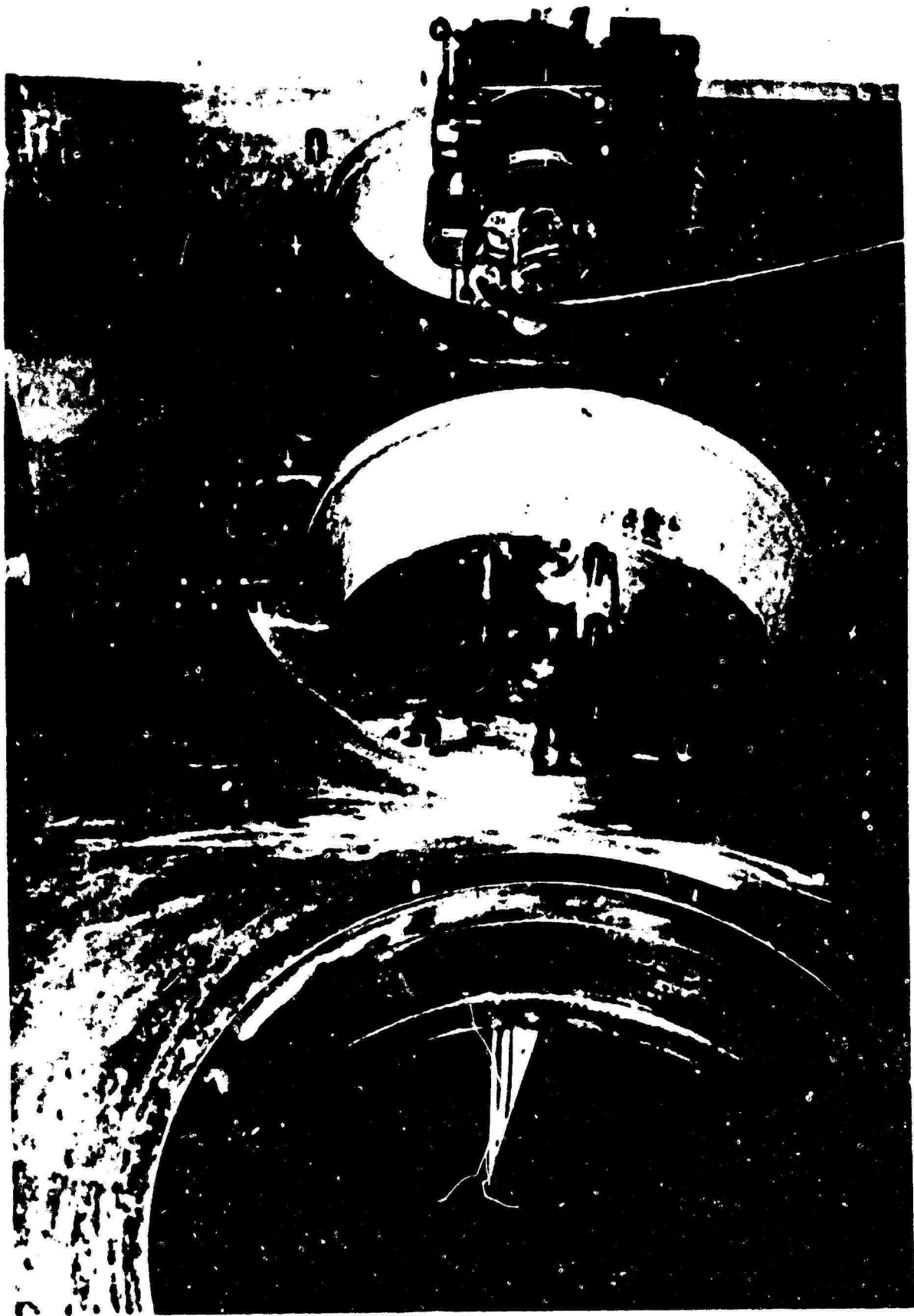


FIGURE 4 TUNNEL WINDOWS ON OPERATING SIDE

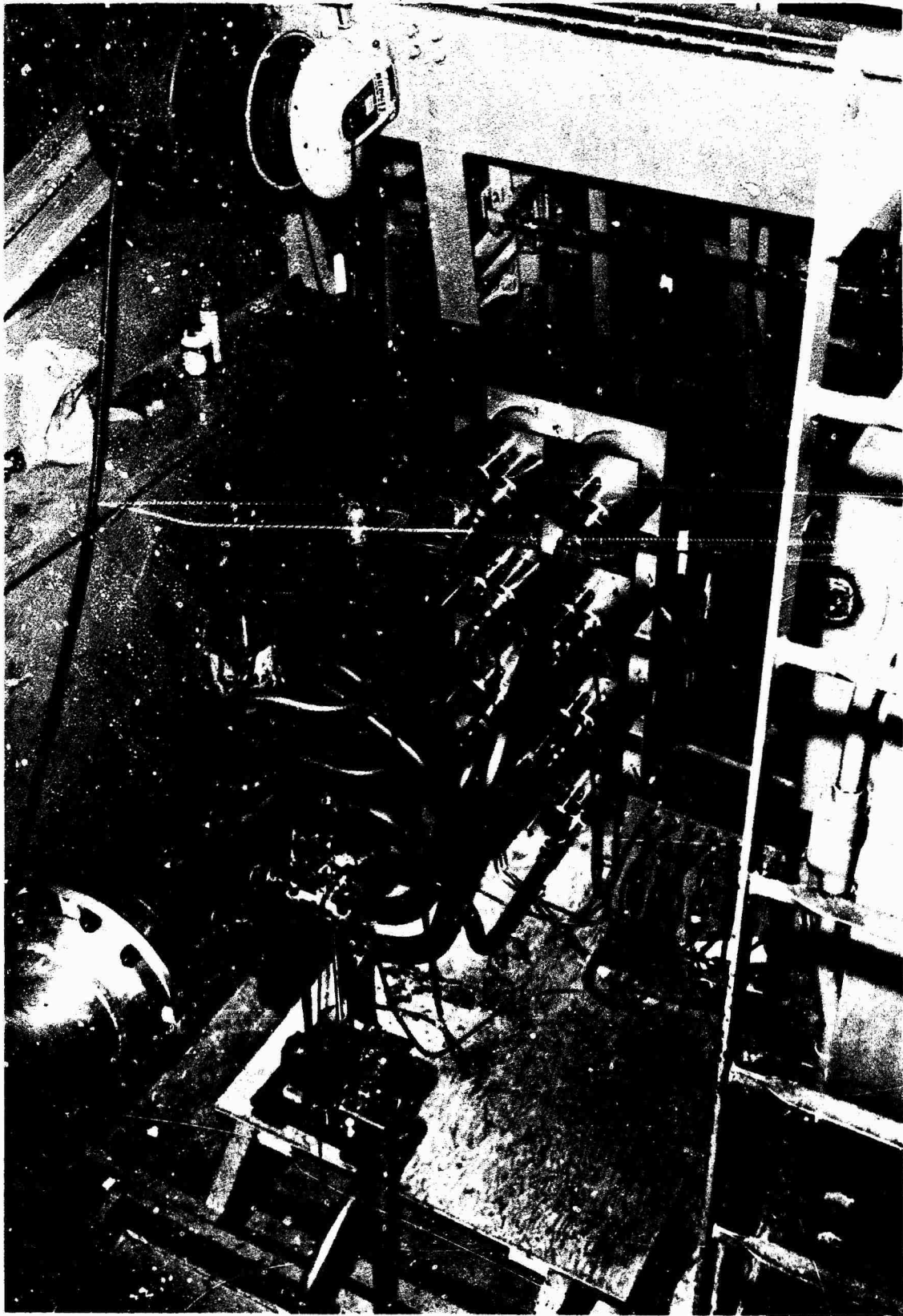


FIGURE 5 SUCTION EQUIPMENT ON NON-OPERATING SIDE OF TUNNEL

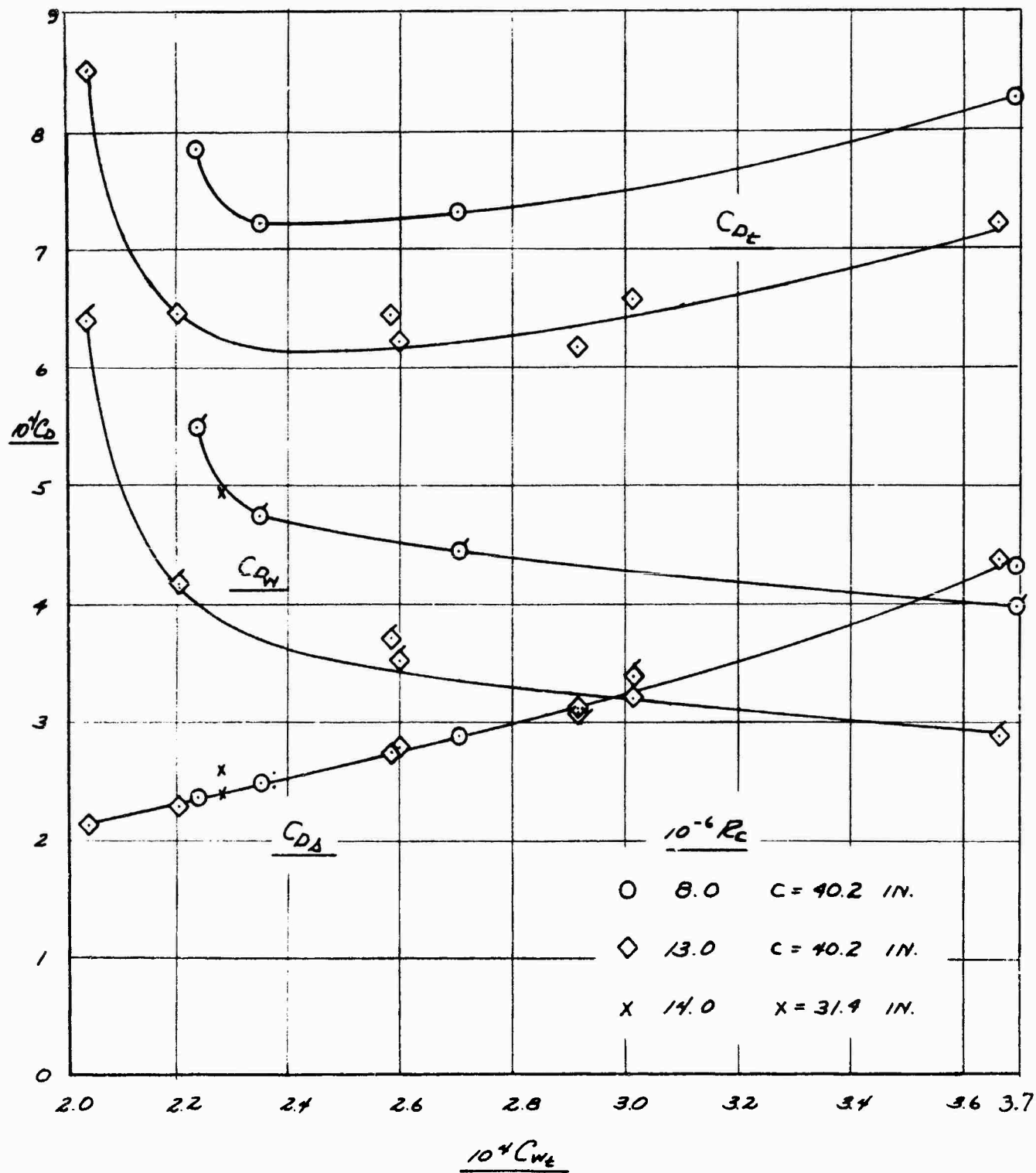


FIGURE 6

WAKE, SUCTION AND TOTAL DRAG COEFFICIENTS VS SUCTION COEFFICIENT

$M = 3.0$ ,  $Re = 8.0$  and  $13.0 \times 10^6$

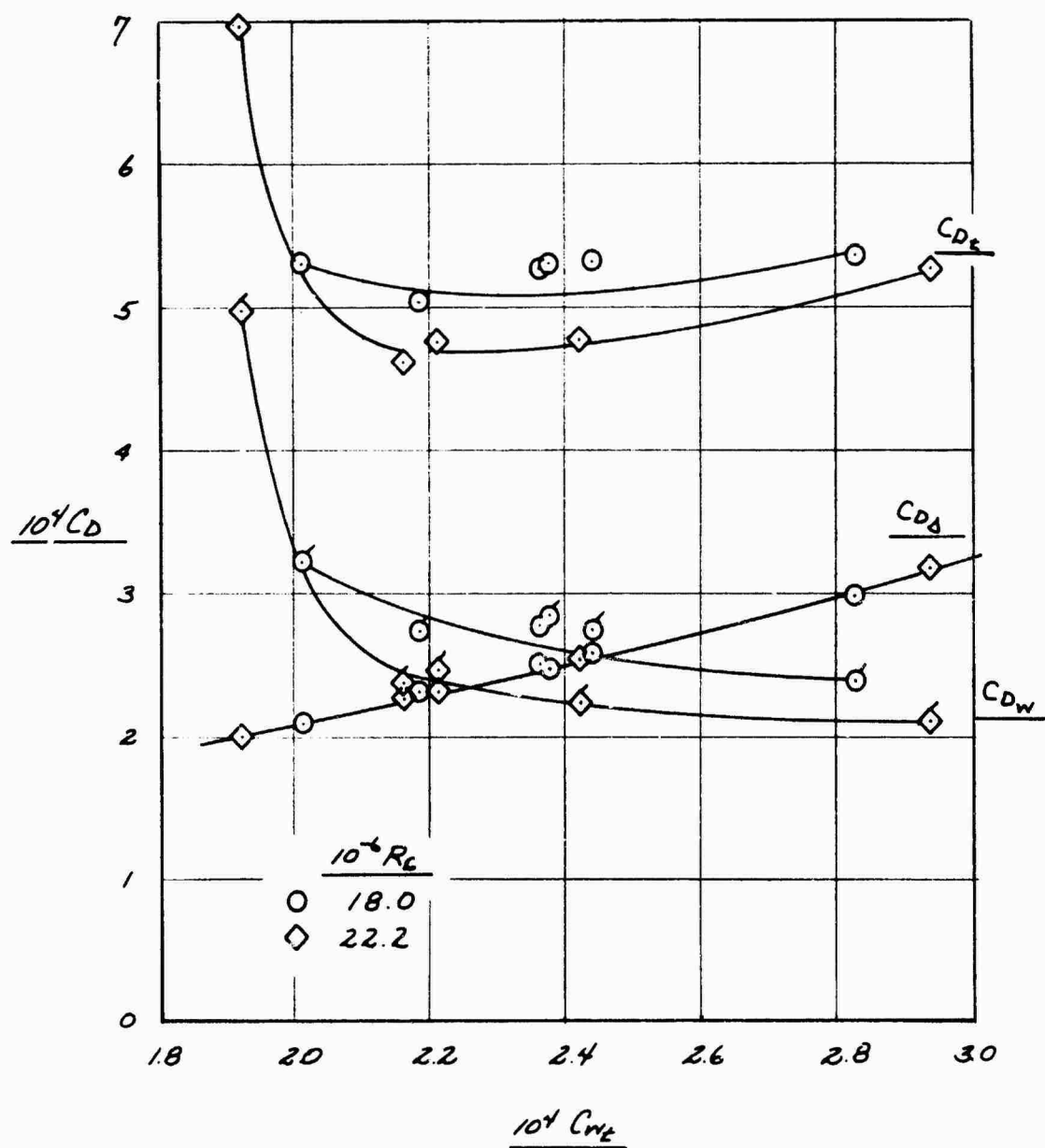


FIGURE 7

WAKE, SUCTION AND TOTAL DRAG COEFFICIENTS VS SUCTION COEFFICIENT

$M = 3.0$ ,  $Re = 18.0$  and  $22.2 \times 10^6$



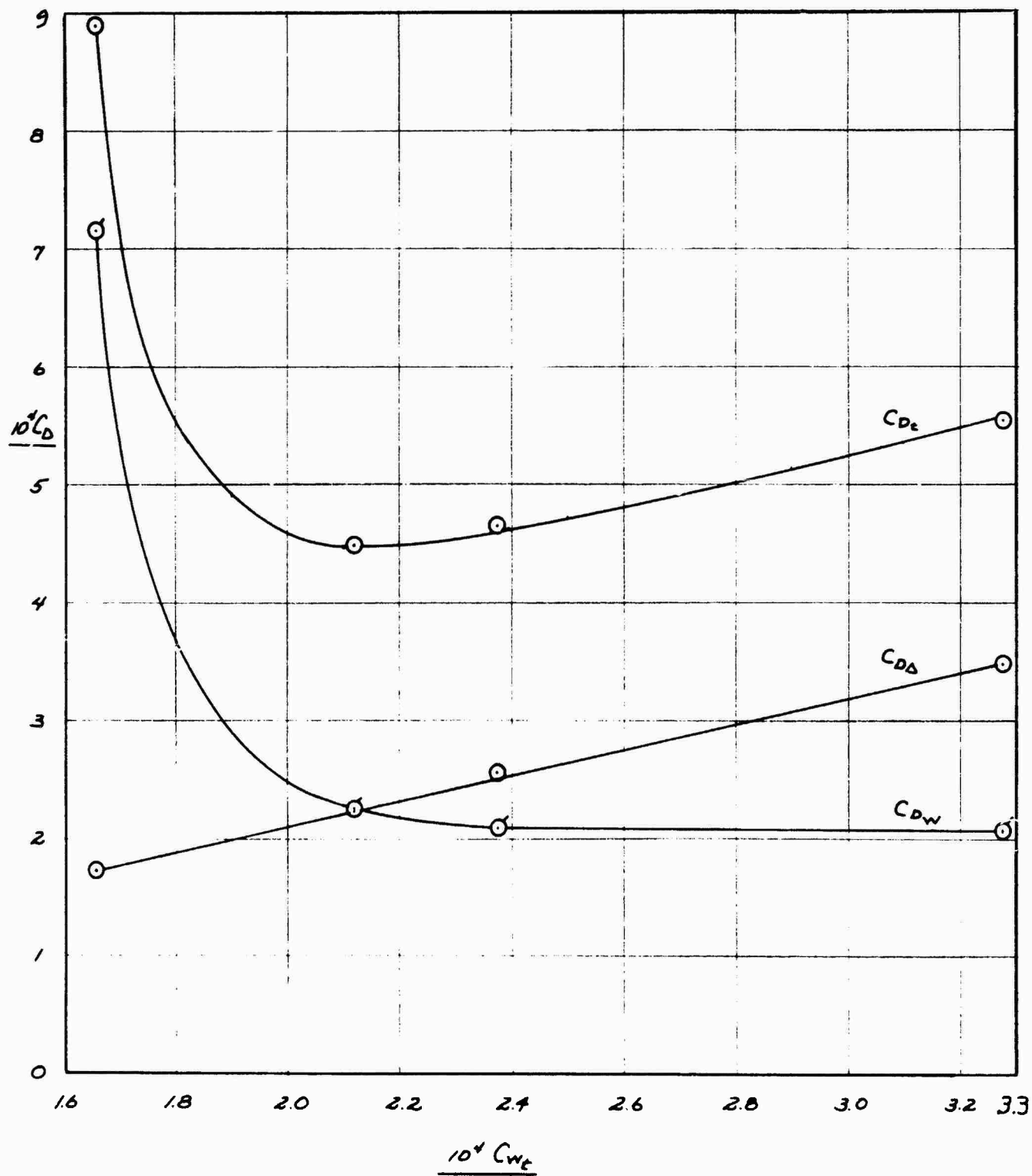


FIGURE 8

WAKE, SUCTION AND TOTAL DRAG COEFFICIENTS VS SUCTION COEFFICIENT

$$M = 3.0, R_c = 25.7 \times 10^6$$

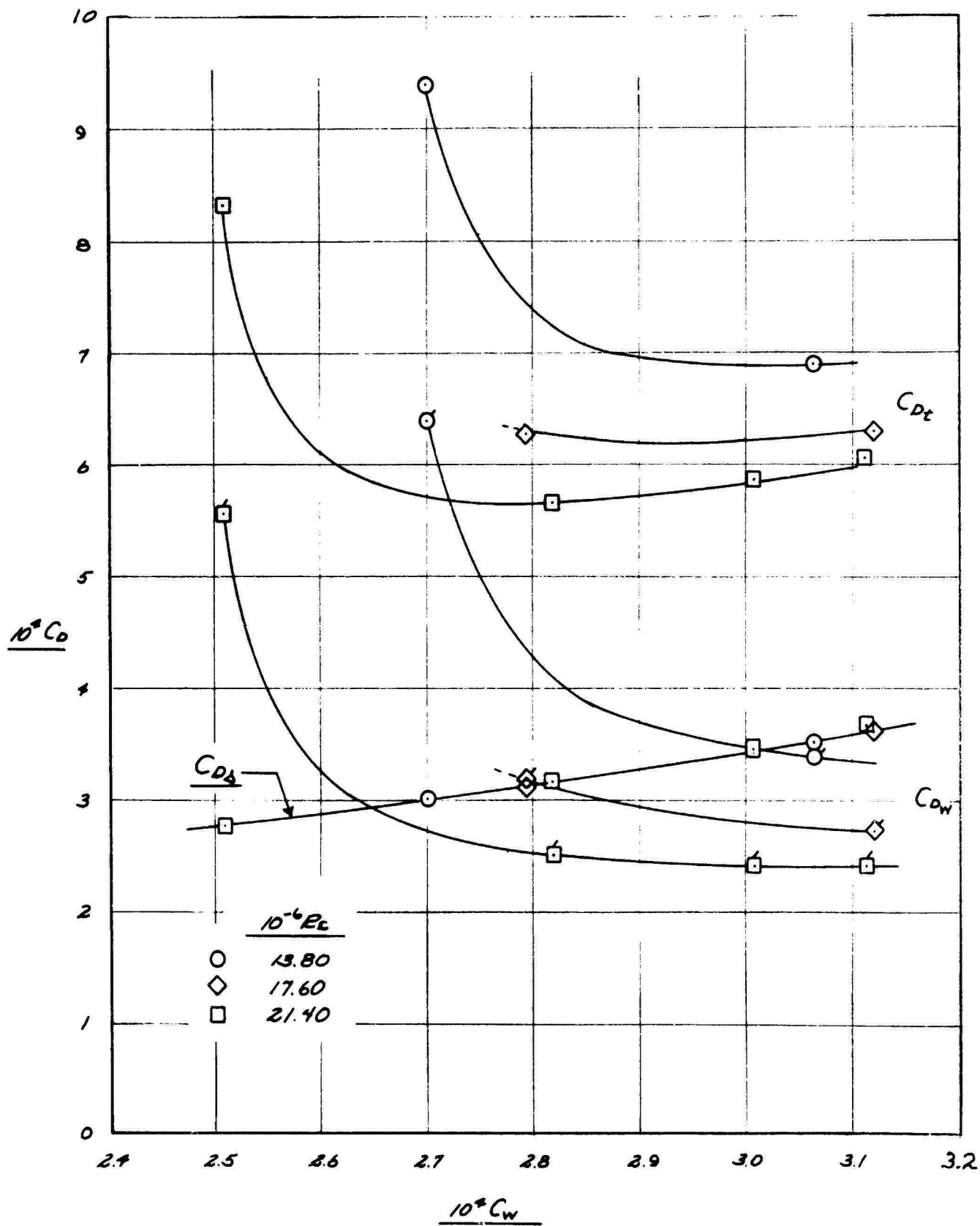


FIGURE 9

WAKE, SUCTION AND TOTAL DRAG COEFFICIENTS VS SUCTION COEFFICIENT

$M = 3.5$ ,  $R_c = 13.8, 17.6$  and  $21.4 \times 10^6$

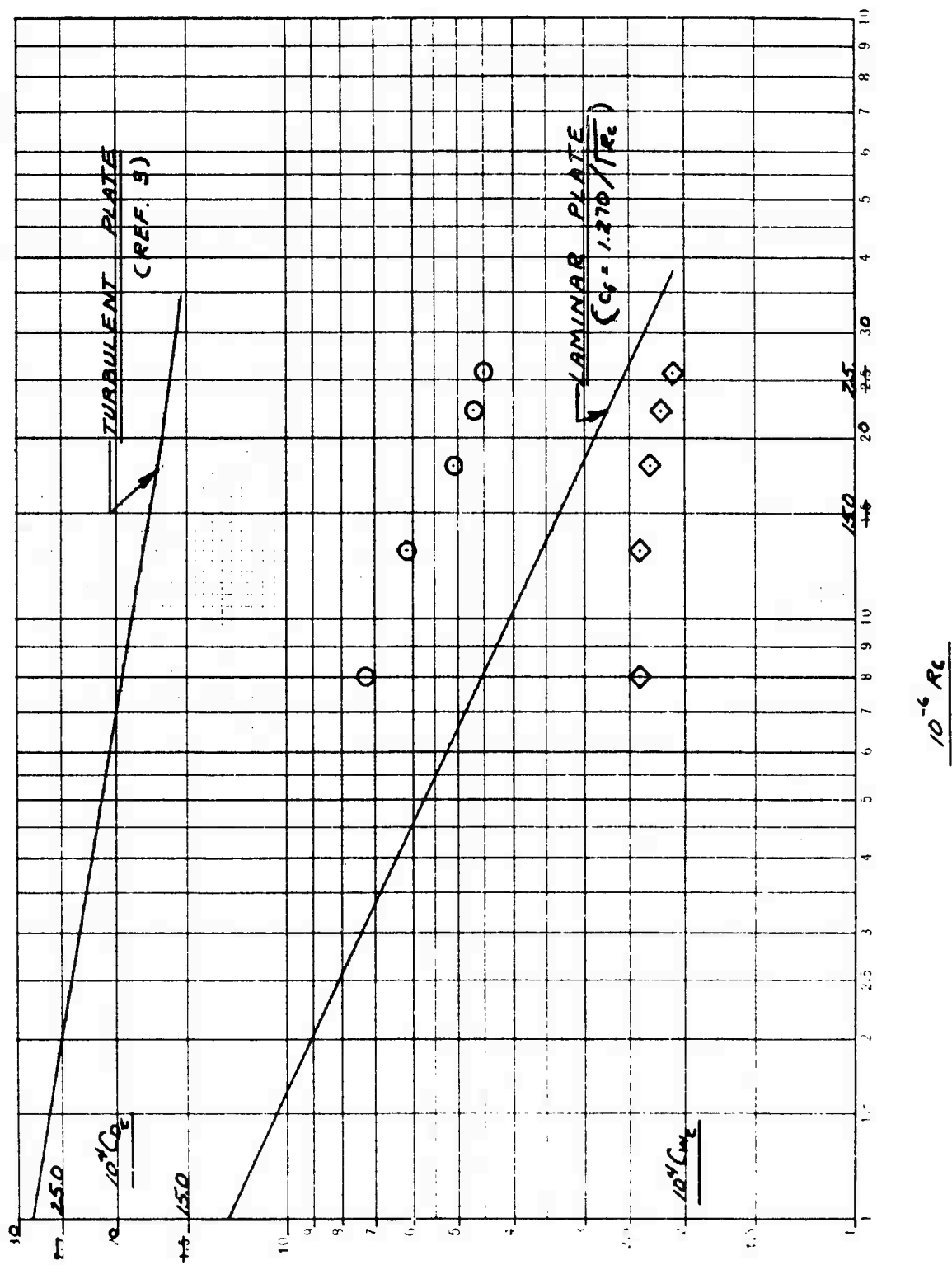


FIGURE 10 MINIMUM TOTAL DRAG AND OPTIMUM SUCTION COEFFICIENTS VS REYNOLDS NUMBER,  $M = 3.0$

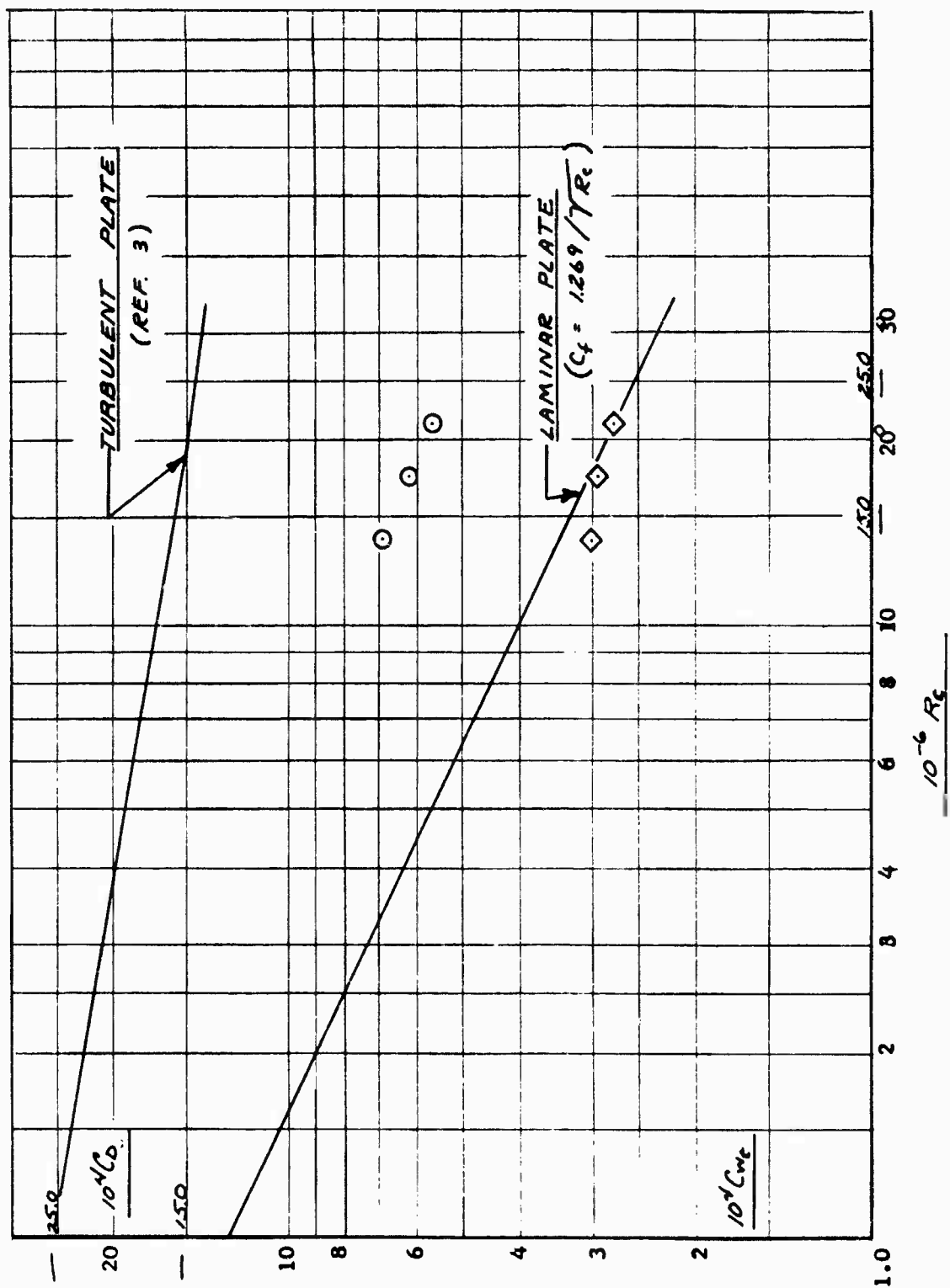


FIGURE 11 MINIMUM TOTAL DRAG AND OPTIMUM SUCTION COEFFICIENTS VS REYNOLDS NUMBER,  $M = 3.5$

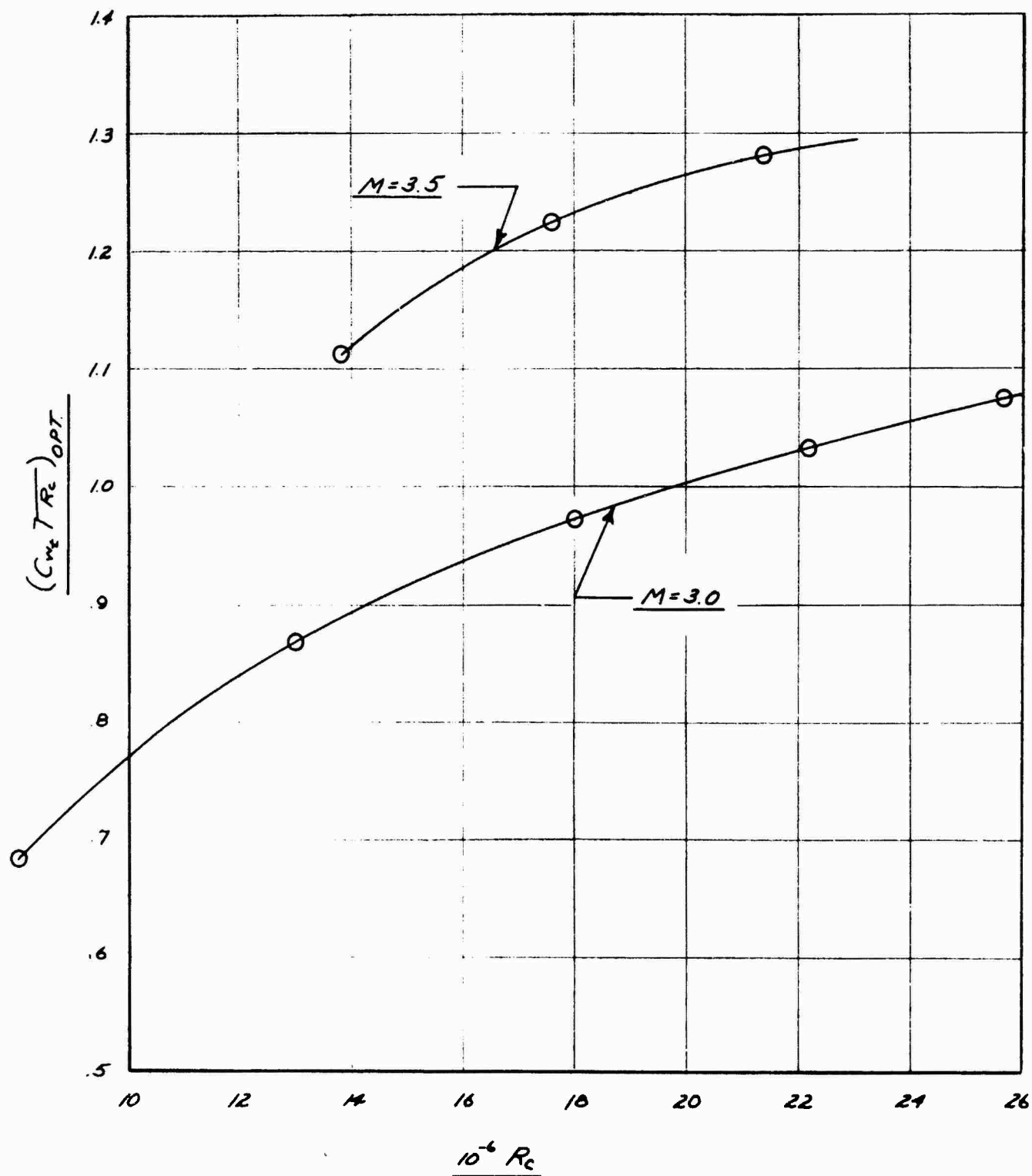


FIGURE 12  
OPTIMUM SUCTION COEFFICIENT VS  
REYNOLDS NUMBER FOR  $M = 3.0$  and  $3.5$

$M_\infty$	$10^4 R_c$	$C_{w,TRC}$
— 3.0	25.8	1.202
--- 3.5	21.7	1.452

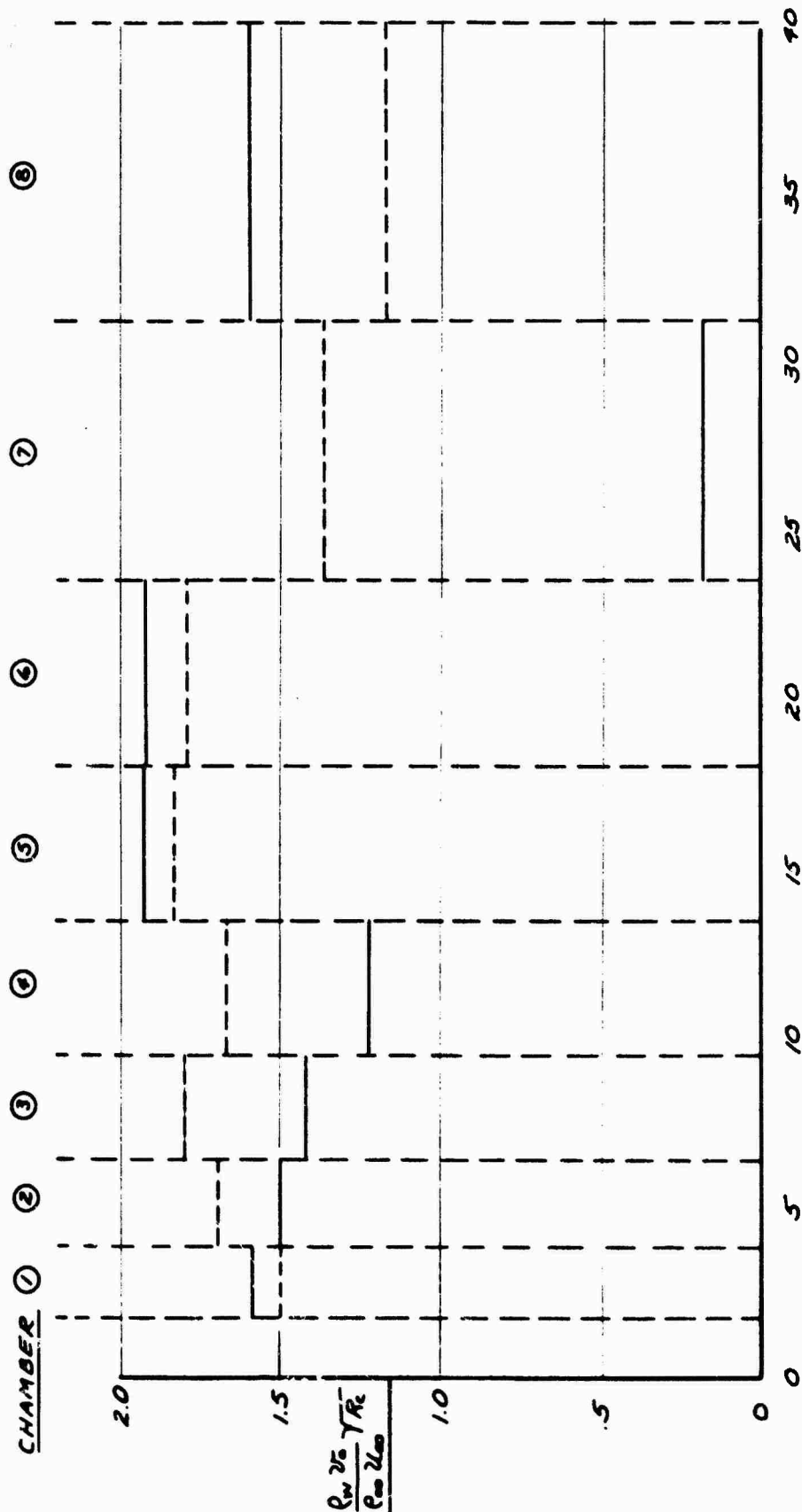


FIGURE 13  
EXPERIMENTAL SUCTION DISTRIBUTIONS FOR  $M_\infty = 3.0$ ,  $R_c = 25.8 \times 10^6$   
AND FOR  $M_\infty = 3.5$ ,  $R_c = 21.7 \times 10^6$

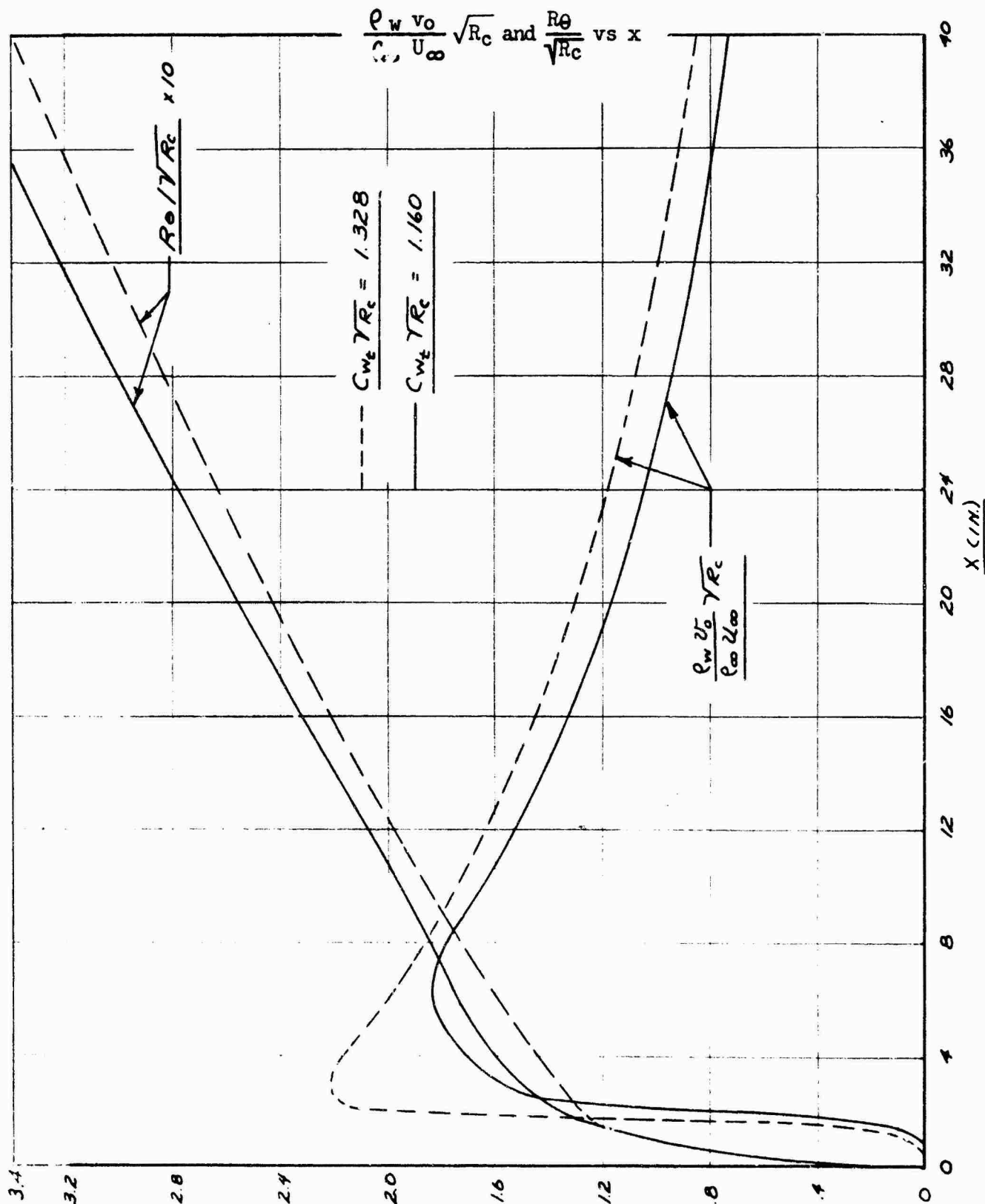


FIGURE 14

SUCTION DISTRIBUTIONS AND MOMENTUM THICKNESS REYNOLDS  
NUMBERS FOR THEORETICAL BOUNDARY LAYER CALCULATIONS

$$\frac{\rho_w v_o}{\rho_\infty U_\infty} \sqrt{R_c} \text{ and } \frac{R_\theta}{\sqrt{R_c}} \text{ vs } x$$

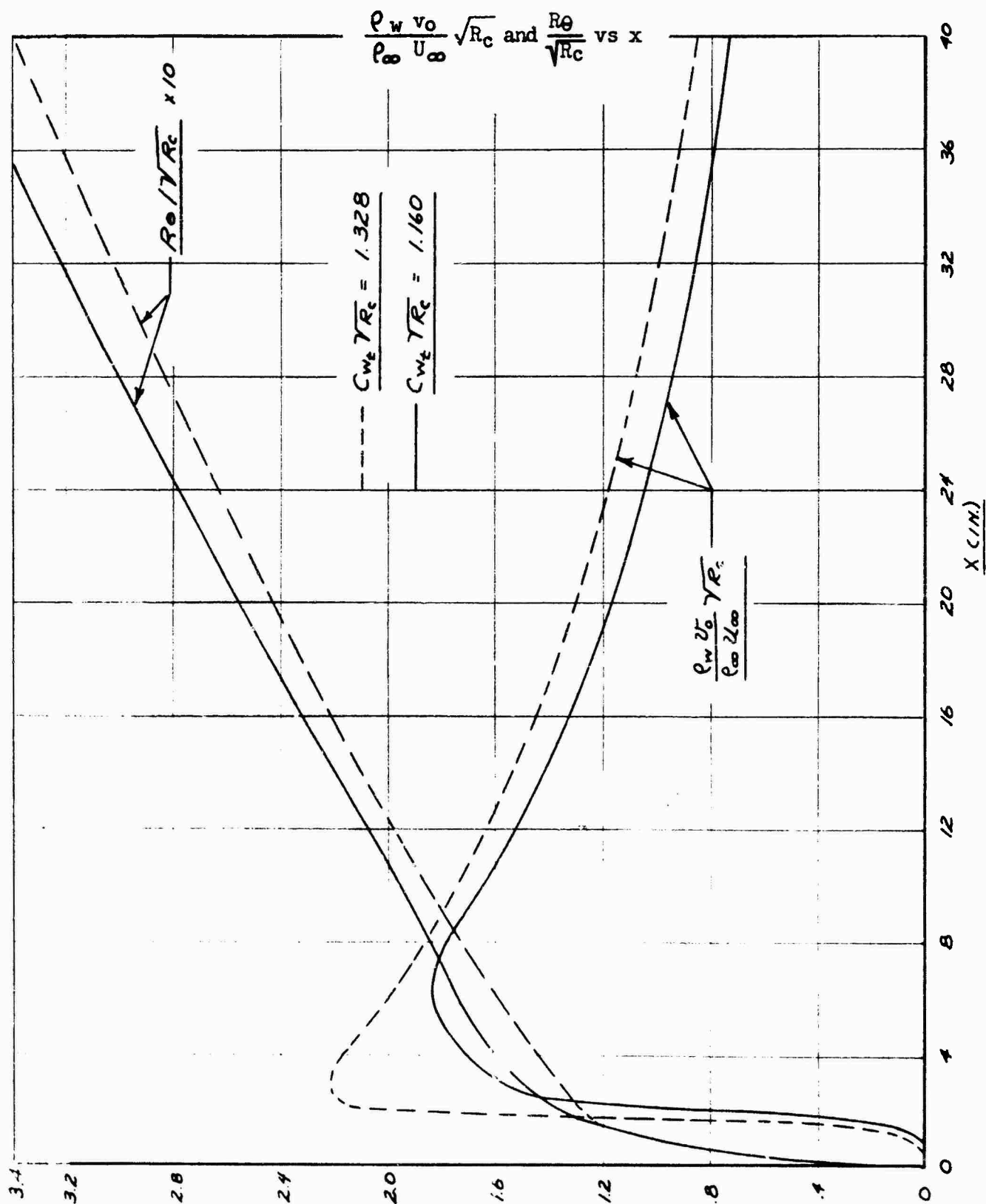


FIGURE 14

SUCTION DISTRIBUTIONS AND MOMENTUM THICKNESS REYNOLDS  
NUMBERS FOR THEORETICAL BOUNDARY LAYER CALCULATIONS

$$\frac{\rho_w v_0}{\rho_\infty U_\infty} \sqrt{R_c} \text{ and } \frac{R_0}{\sqrt{R_c}} \text{ vs } x$$



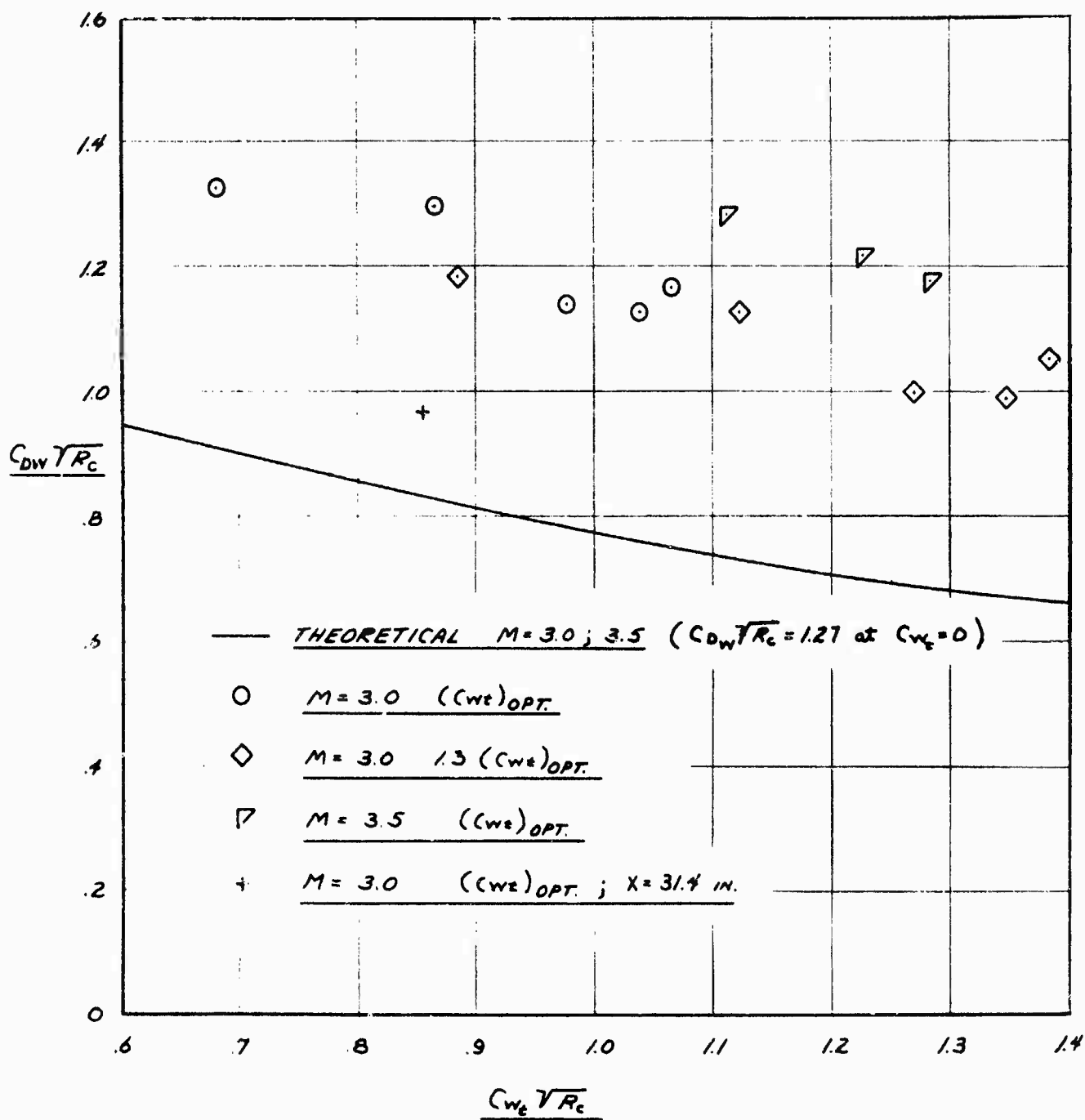


FIGURE 15

COMPARISON OF THEORETICAL AND EXPERIMENTAL  
WAKE DRAG COEFFICIENTS  $C_{DW}/\sqrt{R_c}$  VS  $C_{Wt}/\sqrt{R_c}$

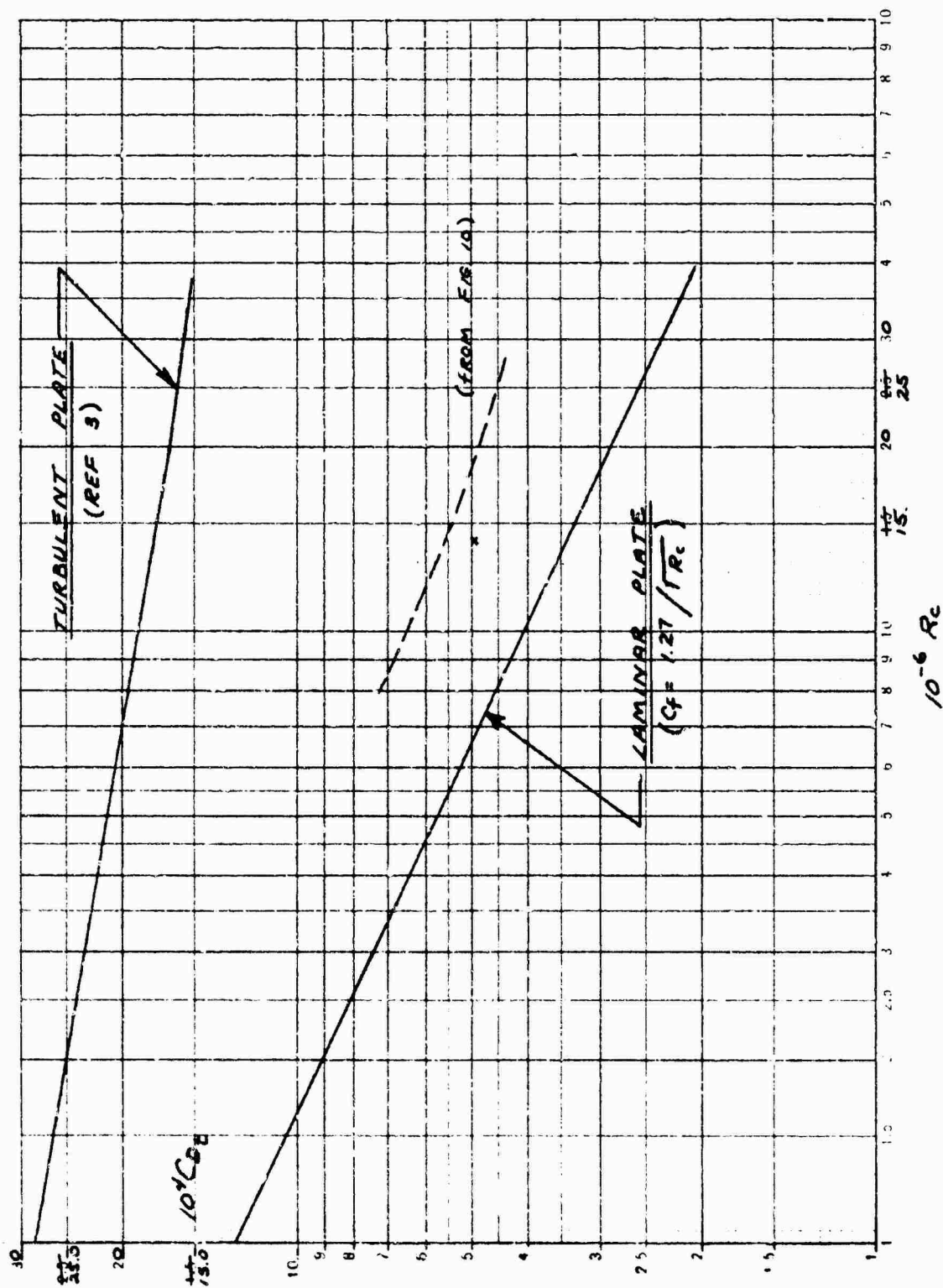


FIGURE 16

COMPARISON OF TOTAL DRAG COEFFICIENT MEASURED AT STATION  
 $x = 31.4$  INCHES WITH MINIMUM TOTAL DRAG COEFFICIENTS  
 MEASURED AT  $c = 40.23$  INCHES FOR  $M_\infty = 3.0$

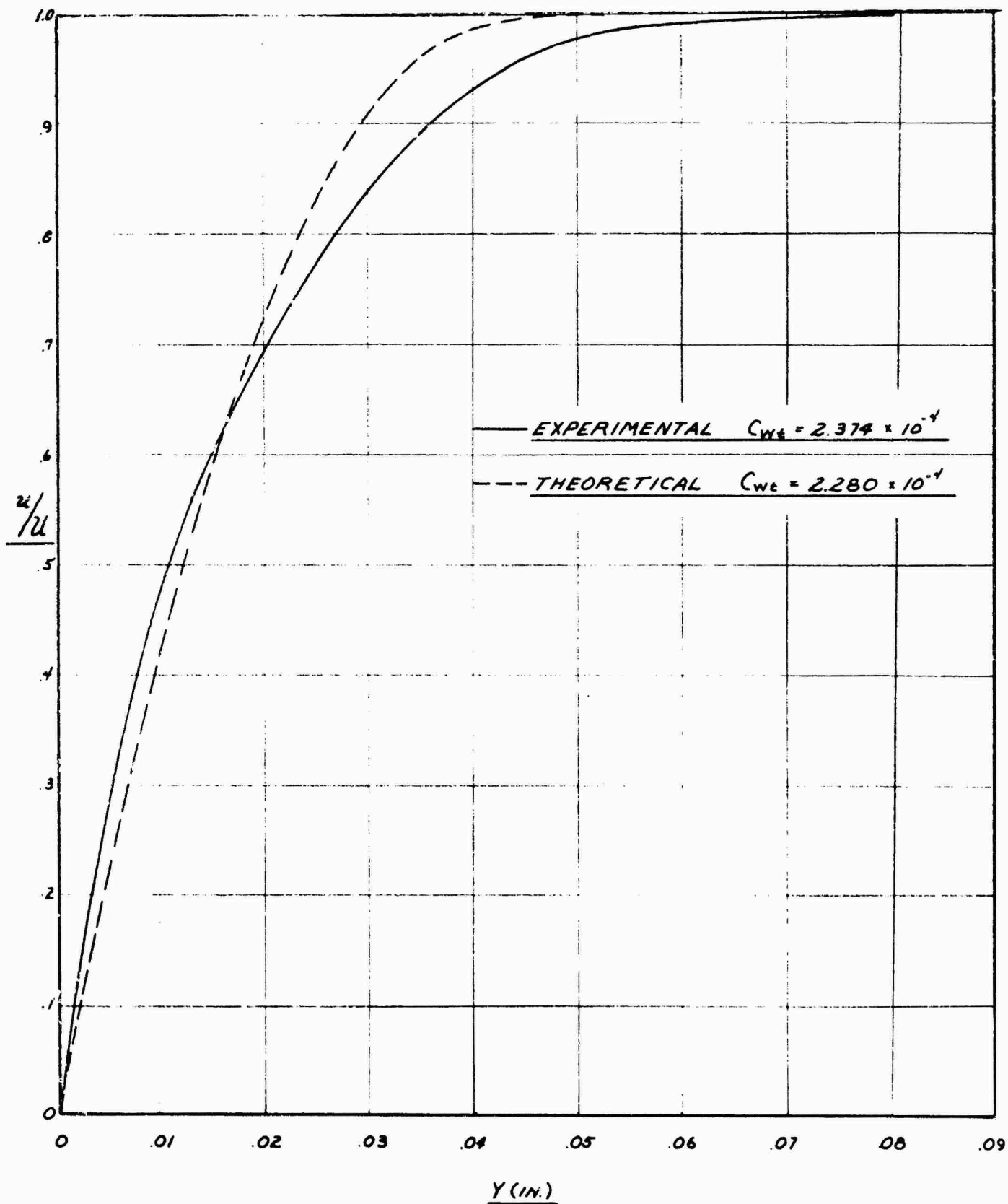


FIGURE 17

COMPARISON OF THEORETICAL AND EXPERIMENTAL BOUNDARY LAYER VELOCITY PROFILES

$M = 3.0$ ,  $R_c = 25.7 \times 10^6$ ,  $c = 40.23$  INCHES

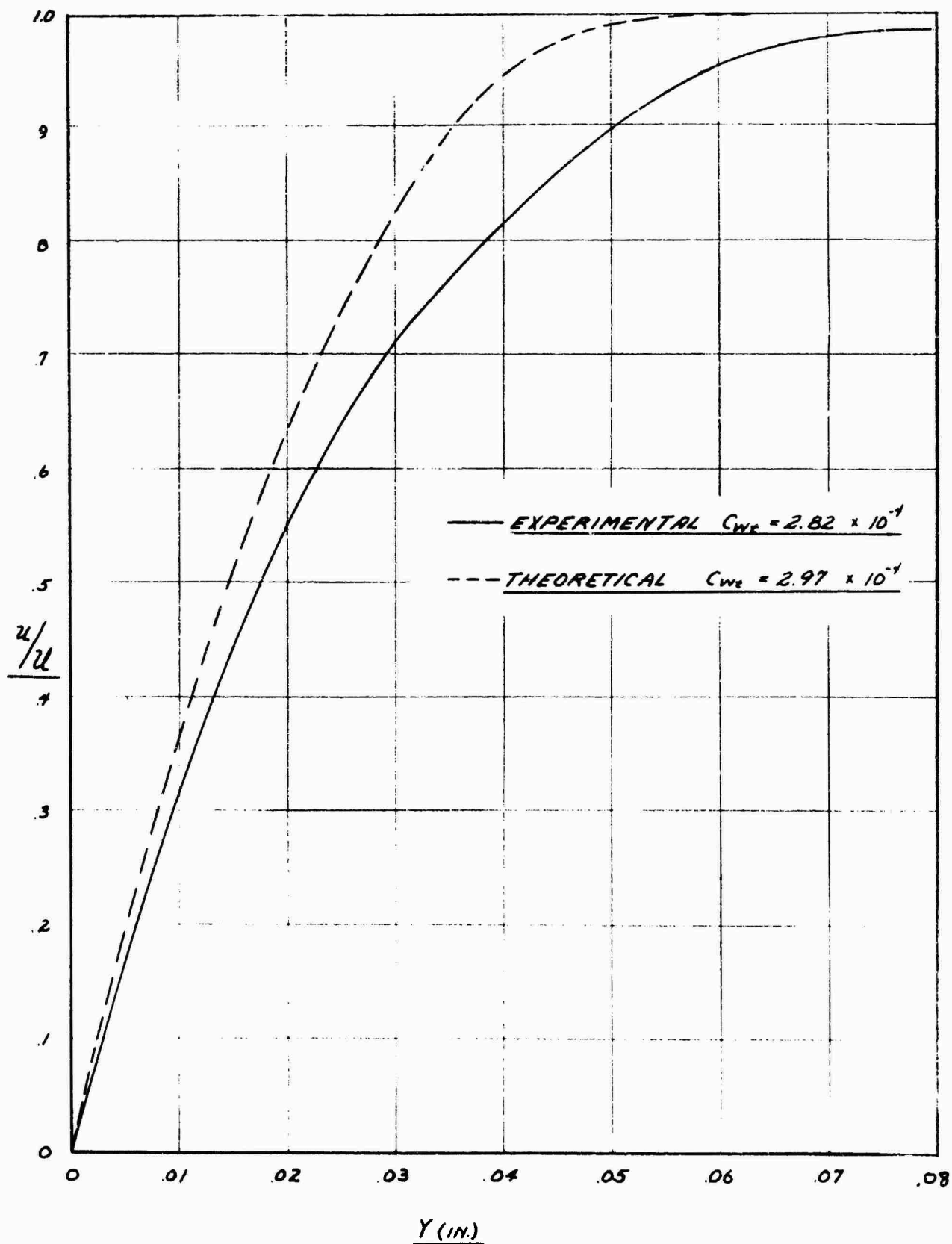


FIGURE 18

COMPARISON OF THEORETICAL AND EXPERIMENTAL BOUNDARY LAYER VELOCITY PROFILES

$M = 3.5$ ,  $R_c = 21.4 \times 10^6$ ,  $c = 40.40$  INCHES

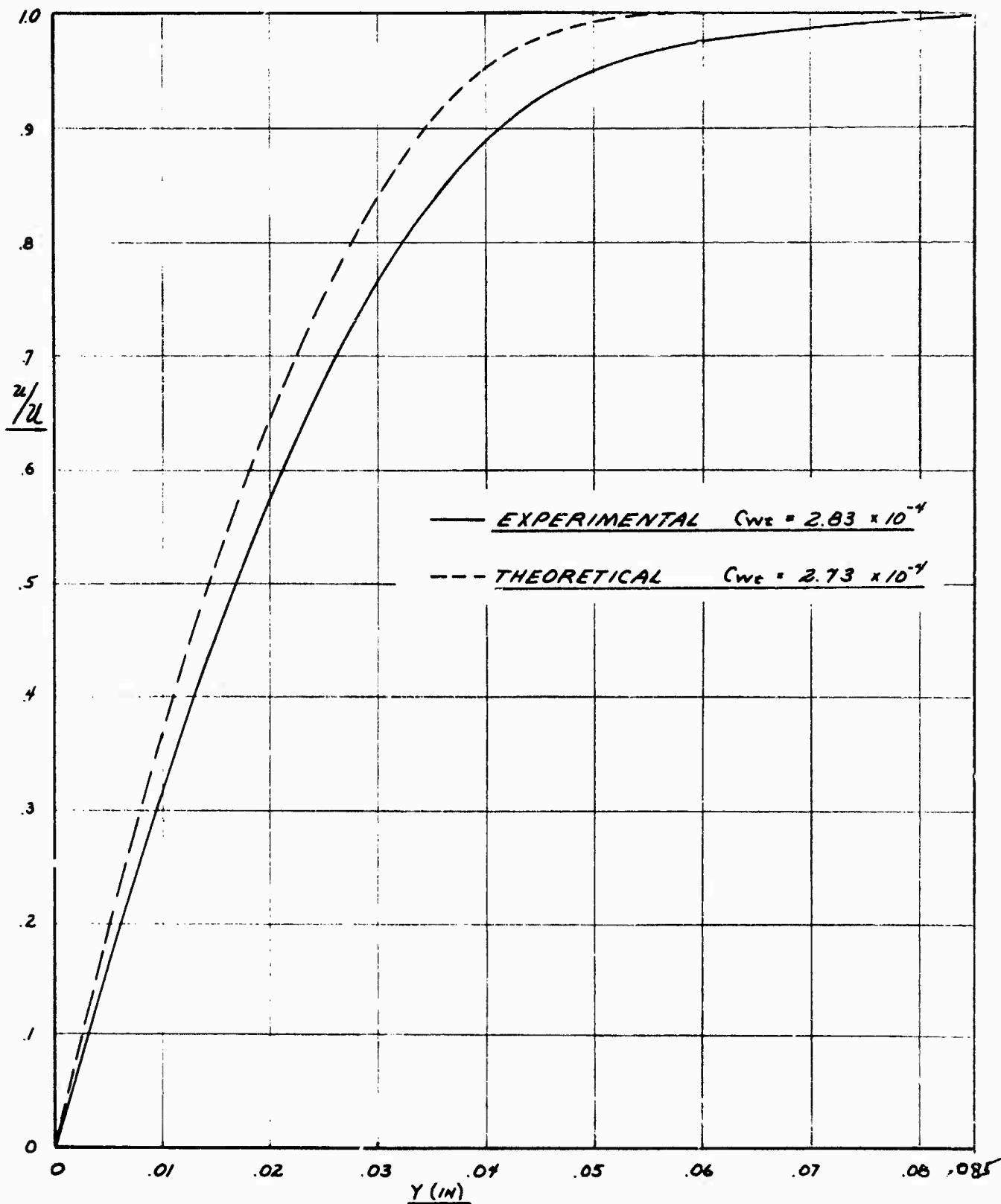


FIGURE 19

COMPARISON OF THEORETICAL AND EXPERIMENTAL BOUNDARY LAYER VELOCITY PROFILES

$M = 3.0$ ,  $R_c = 18.0 \times 10^6$ ,  $c = 40.23$  INCHES

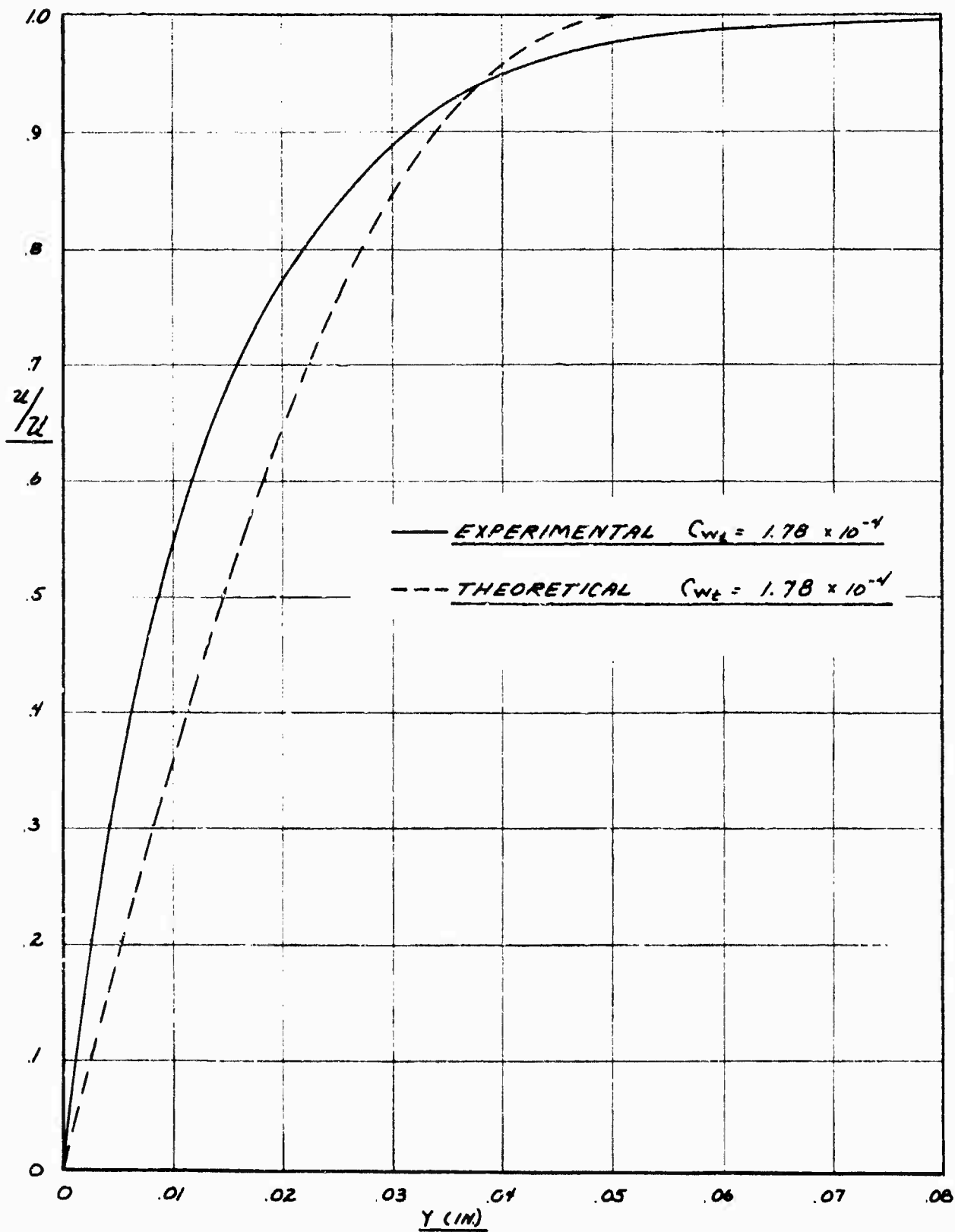


FIGURE 20

COMPARISON OF THEORETICAL AND EXPERIMENTAL BOUNDARY LAYER VELOCITY PROFILES  
 $M = 3.0$ ,  $R_x = 14.0 \times 10^6$ ,  $x = 31.4$  INCHES

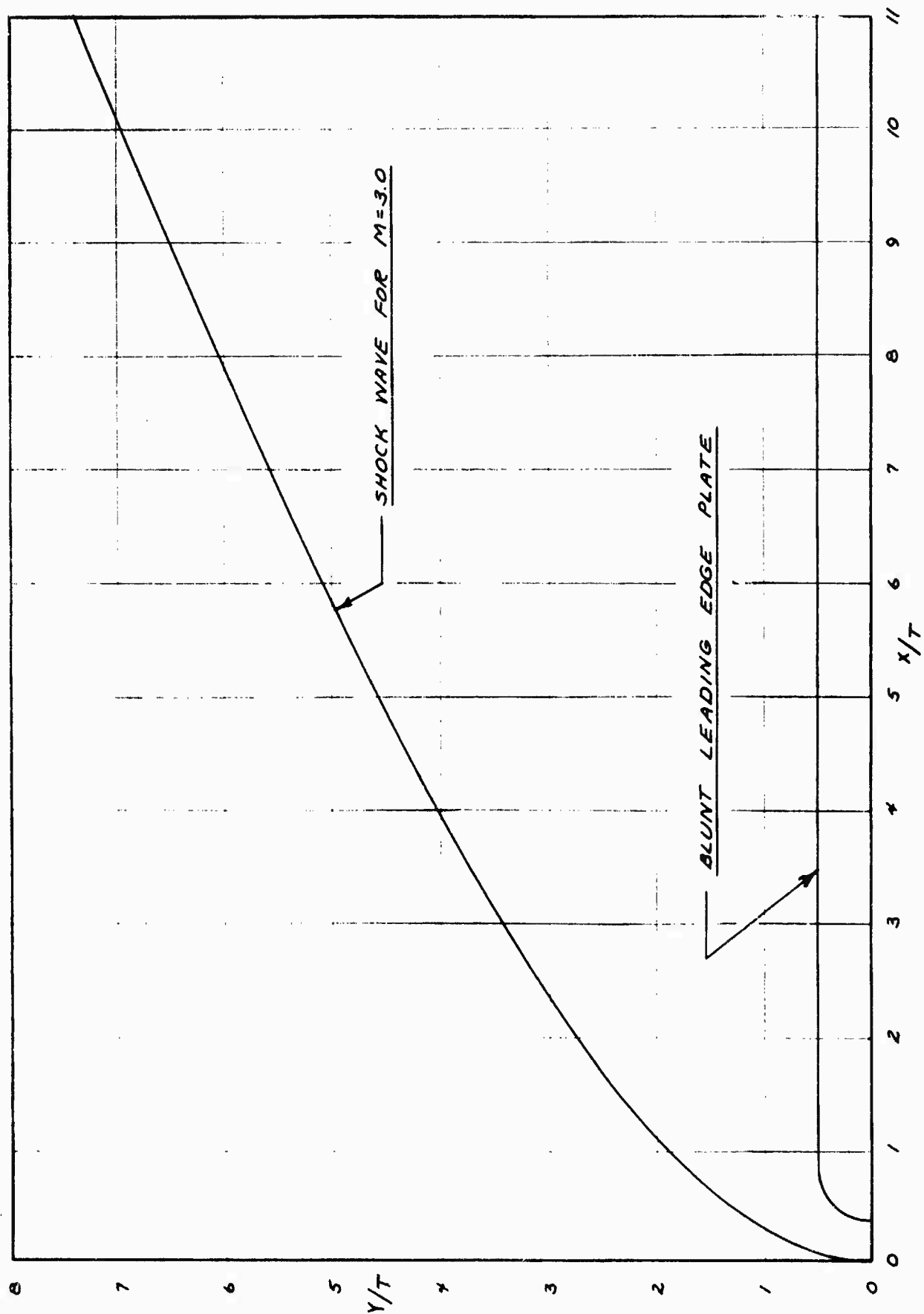


FIGURE 21 BLUNT PLATE AND APPROXIMATE SHOCK WAVE FOR  $M = 3.0$

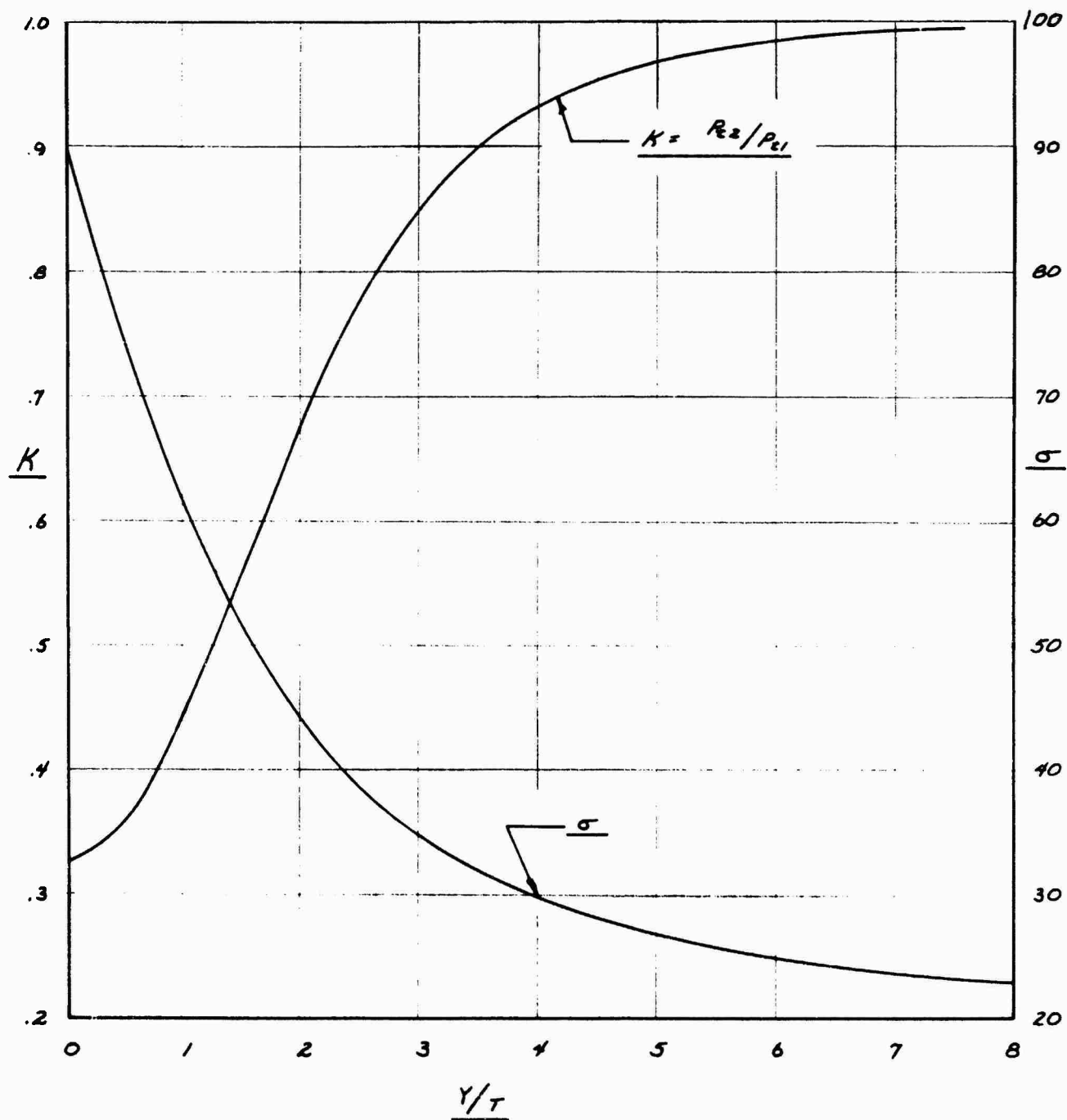


FIGURE 22 SLOPE OF SHOCK WAVE AND TOTAL HEAD LOSS VS HEIGHT  $\frac{y}{t}$



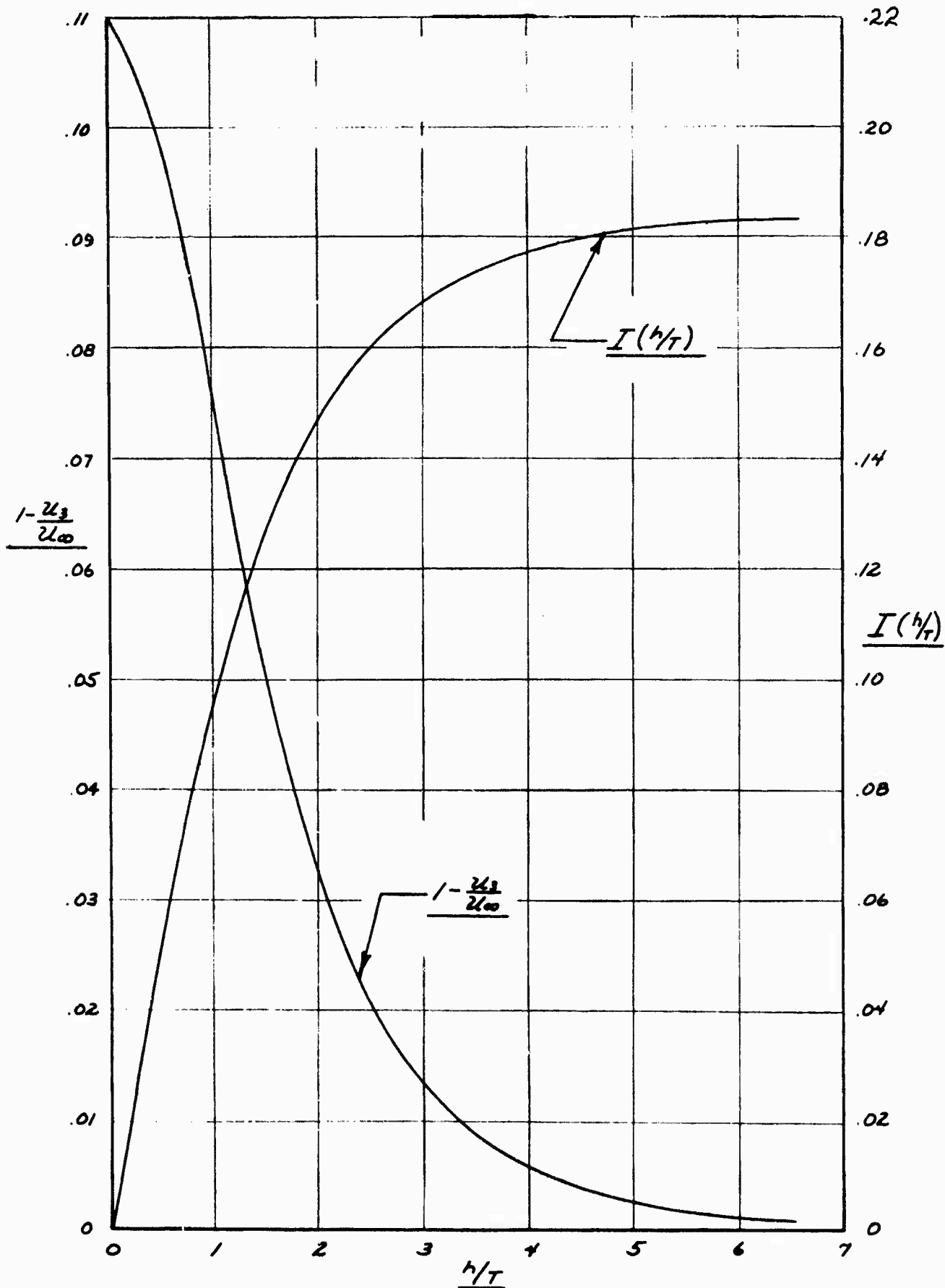


FIGURE 23

VELOCITY RATIO  $1 - \frac{u_3}{u_\infty}$  AND MOMENTUM LOSS FUNCTION  $I(\frac{h}{\tau})$  vs  $\frac{h}{\tau}$

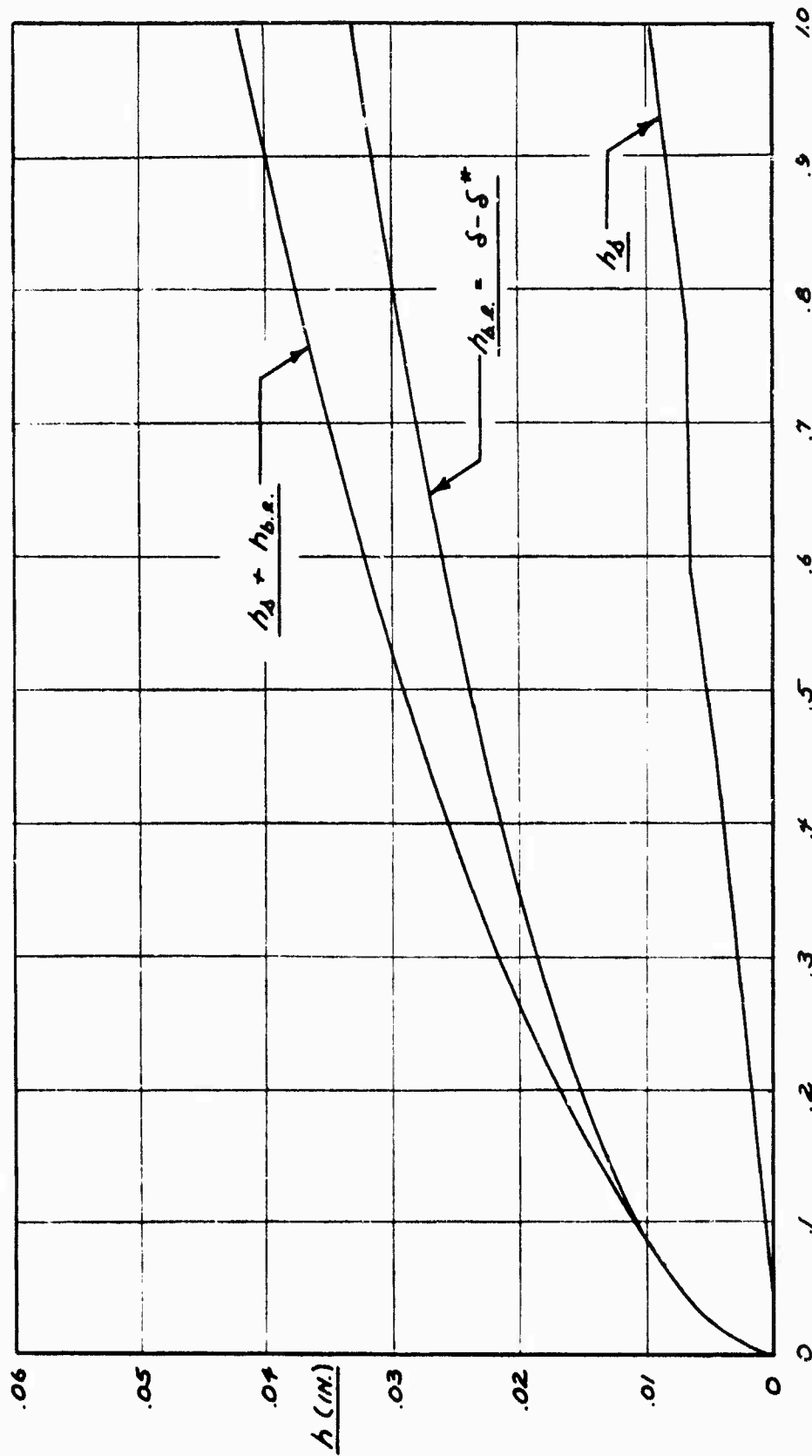


FIGURE 24

CHORDWISE "SUCTION HEIGHT"  $h_s(x)$  AND BOUNDARY LAYER MASS FLOW HEIGHT  $h_{b,l}$   
 vs  $x/c$  for  $M_\infty = 3.0$ ,  $C_{w_t} = 2.374 \times 10^{-4}$ ,  $R_c = 25.7 \times 10^6$

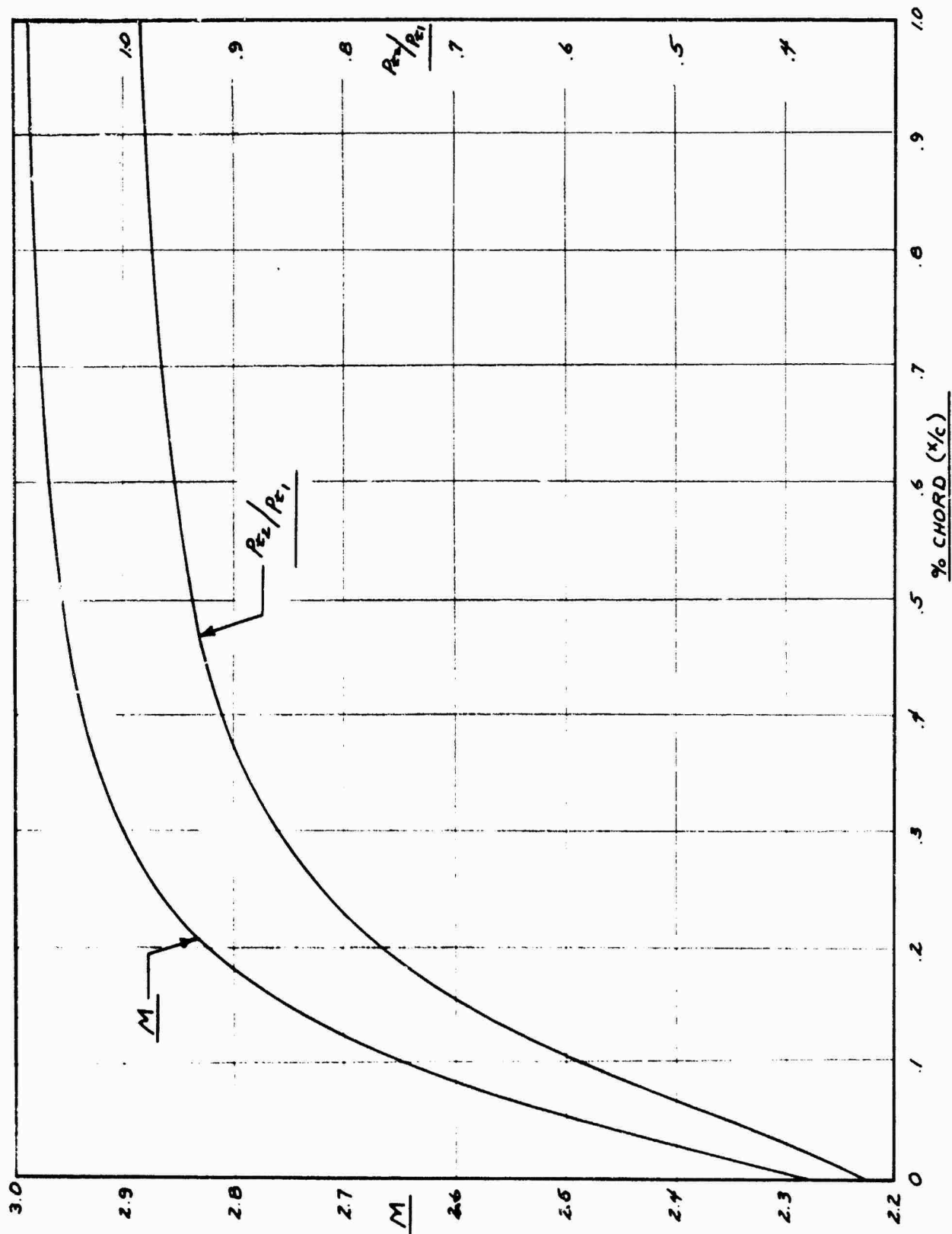


FIGURE 25-1

MACH NUMBER AND TOTAL HEAD DISTRIBUTION AT OUTER EDGE OF BOUNDARY LAYER

FOR  $M_\infty = 3.0$ ,  $C_{Wt} = 2.374 \times 10^{-4}$ ,  $R_c = 25.7 \times 10^6$

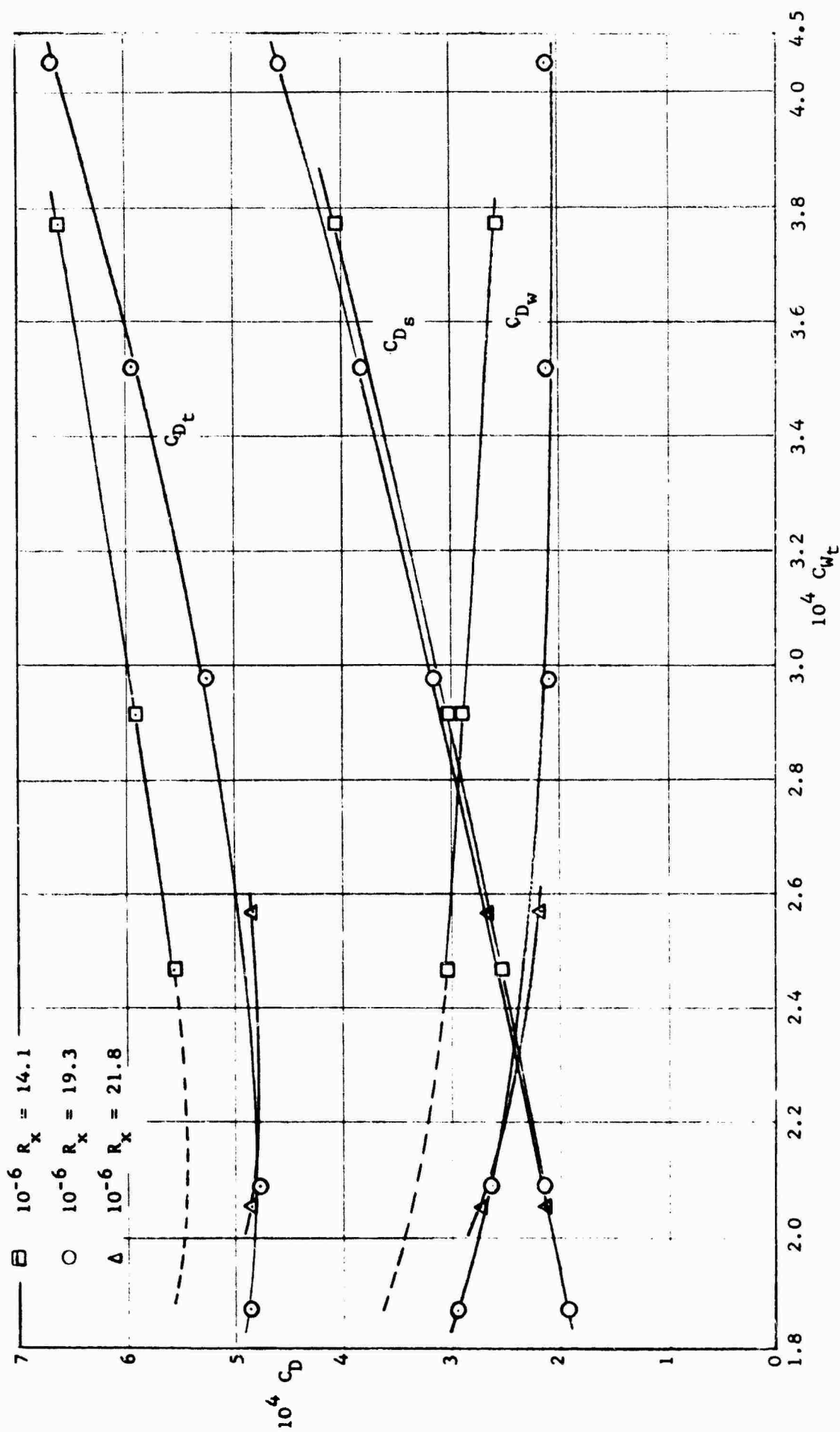


FIGURE 25-2 WAKE, SUCTION AND TOTAL DRAG COEFFICIENTS VS TOTAL SUCTION COEFFICIENT  $M = 2.5$ ,  $X_{rake} = 40.2$  in.

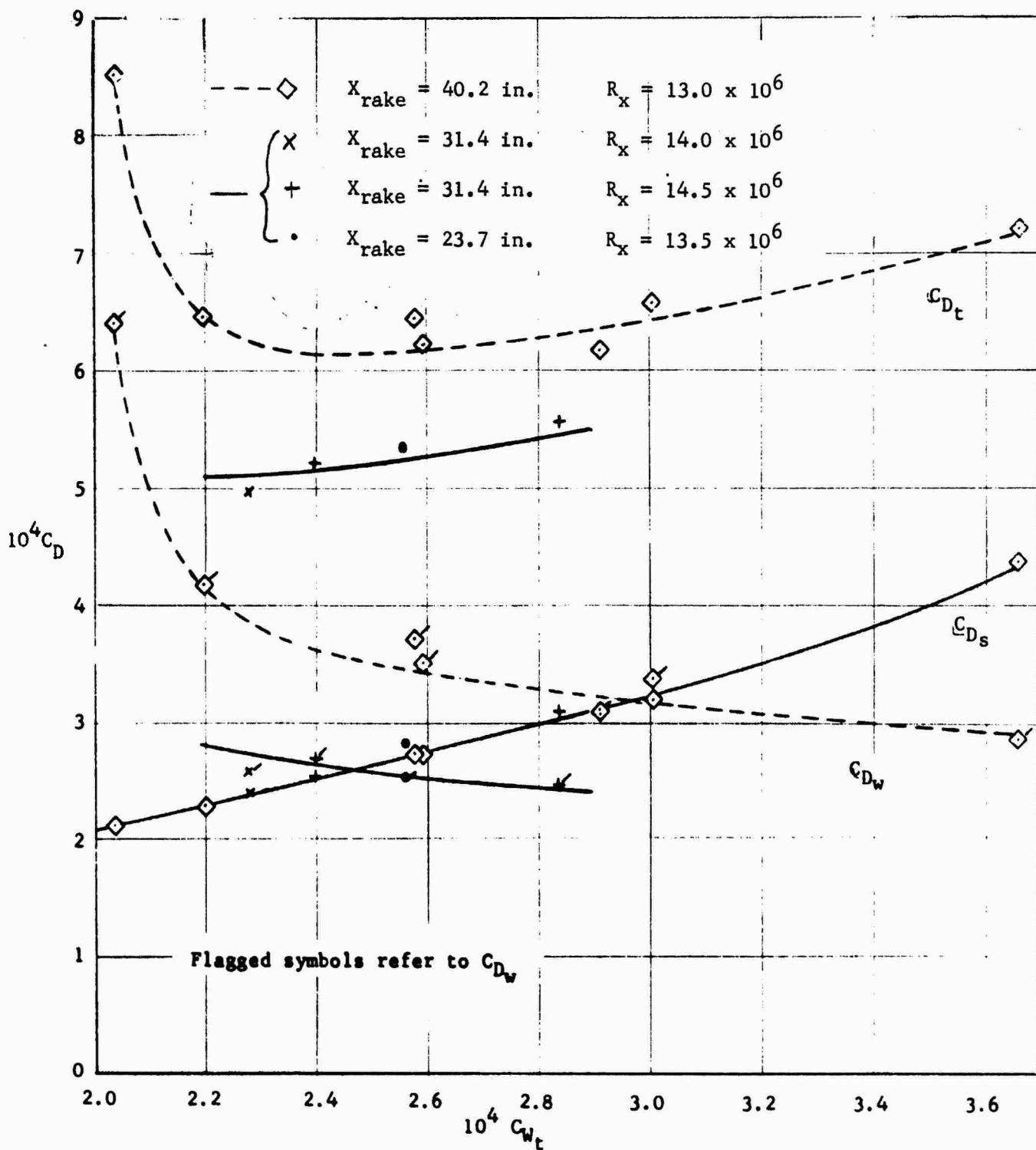


FIGURE 25-3

WAKE, SUCTION, AND TOTAL DRAG COEFFICIENTS  
VS TOTAL SUCTION COEFFICIENT  $M = 3.0$

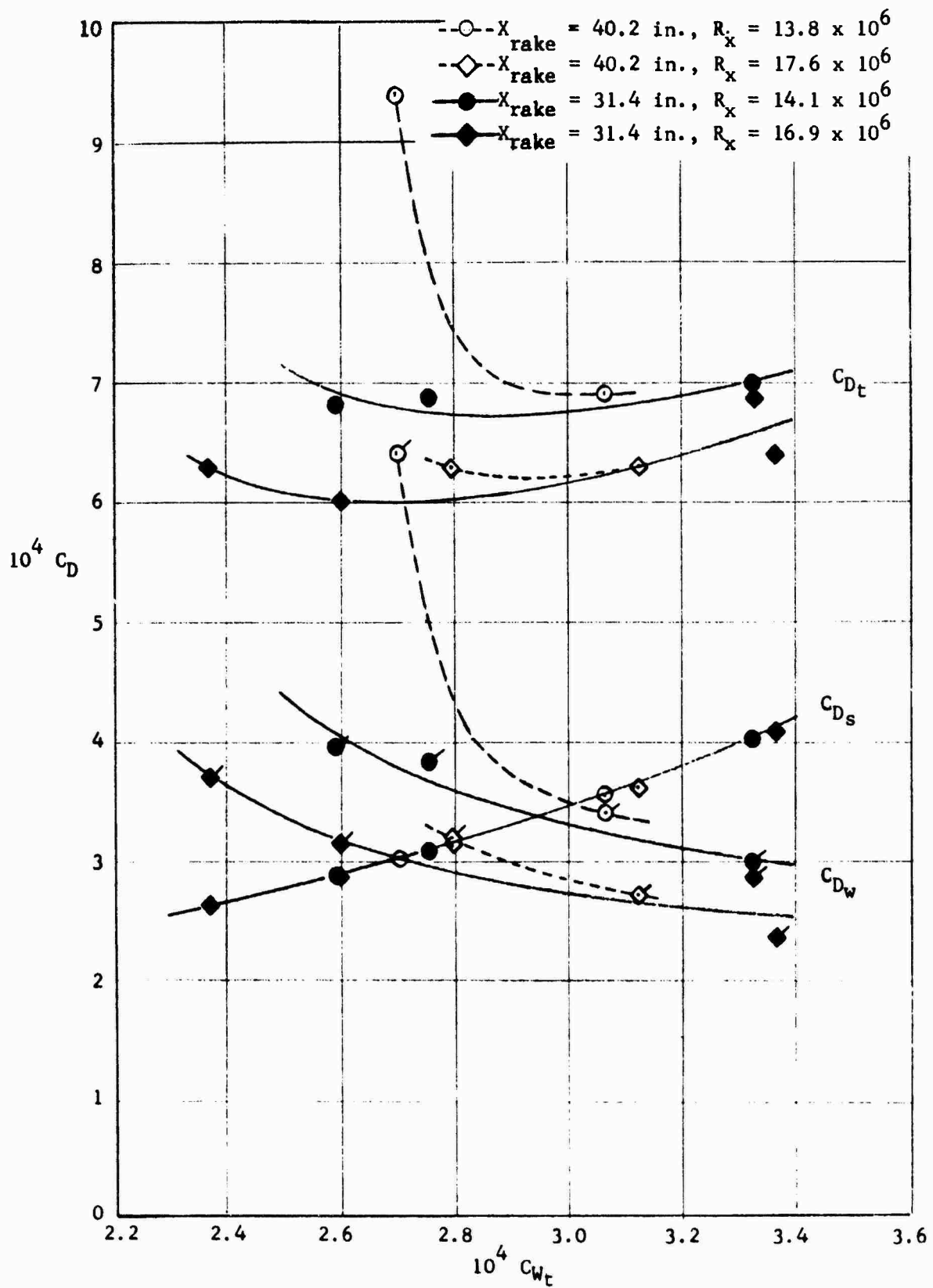


FIGURE 25-4

WAKE, SUCTION, AND TOTAL DRAG COEFFICIENTS  
VS TOTAL SUCTION COEFFICIENT  $M = 3.5$

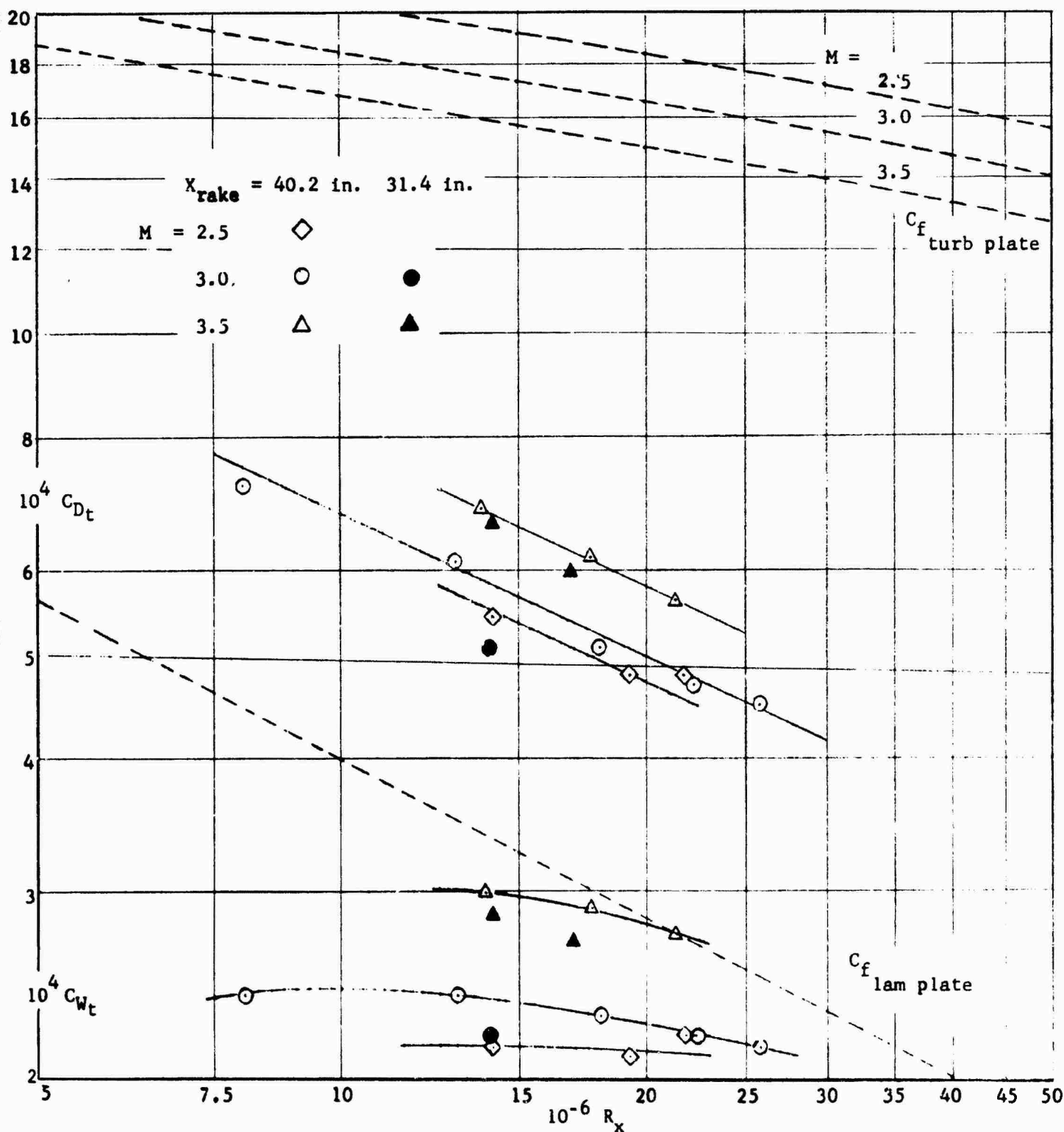


FIGURE 25-5

MINIMUM TOTAL DRAG AND OPTIMUM TOTAL SUCTION  
COEFFICIENTS ON FLAT PLATE SUCTION MODEL

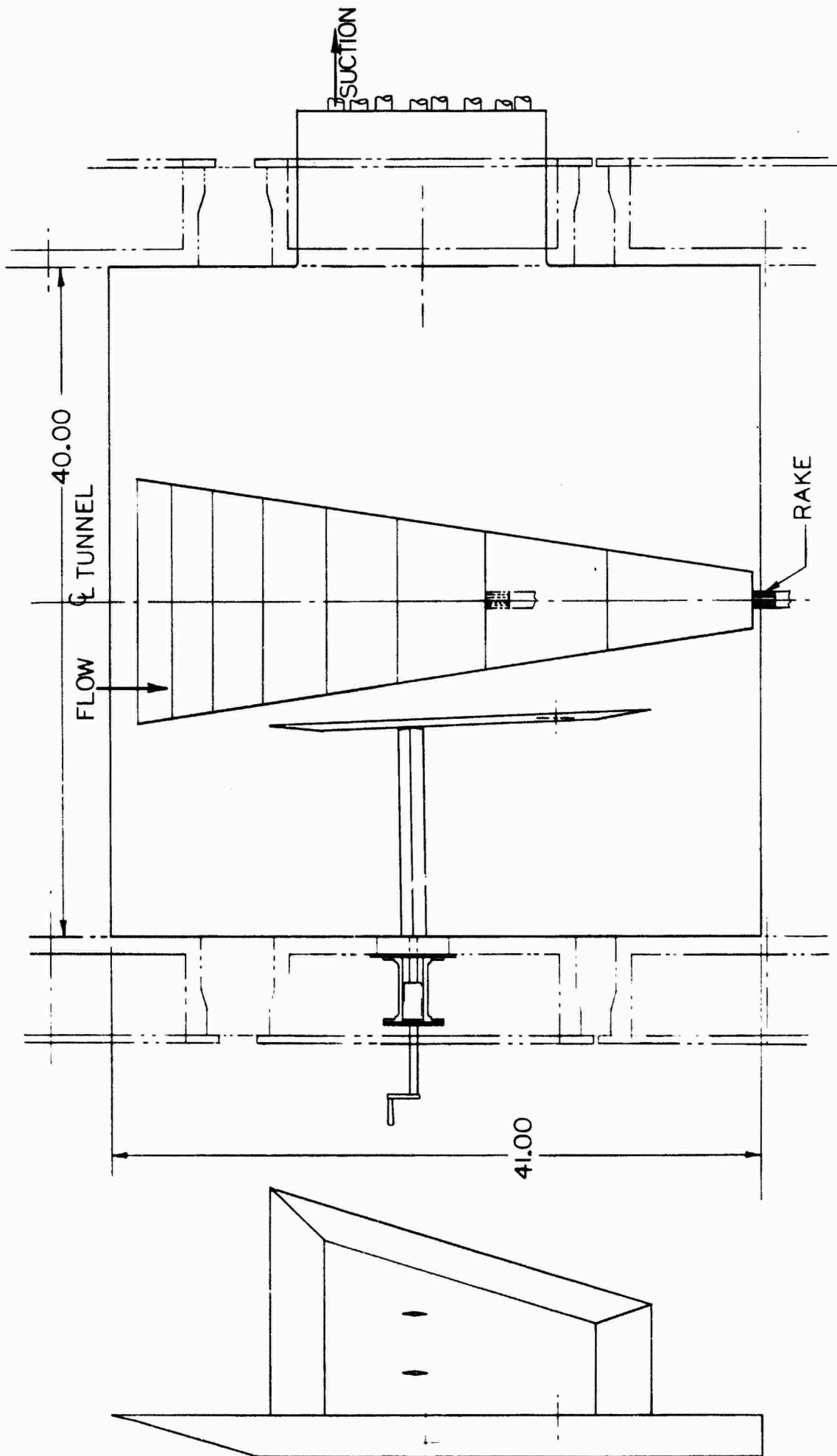


FIGURE 26  
SHOCK GENERATOR MOUNTED ON FLAT PLATE SUCTION MODEL



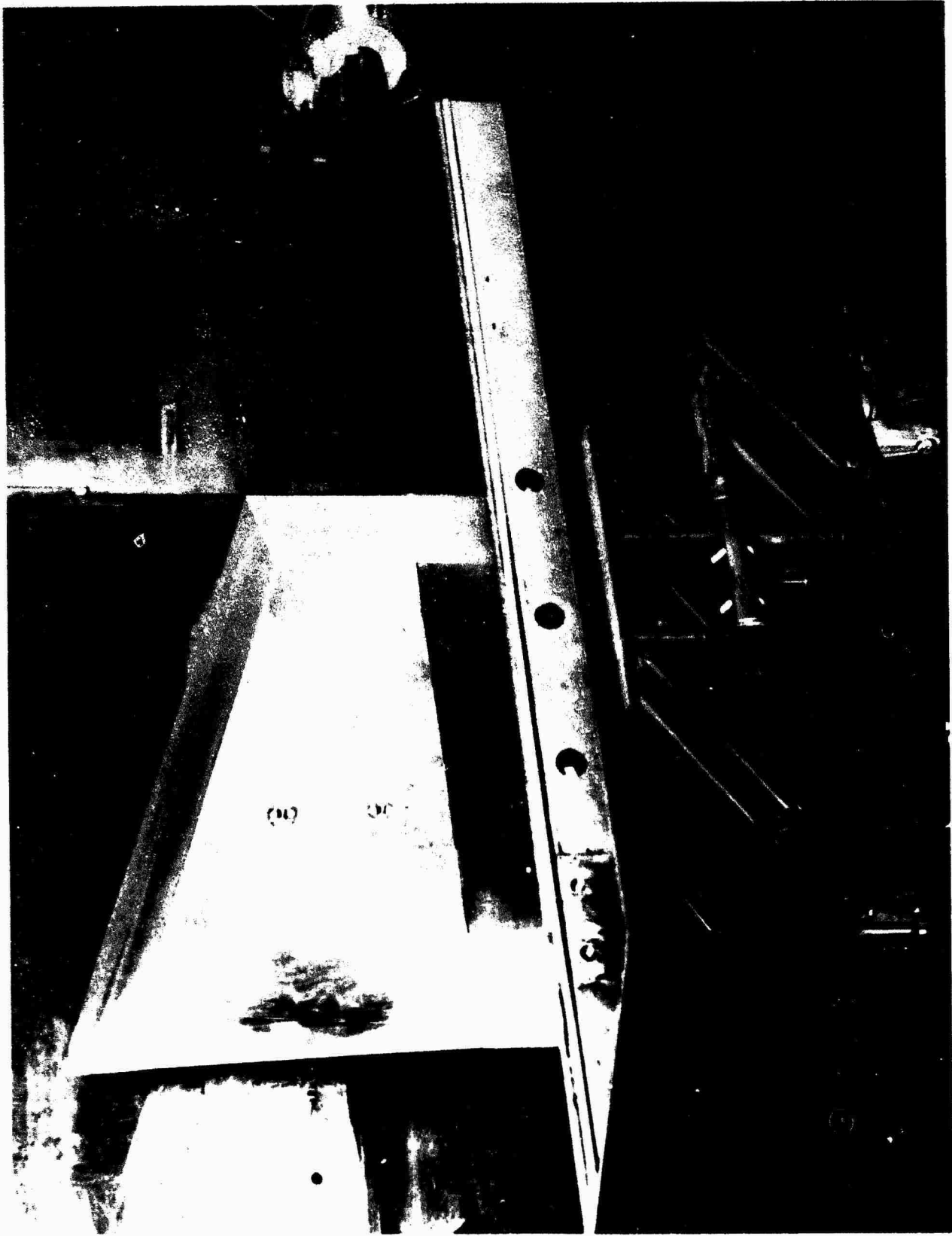


FIGURE 27 INSTALLATION OF THE FLAT PLATE SUCTION MODEL IN WIND TUNNEL

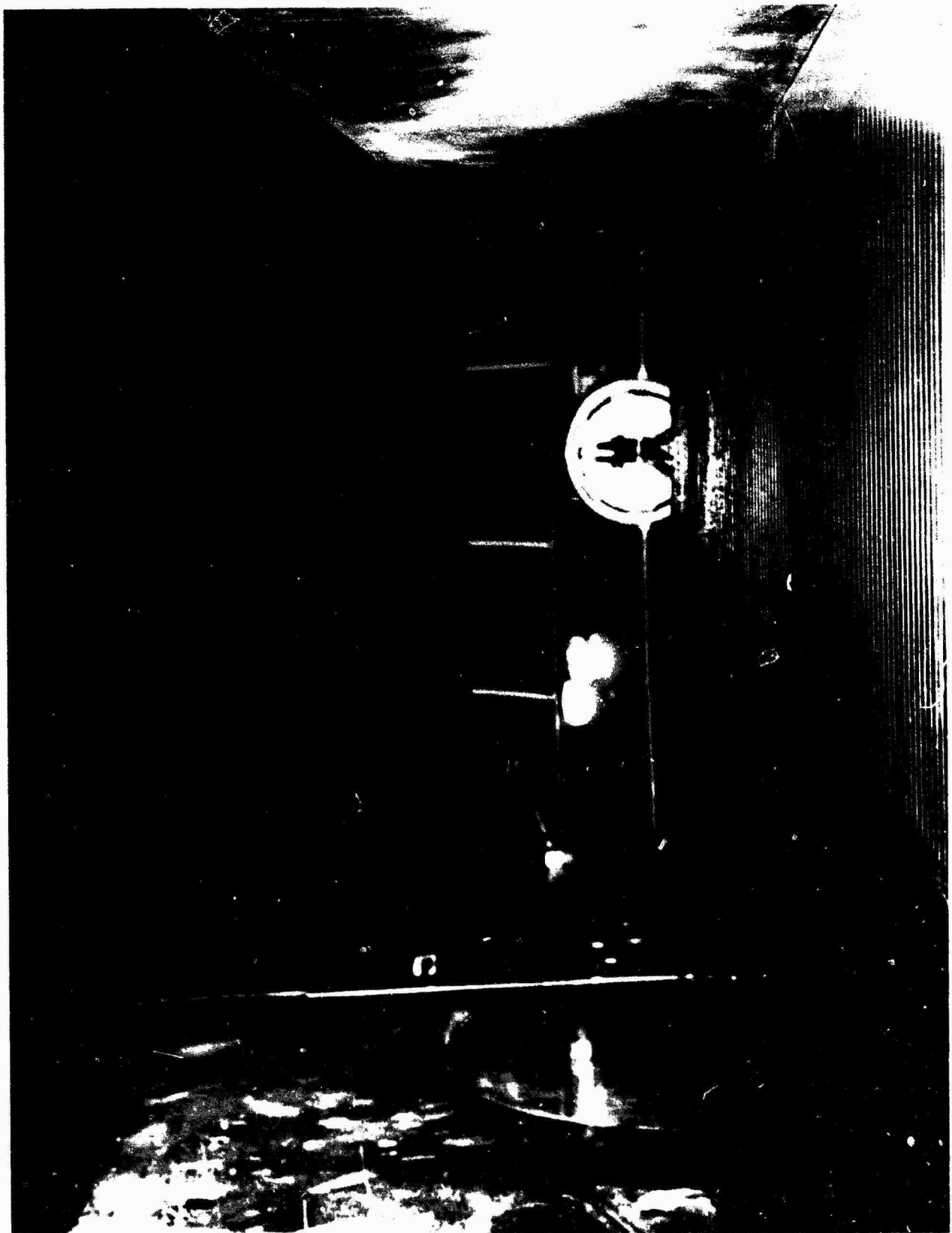


FIGURE 28 INSTALLATION OF THE FLAT PLATE SUCTION MODEL IN WIND TUNNEL

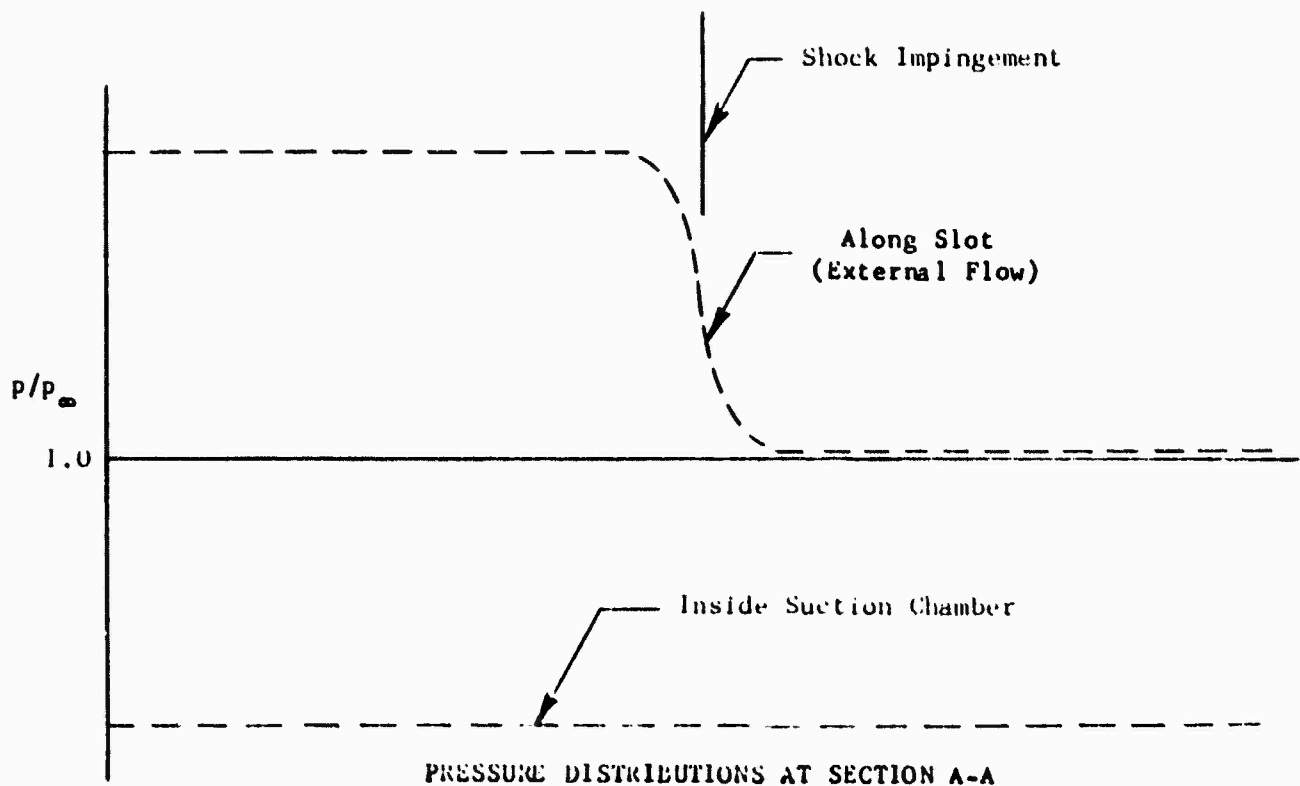
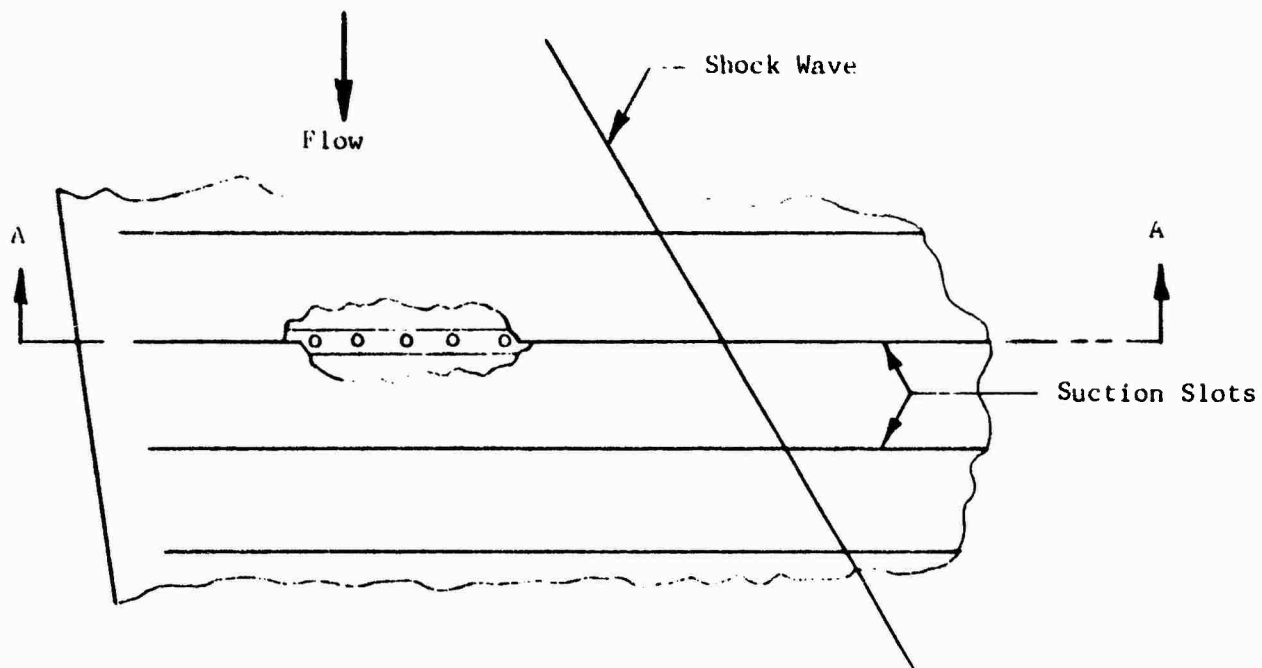


FIGURE 29

INFLUENCE OF SHOCK WAVE ON PRESSURE FIELD IN SLOTTED AREA

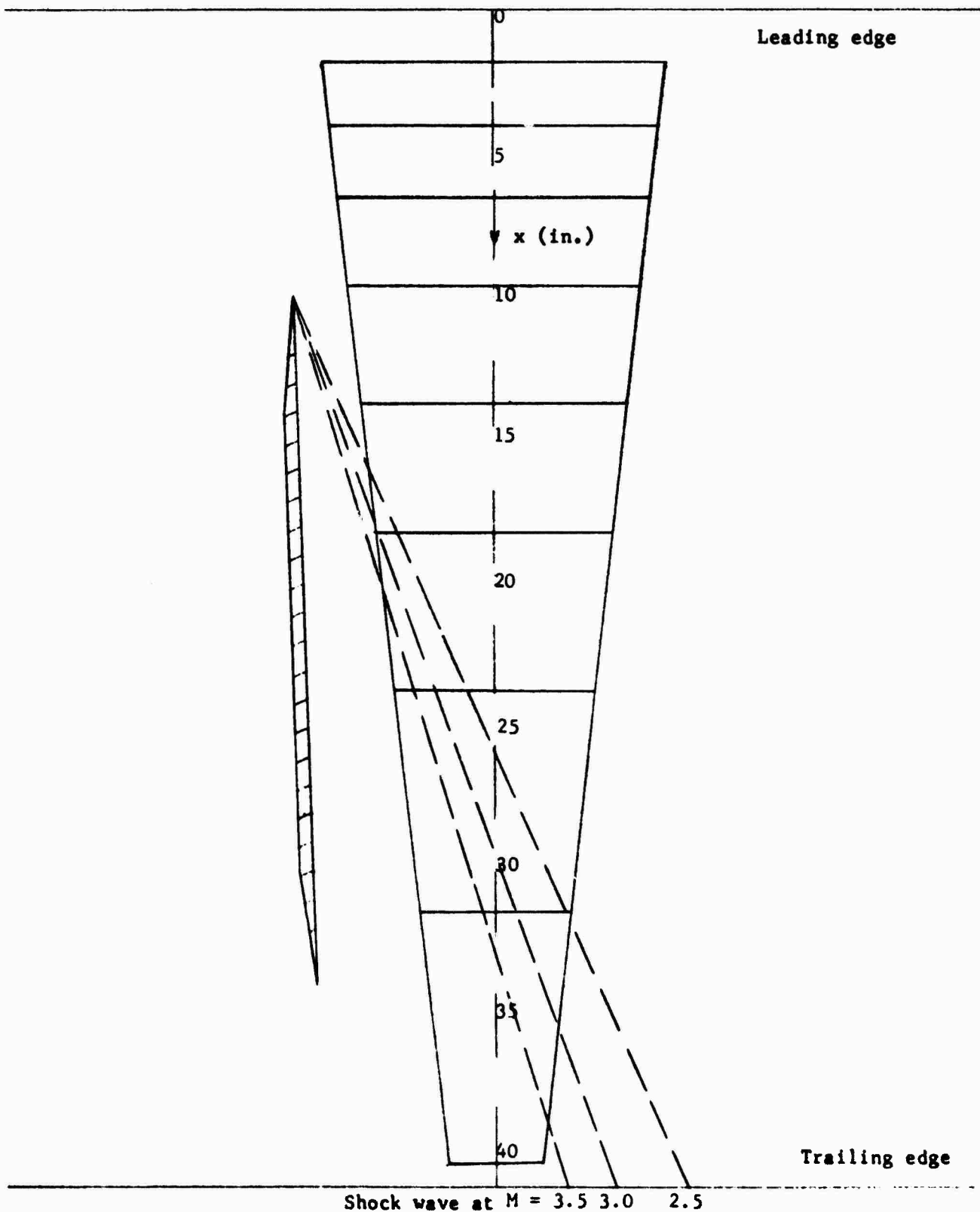


FIGURE 30

LOCATION OF SUCTION CHAMBERS AND SHOCK WAVES FOR  
SHOCK GENERATOR MOUNTED OUTSIDE SUCTION AREA

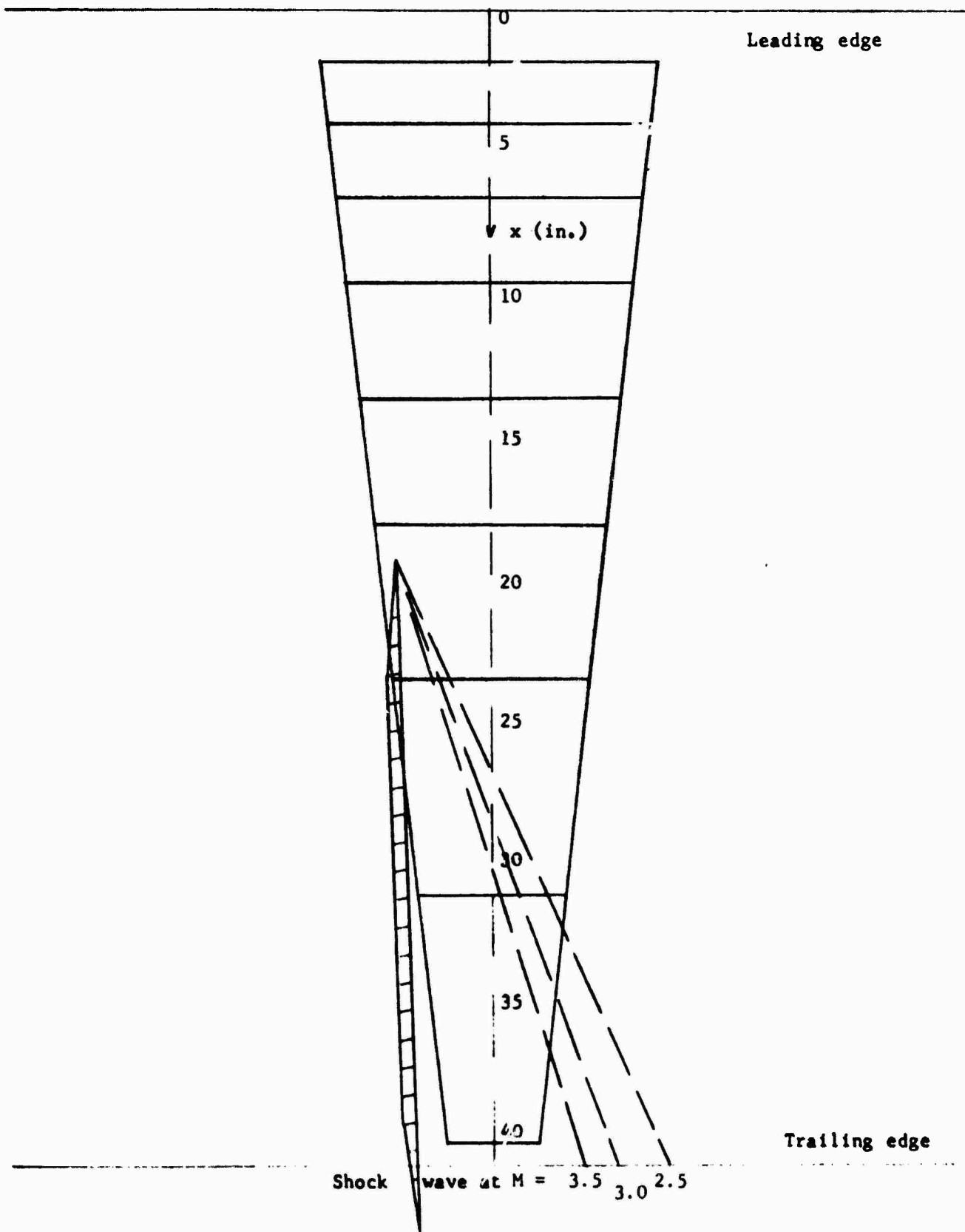


FIGURE 31

LOCATION OF SUCTION CHAMBERS AND SHOCK WAVES FOR SHOCK GENERATOR  
MOUNTED INSIDE SUCTION AREA

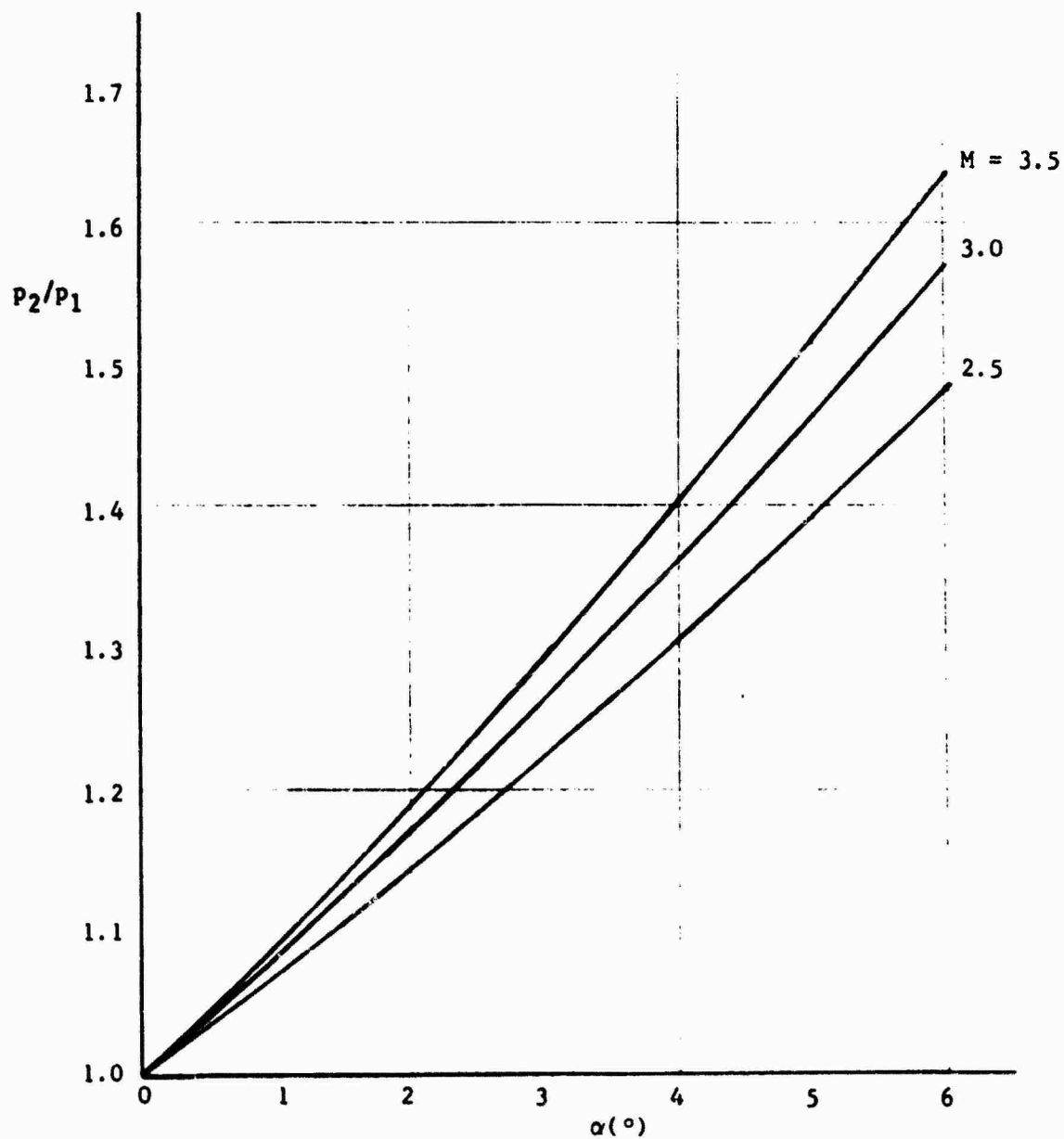


FIGURE 32

THEORETICAL PRESSURE RISE  $\frac{P_2}{P_1}$  VS SHOCK GENERATOR ANGLE  $\alpha$

○ Adjustable shock generator mounted outside suction area

△ Fixed shock generator mounted inside suction area

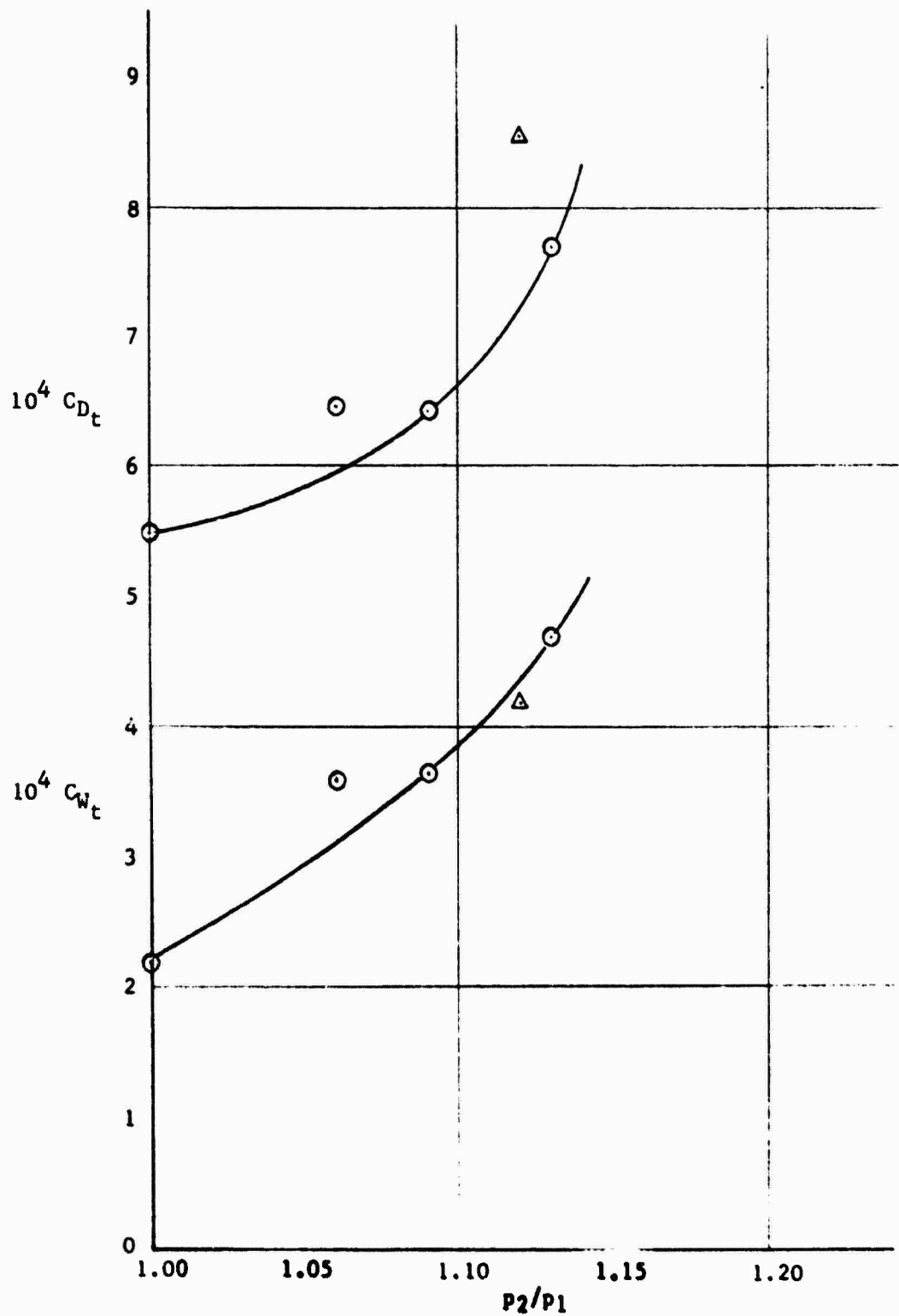


FIGURE 33

TOTAL DRAG AND SUCTION COEFFICIENTS VS SHOCK INTENSITY

$M = 2.5$        $R_x = 14.2 \times 10^6$       ( $x_{rake} = 40.2$  in.)

○ Adjustable shock generator mounted outside suction area

△ Fixed shock generator mounted inside suction area

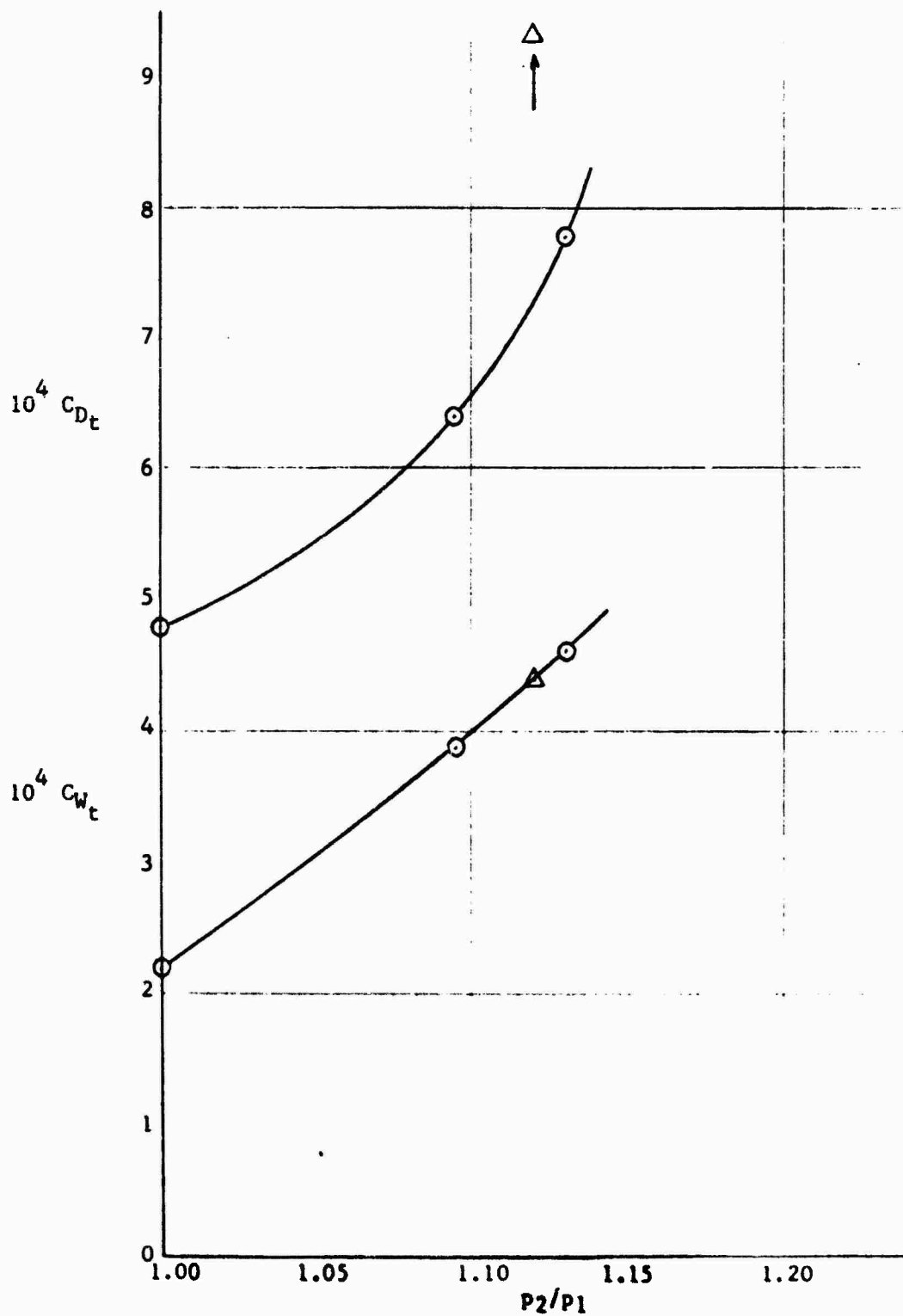


FIGURE 34

TOTAL DRAG AND SUCTION COEFFICIENTS VS SHOCK INTENSITY

$M = 2.5$        $R_x = 19.9 \times 10^6$       ( $x_{rake} = 40.2$  in.)



○ Adjustable shock generator mounted outside suction area

△ Fixed shock generator mounted inside suction area

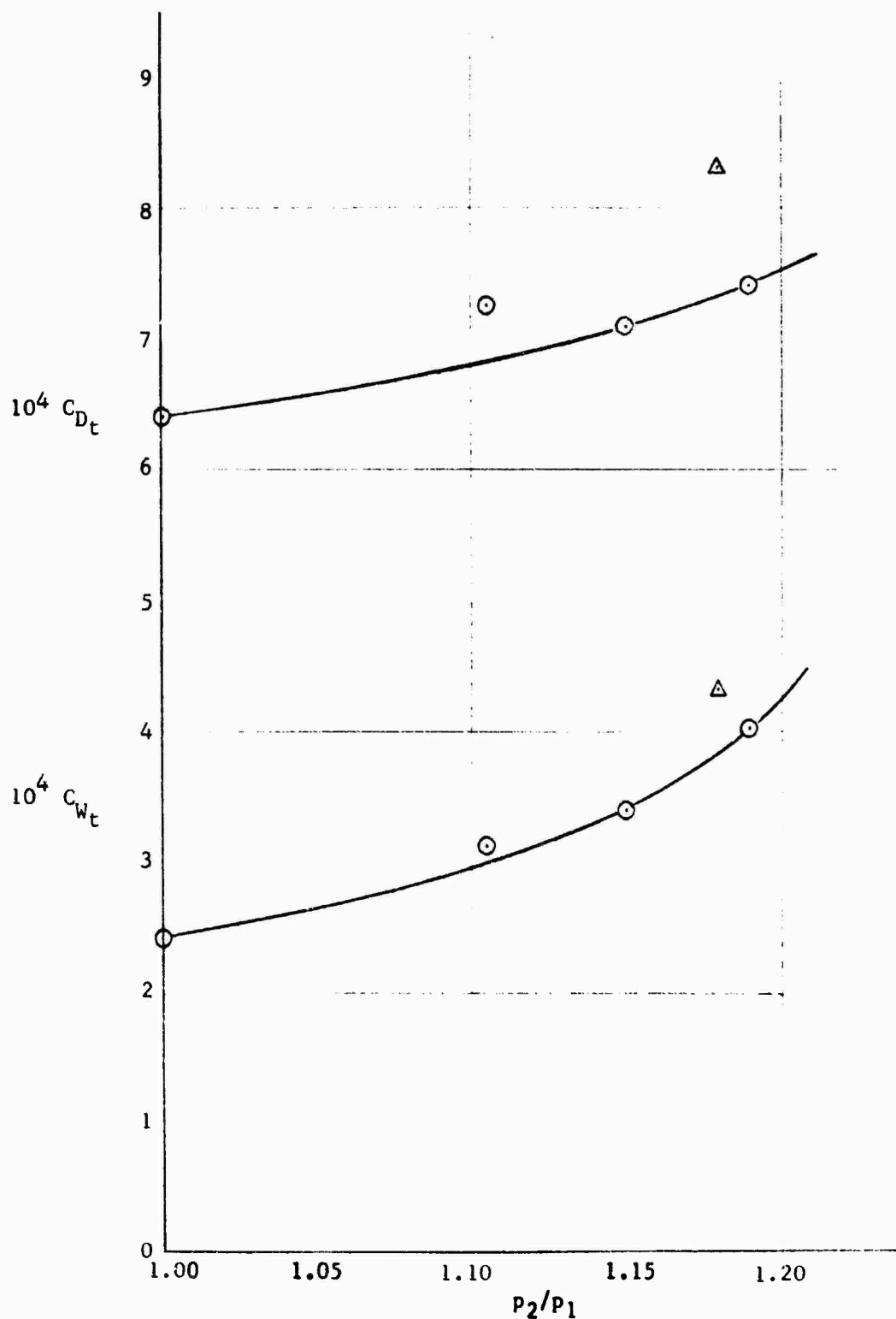


FIGURE 35

TOTAL DRAG AND SUCTION COEFFICIENTS VS SHOCK INTENSITY

$M = 3.0$

$R_x = 11.0 \times 10^6$

( $x_{rake} = 40.2$  in.)

○ Adjustable shock generator mounted outside suction area

△ Fixed shock generator mounted inside suction area

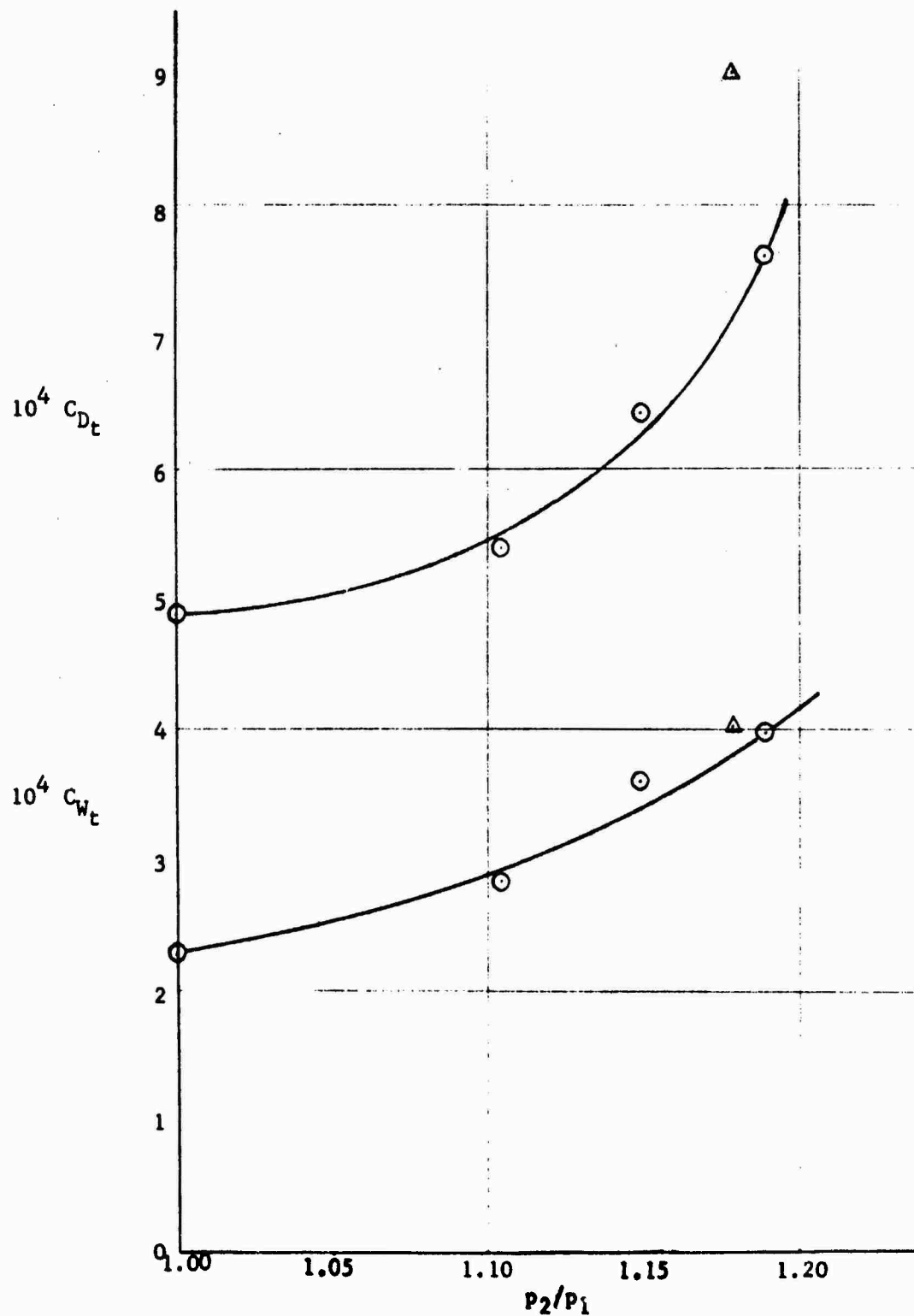


FIGURE 36

TOTAL DRAG AND SUCTION COEFFICIENTS VS SHOCK INTENSITY

$M = 3.0$

$R_x = 19.0 \times 10^6$

( $x_{rake} = 40.2$  in.)

○ Adjustable shock generator mounted    △ outside suction area

△ Fixed shock generator mounted inside suction area

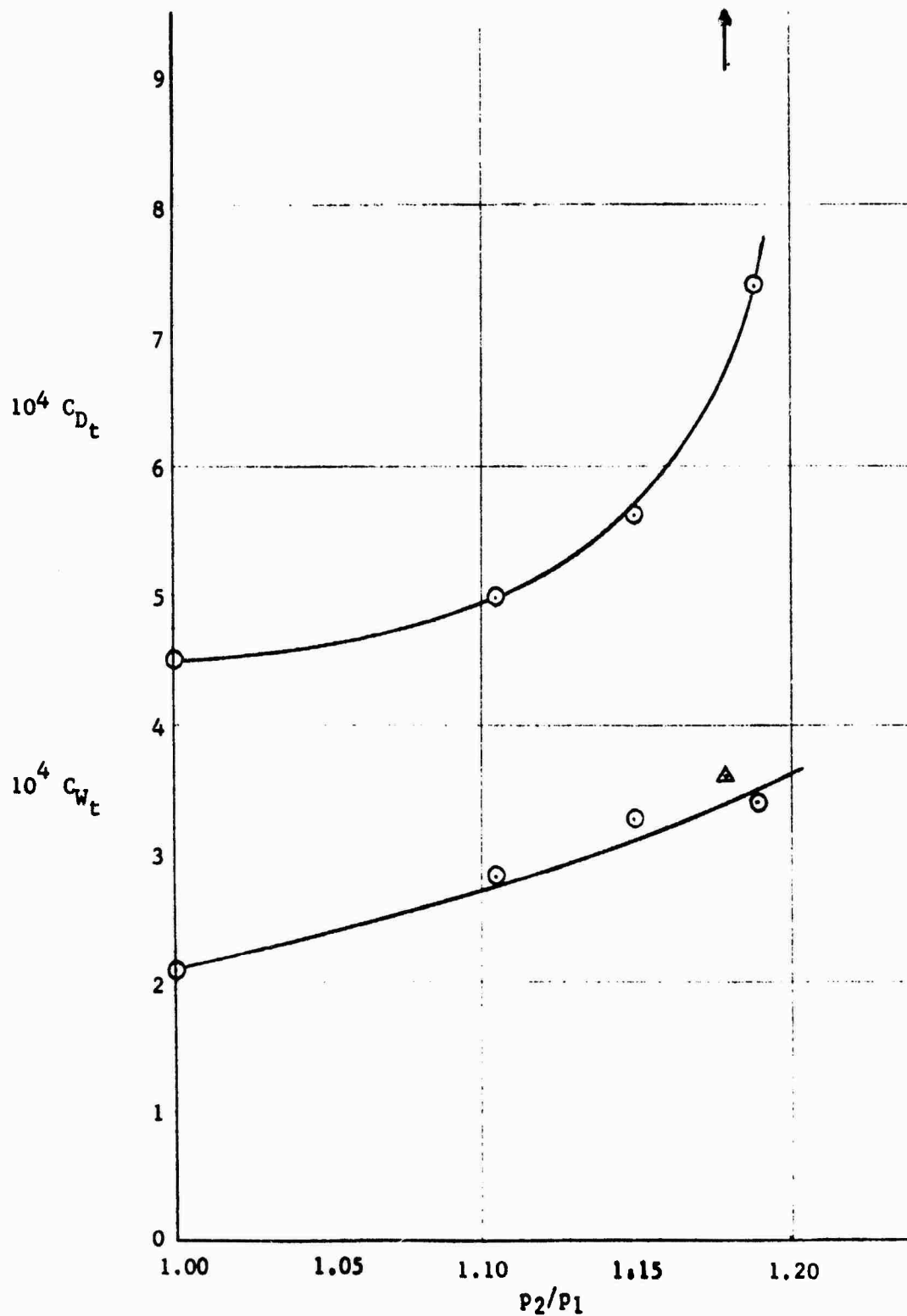


FIGURE 37

TOTAL DRAG AND SUCTION COEFFICIENTS VS SHOCK INTENSITY

$M = 3.0$

$R_x = 26.4 \times 10^6$

( $x_{rake} = 40.2$  in.)

○ Adjustable shock generator mounted outside suction area

△ Fixed shock generator mounted inside suction area

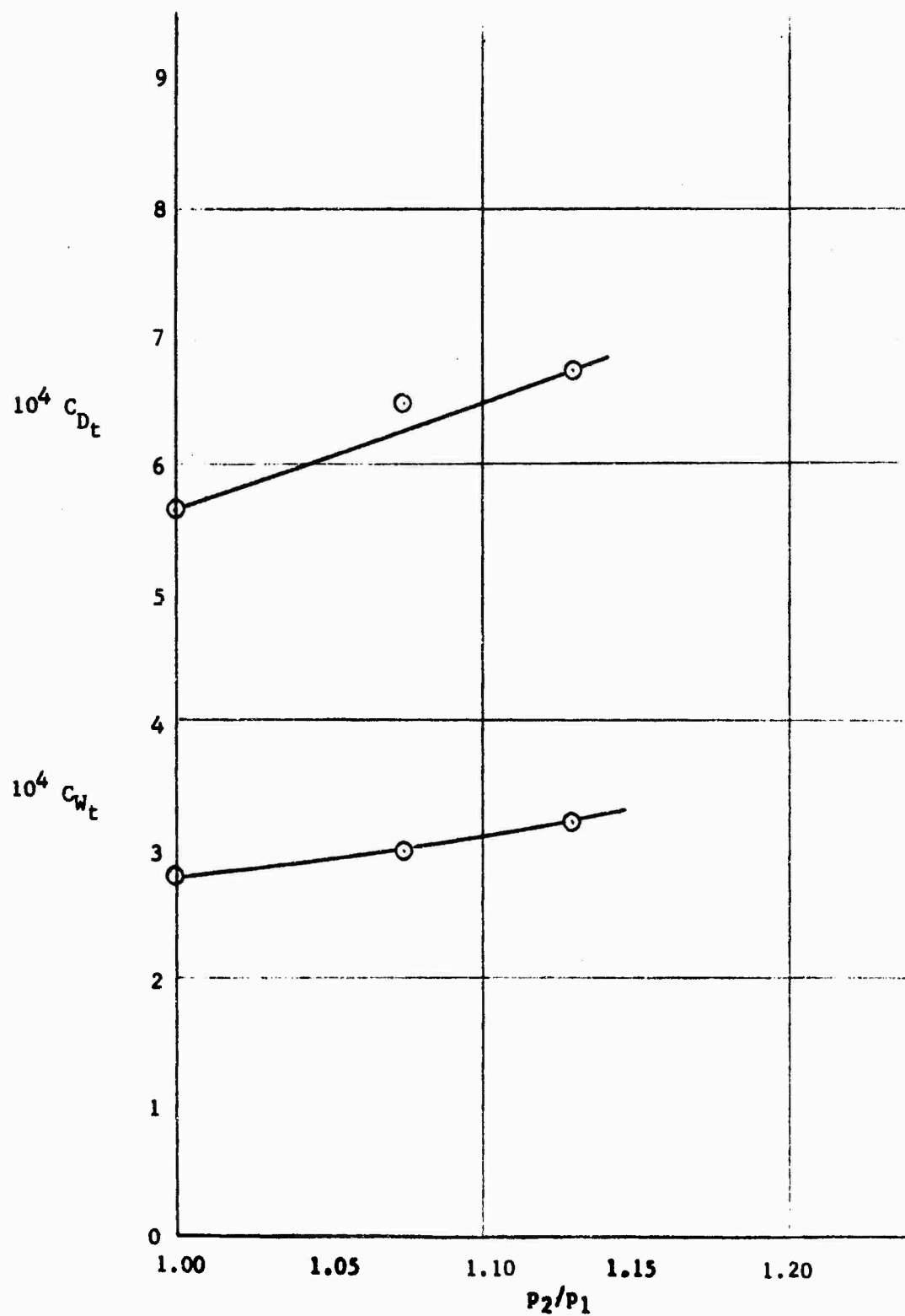


FIGURE 38

TOTAL DRAG AND SUCTION COEFFICIENTS VS SHOCK INTENSITY

$M = 3.5$        $R_x = 21.6 \times 10^6$       ( $x_{rake} = 40.2$  in.)

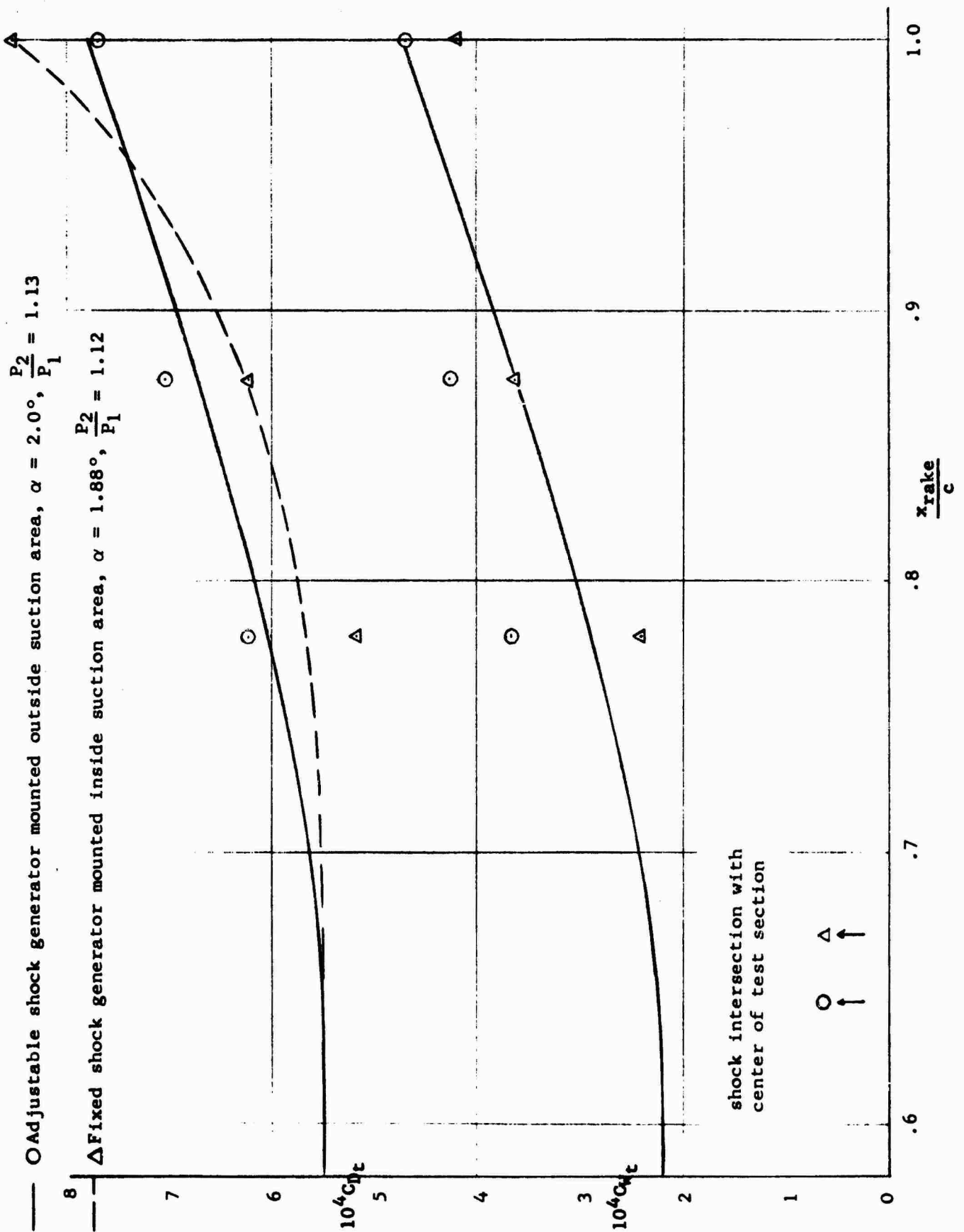


FIGURE 39

TOTAL DRAG AND SUCTION COEFFICIENTS VS CHORDWISE DISTANCE,  $x_{rake}$

$M = 2.5$

$R_c = 14.4 \times 10^6$

( $c = 40.2$  in.)

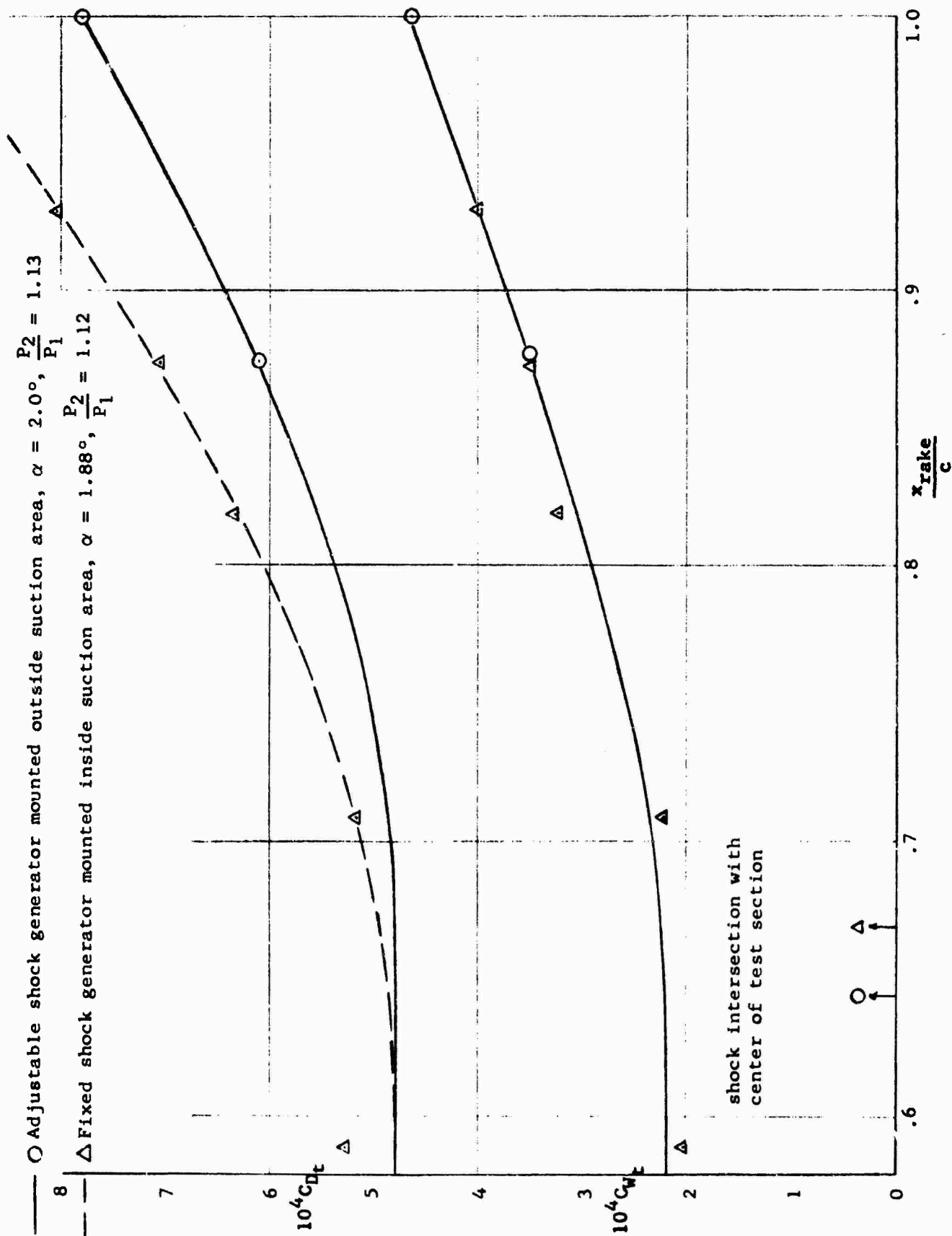


FIGURE 40

TOTAL DRAG AND SUCTION COEFFICIENTS VS CHORDWISE DISTANCE,  $x_{rake}$

$M = 2.5$

$R_c = 19.9 \times 10^6$

( $c = 40.2$  in.)

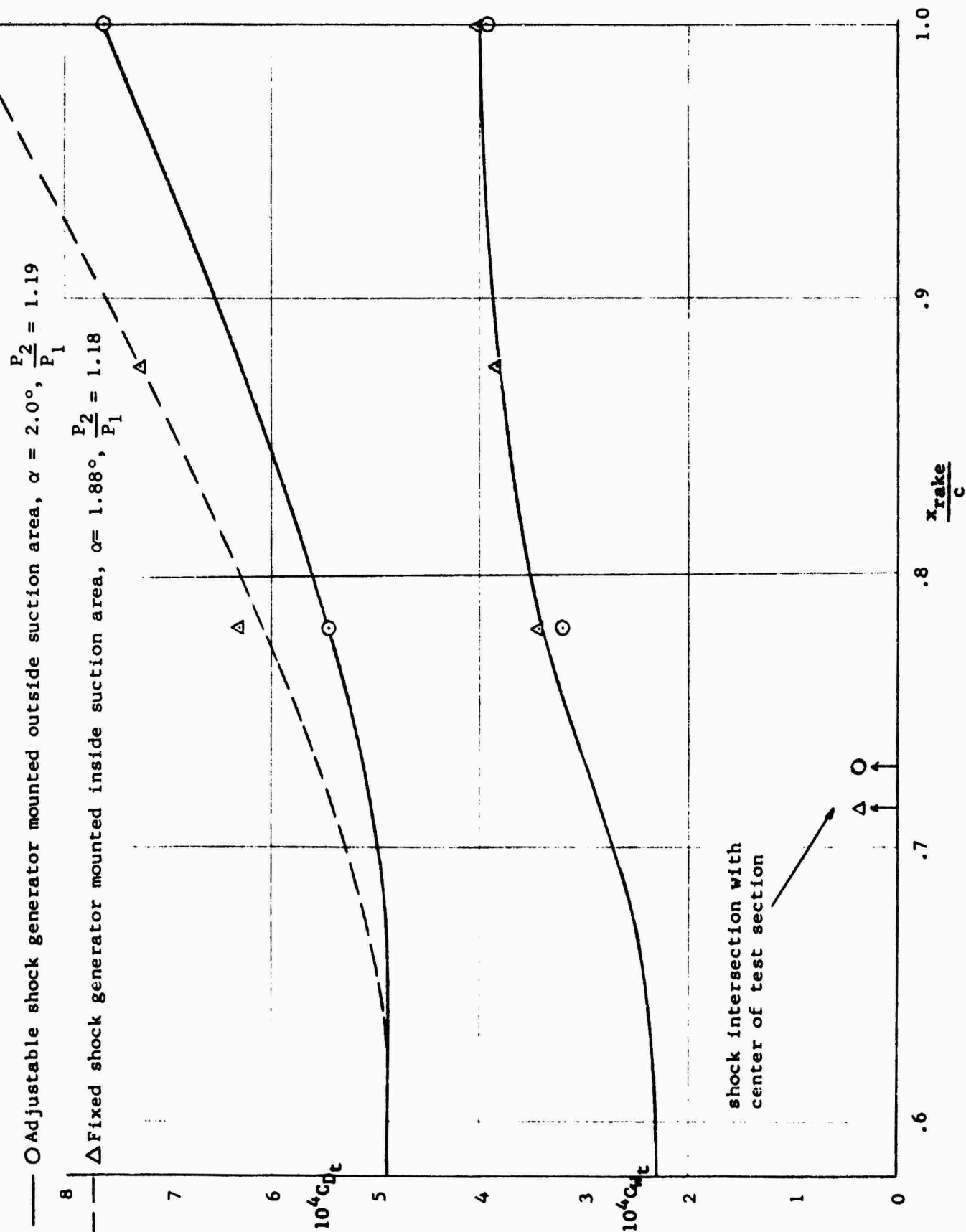


FIGURE 41

TOTAL DRAG AND SUCTION COEFFICIENTS VS CHORDWISE DISTANCE,  $x_{\text{rake}}$   
 $M = 3.0$   $R_c = 19.0 \times 10^6$  ( $c = 40.2$  in.)

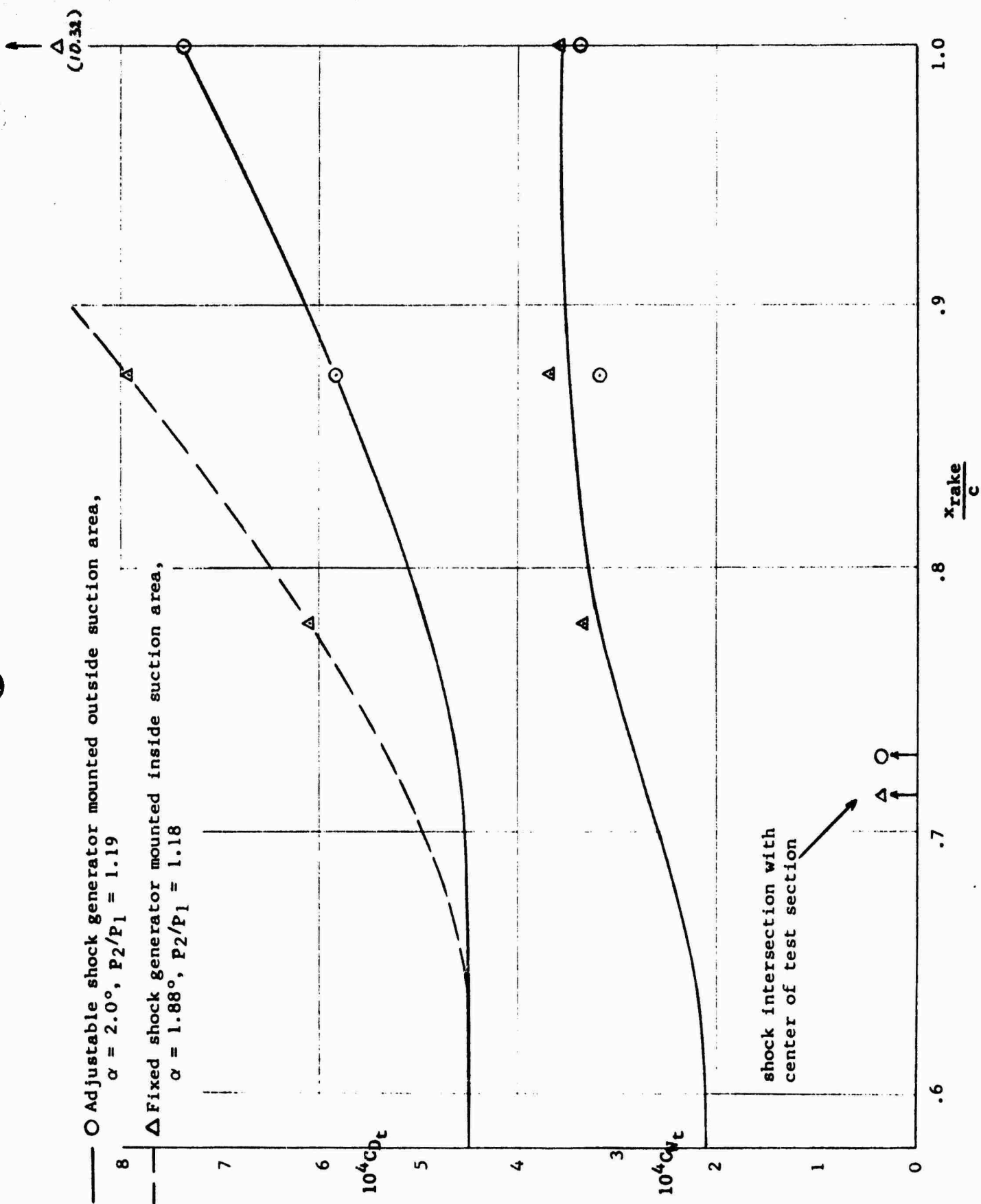


FIGURE 42

TOTAL DRAG AND SUCTION COEFFICIENTS VS CHORDWISE DISTANCE,  $x_{\text{rake}}$

$M = 3.0$

$R_c = 26.4 \times 10^6$

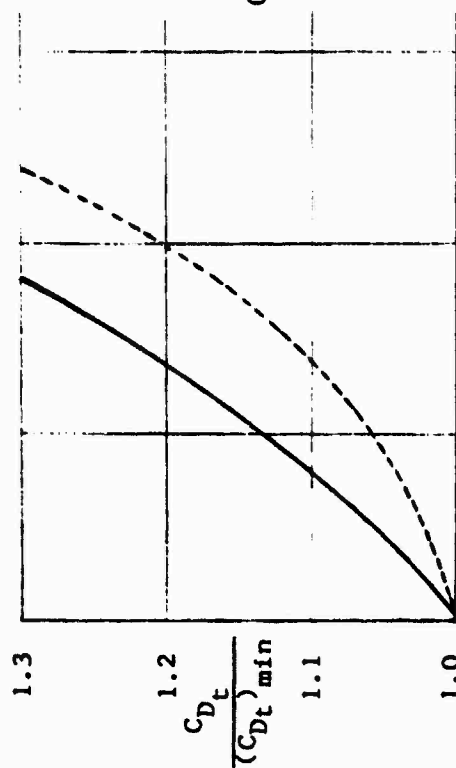
( $c = 40.2$  in.)



M = 2.5

---  $R_C = 14.2 \times 10^6$

—  $R_C = 19.9 \times 10^6$



M = 3.0

---  $R_C = 11.0 \times 10^6$

—  $R_C = 19.0$  and  $26.4 \times 10^6$

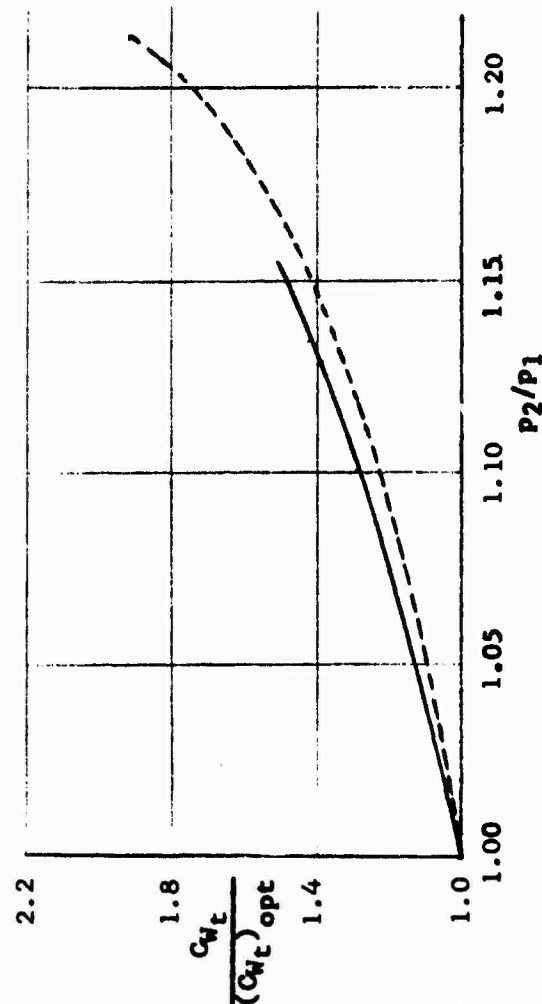
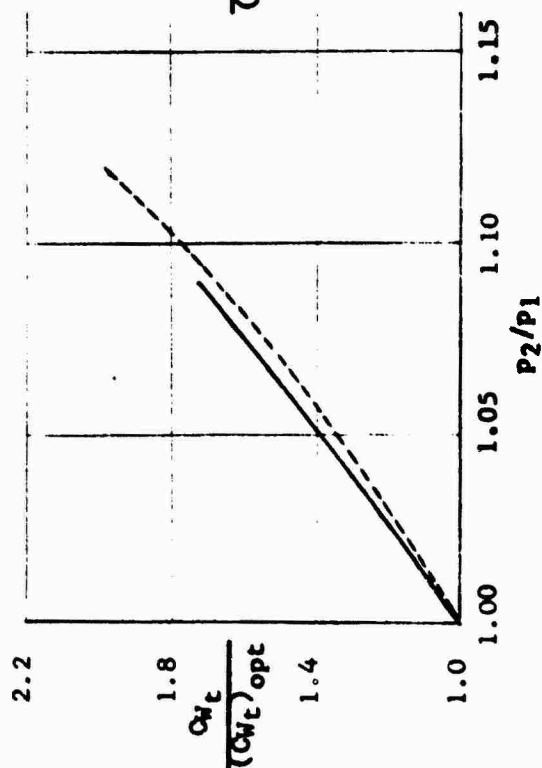
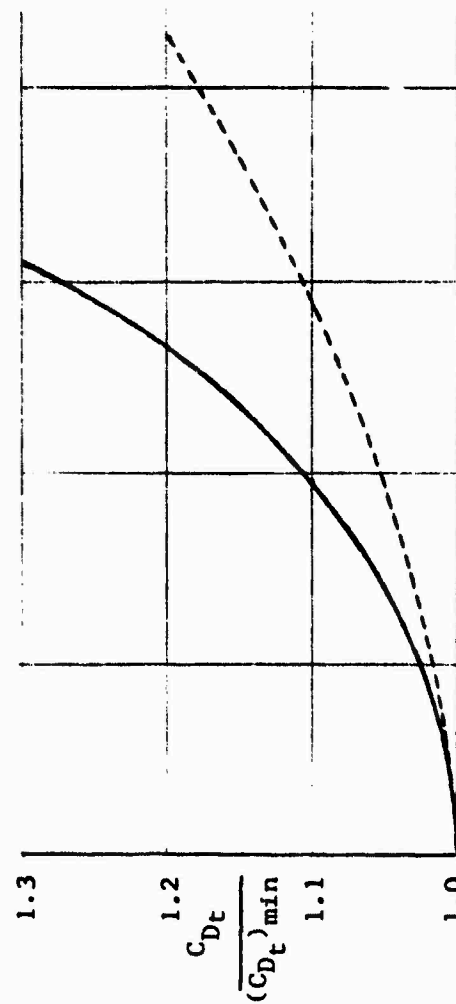


FIGURE 43

INCREASE IN TOTAL DRAG AND SUCTION COEFFICIENTS VS SHOCK INTENSITY

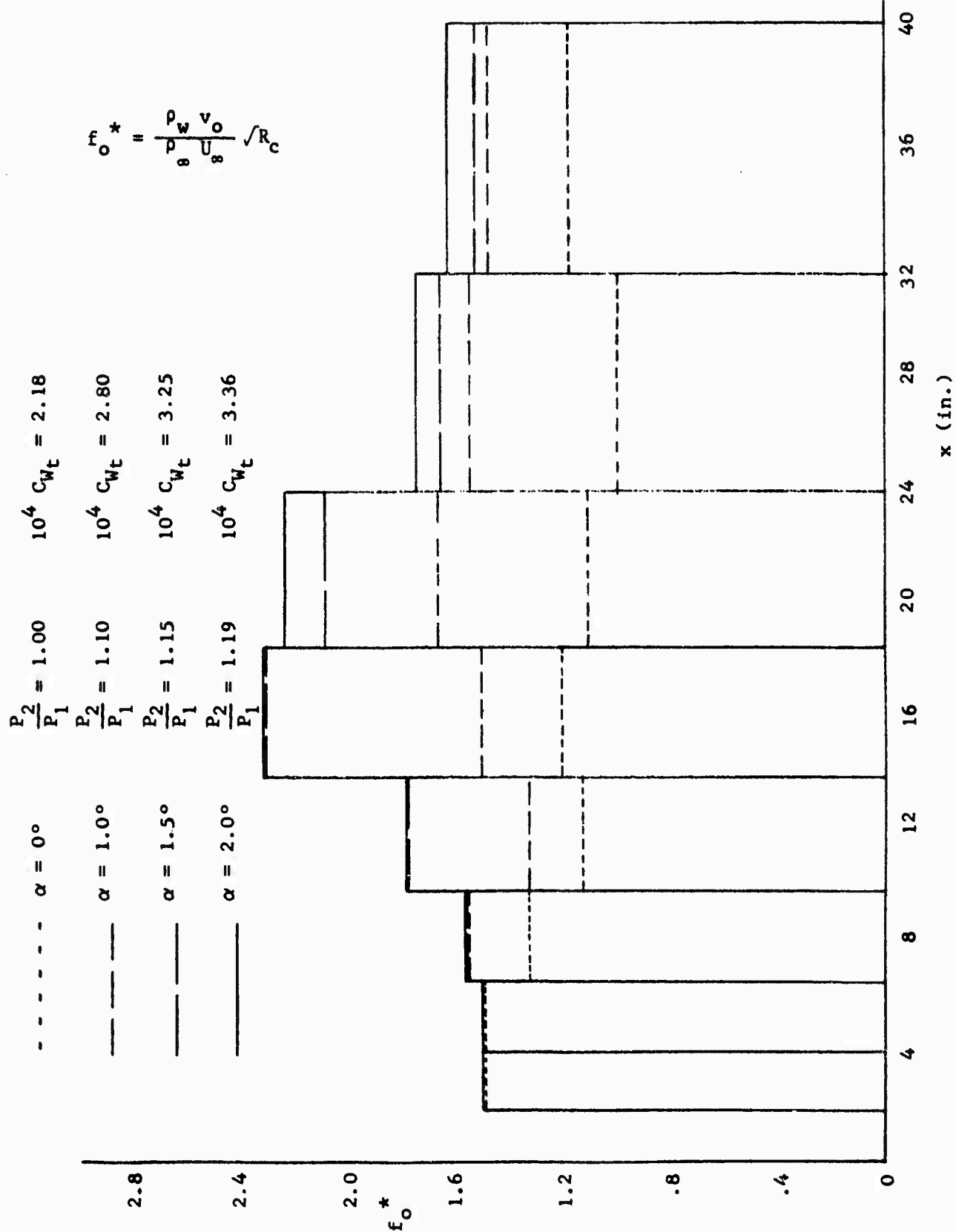


FIGURE 44

SUCTION DISTRIBUTIONS AT DIFFERENT SHOCK INTENSITIES

$M = 3.0$

$R_x = 26.4 \times 10^6$

$x = 40.2 \text{ in.}$

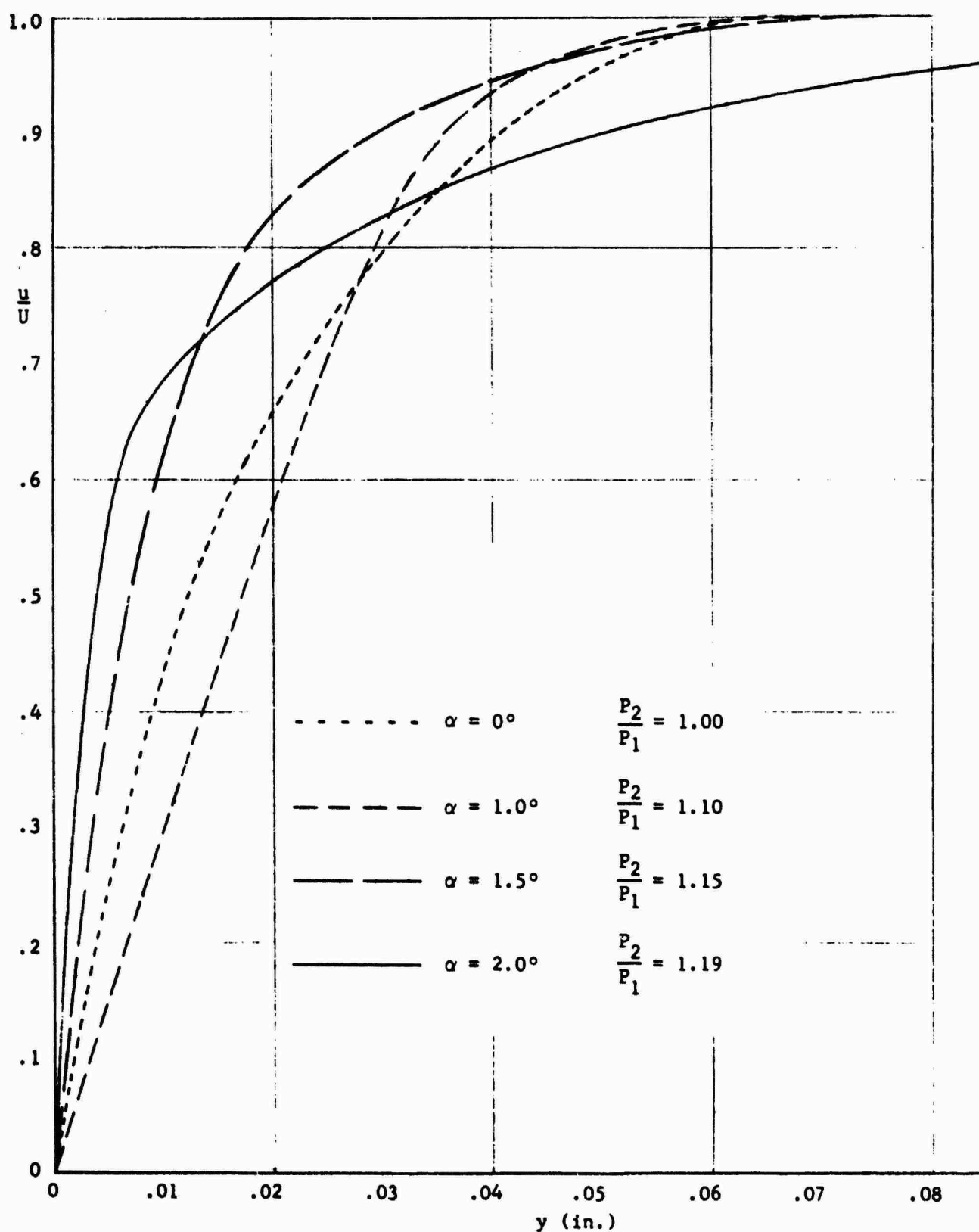


FIGURE 45

BOUNDARY LAYER VELOCITY PROFILES AT DIFFERENT SHOCK INTENSITIES

$M = 3.0$

$R_x = 26.4 \times 10^6$

$x_{rake} = 40.2 \text{ in.}$

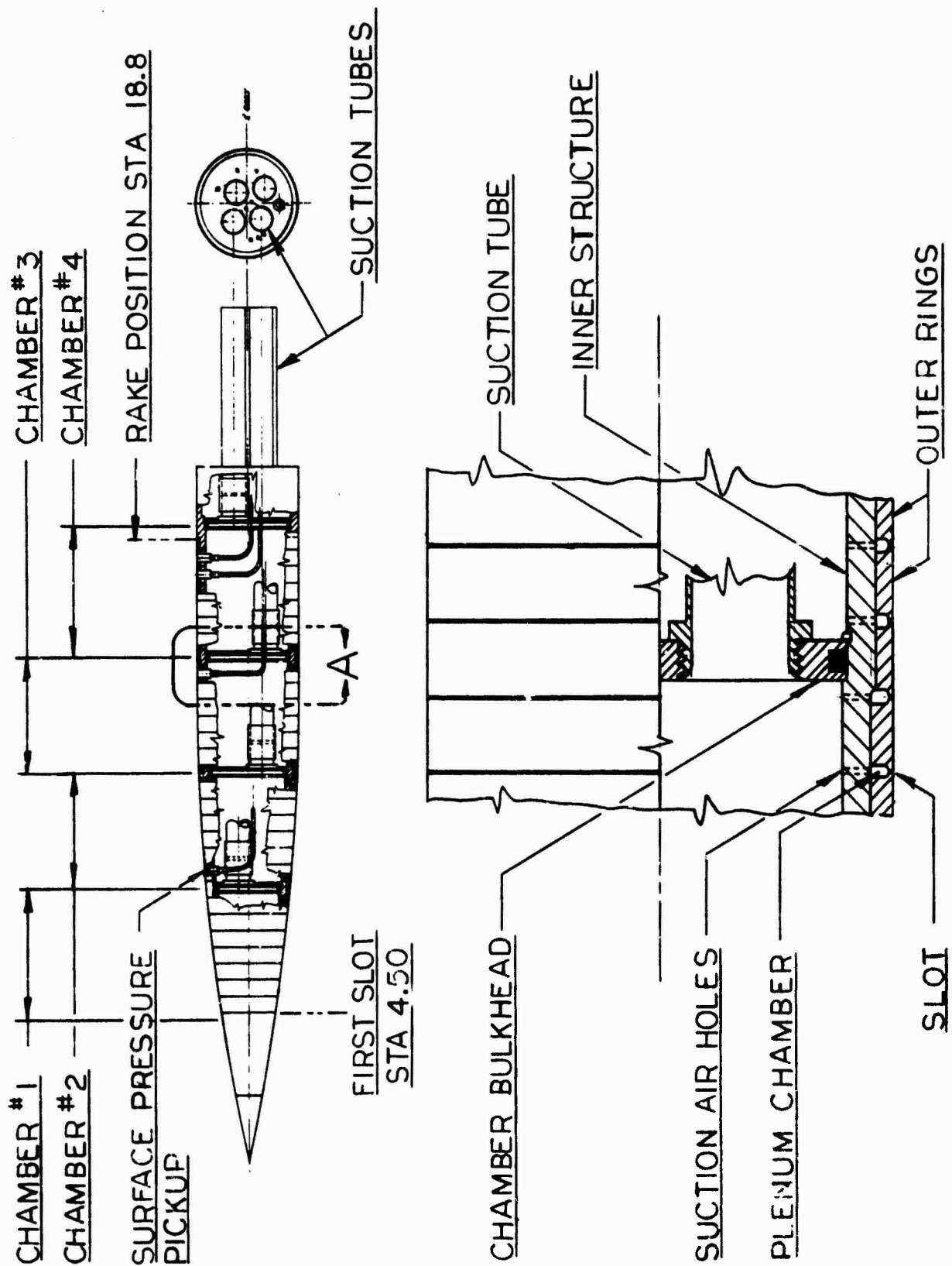


FIGURE 46 SKETCH OF SUCTION MODEL

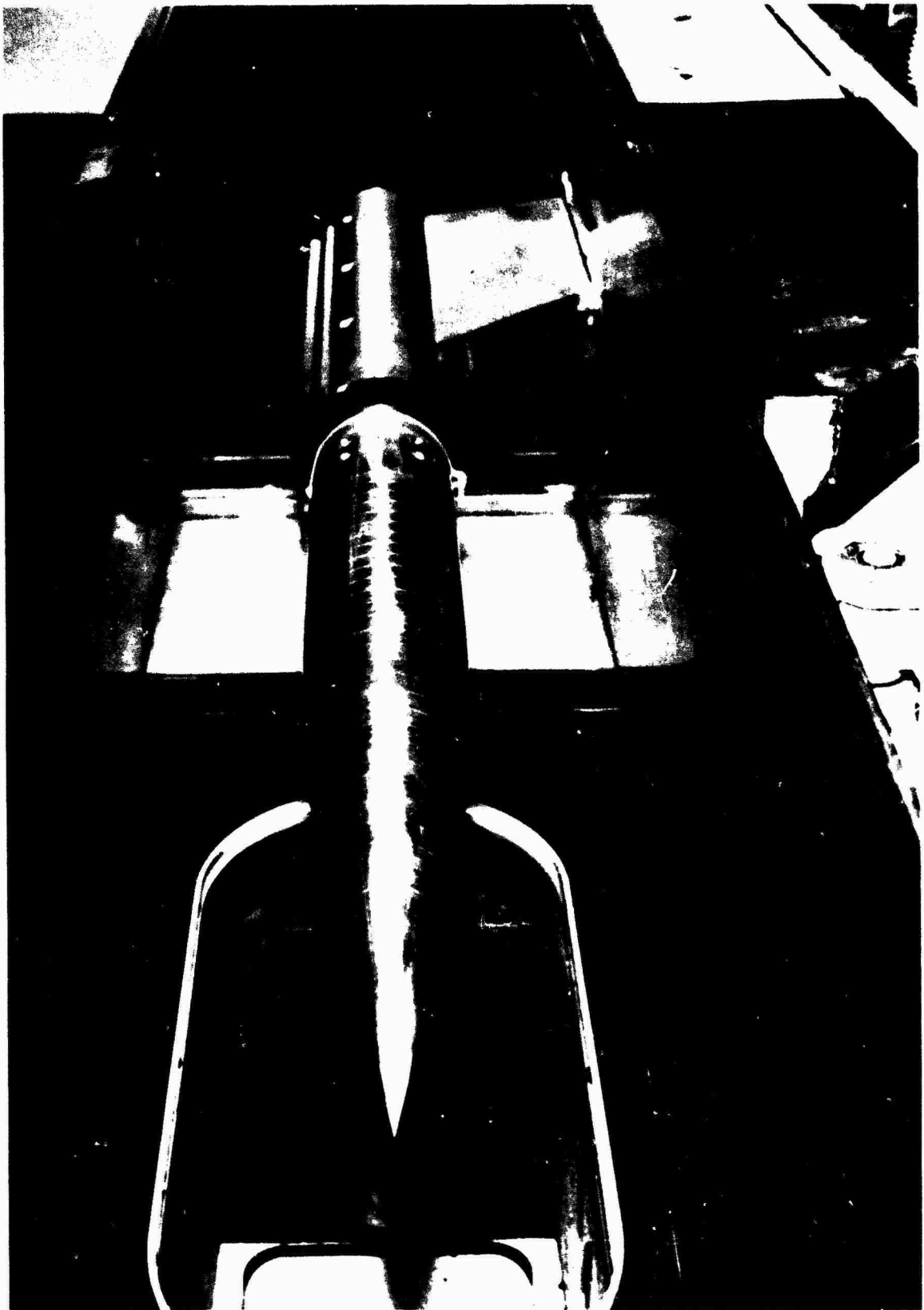


FIGURE 47 PHOTOGRAPH OF MODEL MOUNTED IN TUNNEL E-1

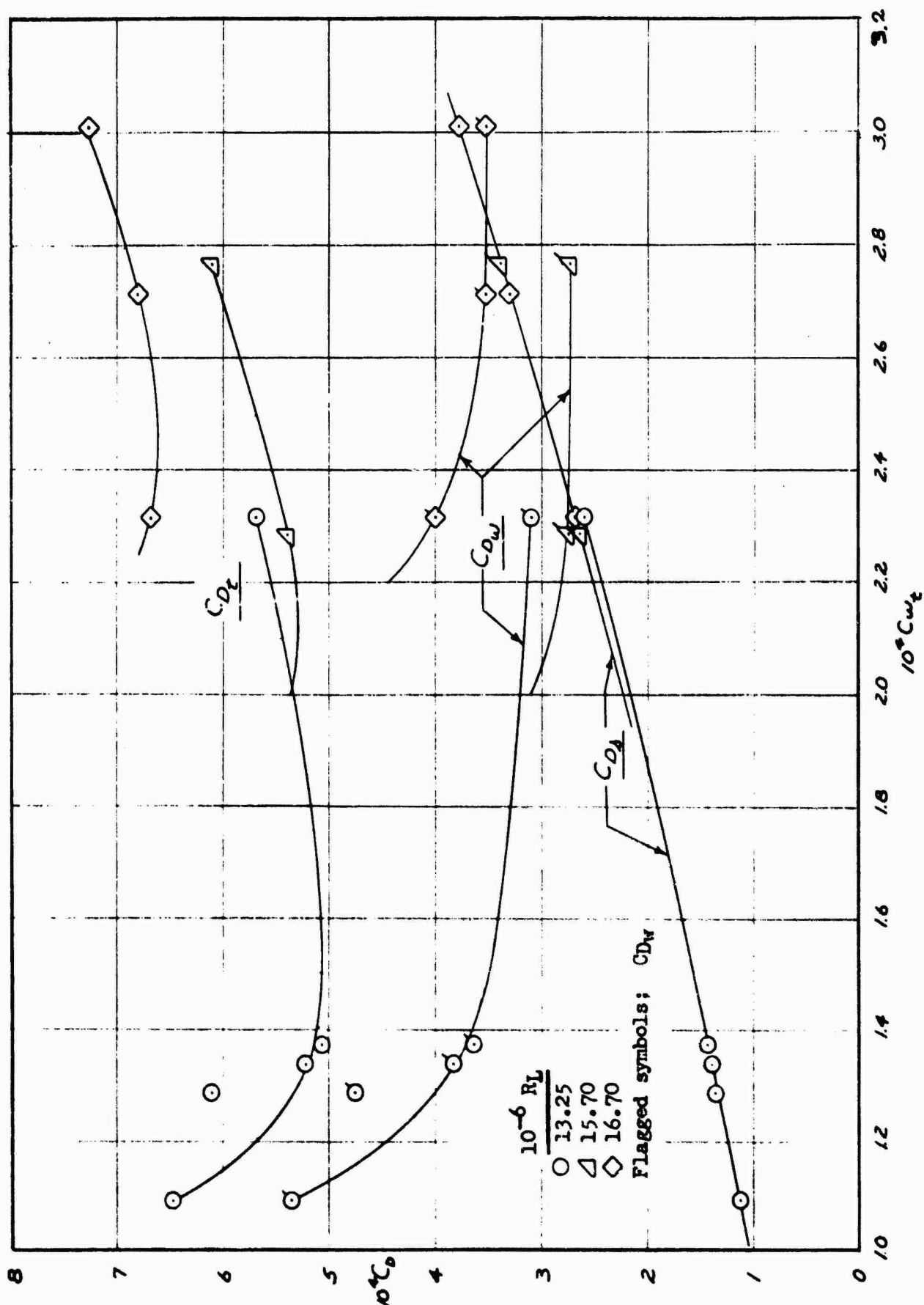


FIGURE 48

WAKE, SUCTION AND TOTAL DRAG COEFFICIENTS VS SUCTION QUANTITIES

AT  $M_\infty = 2.5$

-639-

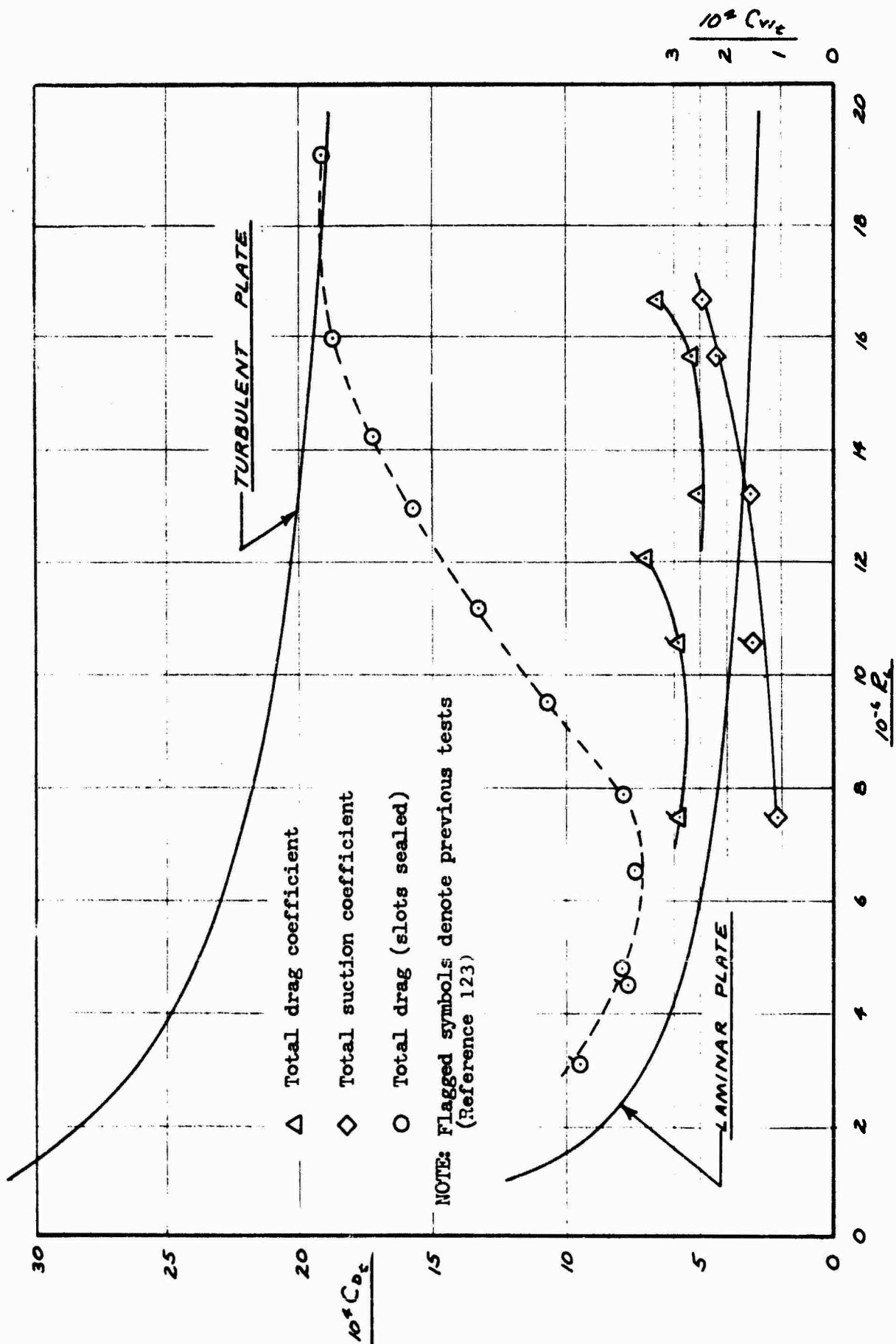


FIGURE 49

MINIMUM TOTAL DRAG AND OPTIMUM TOTAL SUCTION COEFFICIENTS VS  
LENGTH REYNOLDS NUMBER AT  $M_\infty = 2.5$

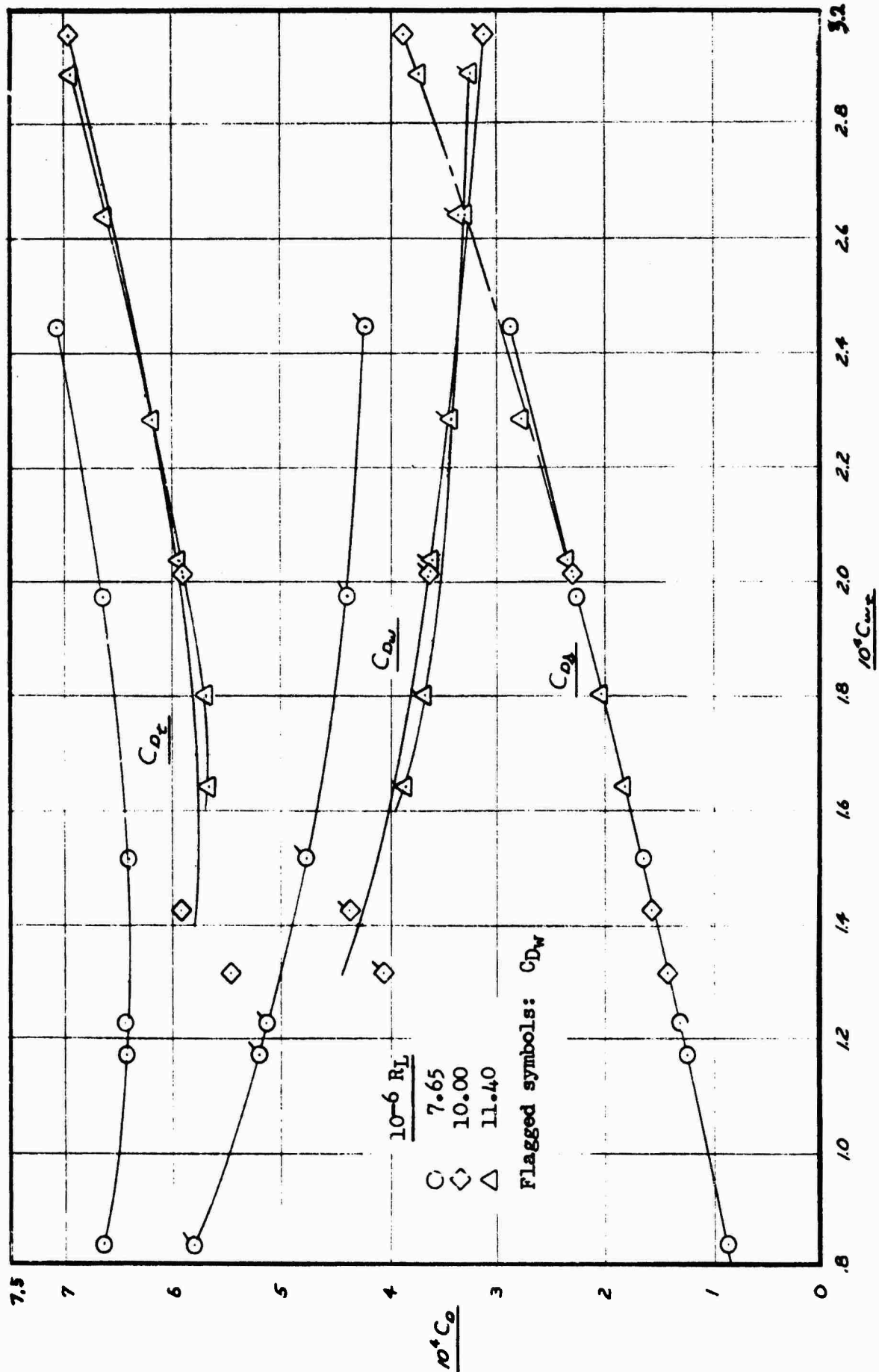


FIGURE 50

WAKE, SUCTION AND TOTAL DRAG COEFFICIENTS VS SUCTION QUANTITIES  
AT  $M_\infty = 3.0$



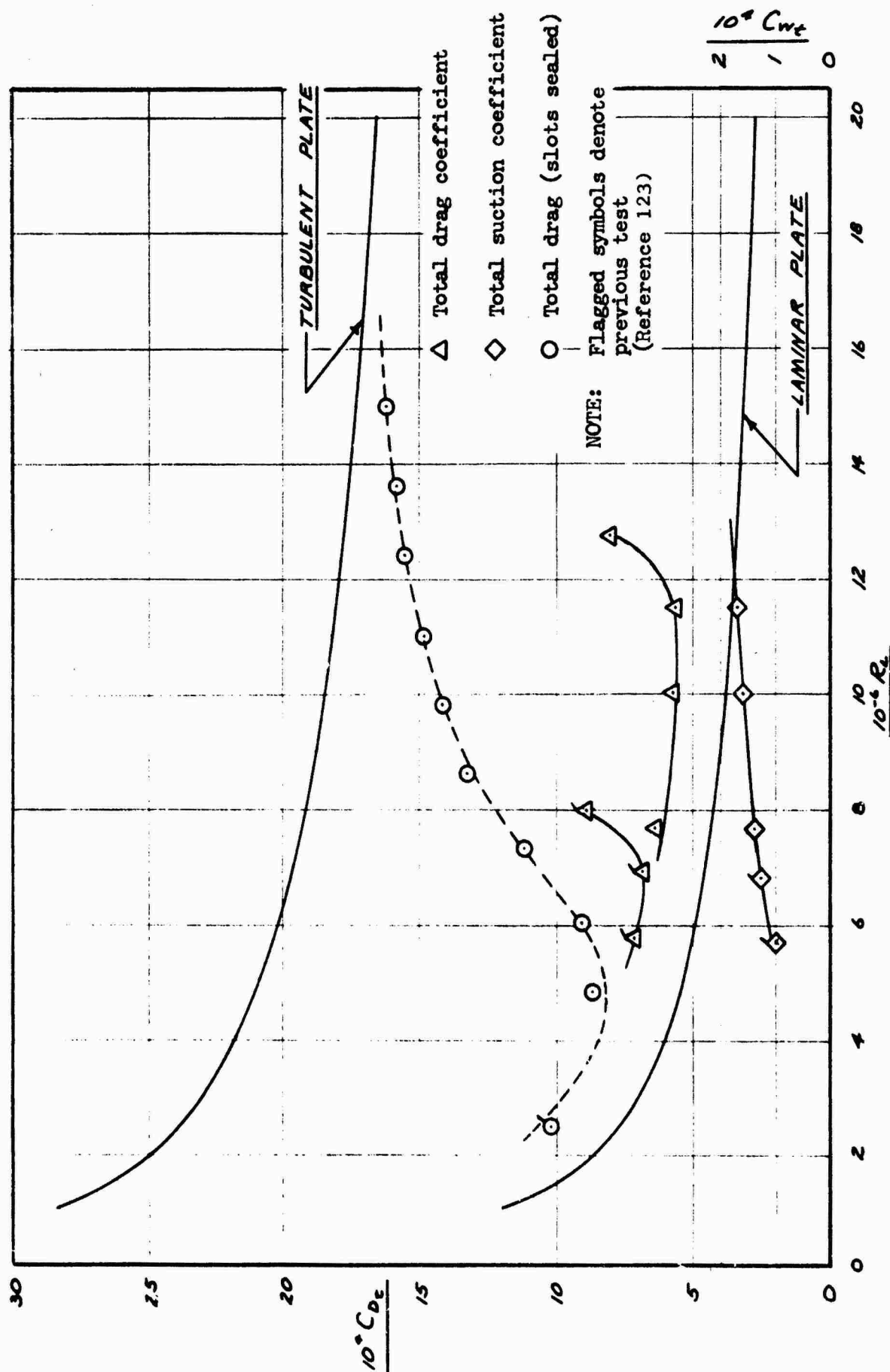


FIGURE 51

MINIMUM TOTAL DRAG AND OPTIMUM TOTAL SUCTION COEFFICIENTS VS  
LENGTH REYNOLDS NUMBER AT  $M_\infty = 3.0$

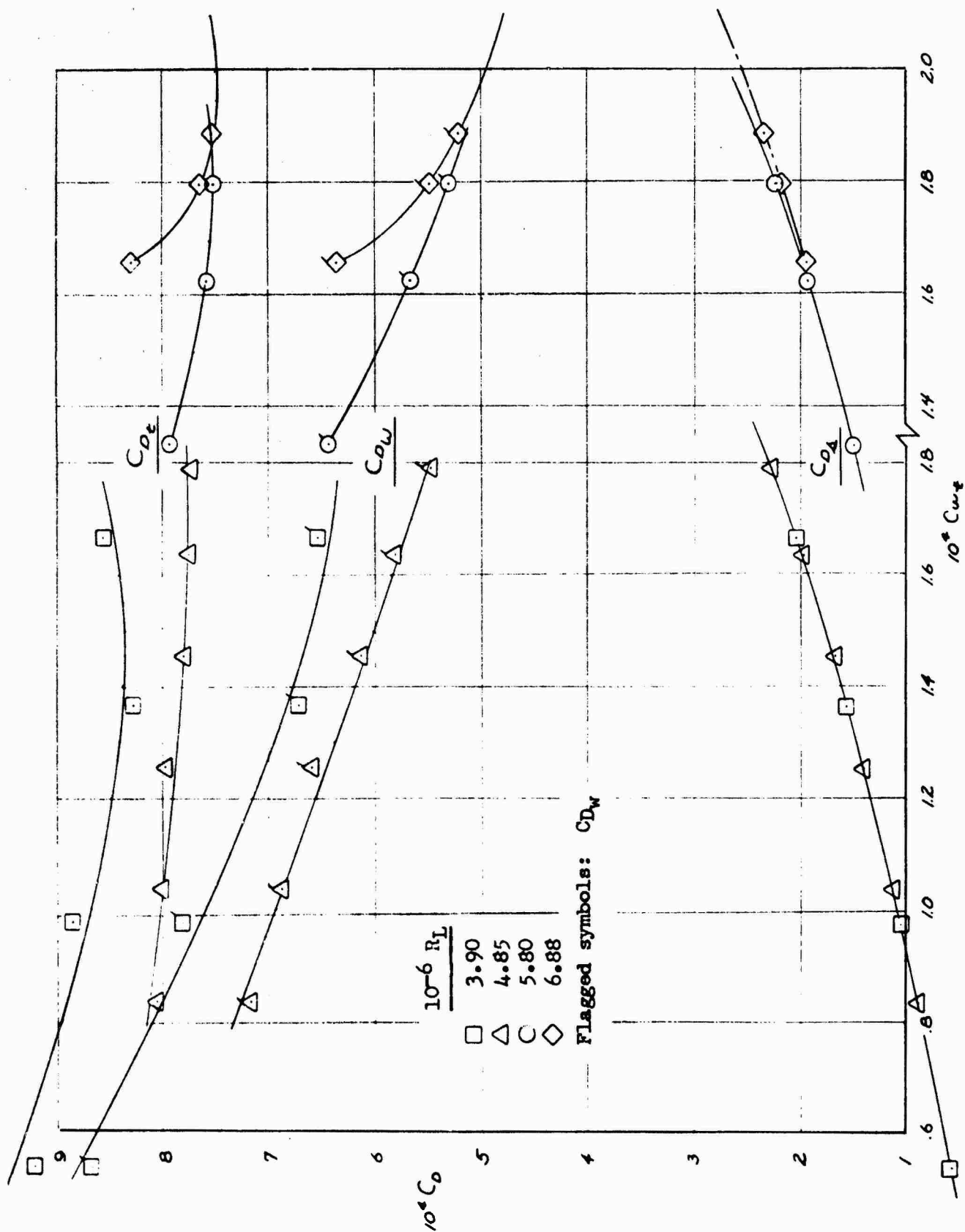


FIGURE 52

WAKE, SUCTION AND TOTAL DRAG COEFFICIENTS VS SUCTION QUANTITIES  
AT  $M_\infty = 3.5$

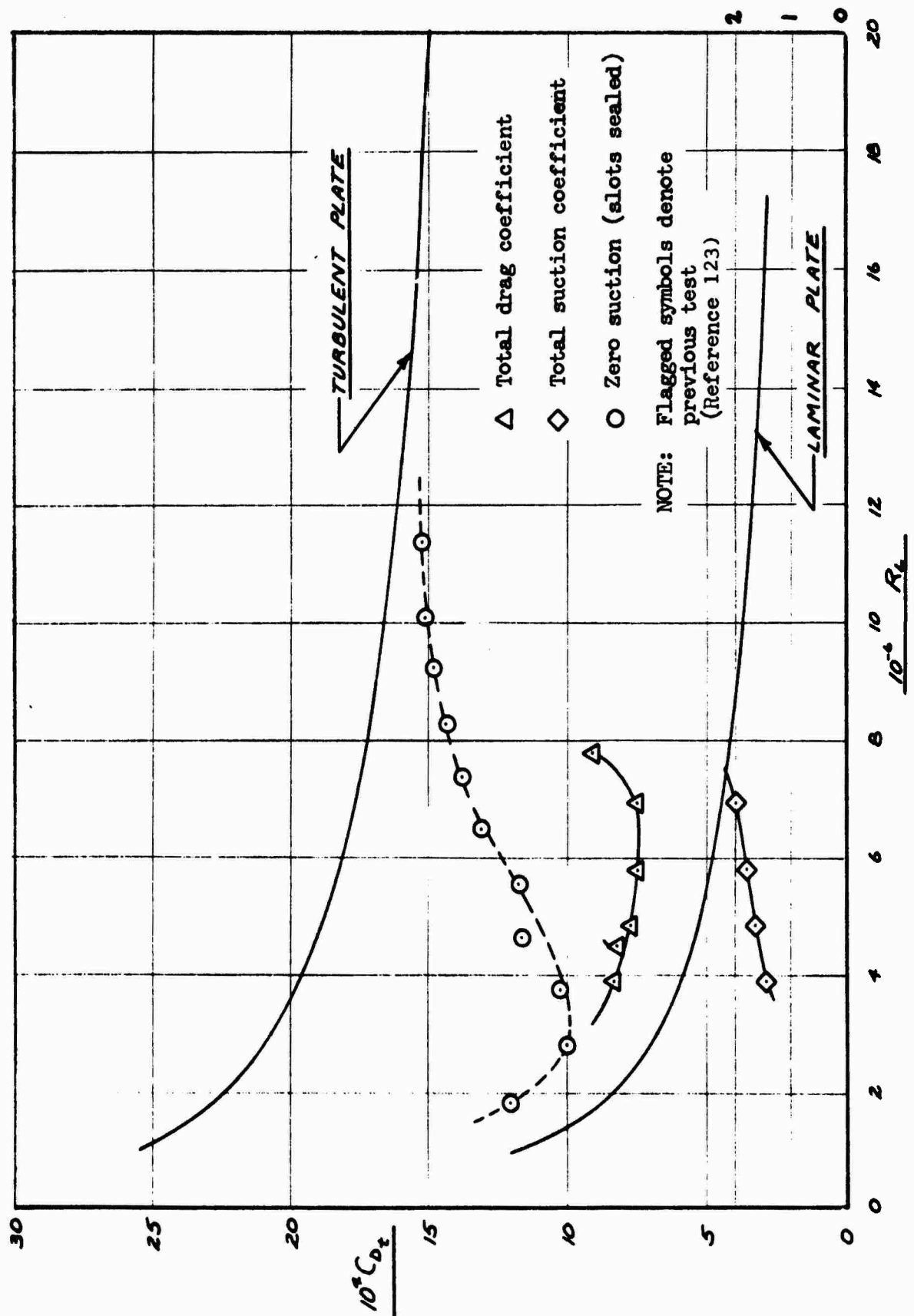


FIGURE 53

MINIMUM TOTAL DRAG AND OPTIMUM TOTAL SUCTION COEFFICIENTS VS  
LENGTH REYNOLDS NUMBER AT  $M_\infty = 3.5$

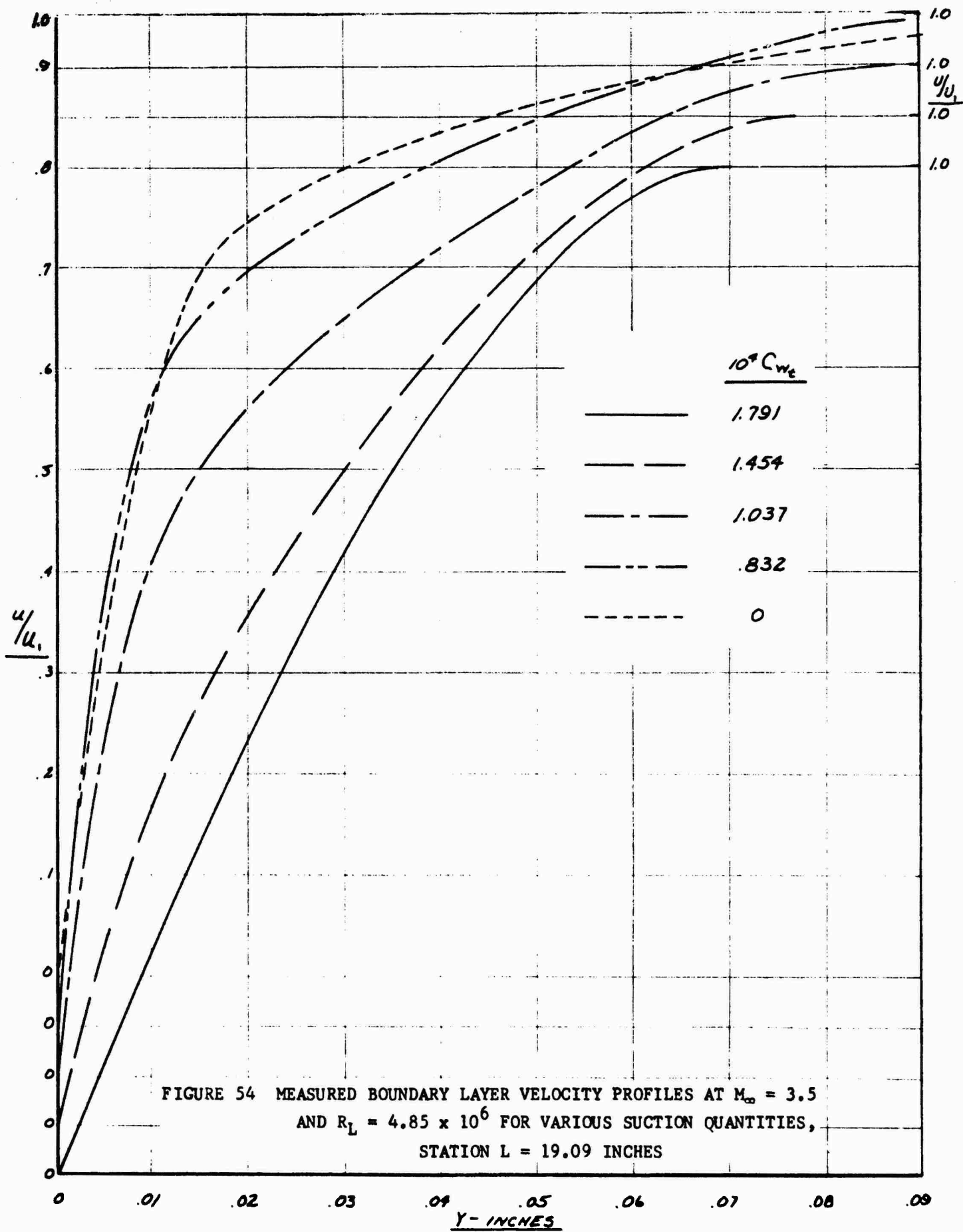


FIGURE 54 MEASURED BOUNDARY LAYER VELOCITY PROFILES AT  $M_\infty = 3.5$   
AND  $R_L = 4.85 \times 10^6$  FOR VARIOUS SUCTION QUANTITIES,  
STATION  $L = 19.09$  INCHES

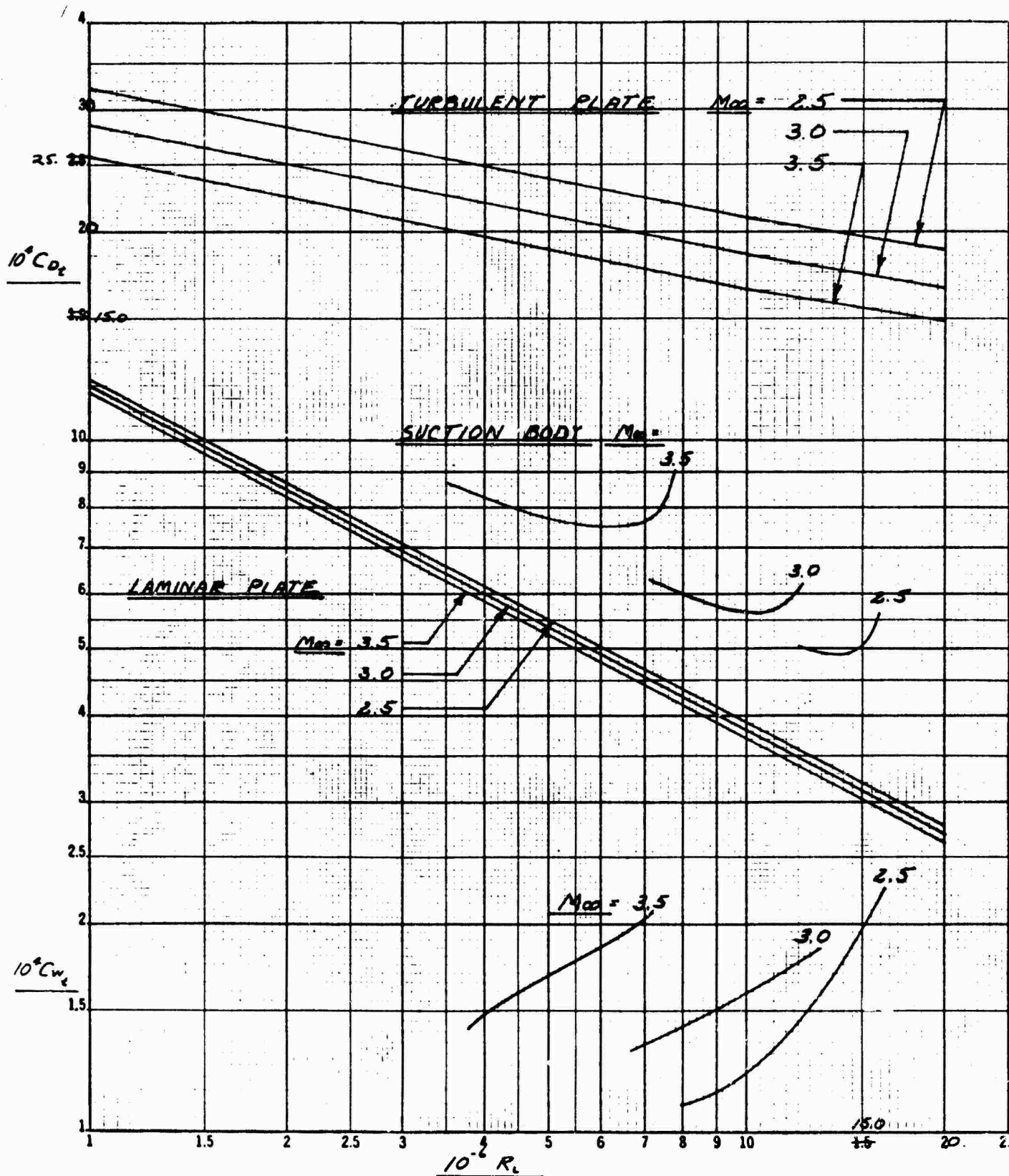


FIGURE 55

VARIATION OF MINIMUM TOTAL DRAG AND OPTIMUM SUCTION COEFFICIENTS WITH REYNOLDS NUMBER FOR  $M_\infty = 2.5, 3.0, \text{ and } 3.5$

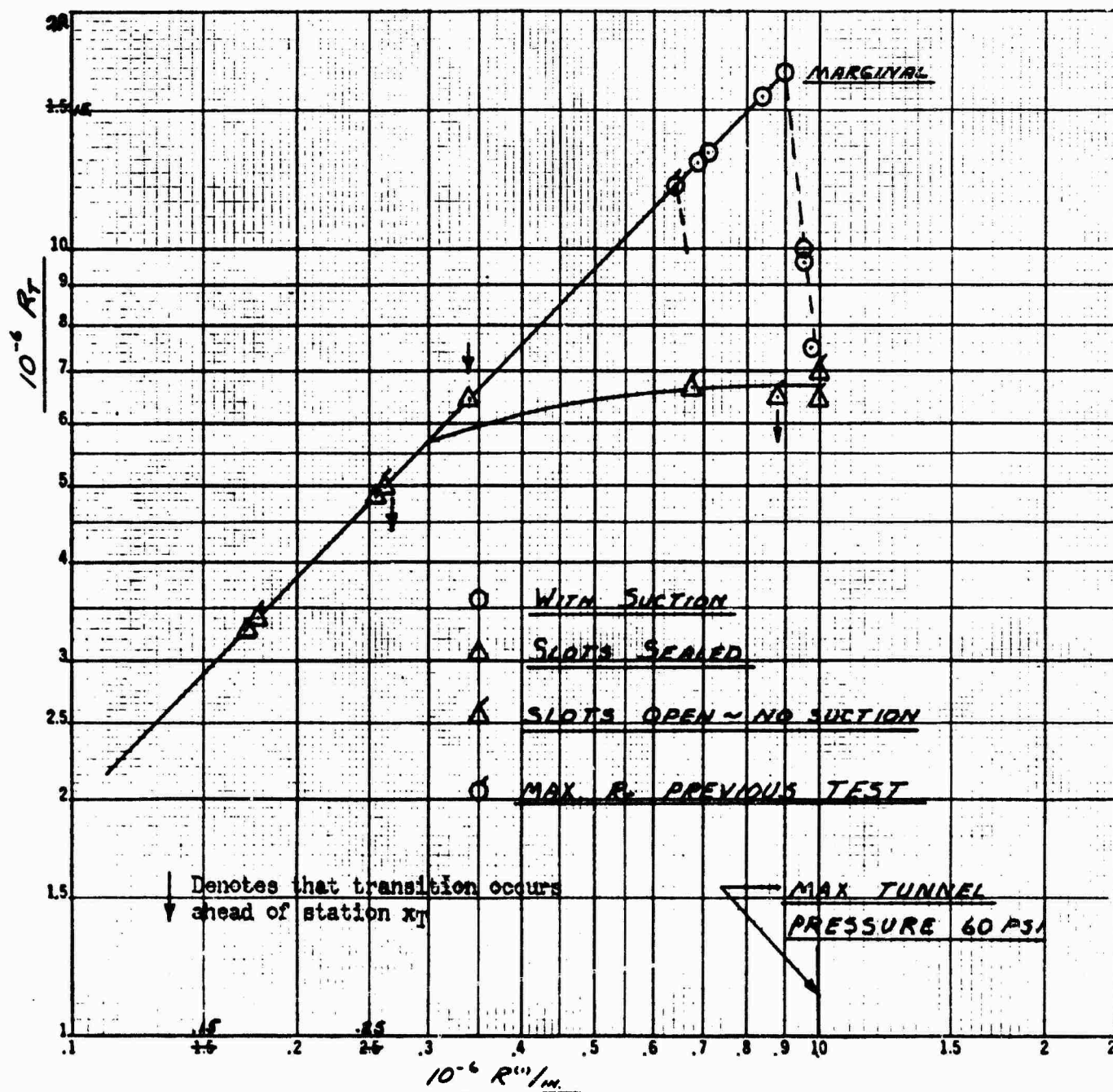


FIGURE 56

TRANSITION REYNOLDS NUMBER VS FREESTREAM UNIT REYNOLDS  
NUMBER AT  $M_\infty = 2.5$

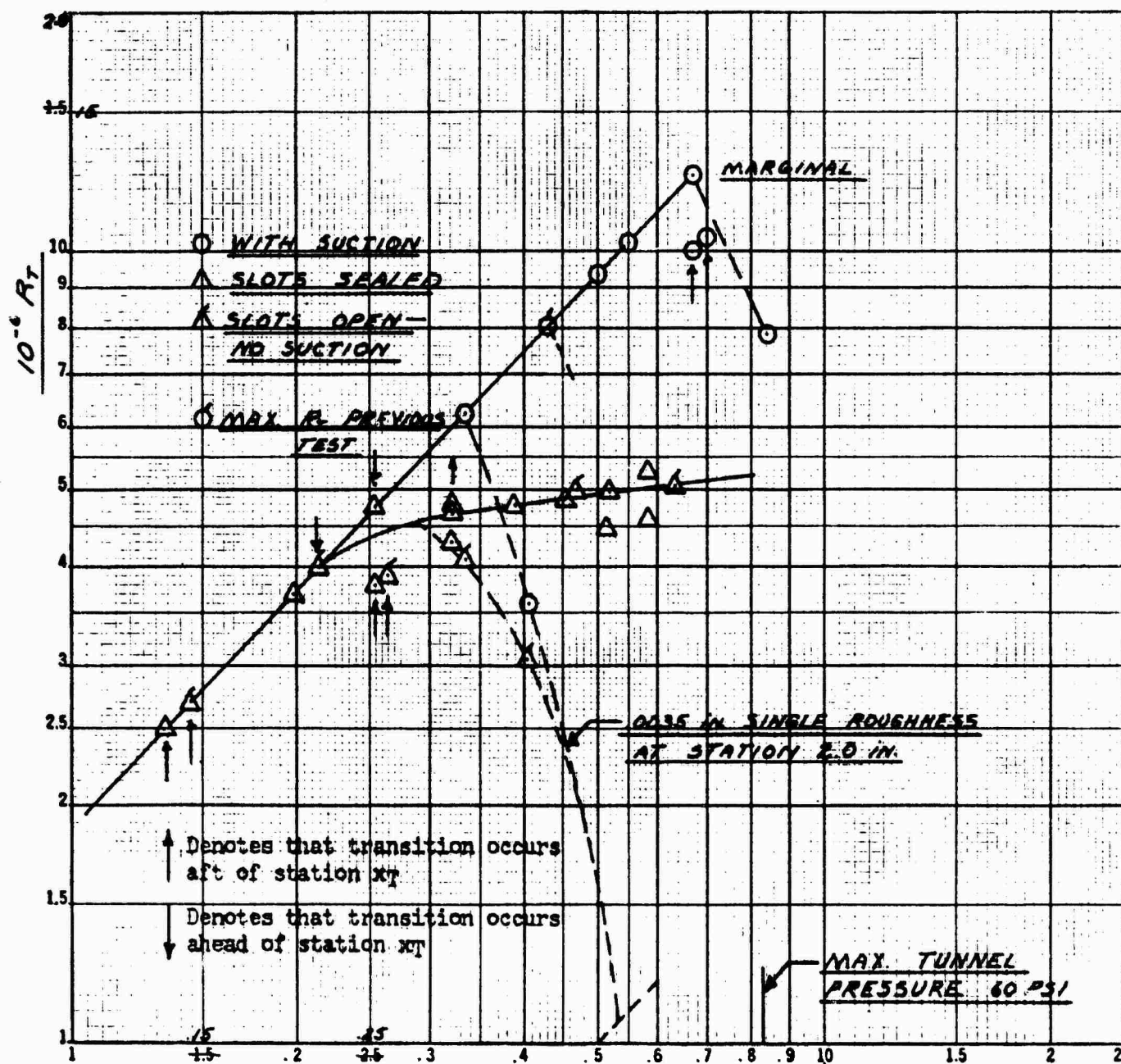


FIGURE 57

TRANSITION REYNOLDS NUMBER VS FREESTREAM UNIT REYNOLDS  
NUMBER AT  $M_\infty = 3.0$



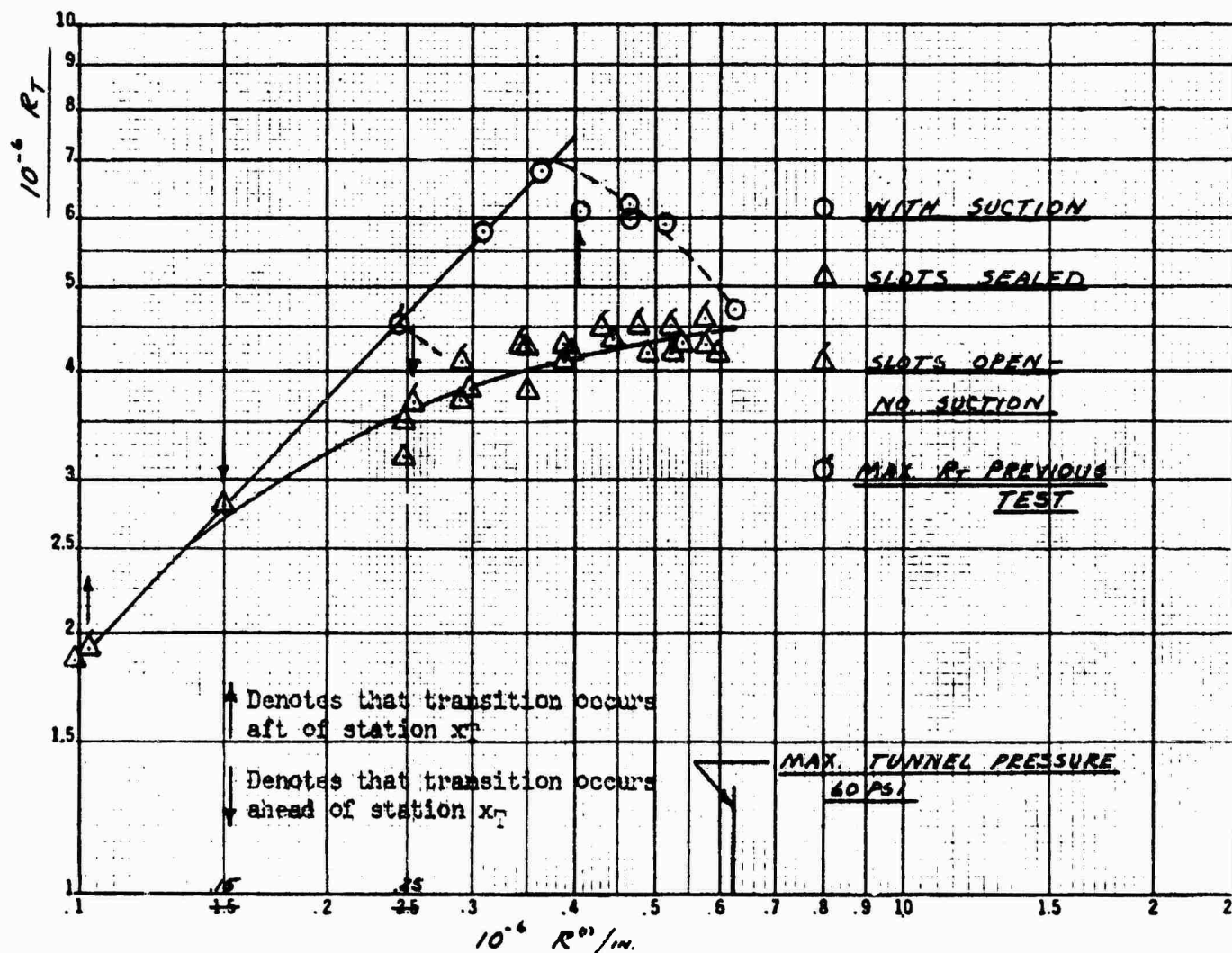


FIGURE 58

TRANSITION REYNOLDS NUMBER VS FREESTREAM UNIT REYNOLDS  
NUMBER AT  $M_{\infty} = 3.5$



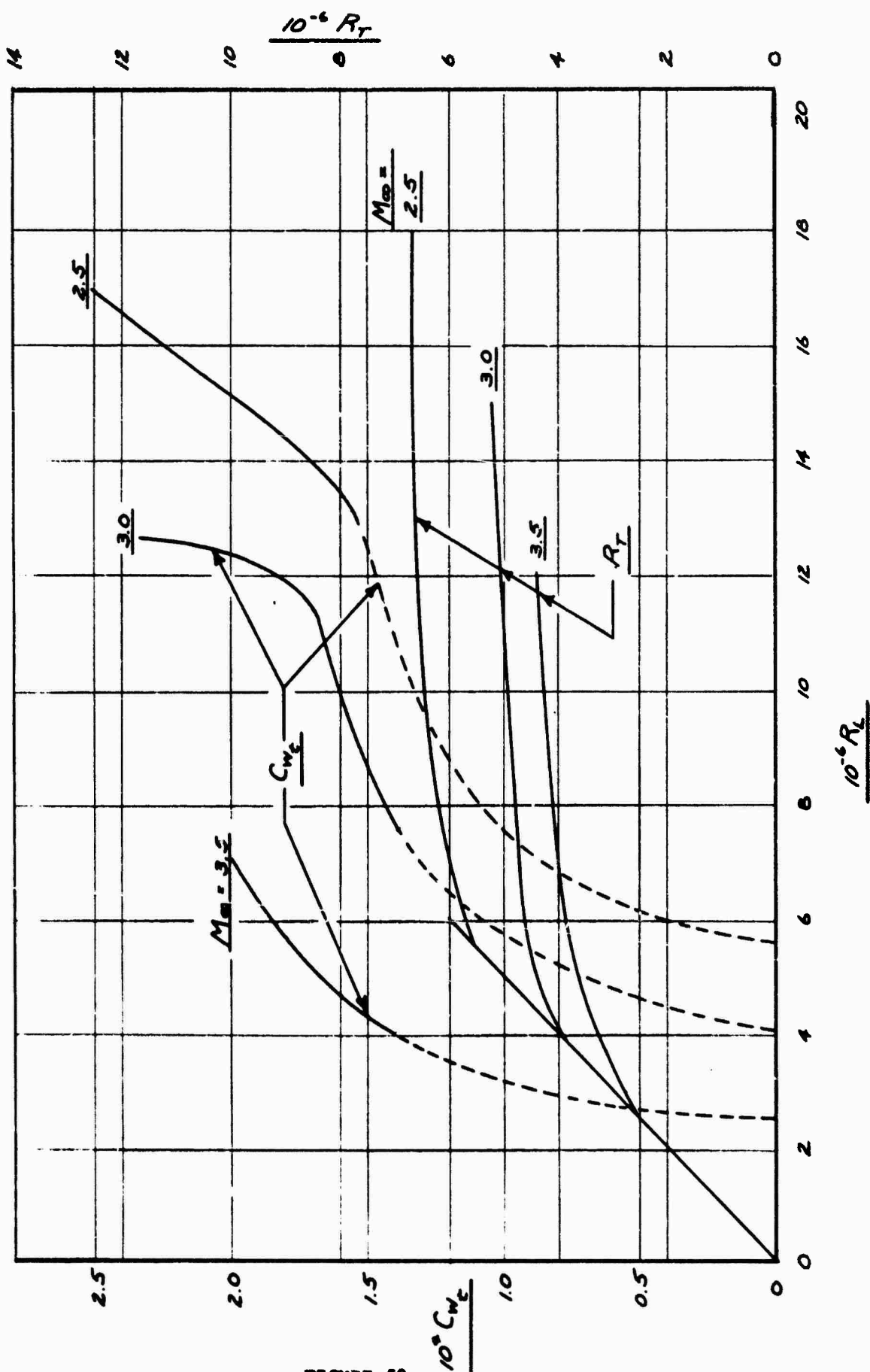


FIGURE 59

OPTIMUM TOTAL SUCTION COEFFICIENT AND NATURAL TRANSITION REYNOLDS  
NUMBER VS REFERENCE LENGTH REYNOLDS NUMBER

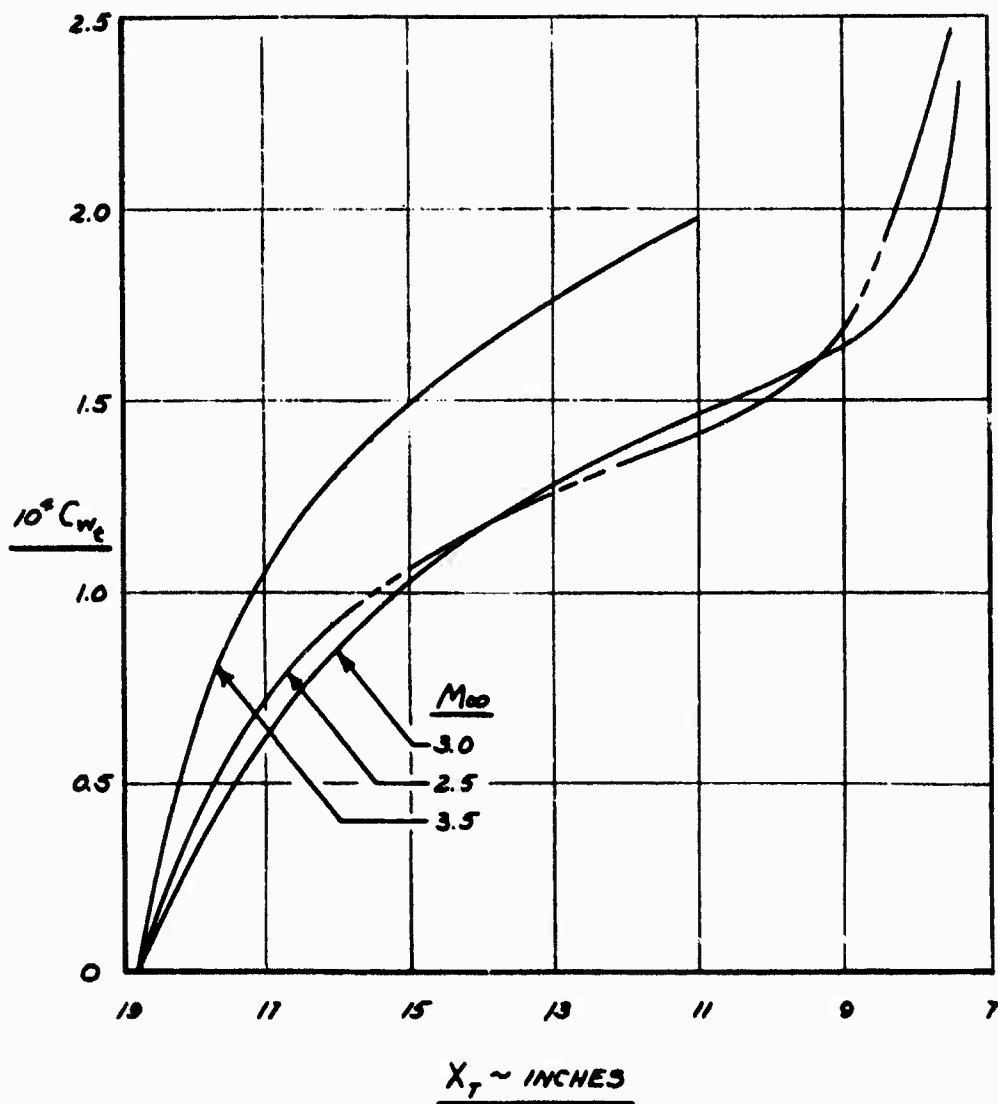


FIGURE 60

OPTIMUM TOTAL SUCTION COEFFICIENT VS LOCATION OF  
TRANSITION WITHOUT SUCTION

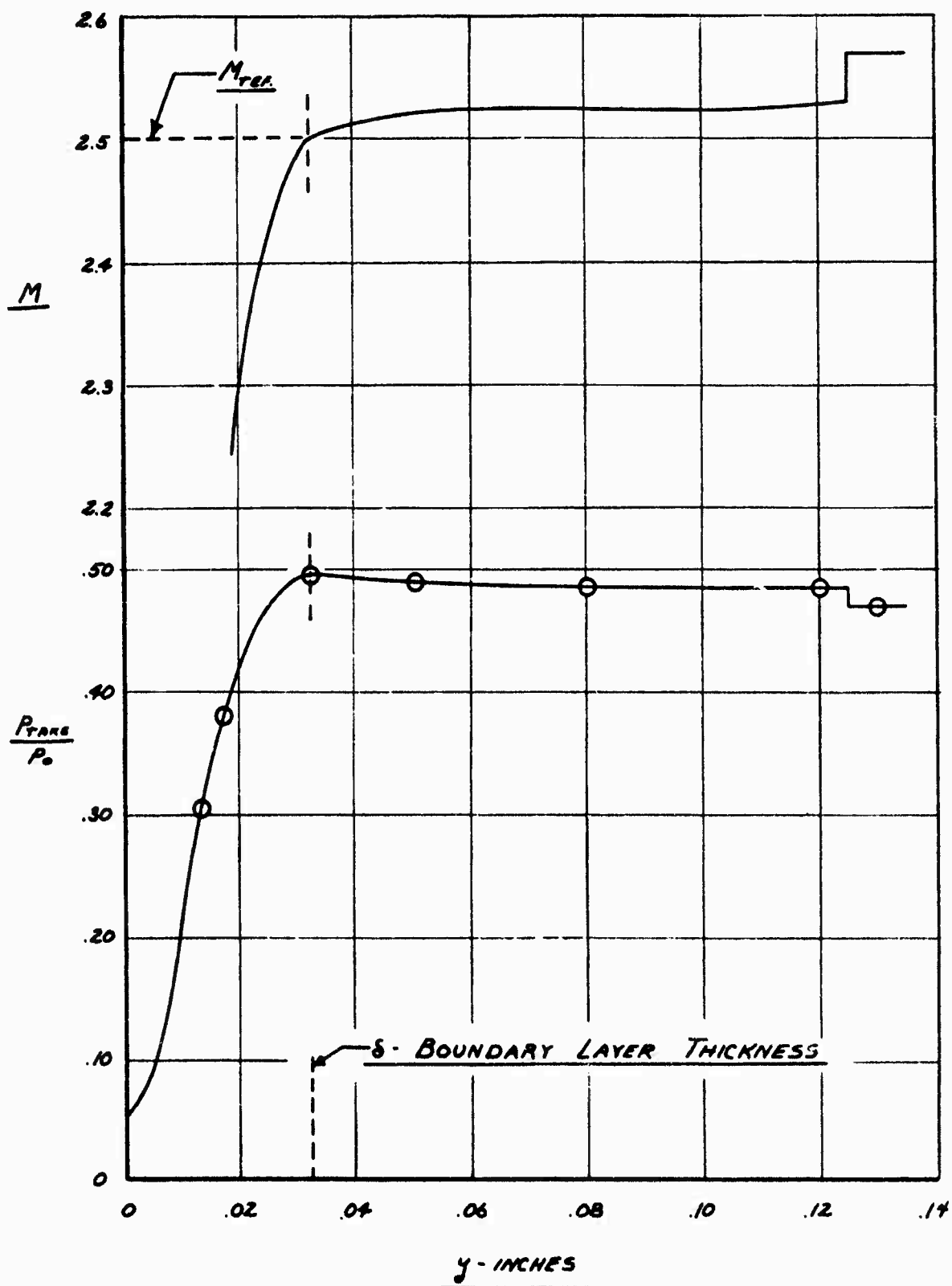


FIGURE 61

RAKE TOTAL HEAD AND CORRESPONDING MACH NUMBER DISTRIBUTION  
 PERPENDICULAR TO MODEL SURFACE AT RAKE LOCATION,  
 STATION 18.81, for  $M_\infty = 2.5$ ,  $R_L = 15.8 \times 10^6$

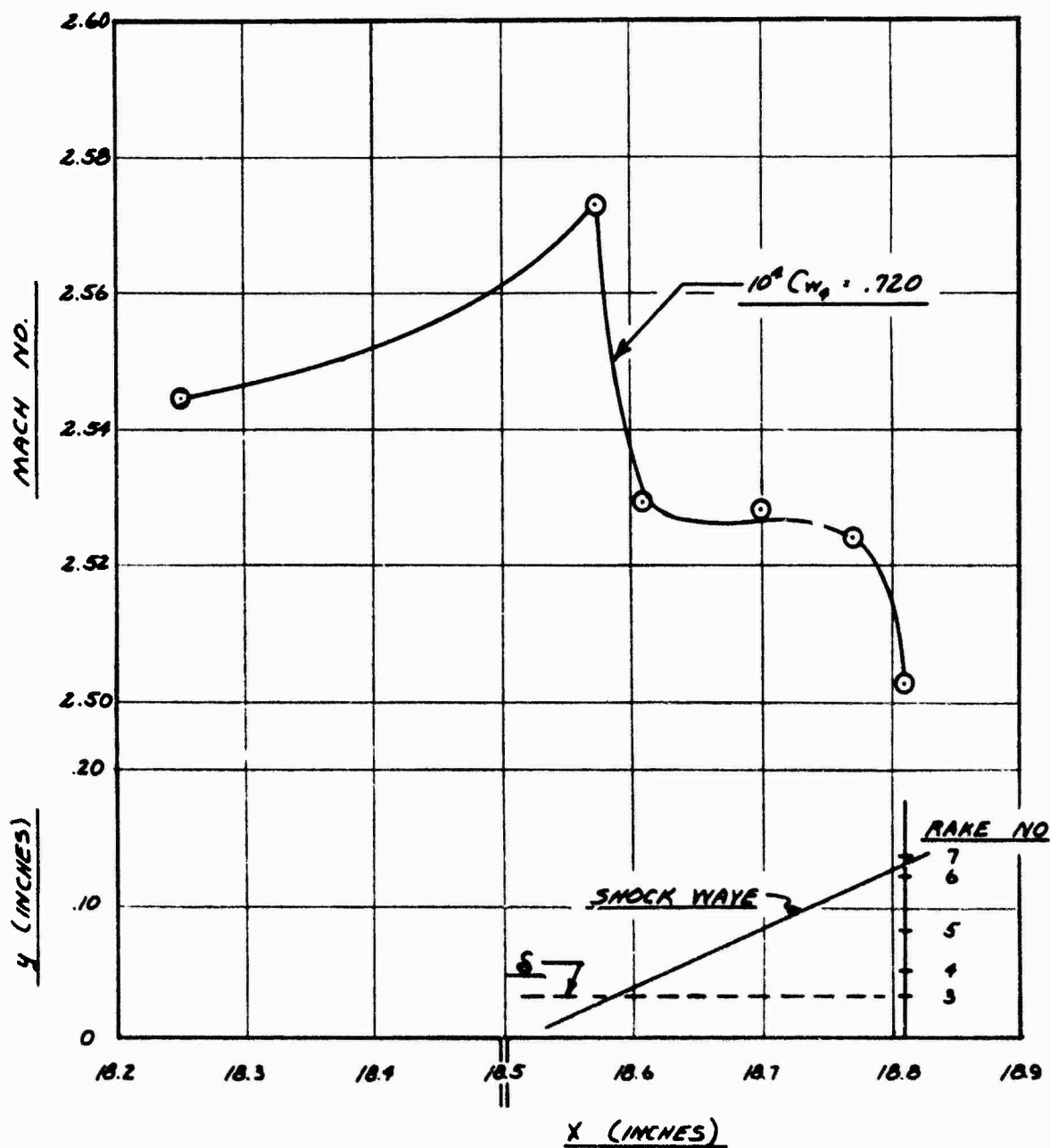


FIGURE 62

EFFECT OF THE SHOCK WAVE FROM THE LAST SLOT (STATION 18.50) ON  
THE LOCAL POTENTIAL FLOW FIELD,  $M_\infty = 2.5$ ,  $R_L = 15.8 \times 10^6$

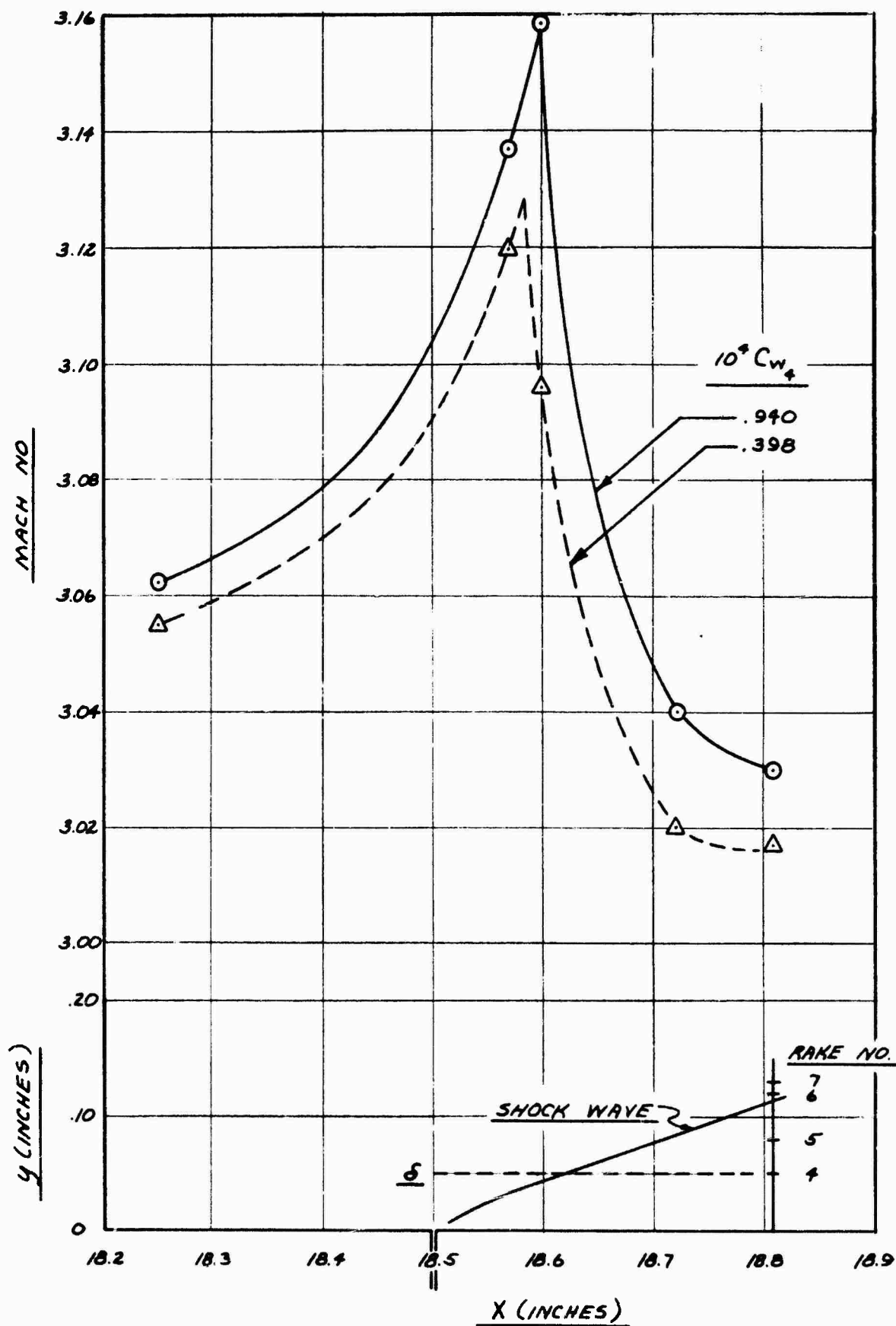


FIGURE 63

EFFECT OF THE SHOCK WAVE FROM THE LAST SLOT (STATION 18.50) ON THE LOCAL POTENTIAL FLOW FIELD,  $M_\infty = 3.0$ ,  $R_L = 7.6 \times 10^6$

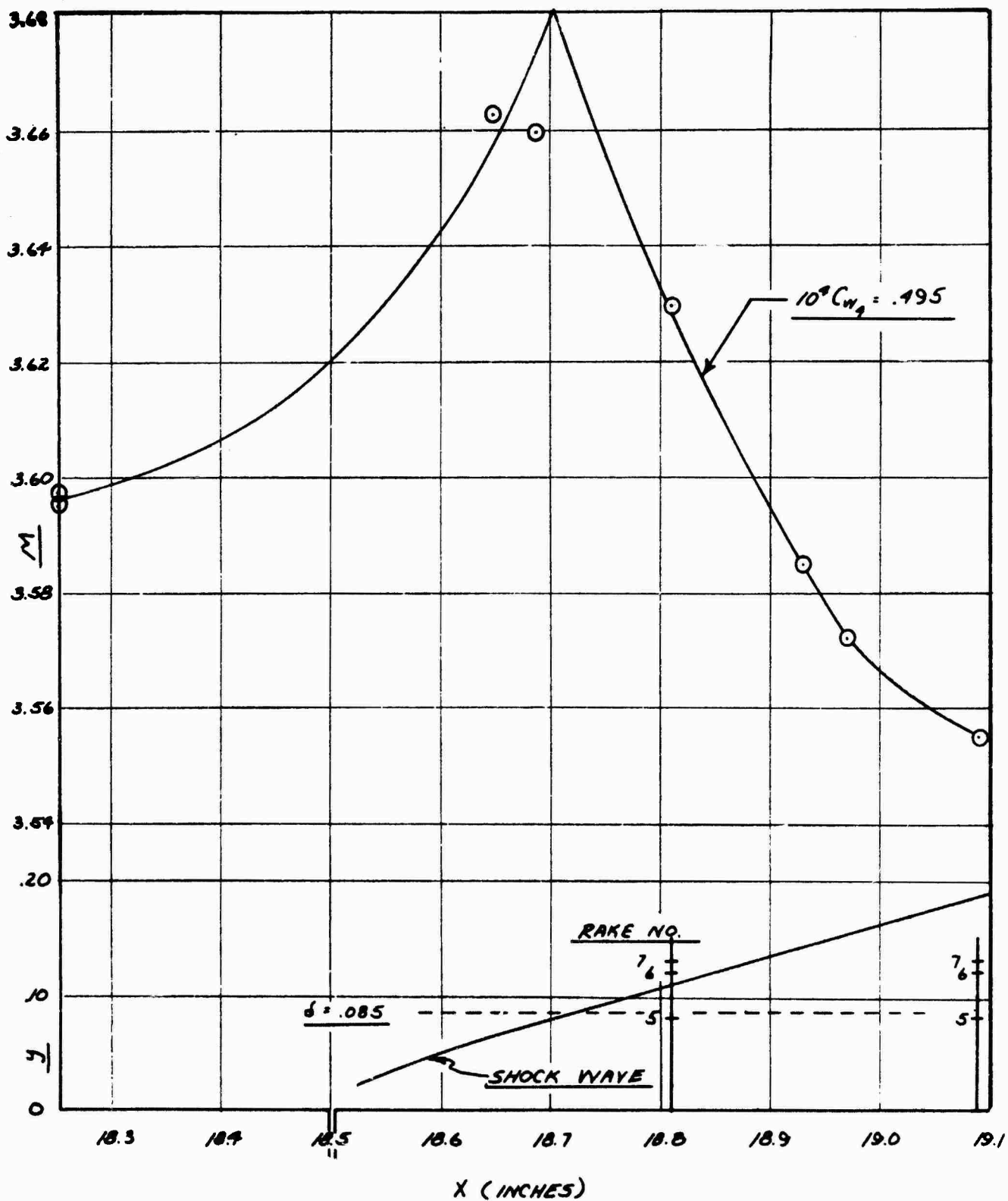


FIGURE 64

EFFECT OF THE SHOCK WAVE FROM THE LAST SLOT (STATION 18.50) ON  
THE LOCAL POTENTIAL FLOW FIELD,  $M_\infty = 3.5$ ,  $R_L = 5.8 \times 10^6$

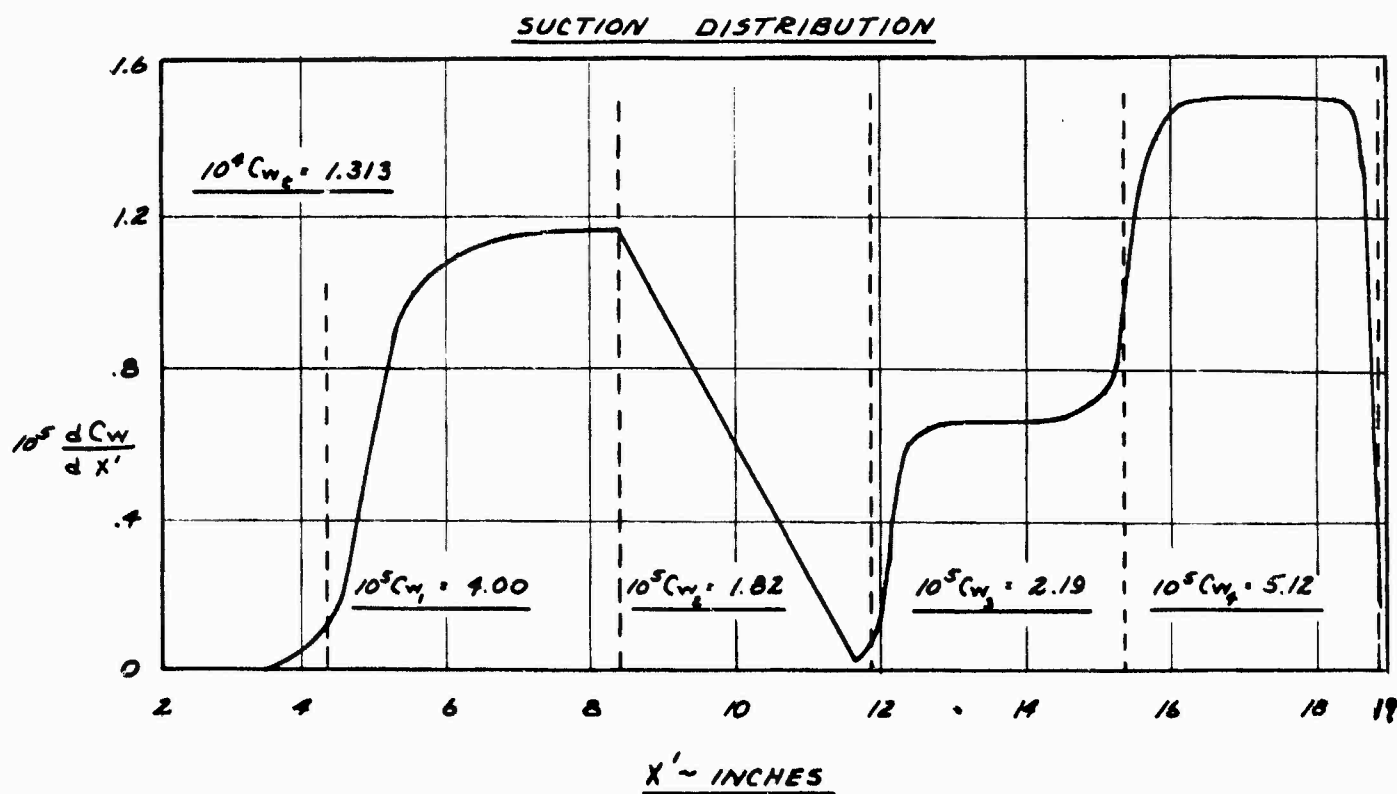
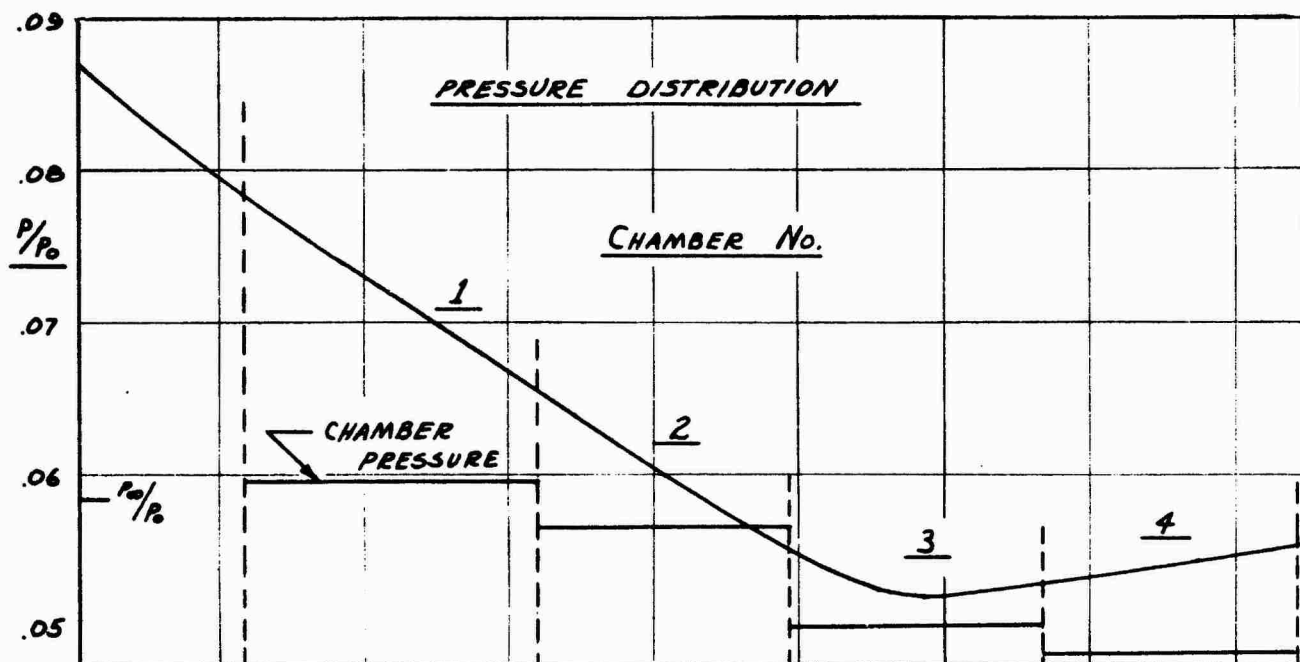


FIGURE 65

EXPERIMENTAL SURFACE PRESSURE AND SUCTION DISTRIBUTION  
 $M_\infty = 2.5$ ,  $R_L = 13.24 \times 10^6$

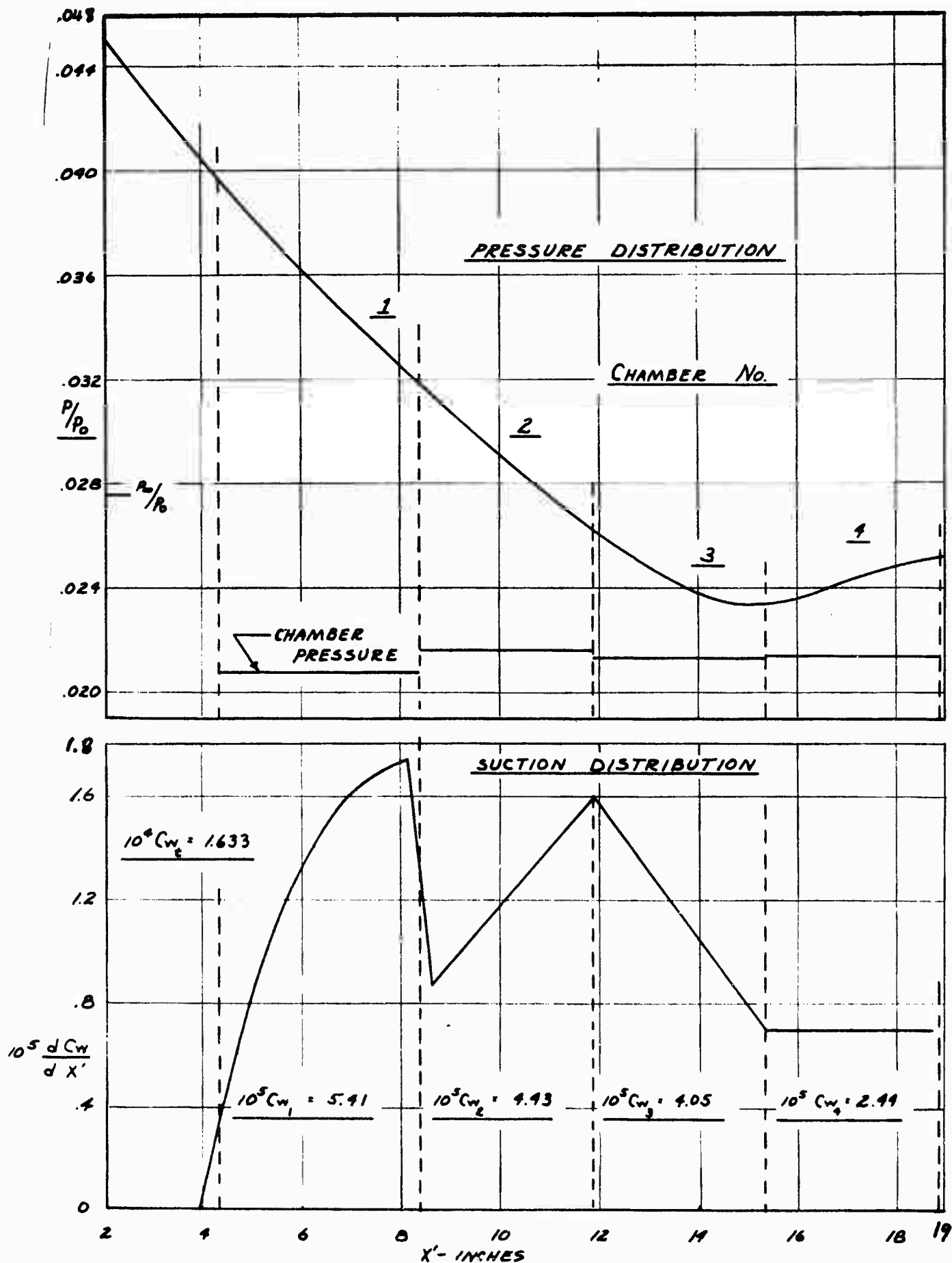


FIGURE 66

EXPERIMENTAL SURFACE PRESSURE AND SUCTION DISTRIBUTION

$M_\infty = 3.0$ ,  $R_L = 11.32 \times 10^6$



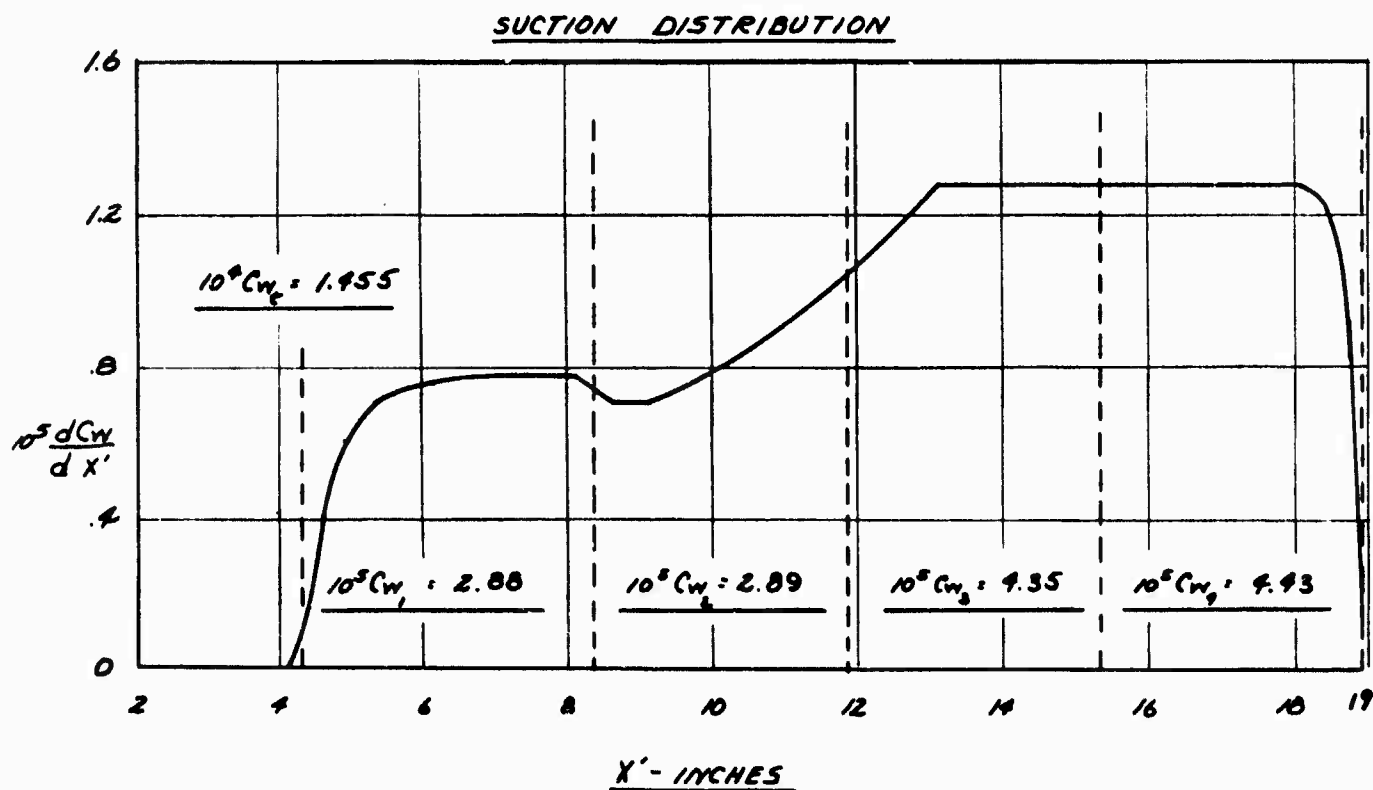
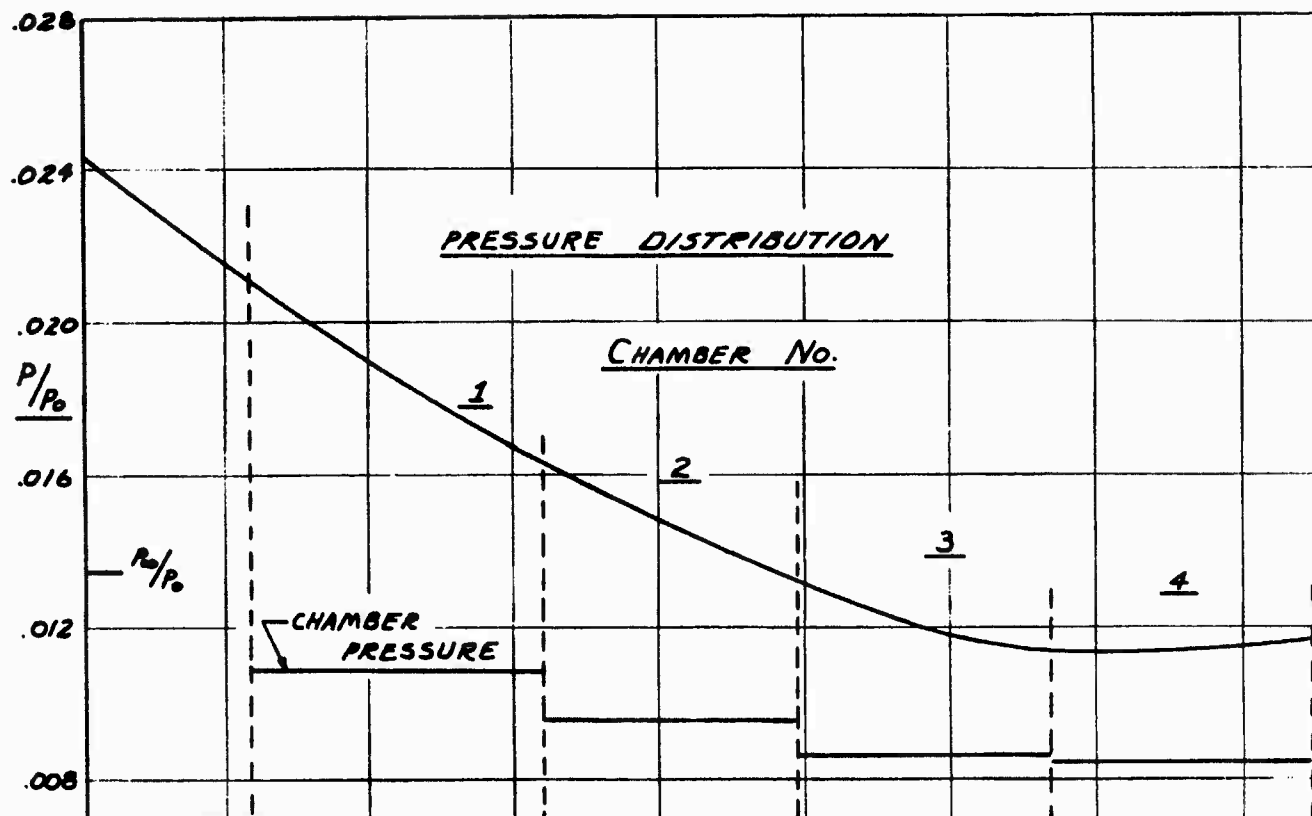


FIGURE 67

EXPERIMENTAL SURFACE PRESSURE AND SUCTION DISTRIBUTION  
 $M_\infty = 3.5$ ,  $R_L = 4.85 \times 10^6$

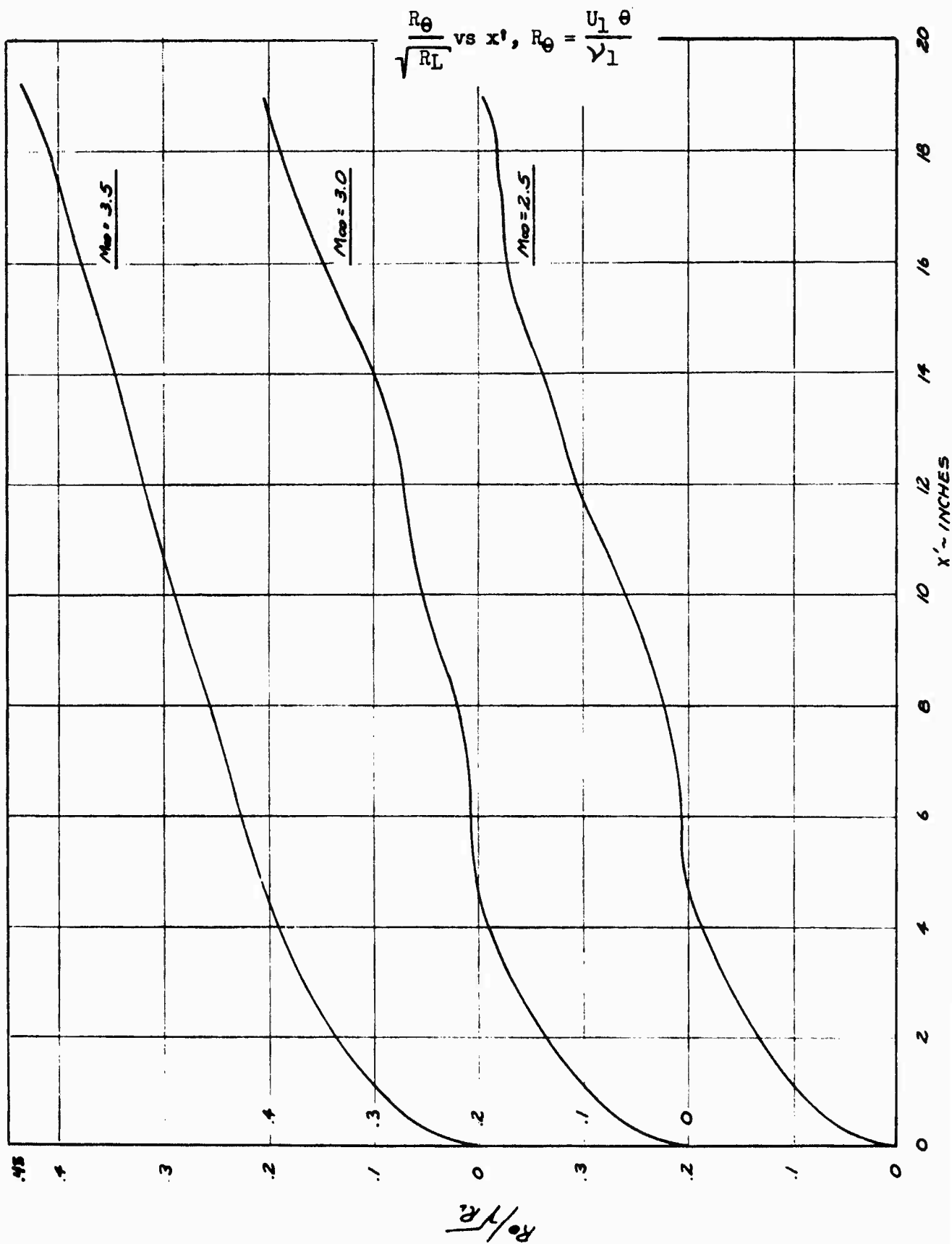


FIGURE 68

THEORETICAL VARIATION OF THE REYNOLDS NUMBER BASED  
ON MOMENTUM THICKNESS ALONG THE MODEL AXIS

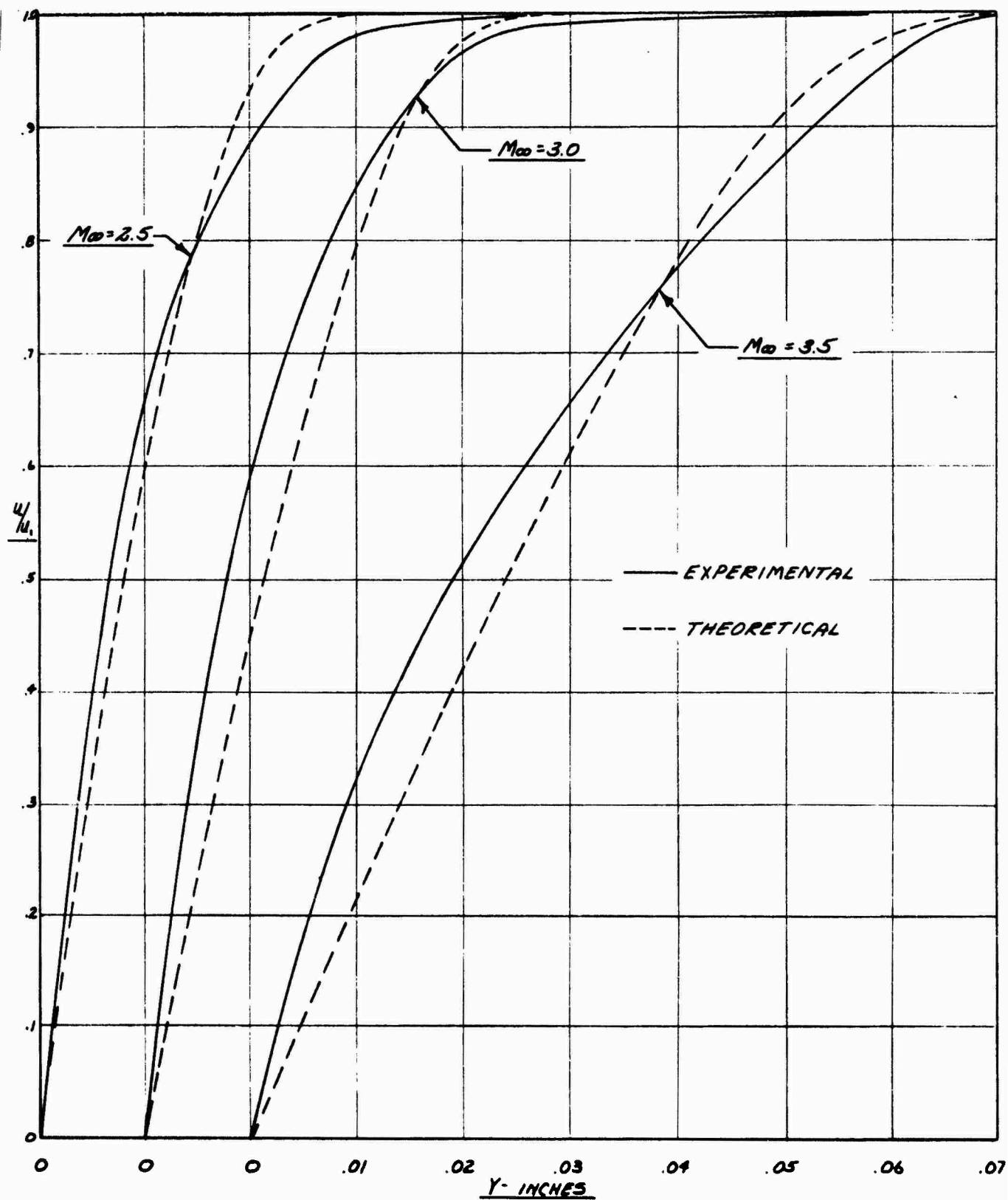


FIGURE 69

THEORETICAL AND EXPERIMENTAL BOUNDARY LAYER VELOCITY  
PROFILES AT THE RAKE LOCATION

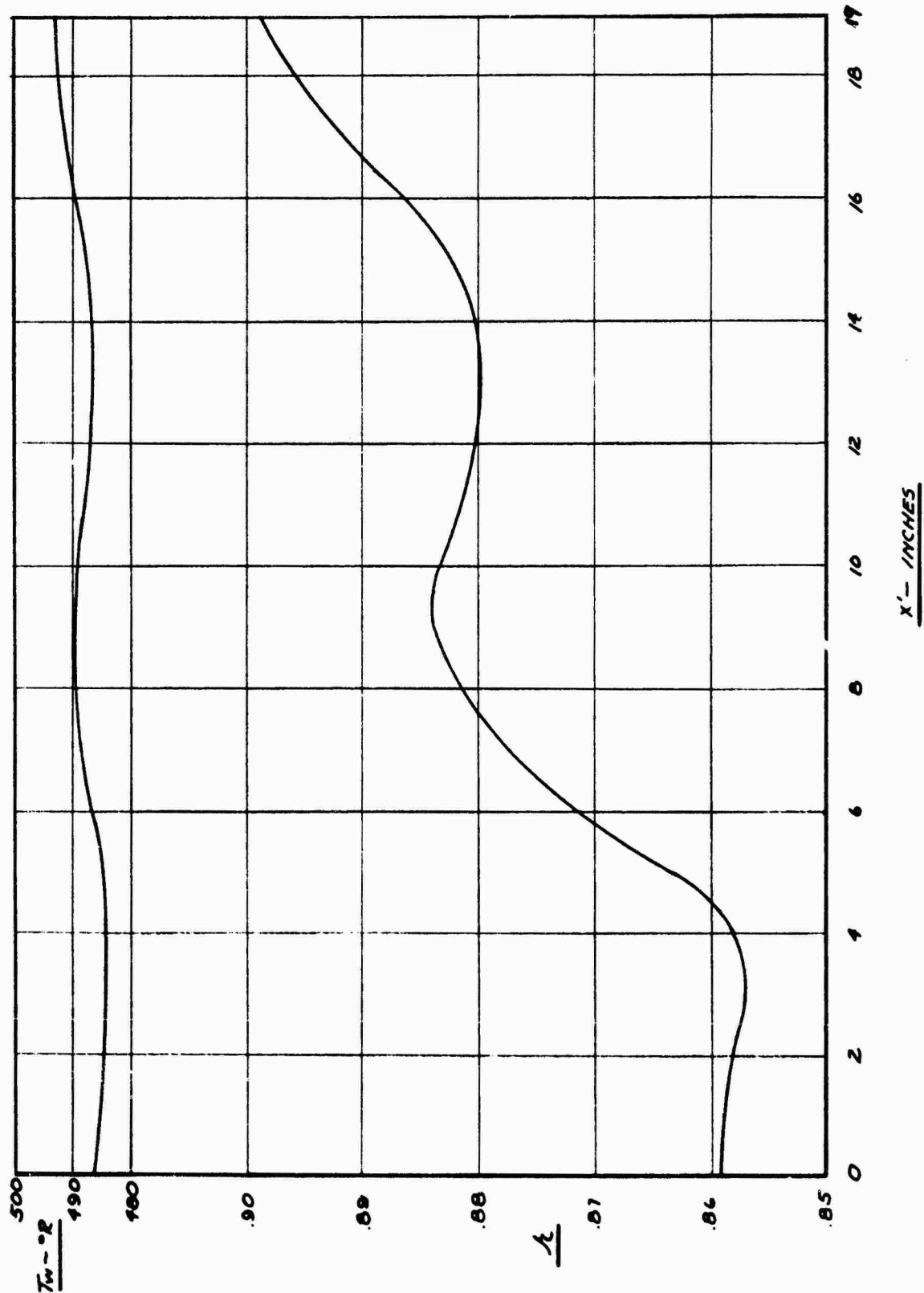


FIGURE 70a

THEORETICAL WALL TEMPERATURES AND TEMPERATURE  
RECOVERY FACTORS ALONG BODY AXIS

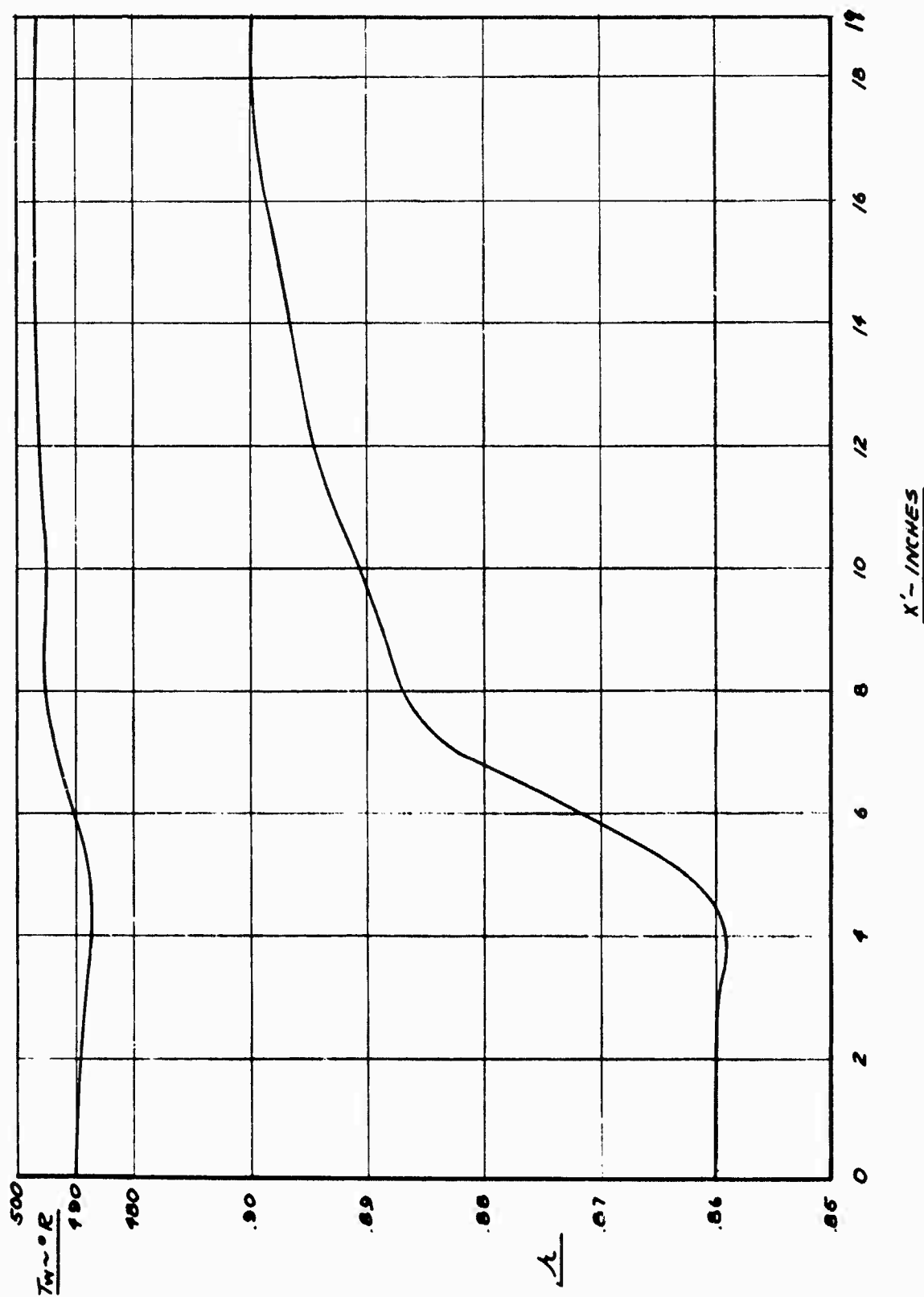


FIGURE 70b

THEORETICAL WALL TEMPERATURES AND TEMPERATURE  
RECOVERY FACTORS ALONG BODY AXIS

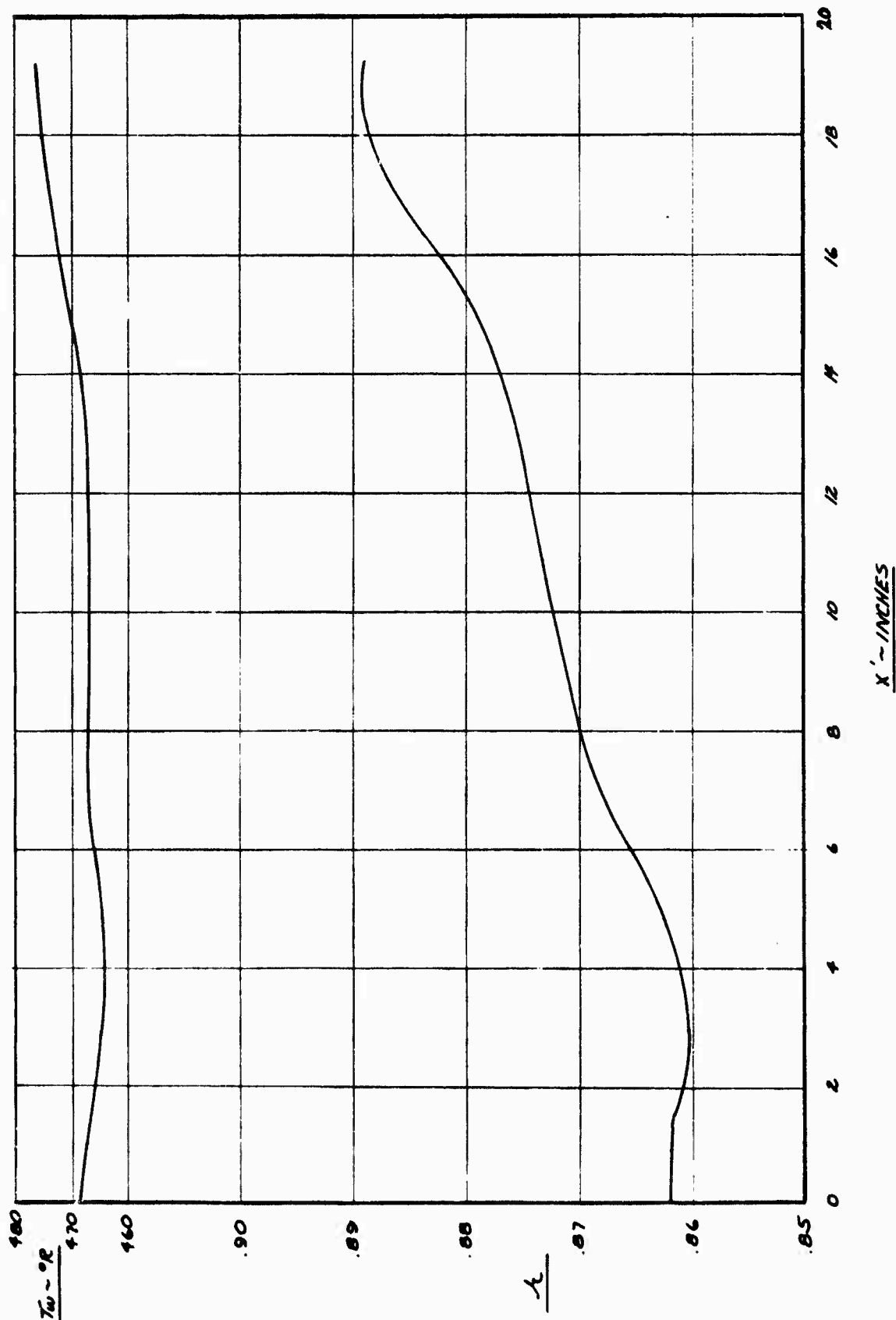


FIGURE 70c

THEORETICAL WALL TEMPERATURES AND TEMPERATURE  
RECOVERY FACTORS ALONG BODY AXIS

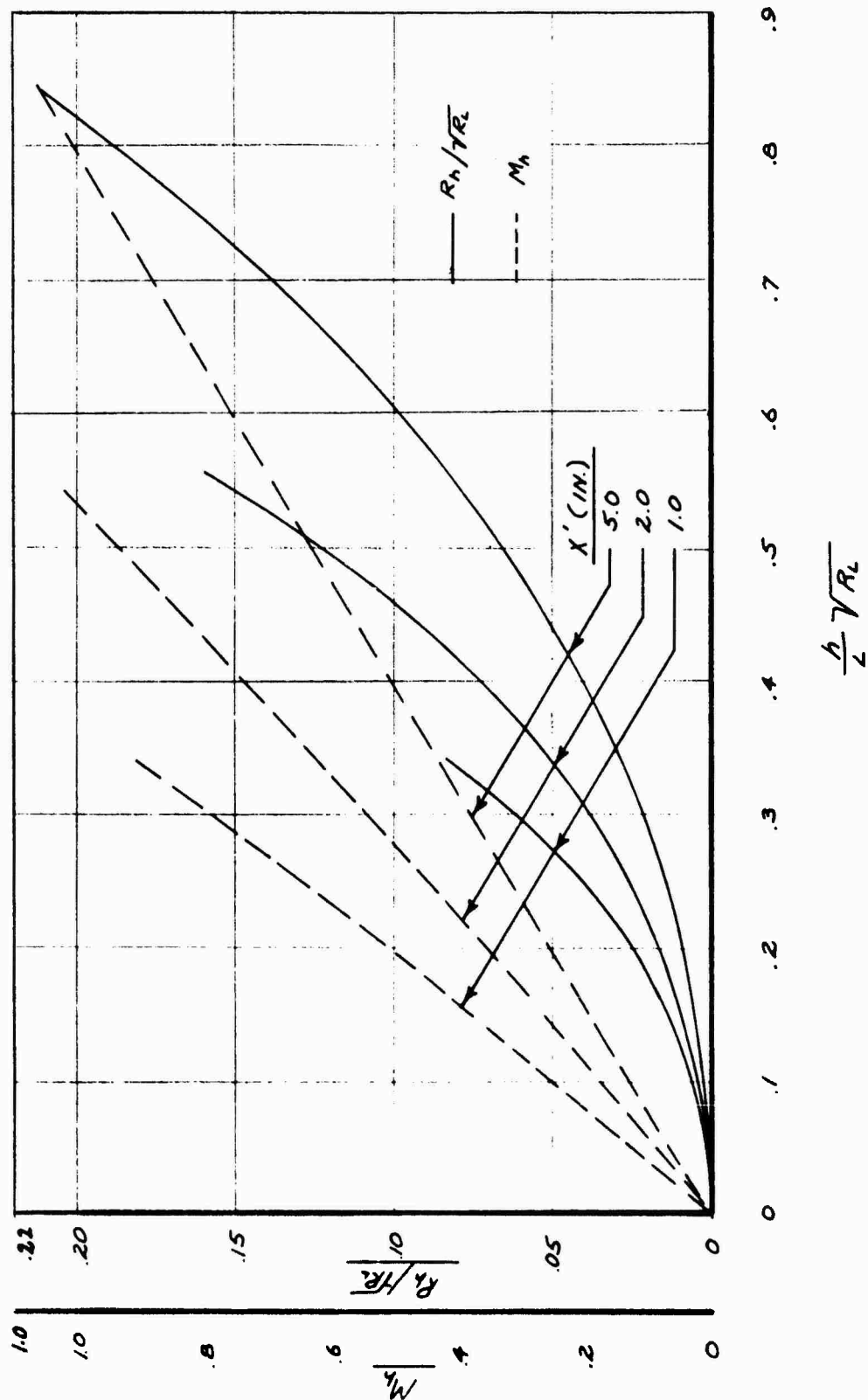


FIGURE 71

ROUGHNESS REYNOLDS NUMBER,  $R_h$ , AND MACH NUMBER AT HEIGHT OF ROUGHNESS PARTICLE,  $M_h$ , VS HEIGHT  $h$  AT  $M_r = 2.5$  AND SEVERAL CHORDWISE STATIONS

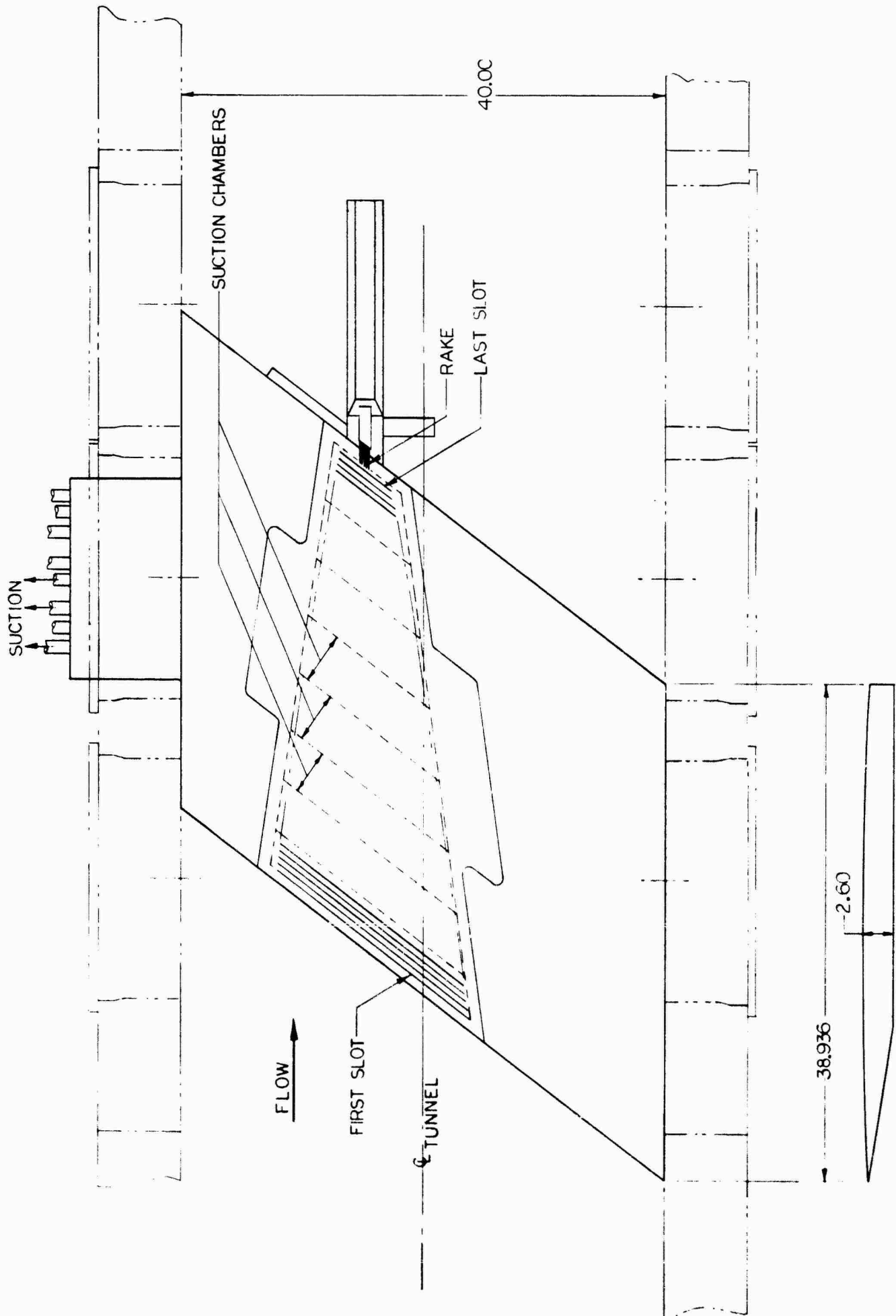


FIGURE 72 SKETCH OF 36° SWEEP SUCTION MODEL INSTALLATION AT AEDC TUNNEL A





FIGURE 73 PHOTOGRAPH OF 36° SWEEP WING SUCTION MODEL

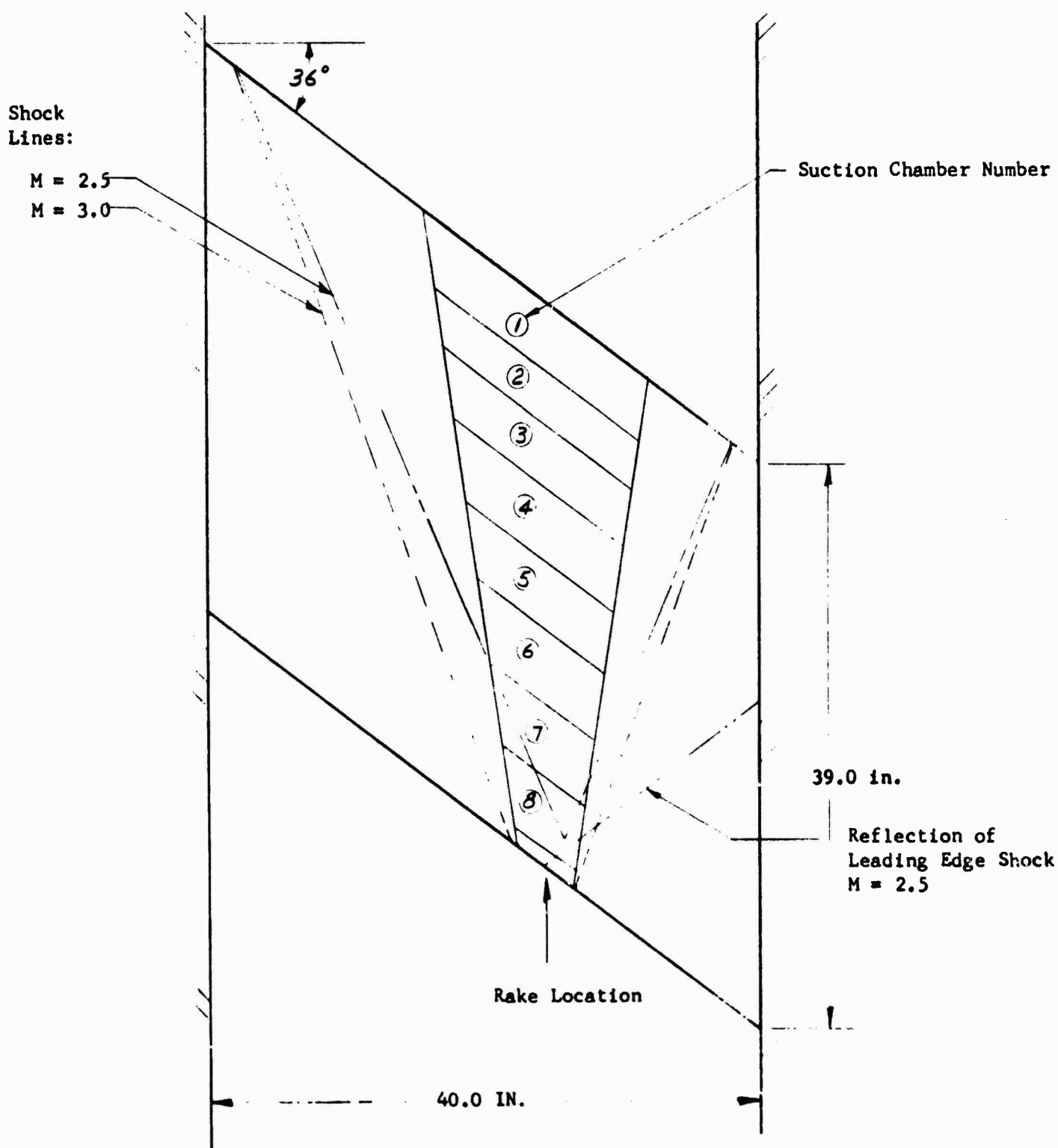


FIGURE 74

SHOCK LINES AND SUCTION AREA ON 36° SWEEP WING MODEL

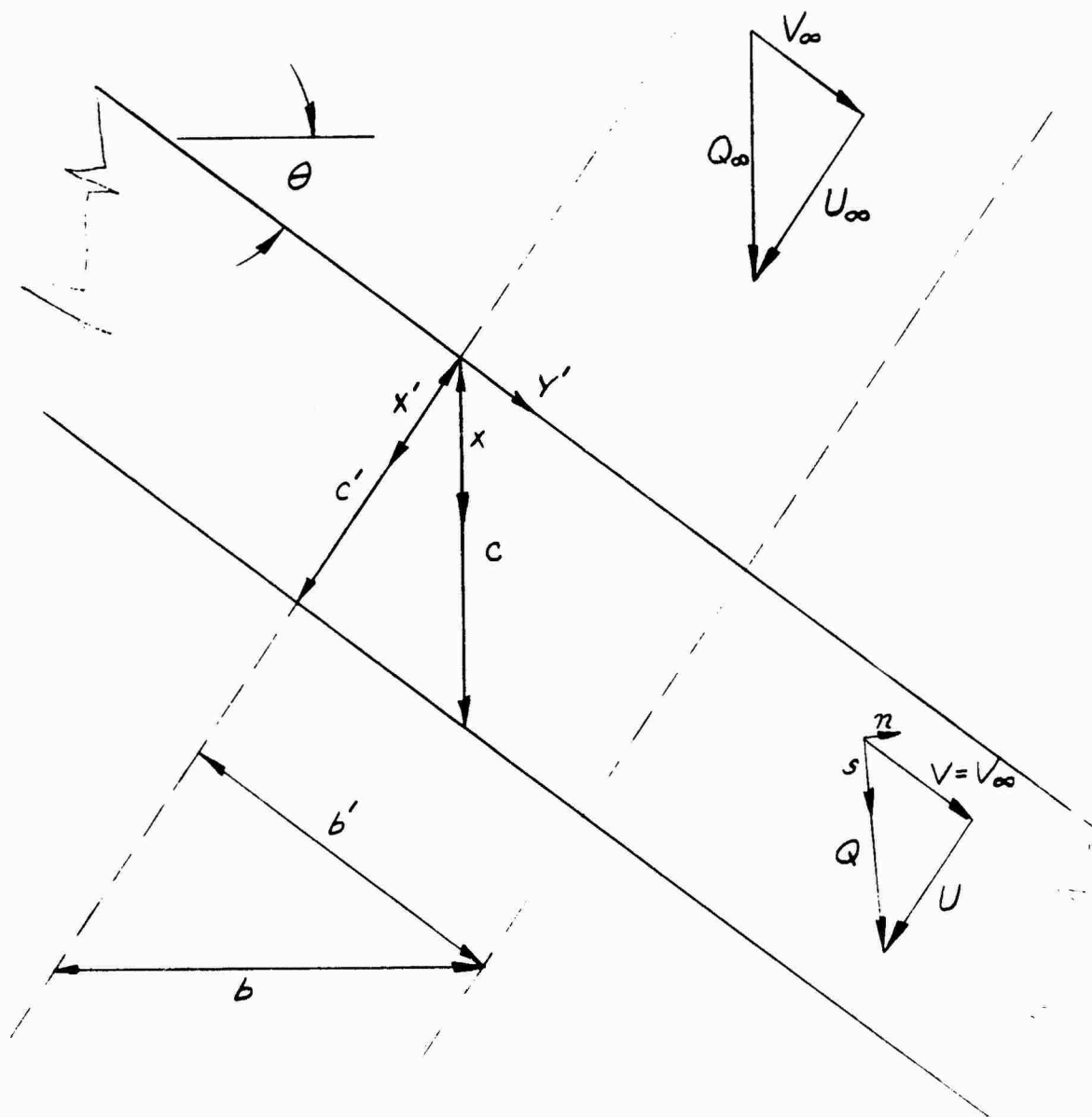


FIGURE 75

SWEPT WING COORDINATES AND VELOCITY COMPONENTS

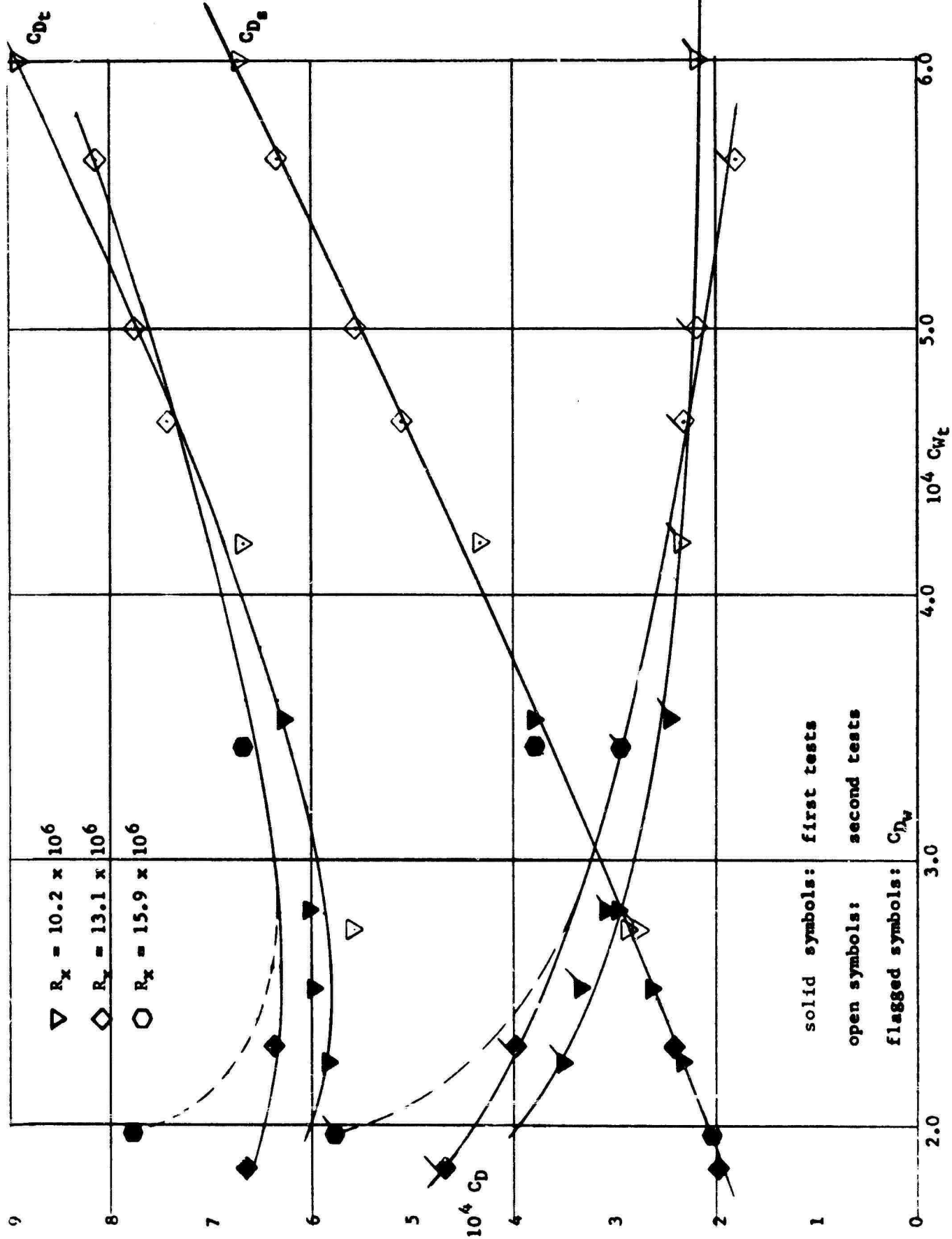


FIGURE 76  
 WAKE SUCTION AND TOTAL DRAG COEFFICIENTS VS TOTAL SUCTION COEFFICIENT  
 $M = 2.5$   $X_{rake} = 37.8$

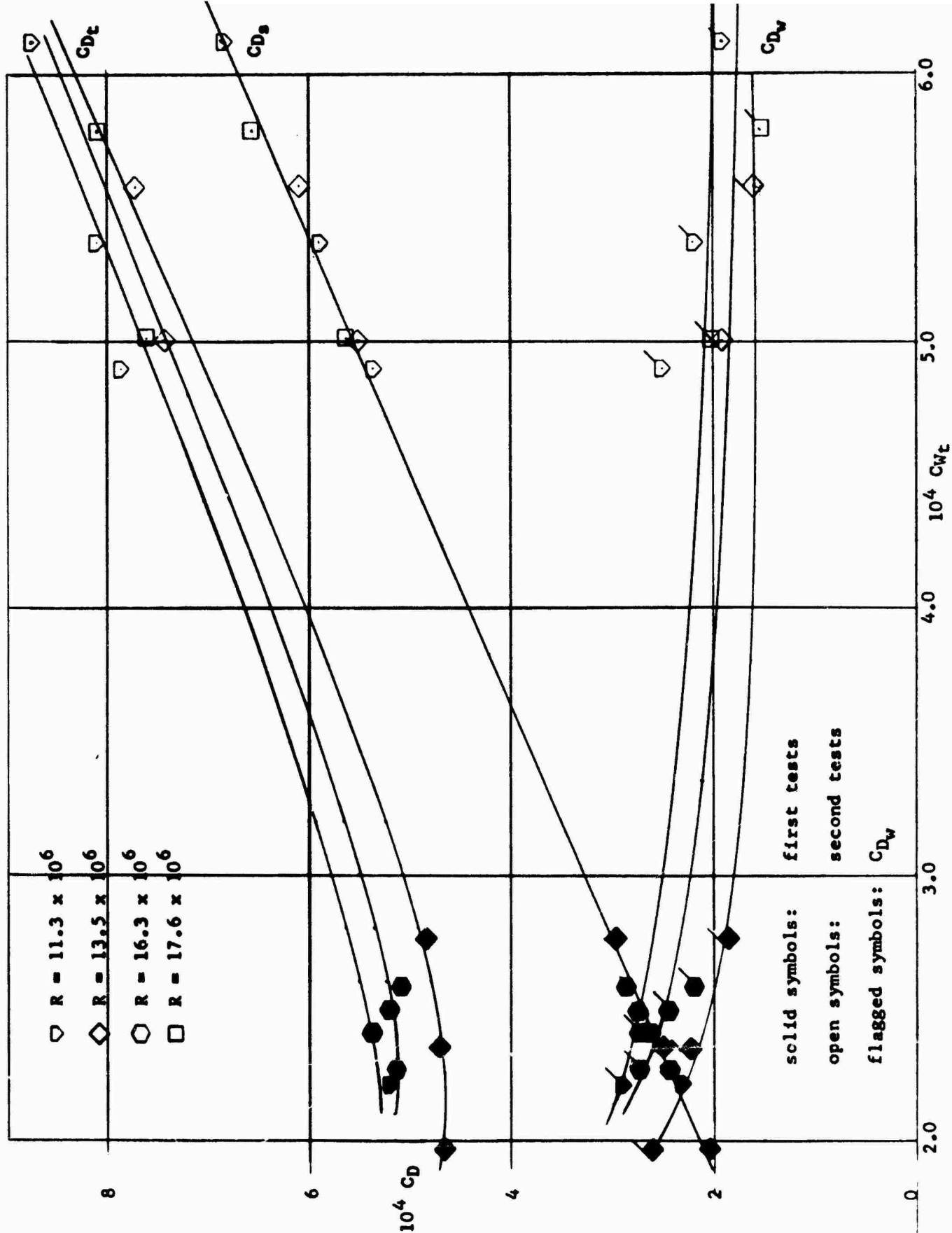


FIGURE 77  
 WAKE, SUCTION AND TOTAL DRAG COEFFICIENTS VS TOTAL SUCTION COEFFICIENT  
 $M = 2.5$   $x_{rake} = 32.8$  in.

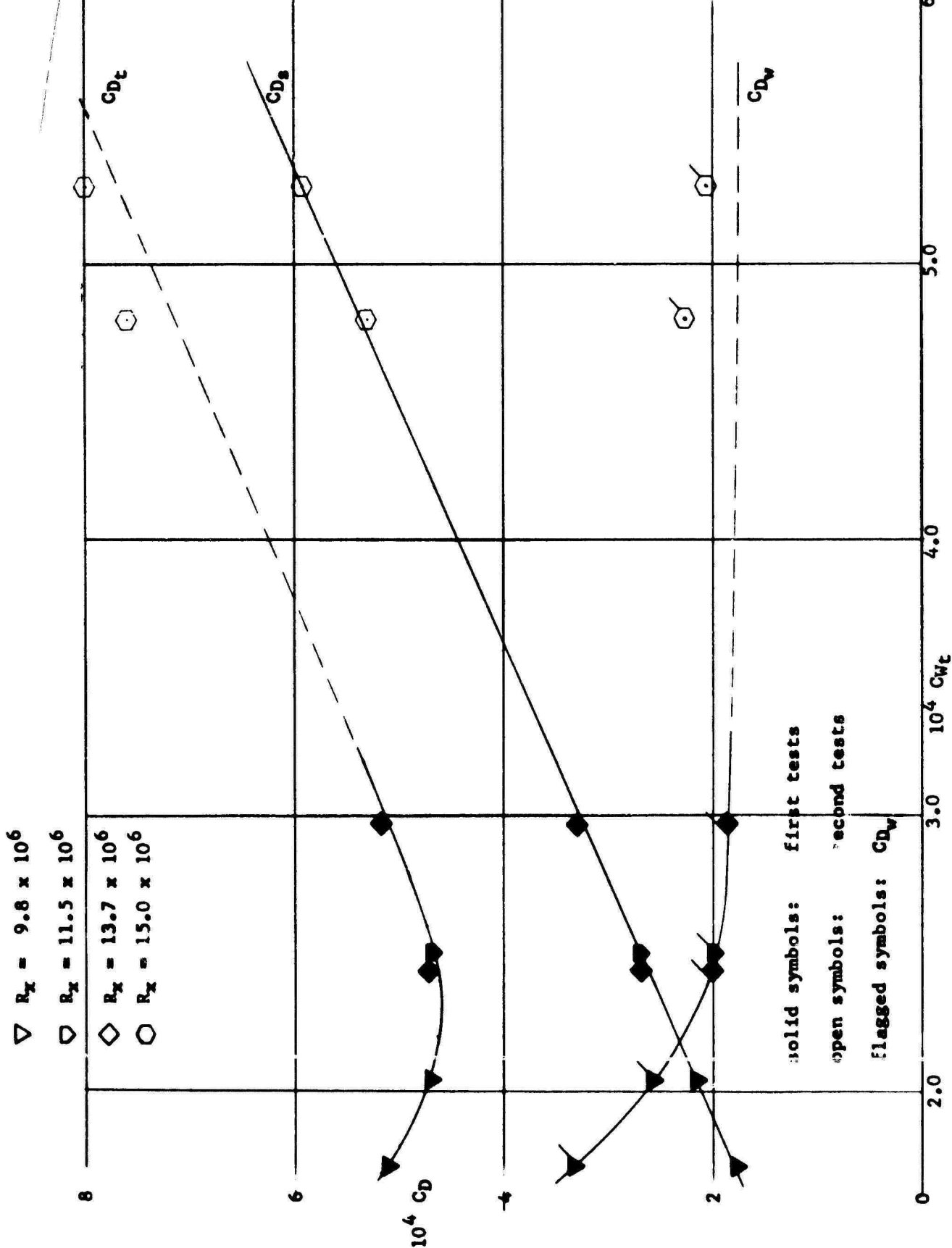


FIGURE 78  
WAKE, SUCTION AND TOTAL DRAG COEFFICIENTS VS TOTAL SUCTION COEFFICIENTS  
 $M = 2.5$   $x_{rake} = 27.7$  in.

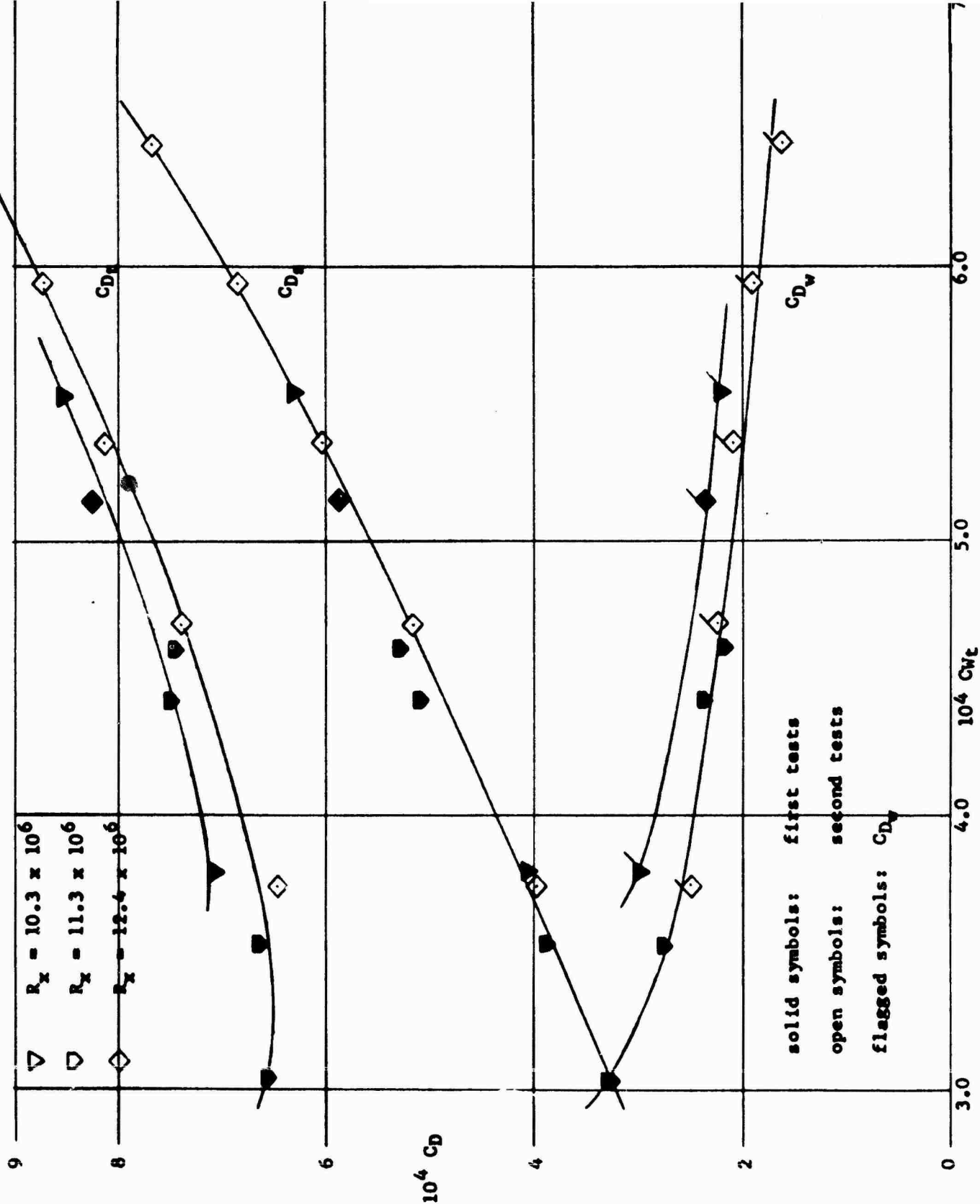


FIGURE 79a

WAKE, SUCTION AND TOTAL DRAG COEFFICIENTS VS TOTAL SUCTION COEFFICIENTS

$M = 3.0$

$x_{rake} = 37.8 \text{ in.}$

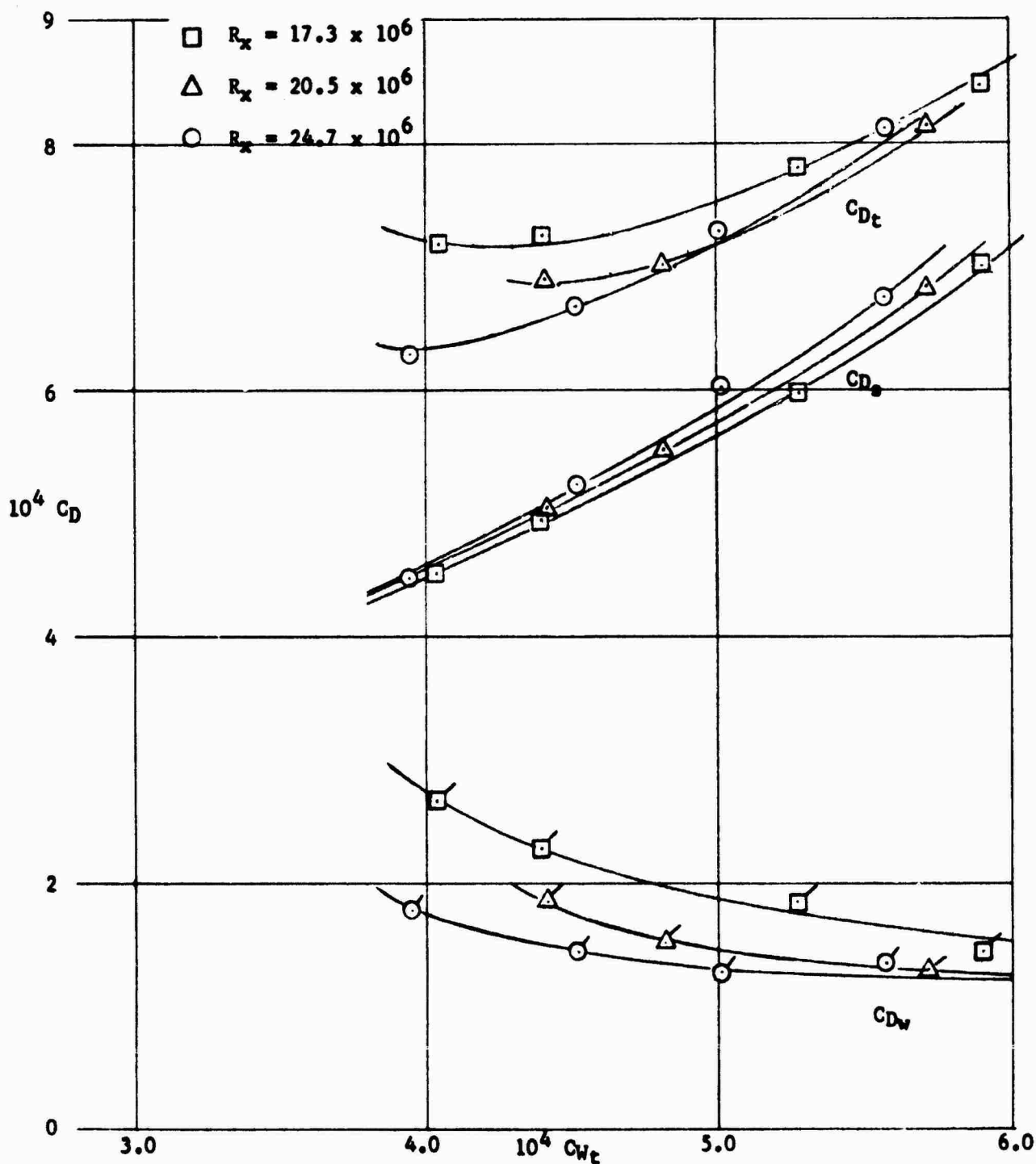


FIGURE 79b

WAKE, SUCTION AND TOTAL DRAG COEFFICIENTS VS TOTAL SUCTION COEFFICIENTS

$M = 3.0$

$x_{rake} = 37.8 \text{ in.}$



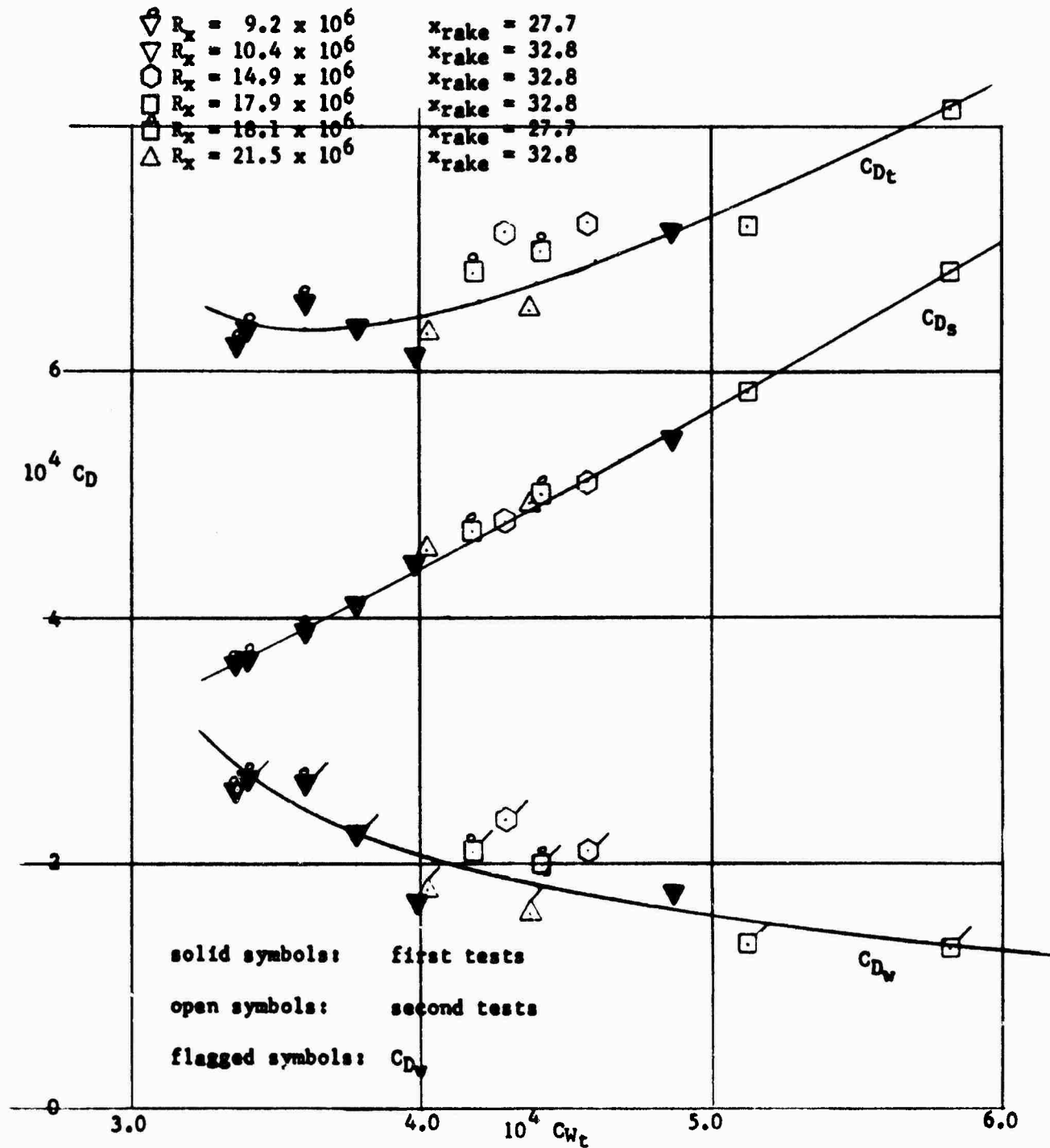


FIGURE 80

WAKE, SUCTION AND TOTAL DRAG COEFFICIENTS VS TOTAL SUCTION COEFFICIENT

$M = 3.0$

$x_{rake} = 27.7$  and  $32.8$  in.

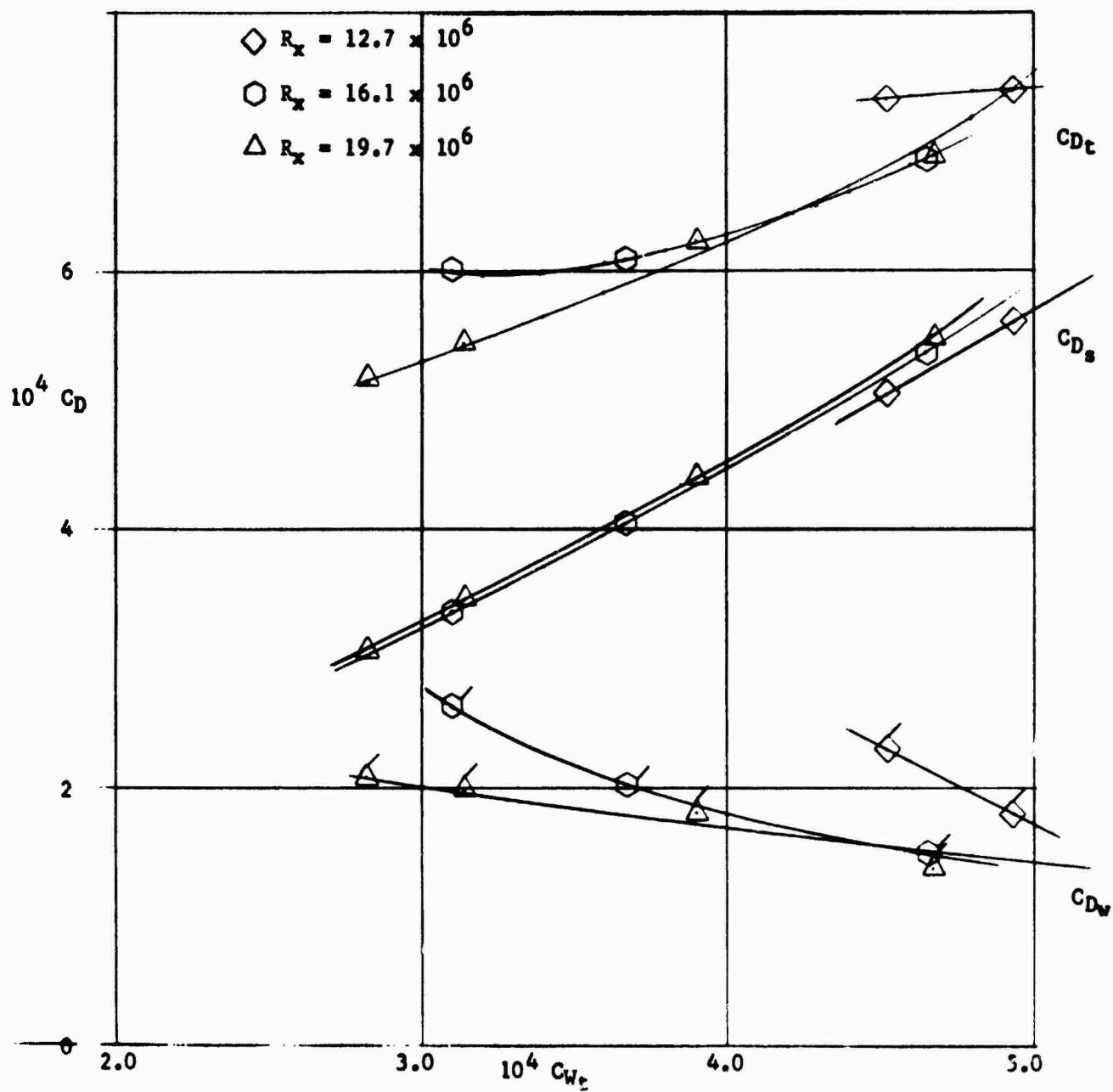


FIGURE 81

WAKE, SUCTION AND TOTAL DRAG COEFFICIENTS VS TOTAL SUCTION COEFFICIENTS

$M = 3.5$

$x_{\text{rake}} = 37.8 \text{ in.}$

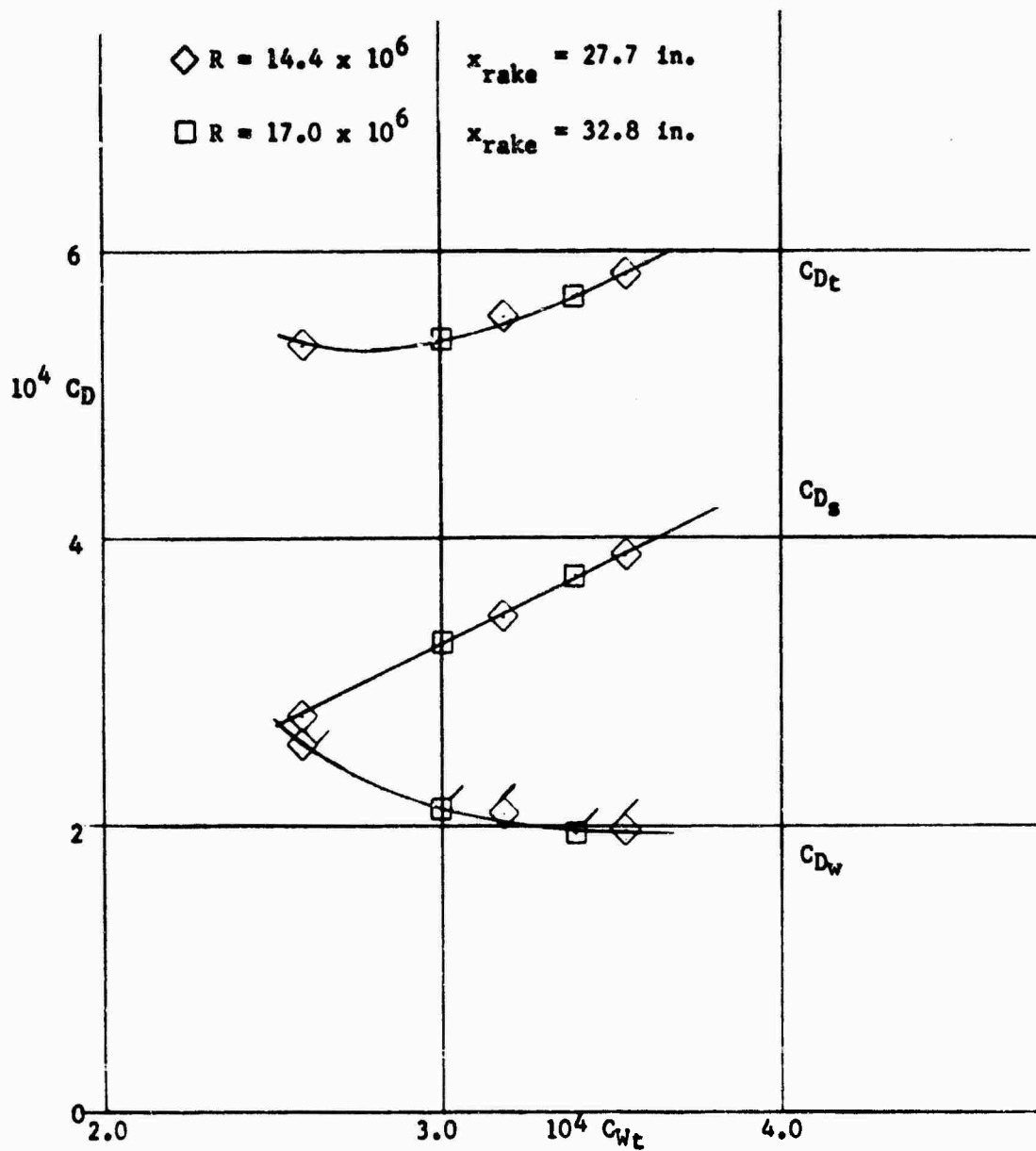


FIGURE 82

WAKE, SUCTION, AND TOTAL DRAG COEFFICIENTS VS TOTAL SUCTION COEFFICIENT

$M = 3.5$

$x_{\text{rake}} = 32.8 \text{ and } 27.7 \text{ in.}$

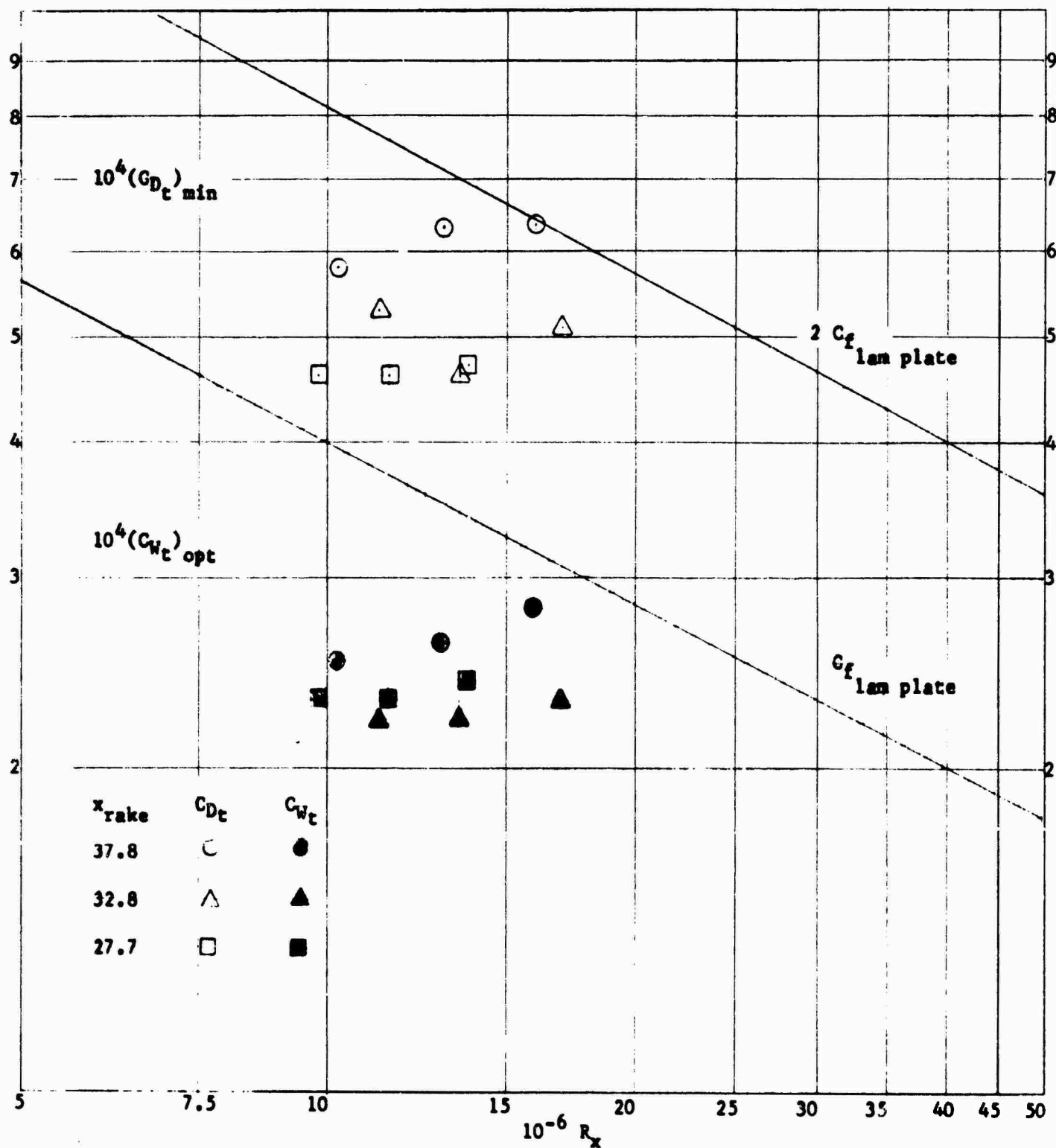


FIGURE 83

MINIMUM TOTAL DRAG AND OPTIMUM TOTAL SUCTION COEFFICIENTS  
VS LENGTH REYNOLDS NUMBERS

$M = 2.5$

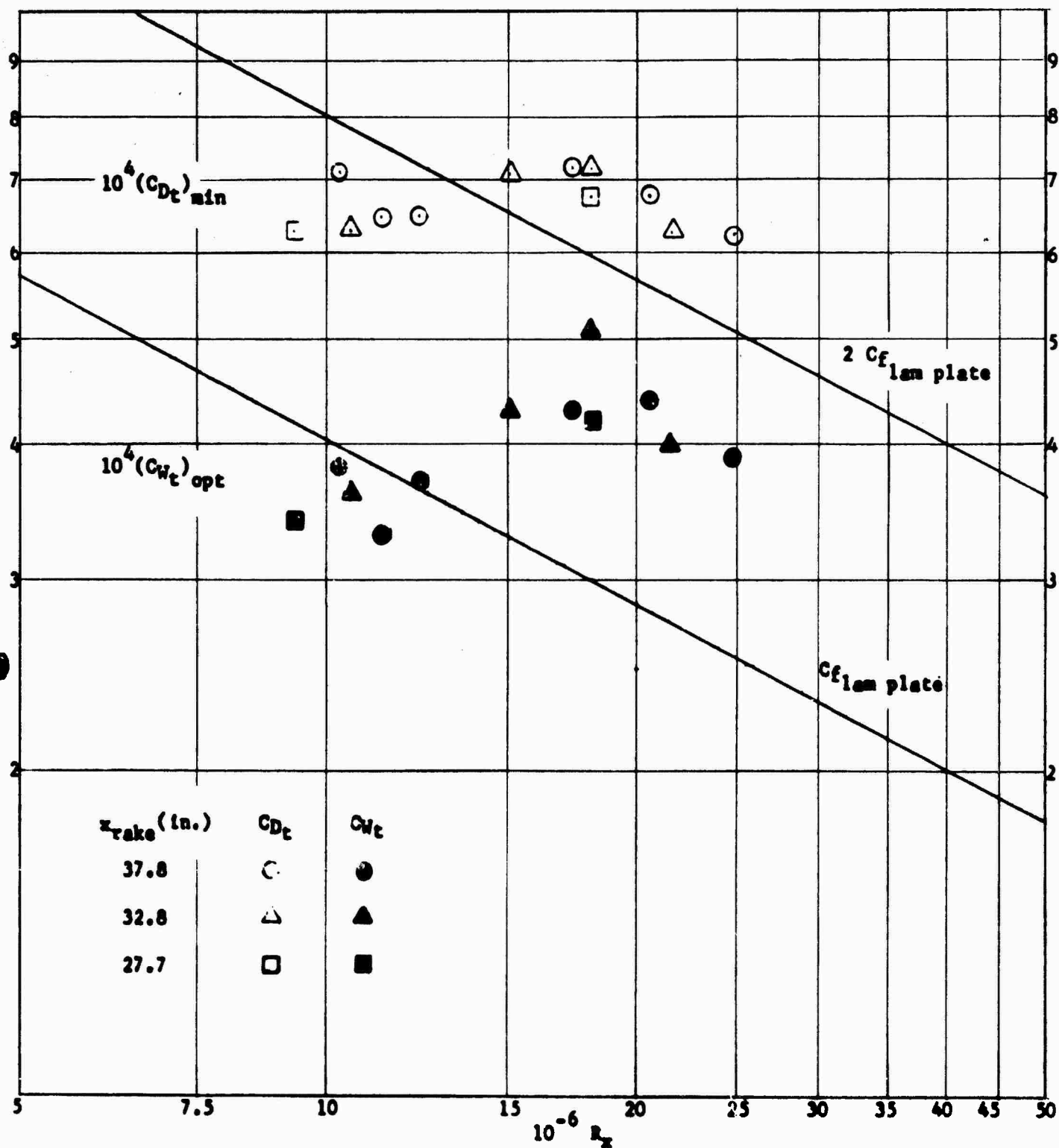


FIGURE 84

MINIMUM TOTAL DRAG AND OPTIMUM TOTAL SUCTION COEFFICIENTS  
VS LENGTH REYNOLDS NUMBER

$M = 3.0$

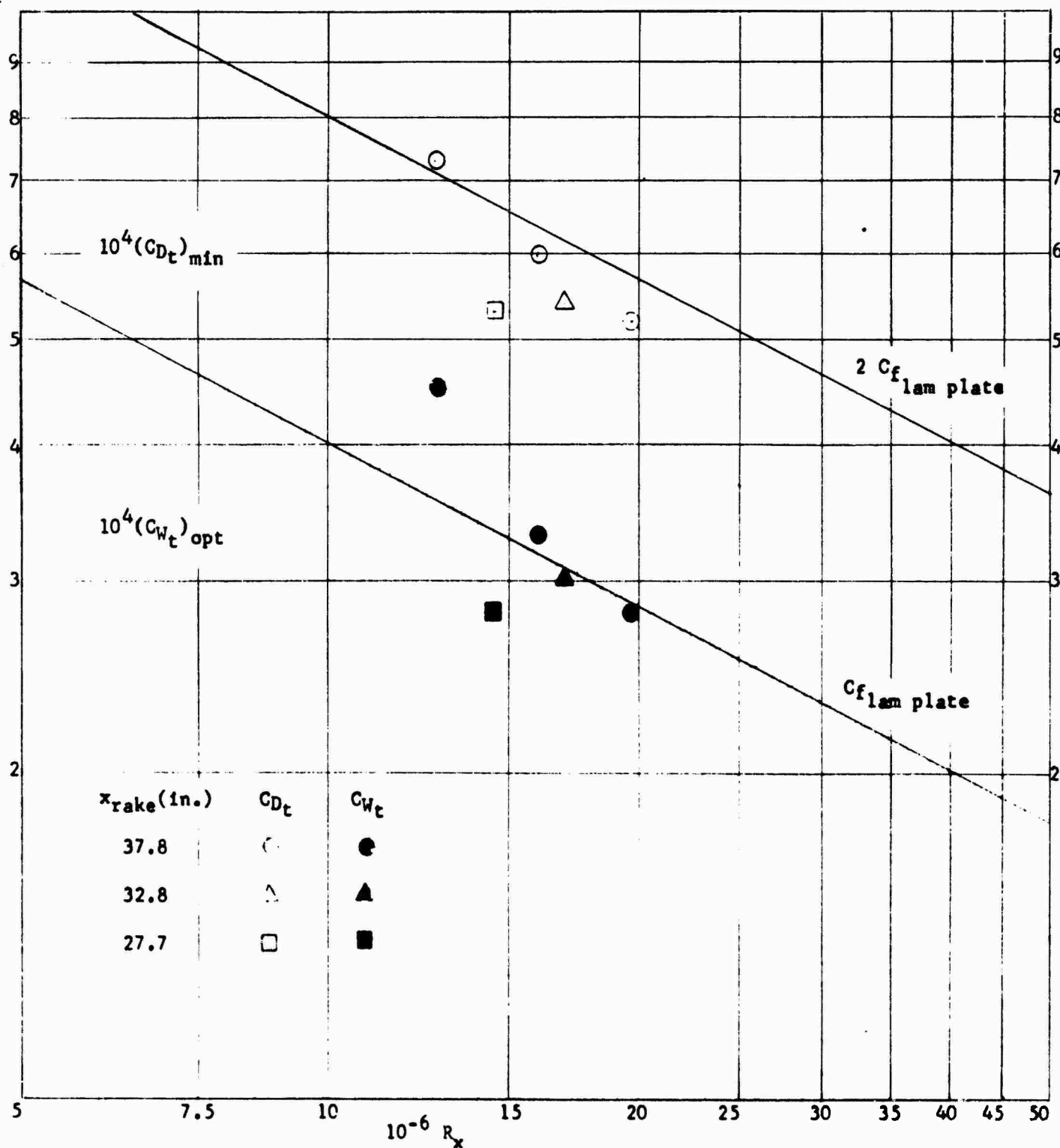


FIGURE 85

TOTAL MINIMUM DRAG AND OPTIMUM SUCTION COEFFICIENTS  
VS LENGTH REYNOLDS NUMBER

$M = 3.5$

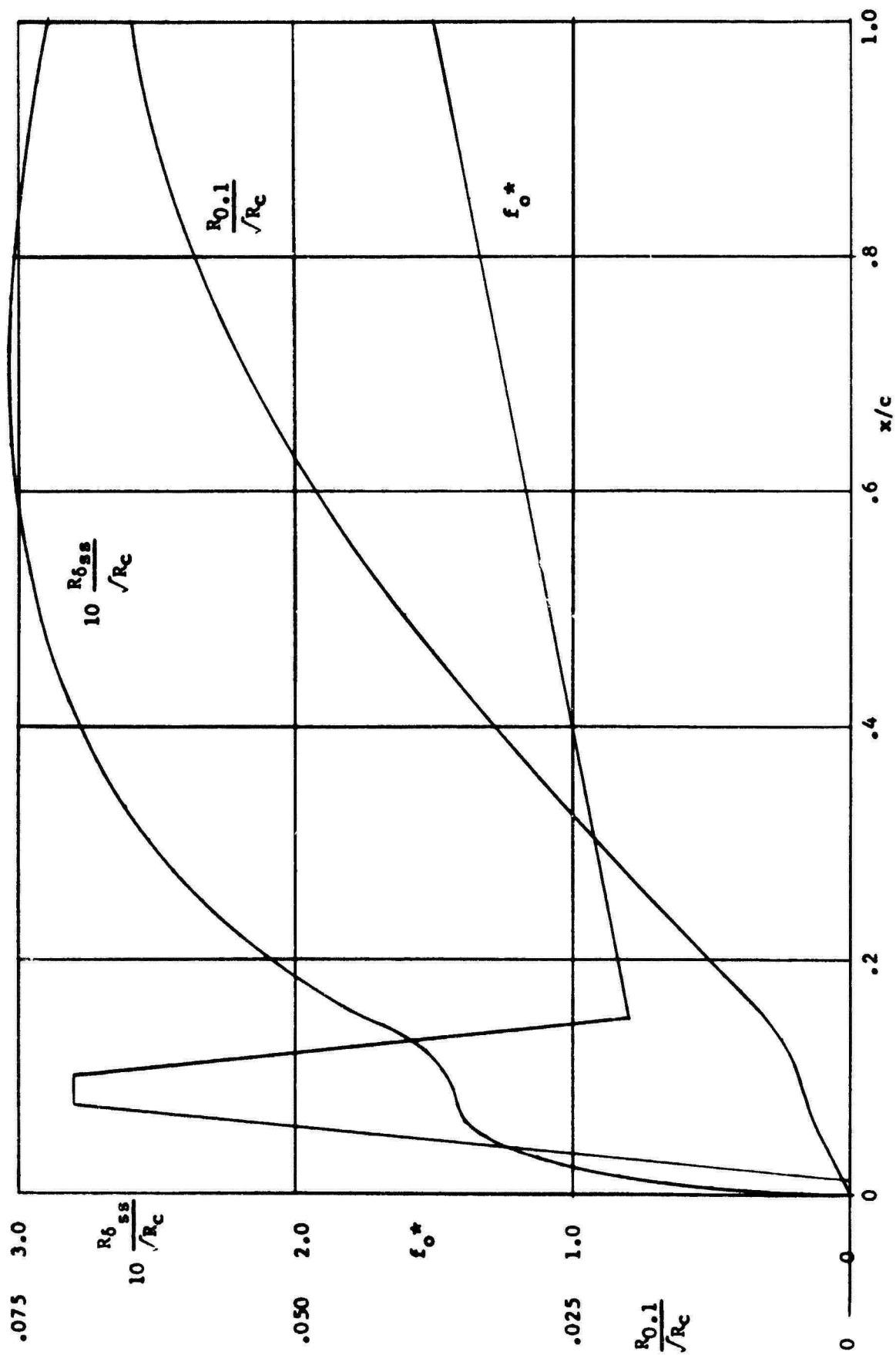


FIGURE 86a  
BOUNDARY LAYER CALCULATION  $M = 2.5$   $C_{wt} \sqrt{R_c} = 1.222$

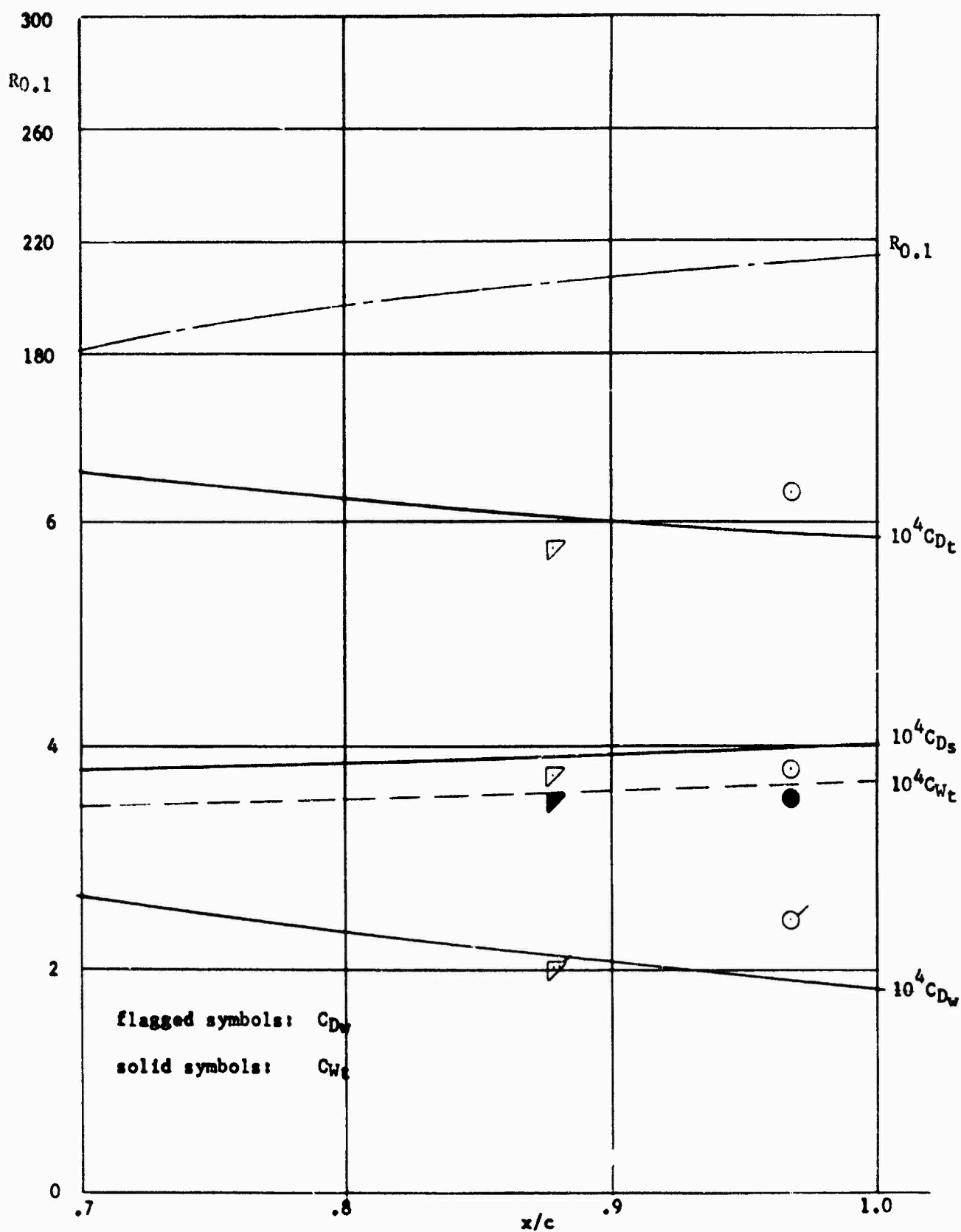


FIGURE 86b

THEORETICAL AND EXPERIMENTAL DRAG COEFFICIENTS AND CROSSFLOW REYNOLDS NO.  
 $M = 2.5$ ,  $c_{wt} / R_c = 1.222$ ,  $R_c = 11.1 \times 10^6$



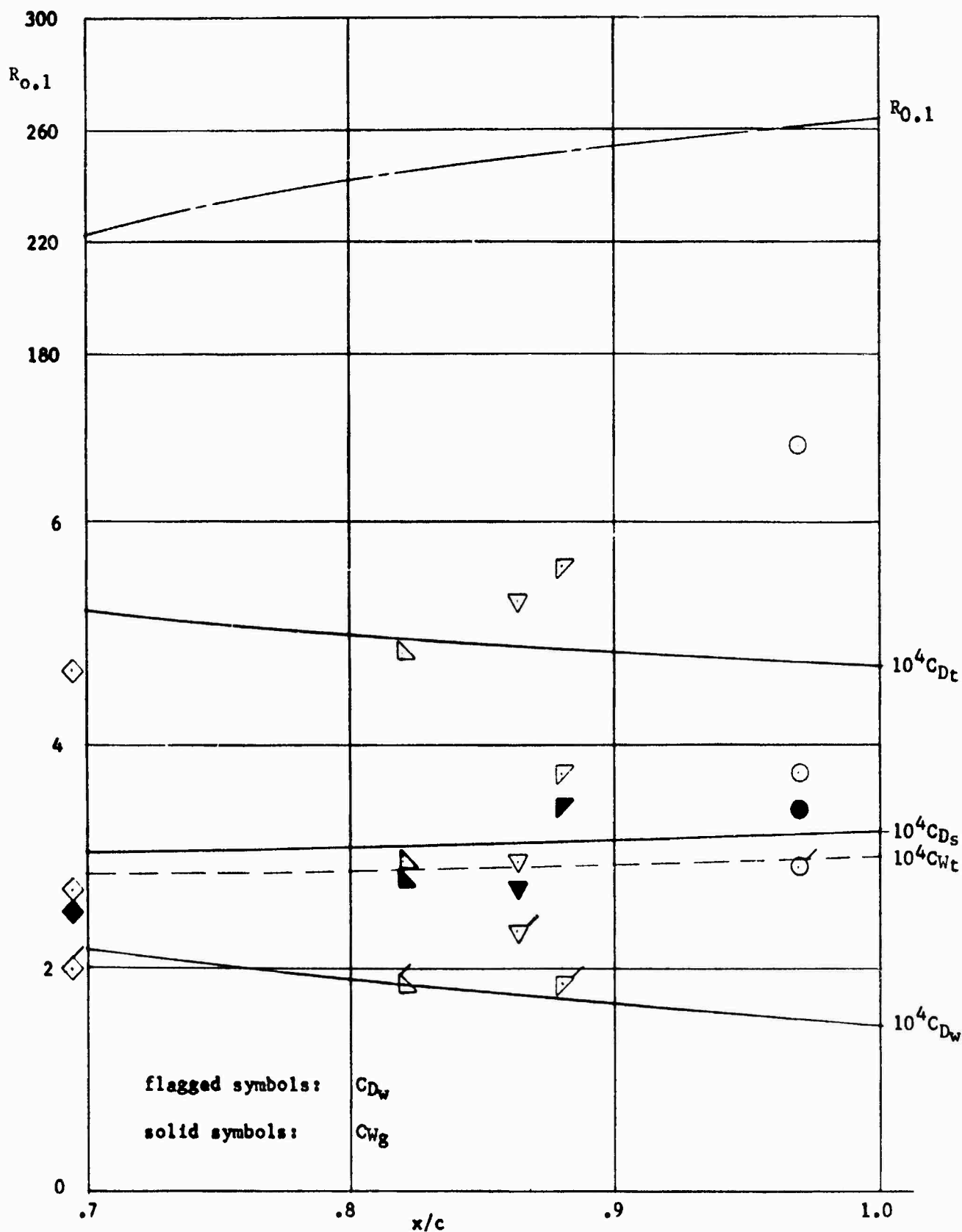


FIGURE 86c  
THEORETICAL AND EXPERIMENTAL DRAG COEFFICIENTS, AND CROSSFLOW  
REYNOLDS NUMBERS  $M = 2.5$ ,  $C_{wt} / R_c = 1.222$ ,  $R_c = 16.6 \times 10^6$

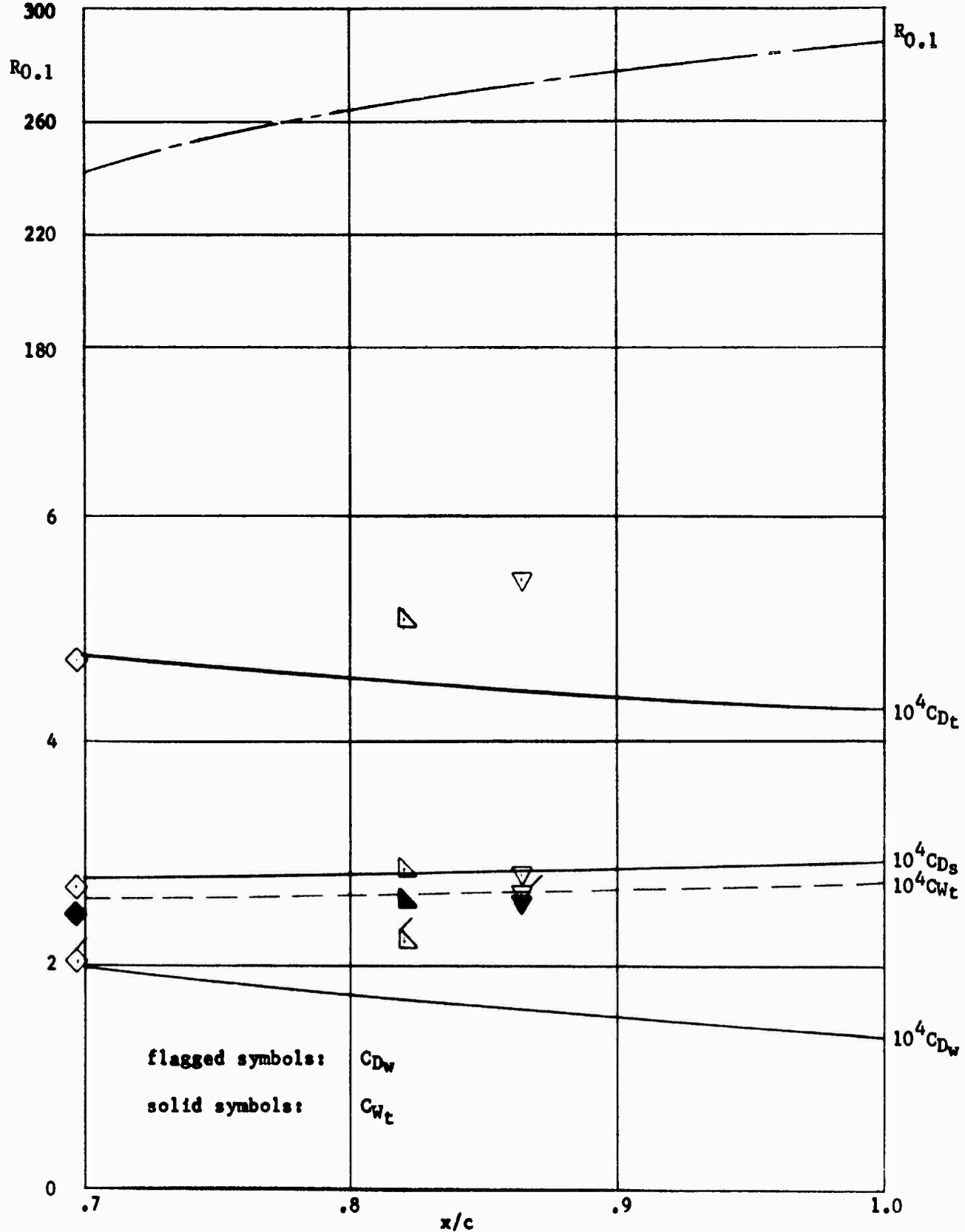


FIGURE 86d  
THEORETICAL AND EXPERIMENTAL DRAG COEFFICIENTS, AND CROSSFLOW REYNOLDS NO.  
 $M = 2.5$ ,  $C_{w_t} / R_c = 1.222$ ,  $R_c = 19.8 \times 10^6$

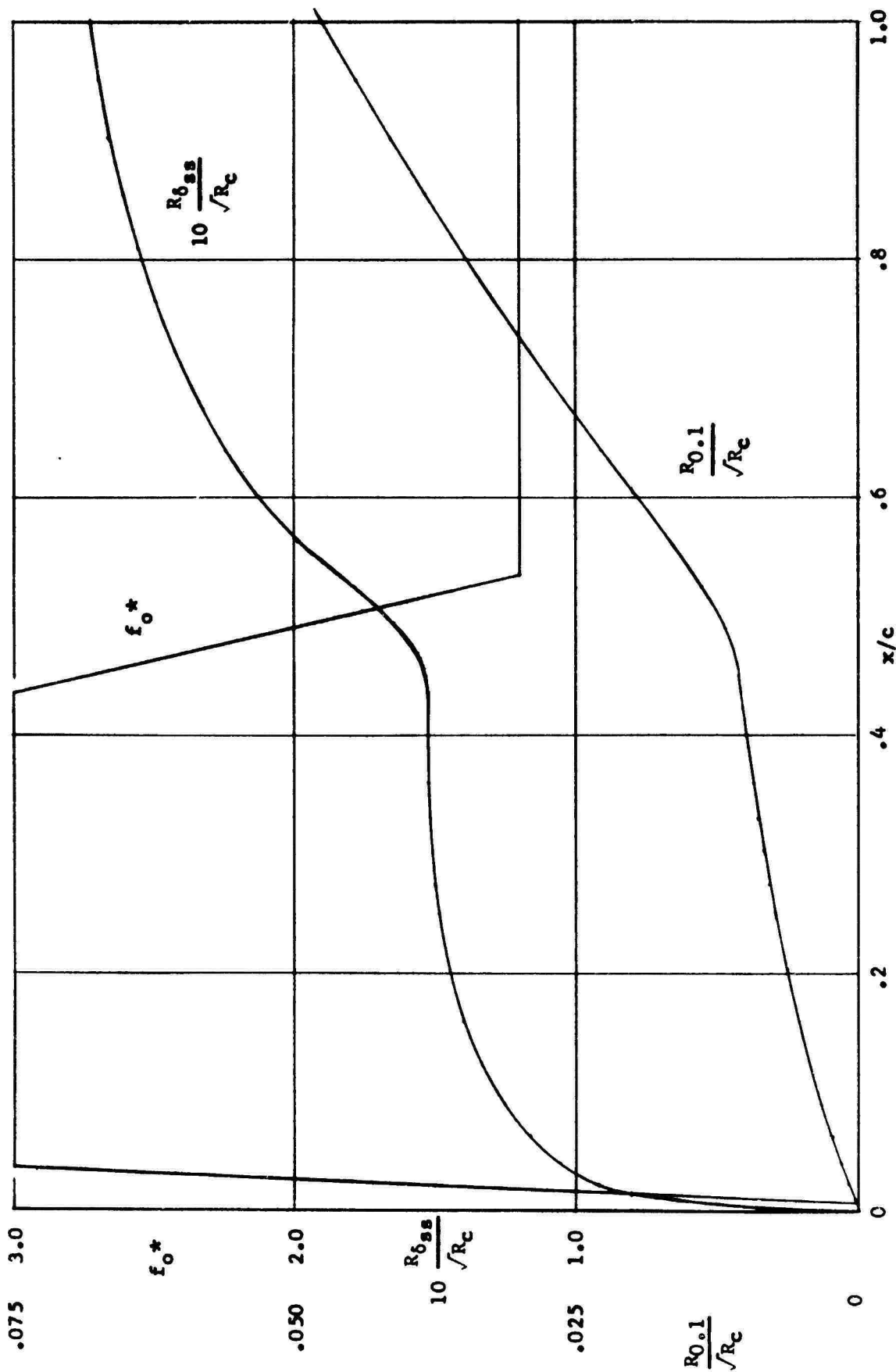


FIGURE 87a  
BOUNDARY LAYER CALCULATION  
 $M = 2.5$ ,  $C_{wt} \sqrt{R_c} = 2.013$

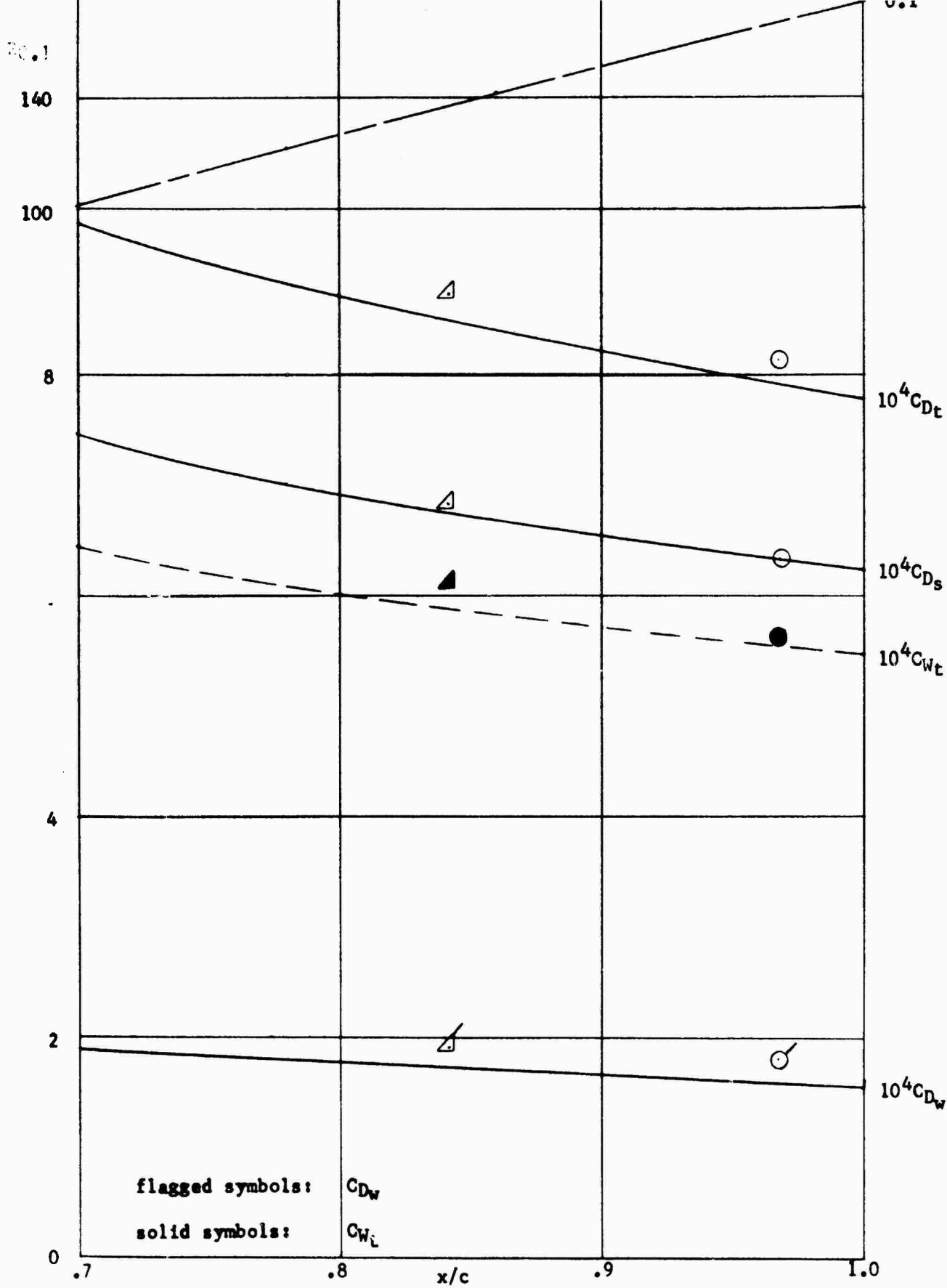


FIGURE 87b  
THEORETICAL AND EXPERIMENTAL DRAG COEFFICIENTS AND CROSSFLOW REYNOLDS NO.  
 $M = 2.5$ ,  $C_{Wt} \sqrt{R_c} = 2.013$ ,  $R_c = 13.5 \times 10^6$

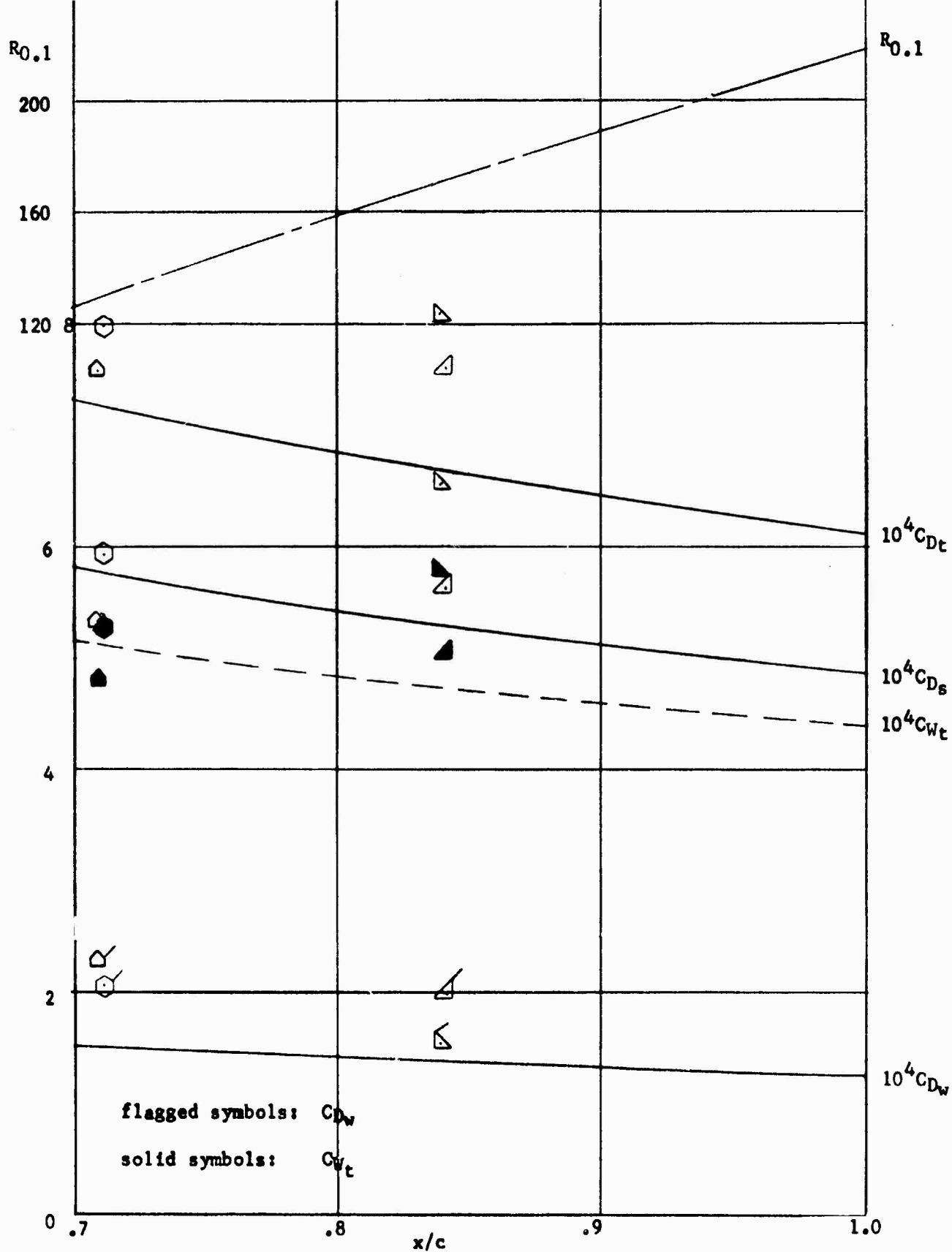


FIGURE 87c

THEORETICAL AND EXPERIMENTAL DRAG COEFFICIENTS, AND CROSSFLOW REYNOLDS NUMBERS  
 $M = 2.5$ ,  $C_{Wt}/R_c = 2.013$ ,  $R_c = 21.0 \times 10^6$

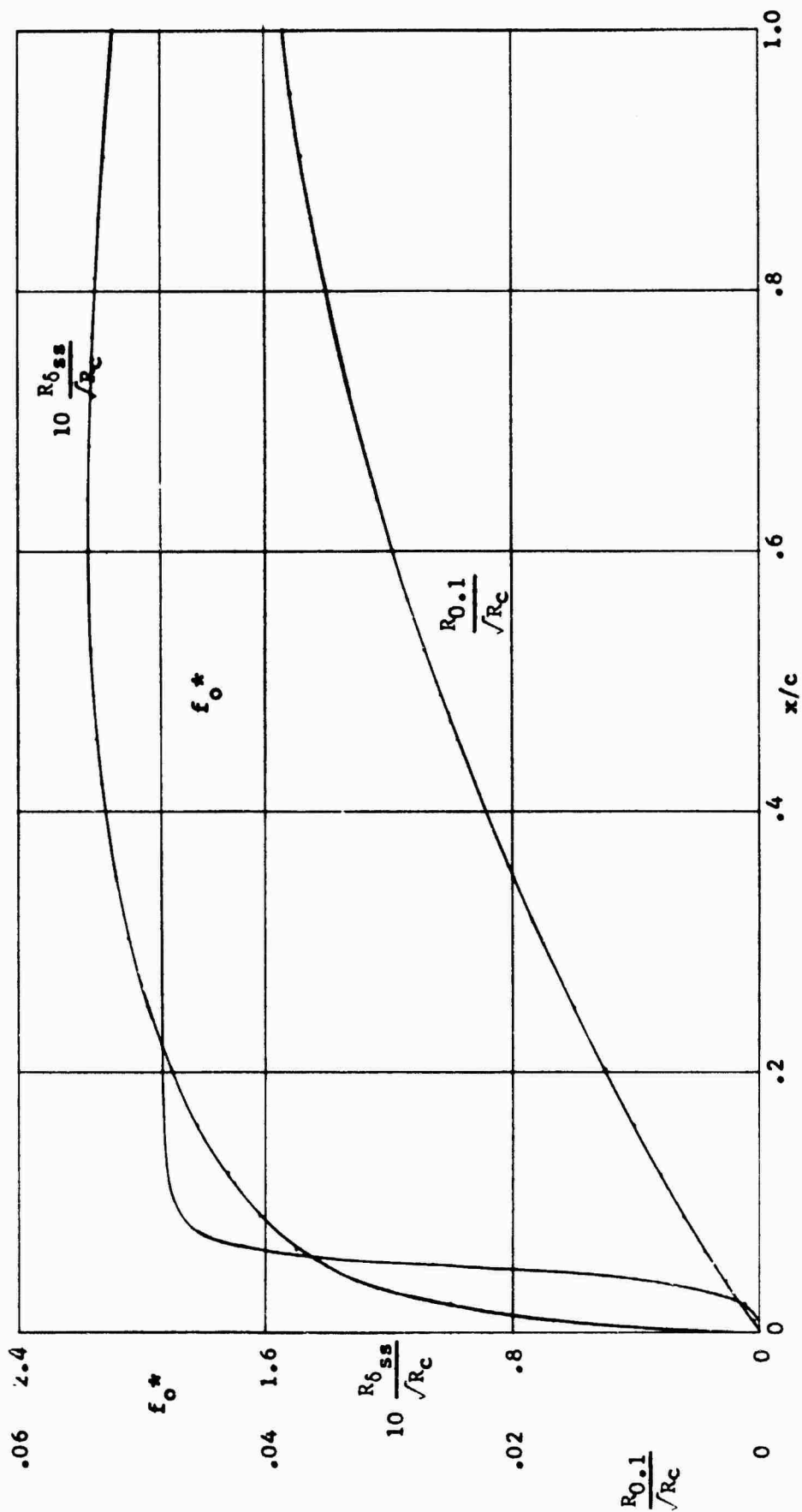


FIGURE 88a

BOUNDARY LAYER CALCULATION  $M = 3.0$ ,  $C_{wt} / R_c = 1.840$

$R_{0.1}$   
180

140

100

8

6

4

2

0

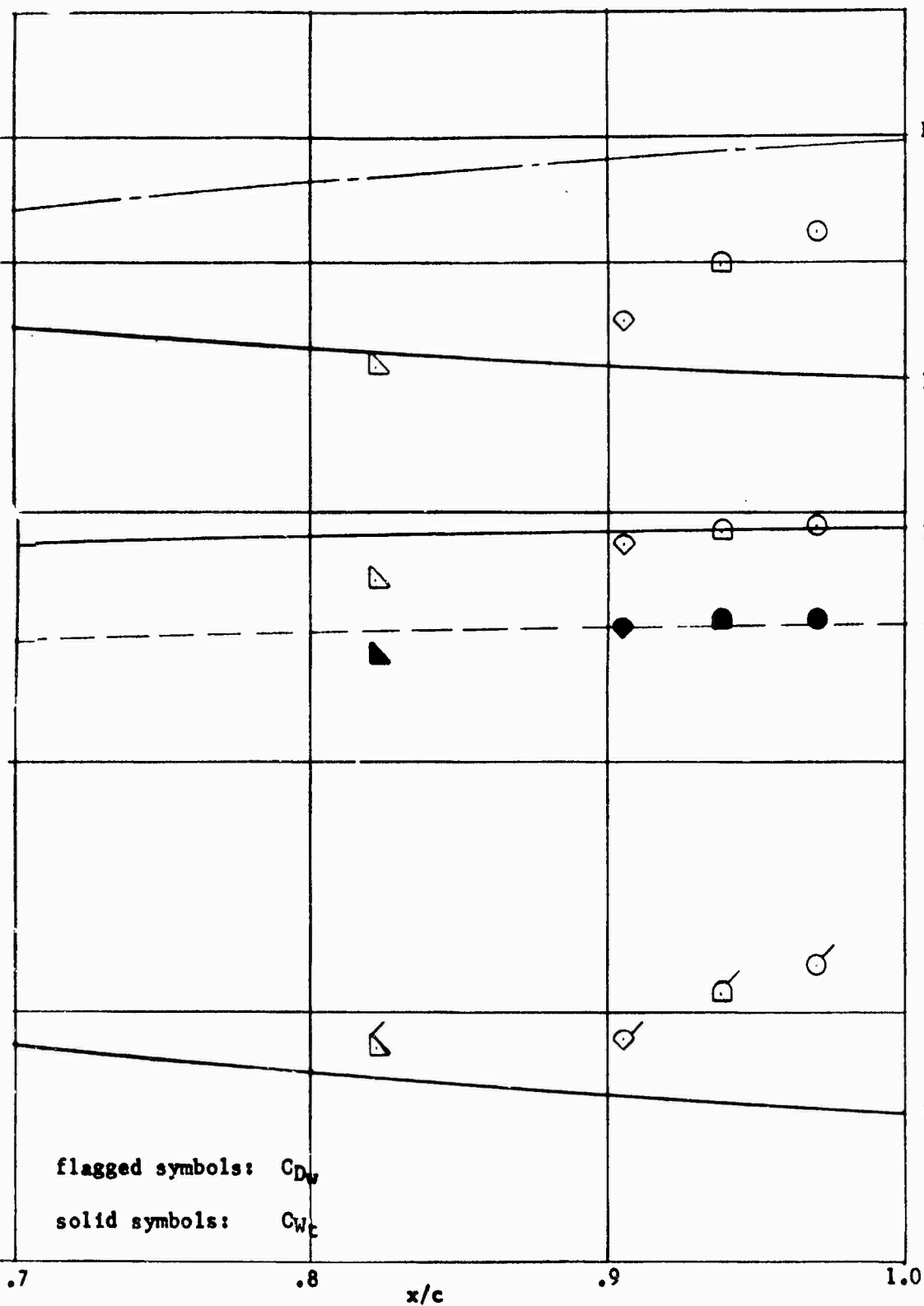


FIGURE 88b

THEORETICAL AND EXPERIMENTAL DRAG COEFFICIENTS, AND CROSSFLOW REYNOLDS NUMBERS  
 $M = 3.0$ ,  $C_{wt} \sqrt{R_c} = 1.840$ ,  $R_c = 13.0 \times 10^6$

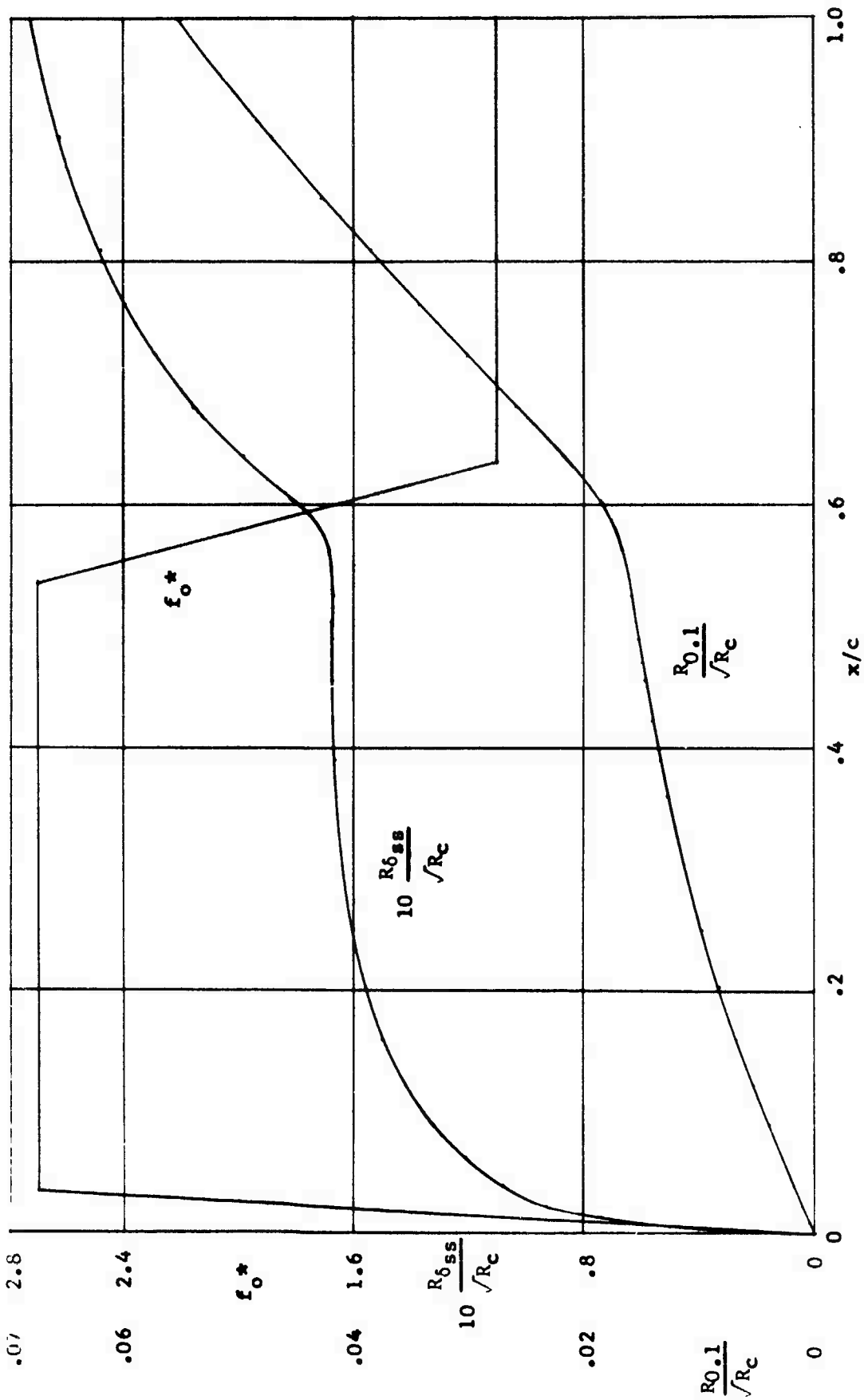


FIGURE 89a  
BOUNDARY LAYER CALCULATION,  $M = 3.0$ ,  $C_{wt}/R_c = 1.982$



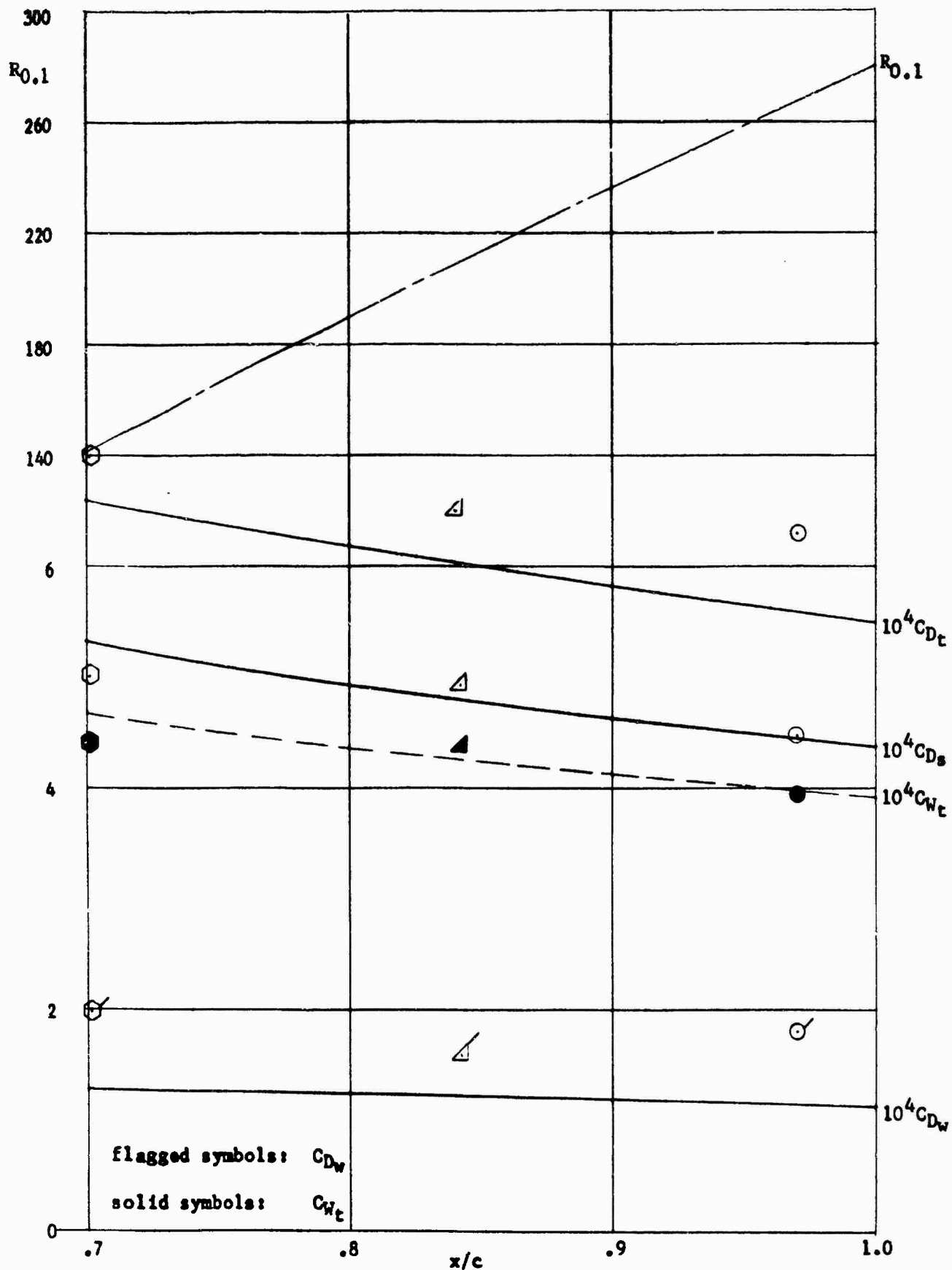


FIGURE 89b  
THEORETICAL AND EXPERIMENTAL DRAG COEFFICIENTS, AND CROSSFLOW  
REYNOLDS NUMBERS  $M = 3.0$ ,  $C_{wt} / R_c = 1.982$ ,  $R_c = 25.5 \times 10^6$

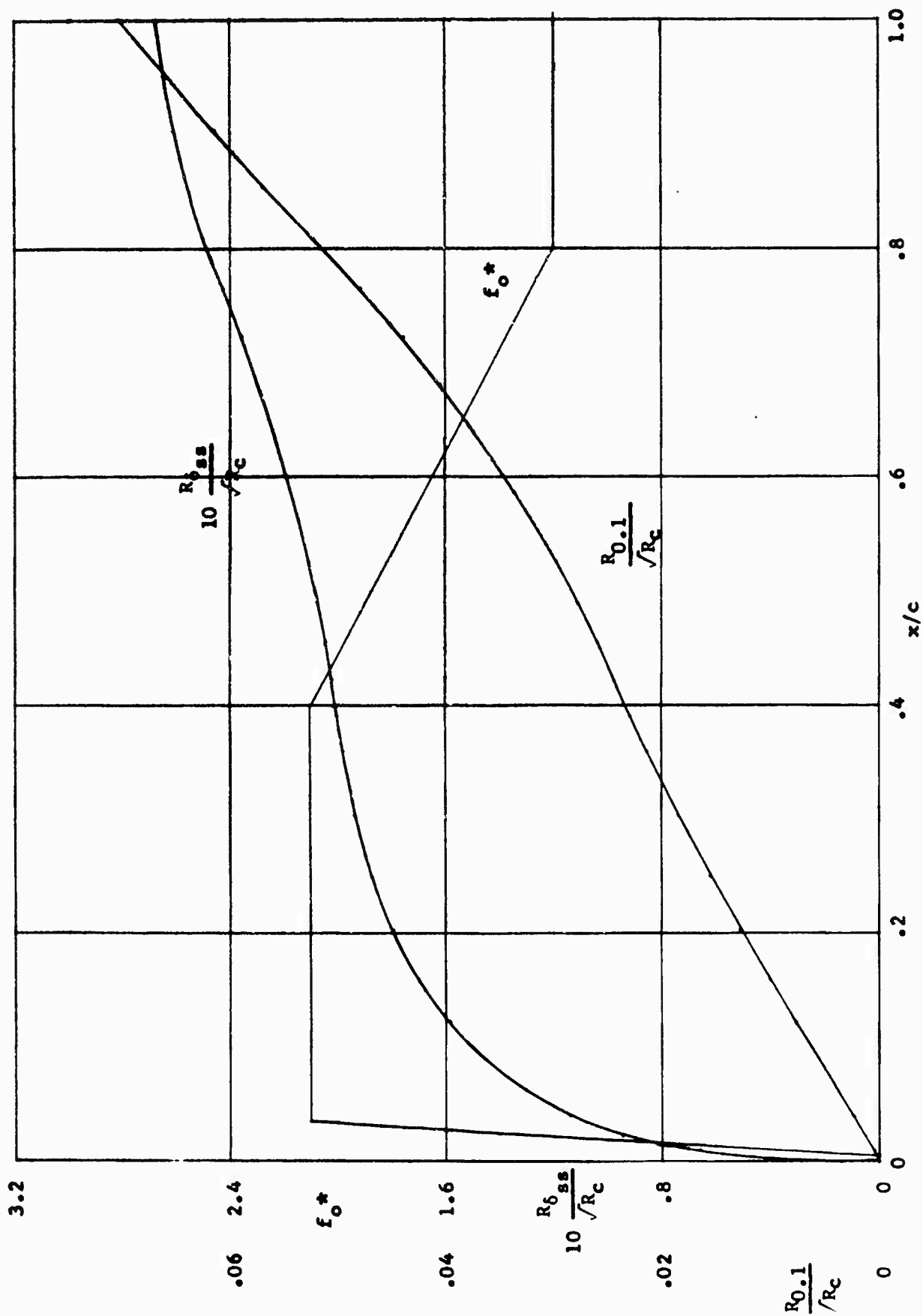


FIGURE 90a  
BOUNDARY LAYER CALCULATION,  $M = 3.5$ ,  $C_{wt}/\sqrt{R_c} = 1.698$

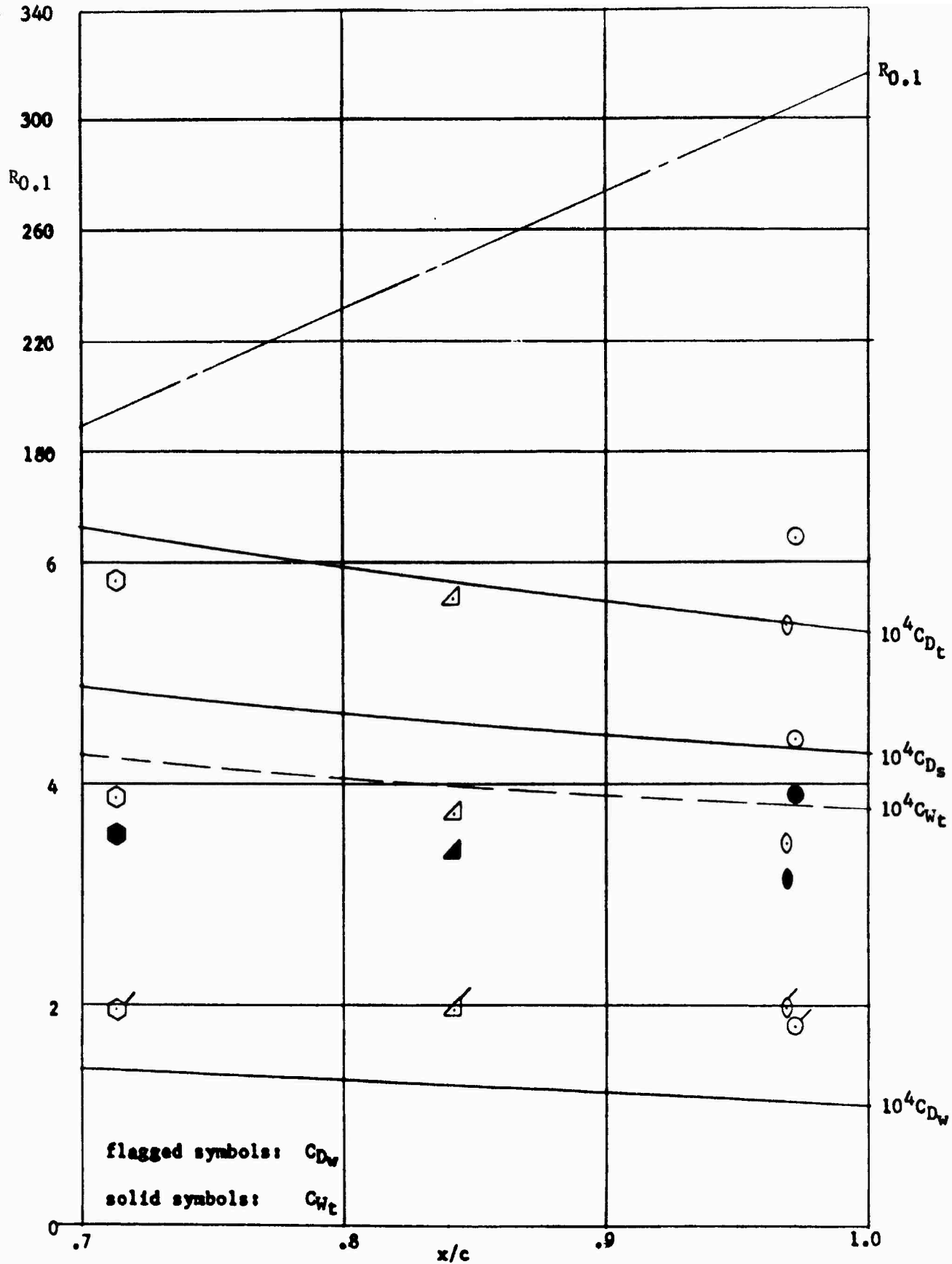


FIGURE 90b  
THEORETICAL AND EXPERIMENTAL DRAG COEFFICIENTS, AND CROSSFLOW  
REYNOLDS NUMBERS  $M = 3.5$ ,  $C_{Wt} / R_c = 1.698$ ,  $R_c = 20.2 \times 10^6$

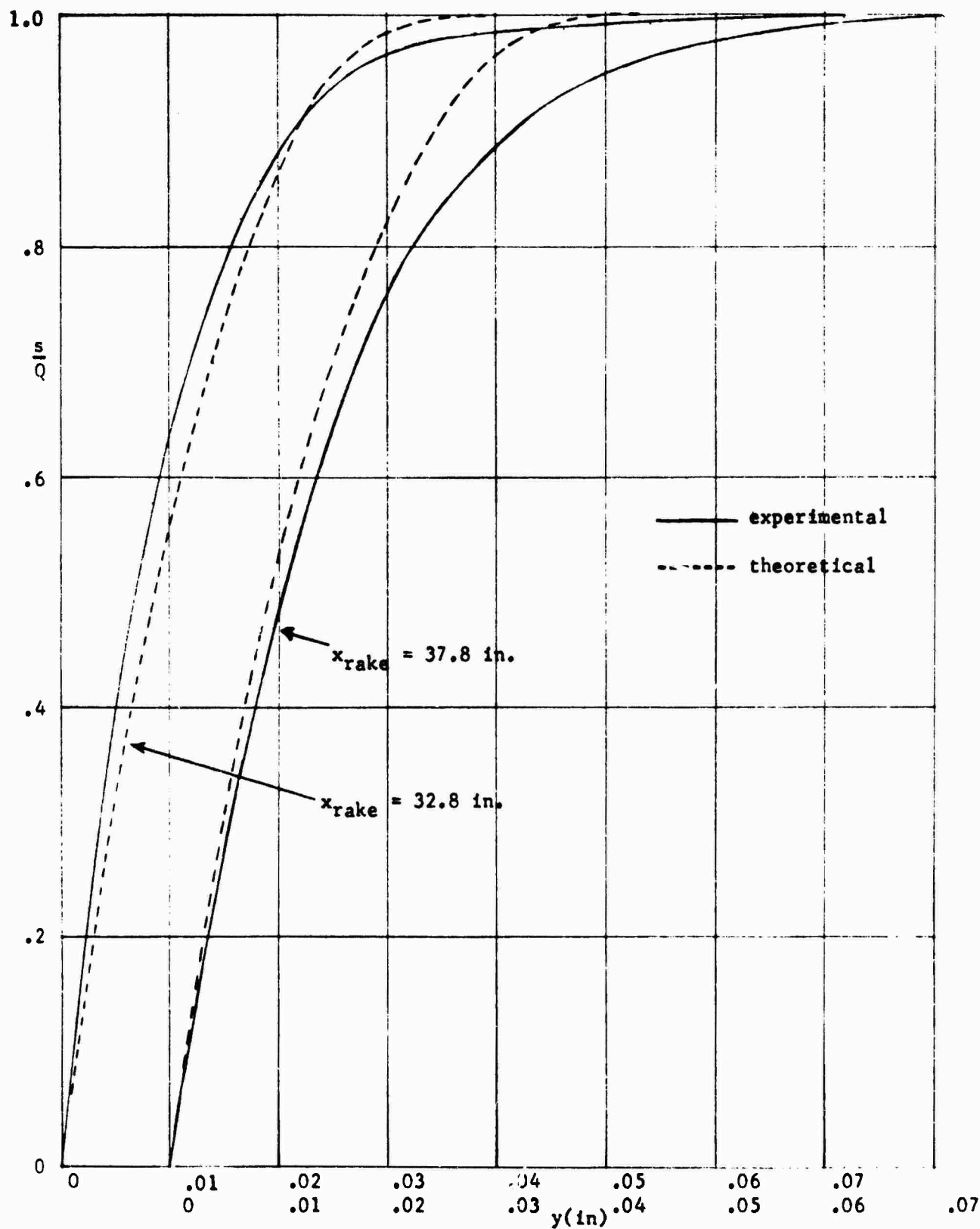


FIGURE 91  
THEORETICAL AND EXPERIMENTAL BOUNDARY LAYER VELOCITY PROFILES  
 $M = 3.0$   $R_c = 25.5 \times 10^6$

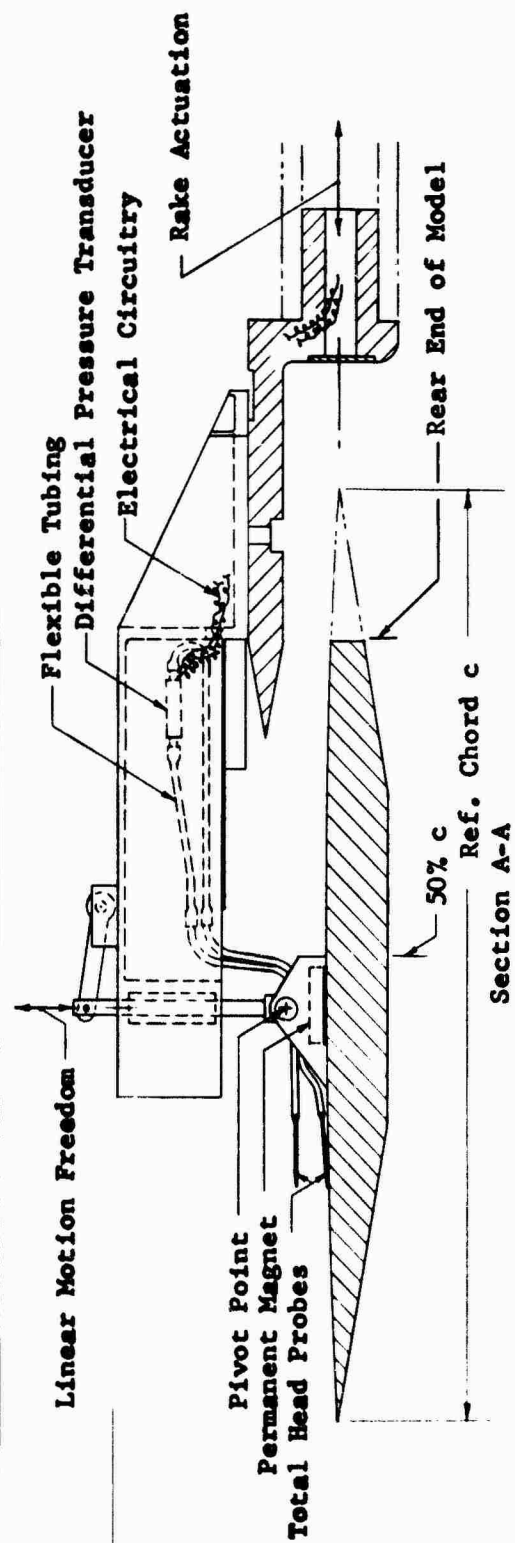
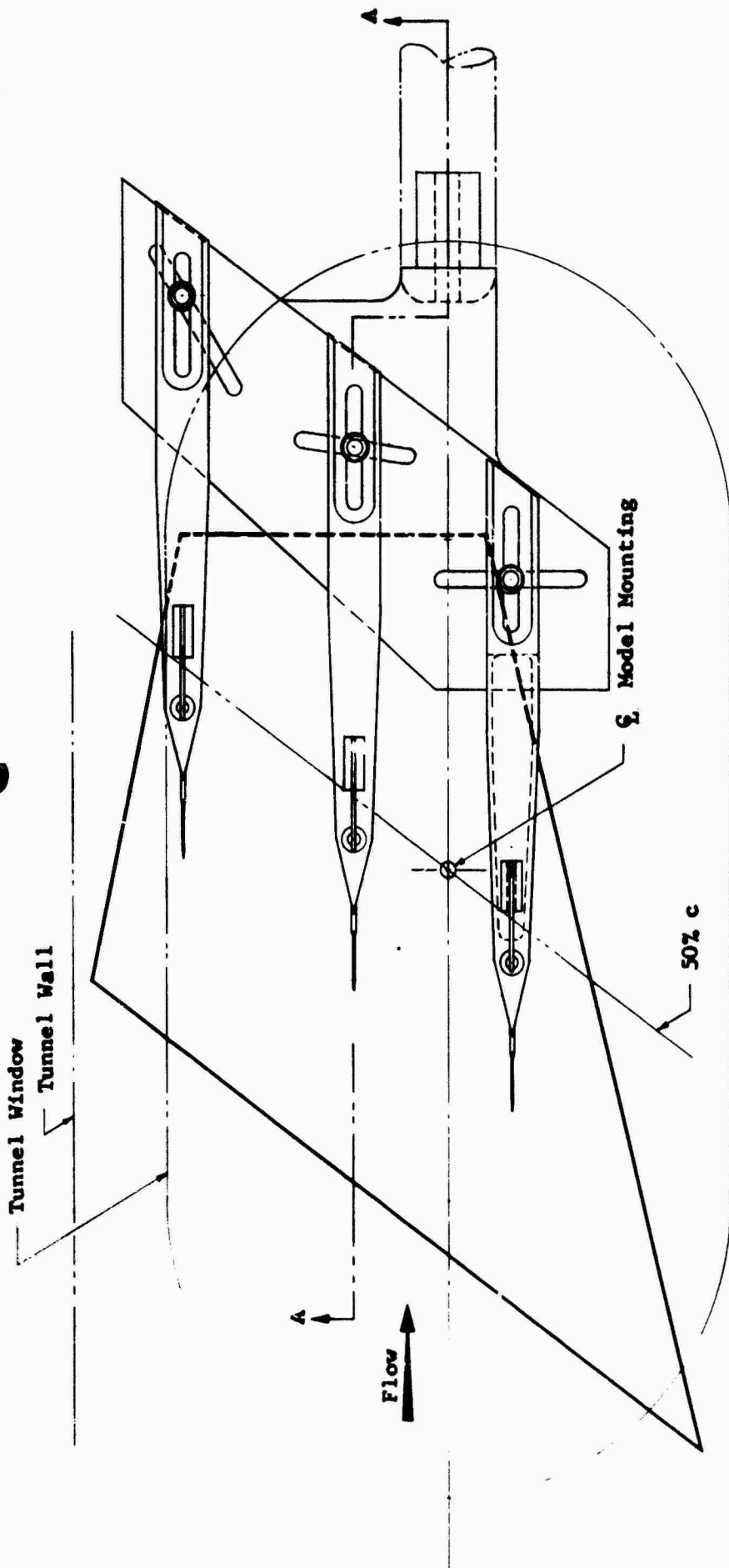


FIGURE 92 SKETCH OF MODEL AT 36° SWEEP AND TRANSITION PROBING MECHANISM

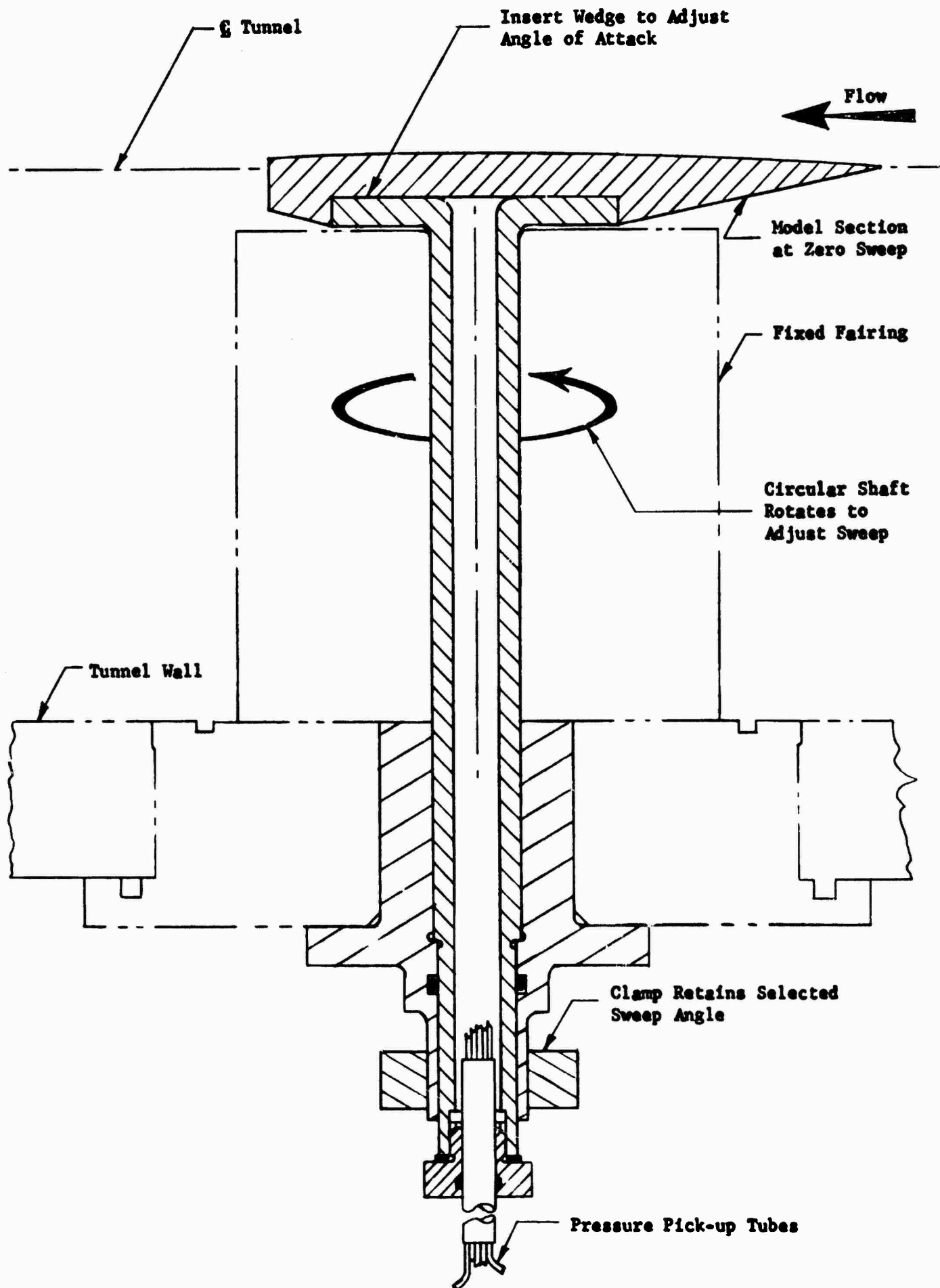


FIGURE 93 SKETCH OF MODEL MOUNTING

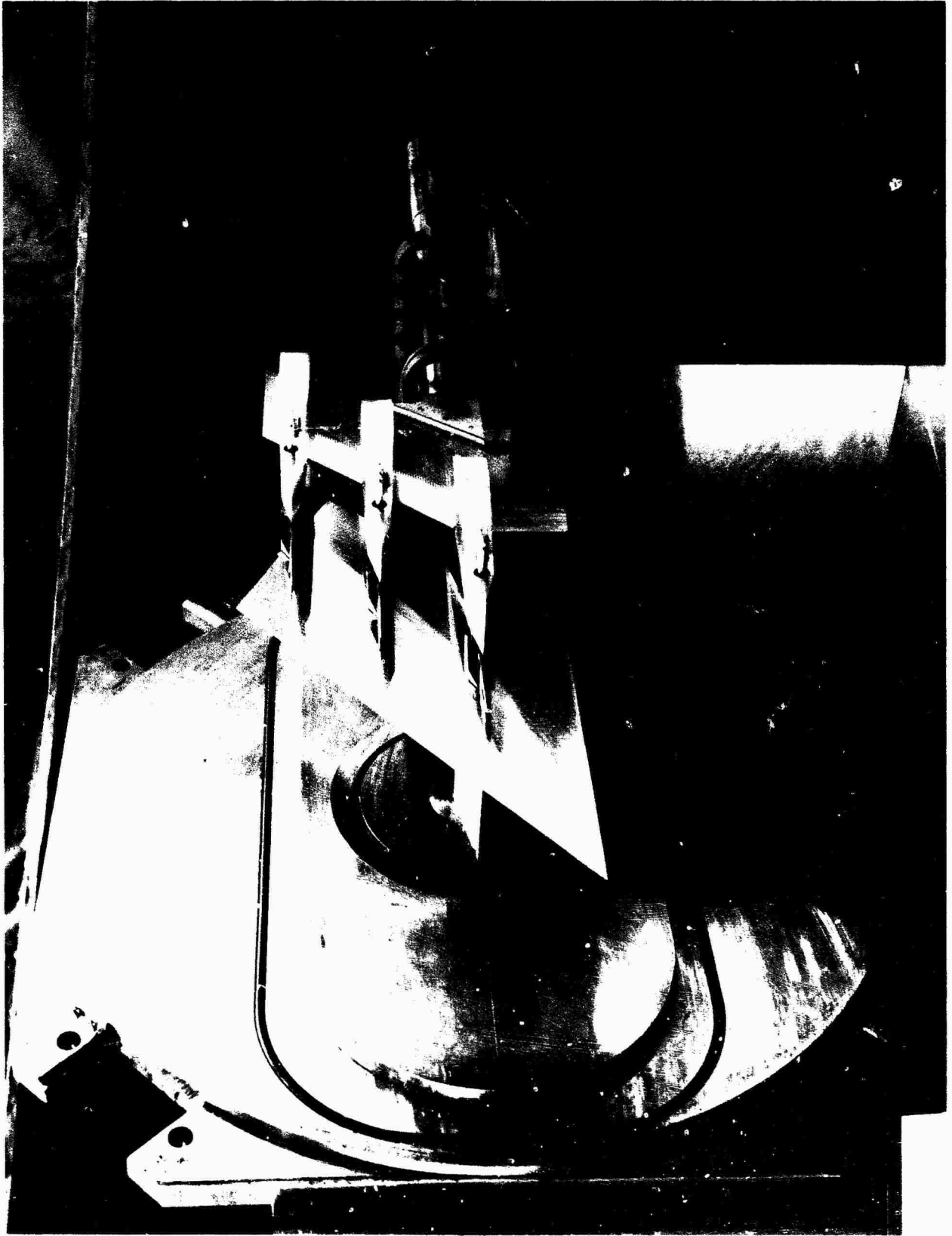


FIGURE 94 PHOTOGRAPH OF MODEL AND TRANSITION PROBING MECHANISM

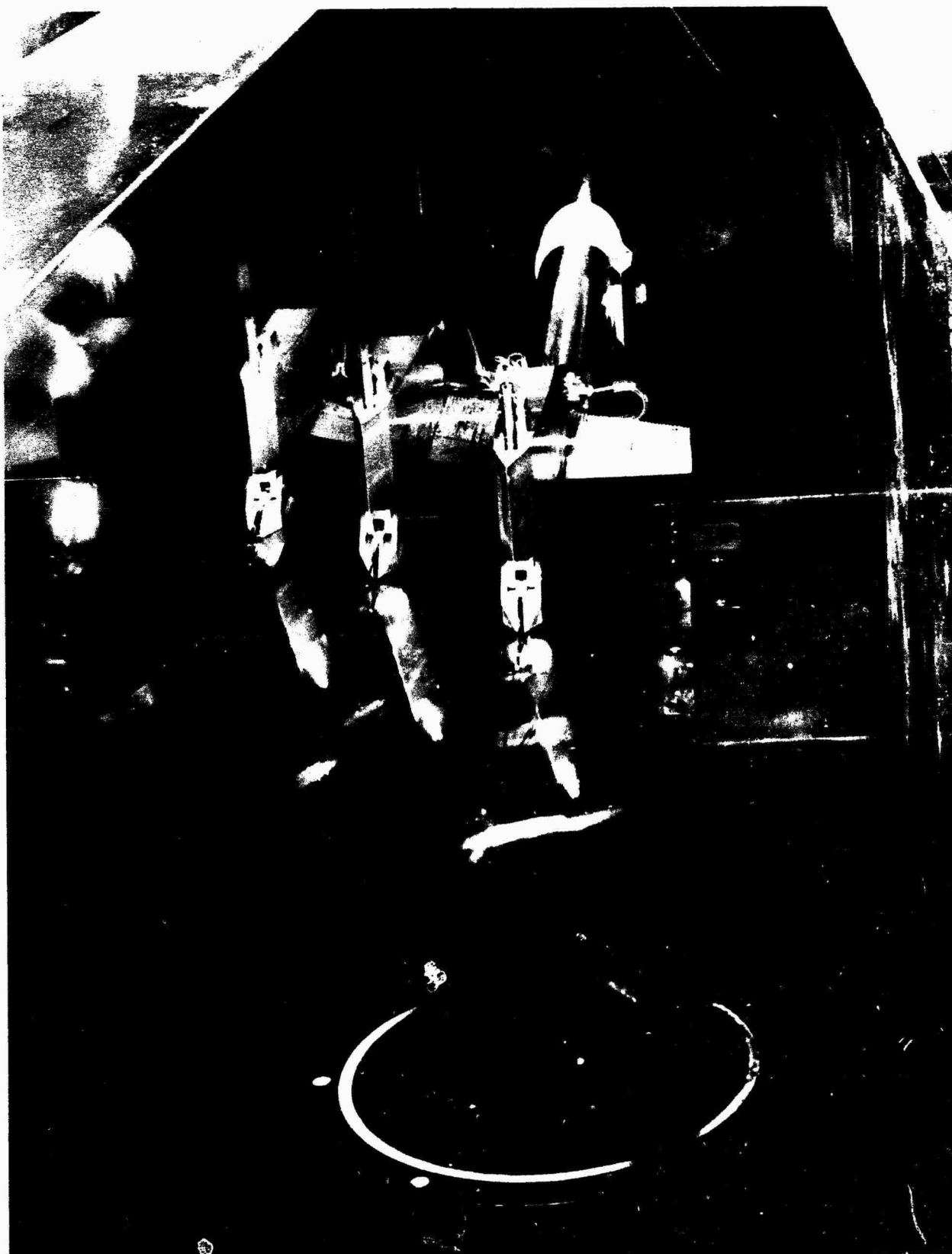


FIGURE 95 PHOTOGRAPH OF MODEL INSTALLED IN TUNNEL E-1



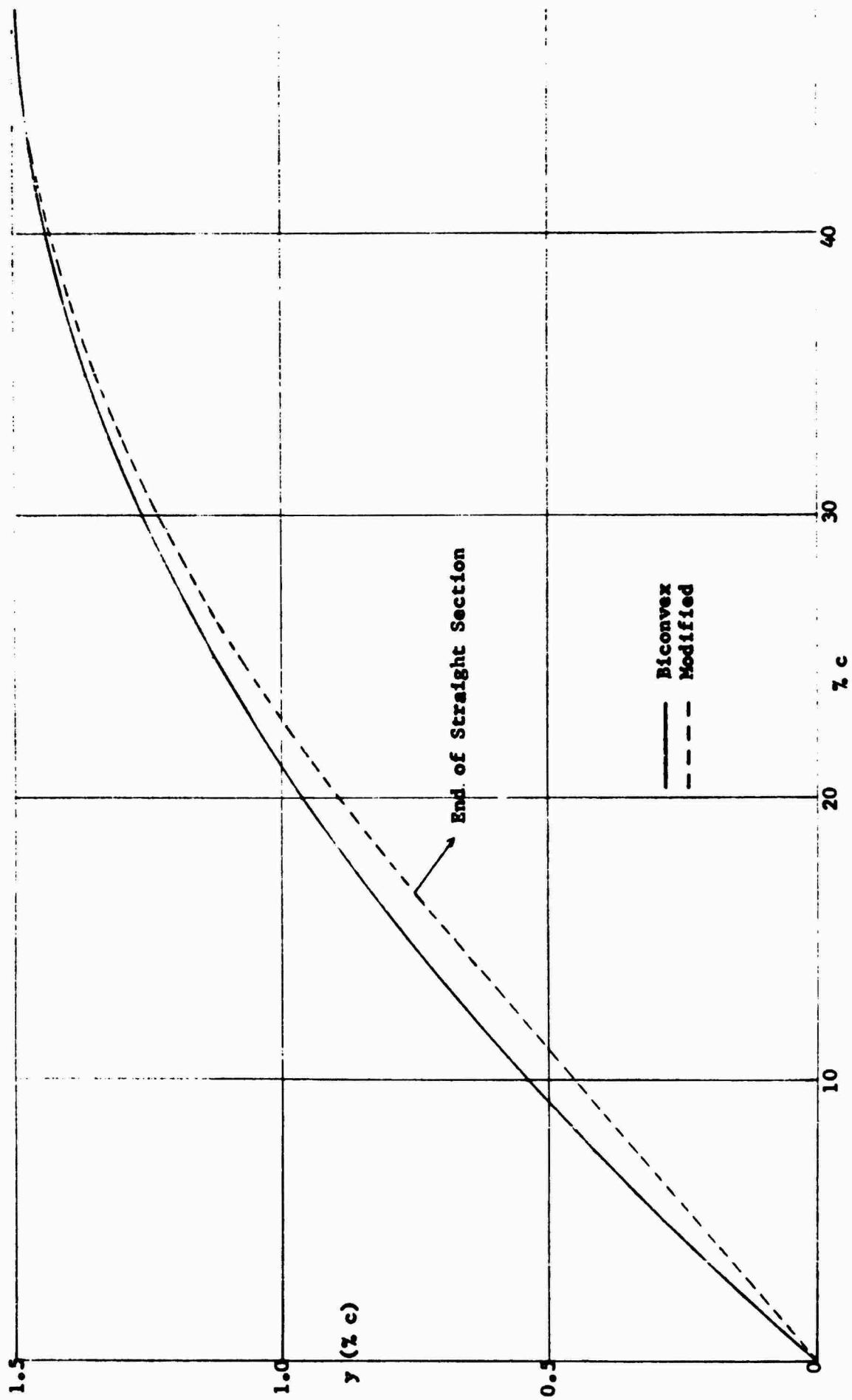


FIGURE 96 BICONVEX AND MODIFIED AIRFOIL SECTIONS

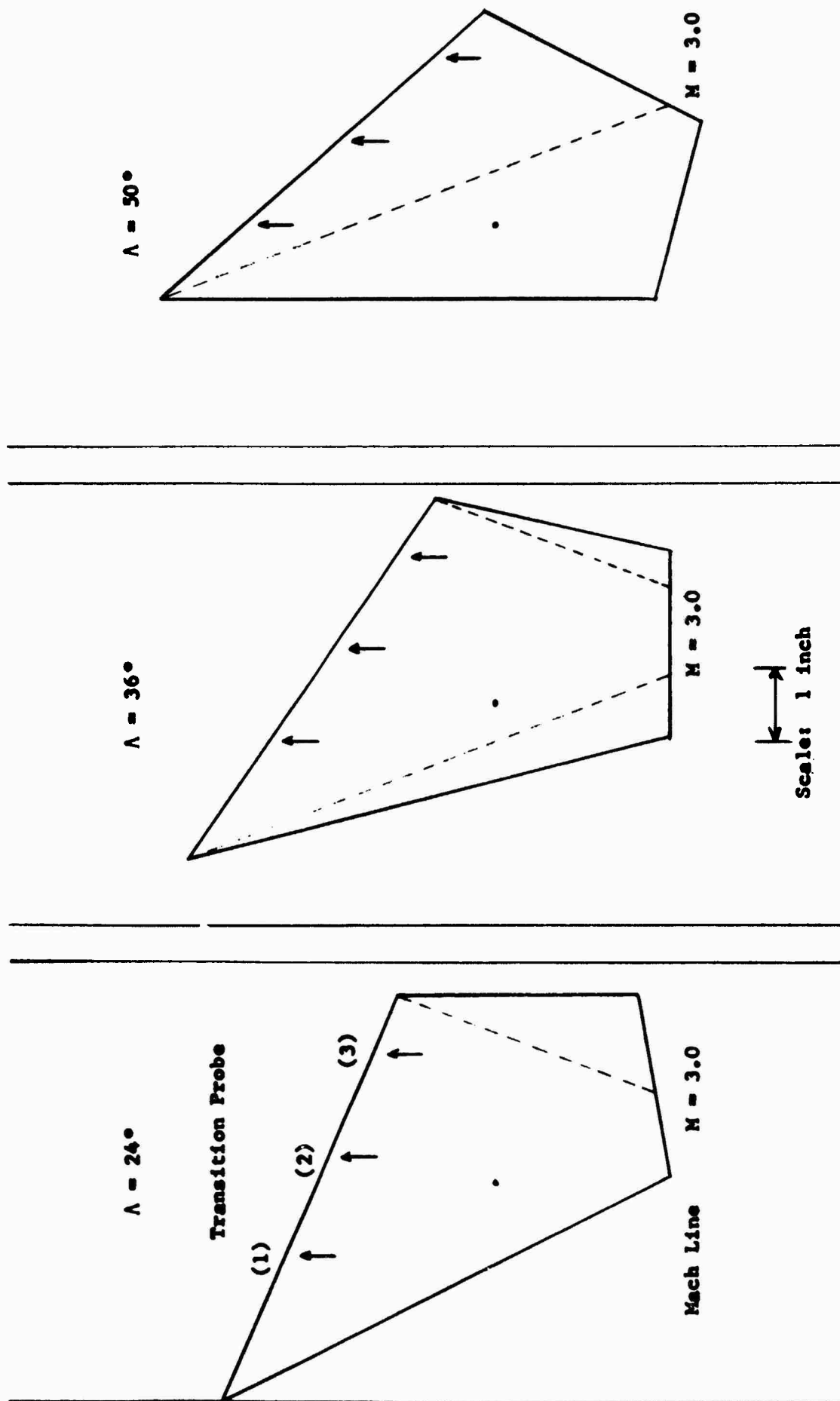


FIGURE 97 SPANWISE LOCATIONS OF TOTAL HEAD PROBES FOR THE THREE SWEEP ANGLES

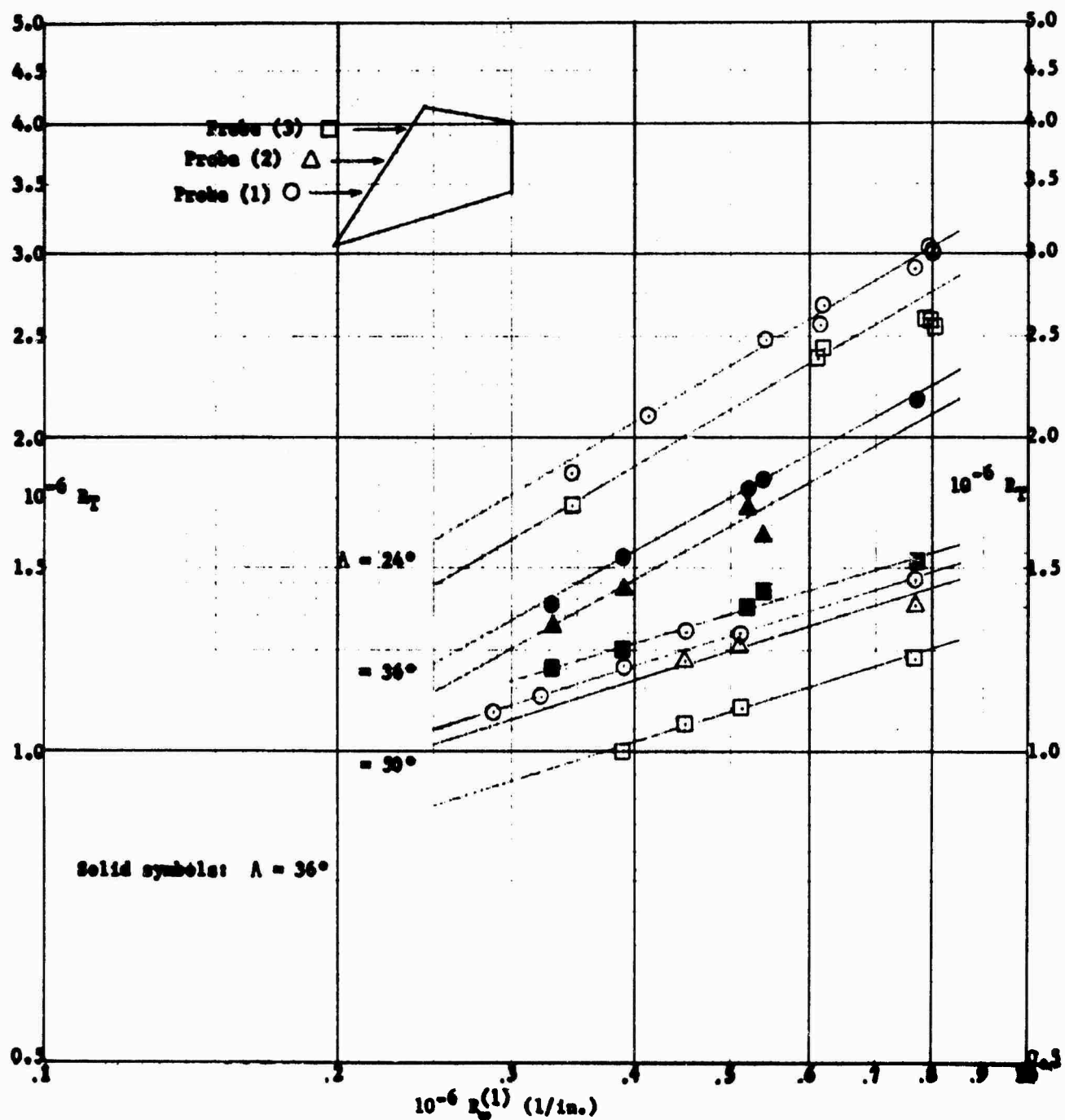


FIGURE 98 TRANSITION VS UNIT REYNOLDS NUMBER, BICONVEX WING,  $M = 3.0$

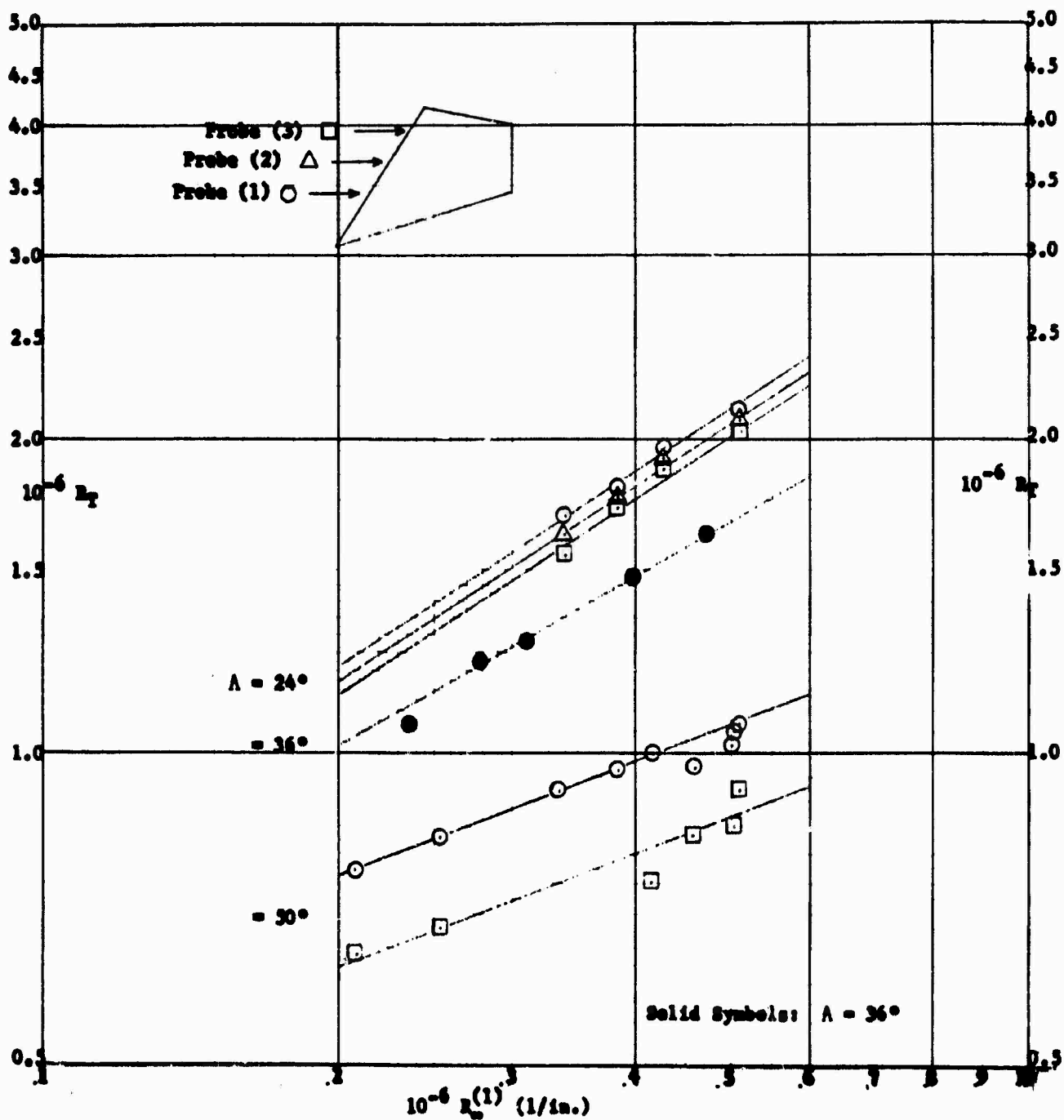


FIGURE 99 TRANSITION VS UNIT REYNOLDS NUMBER, BICONVEX WING,  $M = 4.0$

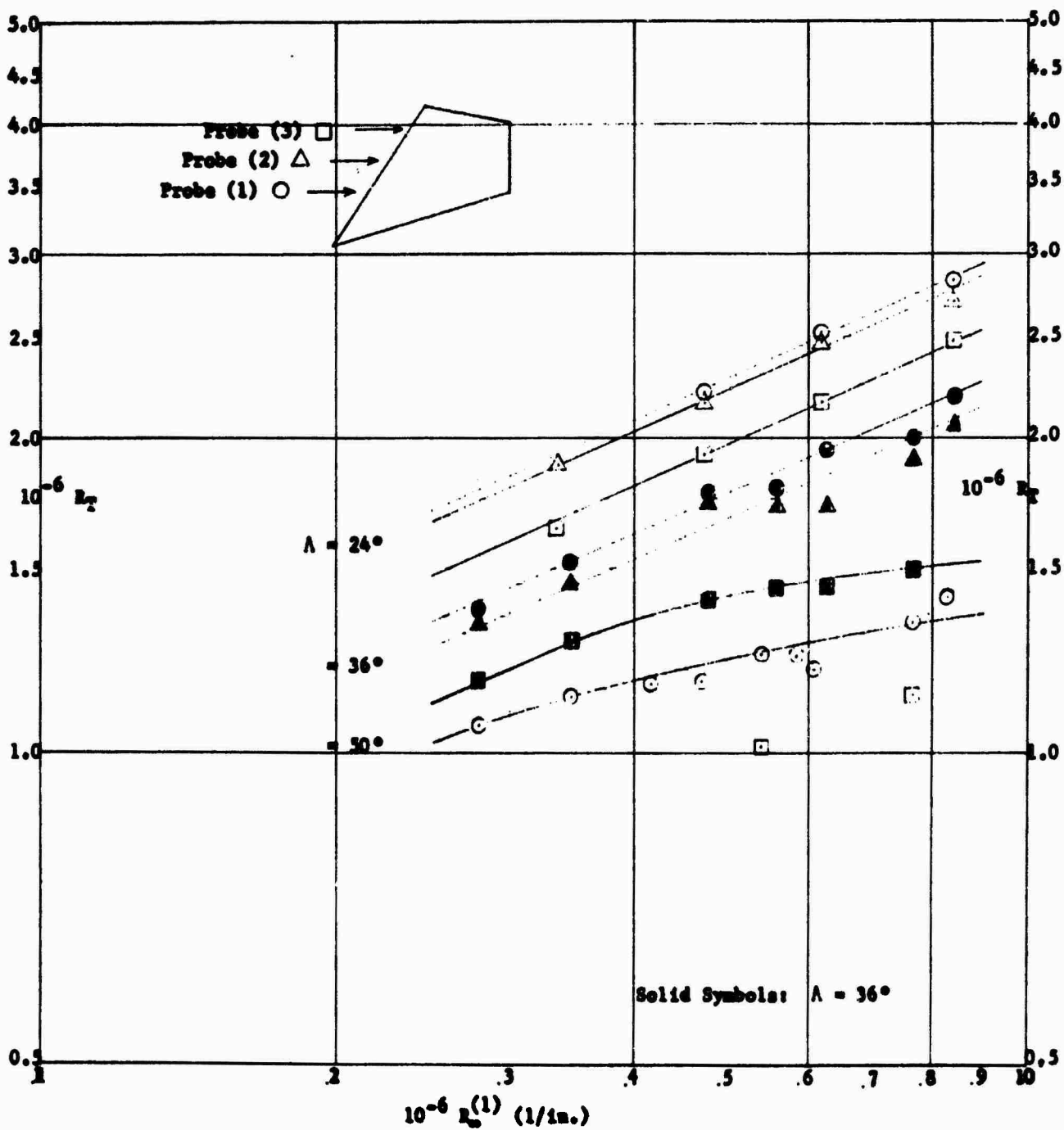


FIGURE 100 TRANSITION VS UNIT REYNOLDS NUMBER, MODIFIED WING,  $M = 3.0$

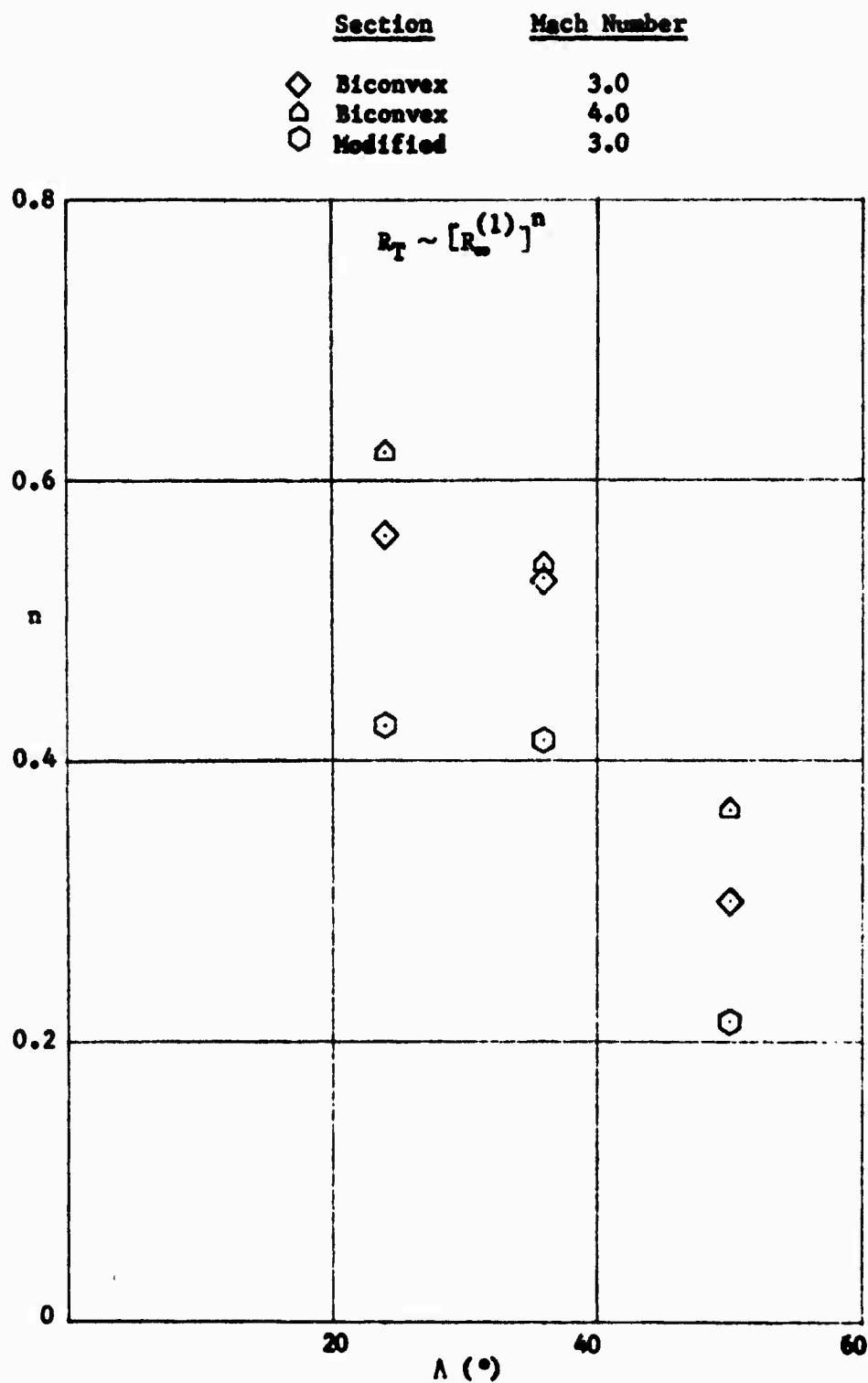


FIGURE 101 EXPONENT  $n$  OF POWER LAW,  $R_T \sim [R_m^{(1)}]^n$  VS SWEEP ANGLE

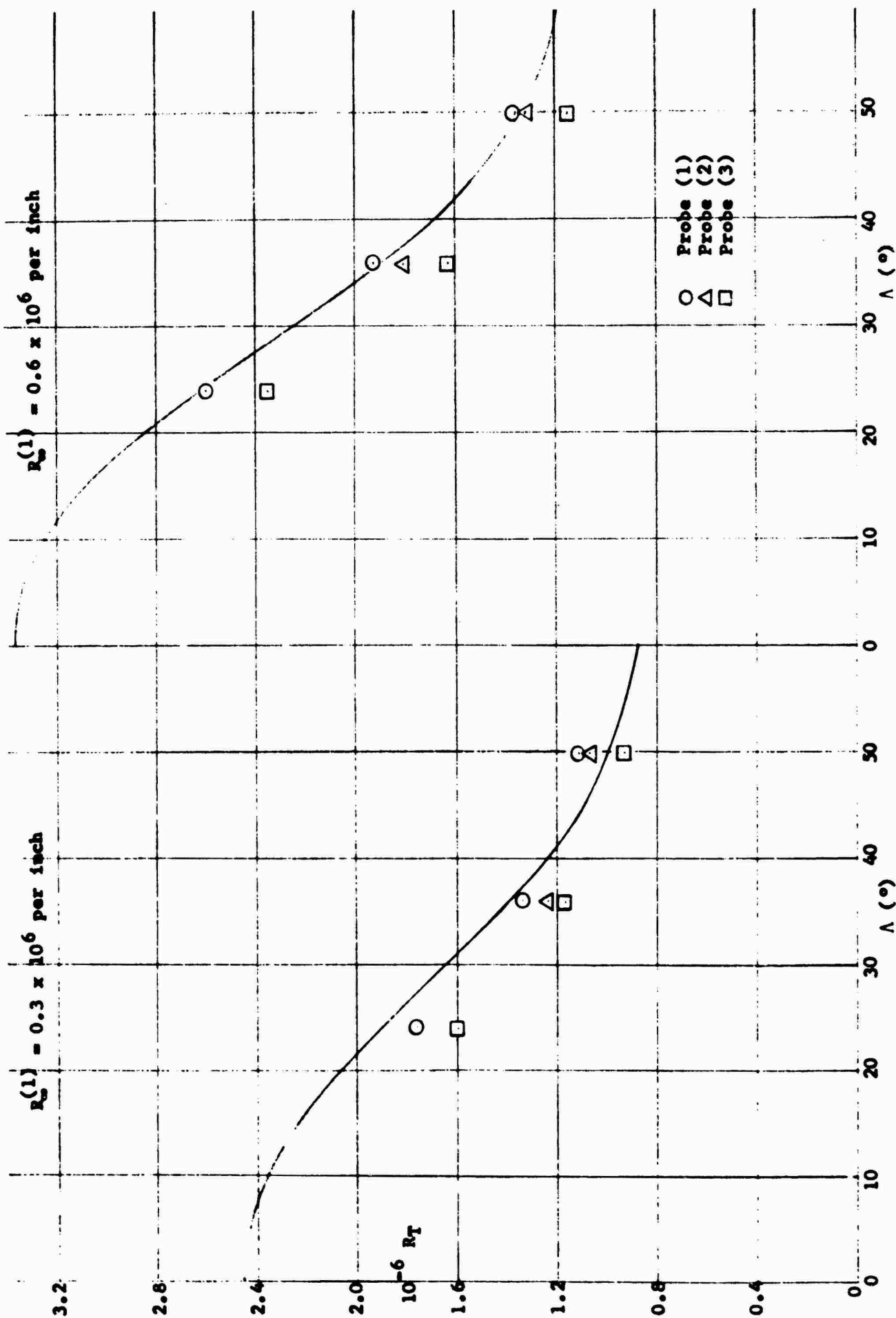


FIGURE 102 VARIATION OF TRANSITION WITH SWEEP, BICONVEX WING,  $M = 3.0$

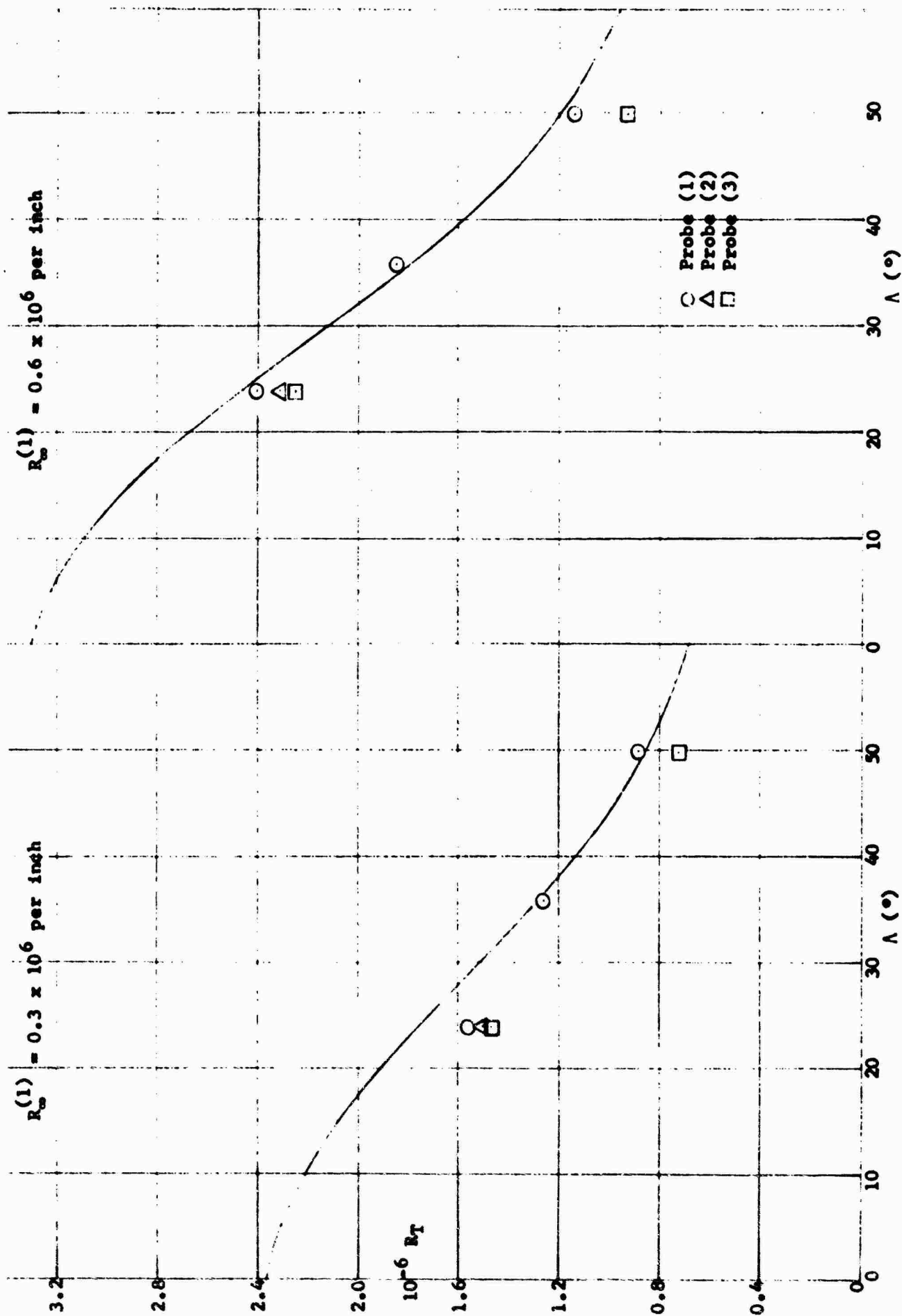


FIGURE 103 VARIATION OF TRANSITION WITH SWEEP, BICONVEX WING,  $M = 4.0$



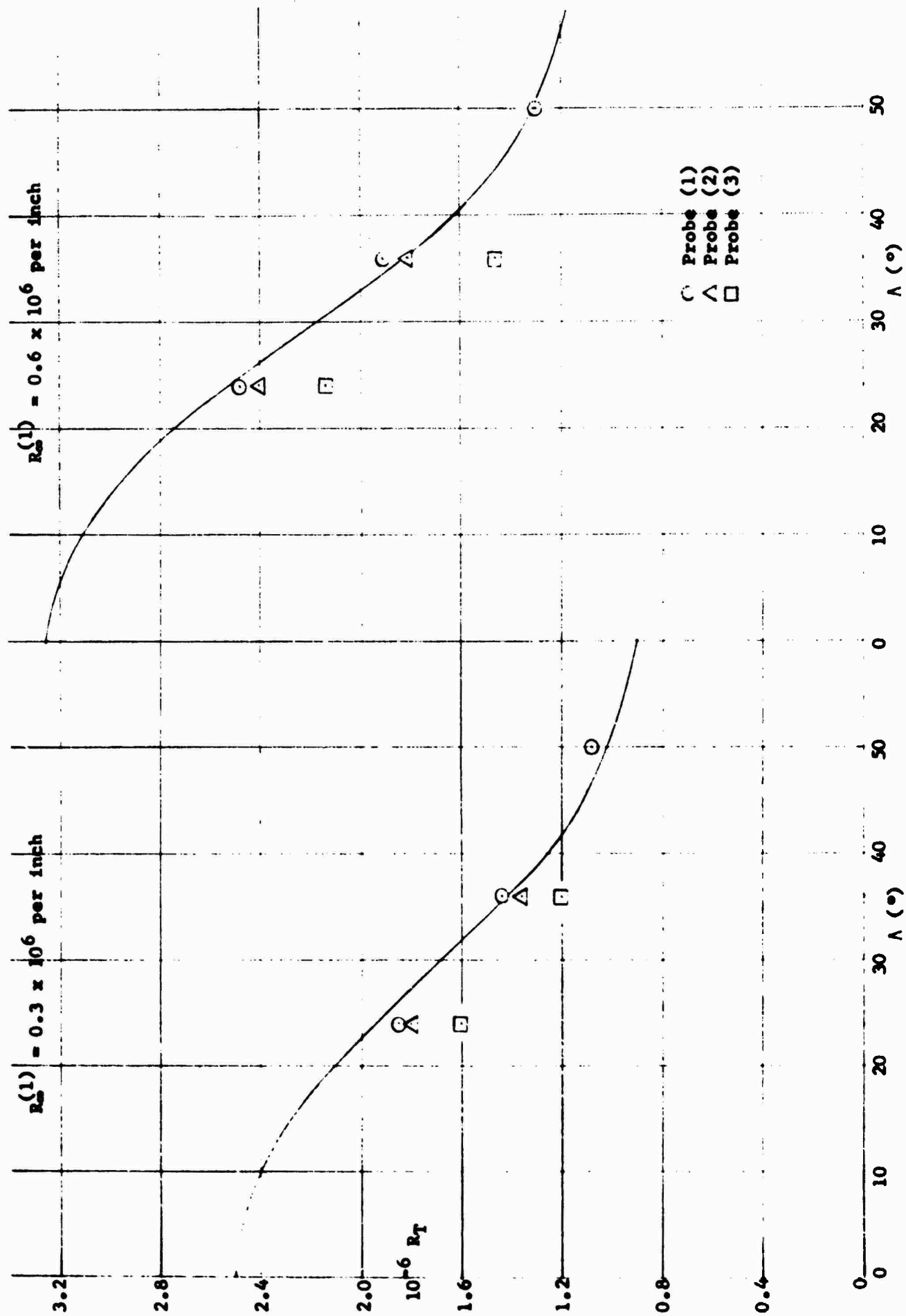


FIGURE 104 VARIATION OF TRANSITION WITH SWEEP, MODIFIED WING,  $M = 3.0$

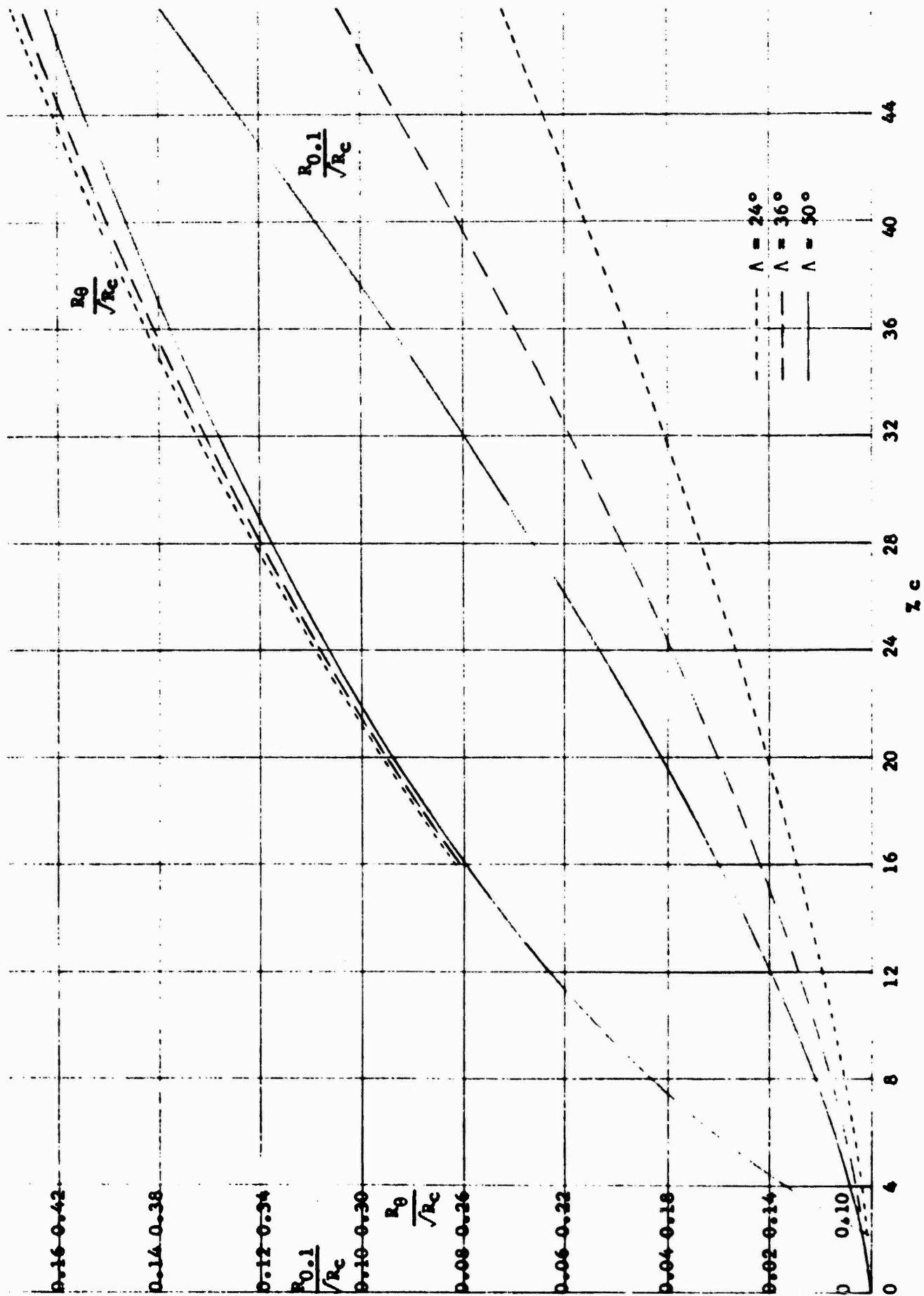


FIGURE 105 RESULTS FROM THEORETICAL BOUNDARY LAYER CALCULATION ON 3-PERCENT BICONVEX WING AT  $M = 3.0$

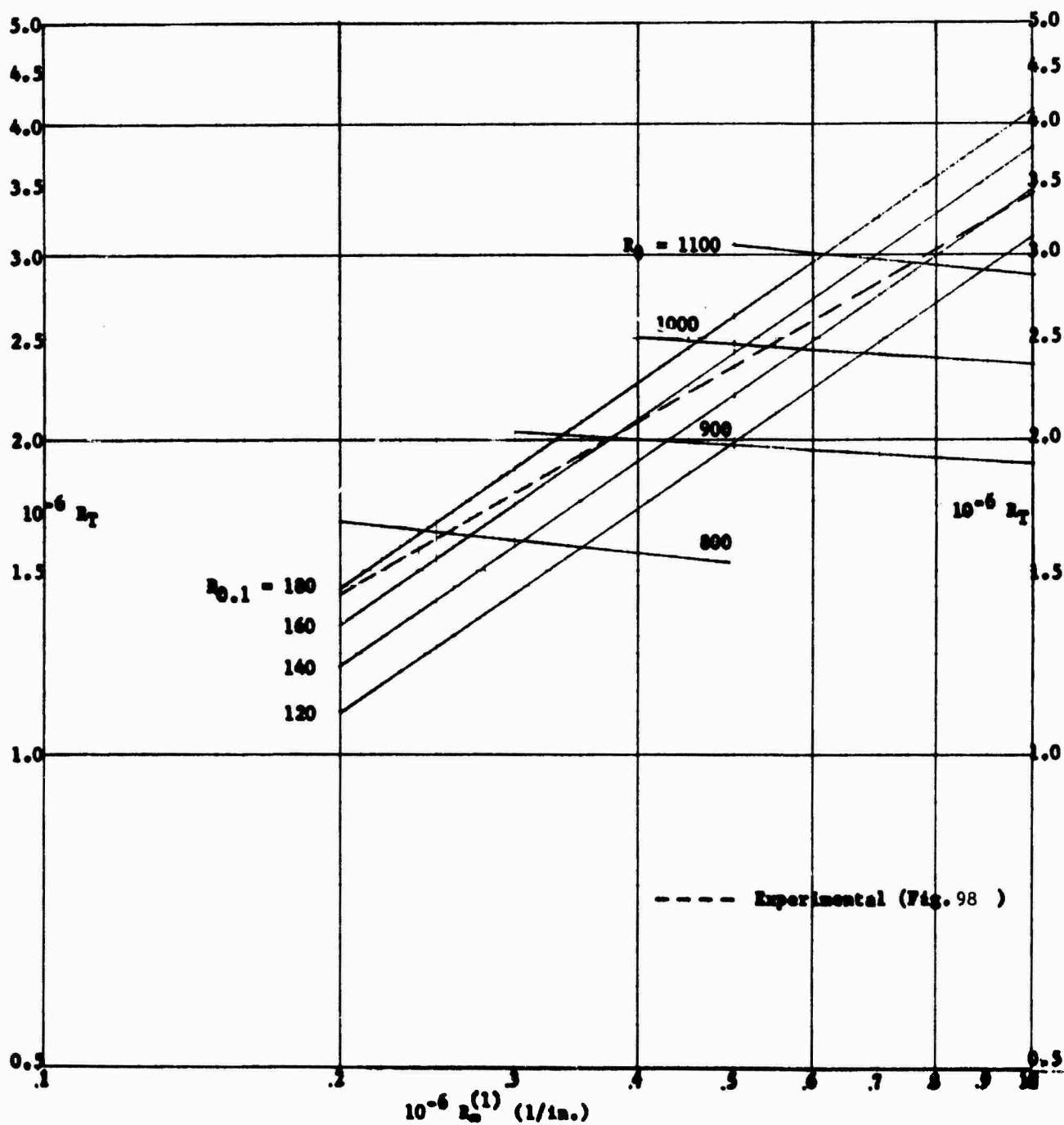


FIGURE 106 CROSSFLOW AND MOMENTUM THICKNESS REYNOLDS NUMBER AT TRANSITION, BICOMPVEX WING,  $M = 3.0$ ,  $\Lambda = 24^\circ$

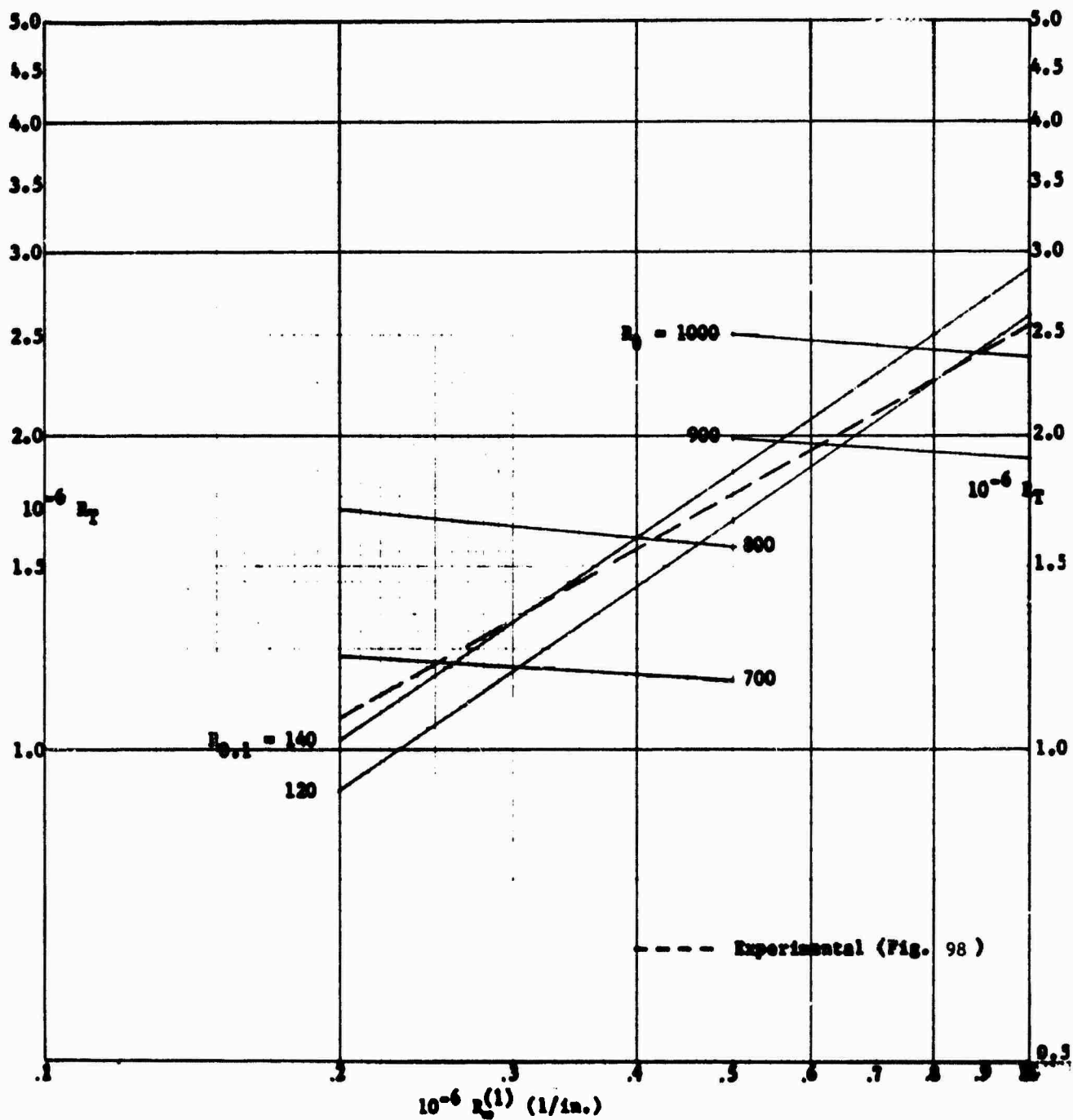


FIGURE 107 CROSSFLOW AND MOMENTUM THICKNESS REYNOLDS NUMBER AT TRANSITION, BICONVEX WING,  $M = 3.0$ ,  $\Lambda = 36^\circ$

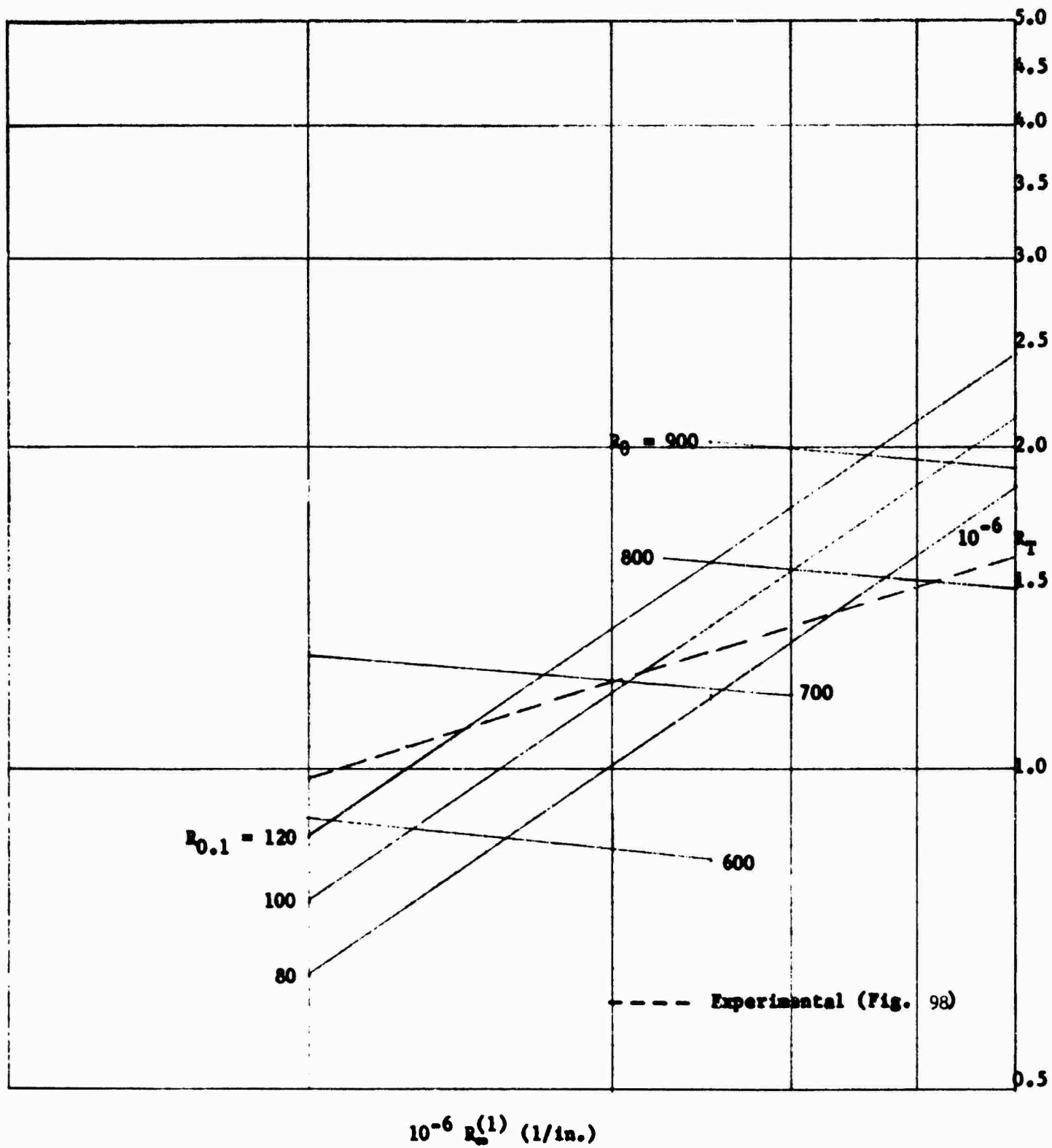
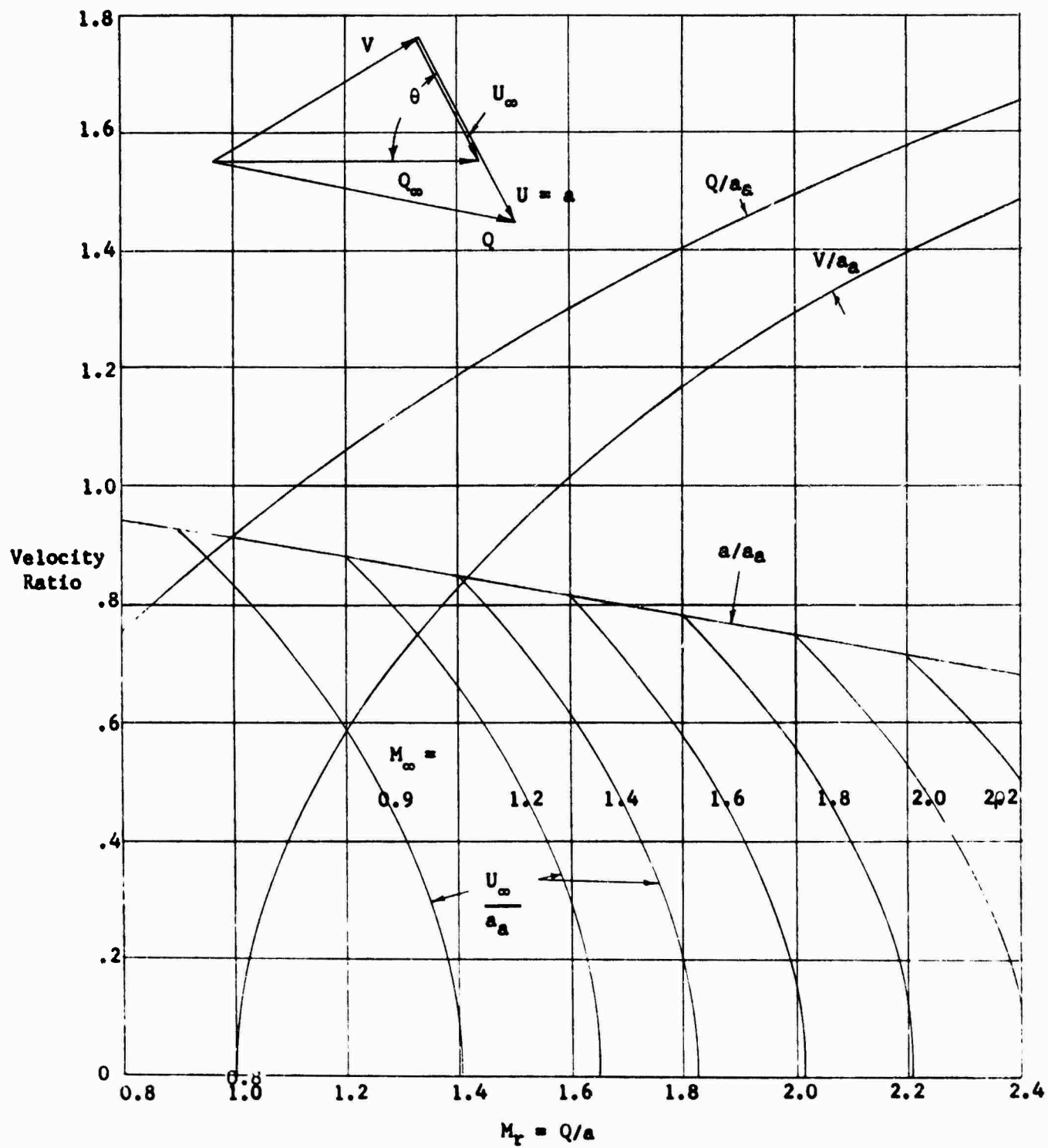


FIGURE 108 CROSSFLOW AND MOMENTUM THICKNESS REYNOLDS NUMBER AT TRANSITION, BICONVEX WING,  $M = 3.0$ ,  $\Lambda = 50^\circ$



VELOCITY COMPONENT RATIOS CORRESPONDING TO  $M_u = 1.0$

FIGURE 109

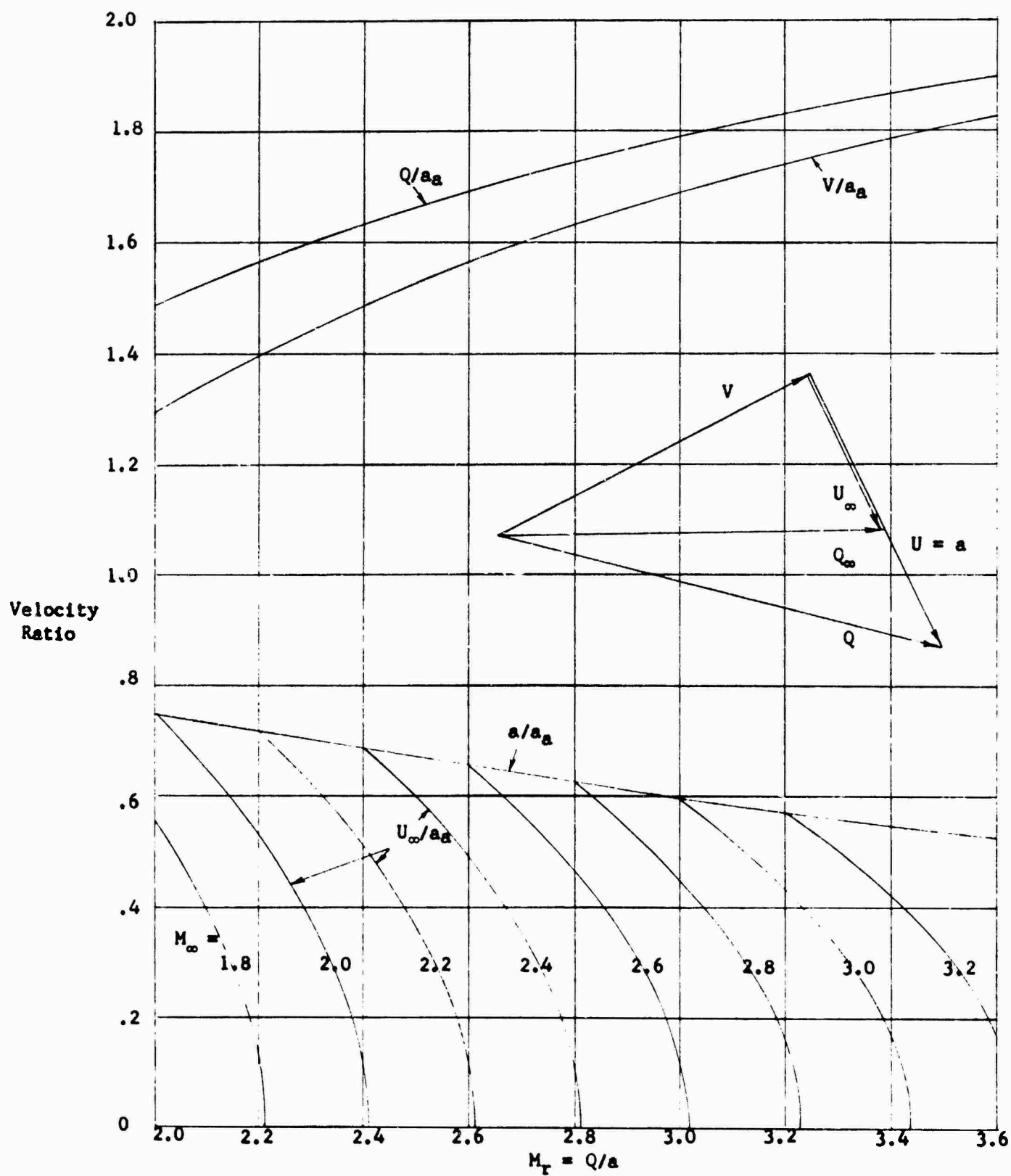
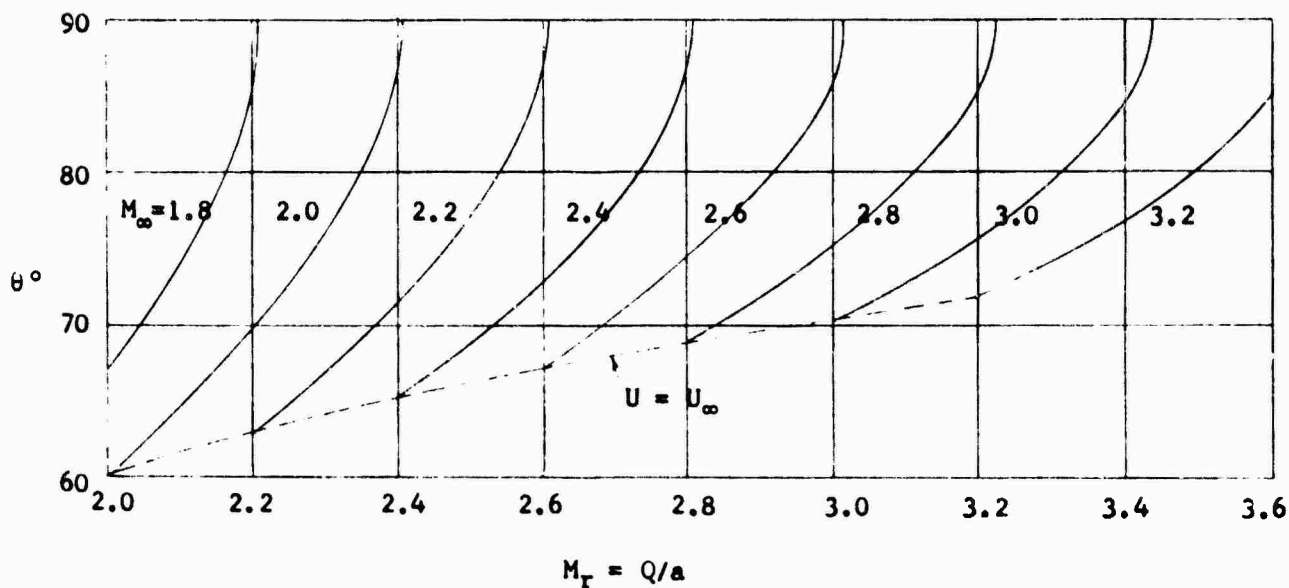
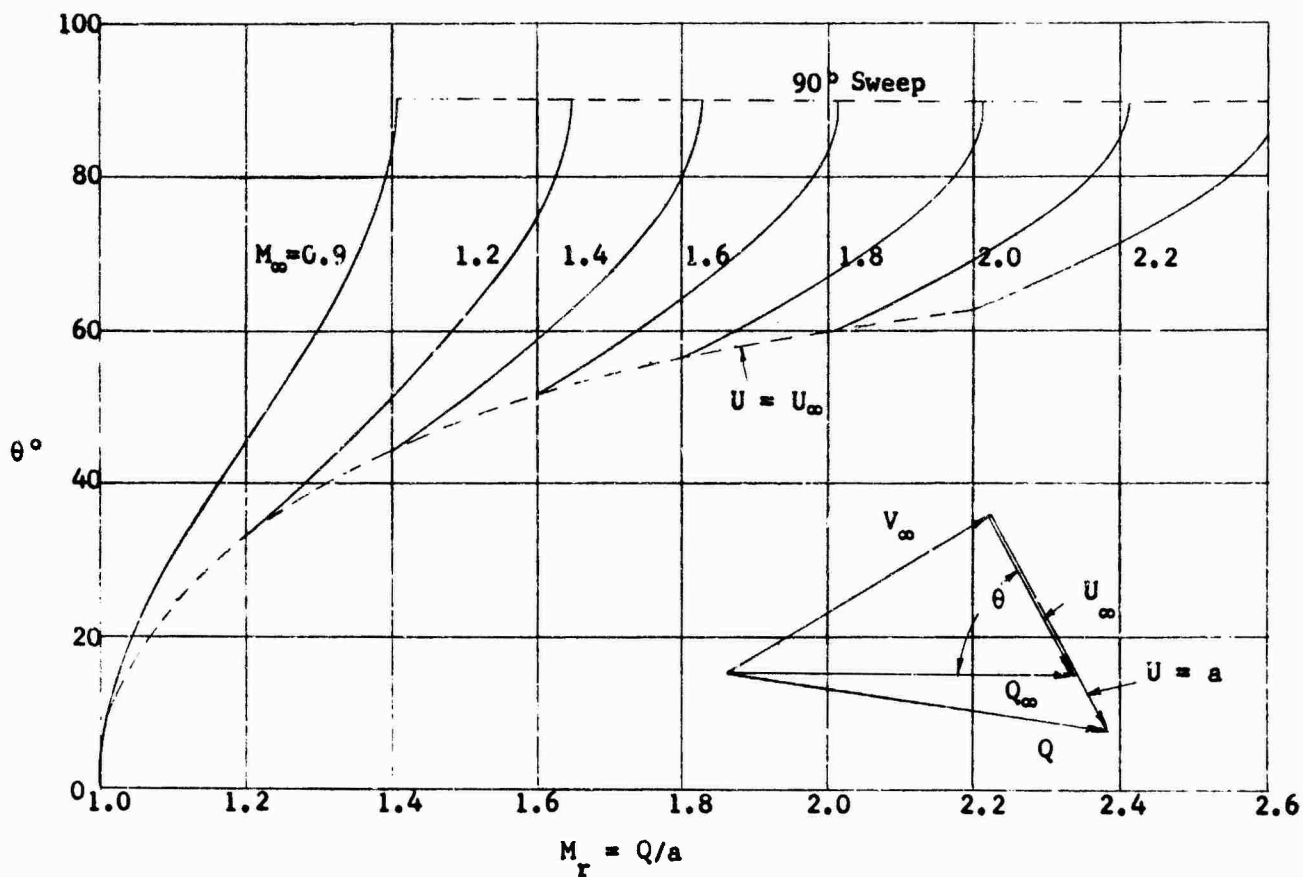


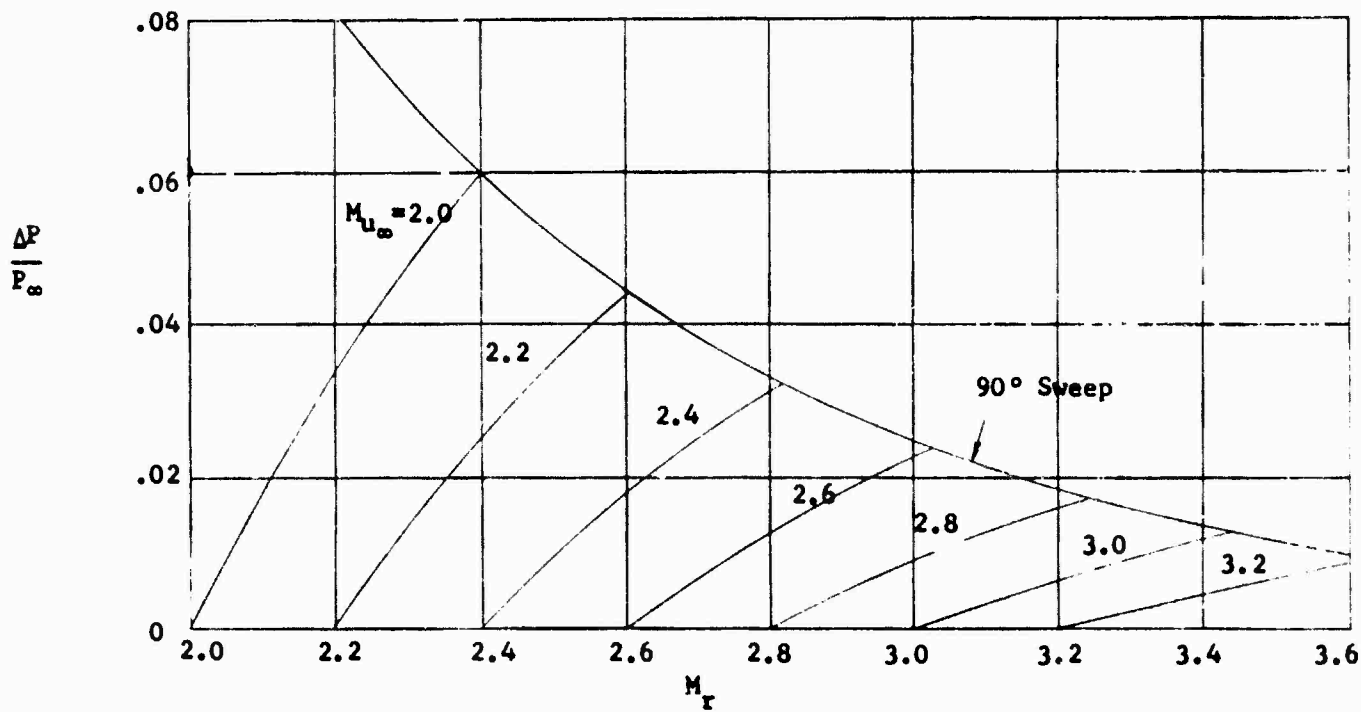
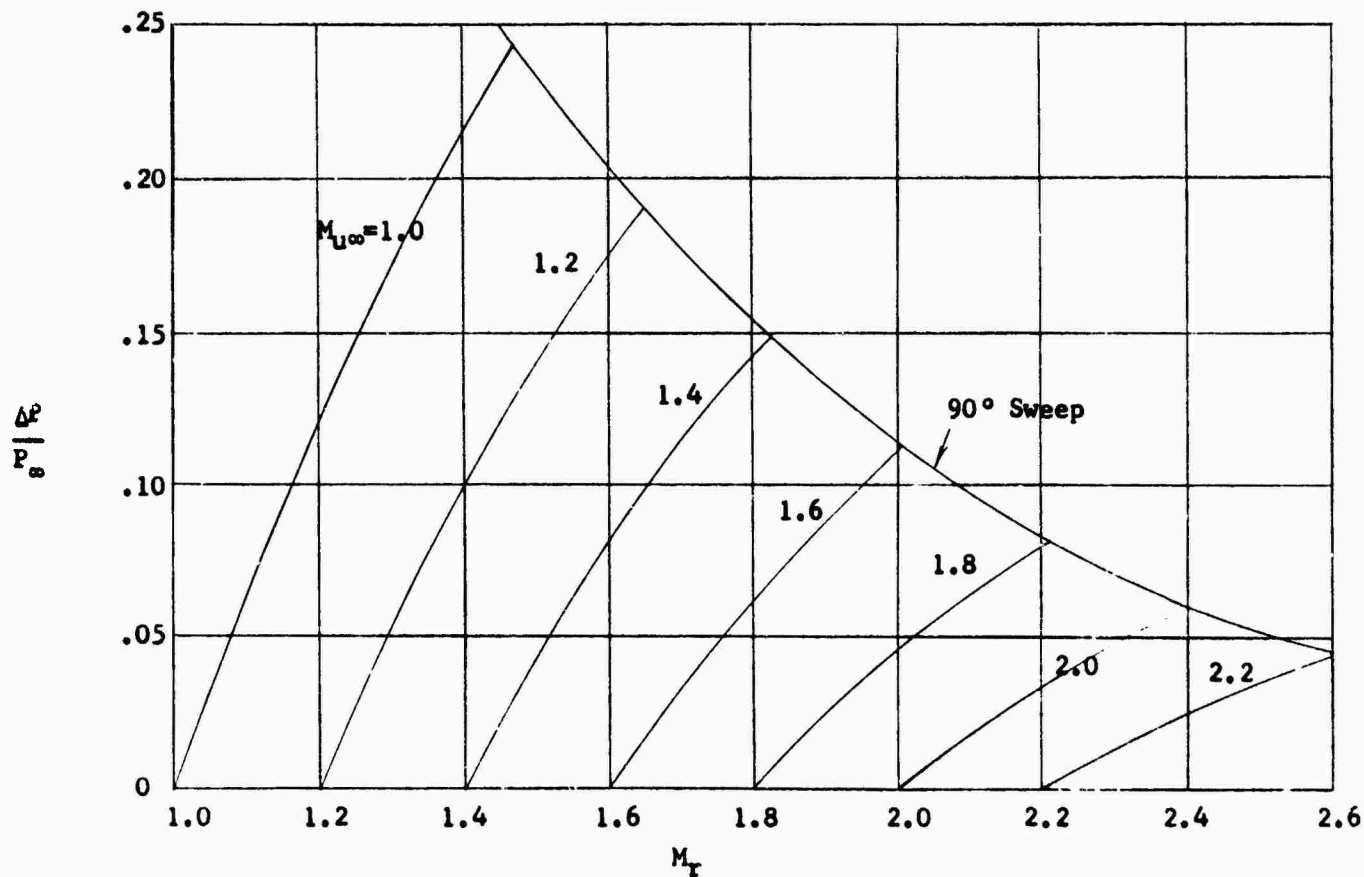
FIGURE 10 (continued)



RELATION BETWEEN FREESTREAM OR RESULTANT MACH AND SWEEP ANGLE FOR  $M_u = 1.0$

FIGURE 110

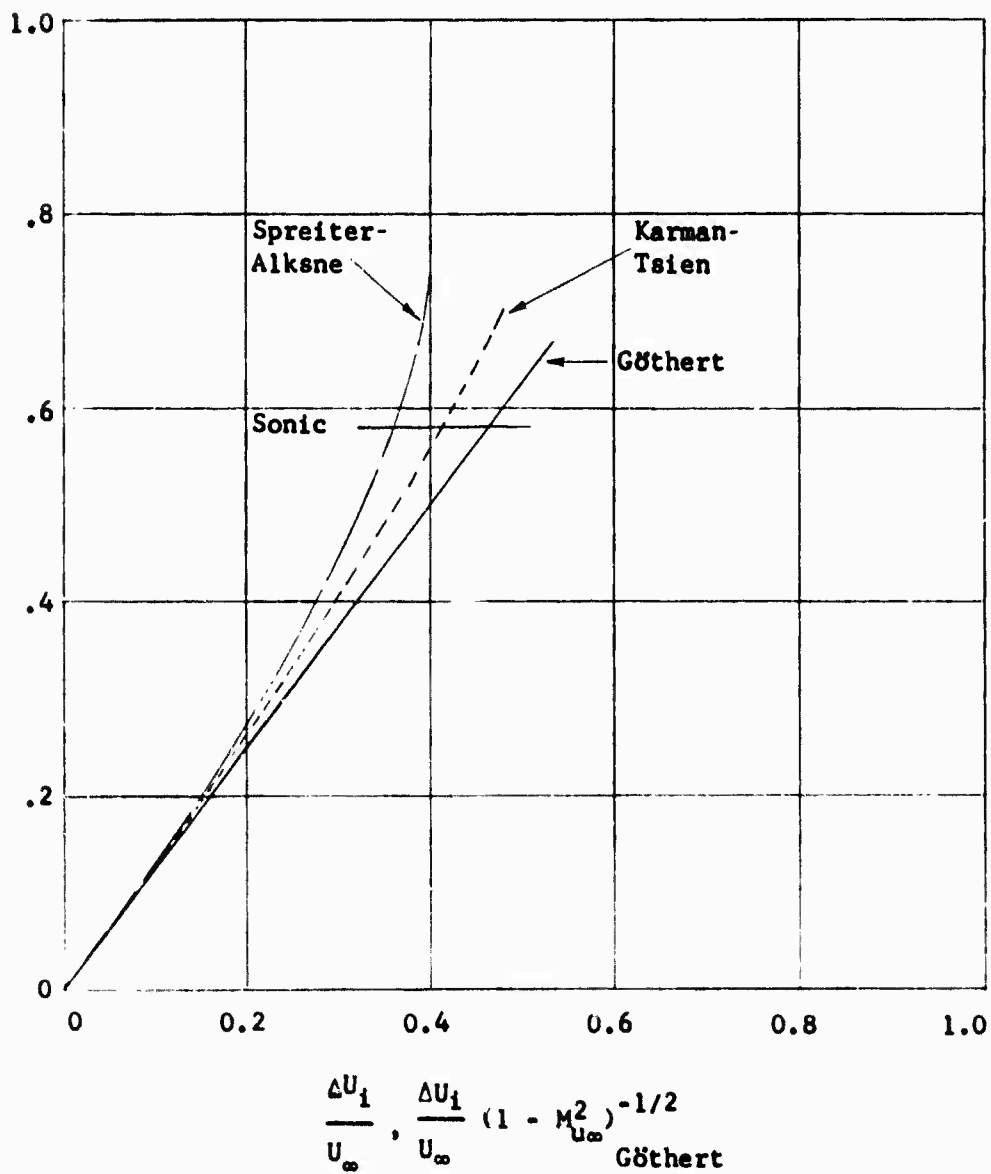




LIMITING PRESSURE RATIO INCREMENTS FOR  $M_u = 1.0$

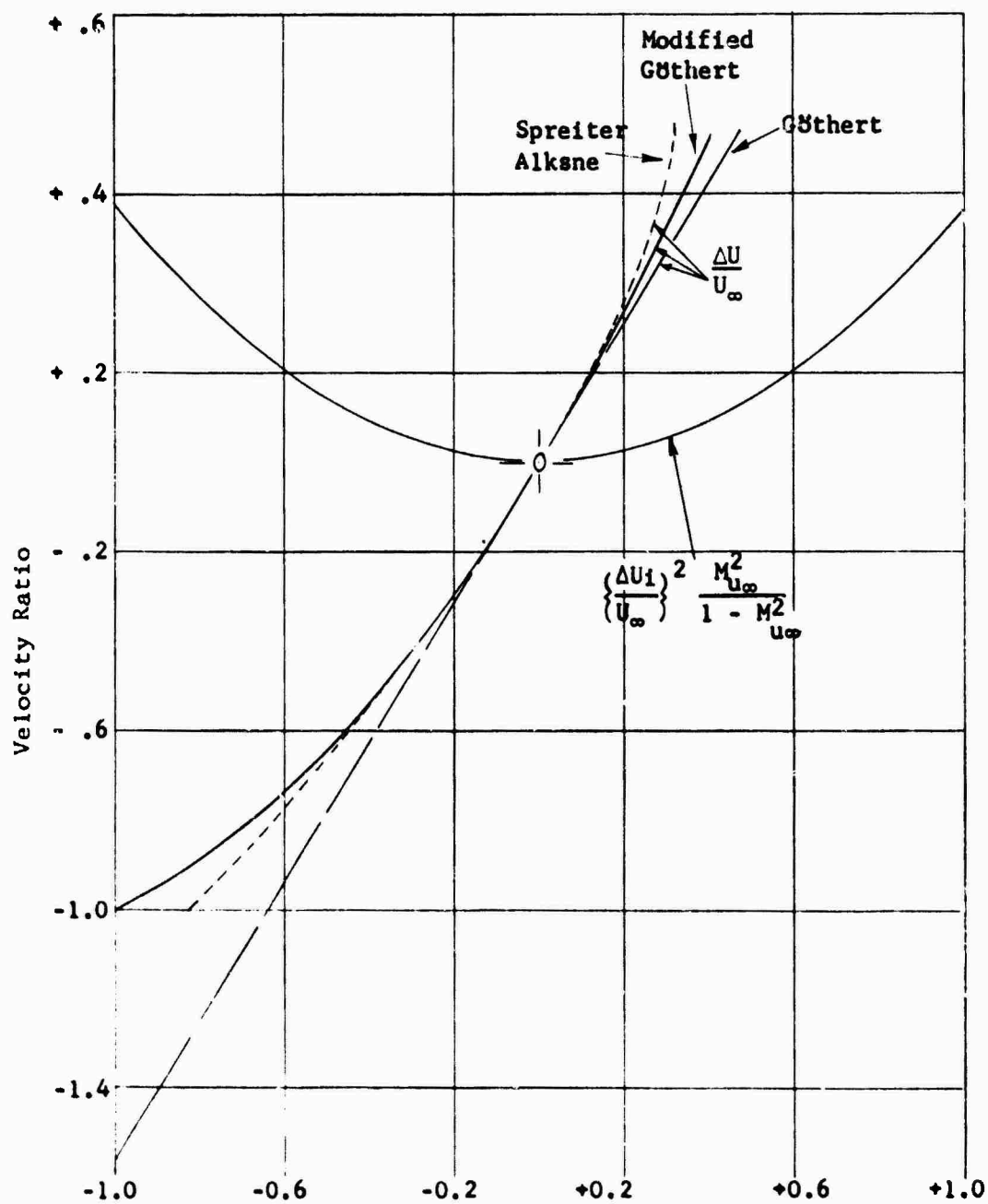
FIGURE 111

$\frac{\Delta U}{U_0}$



COMPARISON OF COMPRESSIBILITY CORRECTIONS AT  $M_{u_\infty} = 0.6$

FIGURE 112



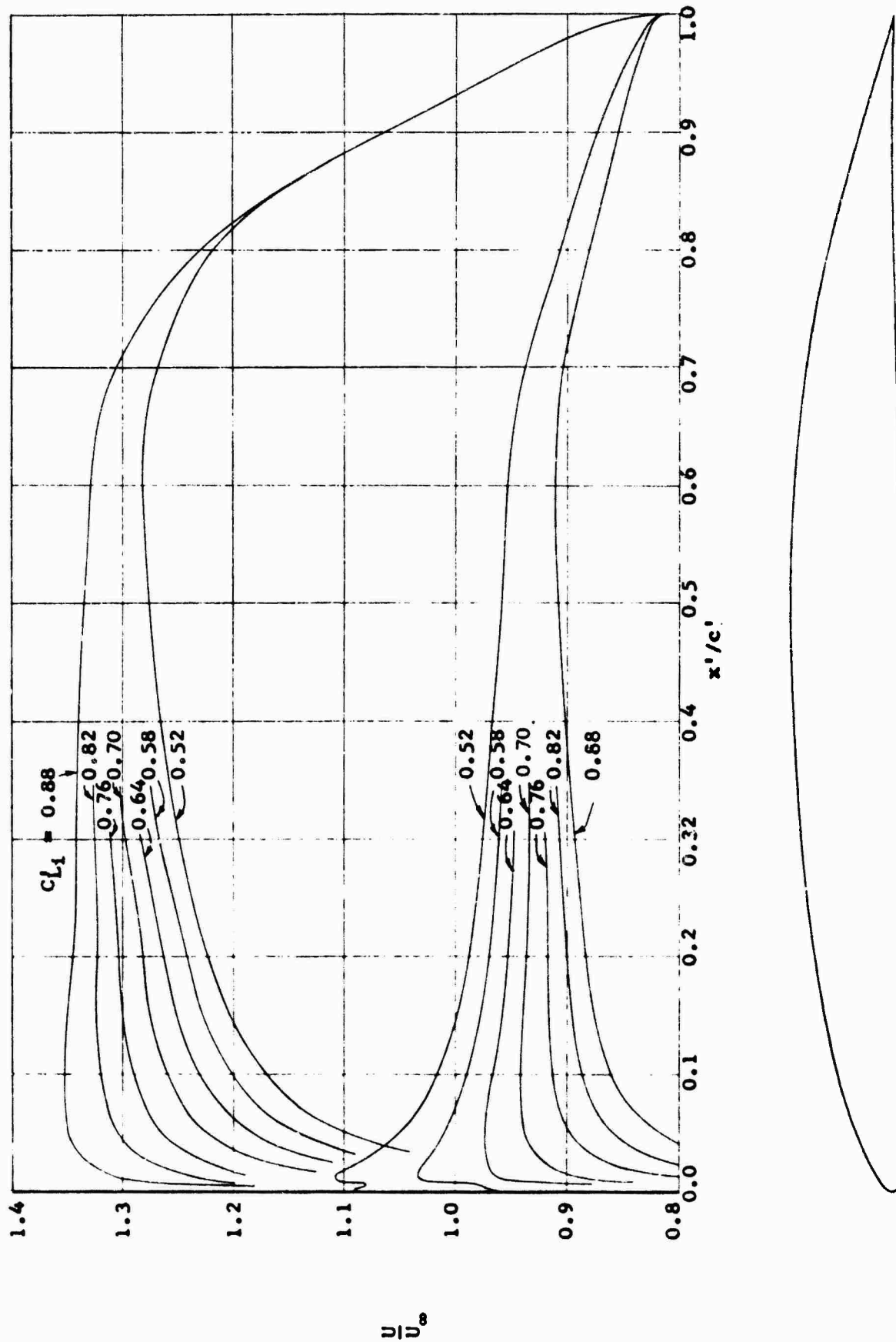
$$\frac{\Delta U}{U_1}, \frac{\Delta U}{U_1} (1 - M_{u_\infty}^2)^{1/2} \text{ Spreiter etc.}$$

$$\frac{\Delta U}{U_\infty} (\text{Göthert}) = \frac{\Delta U_1}{U_0} \frac{1}{1 - M_{u_\infty}^2}$$

$$\frac{\Delta U}{U_\infty} (\text{Modified Göthert}) = \frac{\Delta U}{U_0} (\text{Göthert}) + \left\{ \frac{\Delta U_1}{U_\infty} \right\}^2 \frac{M_{u_\infty}^2}{1 - M_{u_\infty}^2}$$

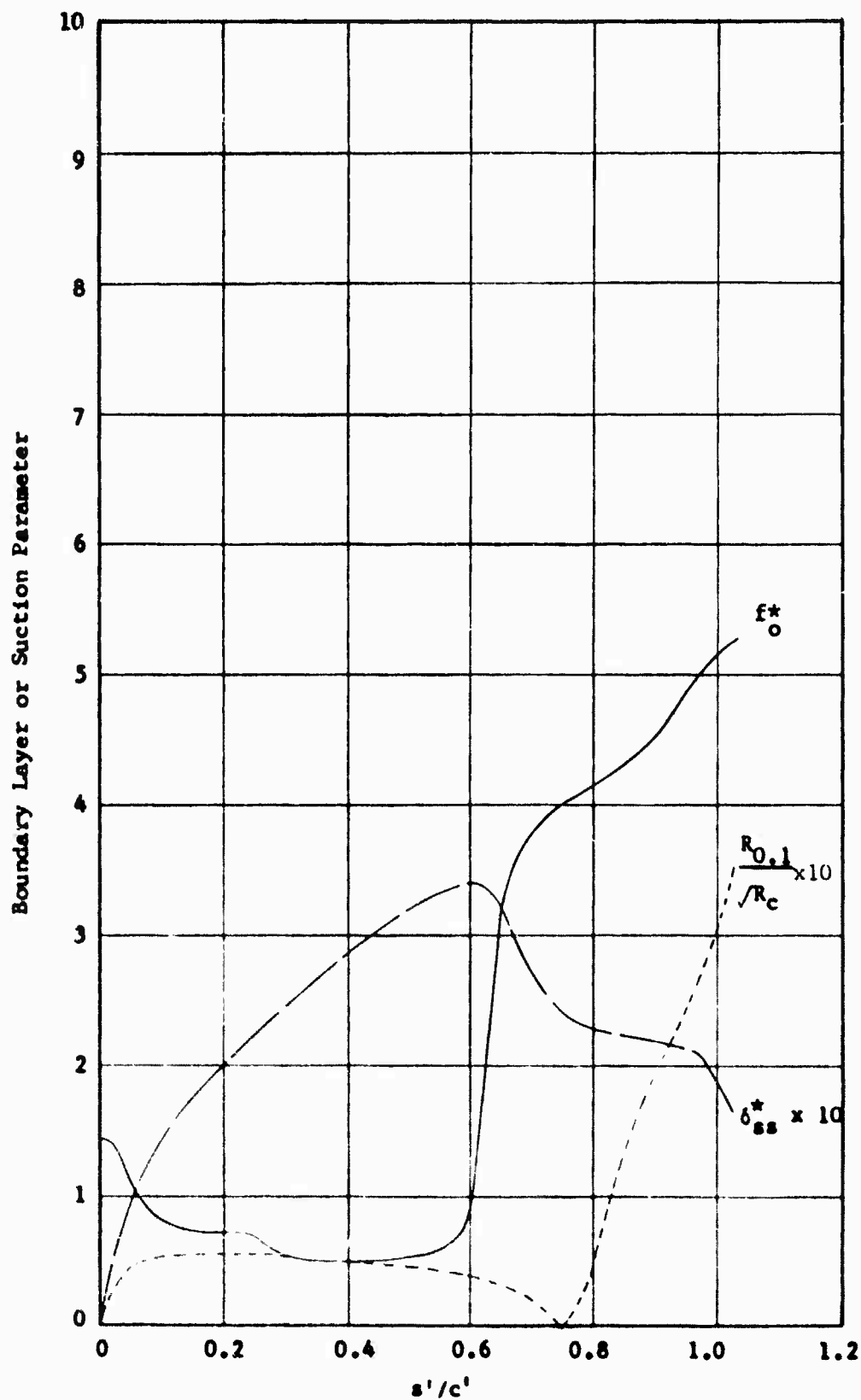
MODIFICATION OF THE GÖTHERT CORRECTION AT  $M_{u_\infty} = 0.6$

FIGURE 113



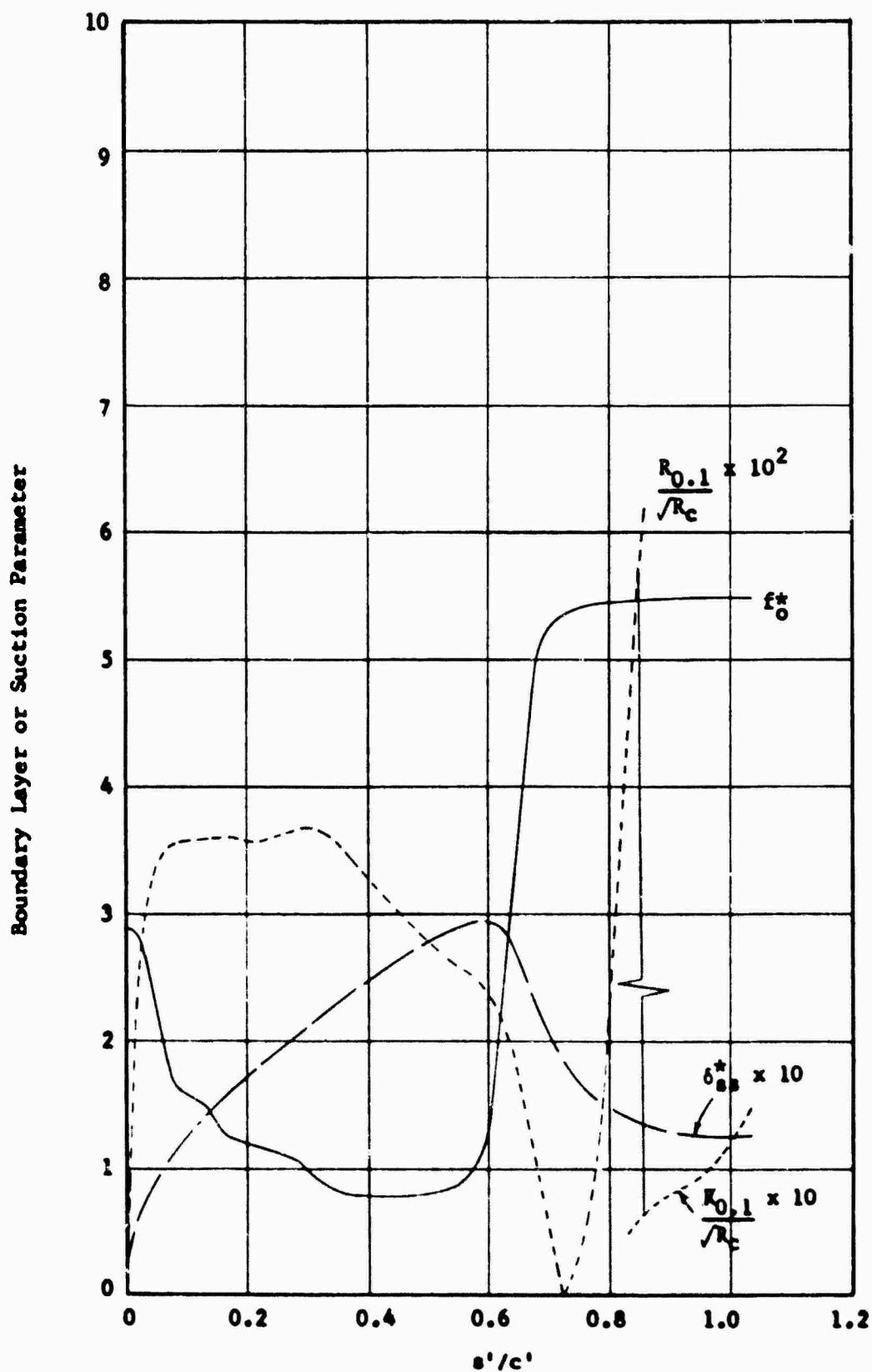
LFC AIRFOIL AND TWO DIMENSIONAL INCOMPRESSIBLE VELOCITY DISTRIBUTION

FIGURE 114

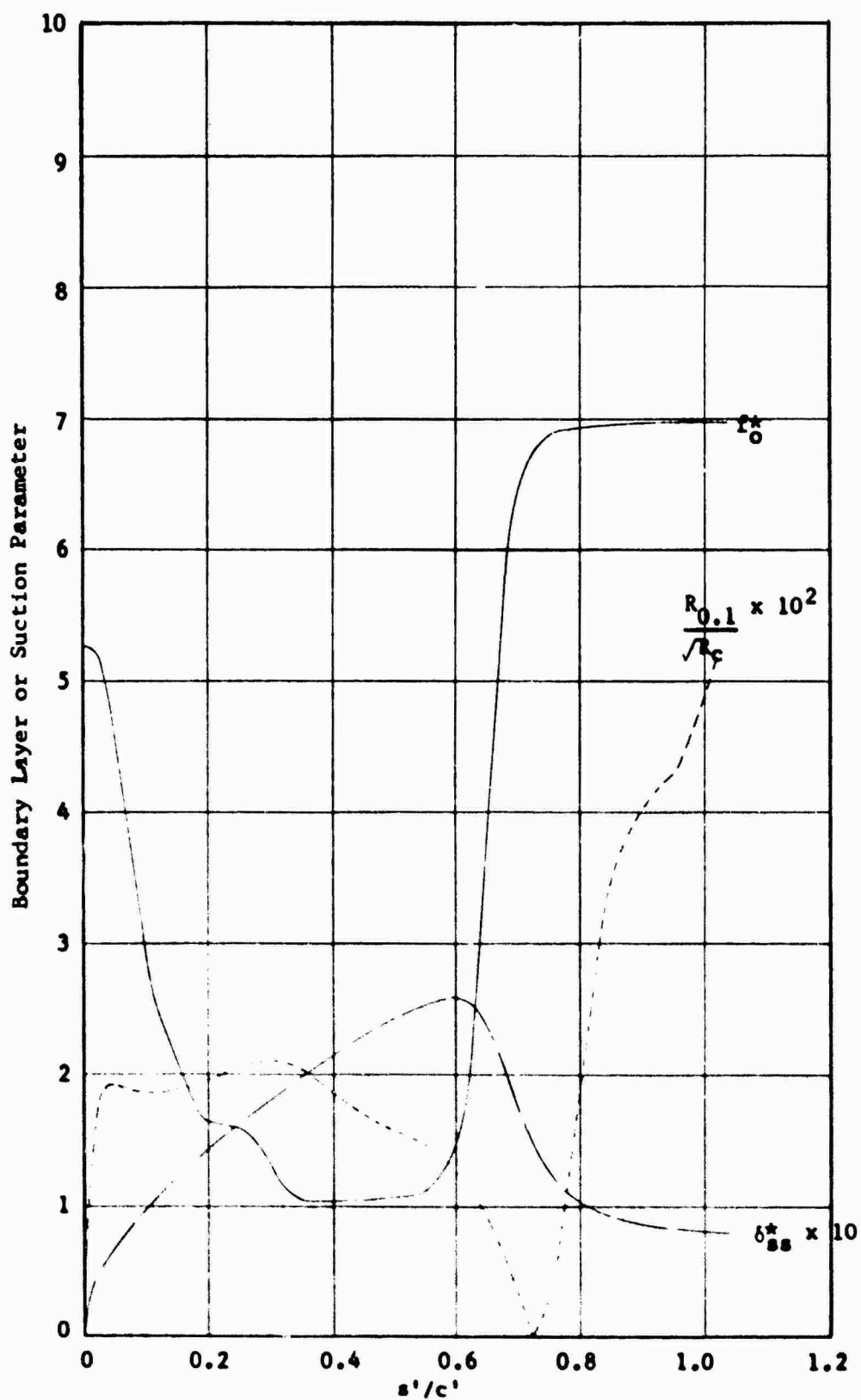


COMPUTED BOUNDARY LAYER PARAMETERS AT  $M_\infty = 2.0$  FOR LOW SUCTION -  
CRITICAL CHORD REYNOLDS NUMBER  $\sim 4 \times 10^6$

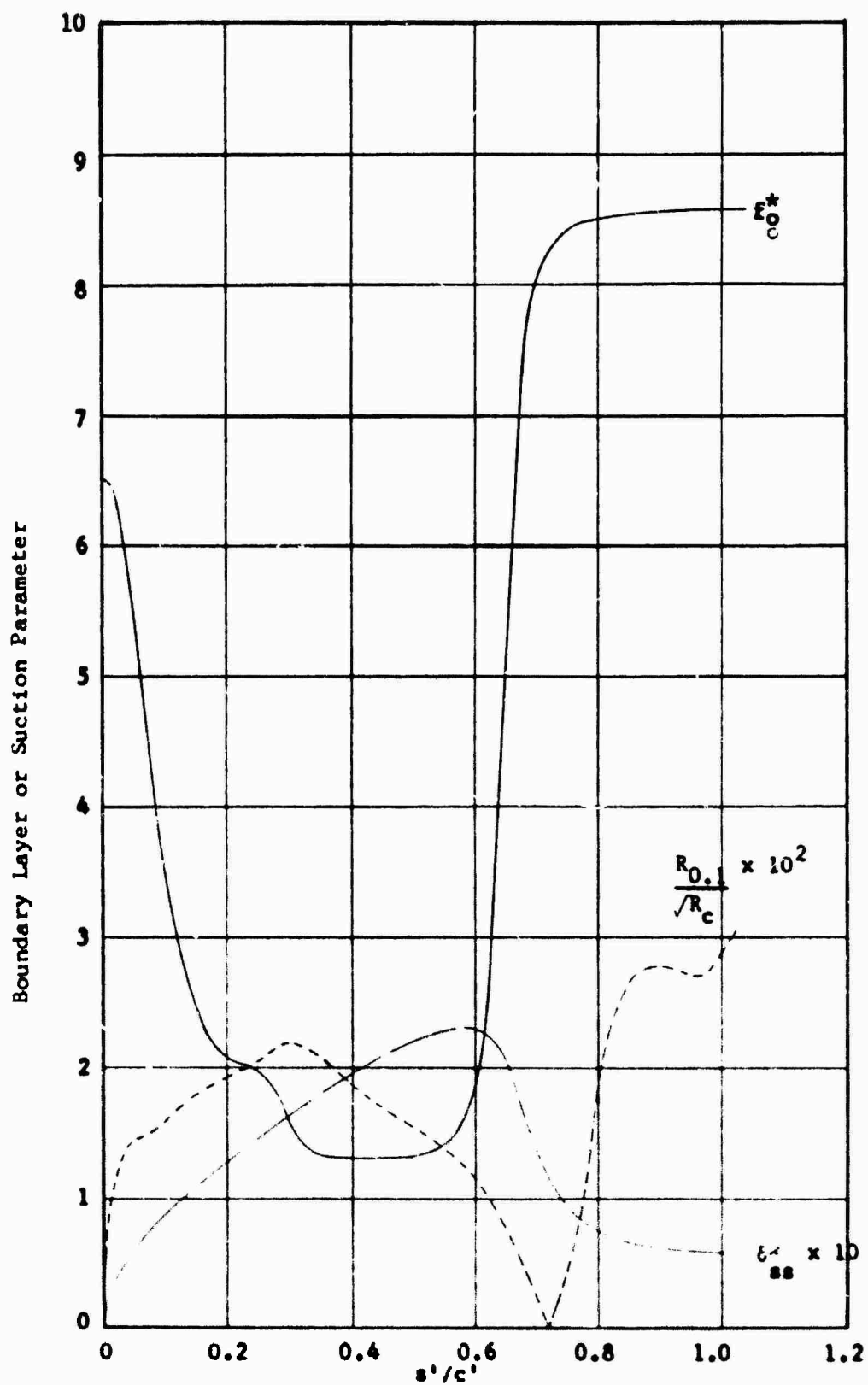
FIGURE 115



COMPUTED BOUNDARY LAYER PARAMETERS AT  $M_\infty = 2.0$  AND MEDIUM  
SUCTION-CRITICAL CHORD REYNOLDS NUMBER  $\approx 10 \times 10^6$



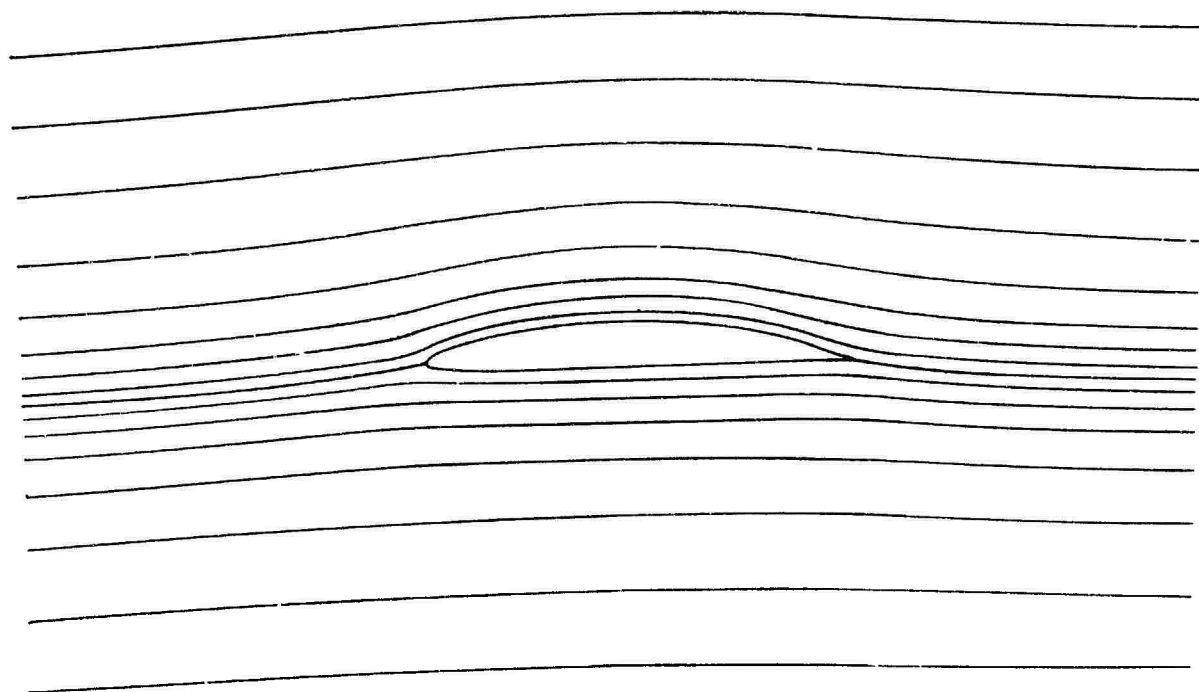
COMPUTED BOUNDARY LAYER PARAMETERS AT  $M_\infty = 2.0$  AND HIGH SUCTION -  
CRITICAL CHORD REYNOLDS NUMBER  $\approx 30 \times 10^6$



COMPUTED BOUNDARY LAYER PARAMETERS AT  $M_\infty = 3.0$  -  
 CRITICAL CHORD REYNOLDS NUMBER  $\approx 30 \times 10^6$

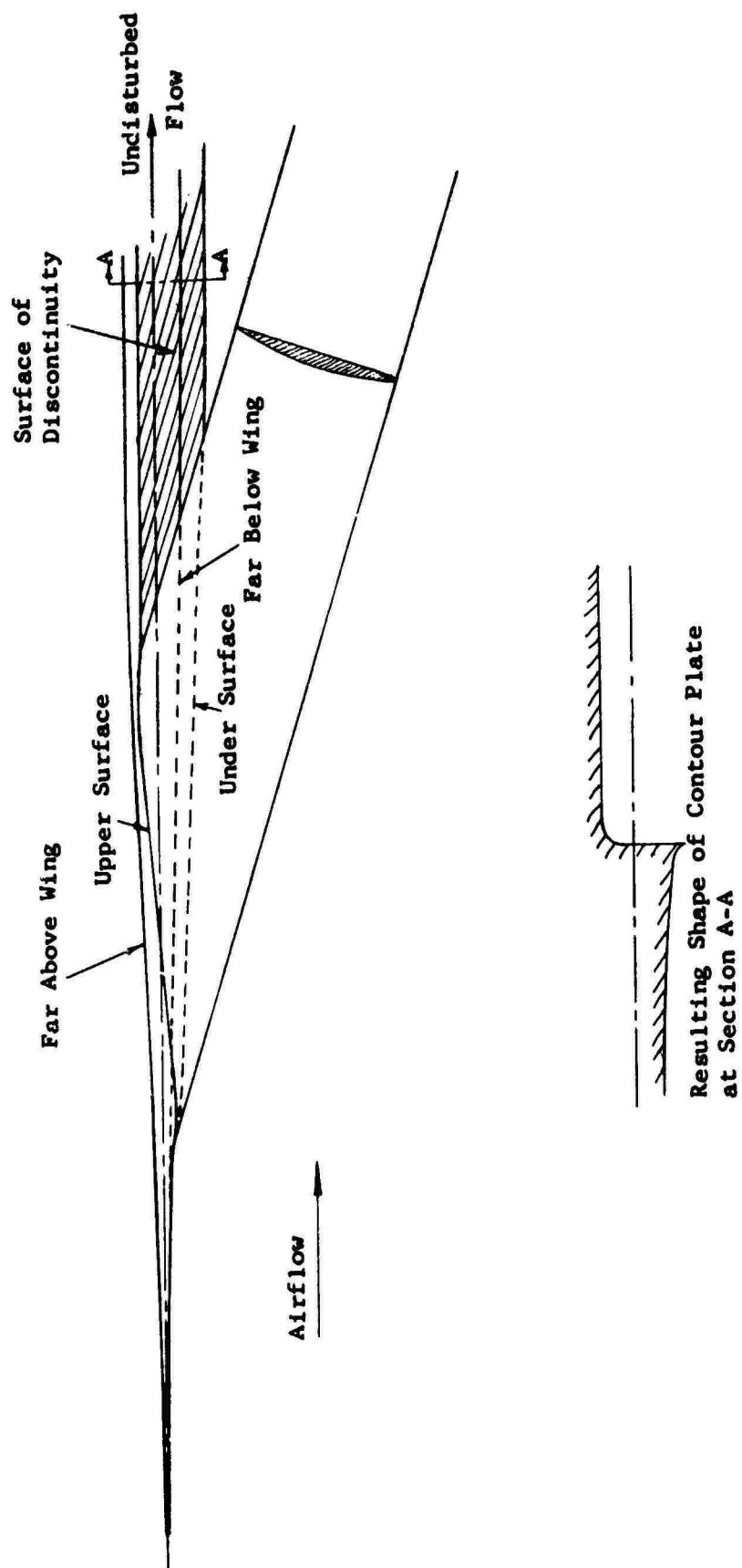
FIGURE 118  
 -721-





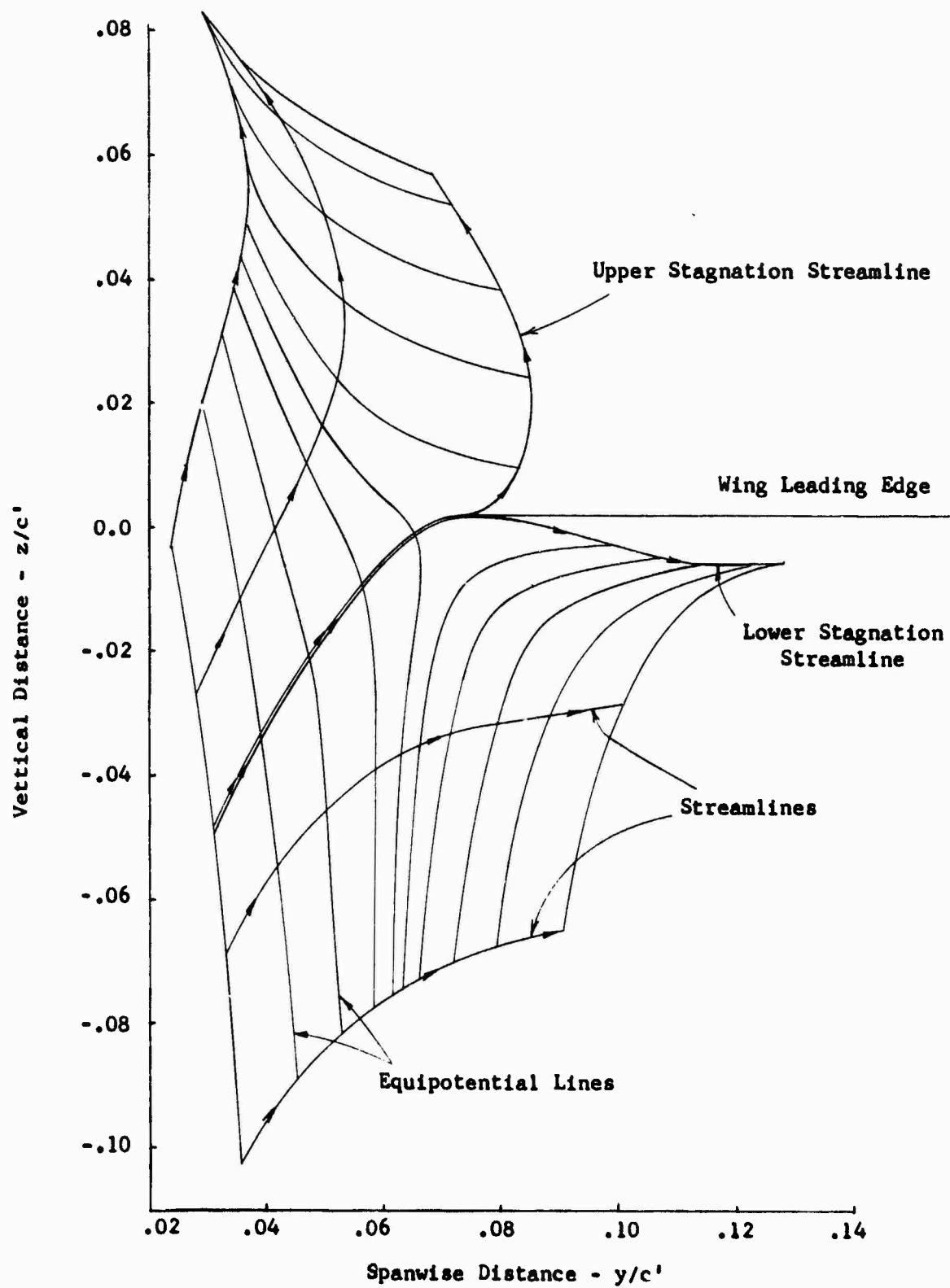
TWO DIMENSIONAL FLOW FIELD FOR LFC AIRFOIL

FIGURE 119



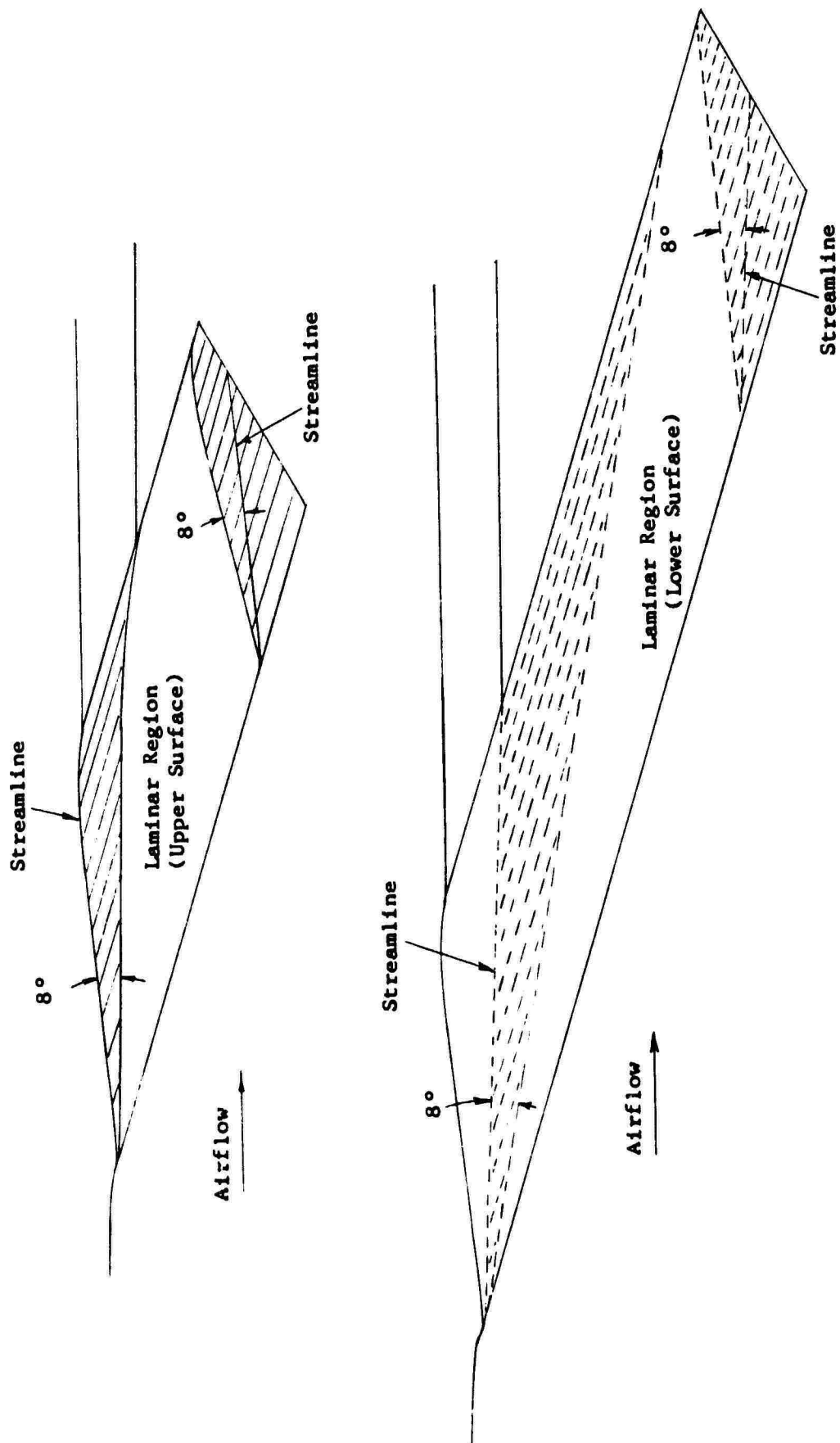
PATH OF STREAMLINES WHICH DEFINE SHAPE OF CONTOURED PLATE

FIGURE 120



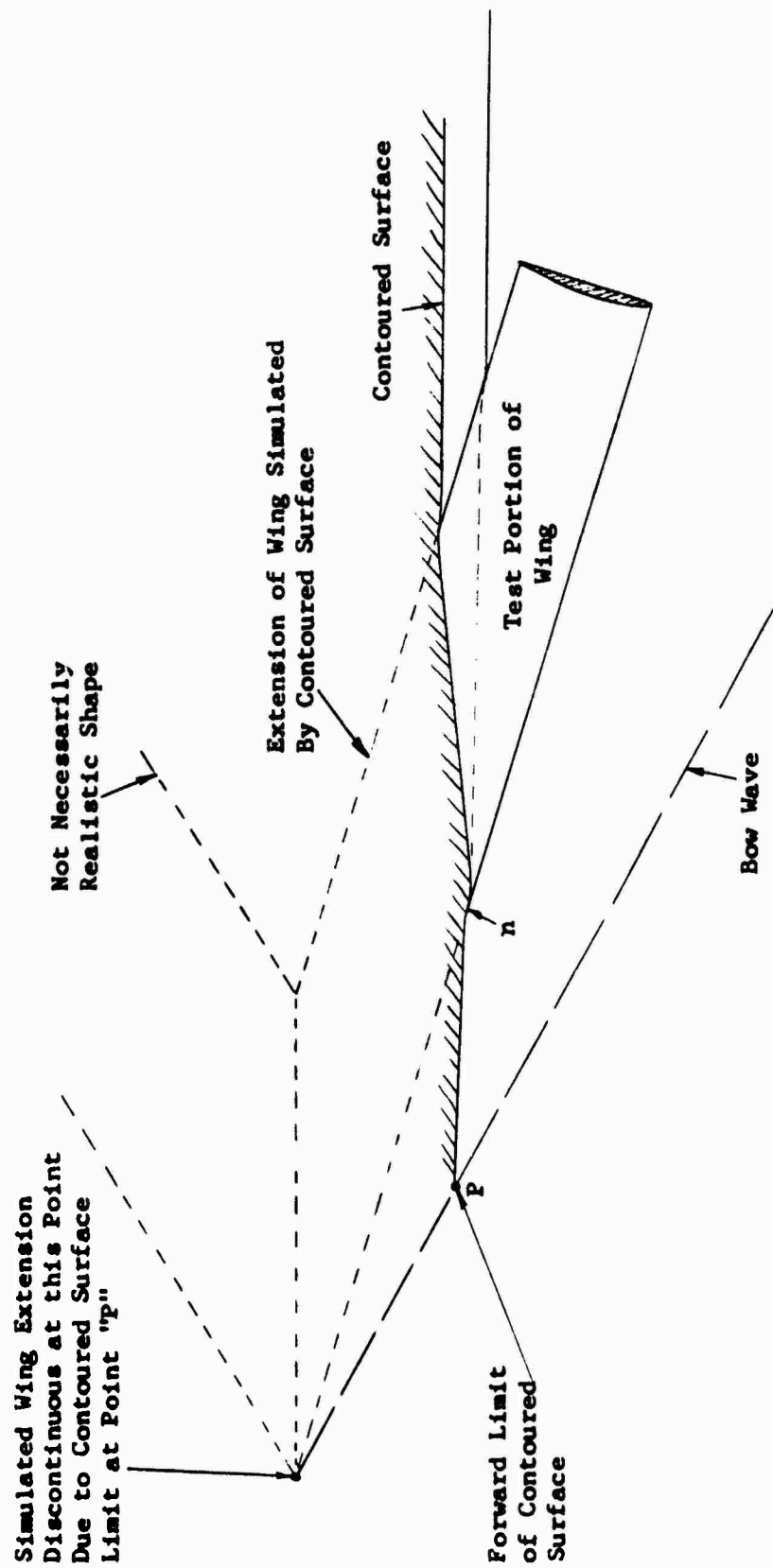
FLOW FIELD NEAR LEADING EDGE ILLUSTRATING EXCESSIVE SPANWISE  
FLOW NEAR AIRFOIL SURFACE

FIGURE 121



LAMINAR & TURBULENT (SHADED) REGIONS AT  $M_\infty = 2.0$

FIGURE 122



EFFECT OF LIMITING CONTOURED WALL TO FINITE DIMENSIONS

FIGURE 123

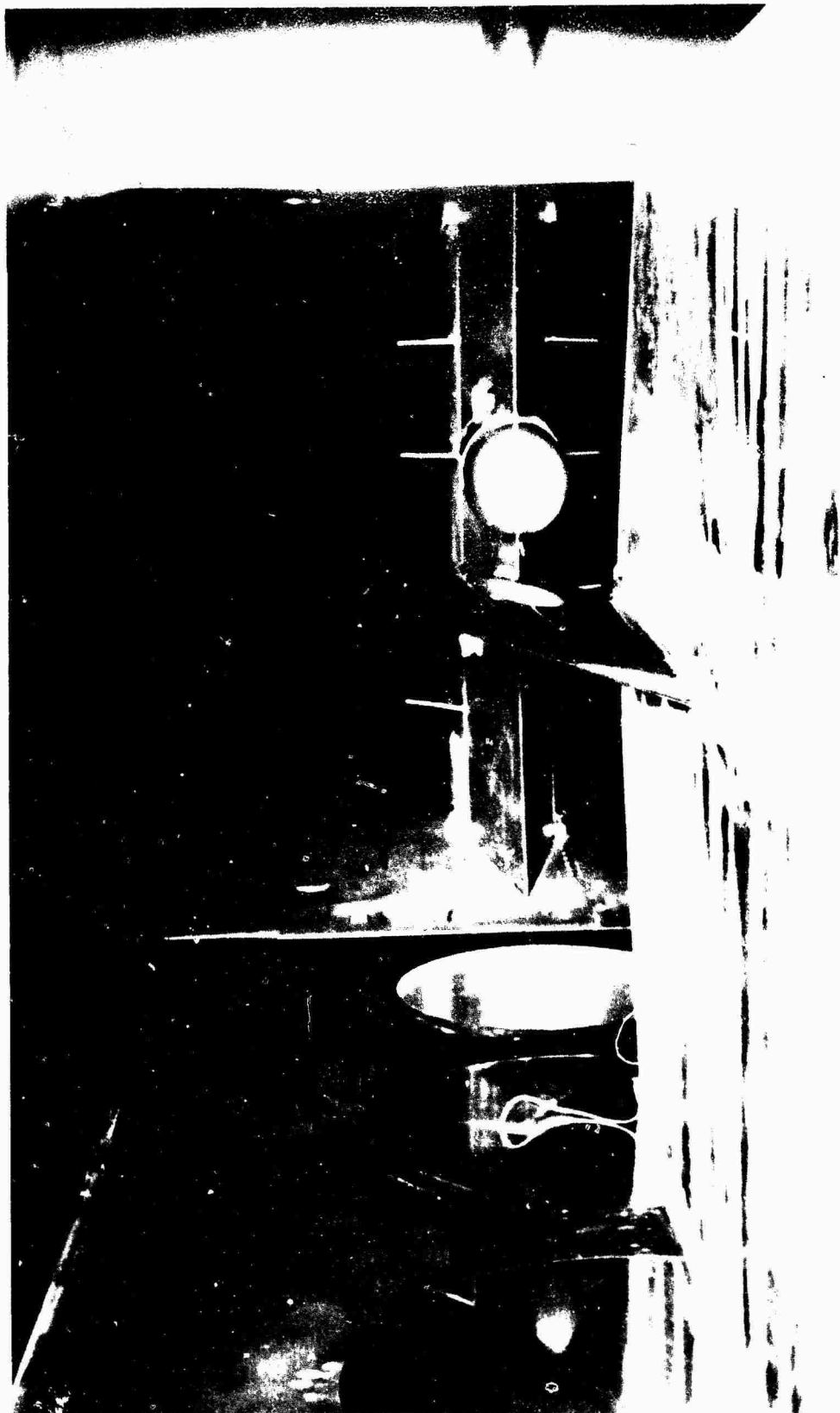
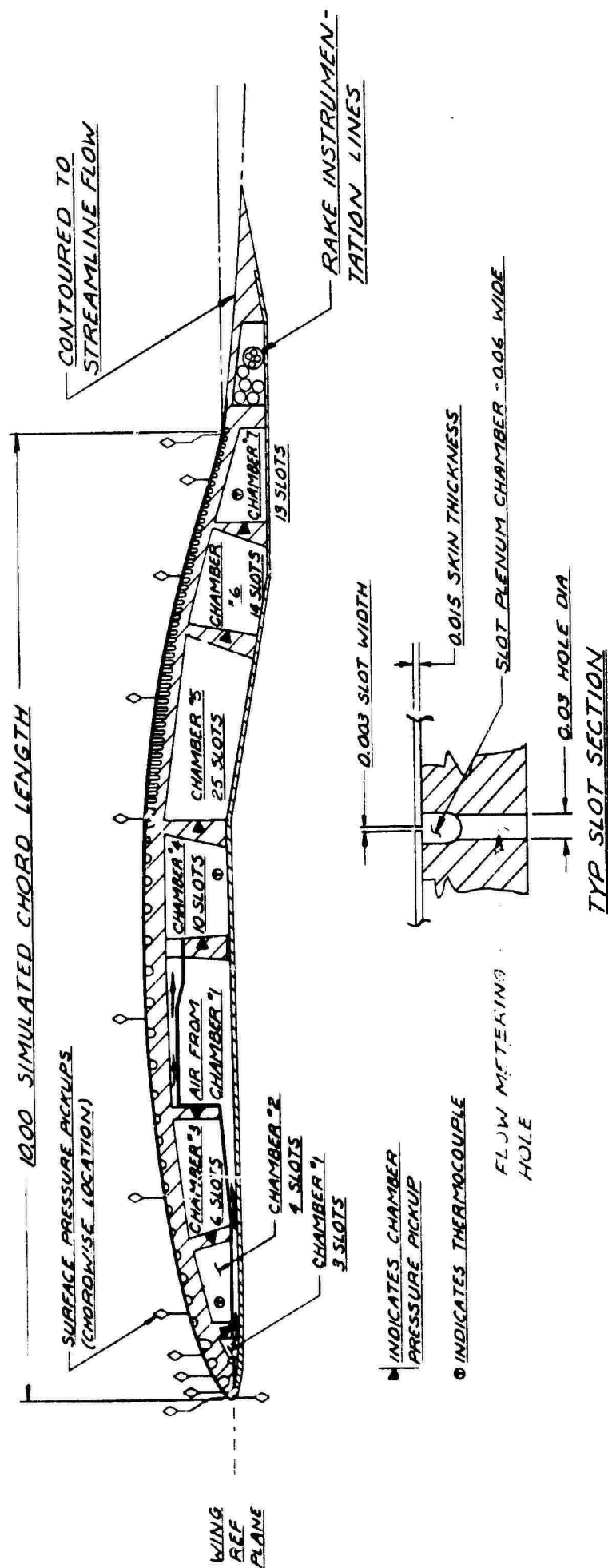


FIGURE 124 INSTALLATION OF MODEL IN 40 x 40 INCH WIND TUNNEL--(RIGHT HAND DOOR REMOVED)



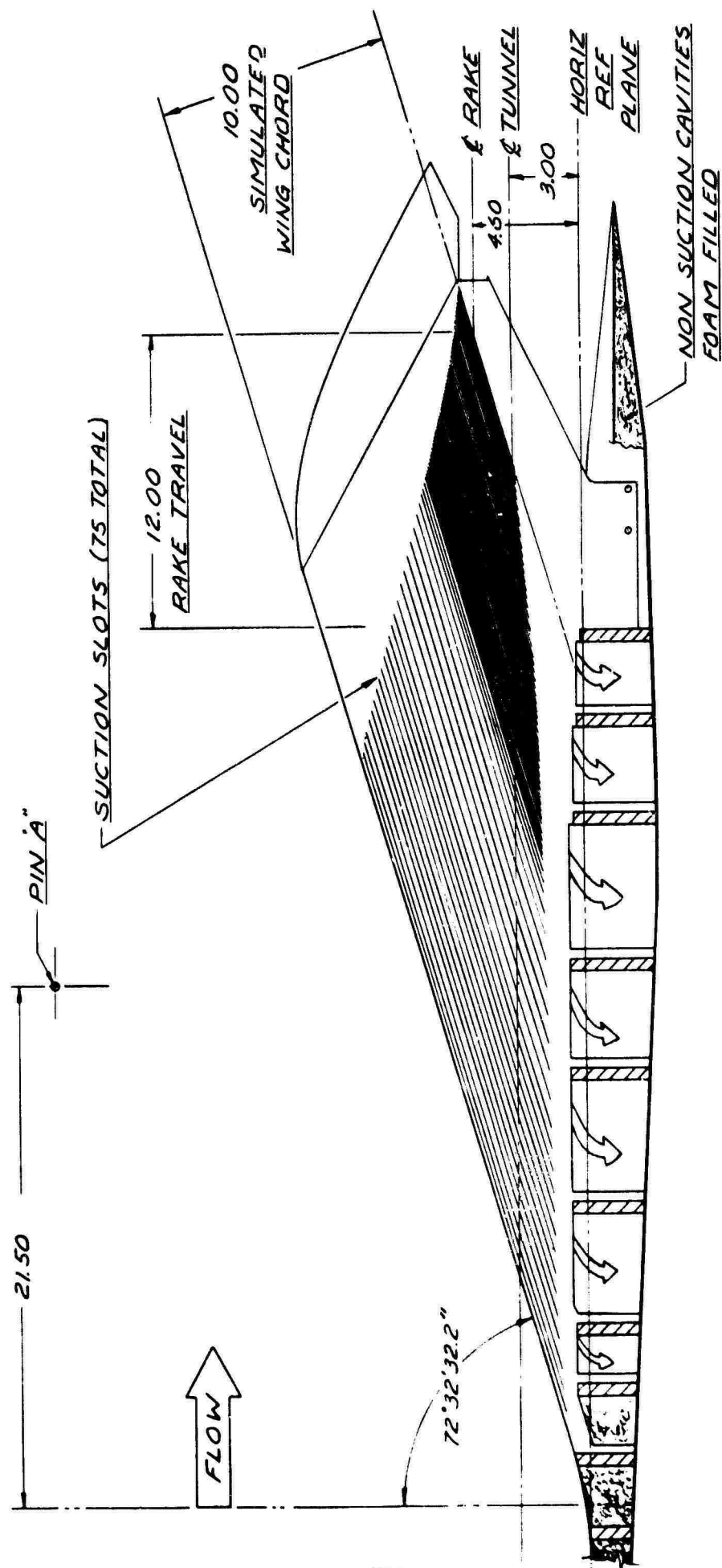
CROSS SECTION OF THE AIRFOIL SHOWING SUCTION CHAMBERS AND TRAILING EDGE EXTENSION

FIGURE 125



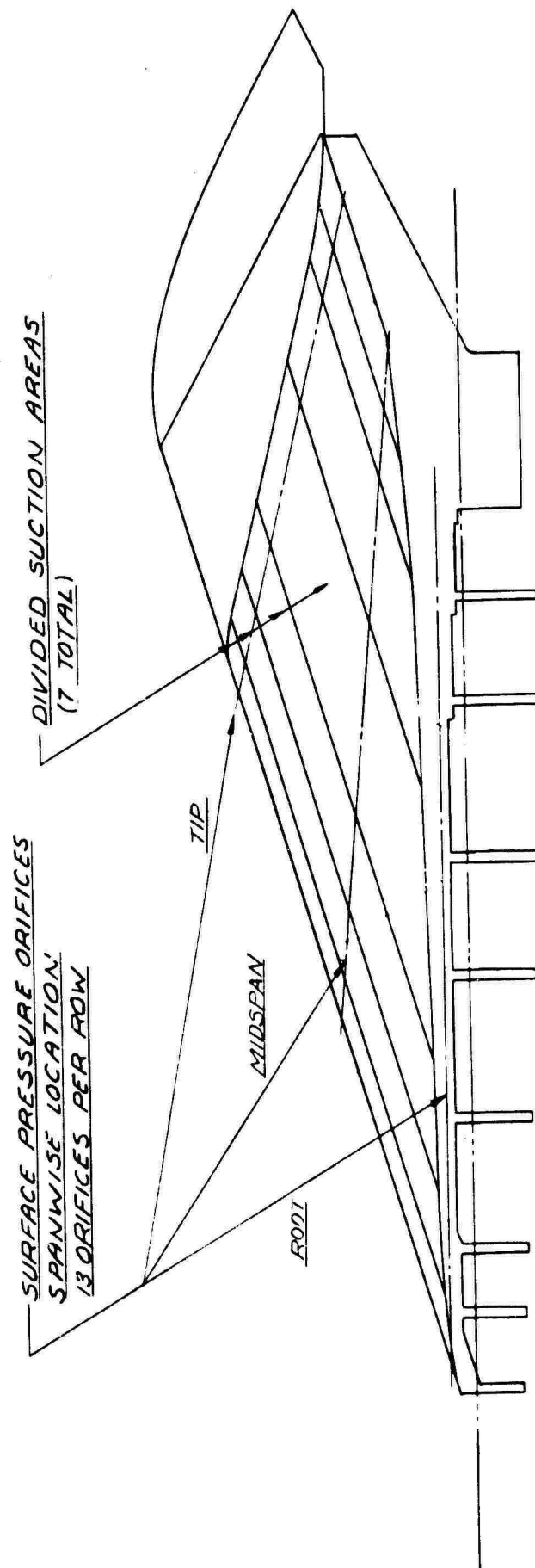
FIGURE 126 STREAMWISE VIEW OF CONTOURED SUPPORT PLATE (SKIN REMOVED) FOR AIRFOIL SHOWING SHAPE OF CONTOUR LINES





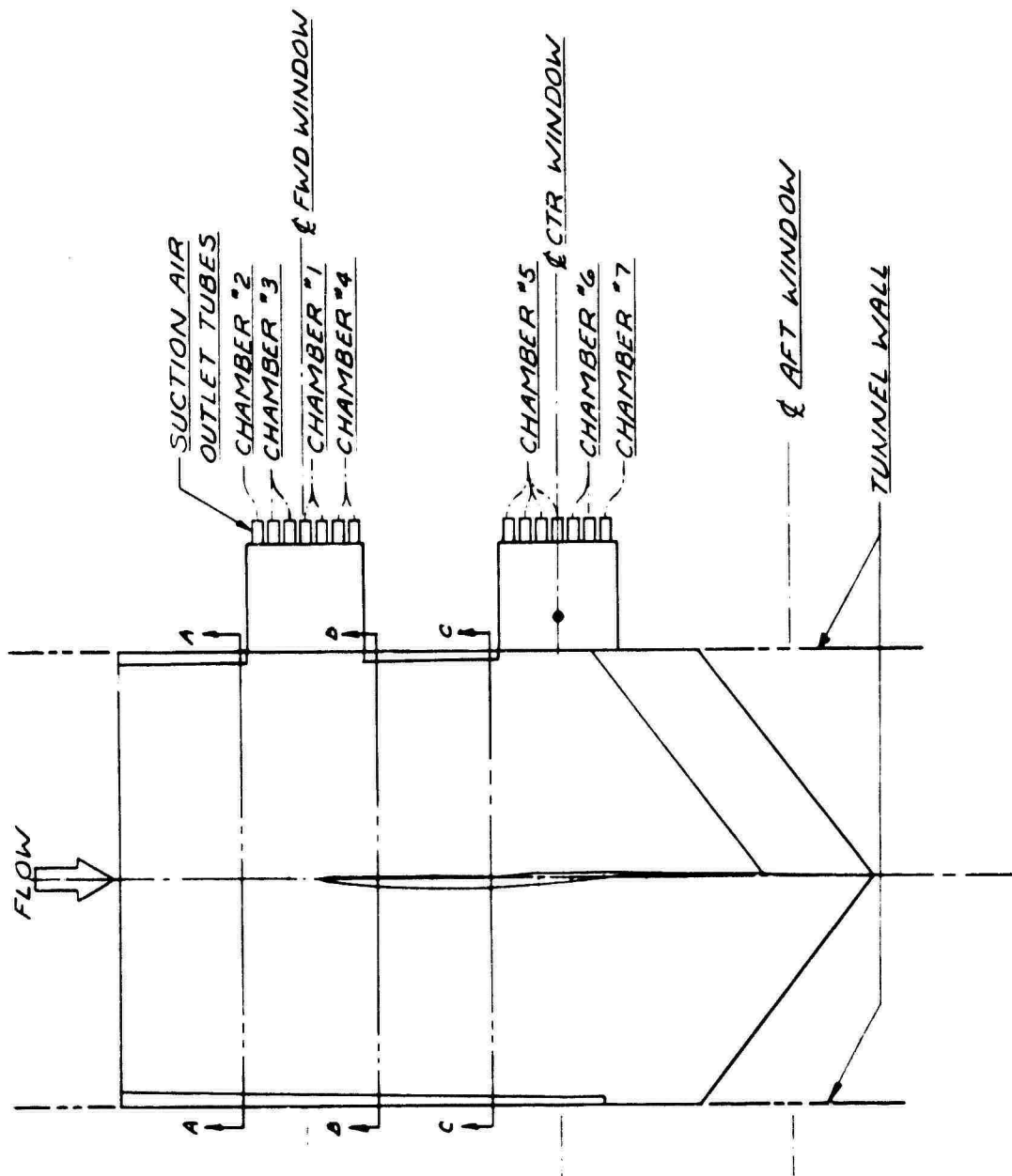
PLAN VIEW OF SIMULATED AIRFOIL SHOWING LOCATION OF SUCTION SLOTS

FIGURE 127



PLAN VIEW OF SUCTION CHAMBERS AND LOCATION OF PRESSURE ORIFICES

FIGURE 128



PLAN VIEW AND SECTIONS OF CONTOUR PLATE

FIGURE 129



FIGURE 130 MODEL INSTALLED IN TUNNEL A - NOTE RAKE LOCATION NEAR TIP OF AIRFOIL TRAILING EDGE

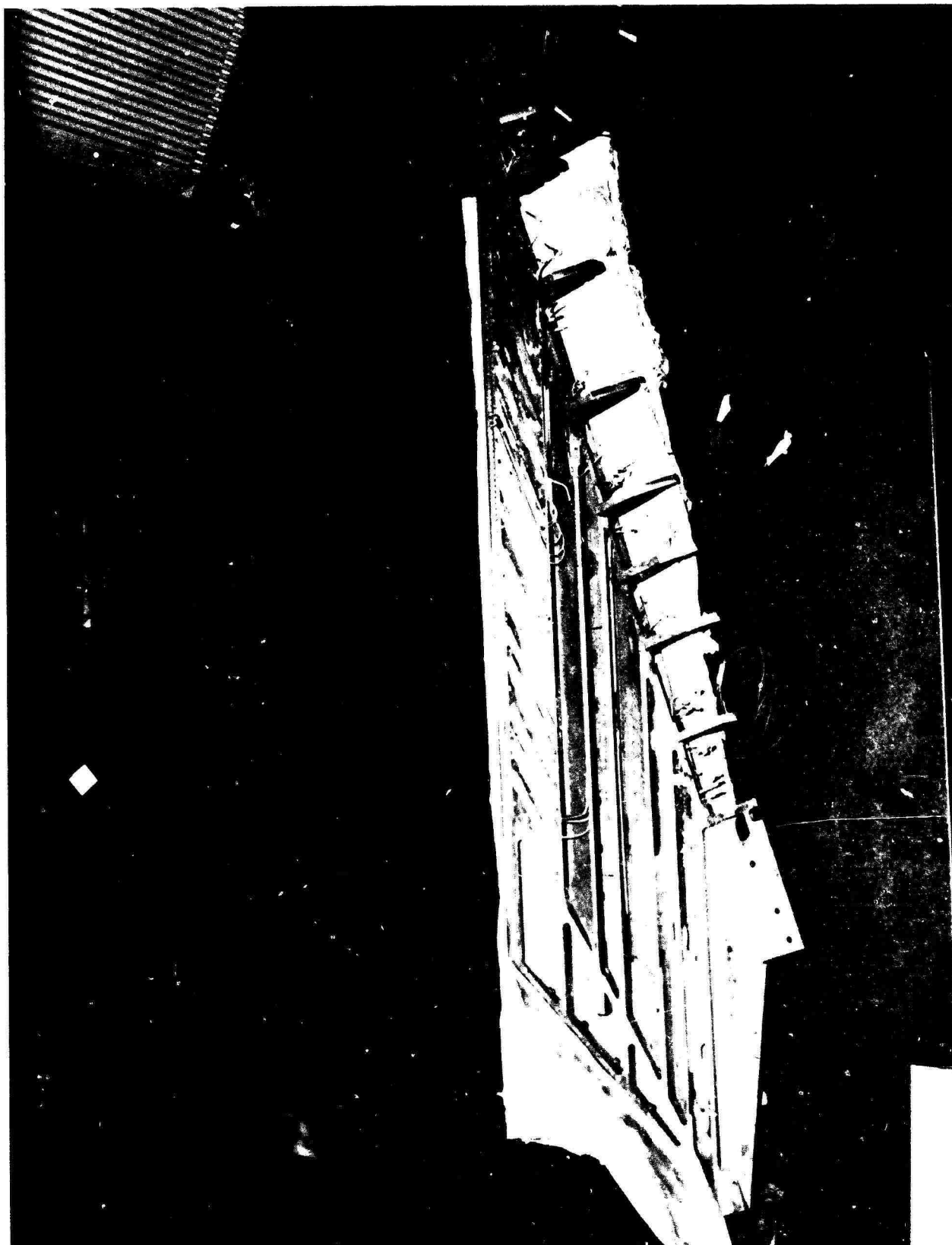


FIGURE 131a BOTTOM VIEW OF MODEL AIRFOIL (LOWER SKIN REMOVED)

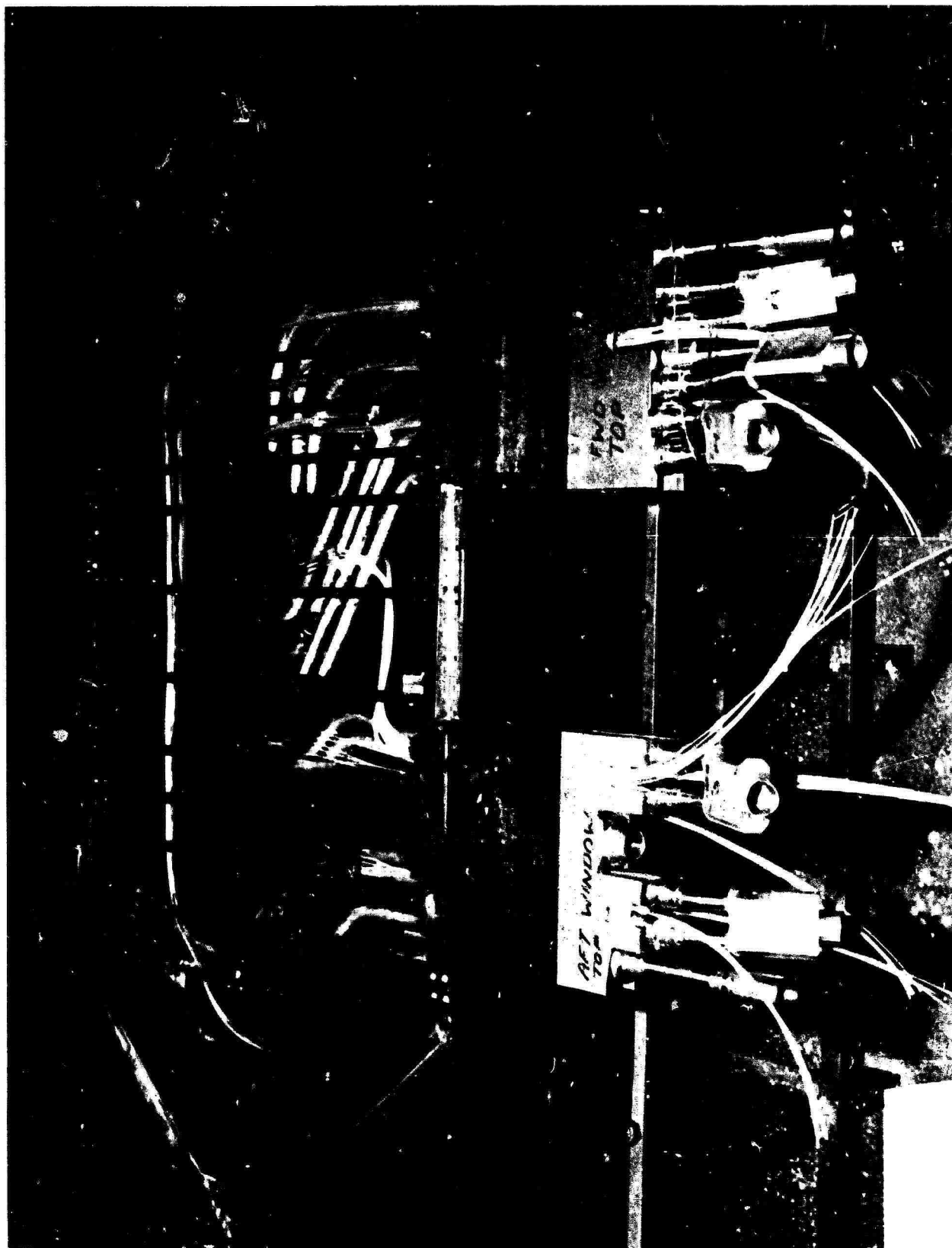


FIGURE 131b DETAILS OF CONTOUR PLATE WITH SKINS REMOVED

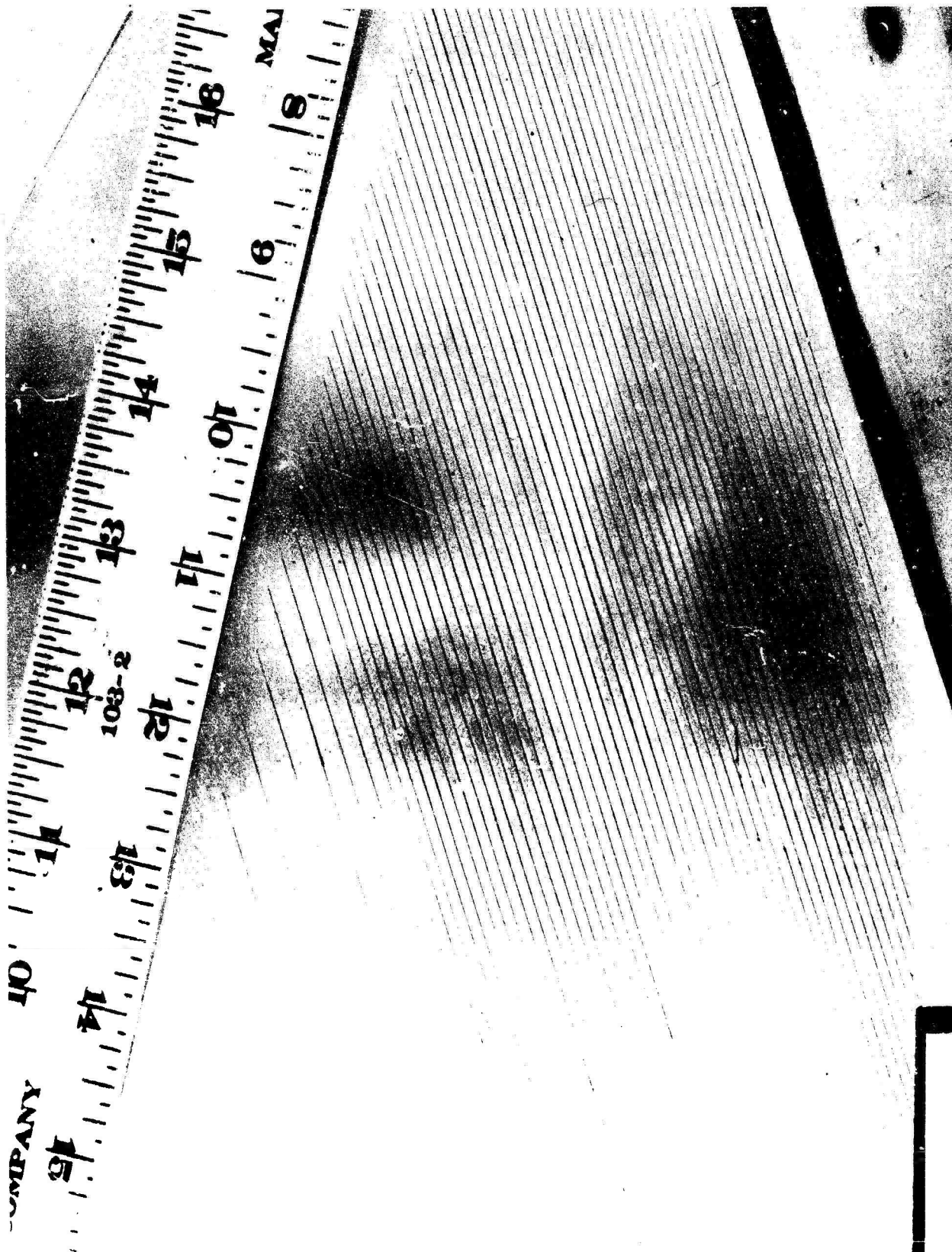
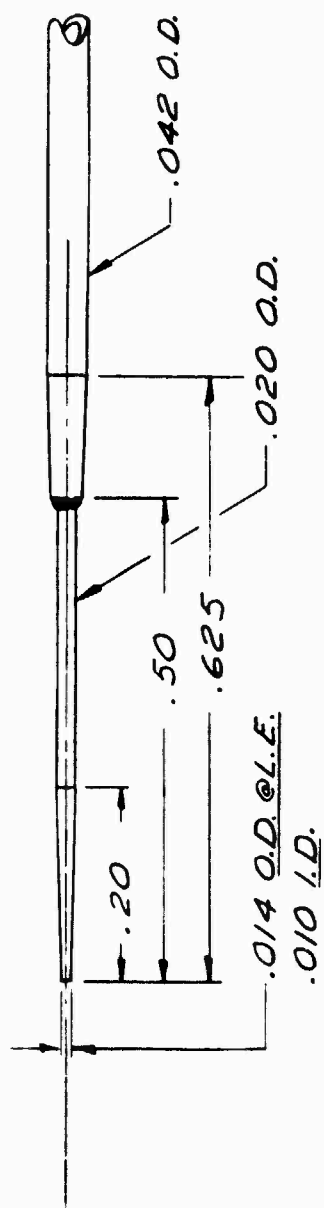
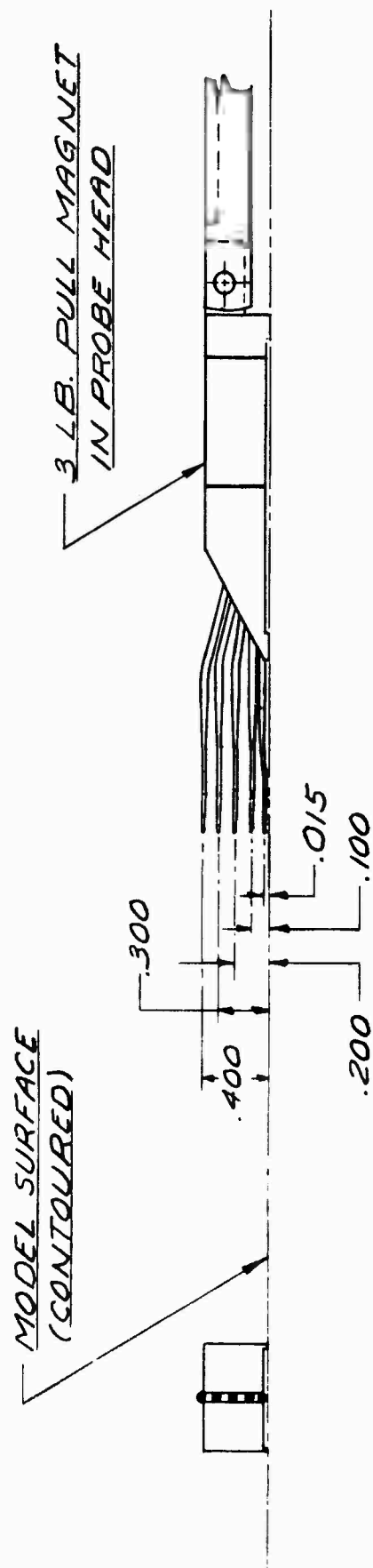
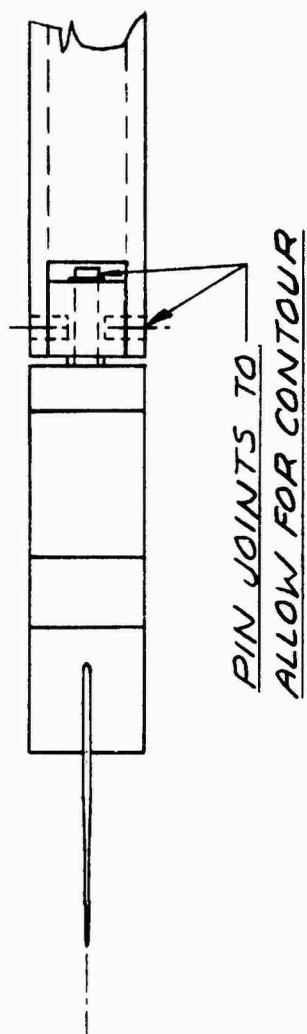


FIGURE 132 CLOSE UP OF SLOTS NEAR AIRFOIL TRAILING EDGE



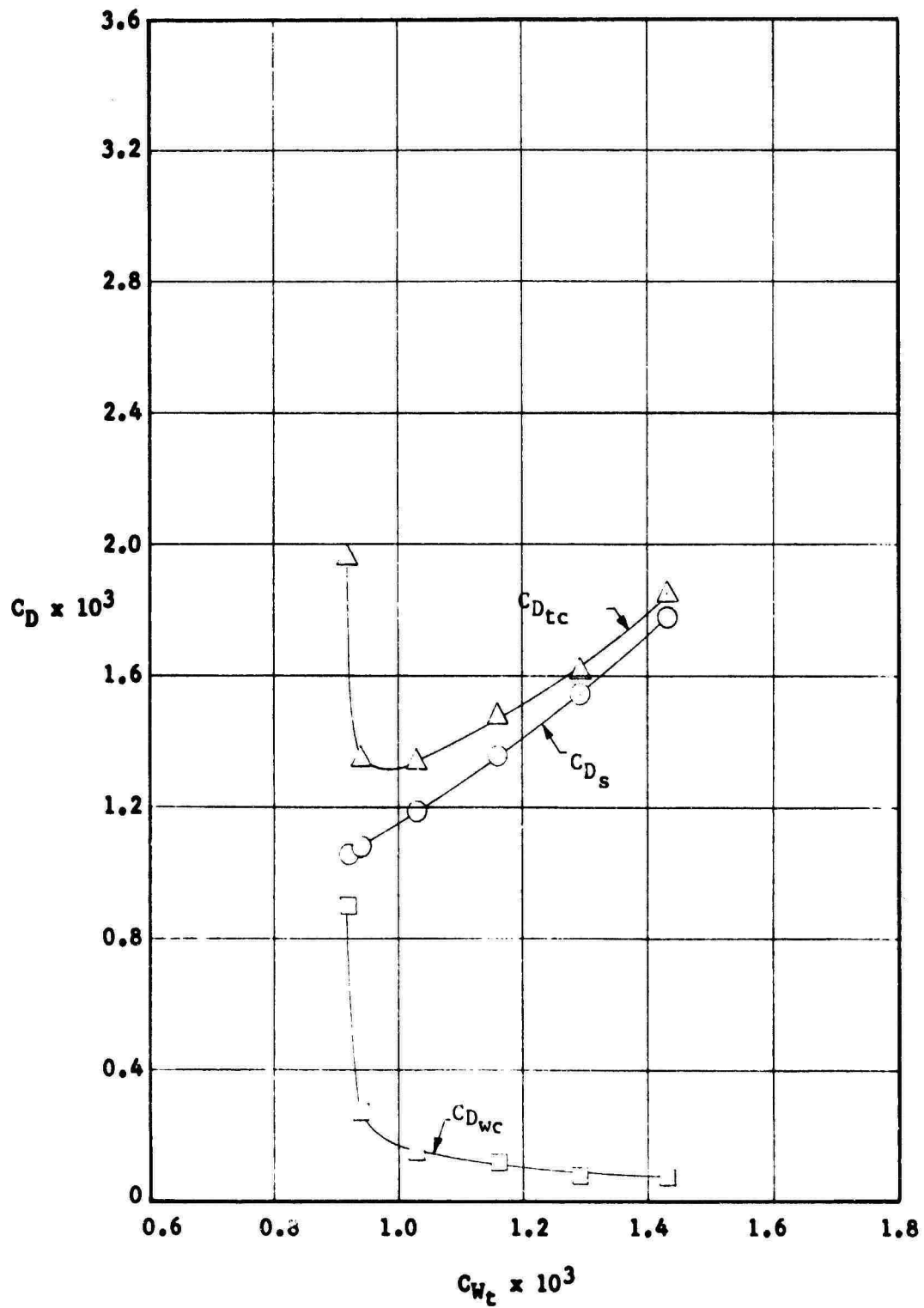
DETAIL OF PROBE



DETAILS OF WAKE RAKE

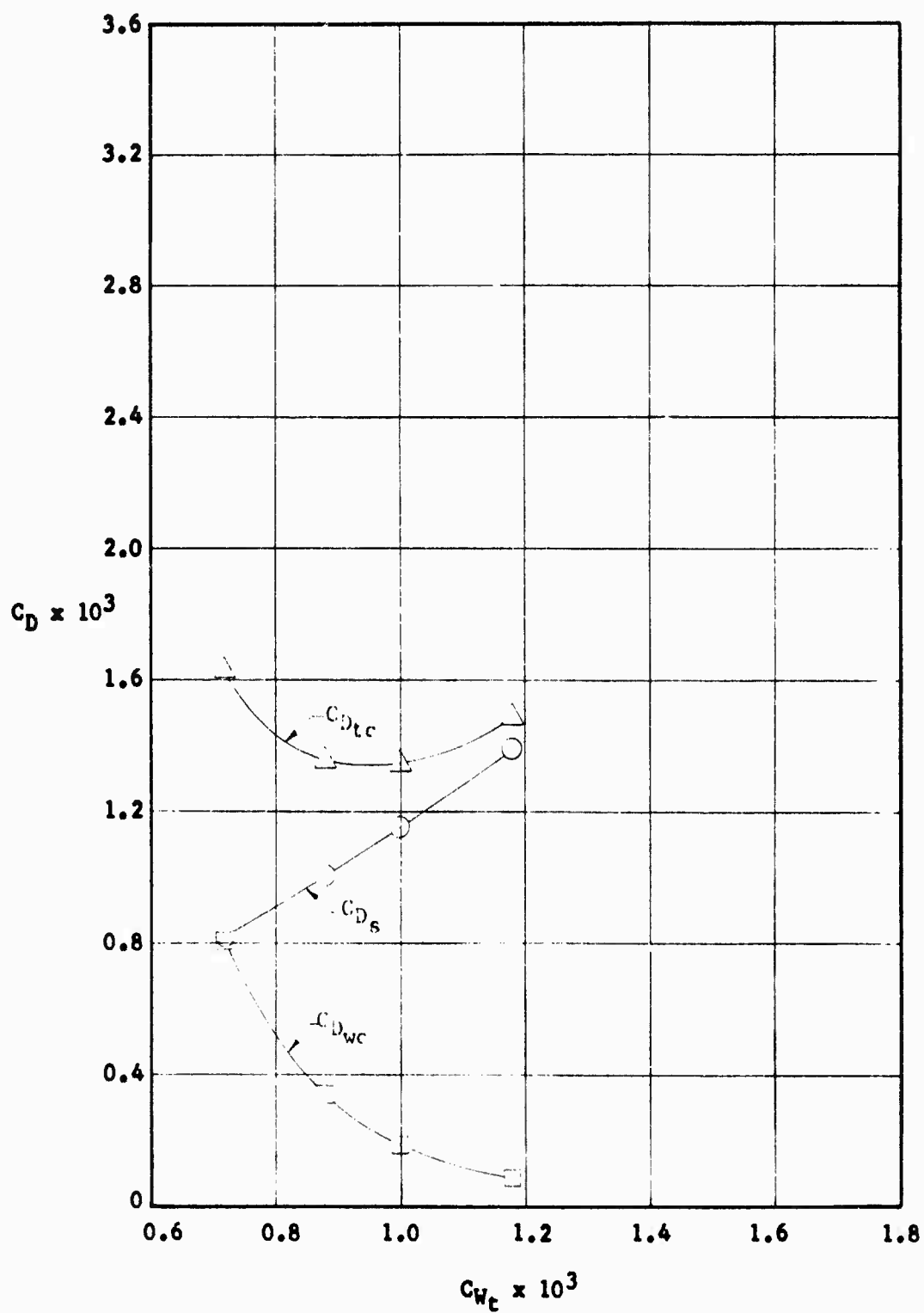
FIGURE 133





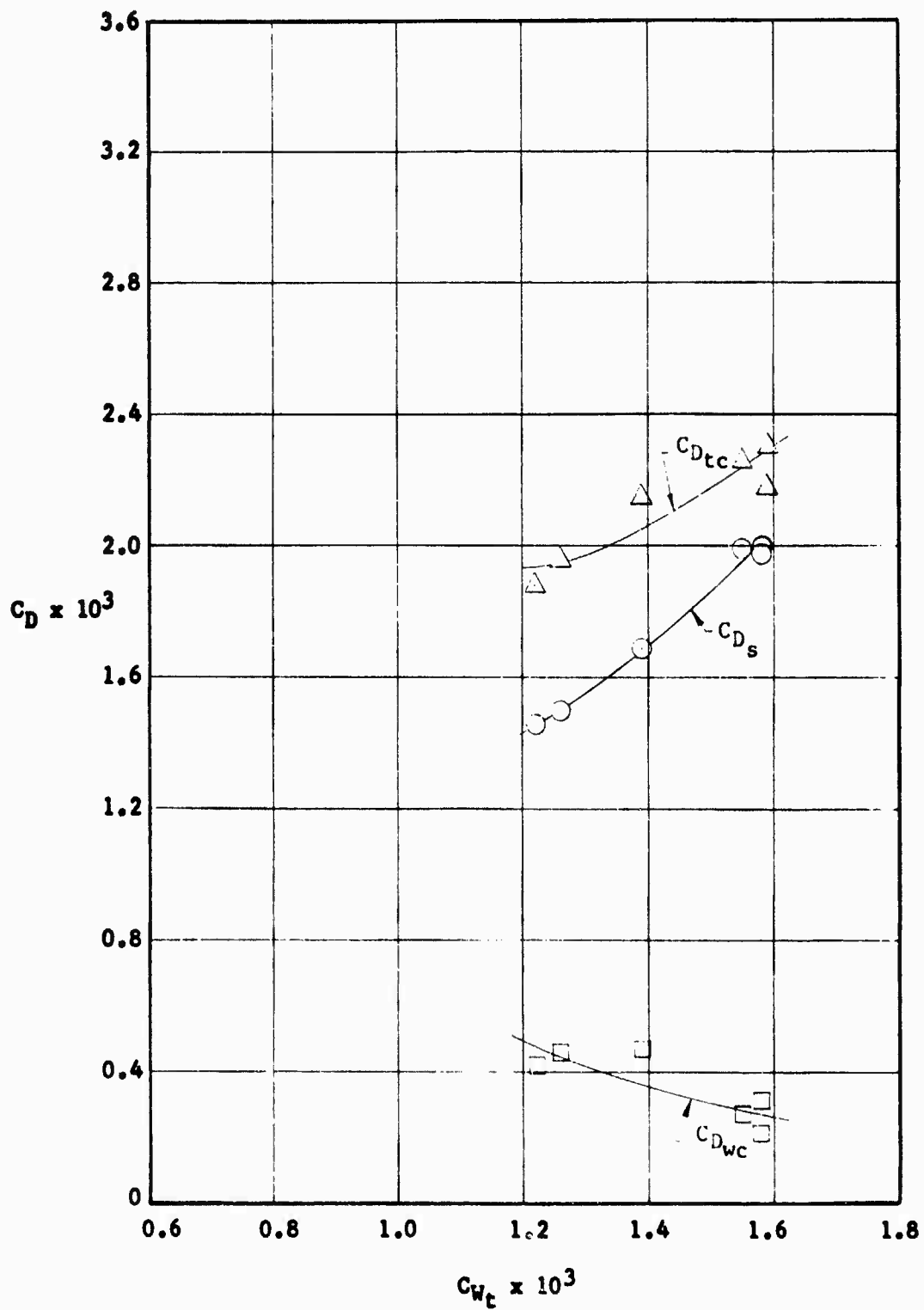
VARIATION OF DRAG COMPONENTS WITH SUCTION COEFFICIENT -  
 $M_\infty \sim 1.99$ ,  $R_c \sim 7.3 \times 10^6$ ,  $\alpha = 0.15^\circ$

FIGURE 134a



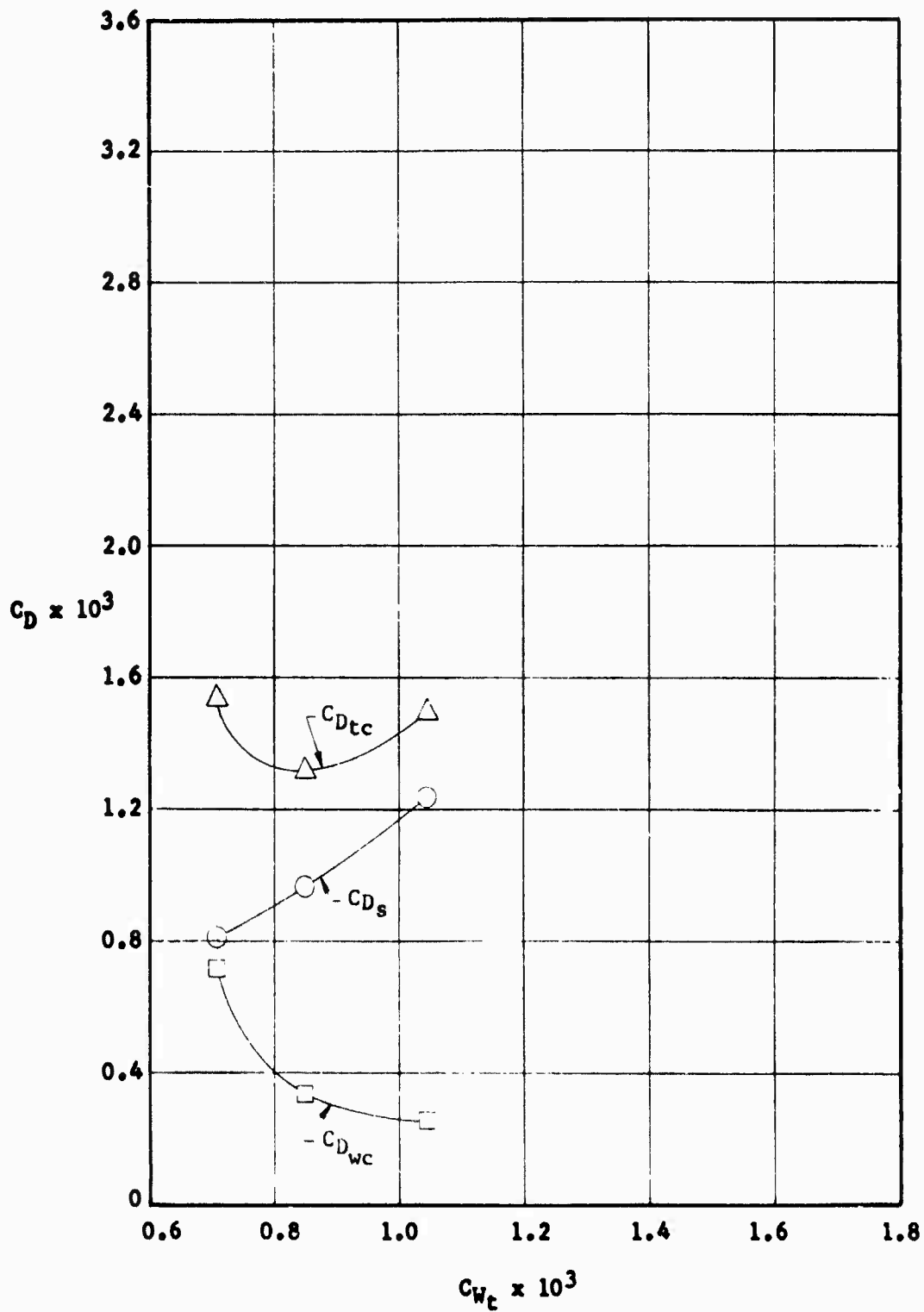
VARIATION OF DRAG COMPONENTS WITH SUCTION COEFFICIENT -  
 $M_\infty = 1.99$ ,  $R_C = 8.8 \times 10^6$ ,  $\gamma = 0.15$

FIGURE 134b



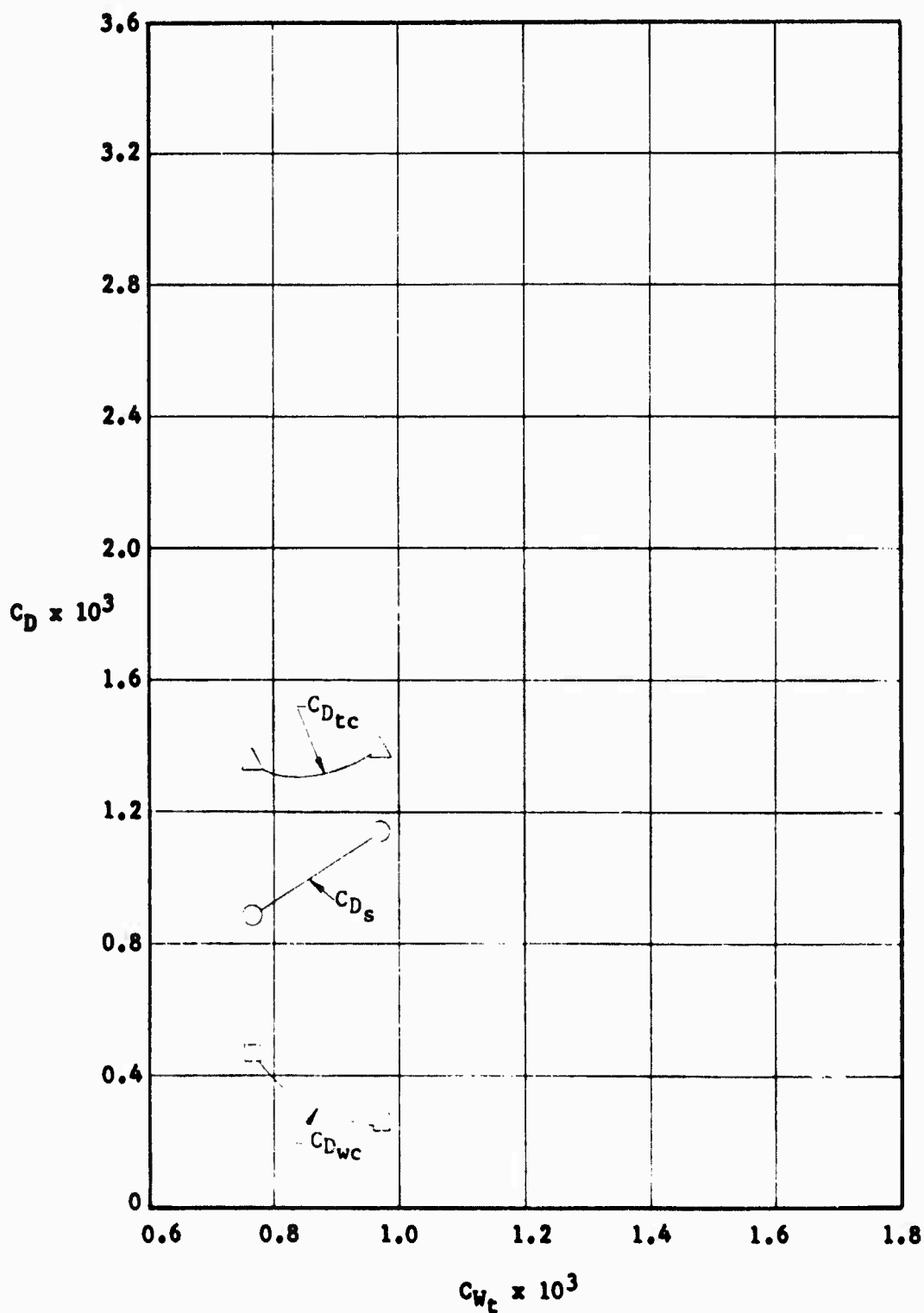
VARIATION OF DRAG COMPONENTS WITH SUCTION COEFFICIENT  
 $M_\infty \sim 1.99$ ,  $R_c \sim 11.0 \times 10^6$ ,  $\gamma = 0.15$

FIGURE 134c



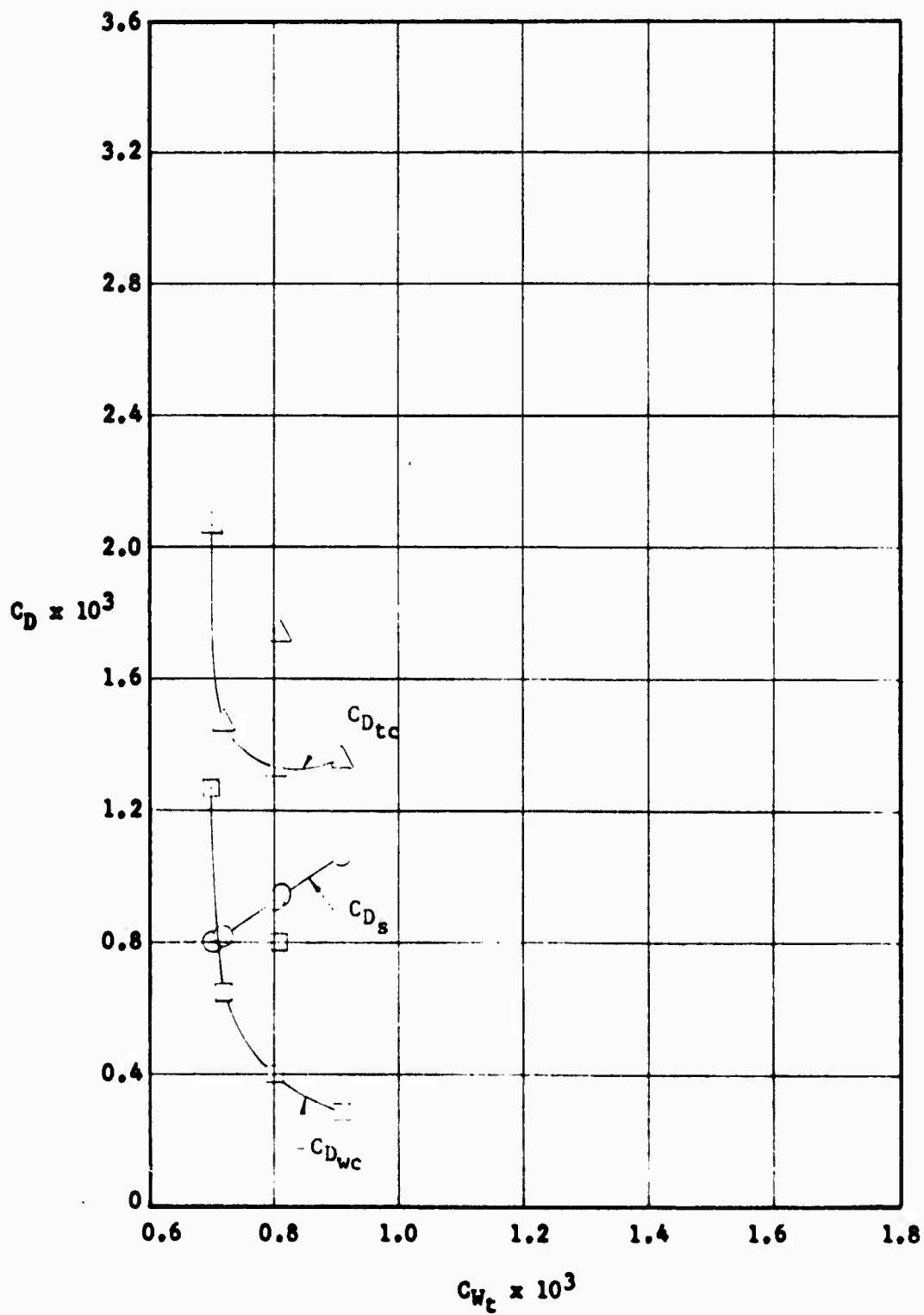
VARIATION OF DRAG COMPONENTS WITH SUCTION COEFFICIENTS  
 $M_\infty \sim 1.99$ ,  $R_c \sim 3.7 \times 10^6$ ,  $\gamma = 0.45^\circ$

FIGURE 135a



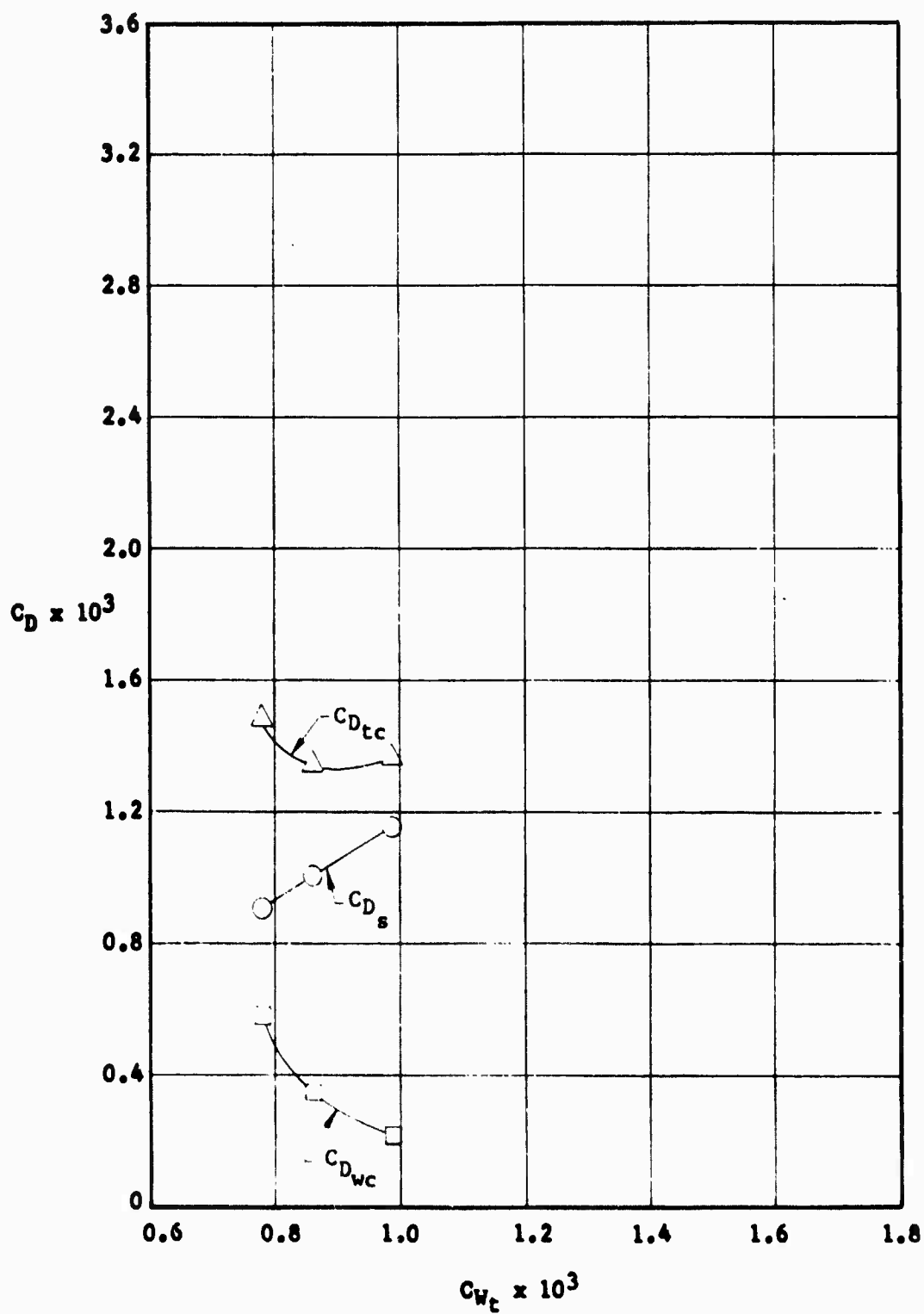
VARIATION OF DRAG COMPONENTS WITH SUCTION COEFFICIENT  
 $M_\infty \sim 1.99$ ,  $R_C \sim 5.3 \times 10^6$ ,  $\gamma = 0.45^\circ$

FIGURE 135b



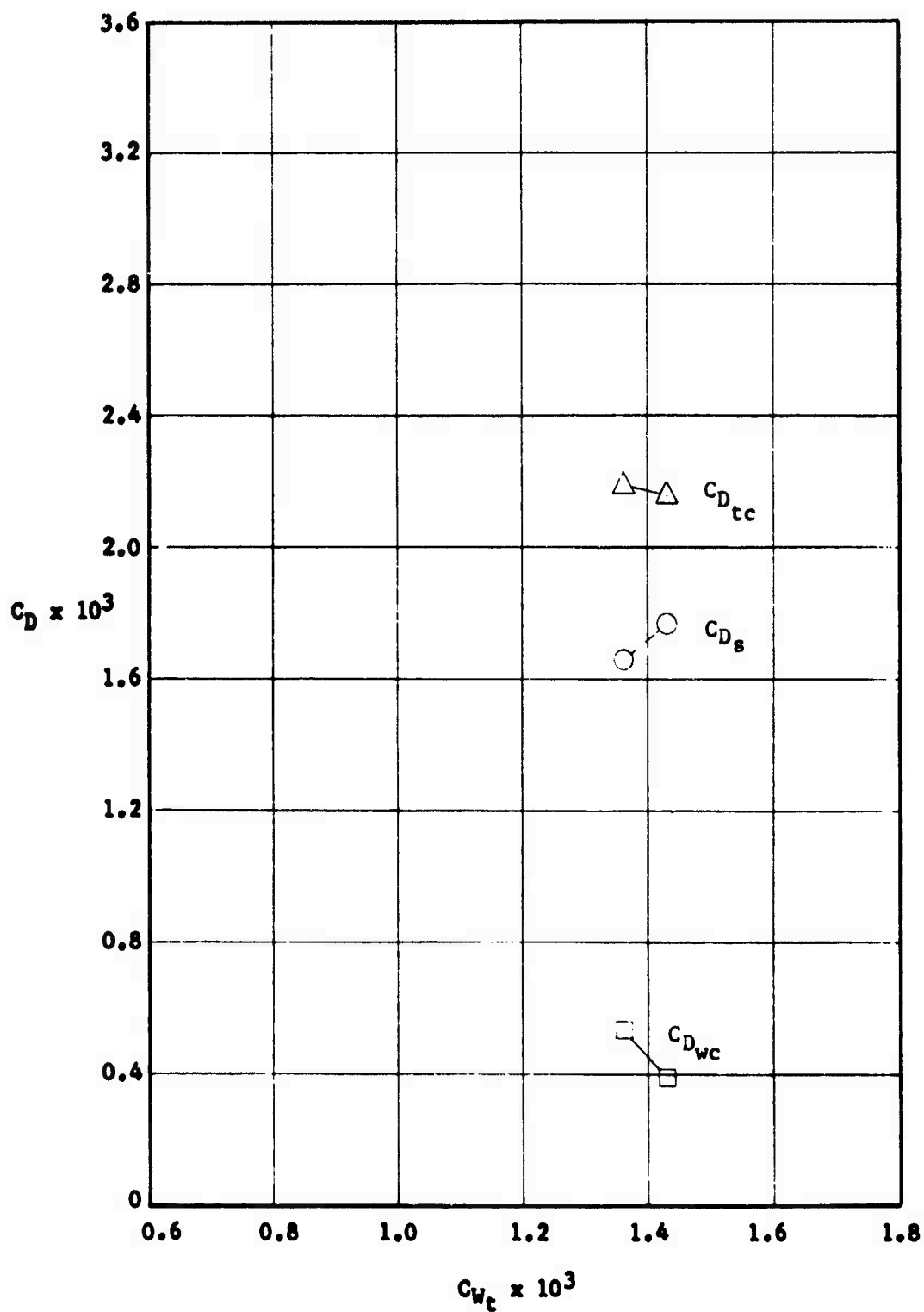
VARIATION OF DRAG COMPONENTS WITH SUCTION COEFFICIENT  
 $M_\infty \sim 1.99$ ,  $R_c \sim 7.5 \times 10^6$ ,  $\alpha = 0.45^\circ$

FIGURE 135c



VARIATION OF DRAG COMPONENTS WITH SUCTION COEFFICIENT  
 $M_\infty \approx 1.99$ ,  $R_c \sim 9.1 \times 10^6$ ,  $\alpha \approx 0.15^\circ$

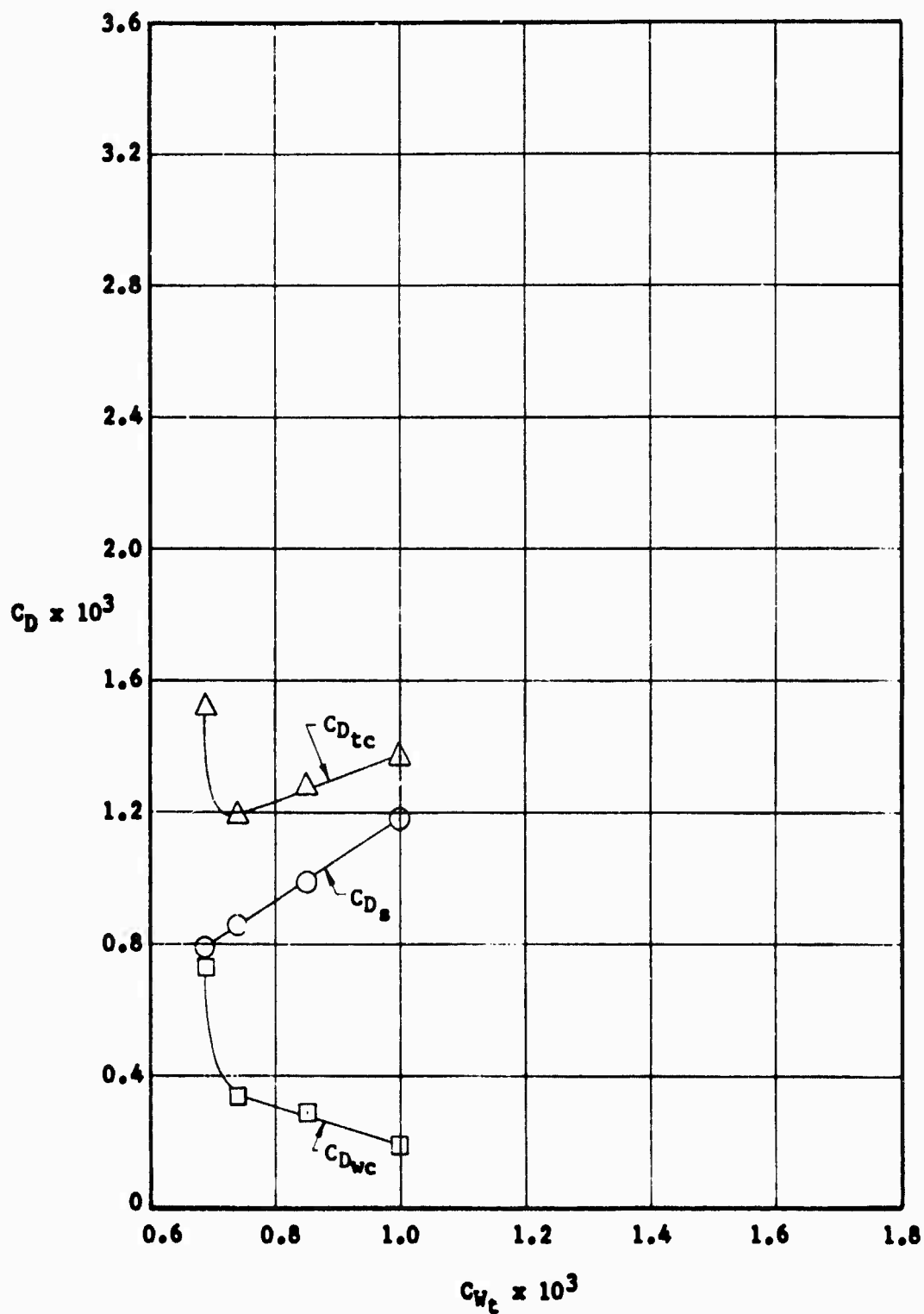
FIGURE 135d



VARIATION OF DRAG COMPONENTS WITH SUCTION COEFFICIENT  
 $M_\infty \sim 1.99$ ,  $R_c \sim 10.8 \times 10^6$ ,  $\alpha = 0.45^\circ$

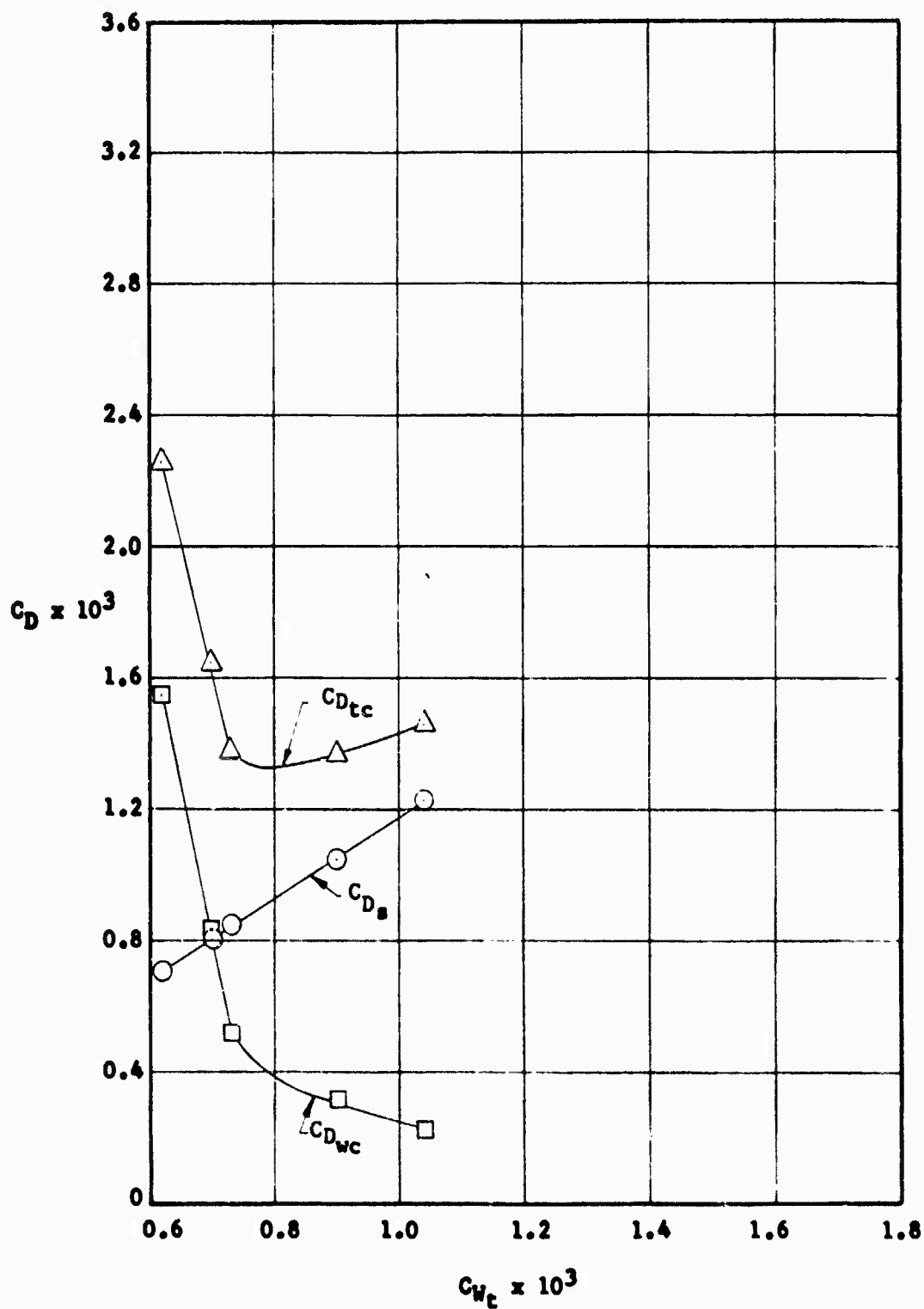
FIGURE 135e





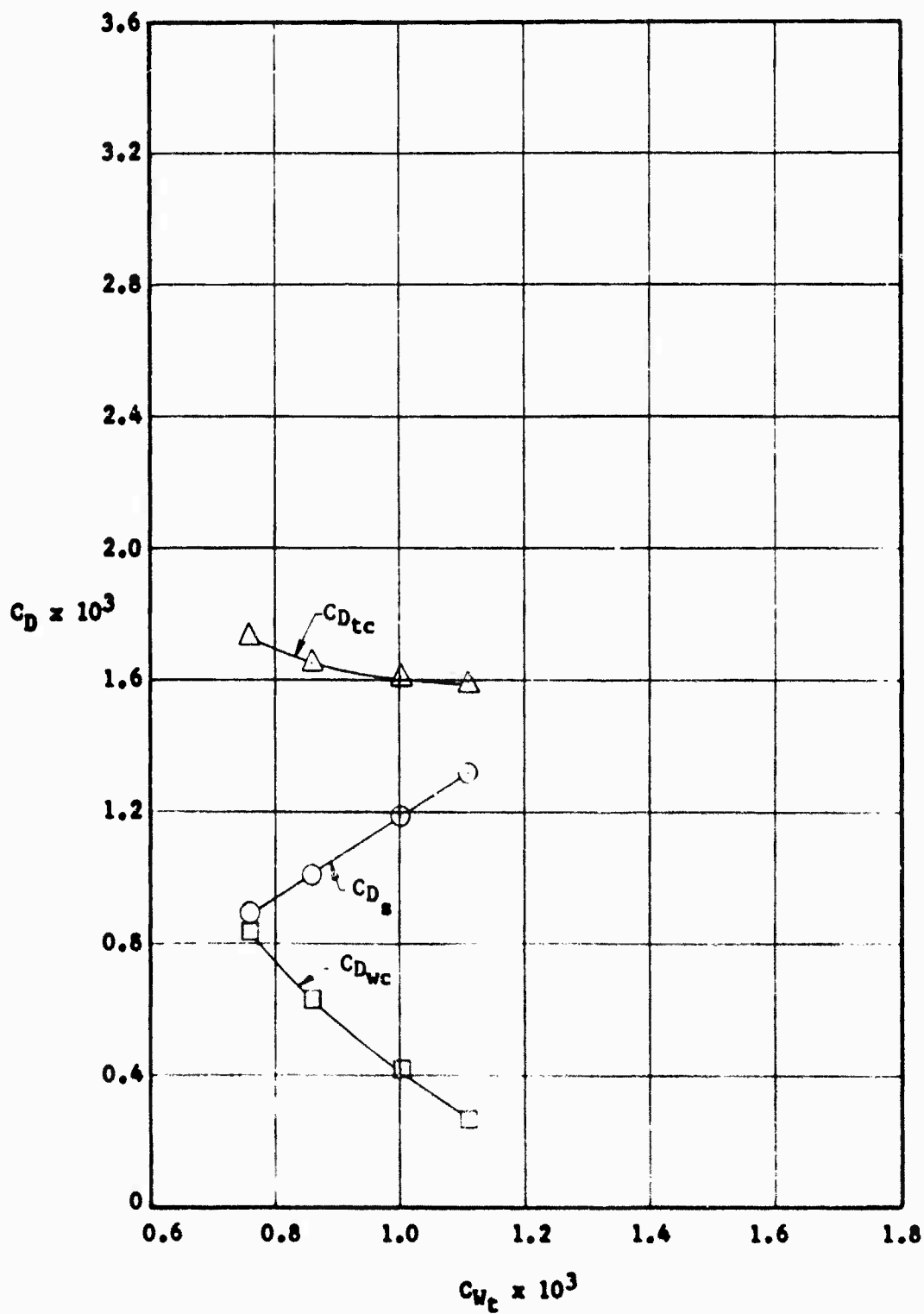
VARIATION OF DRAG COMPONENTS WITH SUCTION COEFFICIENT  
 $M_\infty \approx 1.99$ ,  $R_c \approx 3.5 \times 10^6$ ,  $\alpha = 0.75^\circ$

FIGURE 136a



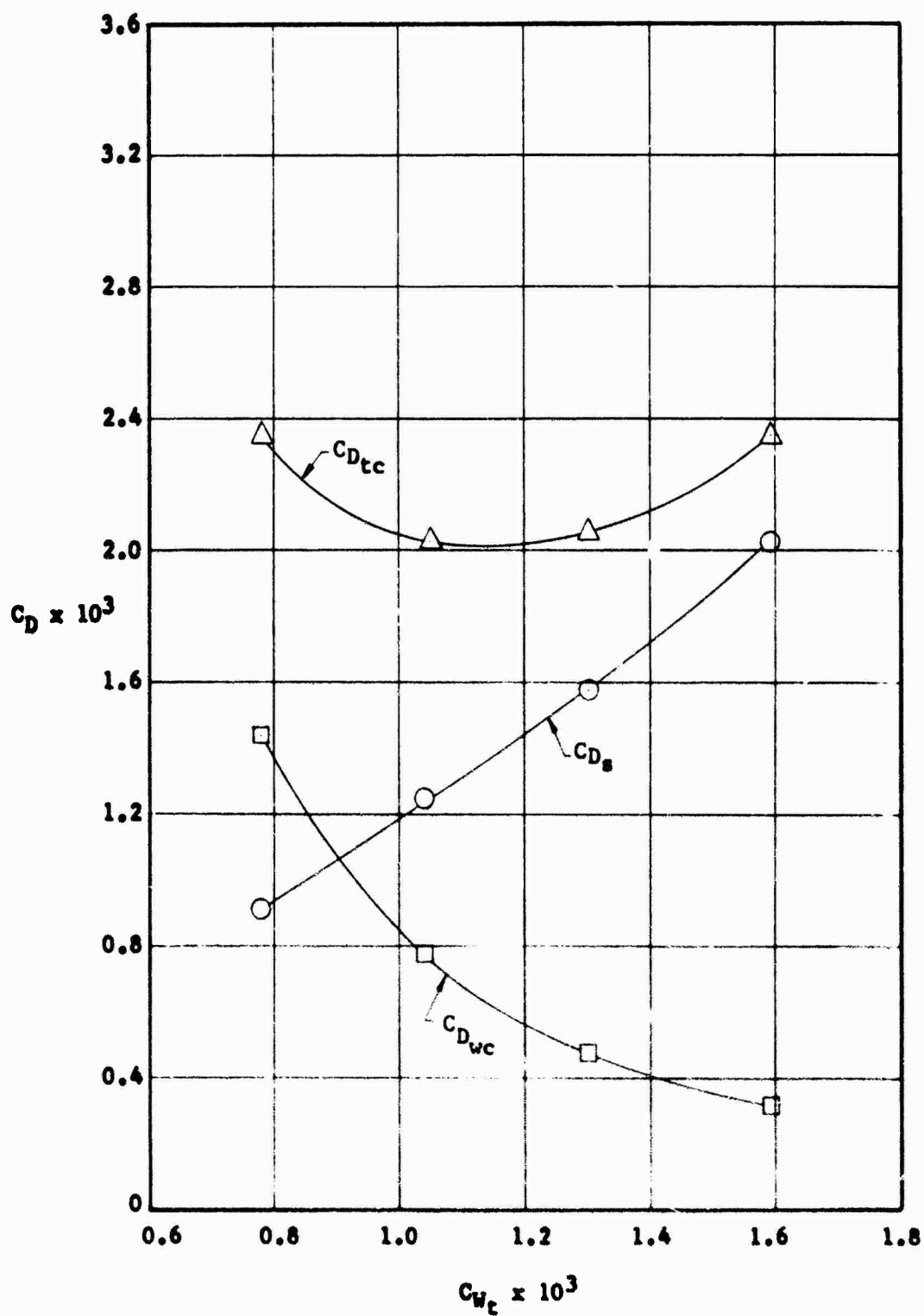
VARIATION OF DRAG COMPONENTS WITH SUCTION COEFFICIENT  
 $M_\infty \approx 1.99$ ,  $R_c \approx 7.1 \times 10^6$ ,  $\alpha = 0.75^\circ$

FIGURE 136b



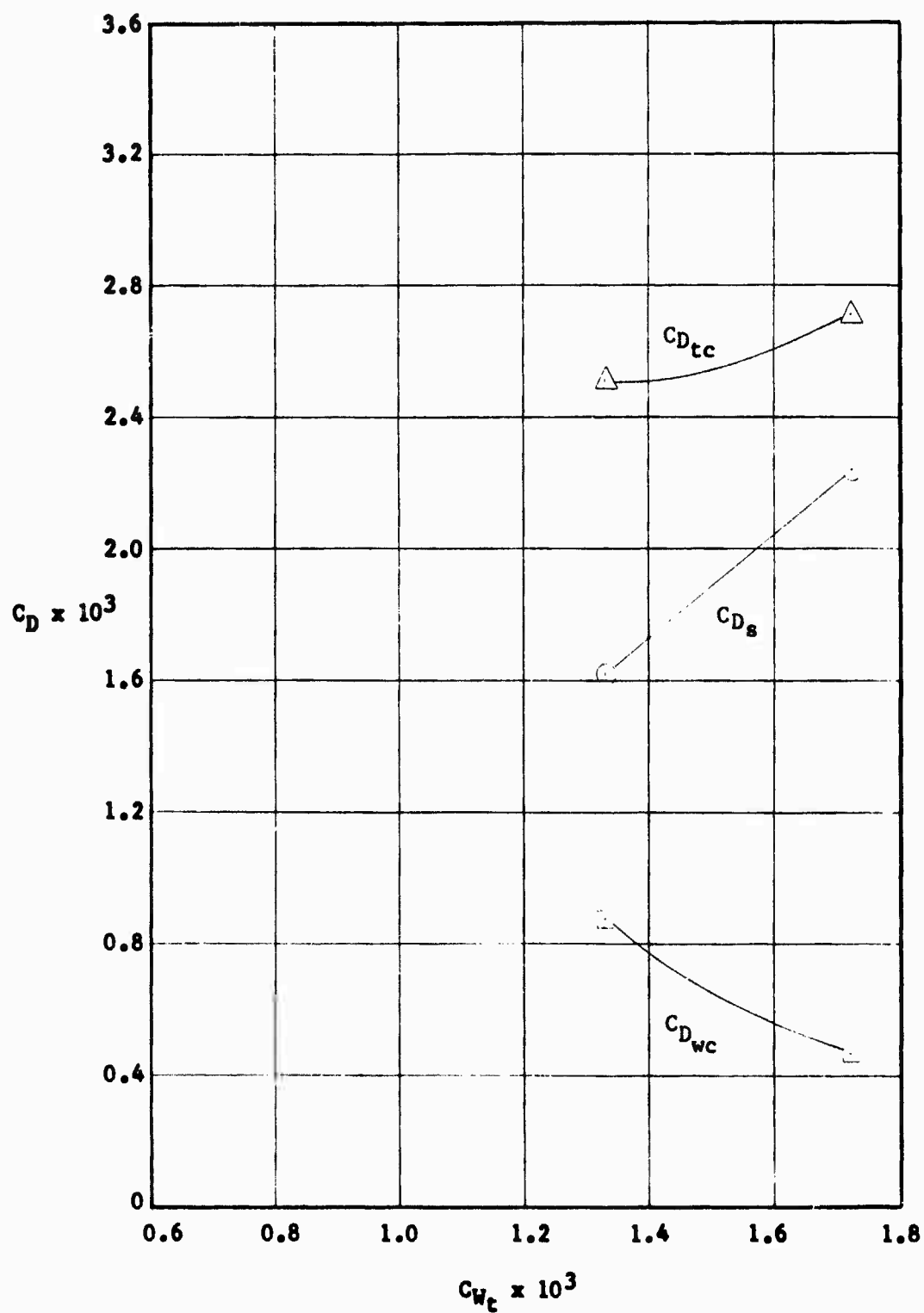
VARIATION OF DRAG COMPONENTS WITH SUCTION COEFFICIENT  
 $M_\infty \approx 1.99$ ,  $R_c \approx 9.2 \times 10^6$ ,  $\alpha = 0.75^\circ$

FIGURE 136c



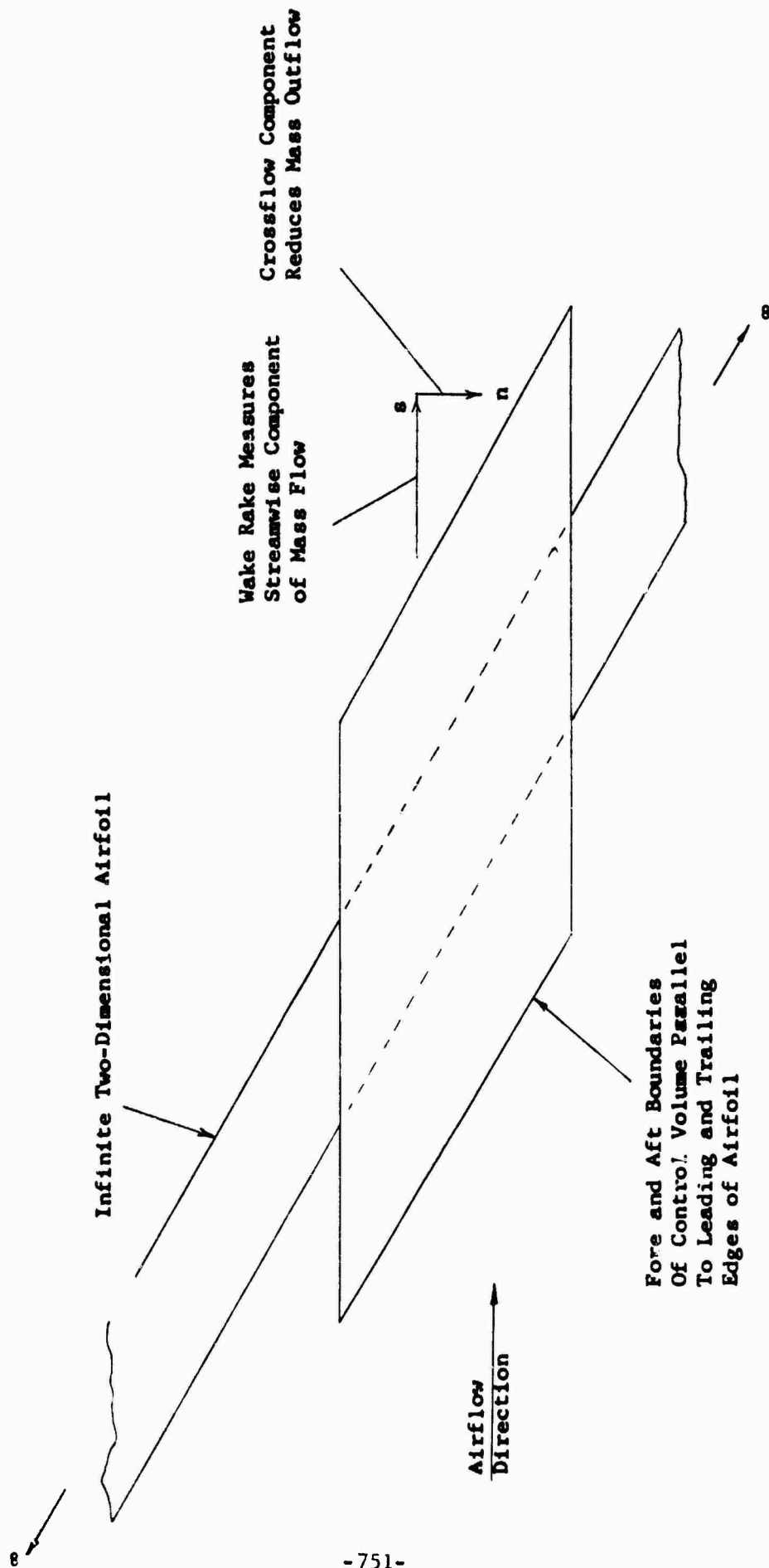
VARIATION OF DRAG COMPONENTS WITH SUCTION COEFFICIENT  
 $M_\infty \approx 1.99$ ,  $R_c \approx 10.7 \times 10^6$ ,  $\alpha = 0.75^\circ$

FIGURE 136d



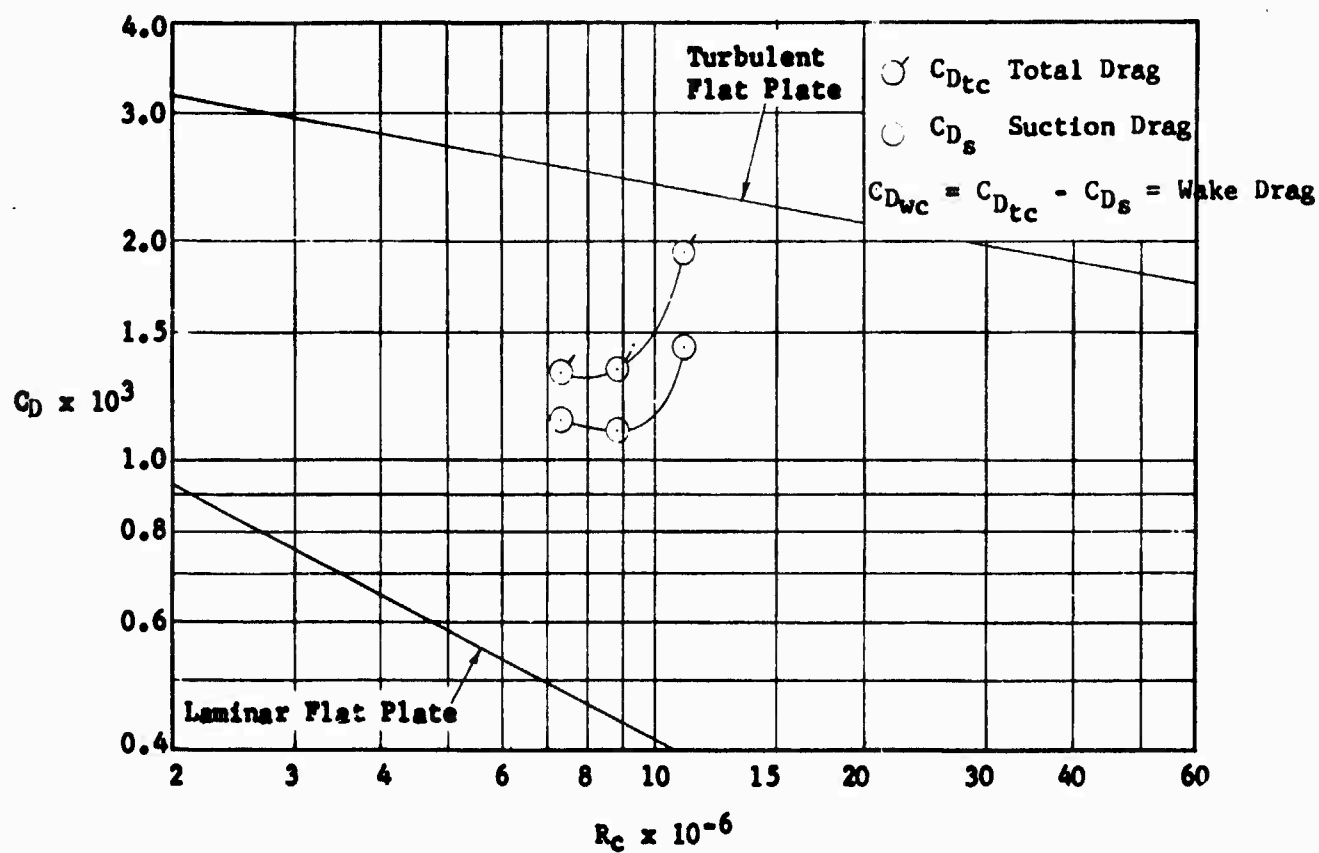
VARIATION OF DRAG COMPONENTS WITH SUCTION COEFFICIENTS  
 $M_\infty \sim 1.99$ ,  $R_c \sim 14.2 \times 10^6$ ,  $\alpha = 0.75^\circ$

FIGURE 136e



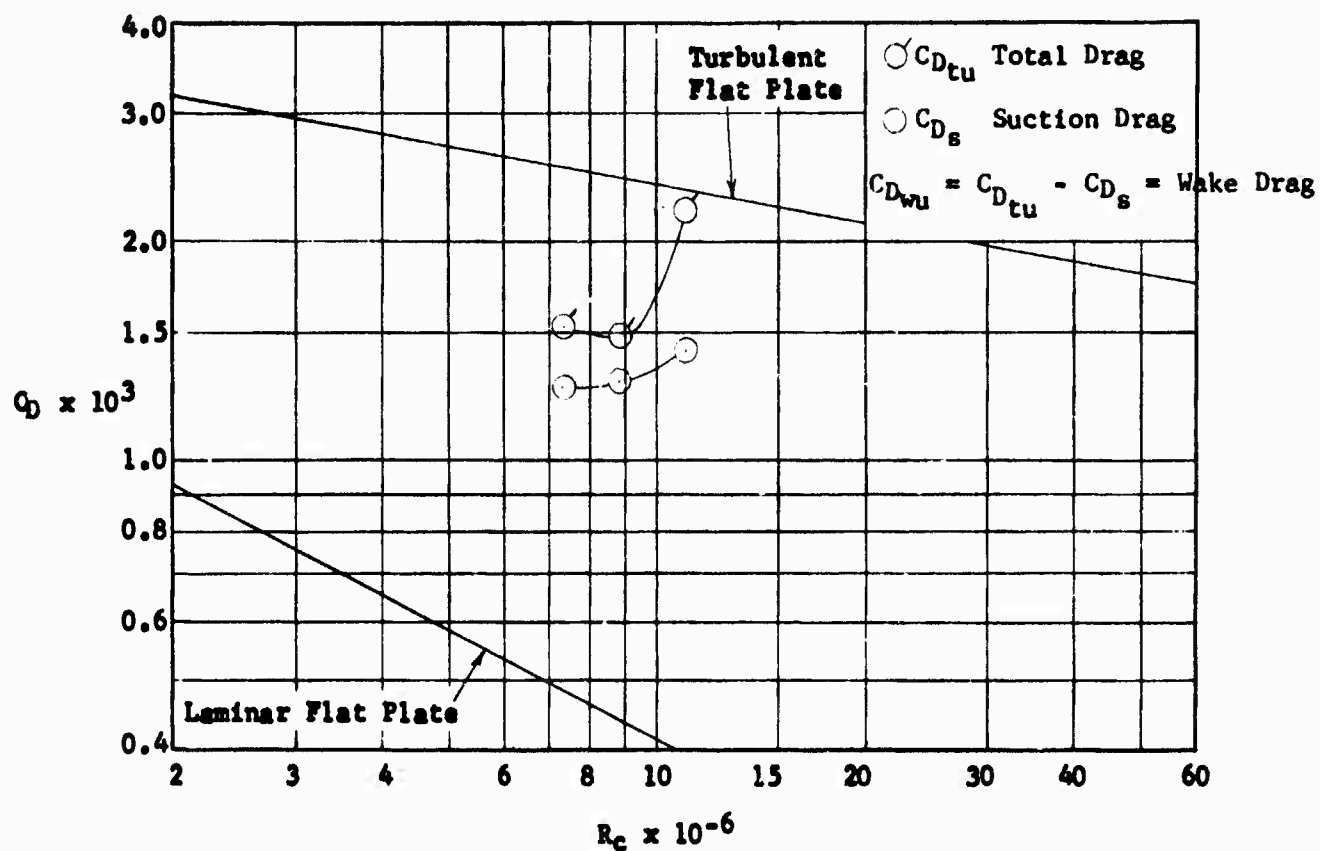
REDUCTION OF WAKE MOMENTUM DEFICIT DUE TO CROSSFLOW VELOCITY IN THE WAKE

FIGURE 137



VARIATION OF CORRECTED OPTIMUM DRAG COEFFICIENTS WITH REYNOLDS NUMBER  
 $M_\infty = 1.99, \alpha = 0.15^\circ$

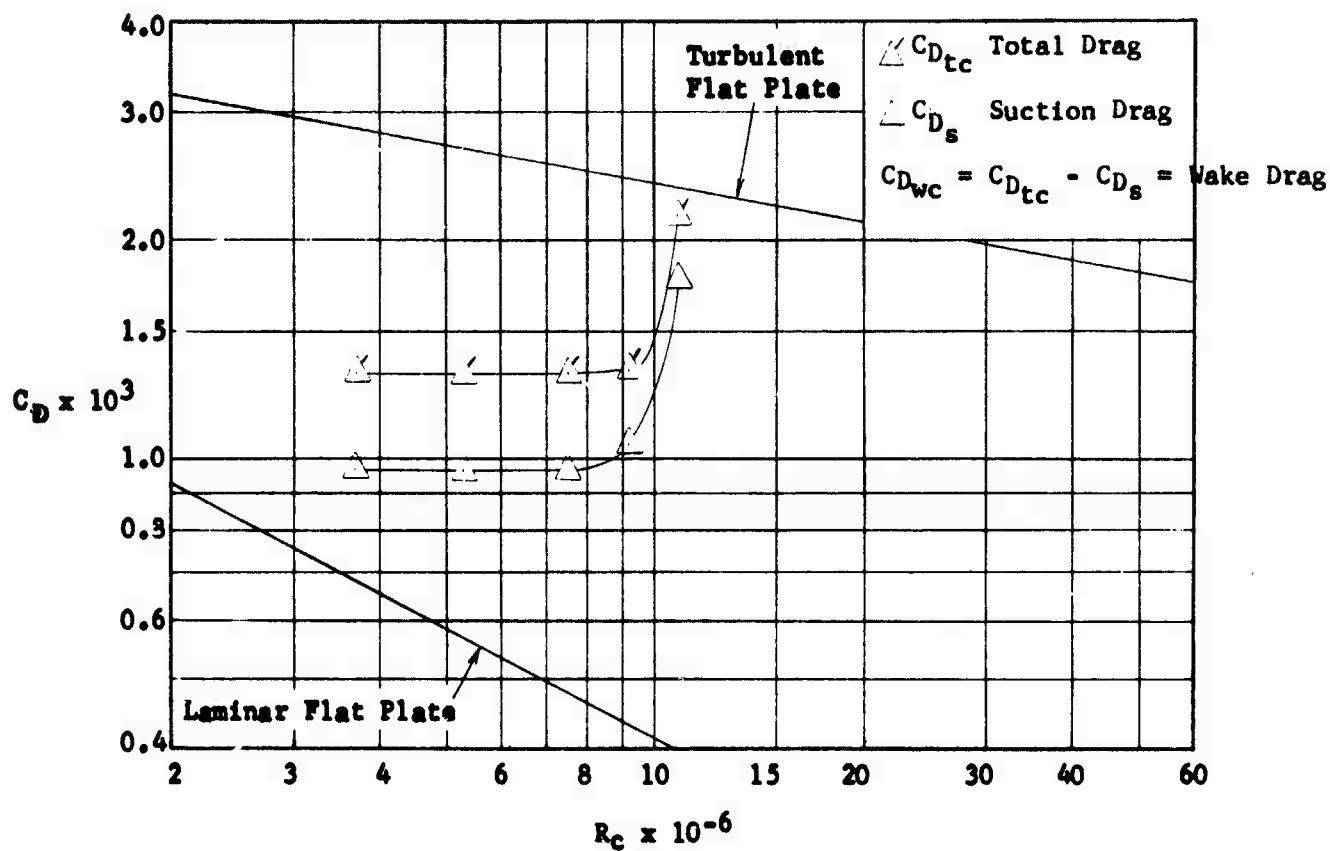
FIGURE 138a



VARIATION OF UNCORRECTED OPTIMUM DRAG COEFFICIENTS WITH REYNOLDS NUMBER  
 $M_\infty = 1.99$ ,  $\alpha = 0.15^\circ$

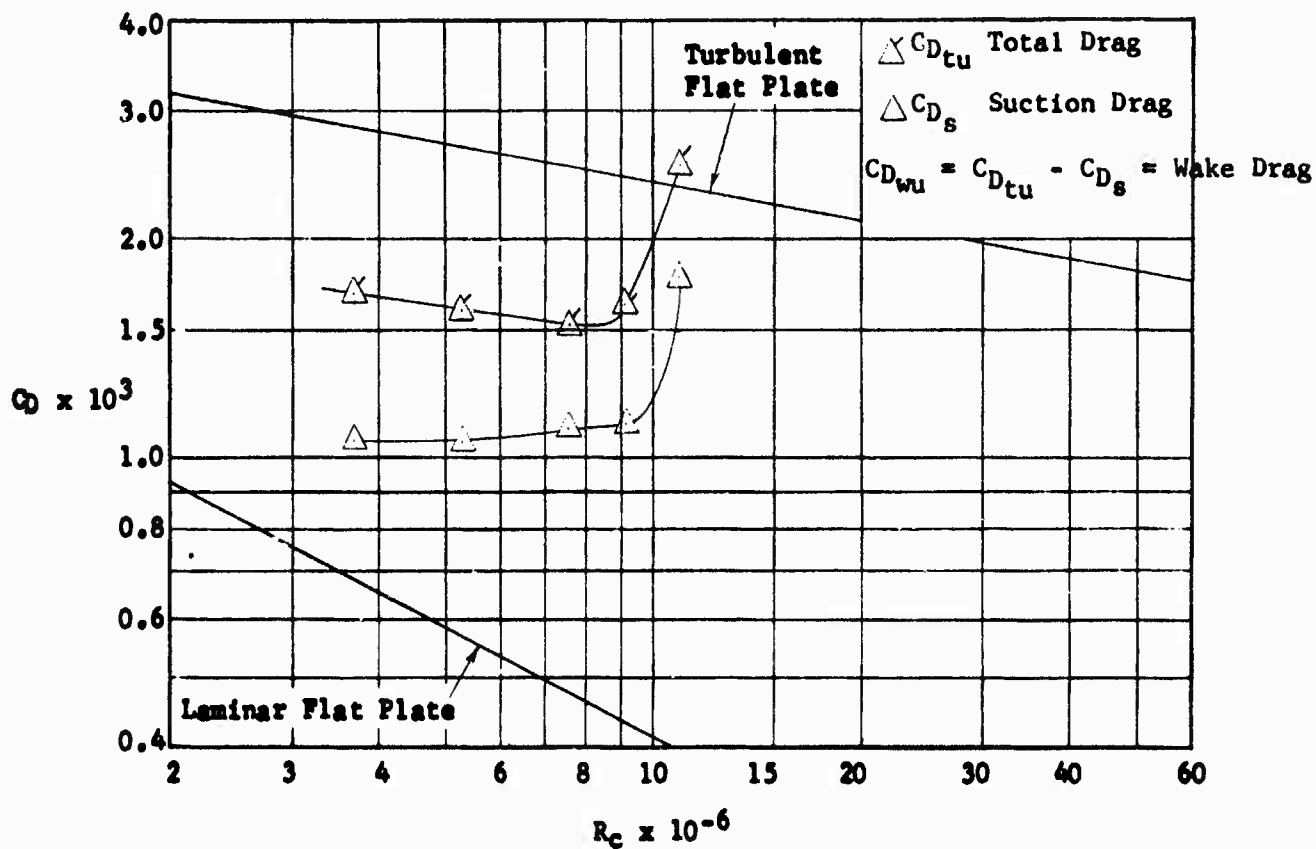
FIGURE 138b





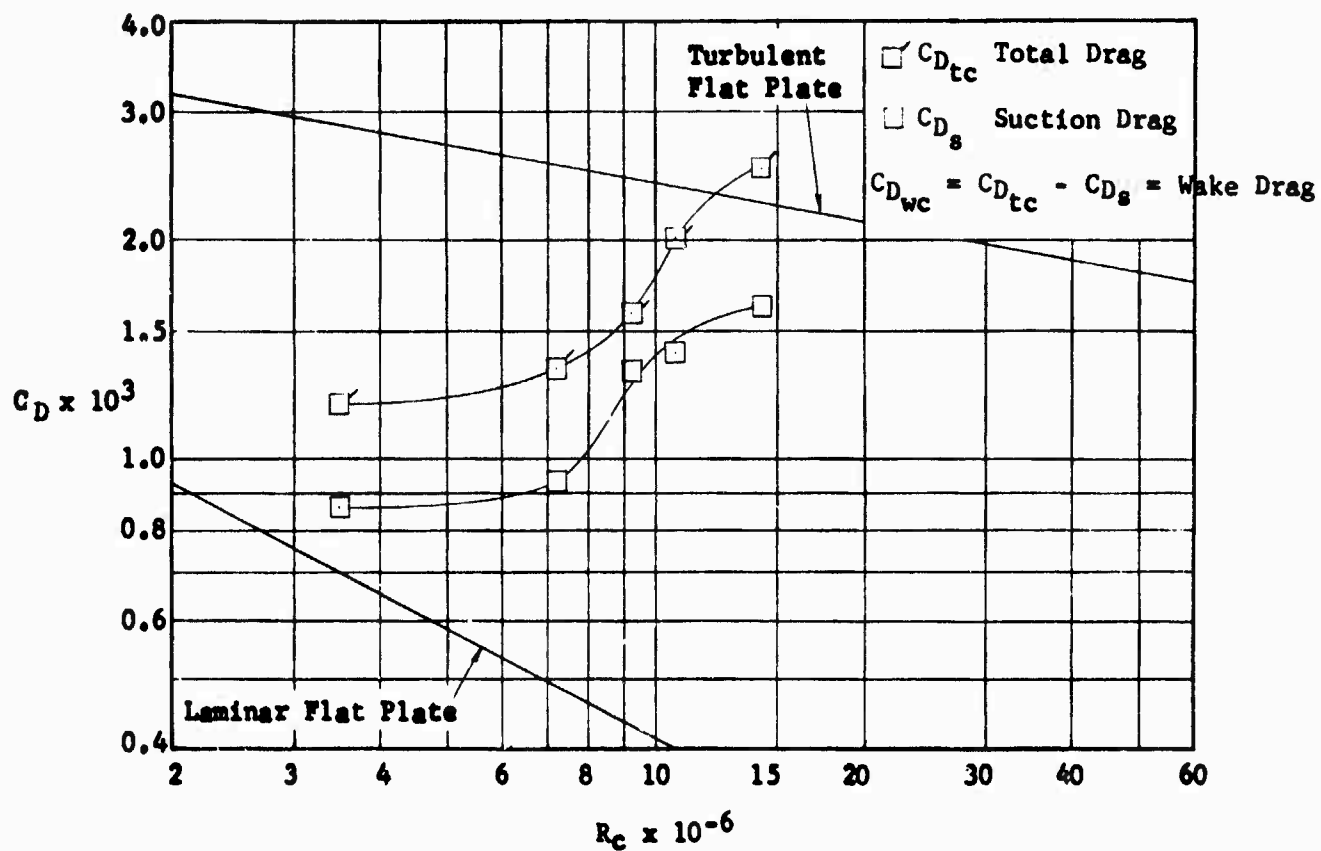
VARIATION OF CORRECTED OPTIMUM DRAG COEFFICIENTS WITH REYNOLDS NUMBER  
 $M_\infty \approx 1.99$ ,  $\alpha = 0.45^\circ$

FIGURE 139a



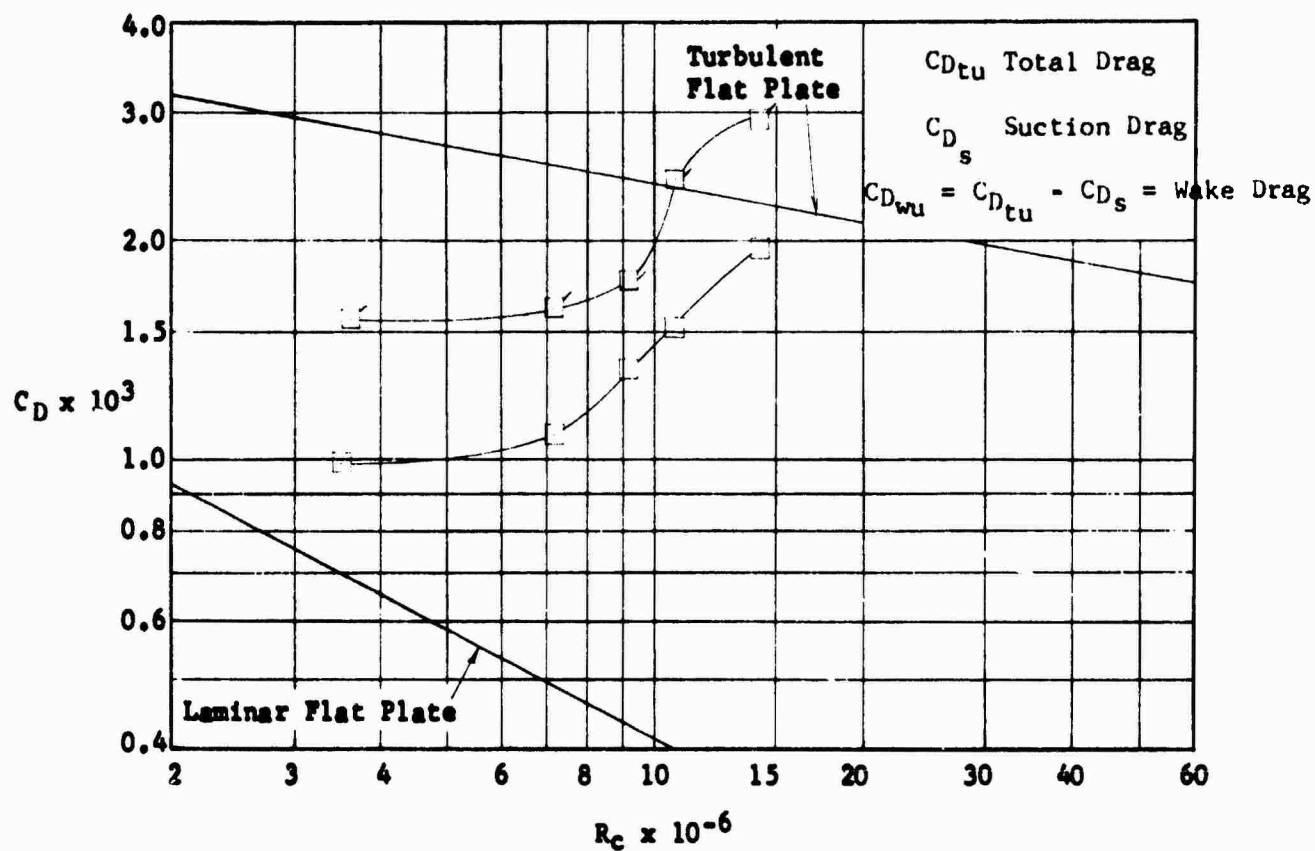
VARIATION OF UNCORRECTED OPTIMUM DRAG COEFFICIENT WITH REYNOLDS NUMBER  
 $M_\infty \approx 1.99$ ,  $\alpha = 0.45^\circ$

FIGURE 139b



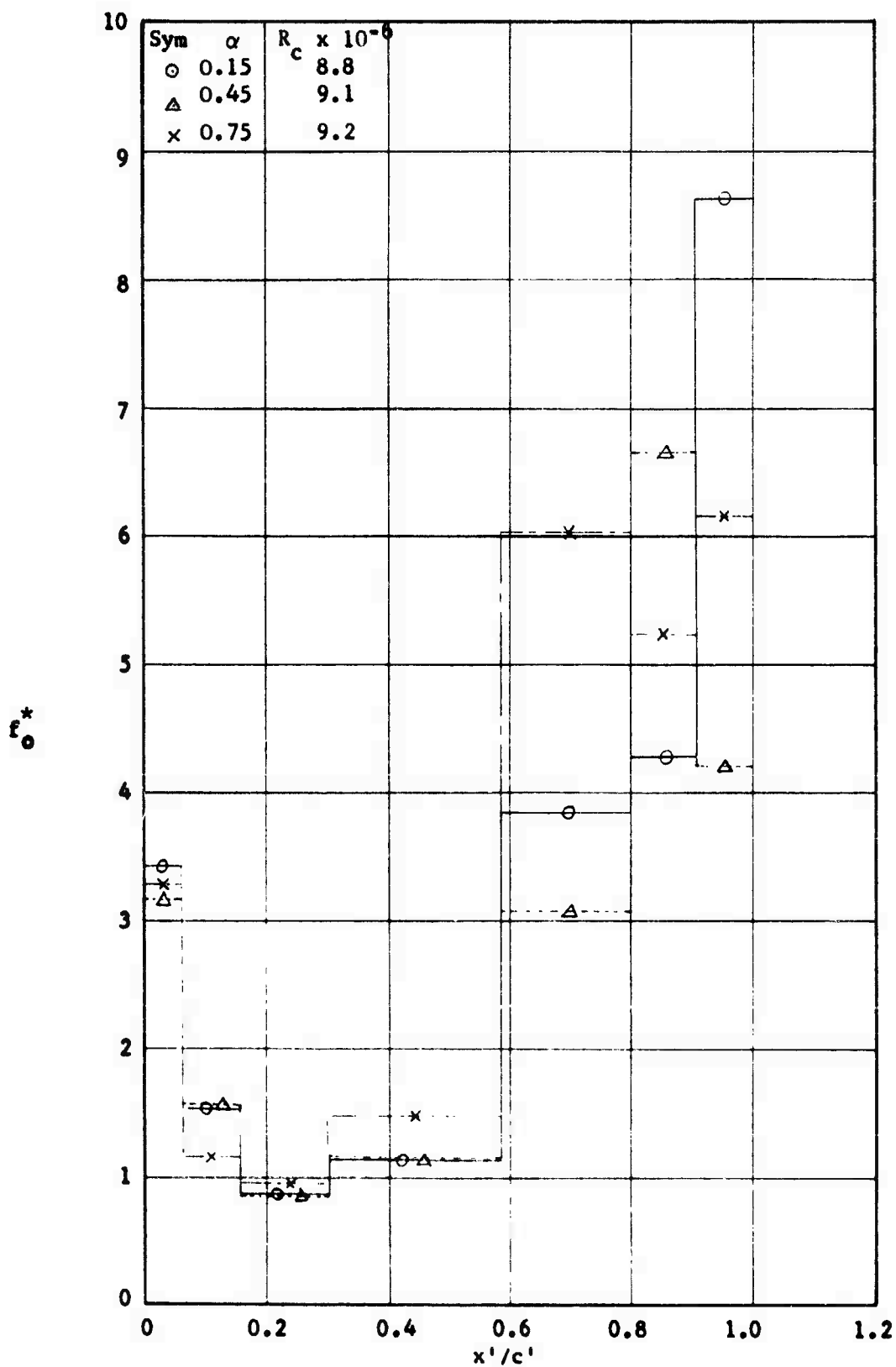
VARIATION OF CORRECTED OPTIMUM DRAG COEFFICIENTS WITH REYNOLDS NUMBER  
 $M_\infty \approx 1.99, \alpha = 0.75^\circ$

FIGURE 140a



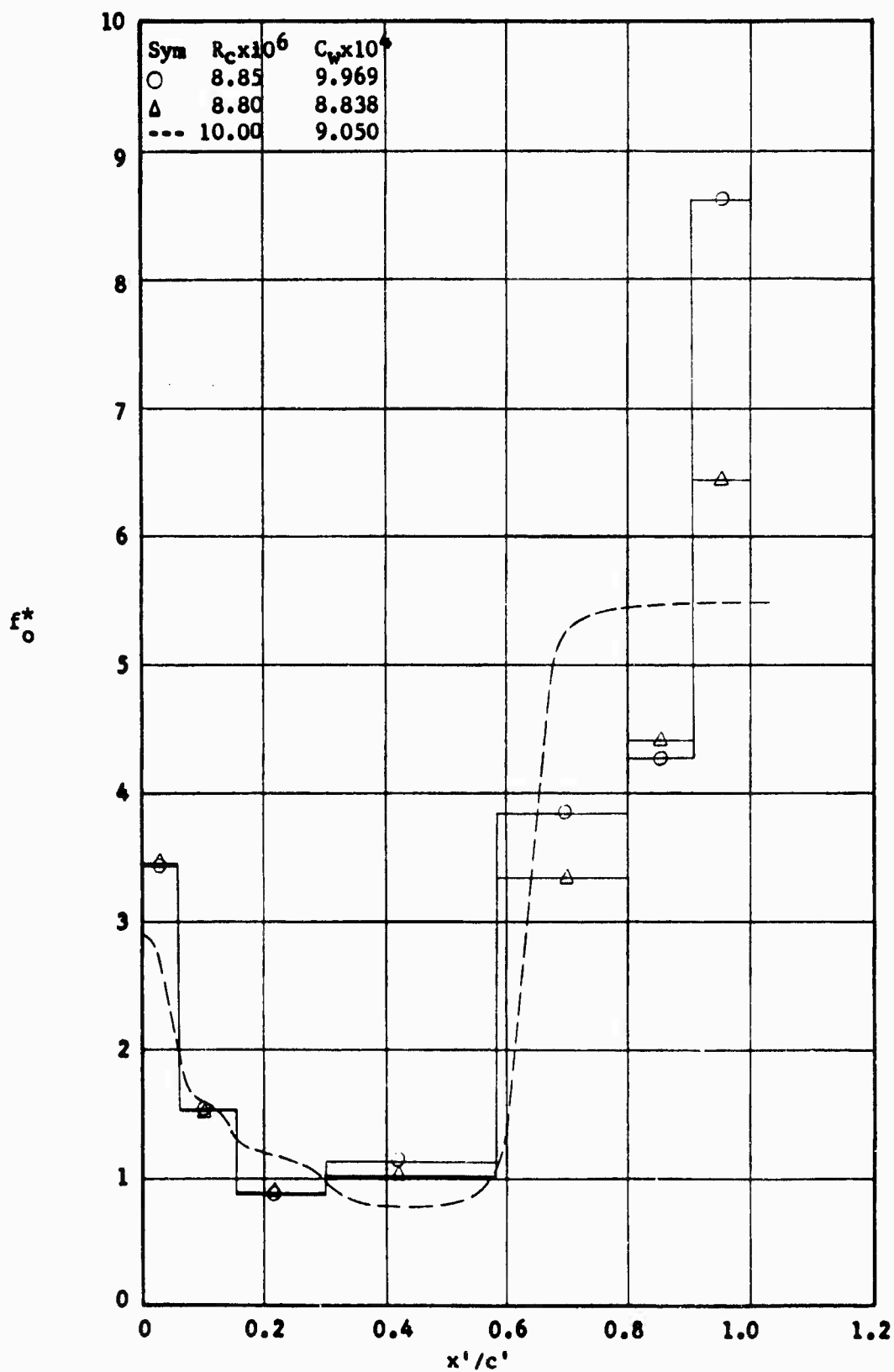
VARIATION OF UNCORRECTED OPTIMUM DRAG COEFFICIENTS WITH REYNOLDS NUMBER  
 $M_\infty \sim 1.99, \alpha = 0.75^\circ$

FIGURE 140b



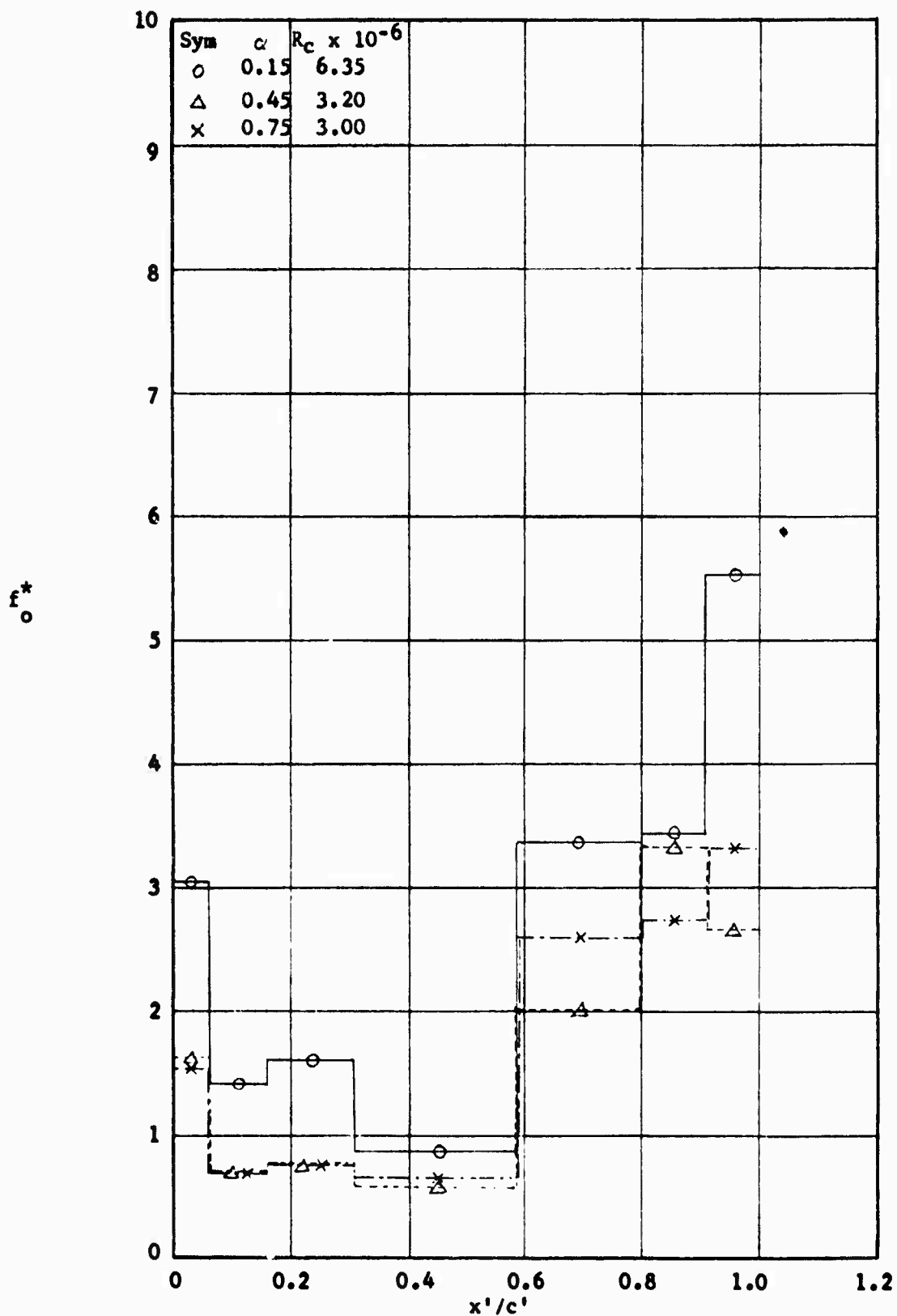
TYPICAL SUCTION DISTRIBUTIONS FOR OPTIMUM SUCTION -  $M_{\infty} \approx 1.99$

FIGURE 141a



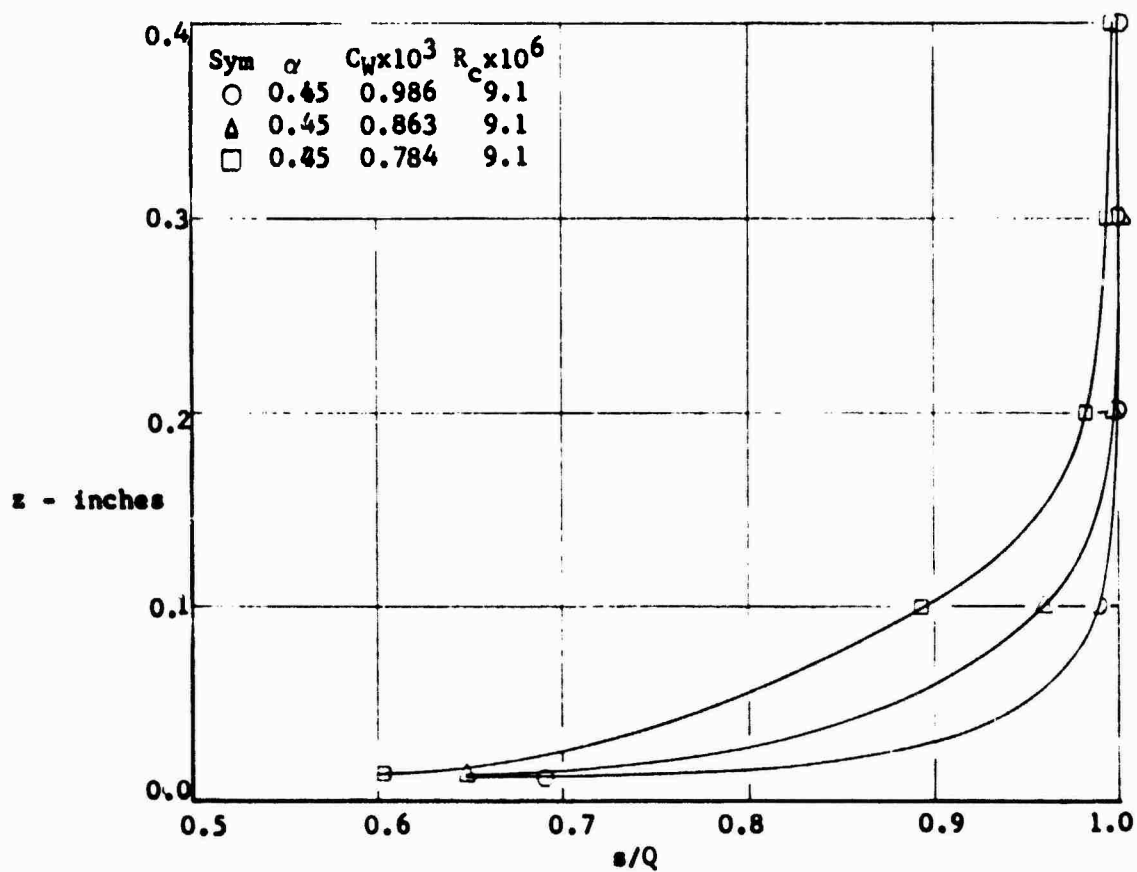
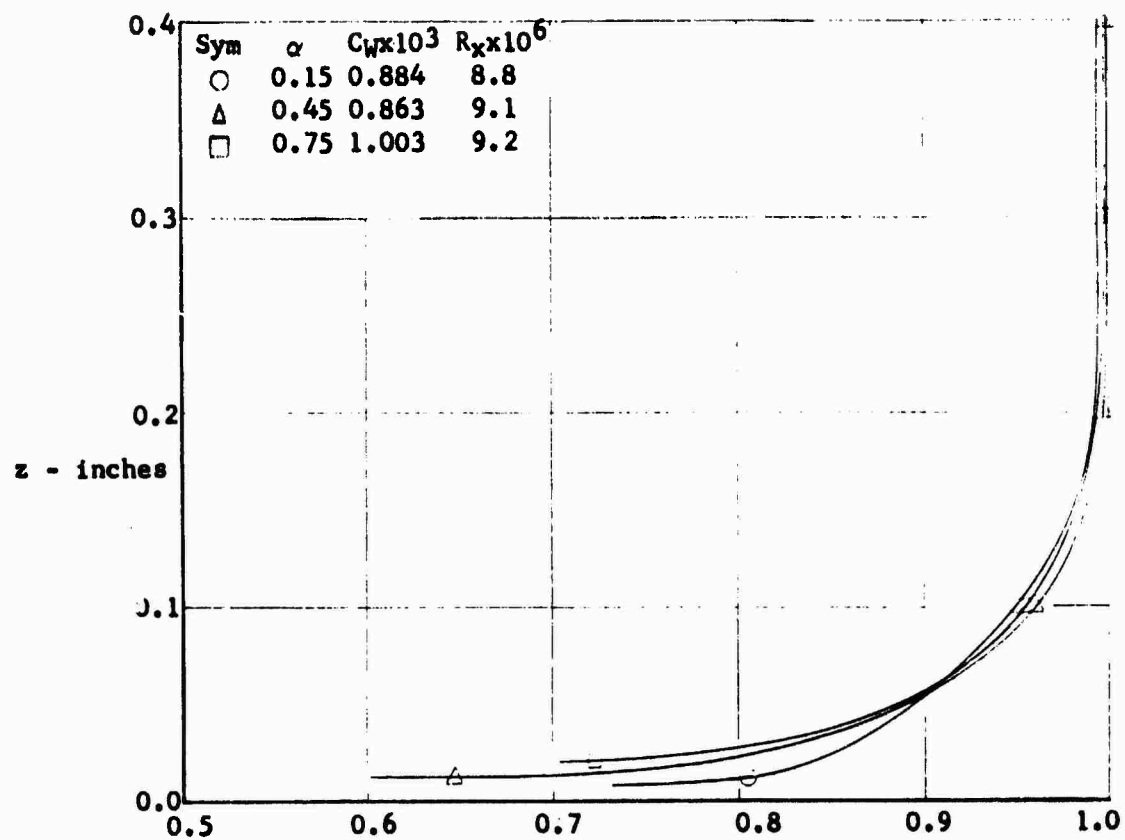
COMPARISON OF CALCULATED AND MEASURED SUCTION DISTRIBUTIONS  
 $M_\infty \approx 1.99$ ,  $\alpha = 0.15^\circ$

FIGURE 141b



TYPICAL SUCTION DISTRIBUTIONS FOR  $M_\infty \approx 2.25$

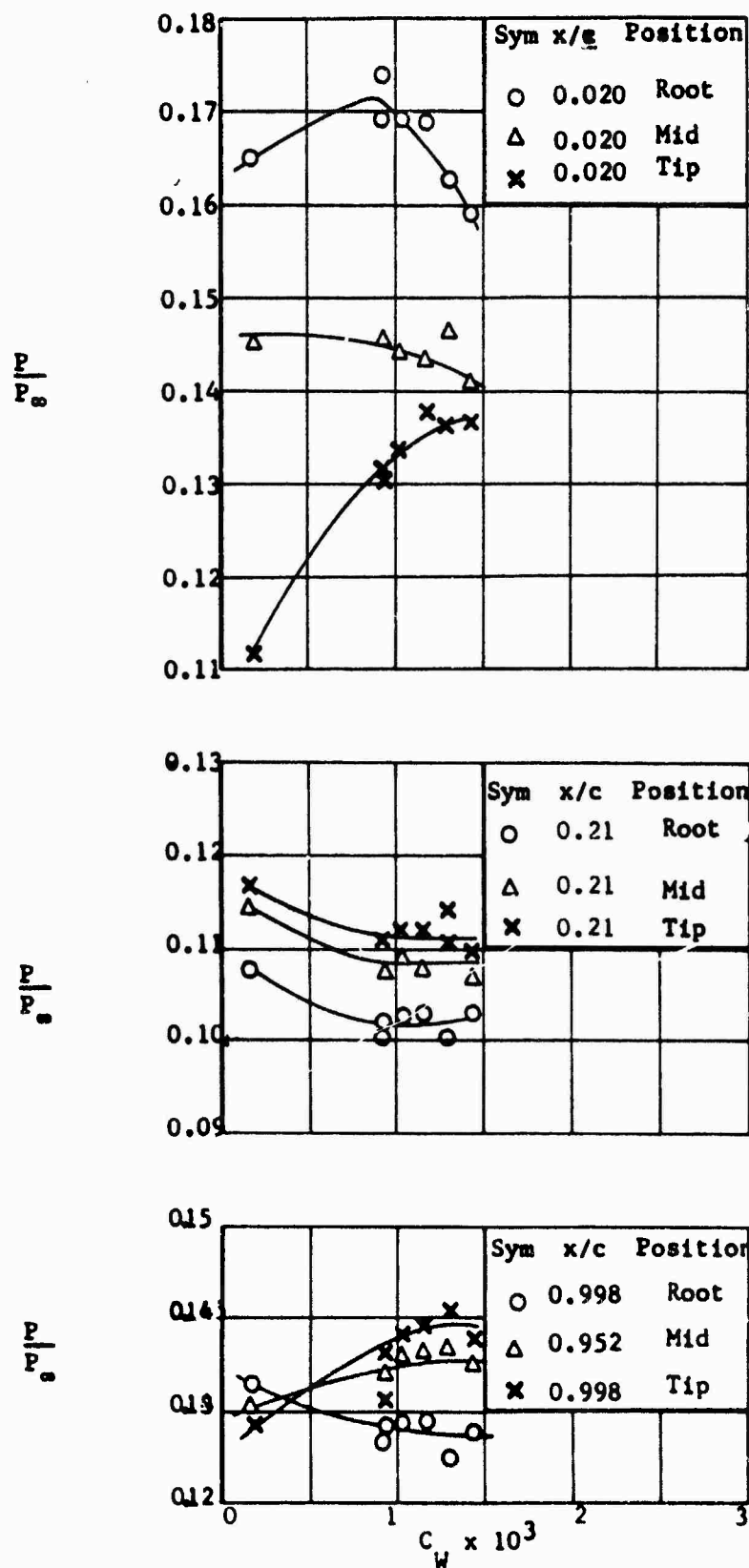
FIGURE 142



TYPICAL MEASURED PROFILES AT  $M_\infty = 2.0$

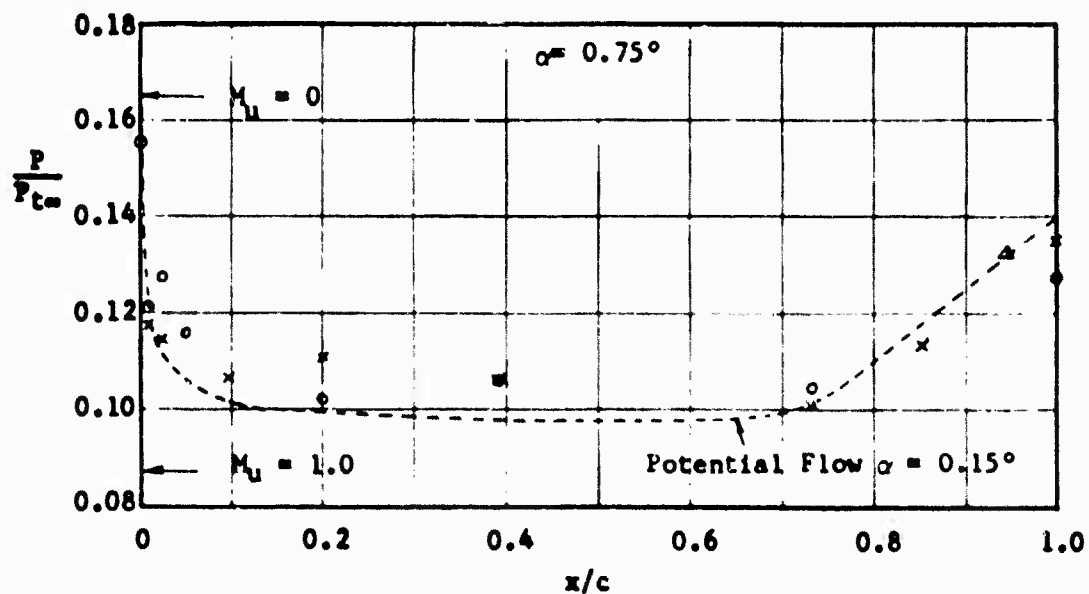
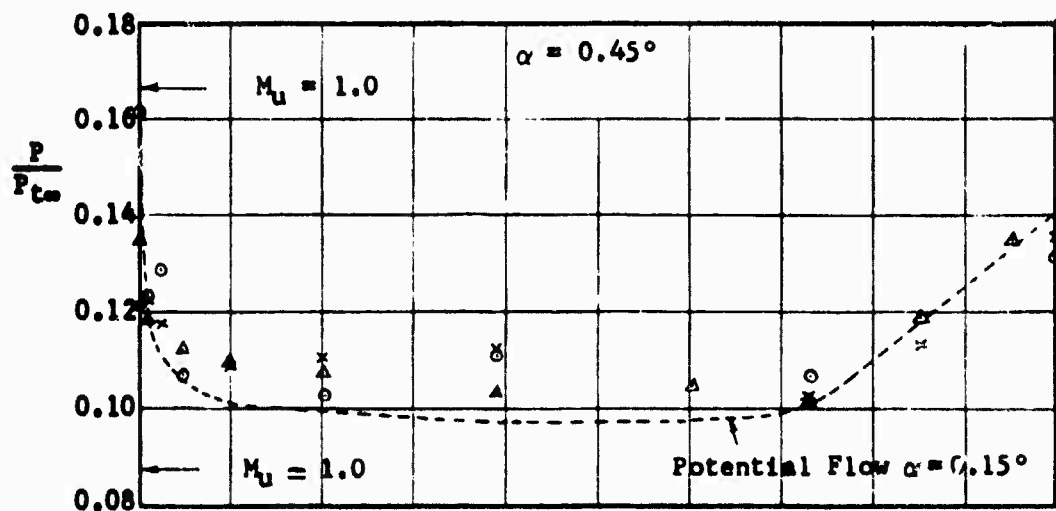
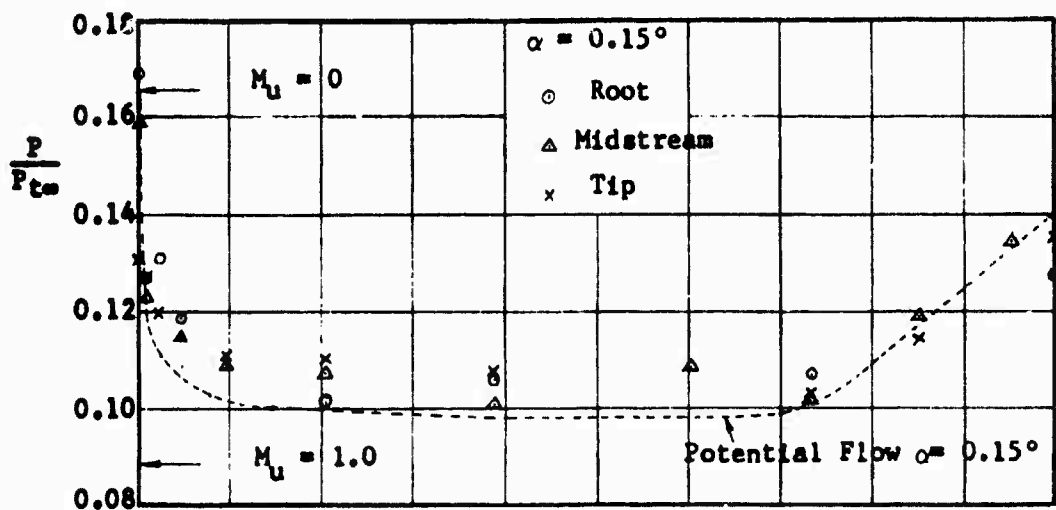
FIGURE 143



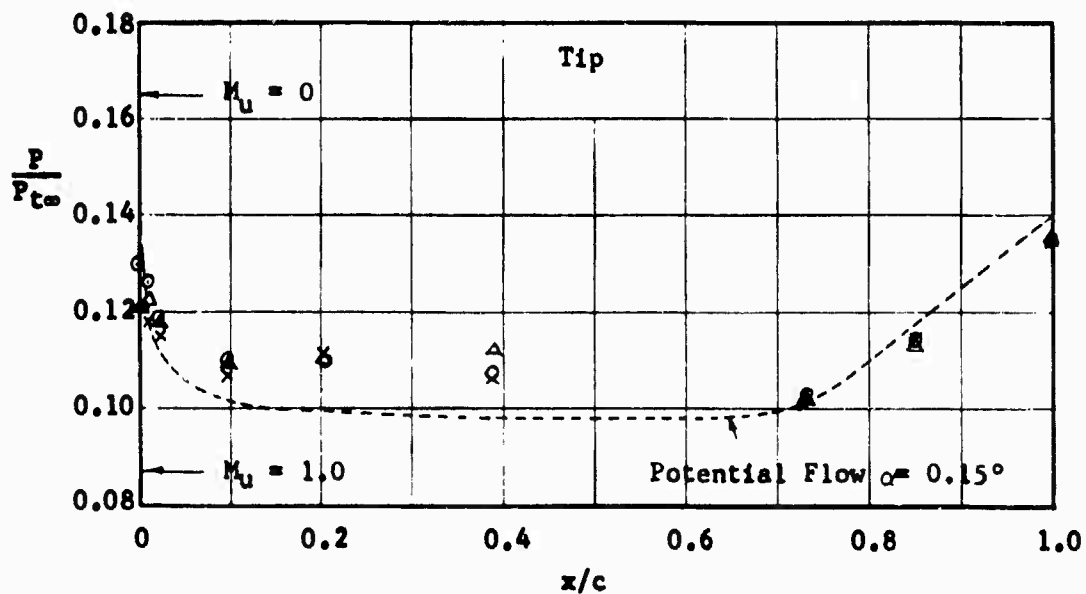
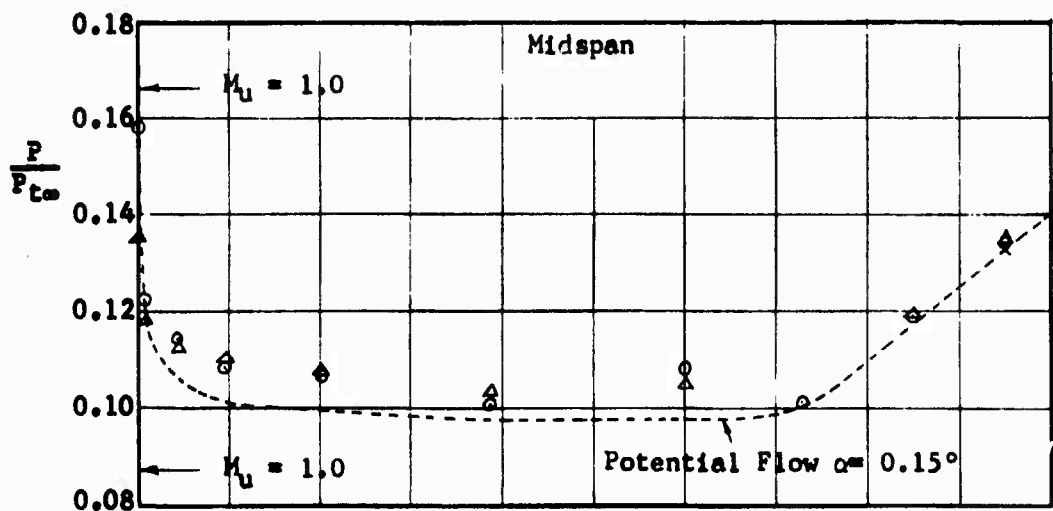
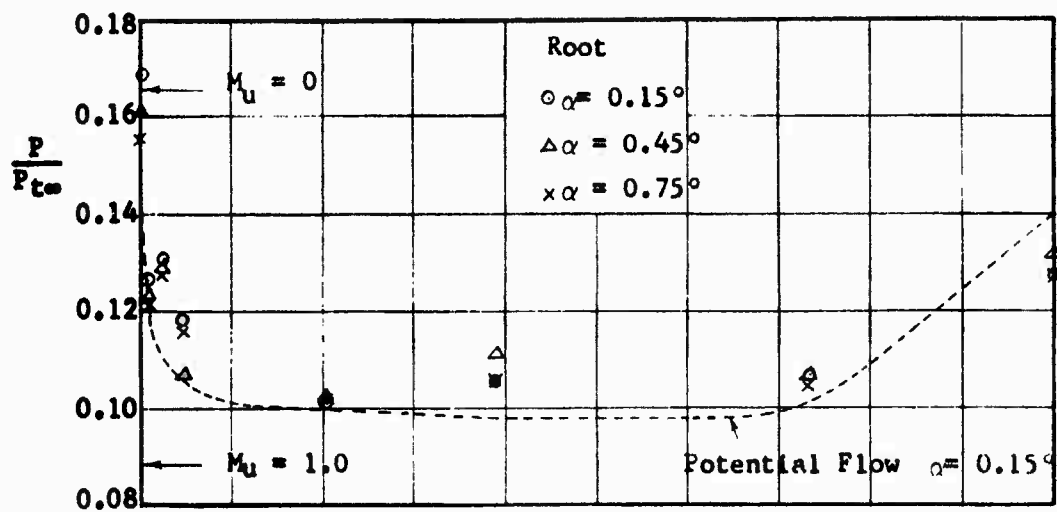


TYPICAL VARIATION OF SURFACE PRESSURE RATIO WITH TOTAL SUCTION =  $M_\infty = 1.99$

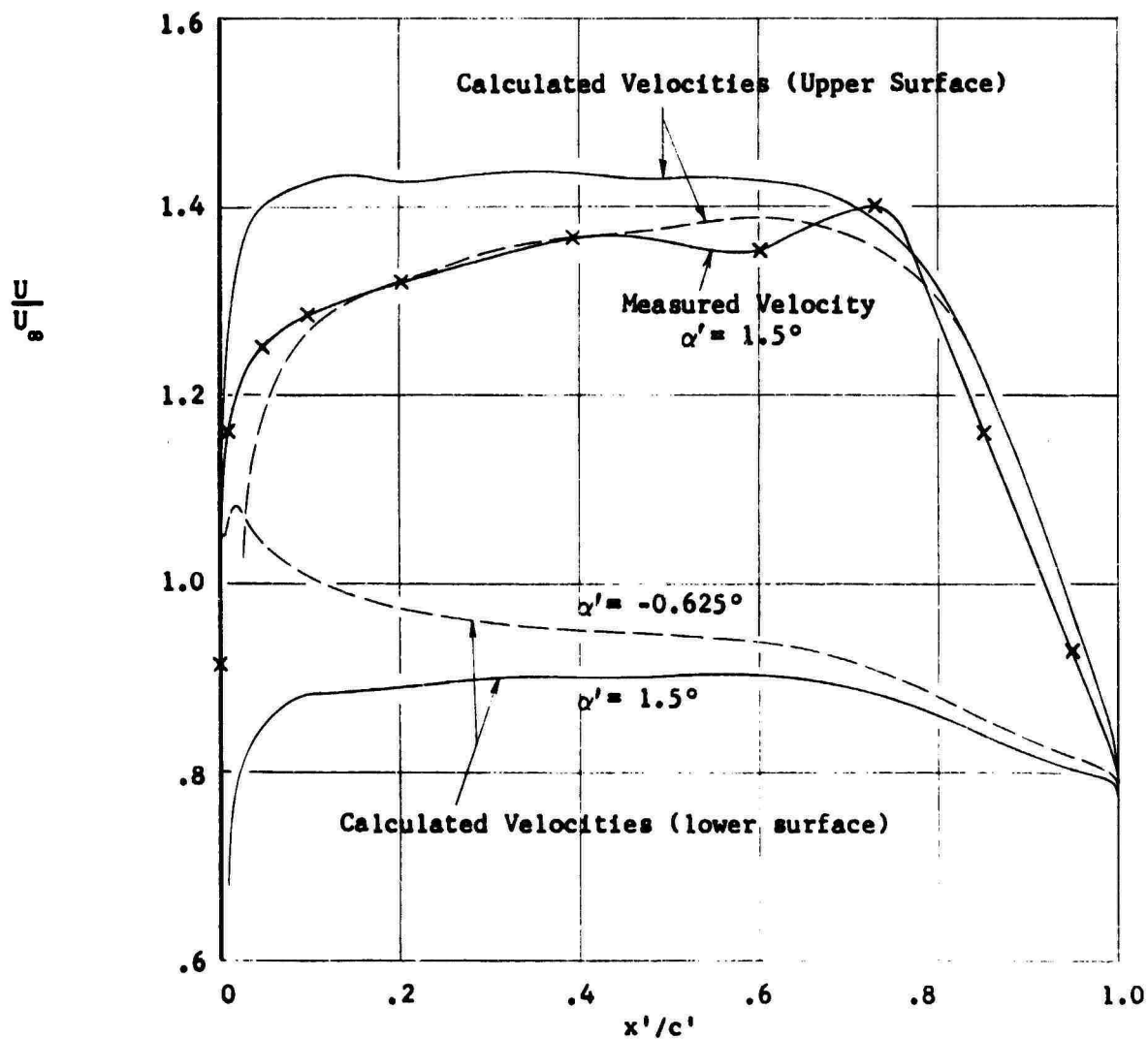
FIGURE 144



COMPARISON OF SURFACE PRESSURES AT THREE SPANWISE STATIONS  
 $M_\infty \sim 1.99$

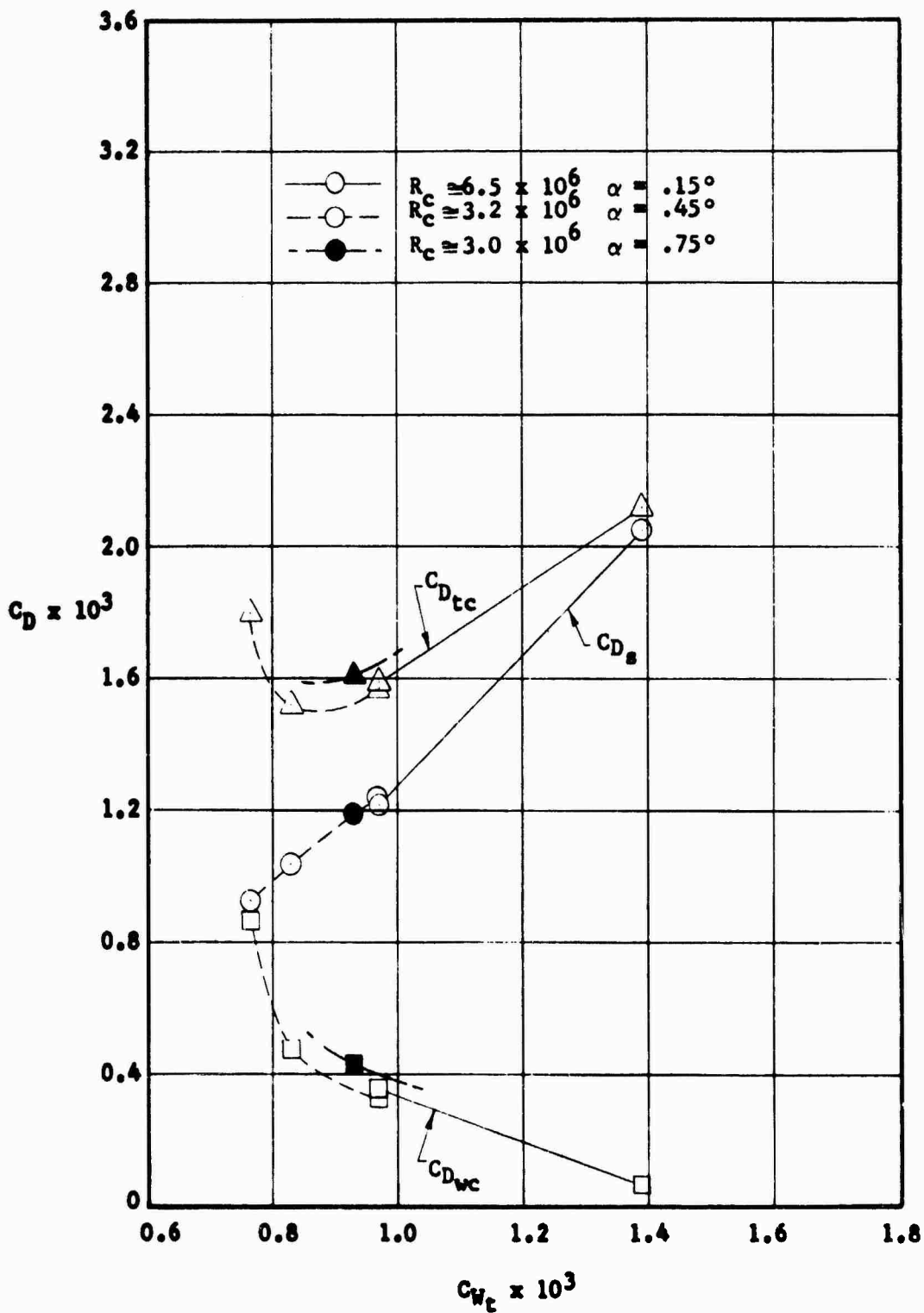


COMPARISON OF SURFACE PRESSURES AT THREE ANGLES OF ATTACK  
 $M_\infty = 1.99$



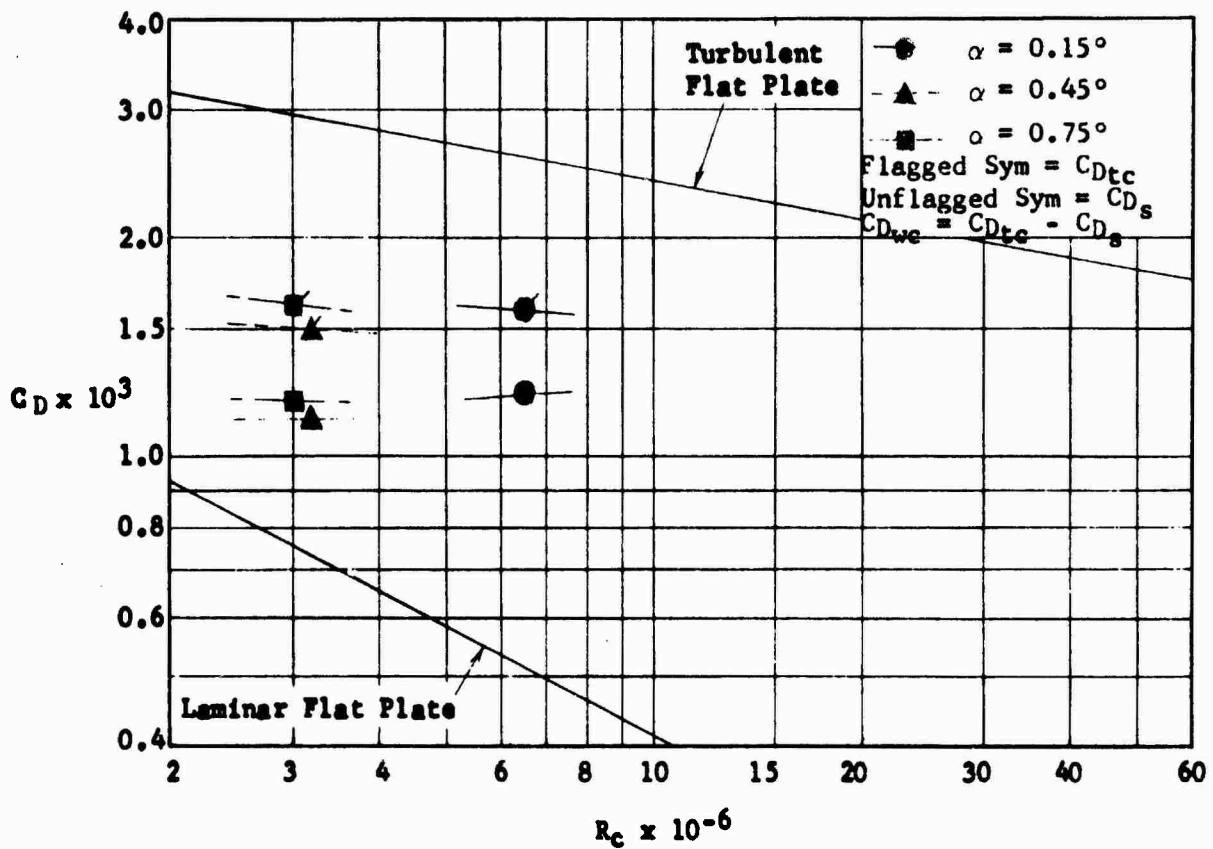
COMPARISON OF MEASURED TWO DIMENSIONAL VELOCITY DISTRIBUTION  
WITH CALCULATED DISTRIBUTION

FIGURE 147



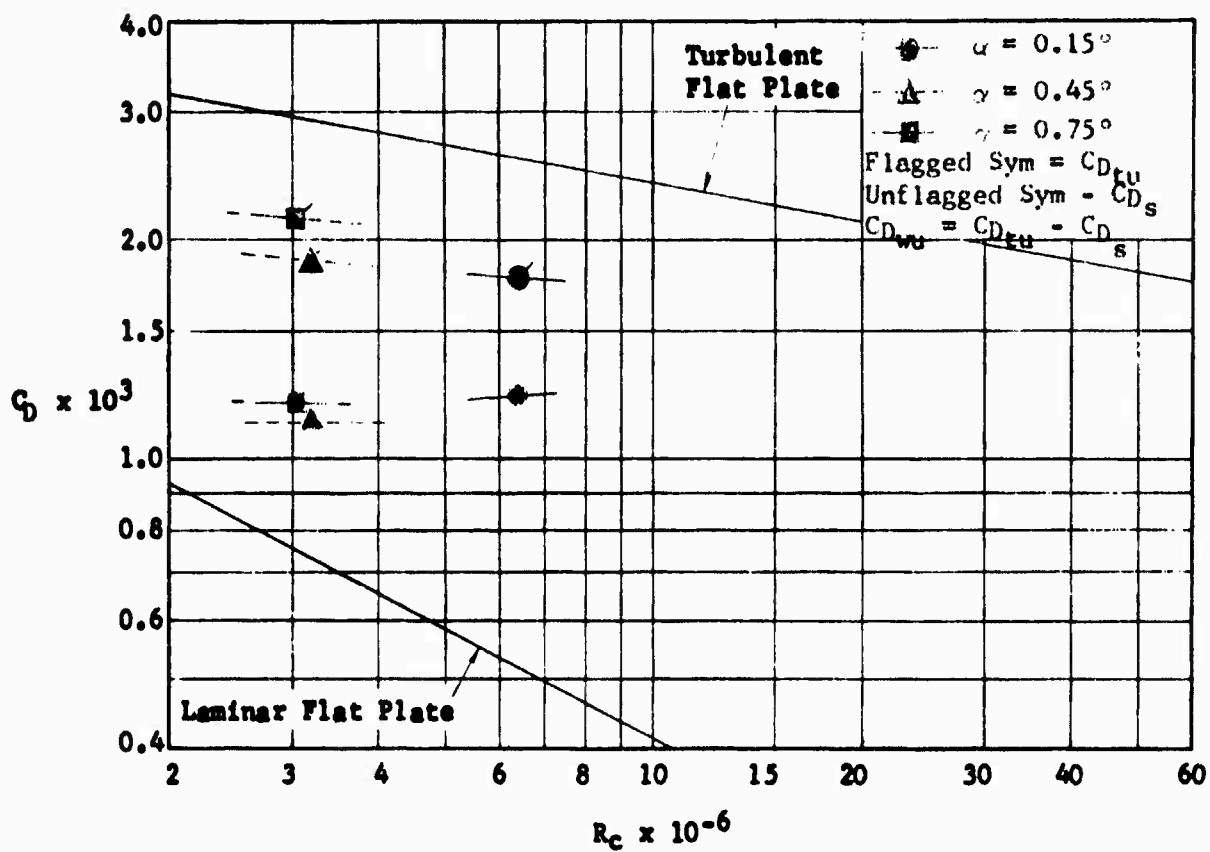
VARIATION OF DRAG COMPONENTS WITH SUCTION COEFFICIENT  
 $M_\infty \approx 2.25$

FIGURE 148



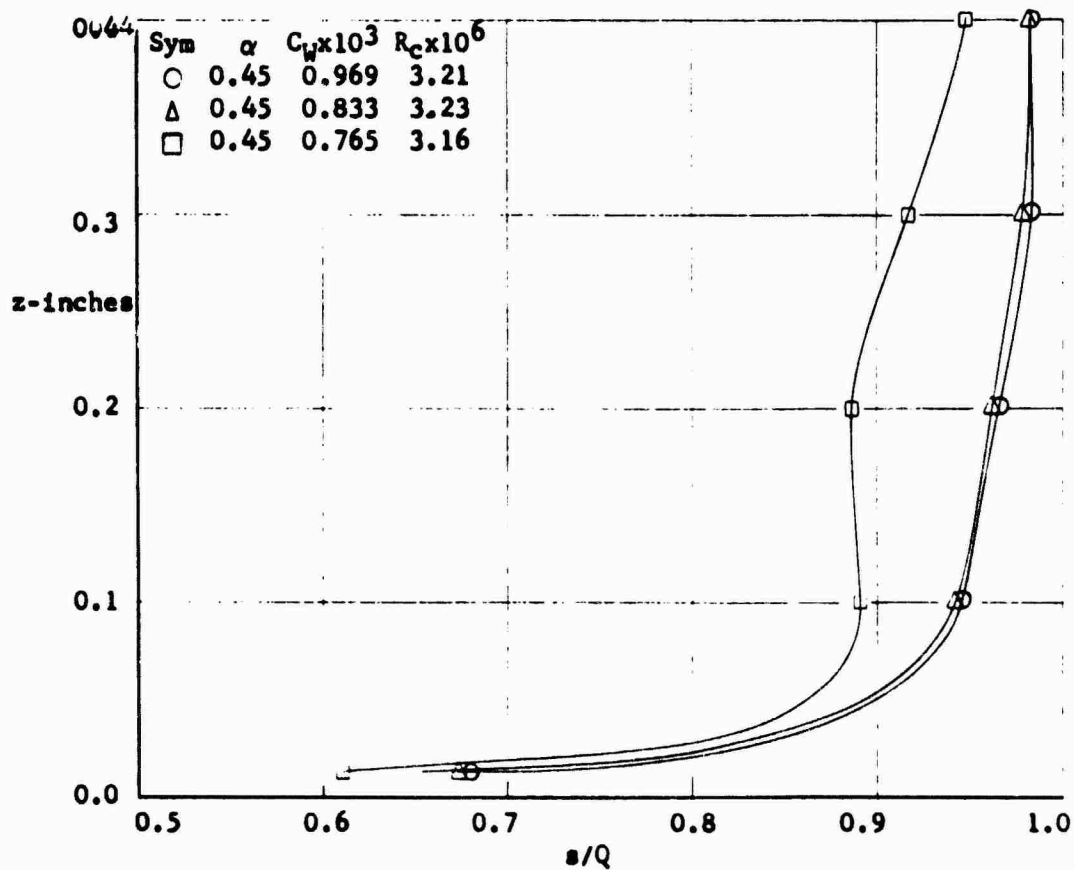
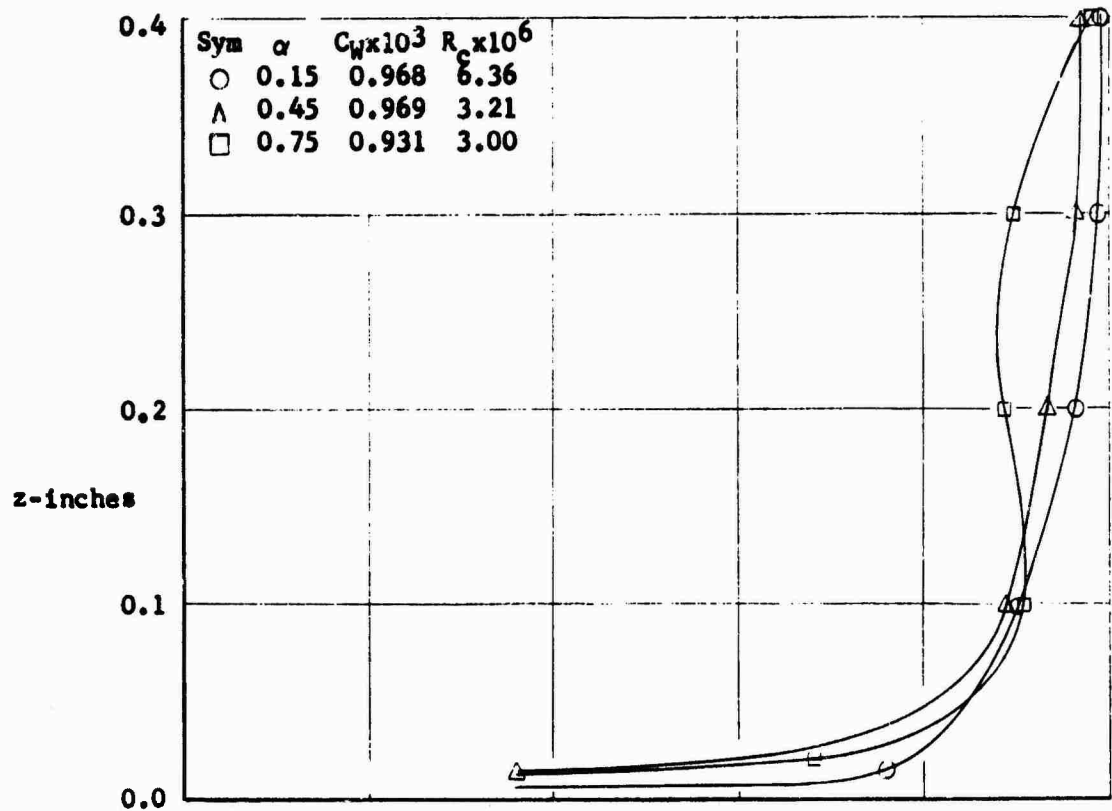
A VARIATION OF CORRECTED DRAG COEFFICIENTS WITH REYNOLDS NUMBER  
 $M_\infty \sim 2.25$

FIGURE 149a



VARIATION OF UNCORRECTED DRAG COEFFICIENTS WITH REYNOLDS NUMBER  
 $M_\infty \sim 2.25$

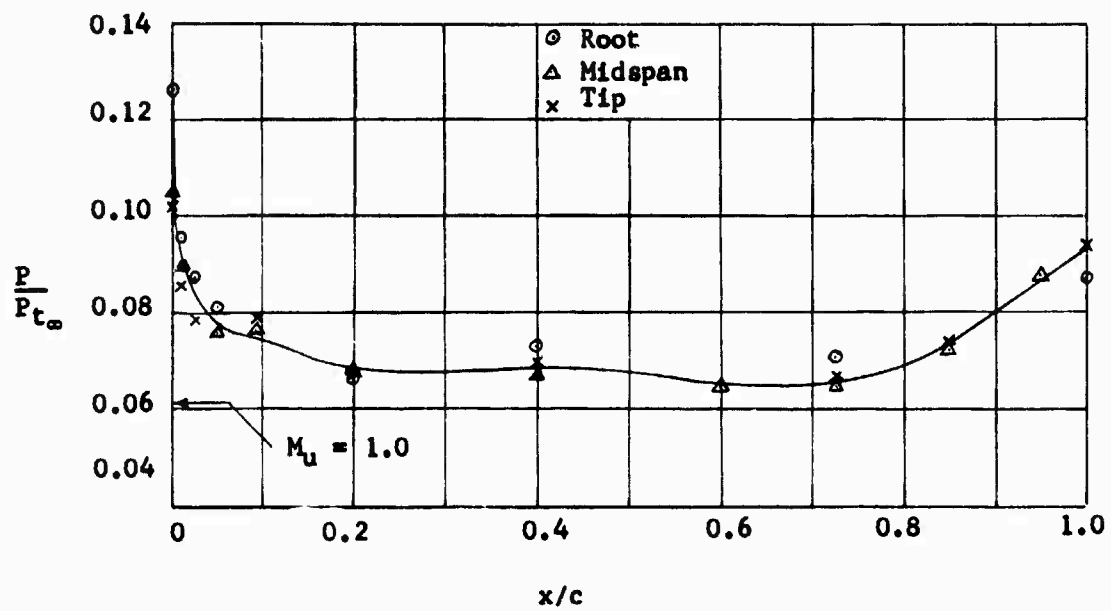
FIGURE 149b



TYPICAL MEASURED WAKE PROFILES AT  $M_\infty = 2.25$

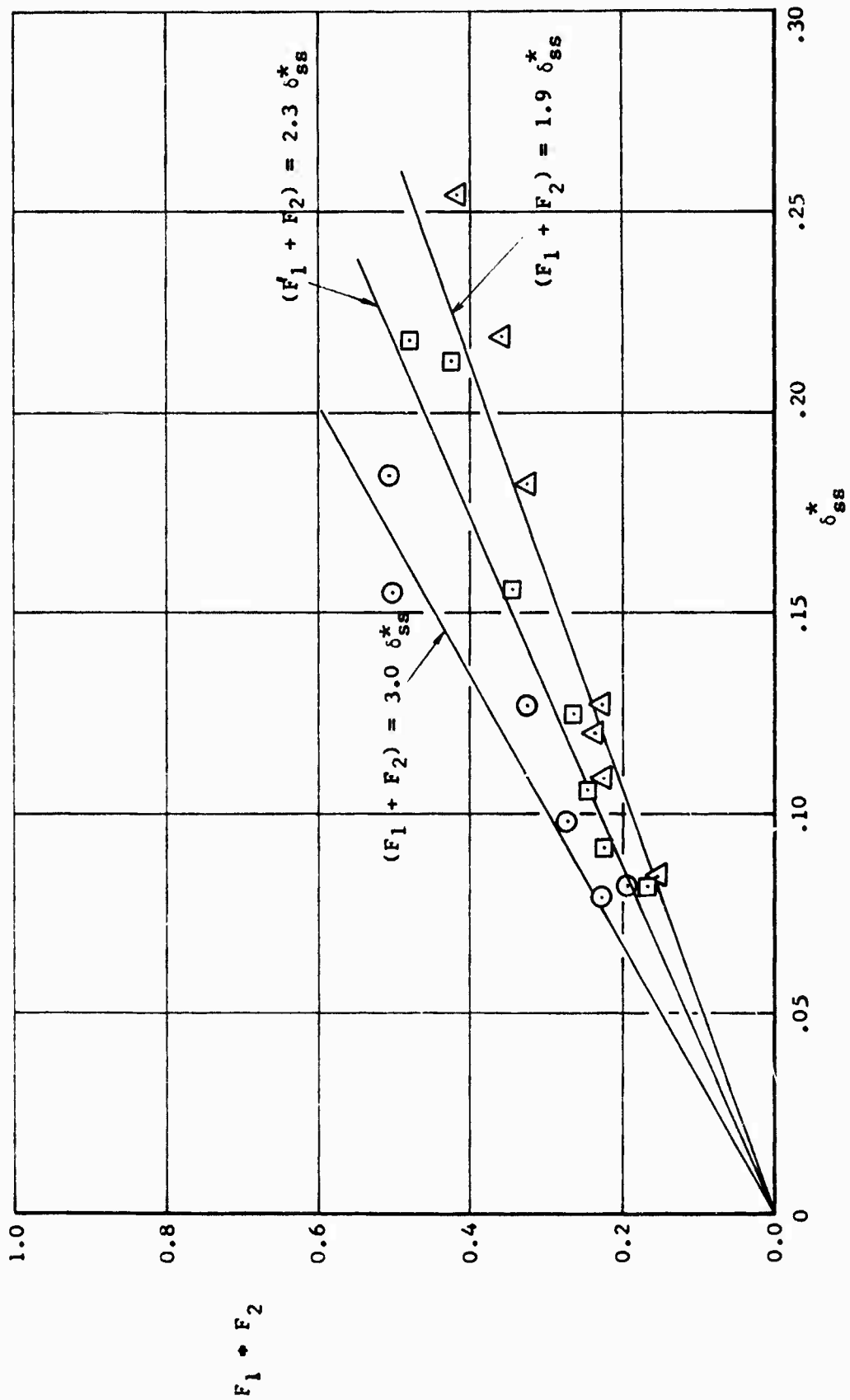
FIGURE 150



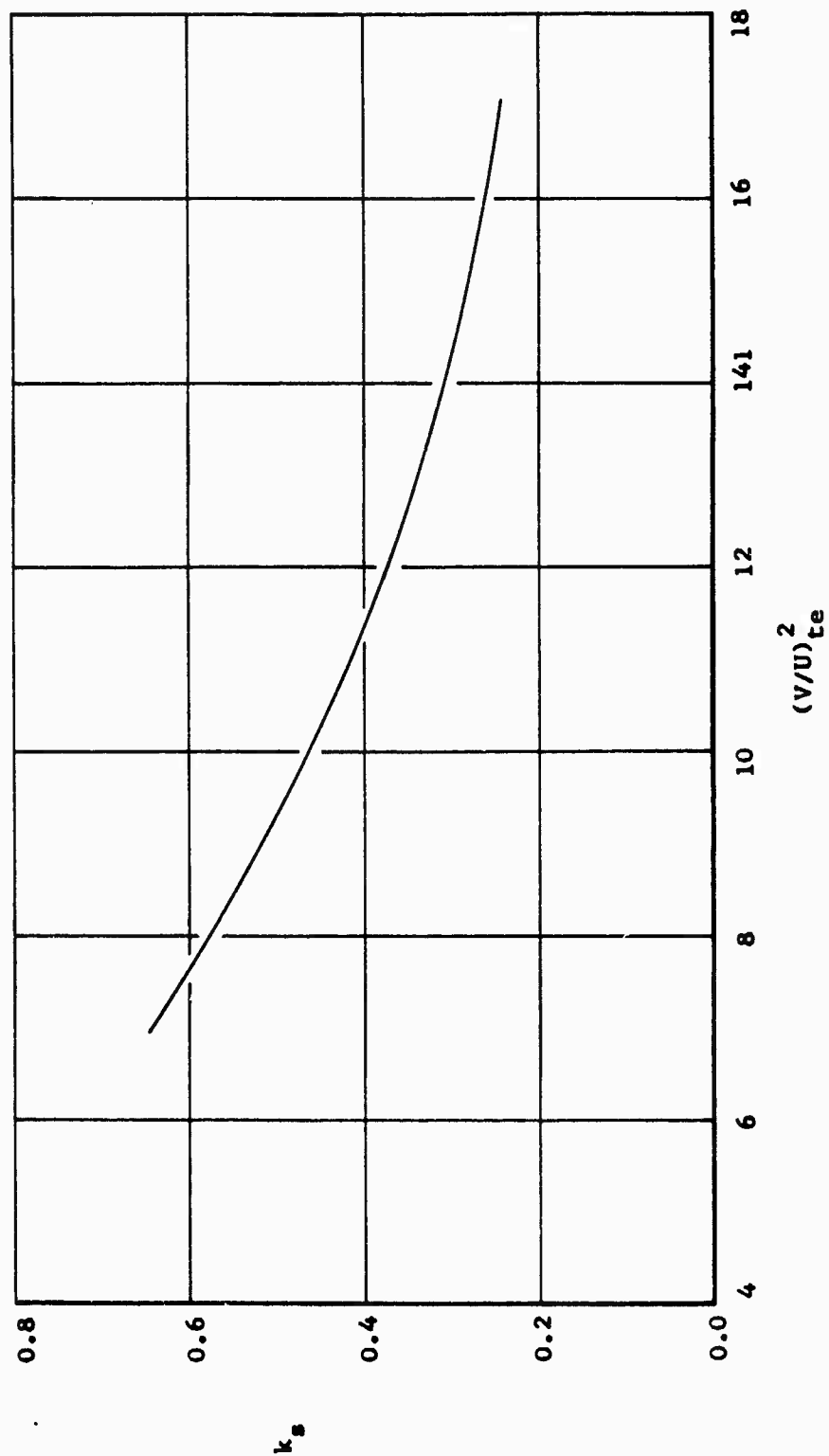


PRESSURE DISTRIBUTION AT  $\alpha = 0.45$  and  $M_\infty = 2.28$

FIGURE 151

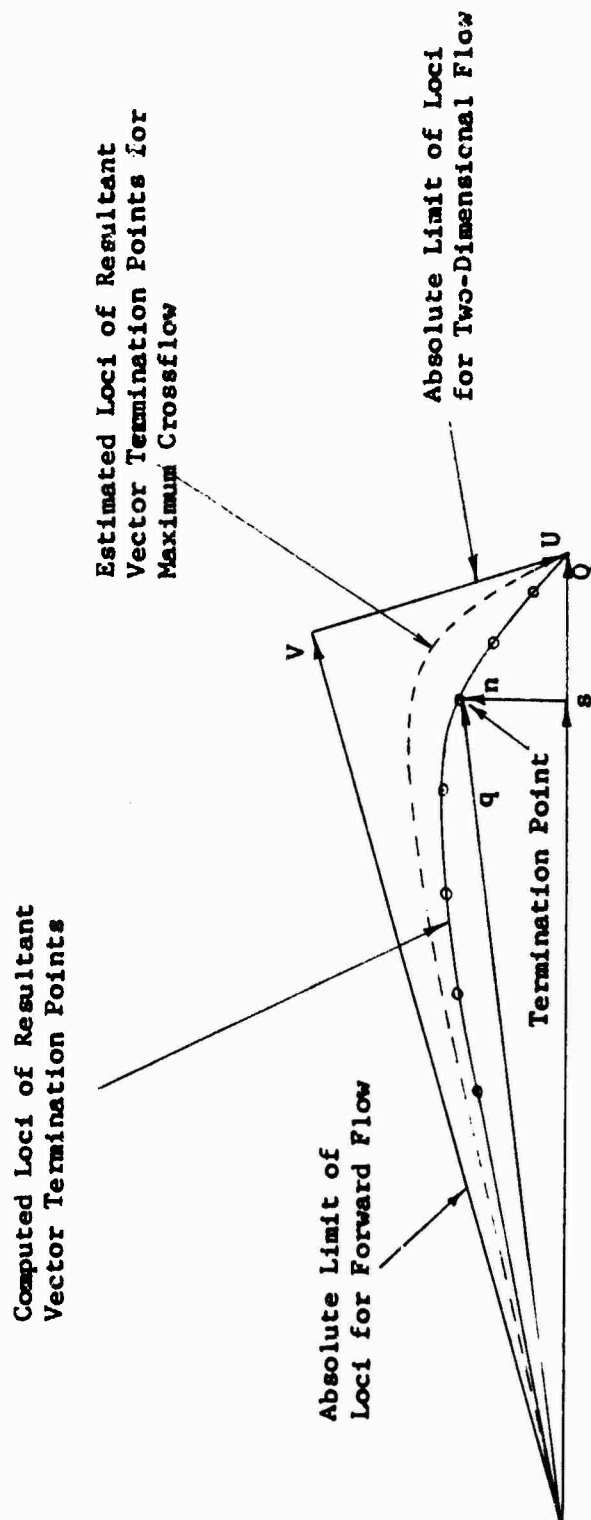


VARIATION OF  $F_1 + F_2$  WITH  $\delta_{SS}^*$



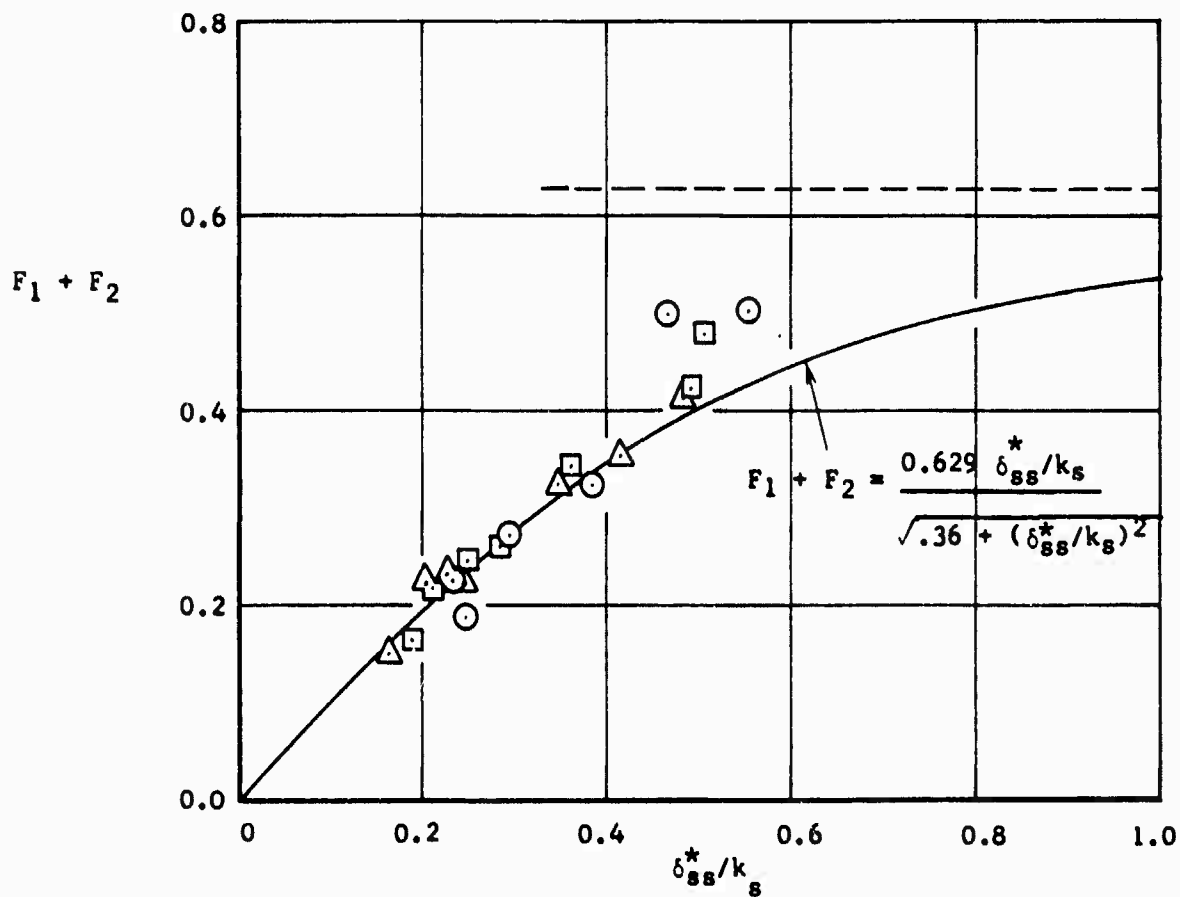
VARIATION OF  $k_s$  WITH  $(V/U)_{te}^2$

FIGURE 153



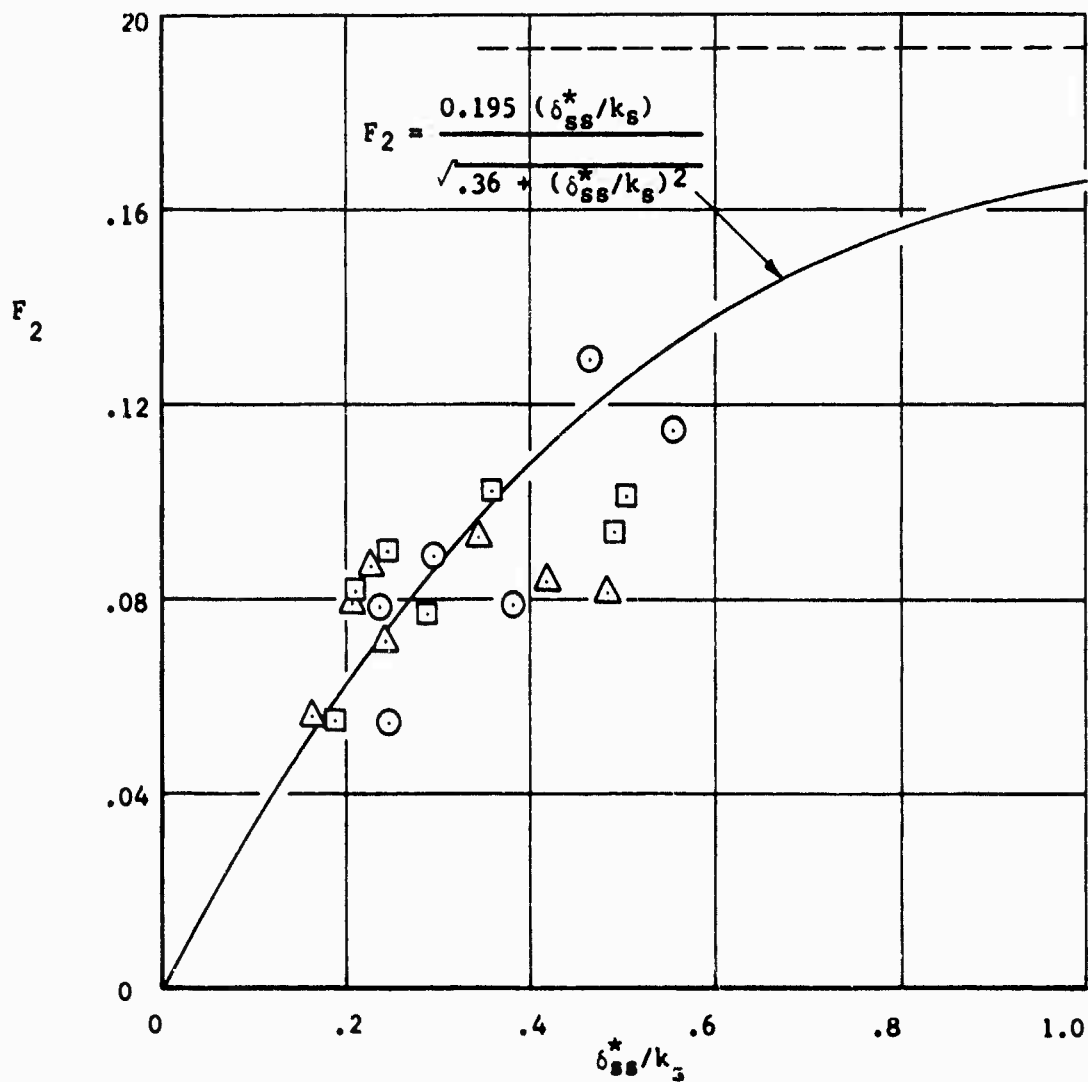
LOCI OF RESULTANT VECTOR TERMINATION POINTS IN THE BOUNDARY LAYER

FIGURE 154



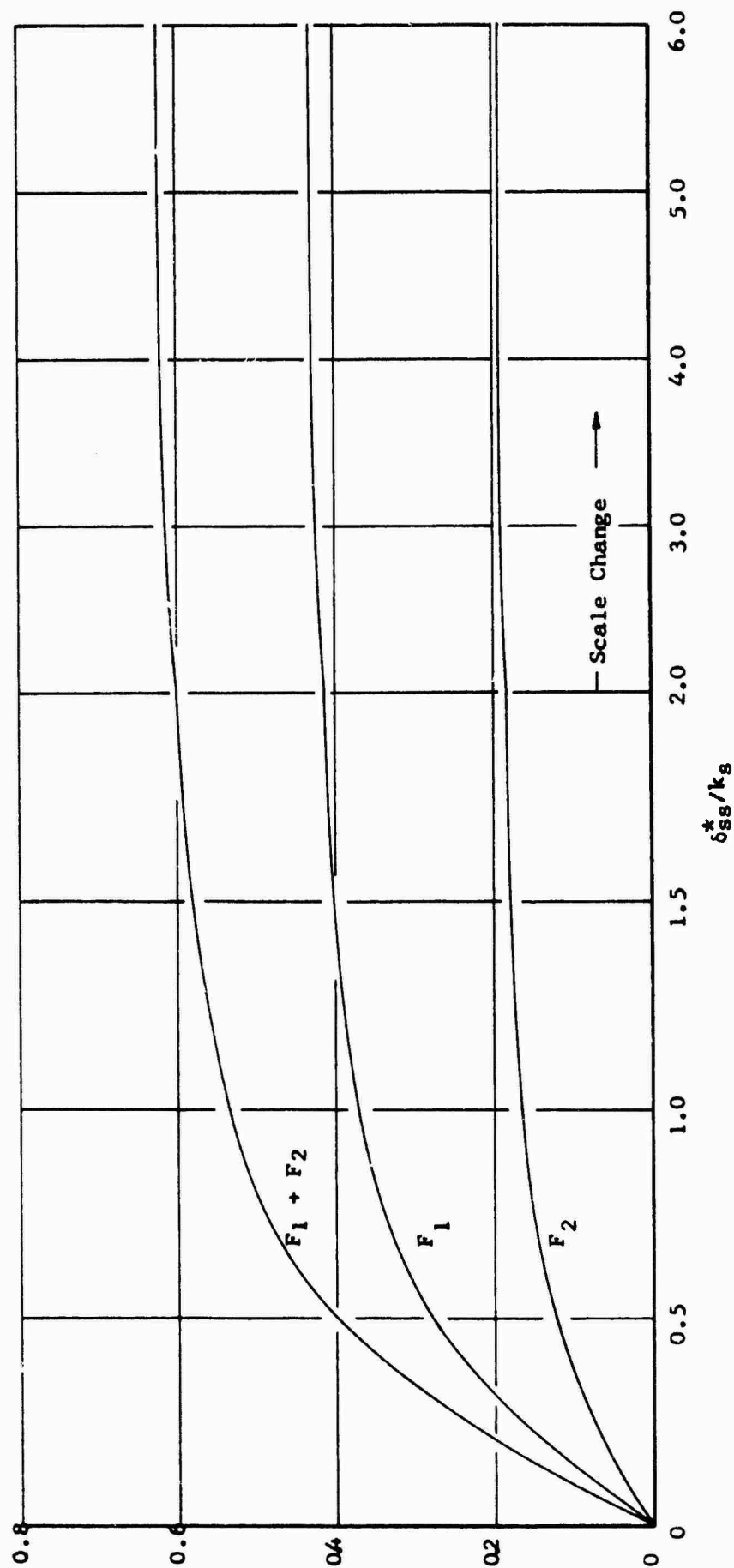
Simulation of  $(F_1 + F_2)$  by Empirical Equation

FIGURE 155



SIMULATION OF  $F_2$  BY EMPIRICAL EQUATION

FIGURE 156



SUMMARY OF EMPIRICAL CROSSFLOW CORRECTION FACTORS

FIGURE 157

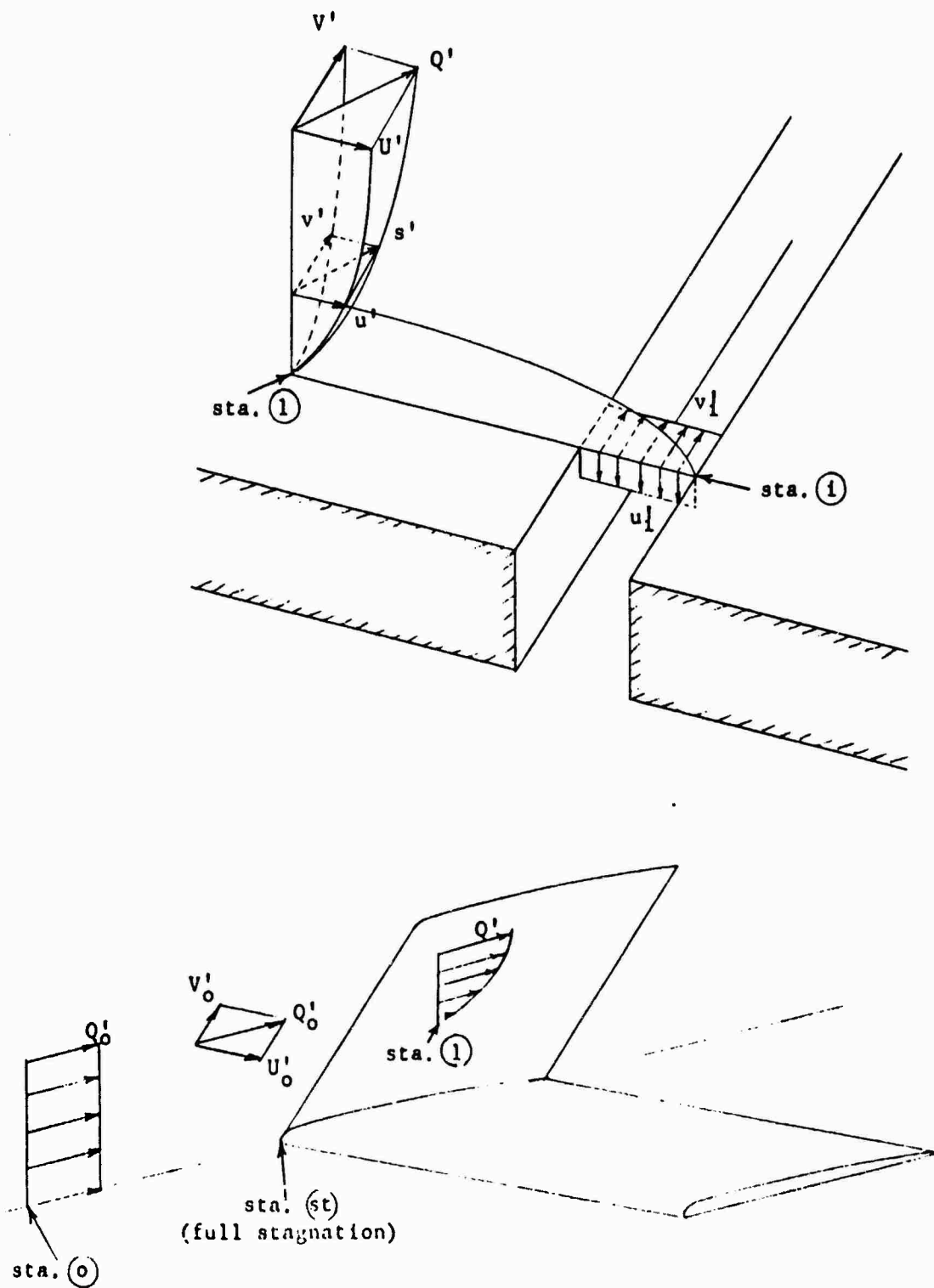


FIGURE 158

EXTERNAL REFERENCE STATIONS FOR LOSS CALCULATIONS  
THROUGH SWEEPED SLOTS



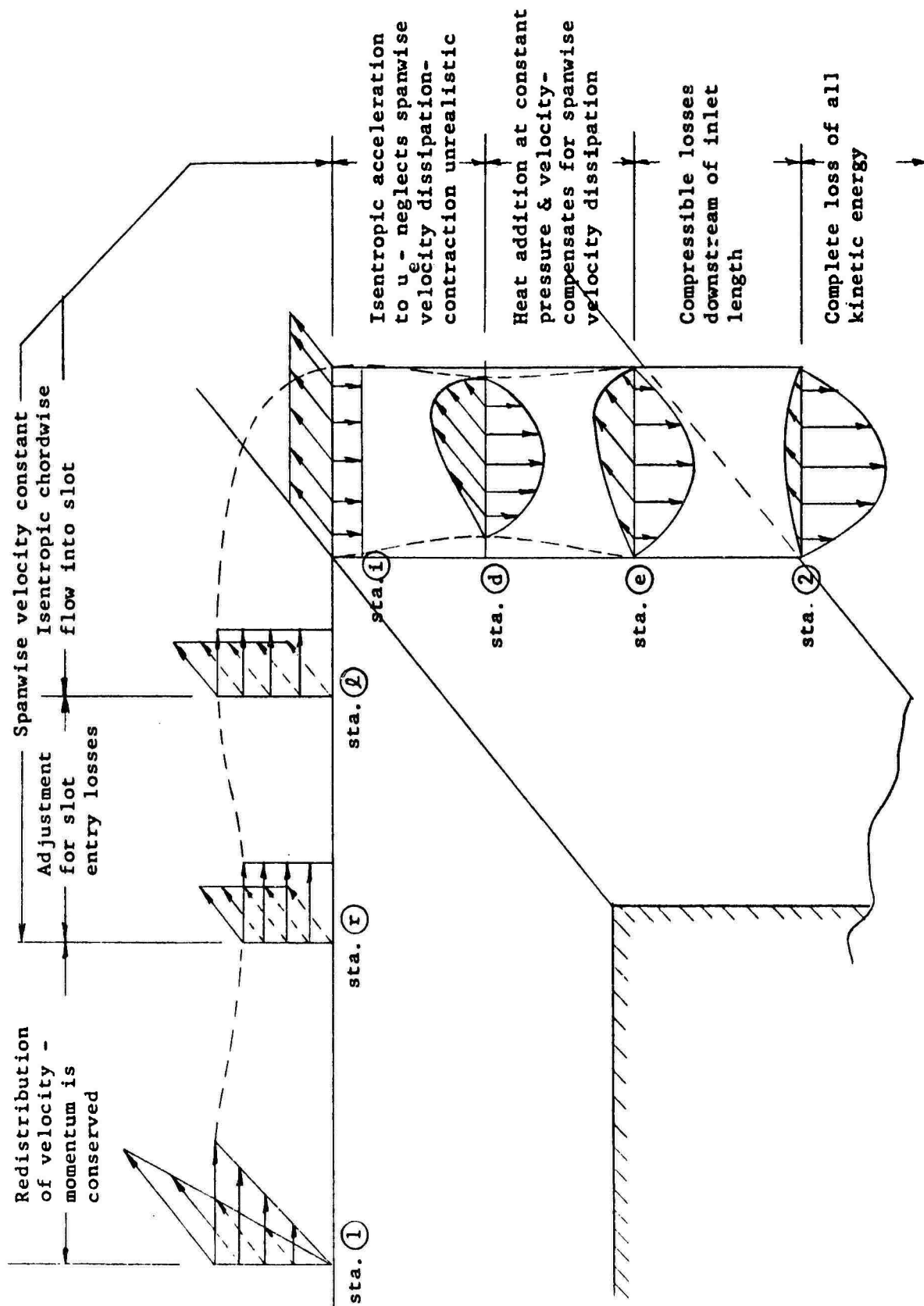


FIGURE 159

LOCAL AND INTERNAL REFERENCE STATIONS FOR LOSS CALCULATIONS THROUGH SLOTS

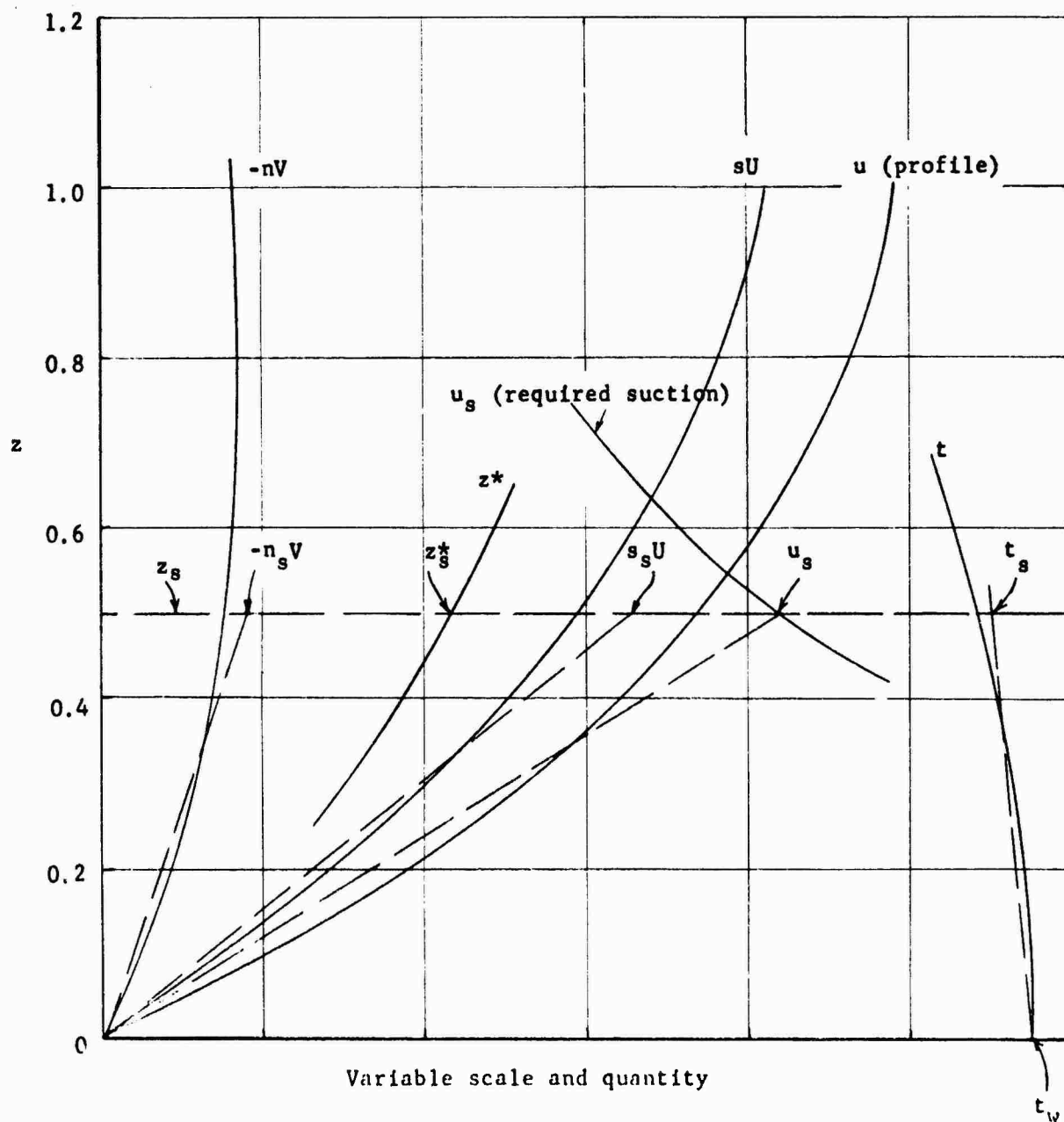
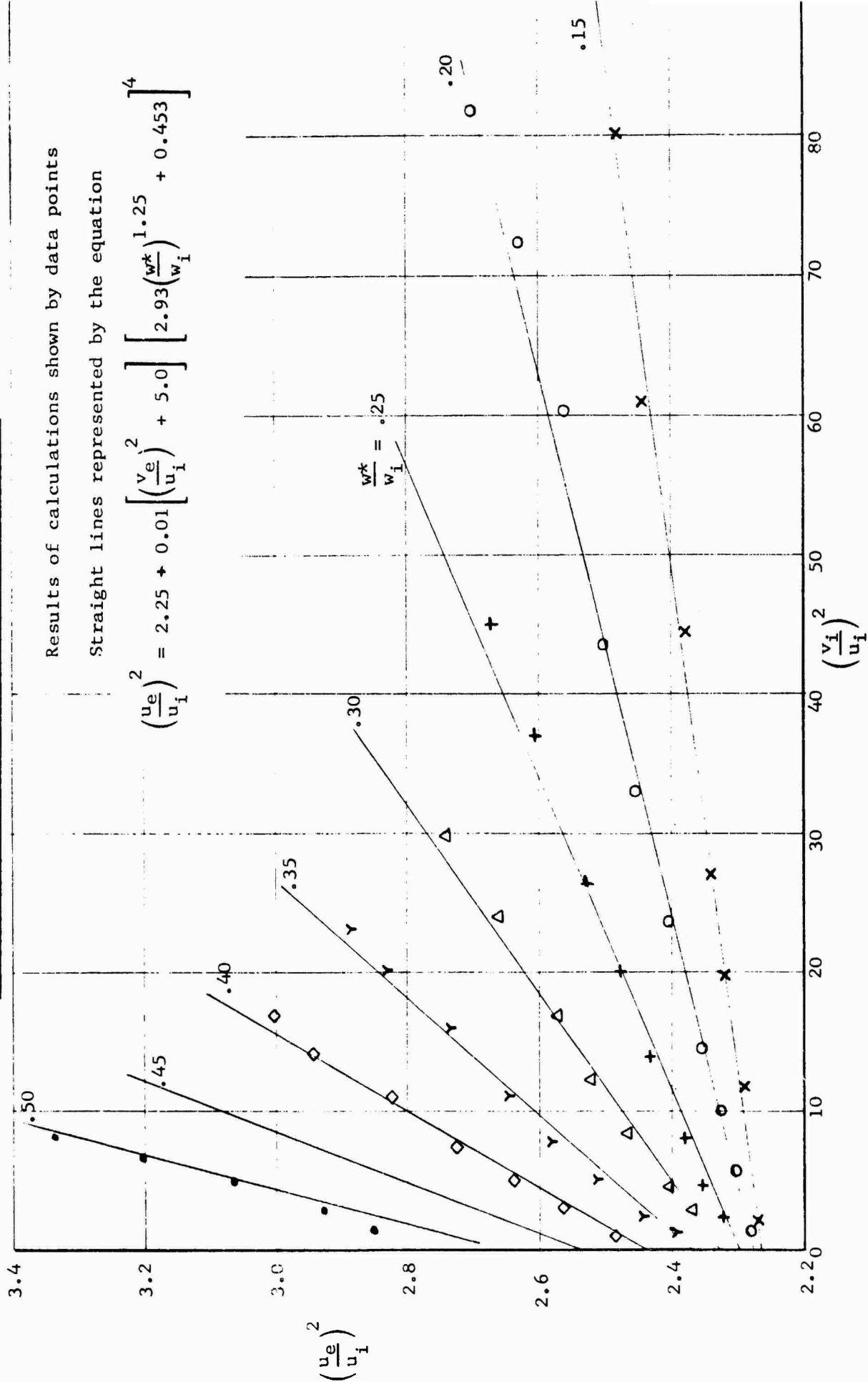


FIGURE 160

SIMULATION OF SUCTION LAYER PROFILE

FIGURE 161  
VELOCITY RATIO FOR THE INLET LENGTH OF SWEEP SLOTS



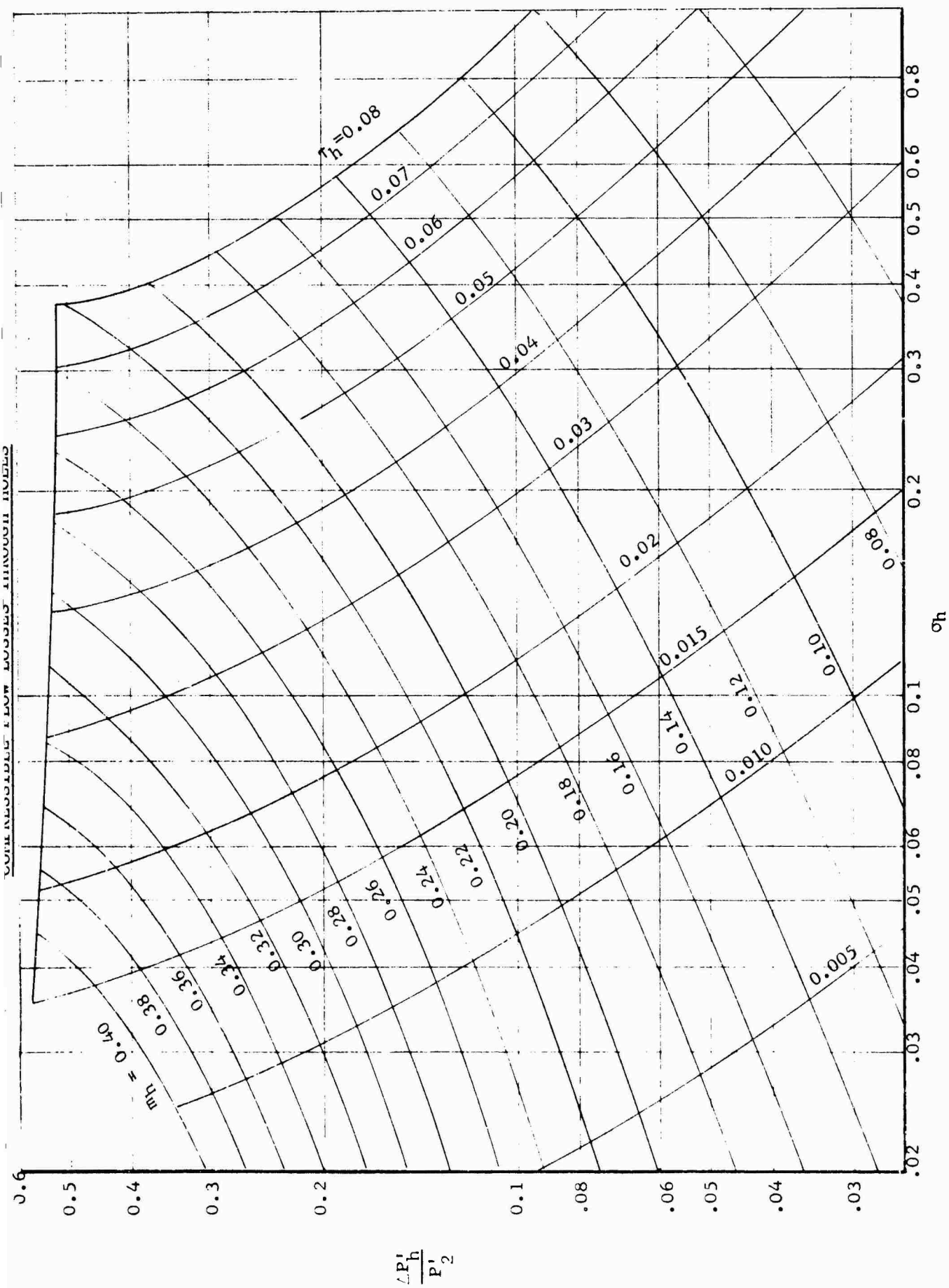


FIGURE 163

APPROXIMATIONS FOR  $w_x/w_i$  AND  $k_{mv}$

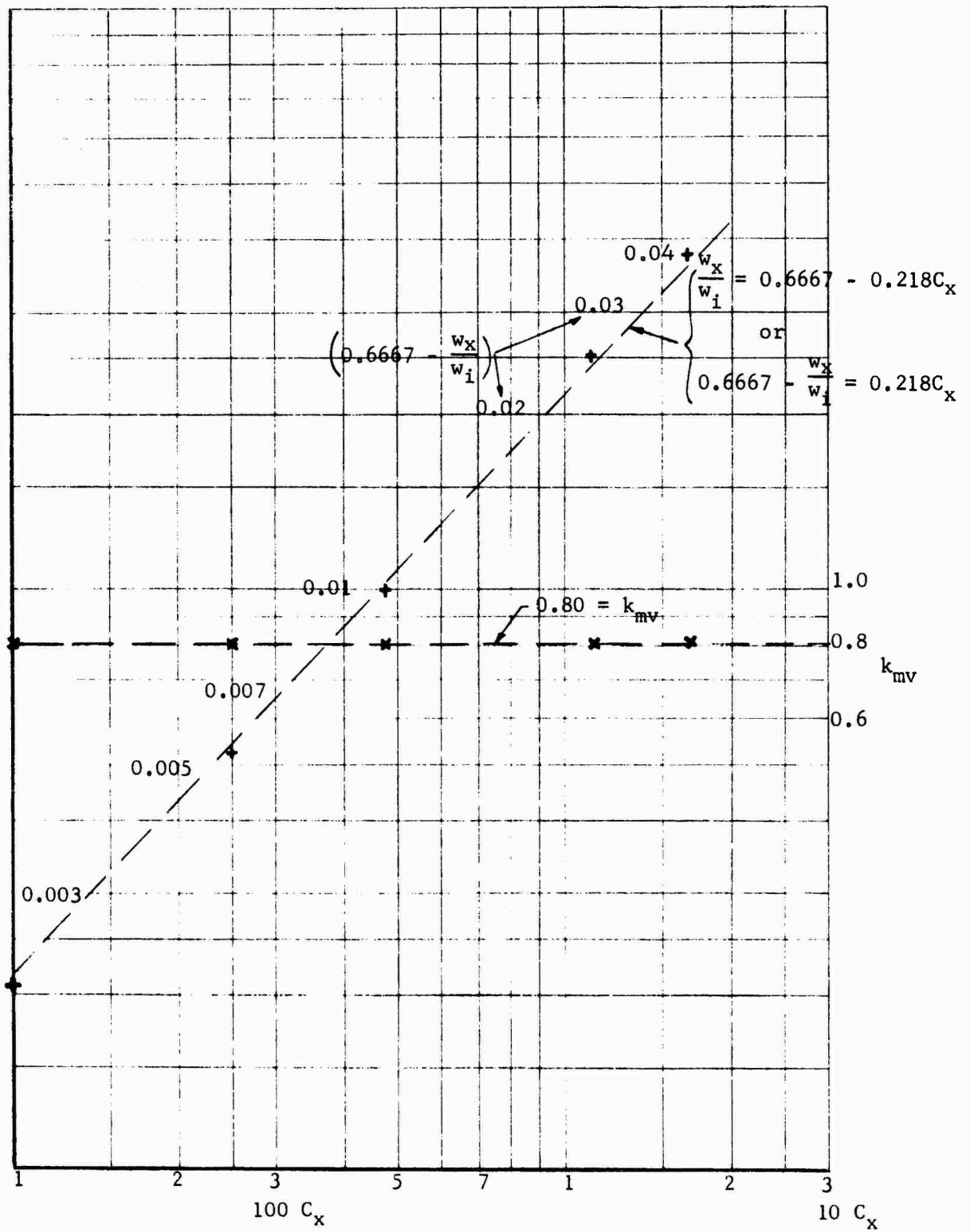


FIGURE 164

WORK CHART FOR FLOW OUTSIDE SLOT

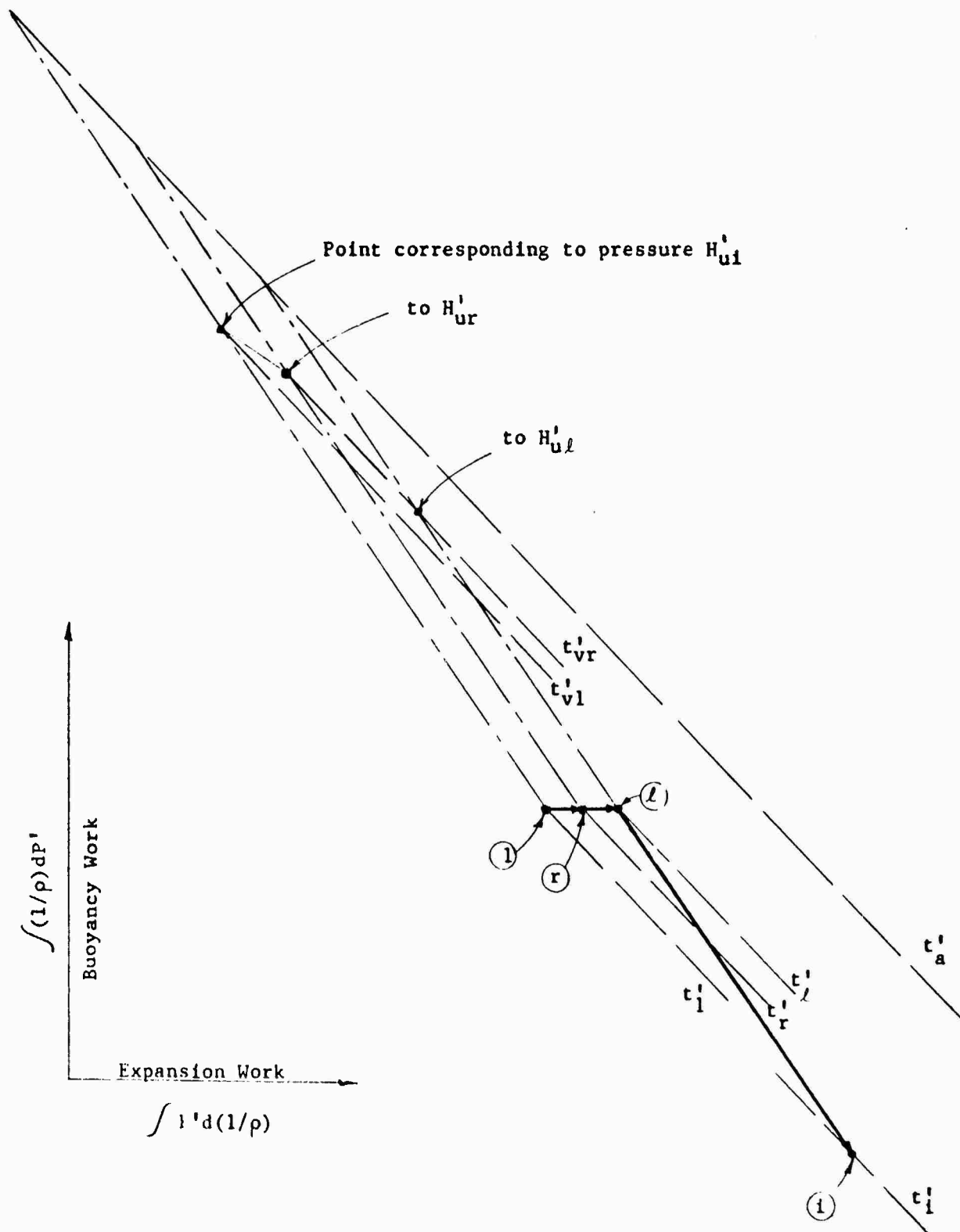
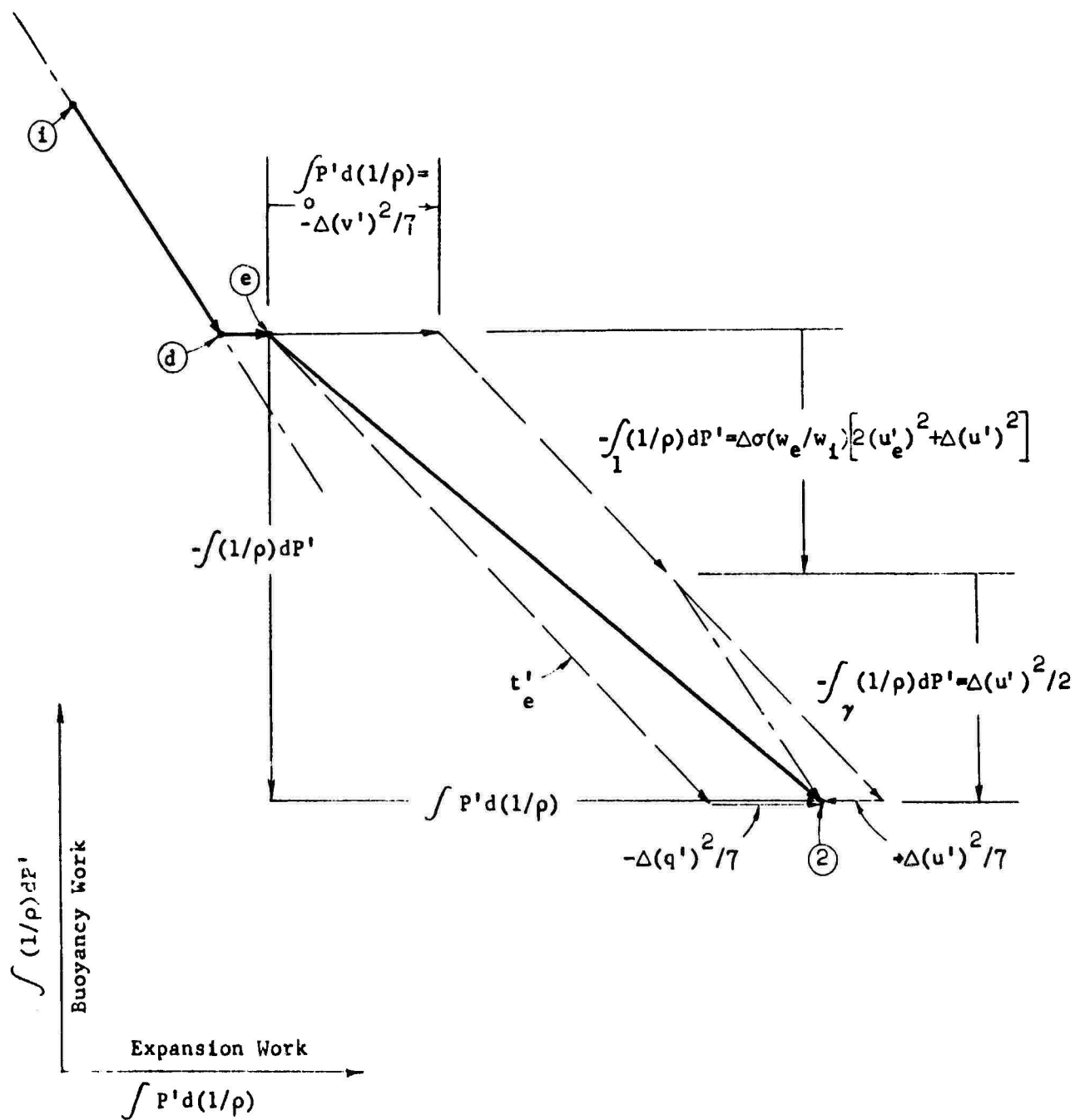


FIGURE 165

WORK CHART FOR FLOW INSIDE SLOT



REF DWG: 5209667 MODEL ASSY - COMPRESSIBLE FLOW TUBE  
4-210761 REWORK

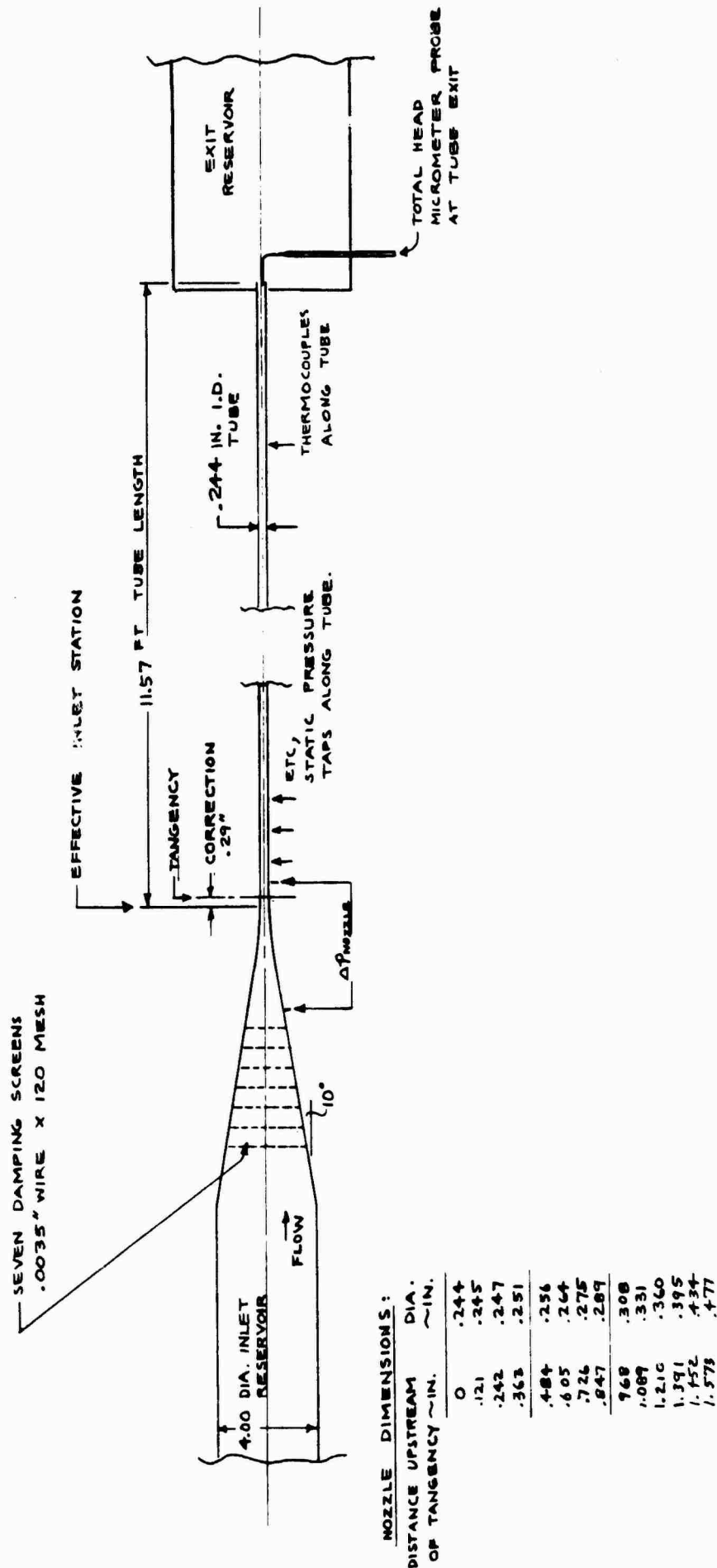


FIGURE 166 SKETCH - COMPRESSIBLE FLOW TUBE



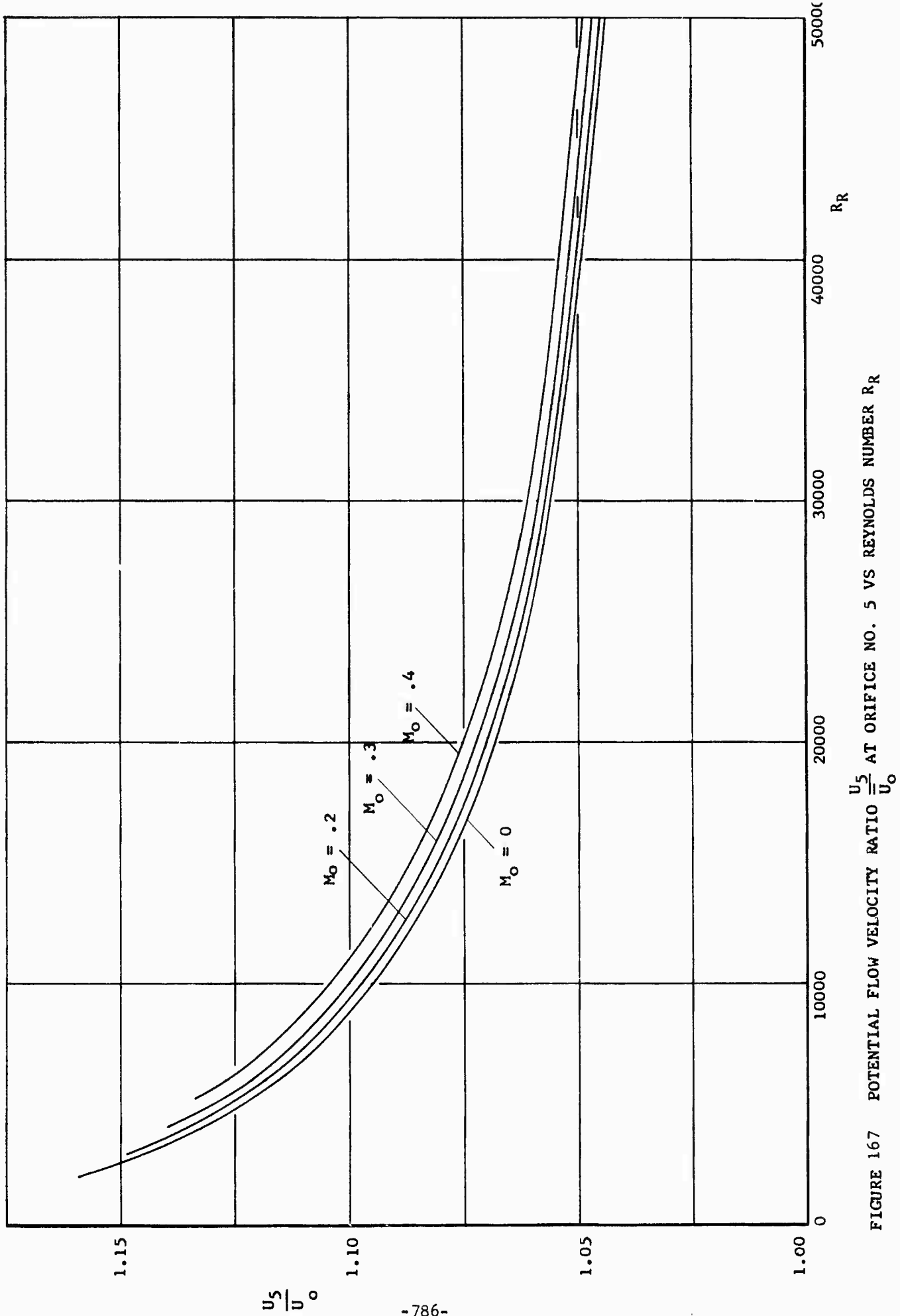


FIGURE 167 POTENTIAL FLOW VELOCITY RATIO  $\frac{U_5}{U_0}$  AT ORIFICE NO. 5 VS REYNOLDS NUMBER  $R_R$

$\frac{x_5}{R}$

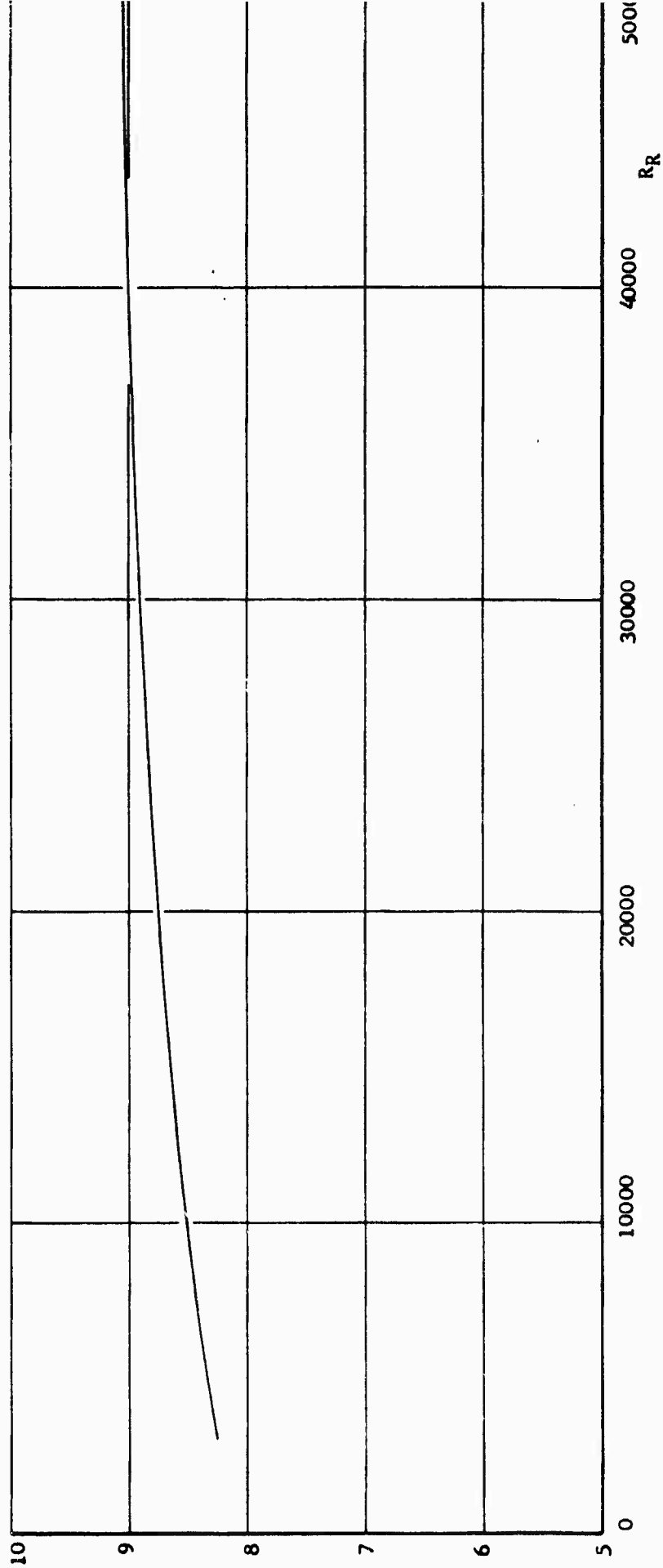


FIGURE 168 DISTANCE  $x_5$  OF ORIFICE NO. 5 FROM FICTITIOUS TUBE INLET VS REYNOLDS NUMBER  $R_R$

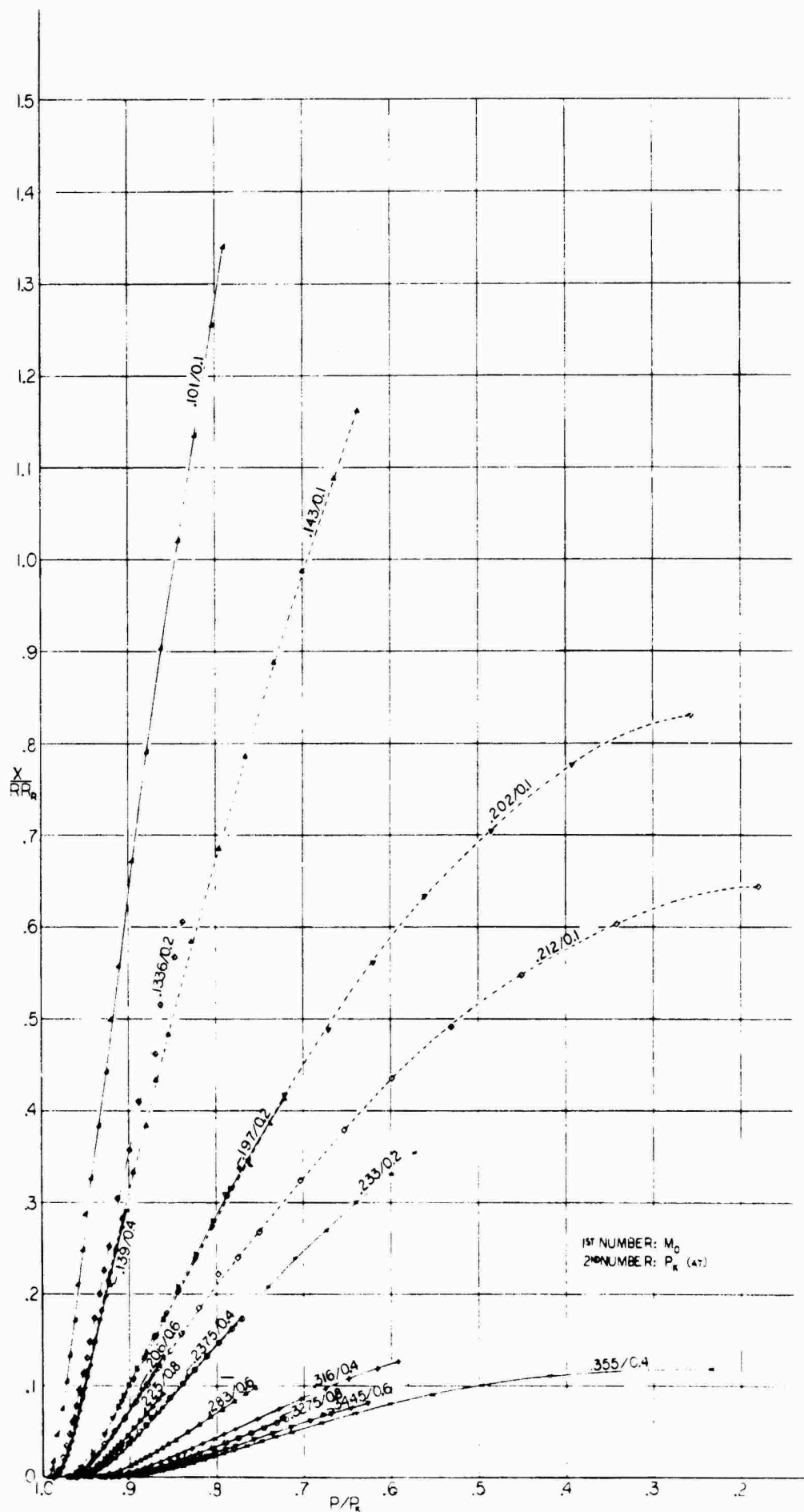


FIGURE 169 PRESSURE RATIO  $P/P_k$  VS NON-DIMENSIONAL TUBE LENGTH  $\frac{X}{R R_R}$  FOR VARIOUS INLET MACH NUMBER  $M_0$

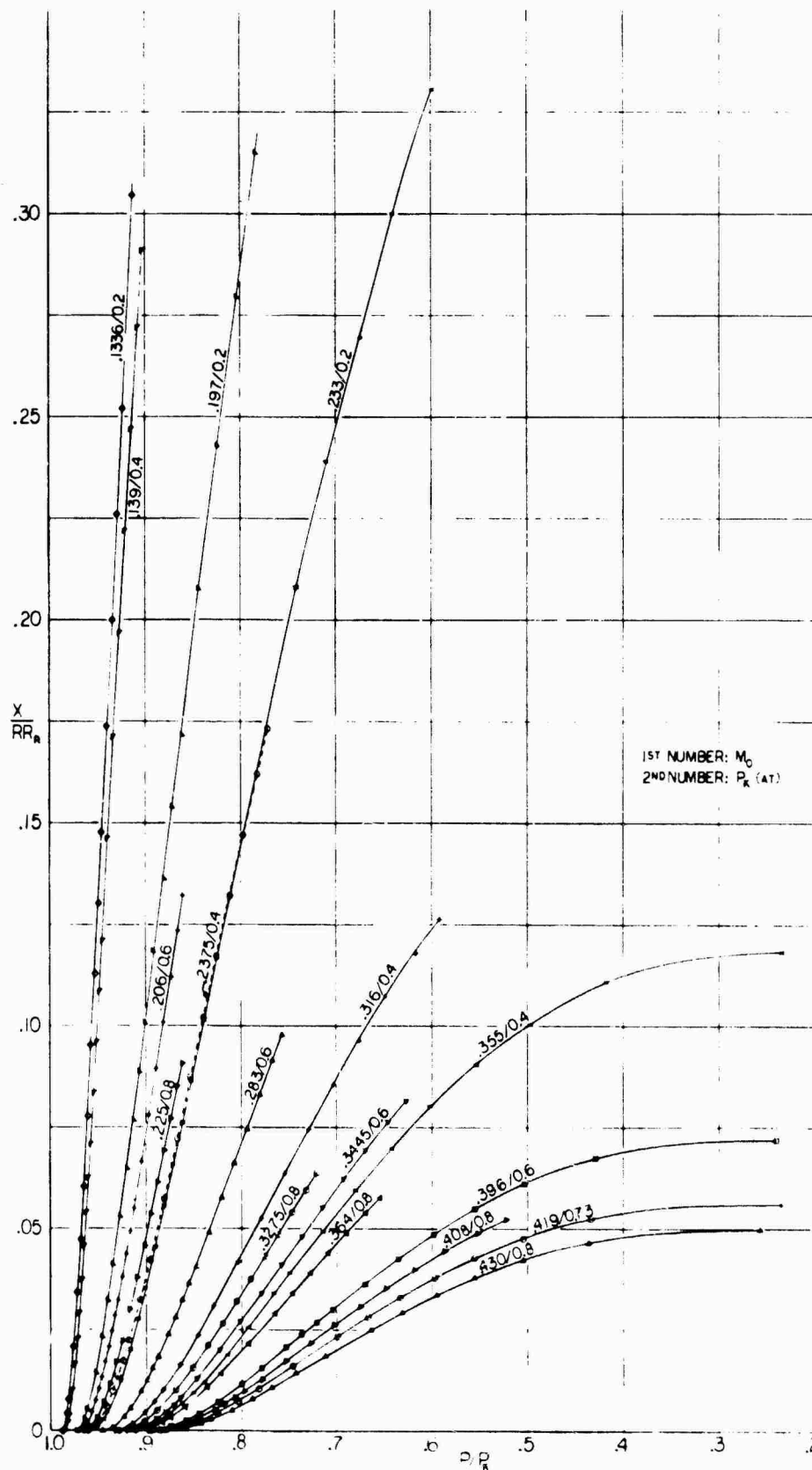


FIGURE 170 PRESSURE RATIO  $P/P_k$  VS NON-DIMENSIONAL TUBE LENGTH  $\frac{X}{R R_k}$  FOR VARIOUS INLET MACH NUMBER  $M_0$

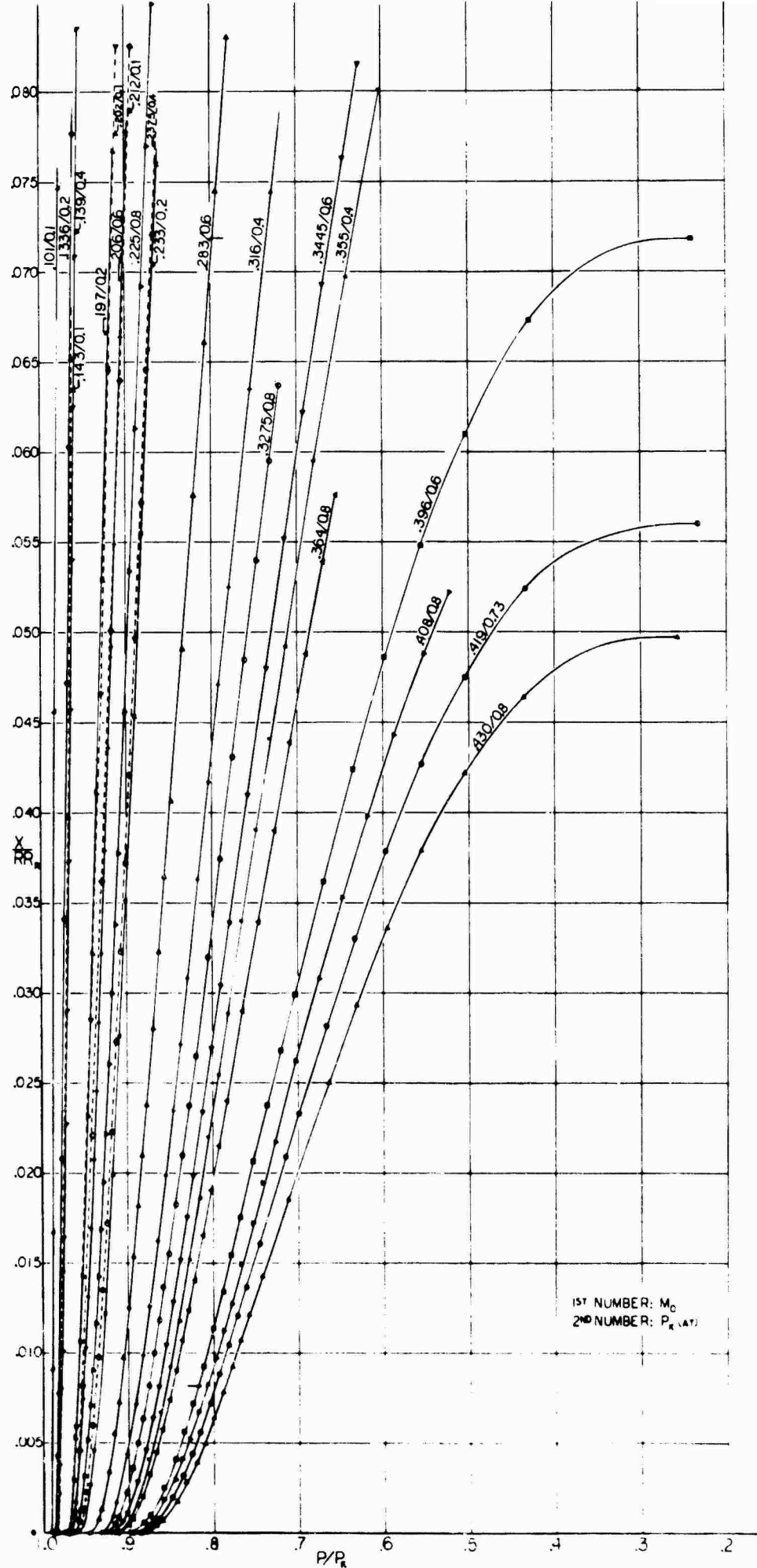


FIGURE 171 PRESSURE RATIO  $P/P_k$  VS NON-DIMENSIONAL TUBE LENGTH  $\frac{X}{R R_R}$  FOR VARIOUS INLET MACH NUMBER  $M_0$

1ST NUMBER:  $M_0$   
2ND NUMBER:  $P_k$  (AT)

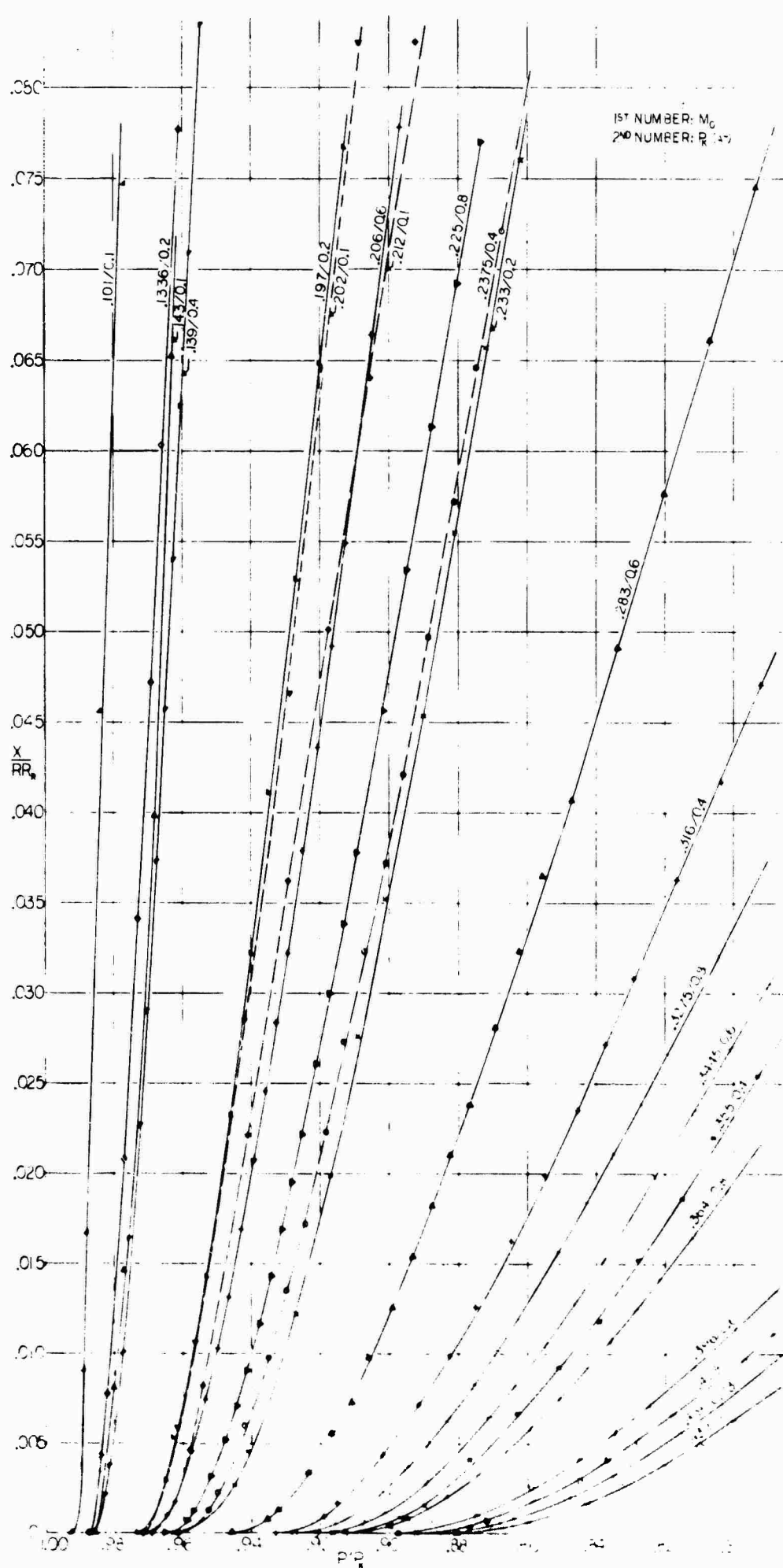


FIGURE 172 PRESSURE RATIO  $p/p_k$  VS NON-DIMENSIONAL TUBE LENGTH  $\frac{x}{R R_0}$  FOR VARIOUS INLET MACH NUMBER  $M_0$

(X/RR<sub>R</sub>) Choking

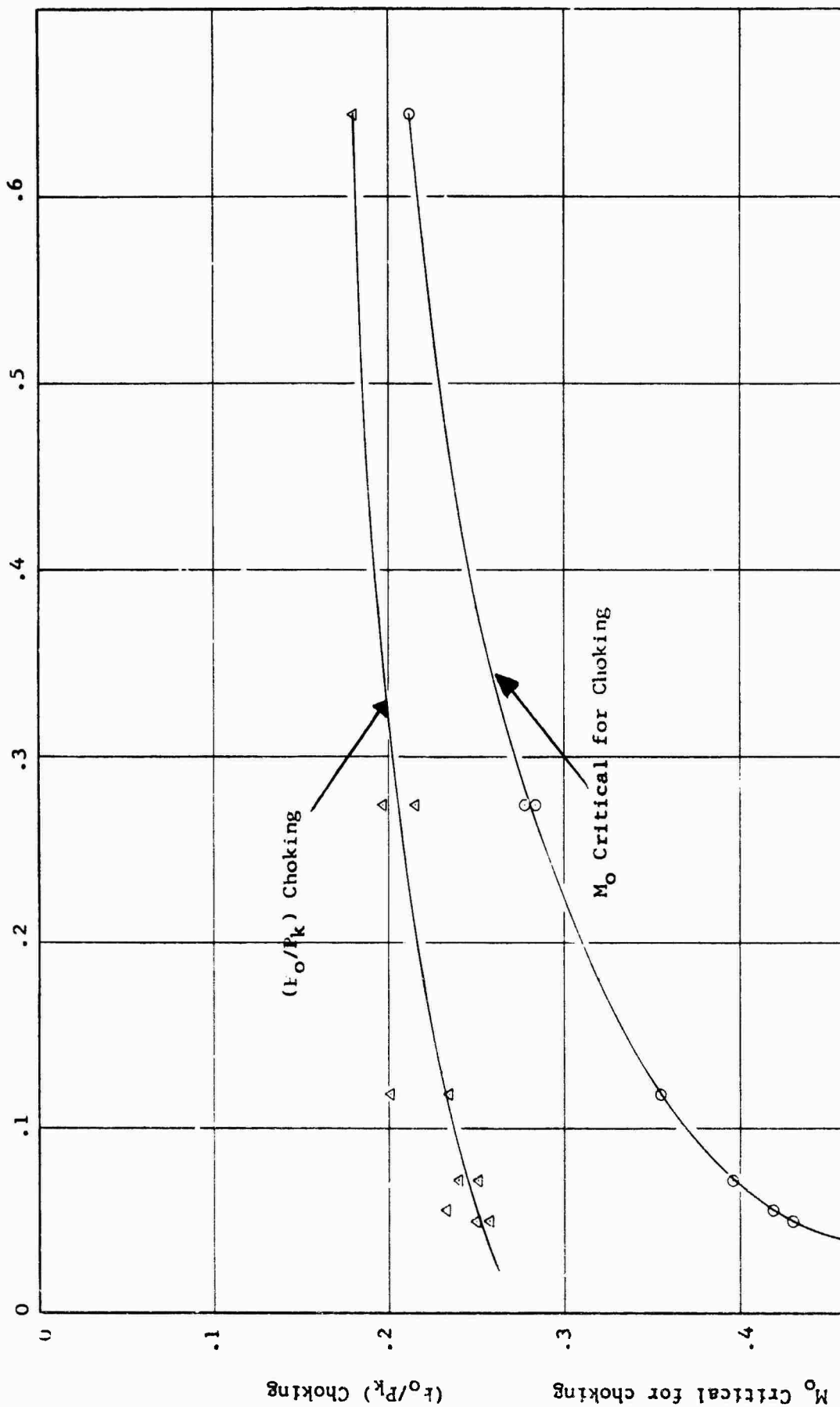


FIGURE 173 CRITICAL VALUES OF PRESSURE RATIO  $P/P_k$ , TUBE LENGTH  $\frac{X}{RR_R}$  AND MACH NUMBER  $M_o$  AT

CHOKING CONDITION

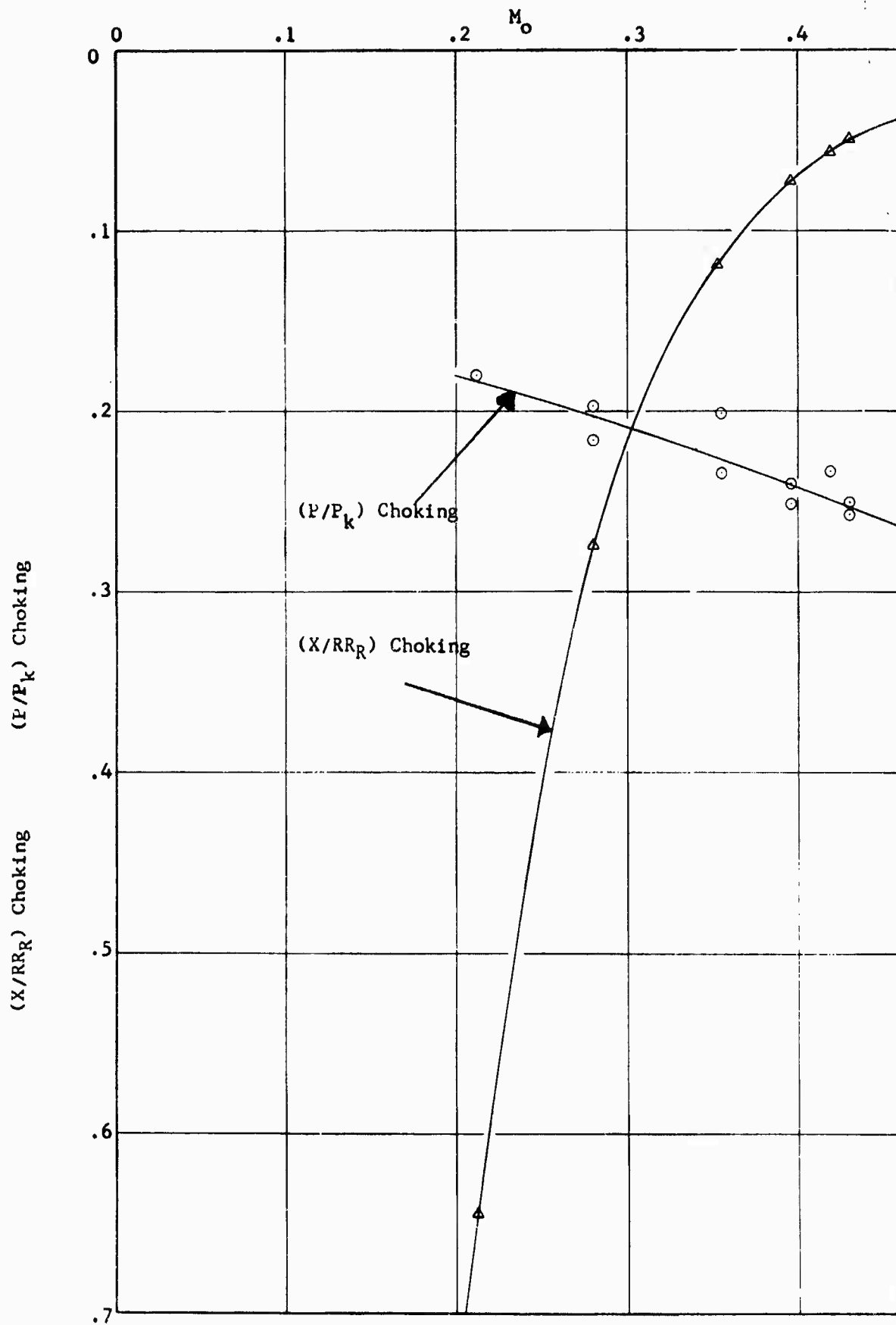


FIGURE 174 CRITICAL VALUES OF PRESSURE RATIO  $P/P_k$ , TUBE LENGTH  $\frac{X}{R R_R}$  AND MACH NUMBER  $M_o$  AT CHOKING CONDITION



**SECTION III**  
**STRUCTURAL INVESTIGATIONS**

## CHAPTER A. STRUCTURAL ASPECTS OF LOW DRAG SUCTION AIRFOILS

J. Wieder  
W. Pfenninger

### (A) Abstract

A description of the structure of low drag suction wings is presented, keyed to a generalized high subsonic wet wing. The results of component load tests, corrosion effects, surface irregularities, concentration factors, and the effects on strength and rigidity are discussed.

### (B) Introduction

Extensive laminar flow on the surfaces of an airplane by means of boundary layer suction will increase its range and endurance. The airplane range depends on the airplane lift to drag ratio, the specific fuel consumption of the propulsion system and the airplane weight ratio between beginning and end of the flight, which in turn is influenced by the airplane structural weight.

With the reduction in friction drag by means of boundary layer suction, the induced drag becomes increasingly important. In order to achieve the full advantage from the application of boundary layer suction, it is desirable to reduce the induced drag at the same time as the friction drag by increasing the wing span. With the large wing spans of an optimized laminar suction airplane, the structural designer is thus immediately faced with the problem of designing these large suction wings with minimum structural weight within the requirements of strength and stiffness, with the suction air ducting system installed, and with the close surface tolerances required for extensive laminar flow. In order to minimize the wing structural weight, the inertial weights should be distributed over the wing span, the walls of the suction air ducts should preferably be combined with the structural elements of the wing, such as wing skin, shear webs, longitudinal stiffeners, ribs, etc. Continuous suction on the wings, being optimum aerodynamically, can be closely approached by removing the slowest boundary layer air particles close to the wing surface through a large number of fine slots. The resulting low flow velocities and small Reynolds numbers for the slot flow enable the use of relatively simple suction slots, which can be cut into a thin outer wing skin, which in turn is bonded to a continuous thicker inner skin. The suction air passes through the slots, spanwise grooves and holes, drilled into the inner skin underneath the slots, into the suction ducts and to the suction compressor. With the exception of the holes in the inner skin, both wing skins are structurally efficient for wing bending strength and stiffness.

### (C) BLC Wing Components

Two current wing skin versions (Figure 1) type A, the solid skin, representative of inboard loading indices, and type B, the honeycomb sandwich, of outboard loading indices and trailing edge surfaces, exemplify upper and lower high subsonic wing surfaces. The range of geometries indicated is determined by the chordwise location of the slot. These are all bonded assemblies with drilled holes and the slots cut by means of a track-mounted saw with a

(C) BLC Wing Components (Continued)

rotating blade. The sheet with plenums in the honeycomb sandwich is chemically milled to the proportions shown.

Previously reported static tension and shear tests of perforated sheets of an aluminum alloy with comparable hole diameter to row ratios (Reference 125) indicate no measurable loss of net area efficiency. Built up panels tested in compression similarly developed net area deformations and buckling stresses. Groups of 4- by 20-inch simply supported panels, representative of low loading indices and trailing edge upper skins, were compressed in the spanwise direction. Figure 2 shows the cross sections of .16-inch over-all depth, and their specific strengths. Of the three types, the chemically milled core sandwich was unreliable due to the narrow bond ledges of the core; the corrugated core type is promising when the core is fabricated with precision dies, and the honeycomb sandwich is a current design choice.

A series of 19 inch long 6061-T6 aluminum alloy tubes was tested in torsion (Figure 3 and Figure 4). The encircled 3 and 5 on the relative rigidity and yield stress diagram designate spacings akin to those of BLC main wing box surfaces and indicate torsional rigidity losses of about 5 percent. The 25 percent decrease in shear yield stress is consistent for all configurations; in actual design, a replacement of local area removed will bring these values close to normal allowables. In those specimens taken to failure, there was the expected elliptical shape of the holes with a 45° major axis; the failure proceeded along the plenum chamber from the top of one ellipse to the bottom of the next following the least net section in a saw-tooth fashion. Figure 5 shows the twist at failure relationship among the slot locations with holes; the fail stress was 22,000 psi based on effective transverse shell thickness. Thus, the strength is a function of the least net area; the rigidity, in the elastic range, approximately of the net cross sectional area transverse to the axis, and the twist, in the plastic range, a non-linear function of the number of slots.

In the region of the main structural box of the wings of large long range or endurance airplanes, the integration of the internal suction air ducting system with the structural layout usually leads to an open double skin panel for the upper and lower wing surface. The small suction velocities on straight as well as swept wings in the area of the main box

$(\frac{v_o}{U_o} = 1 \text{ to } 2 \times 10^{-4})^*$ , with a chordwise slot spacing of approximately 2 percent

of the wing chord, generally permit suction duct arrangements on the basis of structural optimization. Over a range of 8,000 to 20,000 lbs/inch of chord, optimized open sandwiches would give clear duct depths of 1 to 2.7 inch, which are sufficient for keeping duct losses minimal.

The family of open sandwiches is limited to continuous corrugations or a variety of discrete element geometries and cover plates. Corrugated

---

\* $v_o$  = suction velocity for equivalent area suction (FPS)

$U_o$  = freestream velocity (FPS)

(C) BLC Wing Components (Continued)

sandwiches would be a first choice from the standpoint of chordwise stiffness, and as a torsional shear transfer medium from the partial depth intermediate ribs. However, they have the following disadvantages: (1) increased fabrication difficulties of tapering corrugations in planform and elevation to maintain structural efficiency along the span; (2) in some cases the variation of the suction velocities along the chord may lead to a chordwise variation of the depth and spacing of the suction ducts, and certain duct depths may exceed those for structurally optimum corrugation thickness. With the relatively many ribs necessary in a wing with fuel, the use of extruded stiffeners with cover plates eliminates most of these objections and permits more flexibility in arrangement.

A BLC compression skin assembly for a wet wing is shown in Figure 6. The solid upper cover becomes the honeycomb type at the lower loading indices; the "I" sections, or equivalent stringer types, are extruded and machined (with controllable warpage because of their two axis symmetry); the inside face of the skin assembly is a minimum gauge aluminum honeycomb panel. In a BLC airfoil this panel partially functions as a lifting surface and as a fuel liner; it further functions to prevent rolling of the "I" at high stress levels which might wave the skin locally. This type of main box eliminates mechanical fasteners in the upper and lower surfaces of the integral fuel tanks and minimizes leaks into the ducts. All elements are bonded to provide, with the non-wrinkling structural members, smooth suction ducts and to minimize possible local depressions on the outer surface, as in the case of mechanical fasteners. As some prying action occurs, it is important that suitable taper be given the flange legs to decrease peel tendencies; a 1:3 taper ratio is satisfactory for transferring about 100 in-lbs. of moment per square inch of bonded flange surface; the moment is in a plane perpendicular to the bonded flange surface. With this arrangement, bending material and torsional material is kept primarily in the upper skin with a minimum in the lower skin; the neutral axis is for a large part of the span considerably above the geometric center of the open sandwich. All elements are non-buckling to yield. A group of columns 20 inches long and a 3 inch stringer pitch involving equivalent cross sections with riveted Z's and bonded I-stringers gave a favorable specific strength ratio of 1.15 for the cross section of Figure 6. The instability shape of the latter was undistorted in cross section and sinusoidal; some of the former failed in a twisting and explosive tearing of the Z-flange. It is noted that the increasing thickness ratio of the inner skin to outer skin in the outboard half of the wing is a fail-safe aspect of this double skin configuration.

In relation to the wing torsional stiffness, it may be pointed out that for the inboard third of the wing, 85 percent of the skin face material is in the outer face, and for the outboard two-thirds of the wing, it may vary from 85 to 65 percent. A series of torsional load applications for a straight rectangular box 100 inches long and with cross sectional dimensions shown, Figure 7, demonstrated that the "J" value is calculated as a three-cell box or as a single-cell system with the inner and outer skins assumed at the bending center of gravity of the skin system. This may be conservative as the tests were run with no direct attachment of stringers to either the loading devices or reacting column. A possible 5 percent reduction in "J" over a comparable skin stringer arrangement is estimated. It was further demonstrated that the skin system developed full rigidity regardless of the load applications being at inner and outer skins directly or at the inner skin

(C) BLC Wing Components (Continued)

only. It is of significance that this or equivalent systems function in this manner, as a BLC wing would have a minimum of ribs attached to the outer skin since the consequent interruption of the suction airflow in the ducts should be minimized. This, in effect, means that the intermediate ribs, attached to the inside honeycomb sandwich only, transfer airload torsion to the box. The box failed in the web of the stringers, at an applied shear of 2800 lb/in. on the inside surfaces (Reference 126).

In the rear part of the wing in the region of the rear pressure rise, considerably higher suction velocities are required to maintain full chord laminar flow, ( $-v_o/U_o = 5 \text{ to } 8 \times 10^{-4}$ ), as compared with the suction rates in the region of the main structural box. As a result, in order to avoid excessive pressure losses in the suction ducts, the full wing thickness has to be used for the air flow in this part of the wing. In order to minimize the duct losses in critical areas, it may become necessary to deflect the incoming suction air into the direction of the duct flow by means of turning vanes or turning nozzles. The suction air, after passing through the skin, would first be ducted in a spanwise direction through small auxiliary spanwise ducts, formed for example, by closed longitudinal stiffeners or by spanwise corrugations in the outer skin, into turning nozzles and into the main suction ducts. In this manner secondary flow pressure losses in the suction ducts are drastically reduced (References 127 and 128).

One version of the wing trailing edge design is a Warren truss type structure with continuous spanwise honeycomb webs forming smooth full depth duct walls (Figure 8). The eccentric web attachment facilitates assembly; the straight web face is thicker than its opposite. Stress coating showed that a compression web of this type carried its load through the thicker skin acting on an elastic medium. A 9- by 50-inch simple beam of "T" flanges and eccentric sandwich web failed at 90 percent of calculated with a deep buckle at the center; there were no local separations due to the offset of load. Similarly, a two-cell box beam with .25-inch-thick sculptured compression skins loaded in shear and bending failed in a full panel buckle of the eccentric sandwich web (.016-inch faces, .156 inch thick, 4.5 pound honeycomb) at 95 percent ultimate. The all sandwich trailing edge is non-wrinkling; a 24-inch chord deforms about .12 inch at the trailing edge at limit load or a nominal deflection at cruise. Another version of the non-buckling trailing edge consists of chordwise machined truss-like ribs and vertical spanwise sandwich webs, with the rib members streamlined to maintain small suction air duct losses.

With the suction ducts installed in the wing, one might superficially conclude that a laminar suction wing cannot carry as much fuel as a turbulent non-suction wing. However, since wing span and area of an optimized low drag suction airplane are considerably larger than for an optimized turbulent airplane, the wing volume remaining for fuel is generally considerably larger for the optimized low drag suction airplane, as compared with the corresponding turbulent airplane.

#### (D) Surface Limits

Surface irregularities cause velocity fluctuations in the laminar boundary layer leading to transitions. Allowable limits to roughness, steps, gaps and waviness have been established through wind tunnel models and in flight tests. Figures 9 and 10 show these allowable and current production standards. It is observed that high subsonic transports cruising at 30,000 feet and above fall within the surface tolerance limits with the exception of surface steps. This area requires special attention and the submerged splice is a possible solution to this problem. As the down step is more critical, design and manufacturing tolerances should accumulate as positive or up steps. The waviness allowables, in terms of a sinusoidal shape in the chordwise direction are shown in Figure 10. The requirements depicted here are for the one g cruise condition. The limits of contemporary products presently meet a fair proportion of these requirements.

Waviness and slot deformations were frequently checked in the course of axial load 4- by 20-inch specimen testing at one g and two g load levels and found to be within acceptable limits. In the aforementioned torsion box test, the 0.006-inch slots were checked along the span with feeler gauges for all loading conditions to over 3° of box twist; no measurable variation was obtained. The waviness was within 0.001-inch per inch. A leading edge segment 14 inches of cantilever by 2 feet wide, representative of a BLC 6 percent wing and weighing 4 lb/ft<sup>2</sup>, was tested under simulated air load. The maximum tip deformation was .05 inch at 1.25 g and the load induced waviness was .0005 in/in.

Akin to the surface irregularity problem is the surface corrosion problem. An initial effort to evaluate environmental effects was the exposure of 3- by 12-inch solid and honeycomb skin panels to an industrial climate and an ocean and a jungle site. Suction efficiencies subsequent to exposure were checked with and without steam cleaning of surfaces. Results are shown in Figure 11.

Successful anodic treatment of exposed edges and holes on bonded assemblies with no loss of bond strength has been gained. (References 129 and 130).

#### (E) Stress Concentration Factors

In common with most design efforts, we seek to encompass aspects of the safe-life and the fail-safe approach to fatigue problems. One trend of long range or endurance BLC operation which may relax somewhat the criteria of the first is suggested by Figure 12. For an assumed life a BLC long range aircraft type, with an efficient laminar wing and tail, and a turbulent fuselage, cruising at over 40,000 feet has a potentially more favorable cumulative damage history than equivalent turbulent aircraft by about 43 percent in the lower wing surface root area and about 55 percent in the midspan area. These estimates are based on an optimum aircraft usage involving 40 percent fewer ascents and descents, and cruising encounters with 5 to 10 ft/s gusts at one-fourth normal frequency.

Significant design questions are concerned with the concentration factors of holes, plenum chambers and slots. Of these discontinuities,

(E) Stress Concentration Factors (Continued)

the holes are influential in all directions and their small size precludes shaping for possible stress neutralization, or effective symmetrical local reinforcing. Some cycling gains were noted in minimum tests of pre-stressed hole rims. However, the depth of the pre-stressing effect involves areas around the hole which are in multi-axial stress fields where yield increases in one direction may be offset by decreases in another, according to the Bauschinger effect. Although 75ST has been used for BLC specimens, fabrication and tests, it is believed only representative of the aluminum spectrum; for example, 7178 or the more notch accommodating 2024 could be used. To the increasing evidence of reversed high stress levels, is added some evidence of a possible 35 percent gain in nominal fatigue strength over 75ST for sheet with holes such as are encountered in BLC skins (Reference 131). In a single instance of investigation of a row of .04-inch holes in a contour, this percentage was not borne out. However, the use of 2024 for lower main box skins is a design consideration.

The development of maximum tangential stresses in the elastic range of intermediate holes in typical BLC patterns is based on photoelastic results and summarized in Figure 13 (Reference 132). A simple superposition of the tangential stresses at the rim of the hole due to the applied multi-axial stresses results in critical planes at 90° and 135°, to the direction of applied tension or shear. Where the shear stress to spanwise tension stress ratio exceeds 2, the shear effect dominates; below 2, the tension effect dominates, with combined load  $K_T$ 's between 2.75 and 3.5.

The plenum chamber with its full depth radii has notch effects due to loadings in planes transverse to its axis. The effect of tension stress at the base of the fillet for a representative width to depth plenum in a solid skin is shown in Figure 14. For the heavy skins with little induced bending, the ratio  $\sigma_{\max}/\sigma_{\text{gross}} = 3.0$ ; for .1-inch-thick skins  $\sigma_{\max}/\sigma_{\text{gross}}$  is in the vicinity of 3.9. The problem of the thinner skins with increasing eccentricity is circumscribed by the use of the honeycomb sandwich. Results of chordwise tension-tension tests of the honeycomb sandwich type showed the significance of controlling flexibility in the notched sheet. On Figure 15 the dashed S-N curve is a run with the base of the plenum not bonded to the honeycomb and the honeycomb sandwich curve with the base bonded; the life increase is almost 10:1.

If the row of holes is assumed dominant, a  $K_{T_{\text{net}}}$  spanwise = 2.65 and chordwise = 2.40. Assuming  $K_f = 1 + \frac{K_T - 1}{1 + a/r^*}$  and  $a = .02$  inch, a material constant for 75ST sheet, then  $K_f$  at the fatigue limit = 1.82 and 1.70, respectively. The value from the S-N diagram of the spanwise and chordwise honeycomb sandwich at fatigue limit is approximately  $K_{f_{\text{NET}}} = 1.85$ , indicating the prime effect of the holes.

\*r = radius of hole, in.

(E) Stress Concentration Factors (Continued)

Similarly, the solid skin, spanwise, is  $K_{FNET} \approx 1.85$  but, chordwise, is  $K_{FNET} \approx 2.5$  where the plenum eccentricity dominates. (Figure 16.)

There are seemingly more favorable basic shapes for the plenum chamber itself than the one shown; for example, an arc of a circle, "U" type, or elliptical notches. In most of these the presence of the hole in the critical base area of the notch is an additive concentration factor. In the concept shown, the concentrations are adequately separated, at least on the generally verified basis of the very local deterioration of the maximum stress of steep stress gradients. As a result of these investigations, it is believed that with a judicious replacement of material removed from BLC skins, the design  $K_T$  and gross stress of comparable riveted airfoils may be used in the design approach.

It has been noted that wing span is a significant parameter in BLC airplane performance. A traditional method of obtaining additional span within the range of contemporary cantilever deformations is with external bracing. If either a straight or swept wing is braced at one-third of its semi-span with a jury strut system, a potential 15 percent increase in span results in a 12 to 15 percent increase in range (Reference 121). The brace system is composed of laminarized airfoil shapes and designed by reverse loads.



CHAPTER B. SKIN DUCTING SYSTEM CONFIGURSTIONS FOR LFC AIRCRAFT MAIN  
STRUCTURAL BOX

Robert N. Worth

(A) Notation

A	area, sq. inches
E <sub>s</sub>	Young's modulus for face material, psi
G <sub>c</sub>	shear modulus of core material, psi
D <sub>s</sub>	flexural stiffness of isotropic sandwich plate, in./lb
	$= \left( \frac{E_s t_s h^2}{2(1 - \mu_s^2)} \right)$
D <sub>Q</sub>	transverse shear stiffness of isotropic sandwich plate, lb/in.
N <sub>x</sub>	middle surface compressive force, lb/in.
b	stringer spacing, inches
c	core depth, inches
h	depth of sandwich plate measured between middle surfaces of faces, inches
t <sub>s</sub>	thickness of the core faces, inches
f <sub>all</sub>	allowable stress level in the faces, psi
f	Poisson's ratio for face material

## (B) Introduction

The basic objective of a wing skin system configuration for a BLC aircraft is two-fold. It must provide the strength required to support the binding and torsional loads in an efficient manner. It must also provide an efficient ducting system to allow the passage of the suction air from the wing surface to the compressor system.

Since the ducting system is extensive throughout the wing it must be combined with the skin system in an integral manner to provide for an efficient load carrying structure of minimum weight. A double skin configuration is an efficient structure compatible to both basic requirements. This configuration consists of a basic structural outer skin supported on multiple stringers. An inner skin below the stringers imparts stability to the stringer flanges and also provides a lower wall to complete the ducting passage. Air is drawn through a slotted surface skin, and then through plenum chambers and metering holes in the outer skin into the main ducting system. It then passes spanwise along the wing between the inner and outer skins to the compressor system. The entire skin-duct system is load-carrying. The weight penalty inherent in having the inner skin material closer to the neutral axis of the wing rather than at the mold-line is partially offset by the stability it imparts to the stringers.

A bonded skin system with extensive use of honeycomb sandwich material was chosen for several reasons. Of primary importance is the smooth outer surface obtained with a minimum of rivet and bolt heads protruding as a potential source of roughness. The leakage problem both from the external surface and from the integral fuel tank area into the ducting passages is kept to a minimum. In areas where the strength requirements are low, the use of honeycomb sandwich construction allows the use of thinner minimum gauges with a resulting weight saving while maintaining a wrinkle free surface. The use of a honeycomb sandwich construction where feasible allows a maximum variation in stringer spacing with little variation in wing weight enabling the designers to remain close to optimum configuration at all spanwise positions along the wing while remaining compatible with the ducting requirements.

## (C) Detail Design

Design weight charts have been compiled for the configuration shown in Figure 17. The stringers depth and spacing is dictated by the suction air ducting requirements. Since the air is introduced into the ducts from spanwise slots along element lines on the wing, the stringers must also lie along element lines. The spacing therefore increases in relationship to the wing taper ratio as the stringers run inboard from the tip. At various stations along the wing more stringers are added to retain a spacing compatible with strength and ducting requirements.

(c) Detail Design (Continued)

The outer skin in the areas where the loading index (lb/in. of wing chord) is less than 19,000 lb/in. is of honeycomb sandwich construction. While for loading indices over 7,000 lb/in. an optimum corrugated core construction shows up to an 11 percent weight saving over the honeycomb construction it is much more demanding of a specific stringer spacing to maintain this advantage. Since the honeycomb is exceedingly lenient toward variations in stringer spacing and is also easier to manufacture, this type of construction is used. In the inboard portion of the wing where the loading indices are over 19,000 lb/in. a solid outer skin is used.

The inner skin is of minimum gauge honeycomb construction in all cases, providing a stable panel of minimum structural material. This allows the majority of the structural material to be close to the mold-line of the wing for greater efficiency. Figure 18 shows the weight of the skin-system substructure versus the stringer spacing. It is noted that the weight of the inner skins, the slotted skin, and their adhesive systems, plus the adhesive system for the outer skin is constant at .0045 lb/sq. in. of surface area independent of the stringer spacing.

This is based on an interpretation of the work presented in Reference 24 giving two formulae (see Appendix A):

$$h = \frac{\frac{\pi^2}{2(1 - \mu_f^2)} \frac{E_s}{G_c} \frac{t_s^2}{b}}{\left( \frac{\pi^2}{1 - \mu_f^2} \frac{E_s}{f_{all}} \right)^{1/2} - \frac{\pi^2}{2(1 - \mu_f^2)} \frac{E_s}{G_c} \frac{t_s}{b}} \quad (1)$$

or

$$f_{all} = \frac{\frac{\pi^2}{1 - \mu_f^2} E_s}{\left[ \frac{b}{h} - \frac{\pi^2}{2(1 - \mu_f^2)} \frac{E_s}{G_c} \left( \frac{t_s^2}{bh} - \frac{t_s}{b} \right) \right]^2} \quad (2)$$

the radius of curvature which is neglected in these formulae is of relative unimportance for wings whose thickness ratio is less than 20 percent where stringer spacings are compatible with low drag BLC requirements.

For the range of skin thicknesses (up to  $t_f = .125$  inch) and stringer spacings (5.00 to 20.00 inches) of interest for LFC skin design, and if a minimum core weight of 4.5 lb/ft<sup>3</sup> is specified the formulae simplify to:

$$h = \frac{b}{\left( \frac{\pi^2}{1 - \mu_f^2} \frac{E_s}{f_{all}} \right)^{1/2}} \quad (3)$$

(C) Detail Design (Continued)

or

$$f_{all} = \frac{\pi^2}{1 - \mu_f^2} E_s \left( \frac{h}{b} \right)^2 \quad (4)$$

for a close approximation.

In the calculation and plots a design ultimate stress level of 65,000 psi was used so equation (3) becomes:

$$c = h - t_s = .024 b \quad (\text{depth of core}) \quad (5)$$

The depth and therefore the weight of the honeycomb core increases directly as the stringer spacing increases. However, the increase in inner and outer skin core weight as the stringer spacing varies from 10 to 20 inches amounts to only 0.16 lb/ft<sup>2</sup> of surface illustrating the leniency of the honeycomb structure toward the dropping out or addition of stringers without an abrupt change in core depth.

The stringer unit weight (lb/in.<sup>2</sup> of surface) decreases rapidly as the spacing increases towards 10 inches and then decreases more slowly with further increase in spacing. In this region the stringer unit weight decrease is approximately balanced by the increase in core weight resulting in a relatively constant skin substructure weight.

The total substructure unit weight of the honeycomb configuration is given for stringer depths of from 1.00 inch to 2.50 inches. For comparison the substructure weight of a corrugated core configuration is given for a 2.00 inch stringer depth (see Appendix B).

It is noted that where the loading indices get quite low the double skin construction required for the low drag BLC aircraft is relatively inefficient. The minimum gauge skins and stringers provide more area than is needed for the load applied. This situation occurs in the outboard 5 percent to 10 percent of the semi-span so the overall penalty is small. However, in this area the ducting requirements are small so that it may be possible to replace the inner skin and stringers with individual ducts if desirable. Figure 19 shows the load carrying capabilities of the skin substructure versus stringer spacing.

Figure 20 is a design weight chart for honeycomb sandwich construction of the skin duct configuration. Curves are shown of weight of skin surface versus skin loading index for stringer spacings of 5.00 to 20.00 inches. Cross plotted are the facing thicknesses required for loading indices at various stringer spacings. Varying the stringer height required for the ducting moves these cross plots along the stringer spacing curve reflecting the replacement of stringer area with skin area. Curves for the weight of an optimum corrugated core sandwich skin-duct system and a theoretical plate are plotted for comparison. The displacement of the honeycomb curves from

(C) Detail Design (Continued)

the theoretical plate reflects the weight of the non-structural items of core and adhesive. The difference in displacement of the corrugated core curve results from the use of a structural core in the outer skin.

In a design for an actual wing the taper ratio dictates the variation in stringer spacing along the span of a panel since in a low drag BLC wing the stringers should follow element lines. In general the loading index has a small slope in the inboard portion of the wing and drops off rapidly in the outboard third of the wing and is relatively compatible with the stringer spacing variation.

The use of the curves is shown in Figure 21. The loading index is approximated as a straight line variation over the length of the panel. The maximum stringer spacing ( $b_{max}$ ) compatible with the ducting requirements is determined at the inboard end of the panel. The resulting stringer spacing at the outboard end of the panel is matched to the loading index and the line between these points gives the facing thickness taper and the skin system weight at any point along the panel. The core thickness is a direct function of the stringer spacing. The loading index allowable along the panel will be the chosen straight line function between the two end points and can be compared directly to the actual loading index along the span to determine safety margins.

In some areas of the wing the maximum stringer spacing ( $b_{max}$ ) allowed due to the ducting requirements may result in a stringer spacing at the outboard end of the panel which is much too small. In this case stringers are dropped out along the span of the panel to increase the stringer spacing. Since it is desirable to eliminate sudden steps in the facing thickness and core thickness a maximum weight line is added to the design curves as shown in Figure 22. This line was constructed by doubling the number of stringers without changing the skin sandwich design. Its position is relatively constant whether the basic stringer spacing is 5, 10, 15, or 20 inches.

In using this chart the loading index is again approximated as a straight line variation over the length of the panel. The stringer spacing ( $b_{max}$ ) determined by the ducting requirements at the inboard end of the panel locates point B. Line A-A is located at the loading index where

$b = \frac{b_{max}}{2}$  and the intersection of this line with the maximum weight line

gives point C. Line B-C now gives the skin system weight for this portion of the panel. The use of a constant core depth determined by the maximum stringer spacing allows the deletion of every other stringer increasing  $b$  to  $b_{max}$  again. This locates point D and the process is repeated to the end of the panel.

(C) Detail Design (Continued)

The facing skin thickness is determined by the  $b_{\max}$  line giving a straight taper along the panel. The allowable loading index is determined from the actual stringer spacing and the facing thickness giving a stepped line along the panel for comparison to the actual loading index.

(D) Appendix A -- Extension of NACA TN 2601 for Flat Curvature

$$D_s = \frac{E_s}{2(1 - \mu_s^2)} t_s h^2 \quad r_b = \frac{D_s}{D_Q} \frac{\pi^2}{b^2} = \frac{\pi^2}{2(1 - \mu_s^2)} \frac{E_s}{G_c} \frac{t_s (h - t_s)}{b^2}$$

$$D_Q = G_c \frac{h^2}{h - t_s}$$

$$\frac{D_s}{D_Q} = \frac{1}{2(1 - \mu_s^2)} \frac{E_s}{G_c} t_s (h - t_s)$$

$$N_x = 2 f_{all} t_s = \frac{4 D_s \pi^2}{(1 + r_b)^2 b^2} = \frac{4 E_s \pi^2 t_s h^2}{2(1 - \mu_s^2) (1 + r_b)^2 b^2}$$

$$f_{all} = \frac{E_s \pi^2 h^2}{(1 - \mu_s^2) b^2 (1 + r_b)^2} = \frac{\pi^2}{1 - \mu_s^2} \frac{E_s}{b^2} \frac{h^2}{(1 + r_b)^2}$$

$$(1 + r_b)^2 = \frac{\pi^2}{1 - \mu_s^2} \frac{E_s}{f_{all}} \frac{h^2}{b^2}$$

$$\frac{b}{h} + r_b \frac{b}{h} + \sqrt{\frac{\pi^2}{(1 - \mu_s^2) f_{all}} E_s}$$

$$b + \frac{\pi^2}{2(1 - \mu_s^2)} \frac{E_s}{G_c} \frac{t_s (h - t_s)}{b} = \sqrt{\frac{\pi^2}{(1 - \mu_s^2) f_{all}} E_s} h$$

(D) Appendix A -- Extension of NACA TN 2601 for Flat Curvatures  
(Continued)

Solving for this equation gives:

$$b = \frac{\pi^2 E_s t_s^2}{2(1 - \mu_s^2) G_c}$$

$$h = \frac{\pi^2 E_s}{(1 - \mu_s^2) f_{all}} - \frac{\pi^2 E_s t_s}{2(1 - \mu_s^2) G_c b}$$

(E) Appendix B -- Design Weight Charts BLC Skin Configuration

The stringer depth is determined by the suction air flow ducting area requirements and a value of 2.00 was chosen as a design criteria. The I-stringers flanges are designed for bonding to the inner and outer skins.

Stringer Configuration

$$A_{CAP} = .098 \text{ sq. in.}$$

$$A_{WEB} = .162 \text{ sq. in.}$$

$$A_{ST} = .260 \text{ sq. in.}$$

$$b/t = 20$$

$$f_{all} = 65,000 \text{ psi}$$

$$W_{ST} = .026 \text{ lb/in.} = \frac{.026}{b} \text{ lb/sq. in.}$$

$$h = 1.0; 1.5; 2.5$$

$$= .130; .183; .363$$

$$\text{Including bond } W_{ST} = \frac{.0265}{b} \text{ lb/sq. in. surf.}$$

Inner Skin: Same for all configuration designs

$$.008 \text{ skins. } W_{SK1} = .0016 \text{ lb/sq. in.}$$

$$3.1 \text{ lb/cu. ft. core } C = .029 \text{ b } W_{core} = .000,05 \text{ b lb/sq. in. surf.}$$

$$\text{Adhesive } W_t = .001 \text{ lb/sq. in. surf.}$$

$$W_{T1} = .0026 + .000,05 \text{ b lb/sq. in. surf.}$$

(E) Appendix B -- Design Weight Charts BLC Skin Configuration (Continued)

Outer Skin - Slotted:

$$.010 \text{ Skin } W = .001 \text{ lb/sq. in.}$$

$$\text{Adhesive } W = .00035 \text{ lb/sq. in.}$$

$$W_T = .00135 \text{ lb/sq. in.}$$

Upper Skin -

$$Z t_s = \frac{P_{sk}}{65,000}$$

$$\text{Core } \sim 4.5 \text{ lb/cu. ft. } W = .0026 C \text{ lb/sq. in.}$$

$$C = .024 b$$

$$W_C = .000,063 b \text{ lb/sq. in. surf.}$$

$$\text{Adhesive } W = .001 \text{ lb/sq. in.}$$

$$W_{SUB} = \frac{.0265}{b} + .00495 + .000,113 b \text{ lb/sq. in. surf.}$$



## CHAPTER C. EFFECT OF WEATHERING ON TYPICAL BONDED BOUNDARY LAYER CONTROL STRUCTURE

R. N. Worth

### (A) Acknowledgements

The bonding and weathering of all the specimens and the testing of the strength specimens were done by W. L. Hill of the Materials Research Laboratory. The flow rate measurements were conducted by K. H. Rogers of the Boundary Layer Research group.

### (B) Summary

The weathering tests on boundary layer control panels conducted during this program indicated that suction flow rates can be held to within 2.5 percent of the design values with present methods for washing and steam cleaning of aircraft. Results from salt spray exposure tests indicated the desirability of providing protection for the slots and holes by either an anodizing or an Iriditing process. Ground operation or storage of BLC aircraft without special protection seems feasible. Results of the ninety-day industrial exposure and the sixty-day tropical exposure tests indicate that vacuum cleaning from the slot side only can restore the flow rate to within 5 percent of the original value while steam cleaning at 100 psi from the slot side only can restore the flow rate to within 1.5 percent of the original values.

The results of the metal to metal strength tests to determine adhesive strength characteristics showed no deterioration of the bond during the weathering exposures. The results of the honeycomb peel and tensile tests indicated that the adhesive was attacked somewhat by humidity weathering conditions. However, all strength values were adequate for future LFC work.

### (C) Introduction

The object of these tests was:

(1) to determine the effects of various climatic conditions on typical boundary layer control skin configurations with respect to the operational characteristics and maintenance requirements of the suction system, and

(2) to evaluate the strength characteristics of the adhesives, used to bond the test panels, after exposure to the various climatic conditions of the test program.

One of the primary questions concerning the operational capabilities of any boundary layer control equipped aircraft is whether the suction system can be kept within the limits of efficient operation while the aircraft is operated throughout the normal range of climatic environments. The most vulnerable portions of the suction system, with regard to weathering, are the slots and holes provided through the skin for control of the boundary layer.

(C) Introduction (Continued)

The panels tested in this program represent typical boundary layer control skin configurations. Various combinations of materials and surface treatments were subjected to several environmental conditions in the field, as well as to simulated conditions in the laboratory, to provide a background for making recommendations on design, operation, and maintenance of LFC aircraft.

(D) Materials and Equipment

(1) Materials

(a) Metal Details

7075-T6 Alclad sheet aluminum  
2024-T4 Alclad sheet aluminum  
6061-T6 Nonclad sheet aluminum

(b) Honeycomb Details

1/8-inch cell 3003-.001 non-perforated core  
1/4-inch cell 3003-.003 non-perforated core

(c) Adhesives

AF-13 Minnesota Mining and Manufacturing Company  
AF-203 Minnesota Mining and Manufacturing Company  
L-1372 Specialty Resin Company

(2) Test Equipment

- (a) Climbing Drum Peel Jig, per WADC TR-56-386
- (b) Instron Physical Test Machine
- (c) Humidity Chamber
- (d) Salt Spray Chamber

(E) Procedure

(1) Preparation of Specimens

The following two adhesives were used in this program:

- (a) AF-13 for metal to metal bonds;
- (b) AF-203 for metal to honeycomb bonds.

All metal to metal bonds and metal to honeycomb bonds were cured in an autoclave under 32 psi air pressure plus 3 psi vacuum. The temperature was recorded by thermocouples attached to the parts during bonding. The following cure cycles were used.

(E) Procedure (Continued)

(a) Metal to Metal Bonds

- i. The temperature was raised from ambient to 320°F in a minimum time of 45 minutes.
- ii. The temperature was held at 325 ±5°F for a minimum time of 60 minutes.
- iii. The parts were cooled to 150°F before the pressure was removed.

(b) Honeycomb Bonds

- i. The temperature was raised from ambient to 330°F in a minimum time of 65 minutes.
- ii. The temperature was held at 335 ±5°F for a minimum time of 60 minutes.
- iii. The parts were cooled to 150°F before the pressure was removed.

Metal details which were anodized were processed in accordance with Process Bulletin F.P.-3G, using the Type I chromic acid treatment. All anodized metal details were vapor degreased prior to being primed.

The details for metal to metal bonding of Norair Drawing 4209646 panels (Figure 26) were made of 7075-T6 alclad, 2024-T4 alclad and 6061-T6 nonclad aluminum sheet and were surface-treated as follows prior to the application of a thin coat of E.C. 1459 primer to the faying surface. The primed surfaces were air dried for 60 minutes and oven dried for 30 minutes at 160°F.

- (a) All the 6061 skins were anodized.
- (b) The 0.188-inch thick 7075 skins were anodized after the plenum chambers were milled and the holes drilled.
- (c) All the 2024 and the 7075 skins were vapor degreased, etched in a dichromate solution for 10 minutes, and oven dried at 150°F.

The details for metal to metal single lap shear specimens and metal to metal peel specimens were made of the three types of aluminum stock listed in Table II and were surface-treated as follows prior to the application of a thin coat of E.C. 1459 primer (see paragraph above).

- (a) All the 6061 skins were anodized.

(E) Procedure (Continued)

- (b) All of the (a) skins in Table III were anodized.
- (c) All of the (b) skins in Table III with the exception of the 6061 skins, were treated as in paragraph (c) above.

The metal details of Drawing 4209647 (Figure 26) were 7075-T6, 2024-T4, and 6061-T6 skins and 1/8-inch cell 3003-.001 N.P. core. The metal details were surface-treated as follows prior to bonding.

- (a) All 6061 skins were anodized prior to the application of a thin coat of E.C. 1459 primer.
- (b) The lower skin was vapor degreased and etched as outlined above and then coated with E.C. 1682 primer. The primer was air dried for 60 minutes and then oven cured at 200°F for 30 minutes.
- (c) The 2024 and 7075 chem-milled sheets containing the plenum chambers were anodized prior to the application of E.C. 1459 primer to the surface to be bonded with AF-13 and E.C. 1682 primer to the surface to be bonded with AF-203.
- (d) The honeycomb core was vapor degreased prior to bonding.

The metal details for the honeycomb sandwich specimens listed in Table II are 7075-T6 alclad aluminum skins and 1/4-inch cell 3003-.002 N.P. honeycomb core. The metal details were surface-treated as follows prior to the application of a thin coat of E.C. 1682 to the faying surface.

- (a) One skin was anodized (this skin was peeled in the honeycomb peel specimens).
- (b) One skin was vapor degreased and etched as outlined above.
- (c) The honeycomb core was vapor degreased prior to bonding.

The types and quantities of specimens are listed in Table II .

Two types of test panels were fabricated as shown in Table II ,  
(Section I).

- (a) Group "A" panels were of heavy skin configuration typical of the skin structure in the torque box area of a wing. These panels were fabricated by bonding a thin cover skin (A<sub>1</sub> 7075 alclad; A<sub>2</sub> 2024 alclad; A<sub>3</sub> 6061 nonclad, anodized) to an anodized 0.188-inch thick 7075 alclad aluminum skin with plenum chambers

(E) Procedure (Continued)

and holes. AF-13 adhesive was used. The cover skins were then slotted and a thin coat of Iridite was brushed onto the cover skin and slot edges.

- (b) Group "B" panels were of honeycomb sandwich configuration typical of the skin structure in the leading edge and trailing edge areas of a wing. A two-stage bonding operation was used in fabricating these panels. A piece of 1/8-inch cell 3003-.001 N.P. core was first bonded between a primed skin and a primed, anodized chem-milled and drilled skin with plenum chambers using AF-203 adhesive. The holes were then redrilled completely through the panels. The honeycomb panel skin materials were 7075 (B<sub>1</sub>) and 2024 (B<sub>2</sub>) aluminum skins. A 6061 anodized cover skin was then bonded to the chem-milled skin with AF-13 adhesive. The cover skin was then slotted and a thin coat of Iridite was brushed onto the cover skin and slot edges.

The metal to metal single lap shear specimens (Table II , Section III) were fabricated from two pieces of 0.064- by 6.0- by 5.0-inch aluminum with a 1/2-inch bonded overlap using AF-13 adhesive. After exposure to the various conditioning procedures (described below), each panel was cut into five 1.0- by 9.5-inch specimens.

The honeycomb peel specimens (Table II , Section IV) were fabricated by bonding a 0.625- by 12.0- by 15.0-inch core of nonperforated honeycomb between one 0.020- by 12.0- by 15.0-inch primed anodized skin and one 0.020- by 12.0- by 15.0-inch primed skin using AF-203 adhesive. Each panel was cut into four peel test specimens 3.0- by 12.0-inches, with the core ribbon direction parallel to the 12.0-inch dimension.

The honeycomb tensile specimens (Table II , Section IV) were fabricated by cutting 2.0- by 2.0-inch squares from the honeycomb sandwich panels fabricated as described in the paragraph above, and bonding each square between two 1.0- by 2.0- by 2.0-inch 7075 blocks with a room temperature adhesive (L-1372).

The metal to metal peel specimens (Table II , Section II) were fabricated by bonding a strip of 0.020- by 1.0- by 12.0-inch aluminum (skin b) to a strip of 0.064- by 1.5- by 12.0-inch aluminum (skin a) using AF-13 adhesive.

(2) Conditioning of Specimens

The boundary layer control test panels were divided into five groups of two each and were exposed to the following weathering conditions.

- (a) Group 1 - Salt Spray Chamber at 95°F with a 5 percent salt spray solution for a period of twenty days, and then an additional twenty-day period. Panels were removed once every twenty-four hours and rinsed off with tap water.

(E) Procedure (Continued)

- (b) Group 2 - Humidity Chamber at 120°F and 100 percent relative humidity for a period of twenty days, and then an additional twenty-day period. Panels were removed once every twenty-four hours and rinsed off with tap water.
- (c) Group 3 - Roof of the Test Laboratory for a period of ninety days. No cleaning was attempted during this period. Weather variations during the test included a temperature range from 50°F to 90°F, light to heavy smog attacks, a trace of rain, dust, and winds up to 40 mph.
- (d) Group 4 - Panama Canal Zone, Naval Weathering Station, Ocean Site, for a period of sixty days with a temperature and relative humidity range and rainfall average similar to the jungle site. No cleaning was attempted during this test.
- (e) Group 5 - Panama Canal Zone, Naval Weathering Station, Jungle Site, for a period of sixty days with a temperature range of 72 to 87°F, relative humidity range of 56 to 100 percent, an average rainfall of 18.6 inches per month, and an average wind velocity of 5.6 mph. No cleaning was attempted during this test.

The strength test specimens were divided equally into six groups (quantities tabulated in Table II) which were exposed to the following weathering conditions.

- (a) Group 1 - Salt Spray Chamber at 95°F with a 5 percent salt spray for a period of twenty days.
- (b) Group 2 - Humidity Chamber at 120°F and 100 percent relative humidity for a period of twenty days.
- (c) Group 3 - Roof of Test Laboratory for a period of ninety days. Weather same as group 3 above.
- (d) Group 4 - Panama Canal Zone, Naval Weathering Station, Ocean Site, for a period of sixty days. Weather same as group 4 above.
- (e) Group 5 - Panama Canal Zone, Naval Weathering Station, Jungle Site, for a sixty-day period. Weather same as group 5 above.
- (f) Group 6 - Control specimens (no weathering conditions).

(E) Procedure (Continued)

(3) Test Procedures

The test setup used in determining the effect of the various climatic conditions on the suction characteristics of the boundary layer control test panels is shown in Figure 27. A suction source was connected through a nozzle to a sealed chamber containing the test panel. The flow rate was adjusted to obtain a pressure drop of three inches of water through the slots and holes of the test panel for all tests. The pressure drop was measured between the chamber and the nozzle and converted to flow rate by the formula  $Q = 0.0540 \times \sqrt{\Delta p}$ .

Flow rate measurements were taken before any exposure to provide control values. After exposure to the various climatic conditions, the flow rate was determined both before and after cleaning by steam at 100 psi from the slotted side only and the running of shim stock along the slots. The results in terms of percent reduction of flow rate with relation to the control values are tabulated in Table I.

The peel tests were conducted at ambient temperature by means of the climbing drum peel jig mounted in the Instron Physical Test machine with a head travel of five inches per minute. The torque, in pound-inches, necessary to peel the face from the specimen was autographically recorded.

The climbing drum jig was calibrated by peeling unbonded aluminum strips of the same type and thickness as the faces of the bonded specimens.

The torque, in pound-inches, necessary to peel the adhesive was calculated by subtracting the average calibration value from the average test value. Such factors as initial load on the test machine, torque necessary to overcome the weight of the drum, and torque necessary to overcome the resistance of the skin were thus eliminated. The results are tabulated in Table III and Table IV.

The honeycomb tensile specimens were tested to destruction at ambient temperature in the Instron Physical Test machine with a head travel of 0.030 to 0.035 inch per minute. The bonded area was then measured and the failing stress was calculated in psi. The results are tabulated in Table IV.

The metal to metal single lap shear test specimens were tested to destruction at ambient temperature in the Instron Physical Test machine with a head travel of 0.030 to 0.035 inch per minute. The bonded area was then measured and the failing stress calculated in psi. The results are tabulated in Table III.

(F) Results and Discussion

The results of the suction tests on the boundary layer control test panels are tabulated in Table I.

(F) Results and Discussion

(1) Humidity Chamber Exposure Results

The solid skin panels exposed in the humidity chamber for forty days showed no corrosion appearing on the surfaces or in the slots and holes. The maximum reduction in flow rate was 3.5 percent on one panel with an average reduction of 1.5 percent without any cleaning. These panels then were steam cleaned at 15 psi, instead of 100 psi, and the flow rate reduction was 0.5 percent average with the maximum reduction of 1.0 percent.

The honeycomb panels exposed in the humidity chamber for forty days showed no corrosion of the surface or the slots and only slight corrosion of the holes. The maximum reduction of flow rate was 3.7 percent, occurring in the 2024 sandwich panels that exhibited corrosion in the holes. The average flow rate reduction was 1 percent before steam cleaning. After cleaning the flow rate was increased by 1 percent average. This increase over the control valve is attributable to the steam cleaning operation removing some debris left from drilling the holes after the bonding operation.

(2) Salt Spray Chamber Results

The exposure of the solid skin panels in the salt spray chamber for twenty days produced no evidence of corrosion on the surface or in the slots or holes. The flow rate reduction was 1 percent maximum. An additional twenty-day exposure resulted in slight corrosion in the slots of the 2024 cover skins only. The maximum reduction in flow rate was 5.4 percent with an average 2.7 percent reduction. After steam cleaning at 100 psi, the maximum reduction in flow rate was 1.6 percent with a 1 percent average reduction.

The honeycomb panels exposed for a forty-day period in the salt spray chamber exhibited no evidence of corrosion on the surface. However, the slots of the 7075 panels were slightly corroded, while the holes showed extensive corrosion. The holes in the 2024 panels were more extensively corroded. Microscopic inspection showed a white crystalline deposit blocking the holes and, to a lesser extent, the slots. This aluminum hydroxide deposit was probably caused by galvanic action between the basic metal and its cladding material when the edges were exposed by the drilling operation. Shim stock was run along the slots between the first and second twenty-day exposures without re-Iriditing the slots. This removed some of the Iridite coating in places along the slot, allowing corrosion to develop in the slot during the second twenty-day exposure.

Flow rate measurements were taken after twenty days' exposure in the salt spray chamber. The 7075 sandwich panels showed a reduction in flow rate of 9 percent maximum while the 2024 panels exhibited a reduction of 45 percent. Running shim stock along the slots increased the flow rate to within 4 percent of the control measurements on the 7075 panels but to within only 21 percent on the 2024 panels. The second twenty-day exposure resulted in a reduction in flow rate of 20 percent for the 7075 panels and a 56 percent reduction for the 2024 panels. Steam cleaning at 100 psi and running shim stock along the slots resulted in an increase in flow rate to within 5.5 percent of the control values for the 7075 panels and increased the 2024 panels to within 25 percent of the control values.



(F) Results and Discussion

(3) Los Angeles Climate -- Roof of Test Laboratory and Results

The panels on the roof were mounted on a horizontal rack so that condensation remained on the surface. No attempt was made to clean the panels during the ninety-day period of exposure. Upon removal, the 7075 panels showed extensive corrosion on the clad, Iridited cover skin. The 2024 clad, Iridited cover skins were slightly corroded, while no corrosion appeared on the 6061 anodized skins. The slots of all the panels were clogged with sand particles, though no corrosion was found on the edges and the holes were relatively clean of sand and corrosion.

The solid skin panels with 6061 cover skins had more sand clogging the slots than the other panels and showed a flow rate reduction of 59 percent before cleaning. The flow rate reduction of the other panels was 17.4 percent maximum. All of these panels were steam cleaned at 100 psi. This increased the flow rate to within 0.7 percent of the control values with a maximum reduction of 2.5 percent. Running shim stock along the slots further increased the flow rate to within 0.3 percent of the control value.

The measurements taken on the honeycomb panels showed a 30 percent maximum reduction in flow rate before cleaning. Steam cleaning at 100 psi increased the flow rate to within 2.5 percent of the control values and running skim stock along the slots brought the flow rate to within 1.5 percent of the control values.

(4) Panama Jungle Site Results

The panels at the Jungle Site were mounted on a horizontal rack so that condensation and debris remained on the surfaces. No attempt was made to clean the panels during the sixty-day exposure. Upon removal, there was no evidence of corrosion on the surface or in the slots of any of the panels. The holes of the honeycomb panels showed very slight corrosion on both the 7075 and the 2024 panels.

On the solid skin panels there was virtually no difference in the results for the different materials. Before cleaning there was a 10 percent reduction in flow rate. These panels were first cleaned with a brush and a standard model household vacuum cleaner, used on the slotted side only. This operation brought the flow rate up to within 2.5 percent of the control values. Steam cleaning at 100 psi brought the flow rate back to the original value. Running shim stock along the slots had no appreciable effect on the flow rate.

The 7075 honeycomb panels showed a flow rate reduction of 10 percent while the 2024 honeycomb panels showed a 13.5 percent reduction from the control values. Vacuum cleaning brought the flow rate to within 3.5 percent of the control values for the 7075 panels and 4.5 percent for the 2024 panels. Steam cleaning brought the flow rate back to the original value for the 7075 panels and to within 1 percent for the 2024 panels. Running shim stock through the slots increased the flow rate on one panel 2 percent but had no appreciable effect on the other panels.

## (F) Results and Discussion

### (5) Panama Ocean Test Results

The panels at the Ocean Site were mounted on a horizontal rack so that condensation and debris remained on the surface. No cleaning was attempted during the sixty-day exposure. Upon removal there was no evidence of corrosion on the surface or in the slots of any of the panels. The holes of the honeycomb panels showed very slight corrosion on both the 7075 and the 2024 panels with the 7075 panels being somewhat better than the 2024 panels.

Exposure of the solid skin panels resulted in a reduction in flow rate of 15 percent for the 7075 panels, of 10 percent for the 7075-2024 panels, and of 12 percent for the 7075-6061 panels. Vacuum cleaning brought the flow rate to within 7 percent of the control values for all panels while steam cleaning brought the flow rate to within 1 percent of the control values for all the panels. Running shim stock along the slots had no appreciable effect on the flow rate after steam cleaning except in one panel which showed an increase of 4 percent.

The sixty-day exposure of the honeycomb panels at the ocean site resulted in a 14 percent reduction in flow rate for the 2024 panels and a 7 percent reduction for the 7075 panels. Vacuum cleaning with a brush on a standard household vacuum cleaner brought the flow rate up to within 2.5 percent of the control values for all panels. Steam cleaning at 100 psi further increased the flow rate to above the control values while the running of shim stock through the slots did not effect the flow rate appreciably.

### (6) Adhesive Strength Test Results

Results of the physical test data for the metal to metal bonds are contained in Table III. The results derived from the data are indicated below. Visual inspection of the bonded areas after the specimens had been destructively tested indicated a cohesive type of bond failure.

Primed chromic acid anodized surfaces were satisfactory for bonding with AF-13 adhesive. The AF-13 bond in the metal to metal bonded specimens was relatively unaffected by the five different environmental conditions (discussed previously). All of the different aluminum alloys provided satisfactory surfaces for bonding with the AF-13 adhesive.

Of the metal to metal single lap shear specimens the wide range of lap shear values was probably due to warpage in the aluminum panels that were used in fabricating the shear specimens. To achieve maximum glueline strength with AF-13 adhesive, the cured adhesive glueline should be approximately 1.5 mils. As the bonded glueline increases, the strength characteristics of the adhesive decreases. Therefore, a small warpage in the aluminum panels will cause areas of thicker gluelines and thus a reduction of bond strength.

Since all of the metal to metal peel specimens were bonded as described previously, a comparison can be drawn between the bond strength of the four metal combinations:

(F) Results and Discussion

<u>Metal Combination</u>	<u>Aluminum Details</u>	
	<u>.020 Skin</u>	<u>.064 Skin</u>
A	7075 alclad	7075 alclad anodized
B	2024 alclad	7075 alclad anodized
C	6061 nonclad anodized	7075 alclad anodized
D	6061 nonclad anodized	2024 alclad anodized

The physical test data in Table III indicate that metal combination D will probably provide the best peel strength, that metal combinations B and C are equivalent in peel strength but lower than D, and that metal combination A has the poorest peel strength of the four combinations. However, all bond failures were cohesive and the lowest strength results (combination A) were above required peel strengths.

Results of the physical test data for honeycomb core adhesive bond AF-203 are contained in Table IV. The results derived from the data are indicated below. Visual inspection of the tested specimens indicated cohesive failure on the honeycomb side of the bond. All the values for honeycomb tensile and peel specimens are above required values for BLC work.

Primed chromic acid anodized 7075 surfaces were satisfactory for bonding with AF-203 adhesive.

While the AF-203 bonds were somewhat affected by certain of the five environmental conditions (described previously), the strength values were all above the requirements for BLC work. The only changes in strength values were as follows.

- (a) The honeycomb peel result after humidity exposure was 25 percent lower than the control values.
- (b) The honeycomb peel results of the Panama Canal Zone exposure (Jungle and Ocean Sites) were 15 percent higher than the control values. These results cannot be explained at this time.
- (c) The honeycomb tensile results after exposure to the Ocean and Jungle Sites at Panama and the roof of the test laboratory were 10 percent lower than the control values.

Although the results were satisfactory with AF-203, industry investigations have indicated that AF-203 is only suitable for a two- or three-stage bonding operation when full pressure is applied at all times.

## (F) Results and Discussion

Investigations are currently being conducted on three new types of non-perforated core adhesives which are more promising for multistage bonding operations. These are: (1) modified AF-203, Minnesota Mining and Manufacturing Company; (2) FM-61, Bloomingdale Rubber and Asbestos Company; and (3) Metlbond 406, Narmco Resins and Coating Company.

The two commonly used methods of anodizing aluminum alloys are the sulfuric acid and the chromic acid methods. Military Specification MIL-A-8625A prohibits the chromic acid method for anodizing aluminum containing more than 7 percent alloying metals and more than 5 percent copper alloy without obtaining a deviation from the contracting agency. Due to the availability of the chromic acid anodizing facilities at Northrop Corporation, Norair Division all the anodized aluminum details were chromic acid anodized, as is presently being done on details for the Boeing 707. Specific approval for deviations from MIL-A-8625A will be required if the chromic acid method of anodizing is utilized for high aluminum alloys used in the design of a BLC aircraft.

## (G) Conclusions

The flow rate measurements on all BLC panels, except the honeycomb panels in the salt spray chamber, showed reductions of less than 2.5 percent from the control values after steam cleaning. The honeycomb panels in the salt spray chamber showed considerable corrosion in the holes and the flow rate reduction was as much as 25 percent for the 2024 panels, but only 5 percent for the 7075 panels, after cleaning. From the solid skin panel tests it would seem that anodizing the holes and brush-Iriditing the slots gives adequate protection against corrosion. However, running shim stock along the slots should be accompanied by the reapplication of the Iridite coating. The holes in the honeycomb panels were not protected in any way, and while the salt spray test was the only one producing extensive corrosion, it is deemed necessary to devise a method of Iriditing the holes drilled after bonding.

From the tests run on the weathered panels it would seem that the operation or storage of BLC aircraft for periods up to ninety days would require no special covering or protection for the slots and holes. Periodic vacuum cleaning looks promising as a method for the removal of any debris that may settle in the slots, while steam cleaning at 100 psi from the slot side seems adequate for maintaining an efficient ducting system. Running shim stock through the slots does not seem to be necessary, at least during a three-month period, since in only two cases was the flow rate affected more than 1 percent by this action.

The results of the metal to metal strength tests show no deterioration of the bond during the weathering exposures. The results of the honeycomb peel and tensile tests indicate that the adhesive bond is attacked somewhat by humidity weathering exposures, but the strength values are still adequate for BLC work. Both AF-13 and AF-203 adhesives will be used for future boundary layer work pending further investigation of other adhesives (discussed above).

LIST OF TABLES FOR SECTION III

<u>Table No.</u>	<u>Table Title</u>	<u>Page</u>
I	FLOW RATE MEASUREMENTS.....	822
II	TEST SPECIMENS.....	825
III	PHYSICAL PROPERTIES OF AF-12 BONDED SPECIMENS.....	826
IV	PHYSICAL PROPERTIES OF AF-203 BONDED PANEL.....	828

TABLE 1

## FLOW RATE MEASUREMENTS

Solid Skin, 4209646		Alloy		75 - 75		75 - 24		75 - 61	
Q = Flow Rate in cu. ft./sec		Coupon No.		47		48		43	
<u>Humidity Chamber</u>		Q Control		.0656		.0687		.0664	
% Change in Q		20-Day Exposure		-1.0%		-1.1%		-1.7%	
		40-Day Exposure		-0.6%		-1.0%		-3.5%	
		Cleaned (2)		-0.6%		0%		-1.0%	
<u>5% Salt Spray Chamber</u>		Coupon No.		49		50		45	
Q Control		.0655		.0676		.0668		.0614	
% Change in Q		20-Day Exposure		-1.0%		+ 0.8%		-0.4%	
		40-Day Exposure		-4.4%		-1.7%		-5.4%	
		Cleaned (4)		-1.6%		+ 1.5%		-1.4%	
<u>Los Angeles Climate</u>		Coupon No.		26		28		29	
Q Control		.0700		.0698		.0666		.0683	
% Change in Q		90-Day Exposure		-10.7%		-9.0%		-57.3%	
		Cleaned (3)		0%		0%		-0.4%	
		Cleaned (4)		0%		0%		0%	
<u>Panama Jungle Site</u>		Coupon No.		13		14		10	
Q Control		.0700		.0655		.0674		.0649	
% Change in Q		60-Day Exposure		-7.5%		-11.5%		-12.8%	
		Cleaned (5)		-2.5%		-1.5%		-3.5%	
		Cleaned (3)		0%		+ 0.5%		-1.5%	
		Cleaned (4)		0%		+ 0.5%		-1.0%	
<u>Panama Ocean Site</u>		Coupon No.		15		16		18	
Q Control		.0666		.0661		.0623		.0635	
% Change in Q		60-Day Exposure		-16.0%		-14.5%		-10.0%	
		Cleaned (5)		-9.2%		-7.5%		-4.5%	
		Cleaned (3)		-1.8%		0%		-0.6%	
		Cleaned (4)		-2.0%		-1.8%		-0.5%	

TABLE I (Continued)

Honeycomb Skins, 4209647, 6061-T6 Cover Skins		Alloy		75 - 61		24 - 61	
Q = Flow Rate in cu. ft/sec							
<u>Humidity Chamber</u>	Coupon No.	34	35	31	32		
% Change in Q	Q Control	.0580	.0611	.0619	.0604		
	20-Day Exposure	-3.5%	-1.1%	-3.0%	-2.1%		
	40-Day Exposure	0%	-1.1%	-1.5%	-3.7%		
	Cleaned (2)	+ 2.0%	+ 1.5%	+ 2.0%	-0.6%		
<u>5% Salt Spray Chamber</u>	Coupon No.	36	37	33	38		
% Change in Q	Q Control	.0594	.0605	.0604	.0581		
	20-Day Exposure	-9.0%	0%	-44.9%	-25.1%		
	Cleaned (1)	-4.0%	+ 1.0%	-21.2%	-16.5%		
	40-Day Exposure	-13.2%	-20.2%	-56.2%	-50.0%		
	Cleaned (4)	-5.4%	0%	-25.5%	-15.0%		
<u>Los Angeles Climate</u>	Coupon No.	23	24	21	22		
% Change in Q	Q Control	.0605	.0611	.0641	.0639		
	90-Day Exposure	-27.0%	-20.4%	-19.1%	-29.5%		
	Cleaned (3)	- -	-0.4%	-2.5%	+ 1.0%		
	Cleaned (4)	+ 3.0%	+ 2.0%	-0.8%	+ 1.8%		
<u>Panama Jungle Site</u>	Coupon No.	1	2	3	4		
% Change in Q	Q Control	.0605	.0605	.0613	.0584		
	60-Day Exposure	-8.5%	-12.2%	-15.5%	-11.8%		
	Cleaned (5)	-2.5%	-4.2%	-3.6%	-5.6%		
	Cleaned (3)	+ 1.0%	+ 0.5%	+ 0.5%	-1.5%		
	Cleaned (4)	+ 3.0%	+ 1.0%	0%	-0.5%		
<u>Panama Ocean Site</u>	Coupon No.	7	8	5	6		
% Change in Q	Q Control	.0608	.0616	.0599	.0627		
	60-Day Exposure	-6.3%	-8.2%	-11.5%	-17.3%		
	Cleaned (5)	-2.5%	-1.2%	-1.0%	-4.8%		
	Cleaned (3)	+ 4.0%	- -	+ 3.0%	+ 2.0%		
	Cleaned (4)	+ 4.0%	- -	+ 3.0%	+ 2.0%		

TABLE 1 (Continued)

NOTES:

CLEANING:

1. Cleaned by running shim stock along slots.
2. (1) plus 15 psi steam cleaning.
3. 100 psi steam cleaning only.
4. (1) plus 100 psi steam cleaning
5. Cleaned with a standard model vacuum cleaner from slot side only.



TABLE AI

TEST SPECIMENS

		<u>No. of Specimens Fabricated</u>	<u>No. of Specimens in a Typical Group</u>
I.	<u>Boundary Layer Test Panels</u>		
	A. 4209646 Solid Skin Configuration		
	A <sub>1</sub> -1	10	2
	A <sub>2</sub> -3	10	2
	A <sub>3</sub> -5	10	2
	B. 4209647 Honeycomb Skin Configuration		
	B <sub>1</sub> -1	10	2
	B <sub>2</sub> -5	10	2
II.	<u>Metal to Metal Peel</u>		
	<u>Skin (a) (Table II)</u> <u>Skin (b) (Table III)</u>		
	7075-T6                      7075-T6	30	5
	7075-T6                      2024-T4	30	5
	7075-T6                      6061-T6	30	5
	2024-T4                      6061-T6	30	5
III.	<u>Metal to Metal Single Lap Shear Panels</u> <sup>*</sup>		
	<u>Skin (a) (Table III)</u> <u>Skin (b) (Table III)</u>		
	7075-T6                      7075-T6	6	1
	7075-T6                      2024-T4	6	1
	7075-T6                      6061-T6	6	1
	2024-T4                      6061-T6	6	1
IV.	<u>Honeycomb Peel and Tensile Panels</u> <sup>**</sup>		
	1/4-inch cell		
	3003-.004 N.P. core		
	7075-T6 skins	6	1

\*Each lap shear panel was sheared into 5 individual specimens.

\*\*Each panel was sheared into 4 honeycomb peel and 4 honeycomb tensile specimens.

TABLE III

PHYSICAL PROPERTIES OF AF-13 BONDED SPECIMENS(Using three types of aluminum indicated below,  
tested at ambient temperature)

<u>Conditioning of Specimens</u>	<u>Type of Aluminum Used</u>	<u>Metal to Metal Single Lap Shear psi</u>	<u>Metal to Metal Peel lb-in/1" Width</u>
None	(a) 7075 alclad to	1610	87
	(b) 7075 alclad		
	(a) 7075 alclad to	1970	104
	(b) 2024 alclad		
	(a) 7075 alclad to	1900	101
	(b) 6061 nonclad		
	(a) 2024 alclad to	1790	123
	(b) 6061 nonclad		
Salt Spray for 20 Days	(a) 7075 alclad to	2110	95
	(b) 7075 alclad		
	(a) 7075 alclad to	2250	113
	(b) 2024 alclad		
	(a) 7075 alclad to	1970	104
	(b) 6061 nonclad		
	(a) 2024 alclad to	1640	122
	(b) 6061 nonclad		
Humidity Chamber for 20 Days	(a) 7075 alclad to	2010	89
	(b) 7075 alclad		
	(a) 7075 alclad to	1810	118
	(b) 2024 alclad		
	(a) 7075 alclad to	2180	100
	(b) 6061 nonclad		
	(a) 2024 alclad to	2040	124
	(b) 6061 nonclad		

TABLE III (Continued)

Conditioning of Specimens	Type of Aluminum Used	Metal to Metal Single Lap Shear psi	Metal to Metal Peel 1/16-in/1" Width
Roof of the Test Laboratory for 90 Days	(a) 7075 alclad to	2340	85
	(b) 7075 alclad		
	(a) 7075 alclad to	2215	97
	(b) 2024 alclad		
	(a) 7075 alclad to	2300	102
	(b) 6061 nonclad		
	(a) 2024 alclad to	2170	118
	(b) 6061 nonclad		
Panama Canal Zone Jungle Site for 60 Days	(a) 7075 alclad to	1740	94
	(b) 7075 alclad		
	(a) 7075 alclad to	1820	109
	(b) 2024 alclad		
	(a) 7075 alclad to	1900	102
	(b) 6061 nonclad		
	(a) 2024 alclad to	1900	105
	(b) 6061 nonclad		
Panama Canal Zone Ocean Site for 60 Days	(a) 7075 alclad to	1790	91
	(b) 7075 alclad		
	(a) 7075 alclad to	1880	115
	(b) 2024 alclad		
	(a) 7075 alclad to	1640	96
	(b) 6061 nonclad		
	(a) 2024 alclad to	2220	124
	(b) 6061 nonclad		

1. All (a) skins were anodized before bonding.

2. All 61 nonclad (b) skins were anodized before bonding.  
All other (b) skins were not anodized.

TABLE IV

PHYSICAL PROPERTIES OF AF-203 BONDED PANEL

(Using .020-inch 7075-T6 alclad skins and 1/4-inch cell size 3003-.004 N.P. honeycomb core, tested at ambient temperature)

<u>Conditioning of Test Specimens</u>	<u>Honeycomb Tensile psi</u>	<u>Honeycomb Peel lb-in/3" Width</u>
None	1310	121
Salt Spray for 20 Days	1320	112
Humidity Chamber for 20 Days	1340	86
Roof of Test Laboratory for 90 Days	1190	118
Panama Canal Zone, Ocean Site, for 60 Days	1190	151
Panama Canal Zone, Jungle Site, for 60 Days	1210	157

# LIST OF FIGURES FOR SECTION III

<u>Figure No.</u>	<u>Figure Title</u>	<u>Page</u>
1	BLC WING SKINS.....	831
2	OUTBCARD AND TRAILING EDGE SKINS.....	832
3	20 INCH LONG TORSION TUBES.....	833
4	RELATIVE RIGIDITY AND YIELD STRESS.....	834
5	TWIST AT FAILURE.....	835
6	ALL BONDED UPPER AND LOWER SKIN ASSEMBLY.....	836
7	UNTAPERED TORSION BOX.....	837
8	CONTINUOUS TRUSS TYPE TRAILING EDGE.....	838
9	ALTITUDE-LOCAL DISTURBANCES.....	839
10	ALTITUDE-WAVINESS CHART.....	840
11	CORROSION TEST RESULTS.....	841
12	POTENTIAL CUMULATIVE DAMAGE REDUCTION FOR BLC AIRCRAFT.....	842
13	ENVELOPE OF MAXIMUM STRESSES INTERIOR HOLES.....	843
14	SOLID SKIN FLENUMS CHORDWISE TENSION.....	844
15	S - N CURVE-CHORDWISE SPECIMENS.....	845
16	S - N CURVE-SPANWISE SPECIMENS.....	846
17	TYPICAL WING SKIN STRUCTURE WITH SUCTION DUCTING.....	847
18	DESIGN WEIGHT SANDWICH CONSTRUCTION BLC CONFIGURATION $F_{allult} = 65,000 \text{ psi}$ .....	848
19	HONEYCOMB SUBSTRUCTURE LOAD CARRYING CAPABILITY, $F_{all} =$ $65,000 \text{ psi}$ .....	849
20	DESIGN-WEIGHT SKIN-DUCT CONFIGURATION HONEYCOMB SANDWICH....	850
21	DESIGN-WEIGHT SKIN-DUCT CONFIGURATION.....	851
22	DESIGN-WEIGHT SKIN-DUCT CONFIGURATION.....	852
23	DESIGN-WEIGHT SKIN-DUCT CONFIGURATION.....	853
24	DESIGN-WEIGHT SKIN-DUCT CONFIGURATION.....	854

LIST OF FIGURES FOR SECTION III (continued)

<u>Figure No.</u>	<u>Figure Title</u>	<u>Page</u>
25	DESIGN-WEIGHT SKIN-DUCT CONFIGURATION.....	855
26	FLOW RATE TEST SETUP.....	856
27	BOUNDARY LAYER CONTROL PANELS .....	857

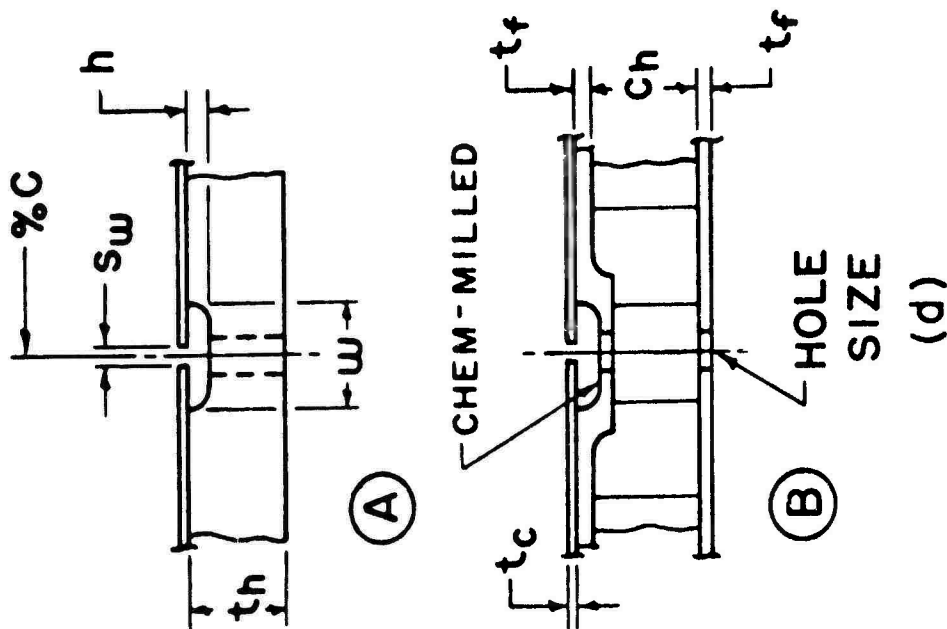


FIGURE 1 BLG WING SKINS

# RANGE OF TYPICAL DIMENSIONS

SLOT WIDTH ( $s_w$ )	.006 -.010
SLOT SPACING (% CHORD)	0.5%-3%
CHAMBER HEIGHT ( $h$ )	.012 -.020
CHAMBER WIDTH ( $w$ )	.15 -.30
COVER SKIN THICKNESS ( $t_c$ )	.012 -.020
HEAVY SKIN THICKNESS ( $t_h$ )	.10 UP
HONEYCOMB SKIN THICKNESS ( $t_f$ )	.012 -.100
HONEYCOMB CORE THICKNESS ( $c_h$ )	.25 -.60
HOLE SIZE ( $d$ )	.03 -.06
SPANWISE HOLE SPACING	4d - 6d

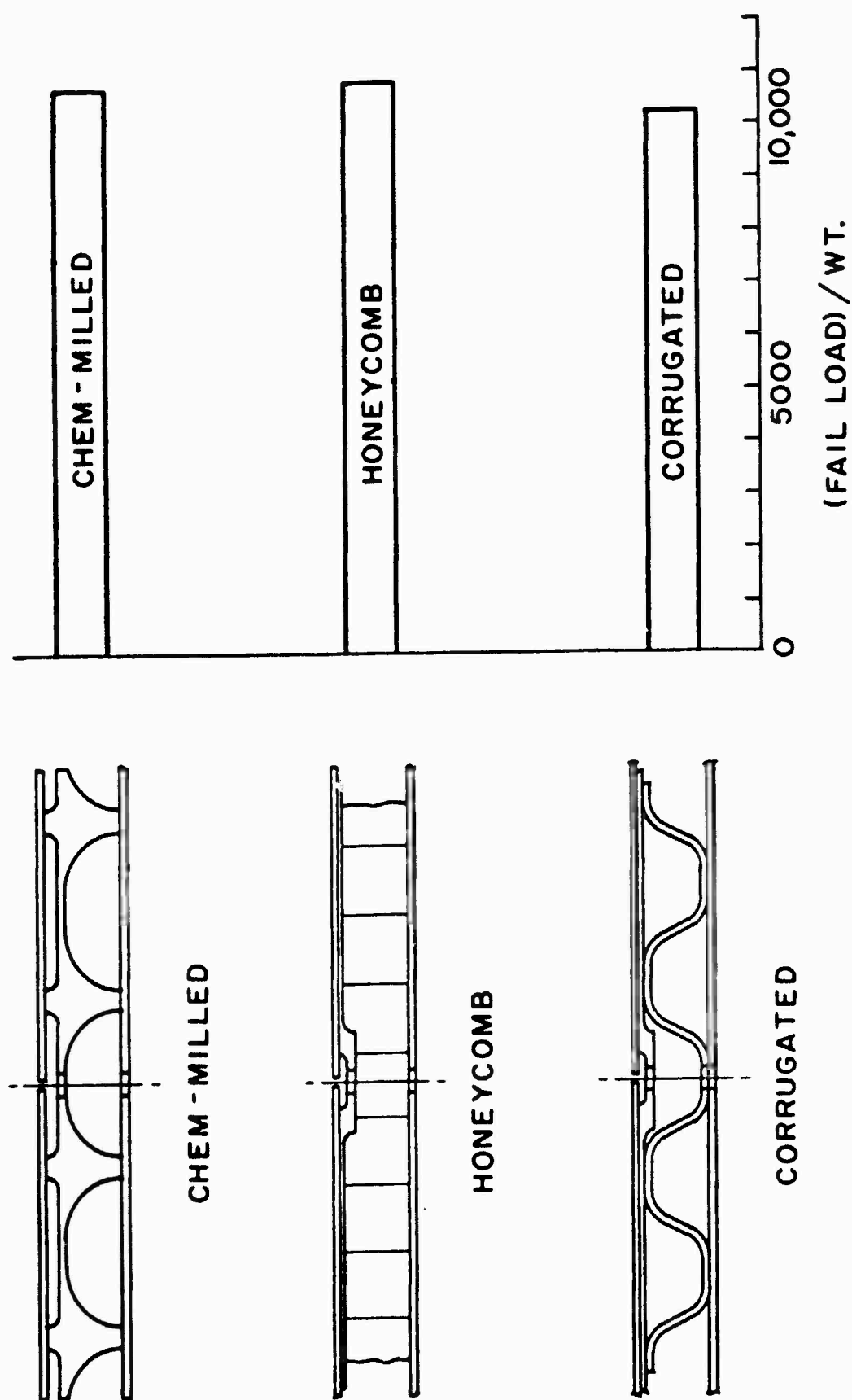


FIGURE 2 OUTBOARD AND TRAILING EDGE SKINS



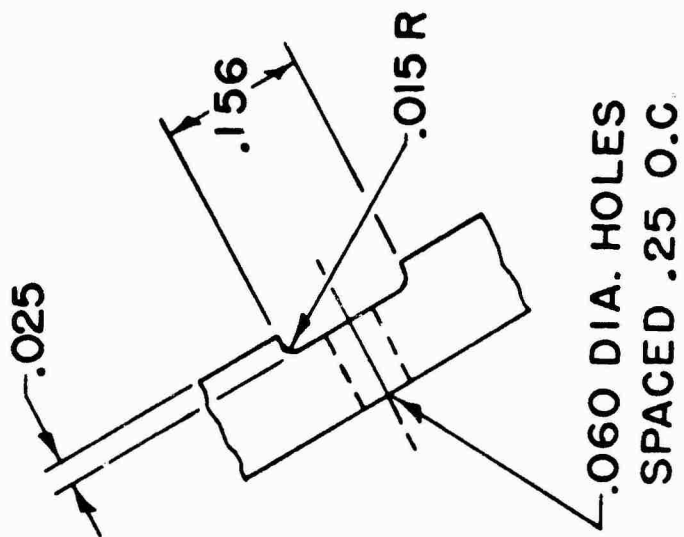
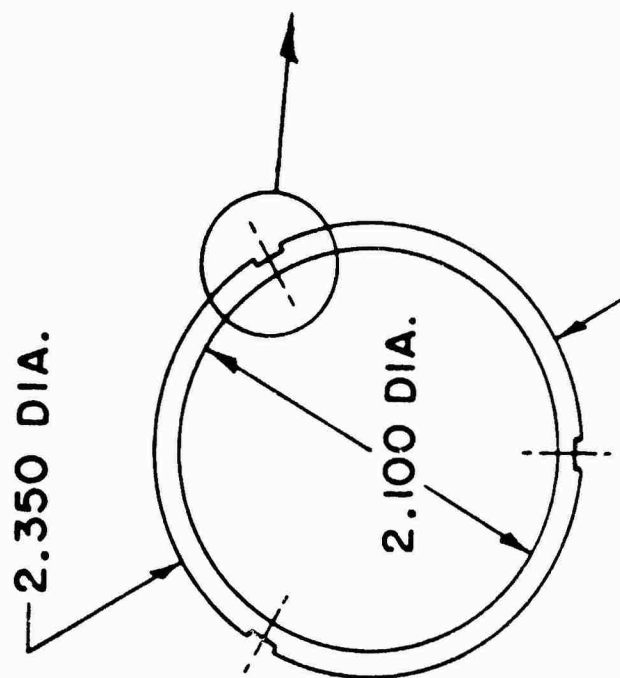


FIGURE 3 20 INCH LONG TORSION TUBES

- ⊙ RIGIDITY-GROOVES
- ◻ RIGIDITY-GROOVES & HOLES
- △ YIELD-GROOVES
- ▽ YIELD-GROOVES & HOLES
- ① 3 GROOVES
- ② 6 GROOVES
- ③ 3 GROOVES & HOLES
- ④ 12 GROOVES
- ⑤ 6 GROOVES & HOLES
- ⑥ 12 GROOVES & HOLES

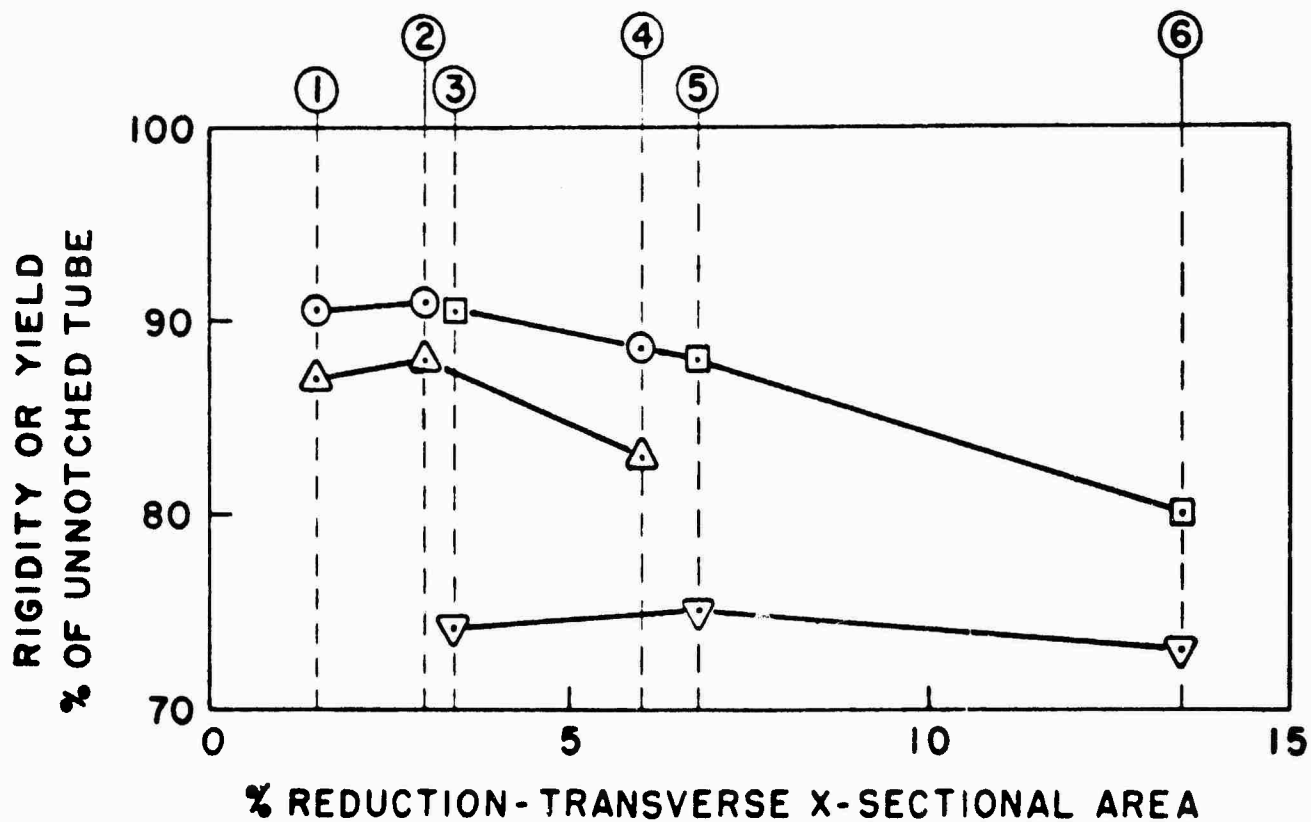


FIGURE 4 RELATIVE RIGIDITY AND YIELD STRESS

- ① 3 GROOVES & HOLES
- ② 6 GROOVES & HOLES
- ③ 12 GROOVES & HOLES

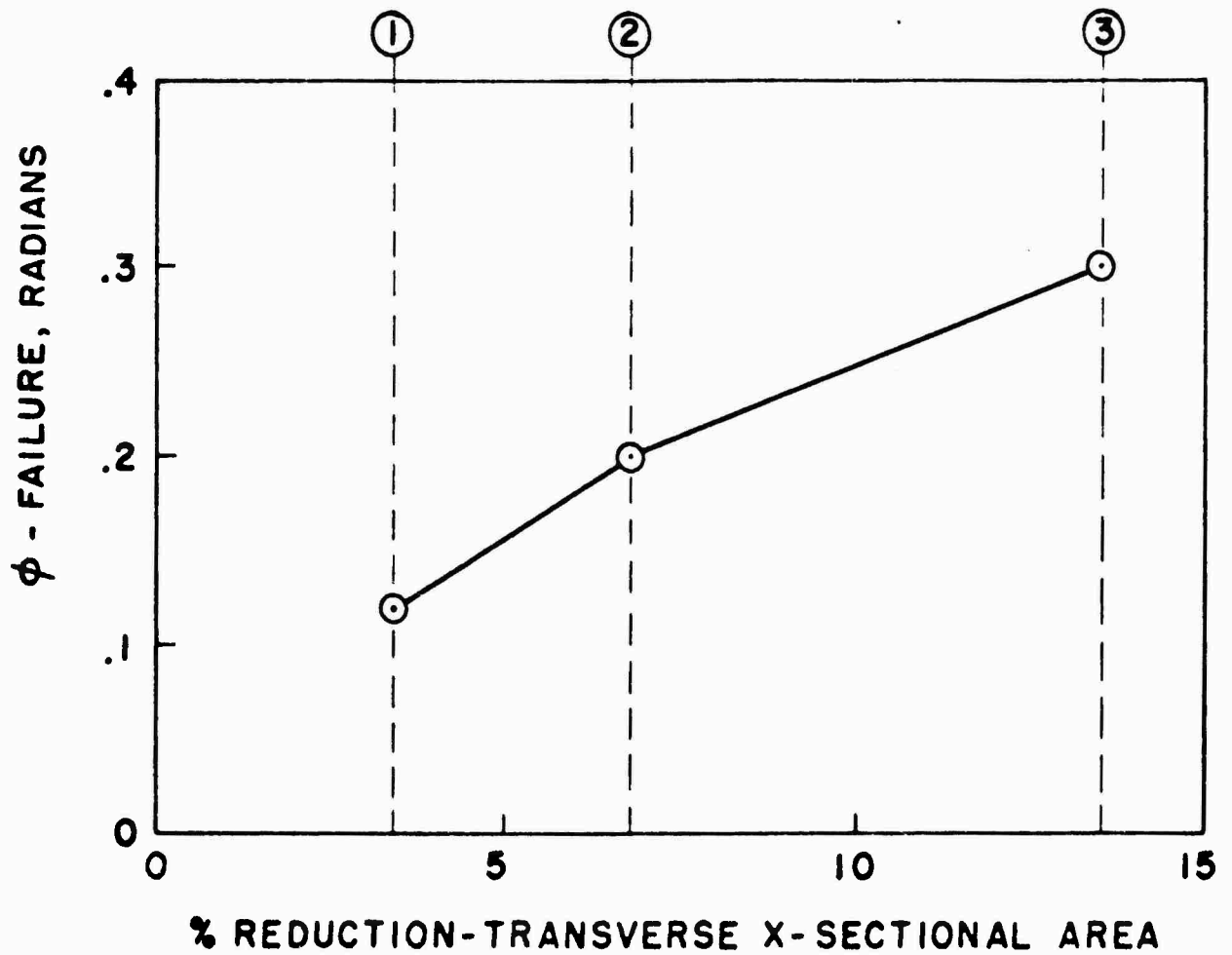


FIGURE 5 TWIST AT FAILURE

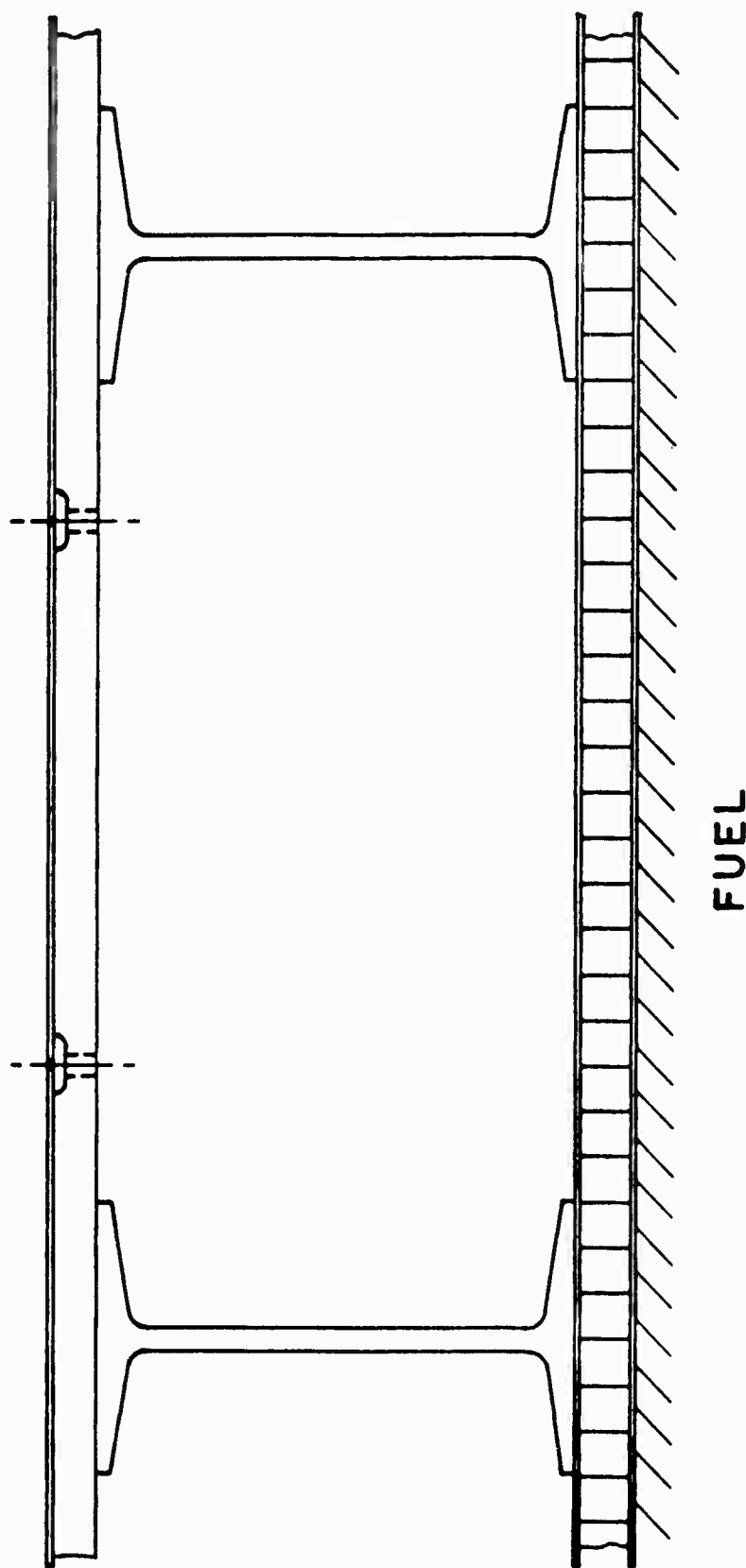


FIGURE 6 ALL BONDED UPPER AND LOWER SKIN ASSEMBLY

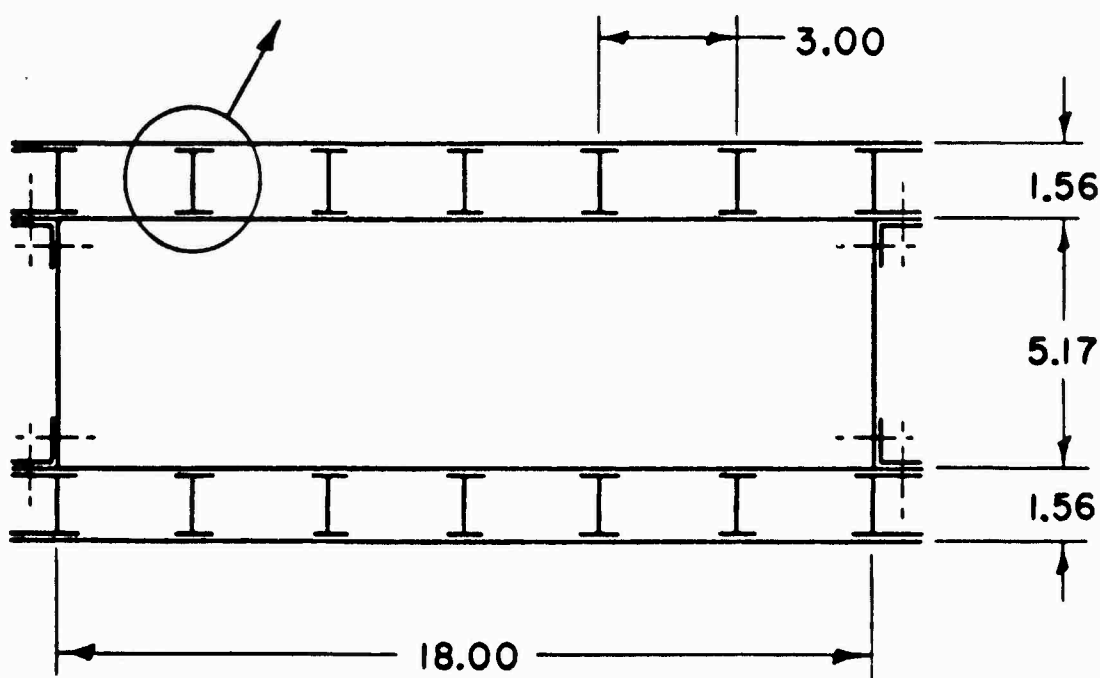
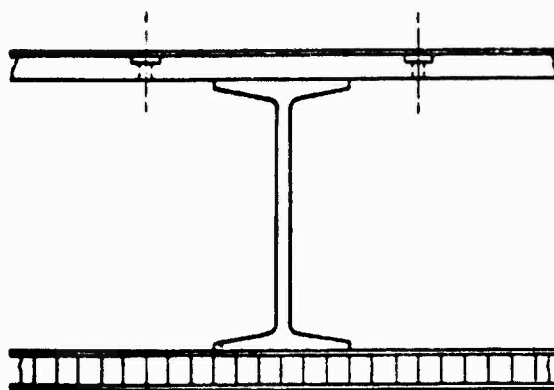


FIGURE 7 UNTAPERED TORSION BOX

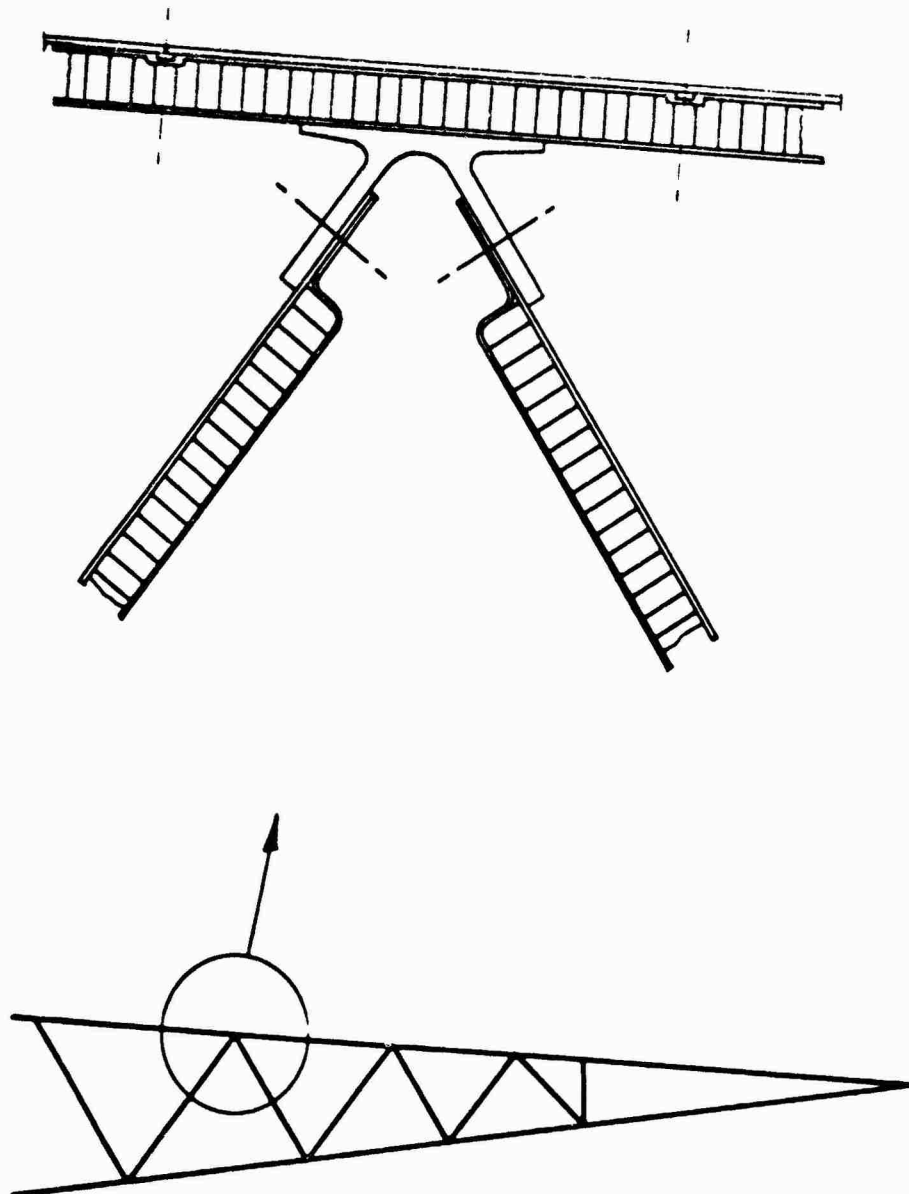


FIGURE 8 CONTINUOUS TRUSS TYPE TRAILING EDGE

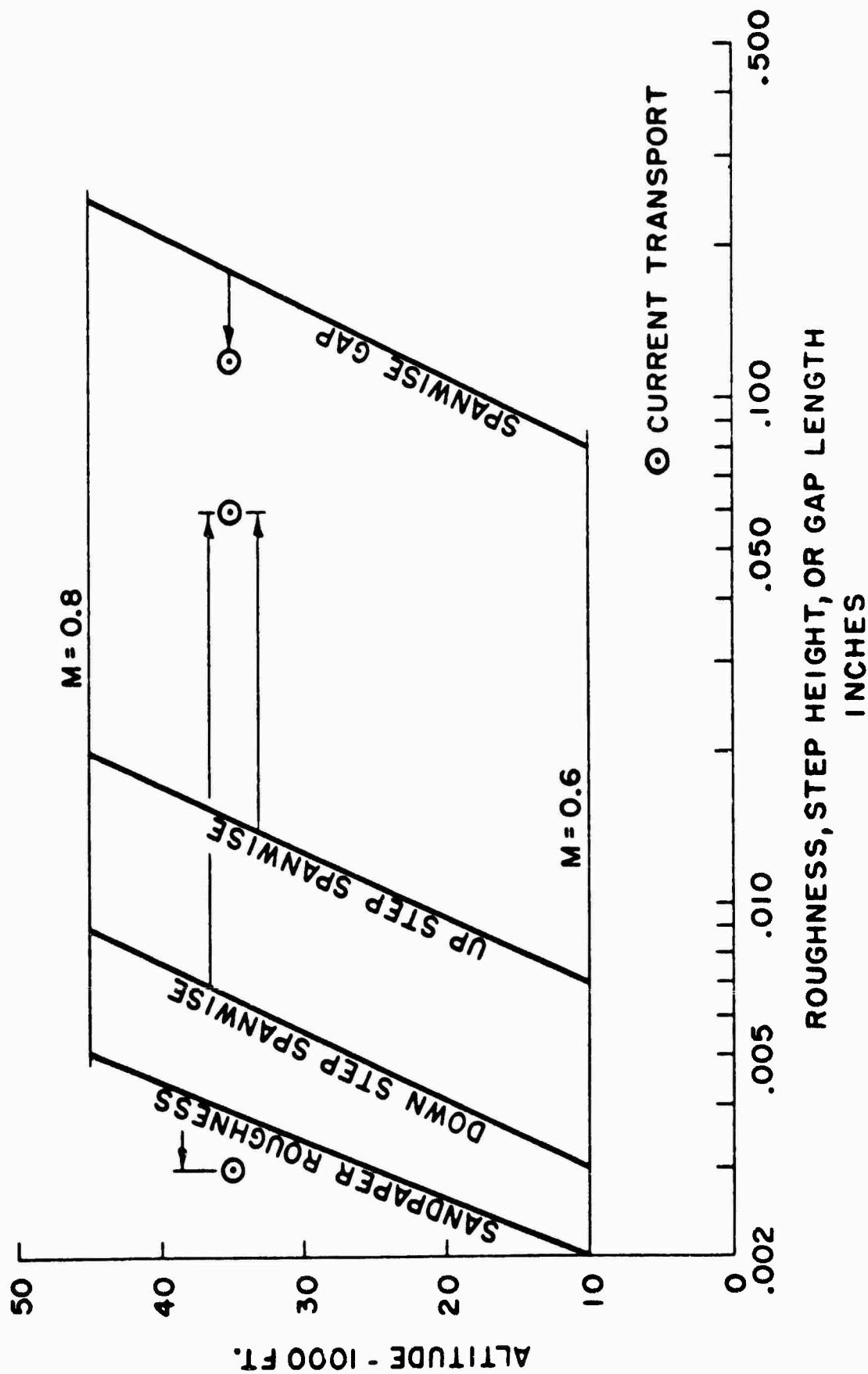


FIGURE 9 ALTITUDE - LOCAL DISTURBANCES

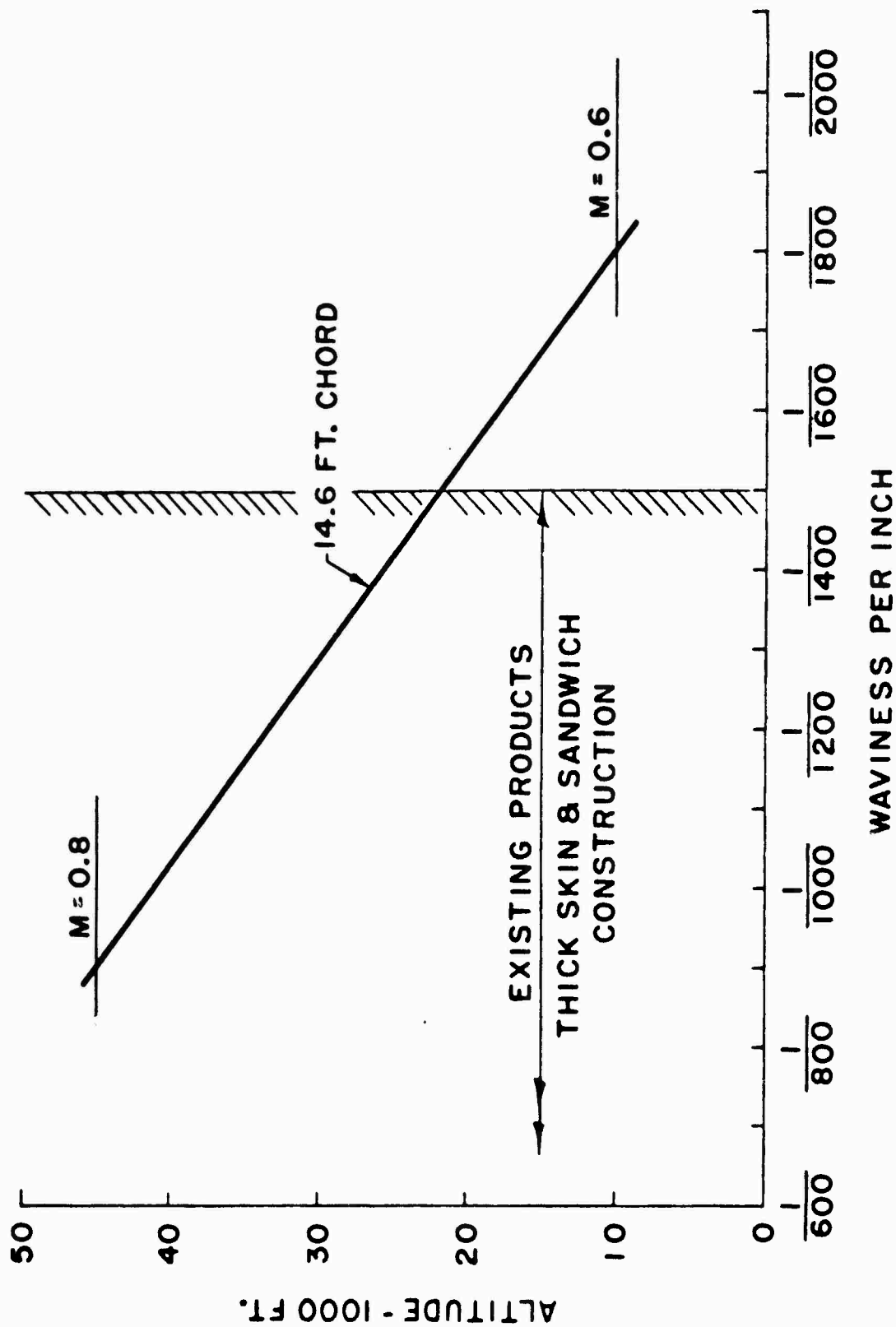


FIGURE 10 ALTITUDE - WAVINESS CHART



--- BEFORE CLEANING  
 — AFTER CLEANING

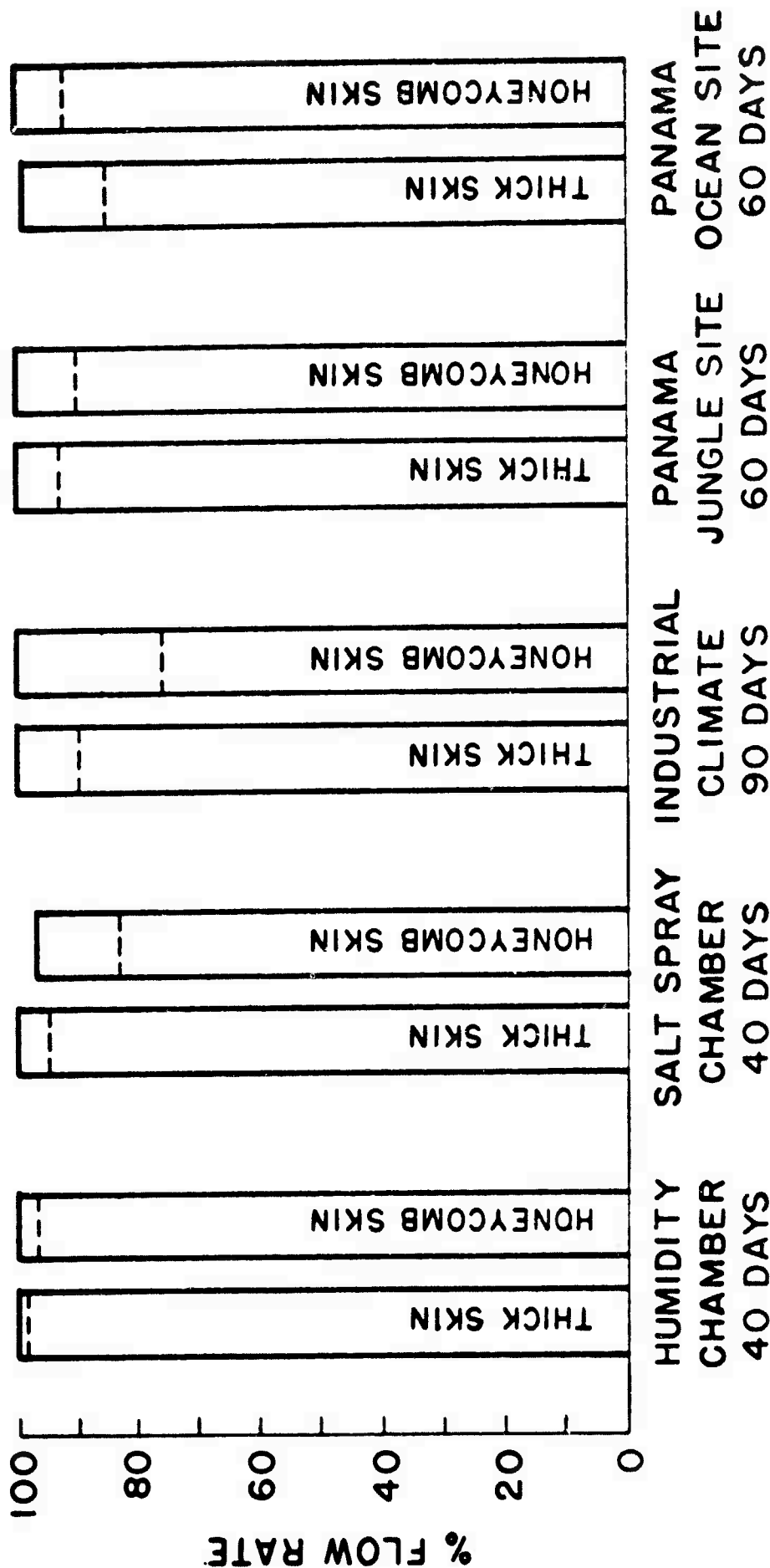


FIGURE 11 CORROSION TEST RESULTS

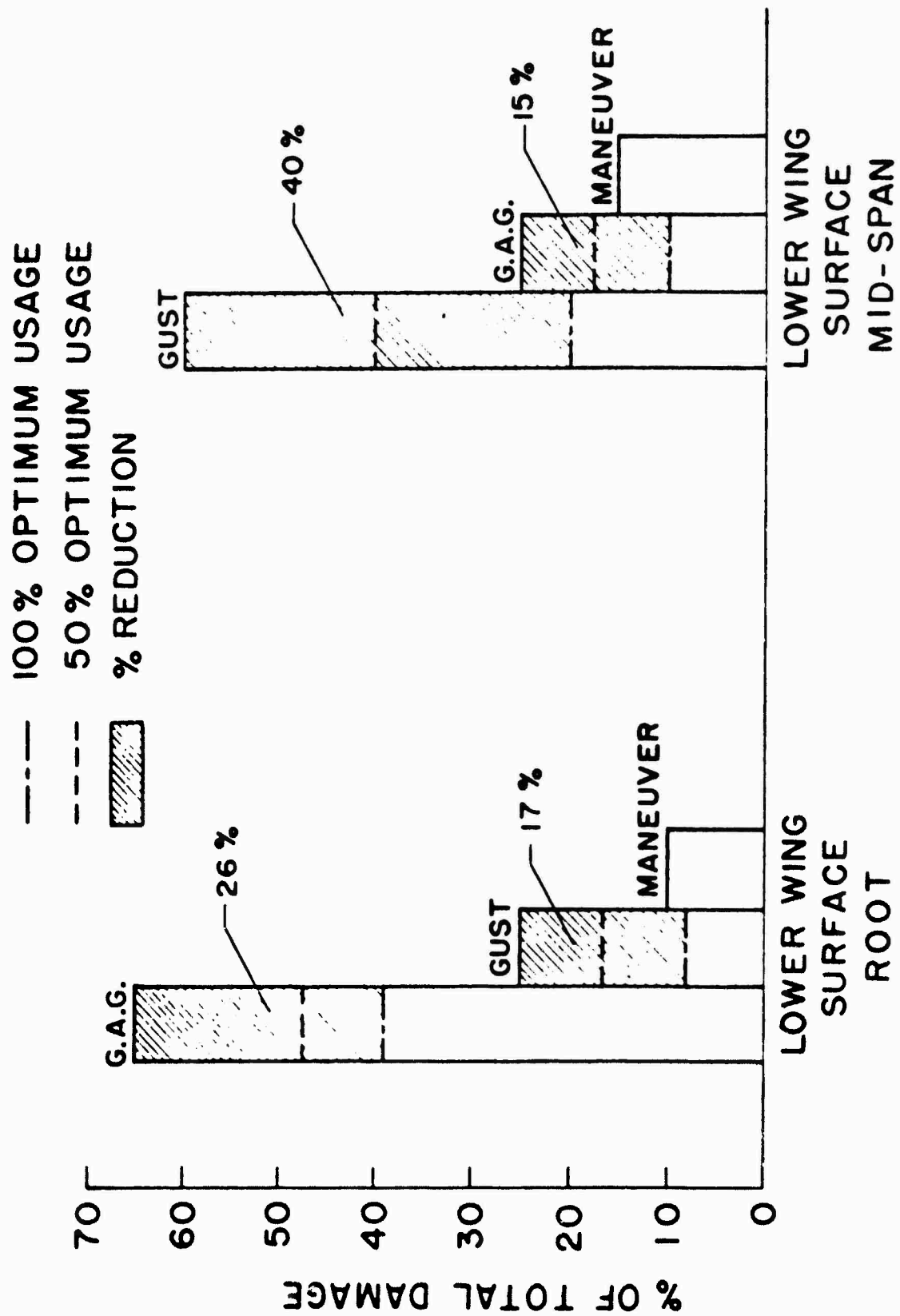
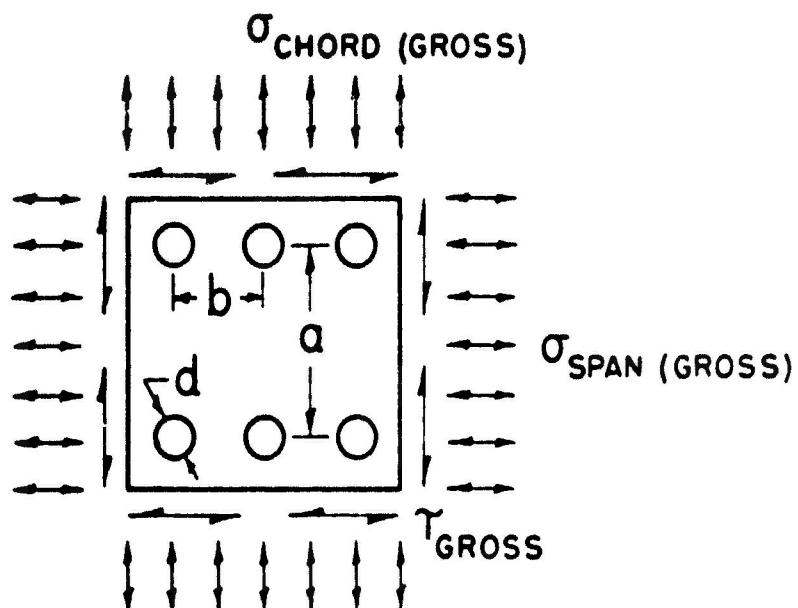


FIGURE 12 POTENTIAL CUMULATIVE DAMAGE REDUCTION FOR BLC AIRCRAFT



$$.2 \leq d/b \leq .3$$

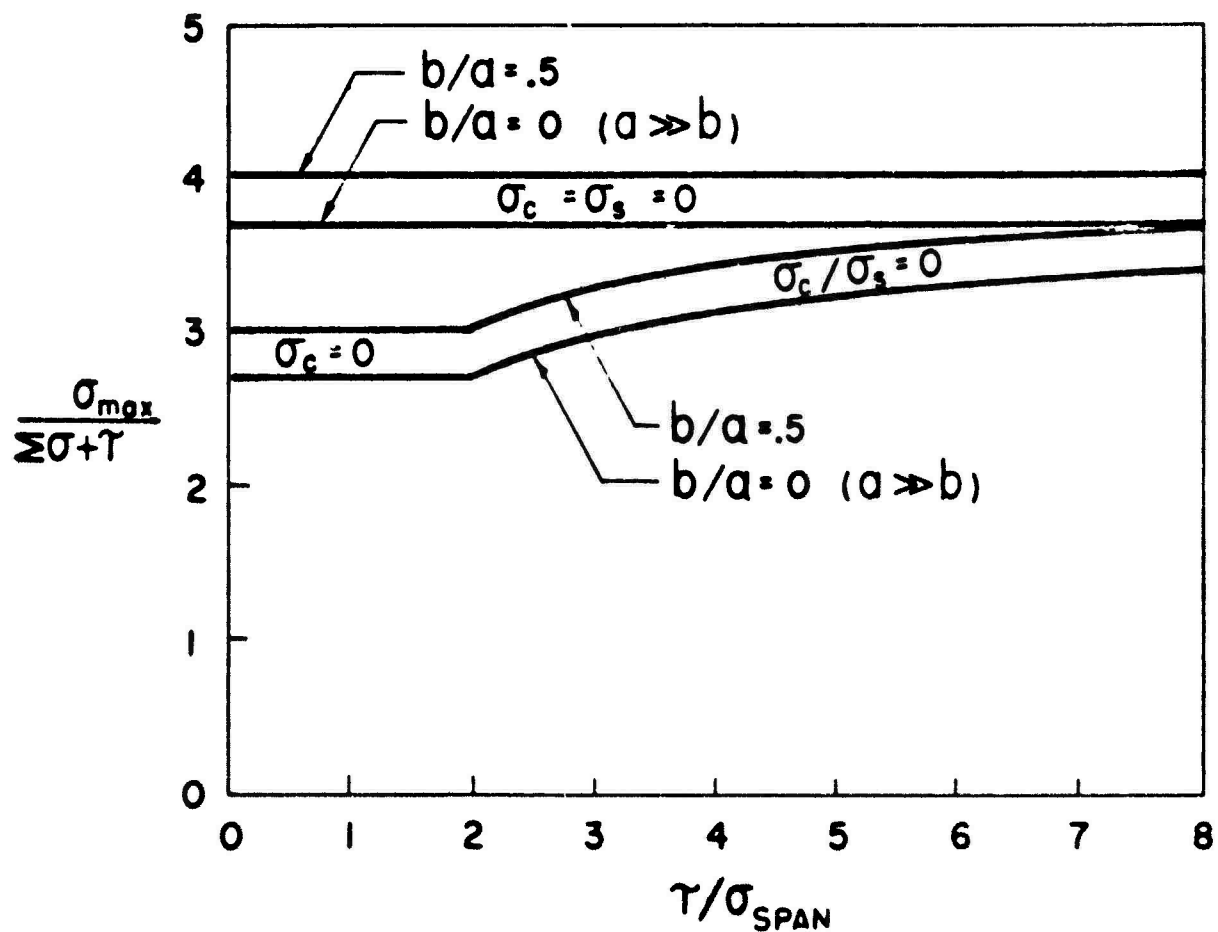


FIGURE 13 ENVELOPE OF MAXIMUM STRESSES INTERIOR HOLES

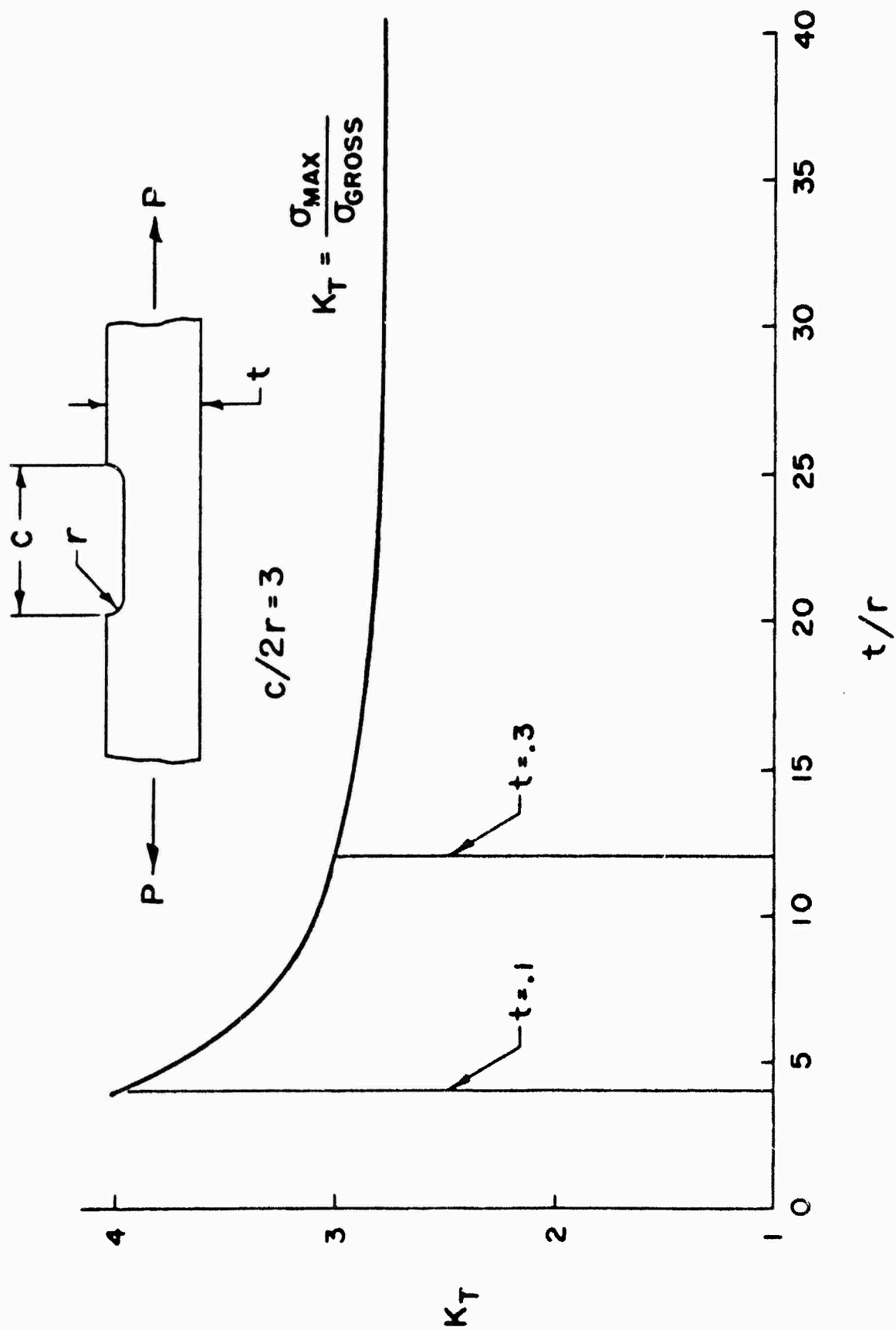


FIGURE 14 SOLID SKIN PLENUMS CHORDWISE TENSION

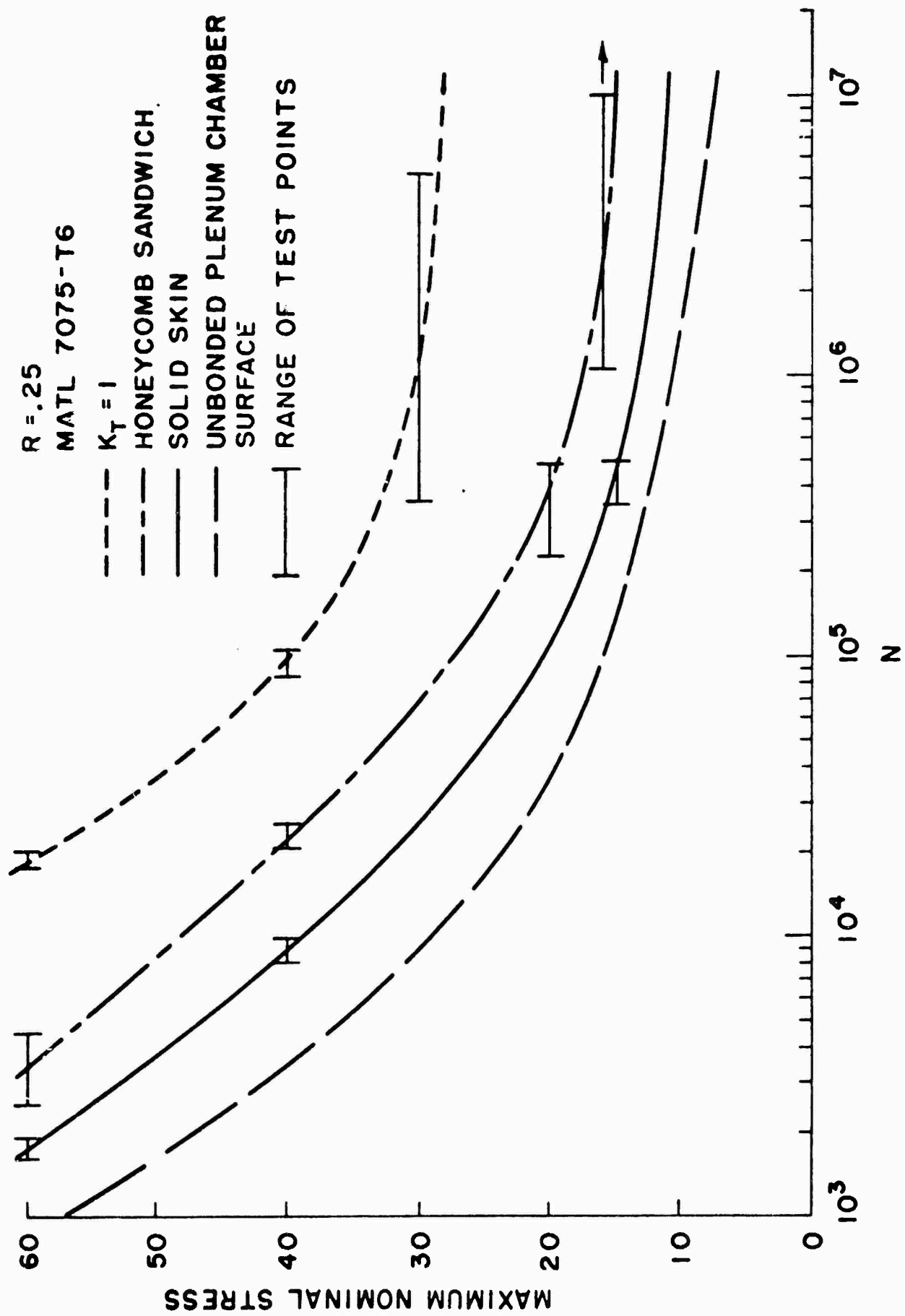


FIGURE 15 S-N CURVE - CHORDWISE SPECIMENS

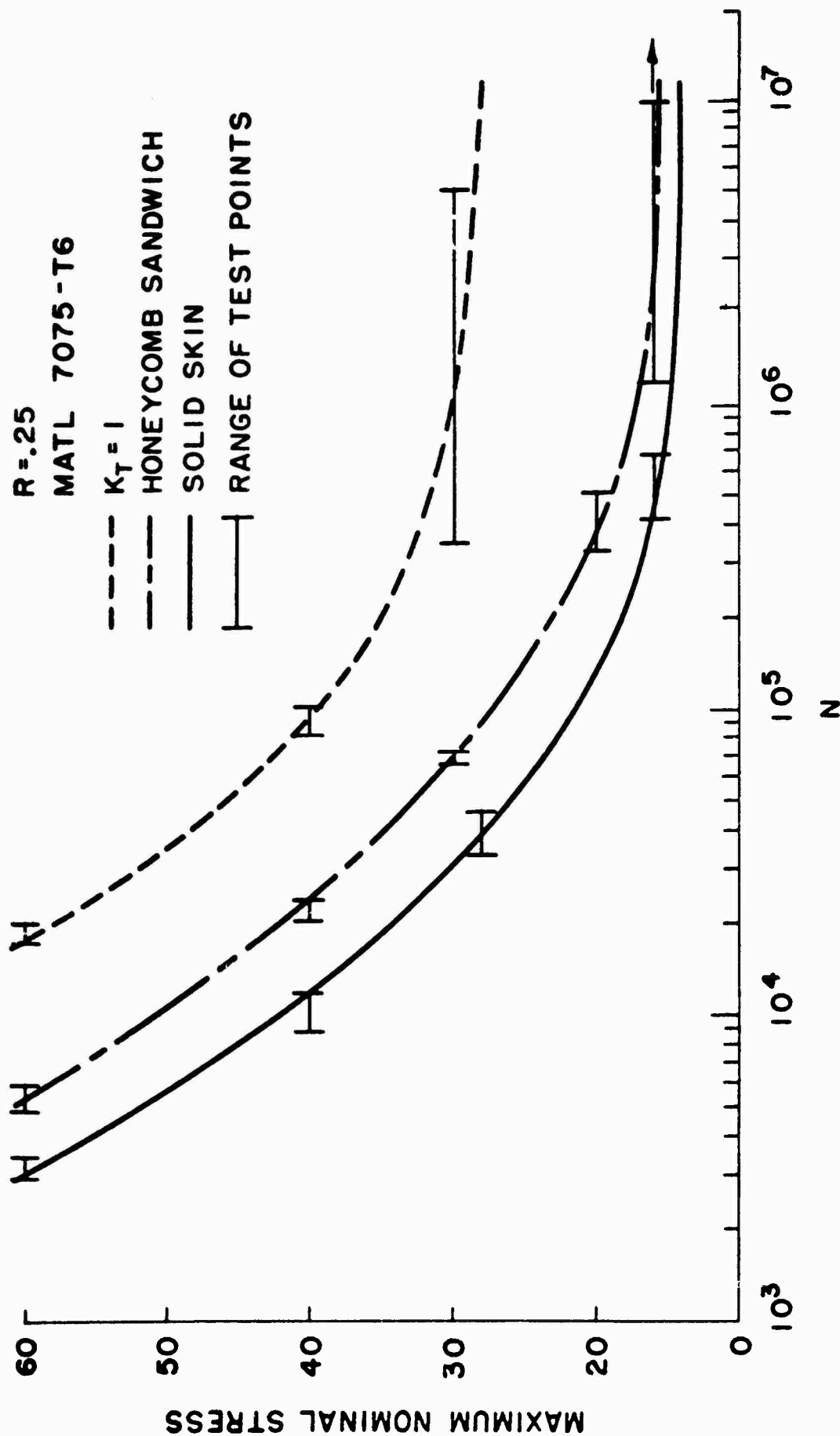


FIGURE 16 S-N CURVE - SPANWISE SPECIMENS

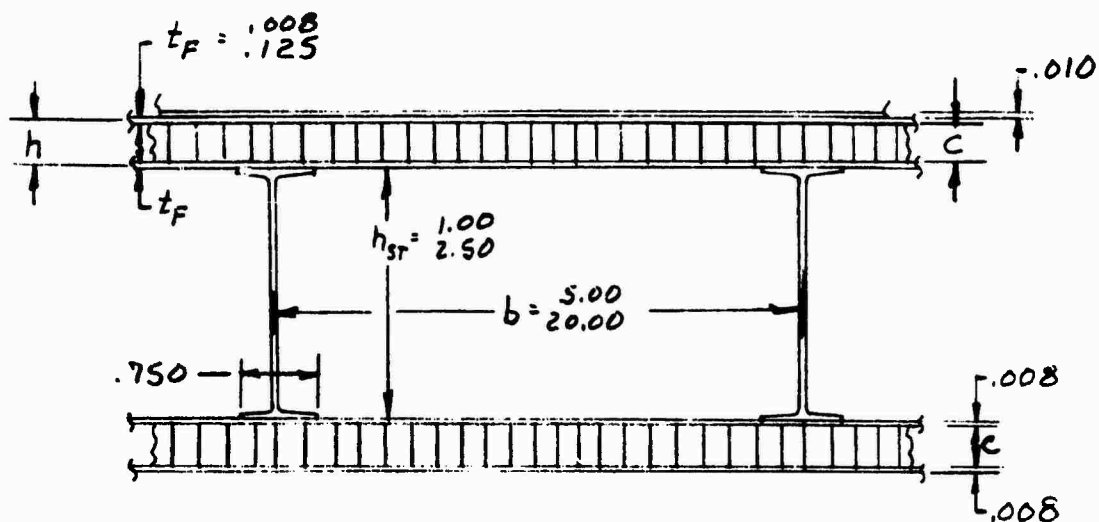
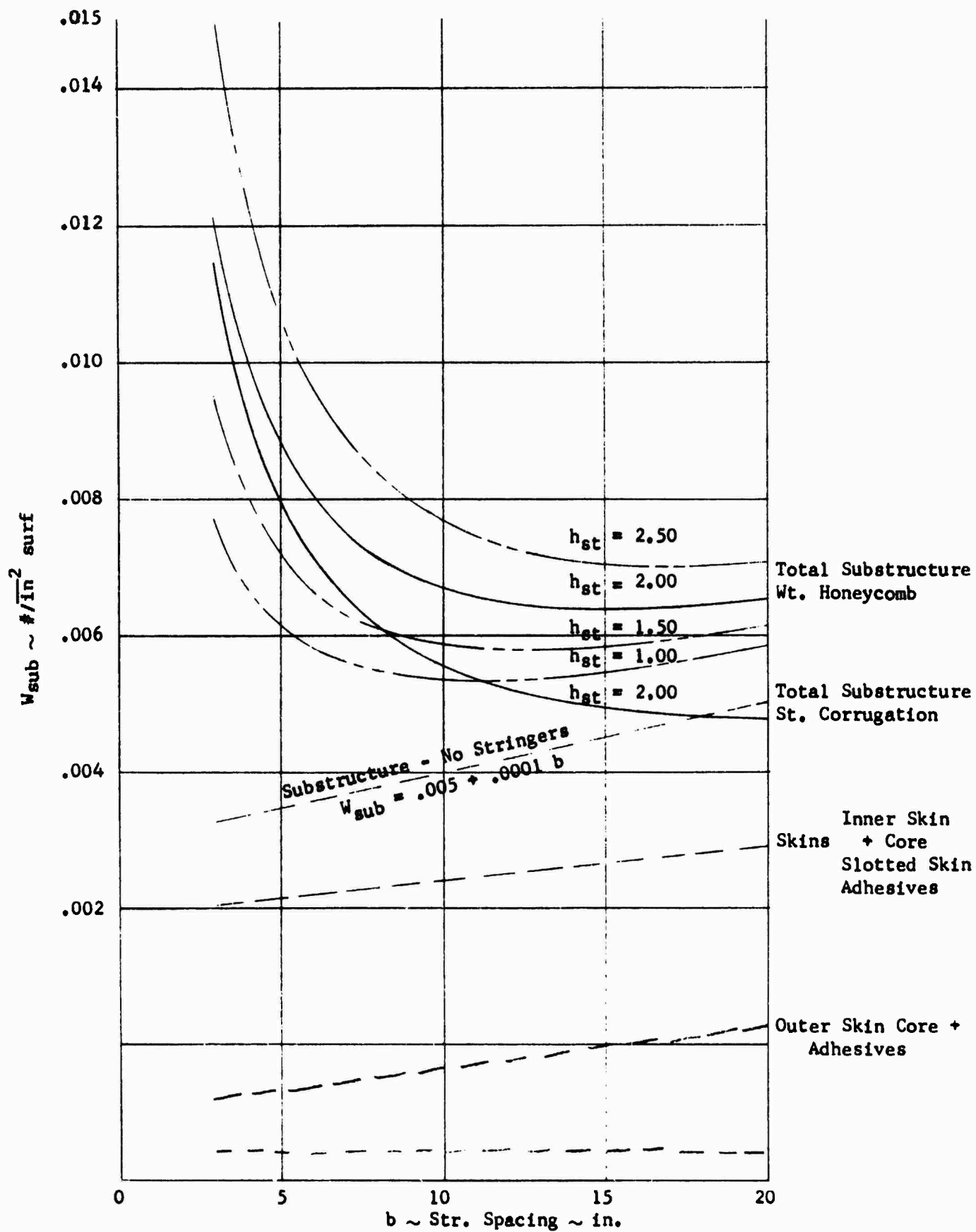


FIGURE 17 TYPICAL WING SKIN STRUCTURE WITH SUCTION DUCTING

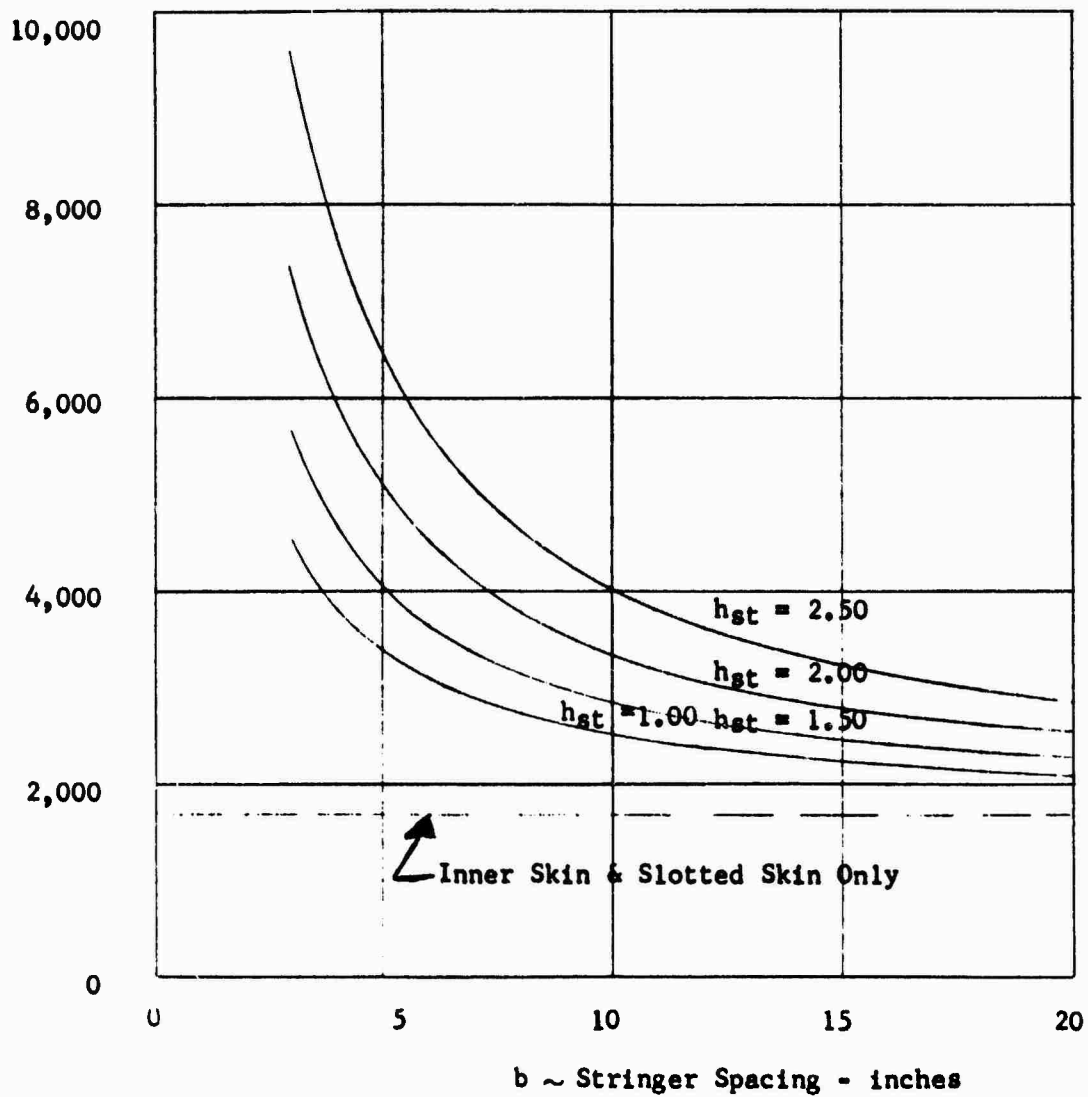
FIGURE 17



DESIGN WEIGHT SANDWICH CONSTRUCTION BLC CONFIGURATION  $F_{all,ult} = 65,000\text{psi}$

FIGURE 18





HONEYCOMB SUBSTRUCTURE LOAD CARRYING CAPABILITY,  $F_{all} = 65,000\text{psi}$

FIGURE 19

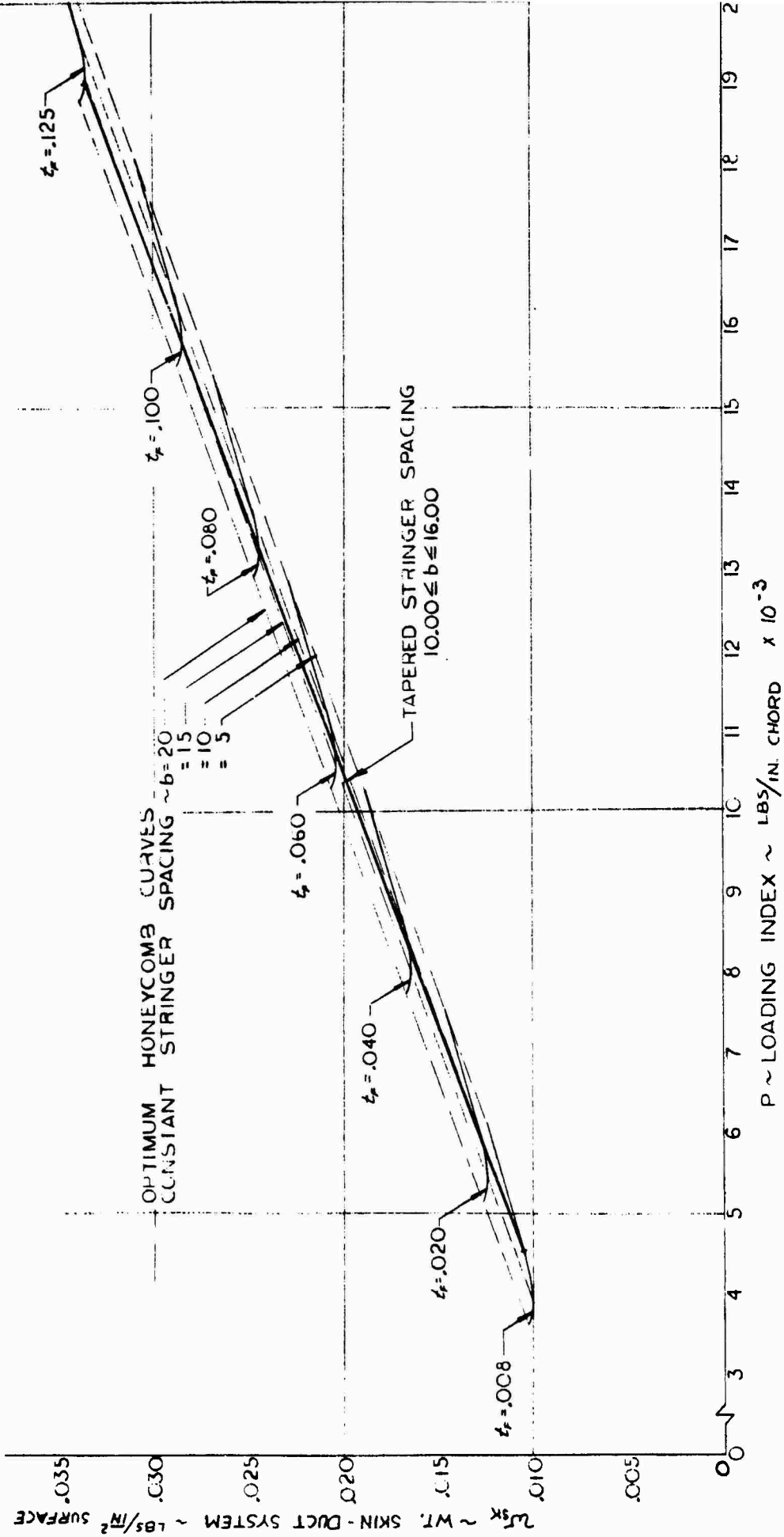


FIGURE 20

DESIGN WEIGHT SKIN-DUCT CONFIGURATION HONEYCOMB SANDWICH

2.00 Stringer height

FALL = 65,000 psi

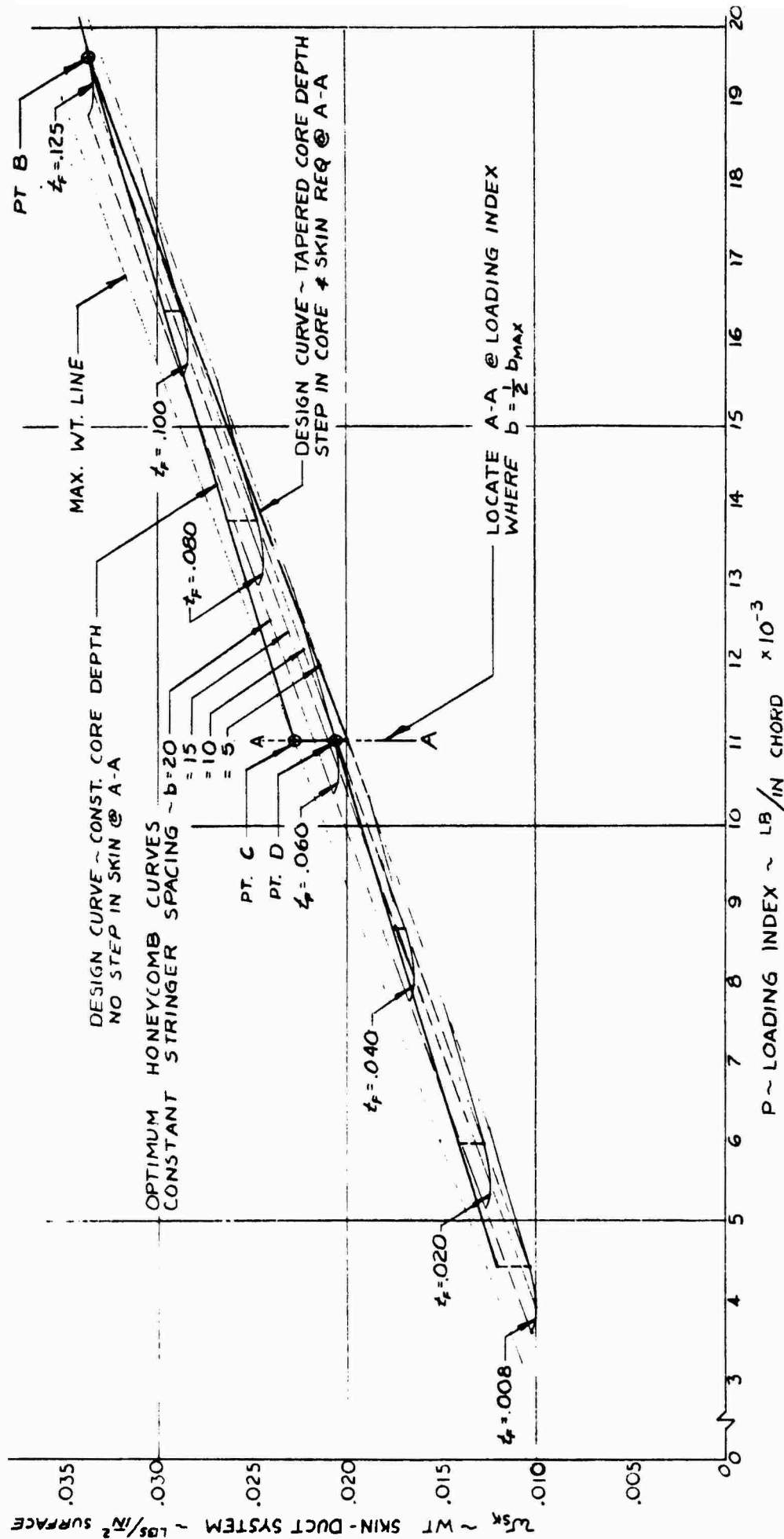


FIGURE 21

DESIGN WEIGHT SKIN-DUCT CONFIGURATION

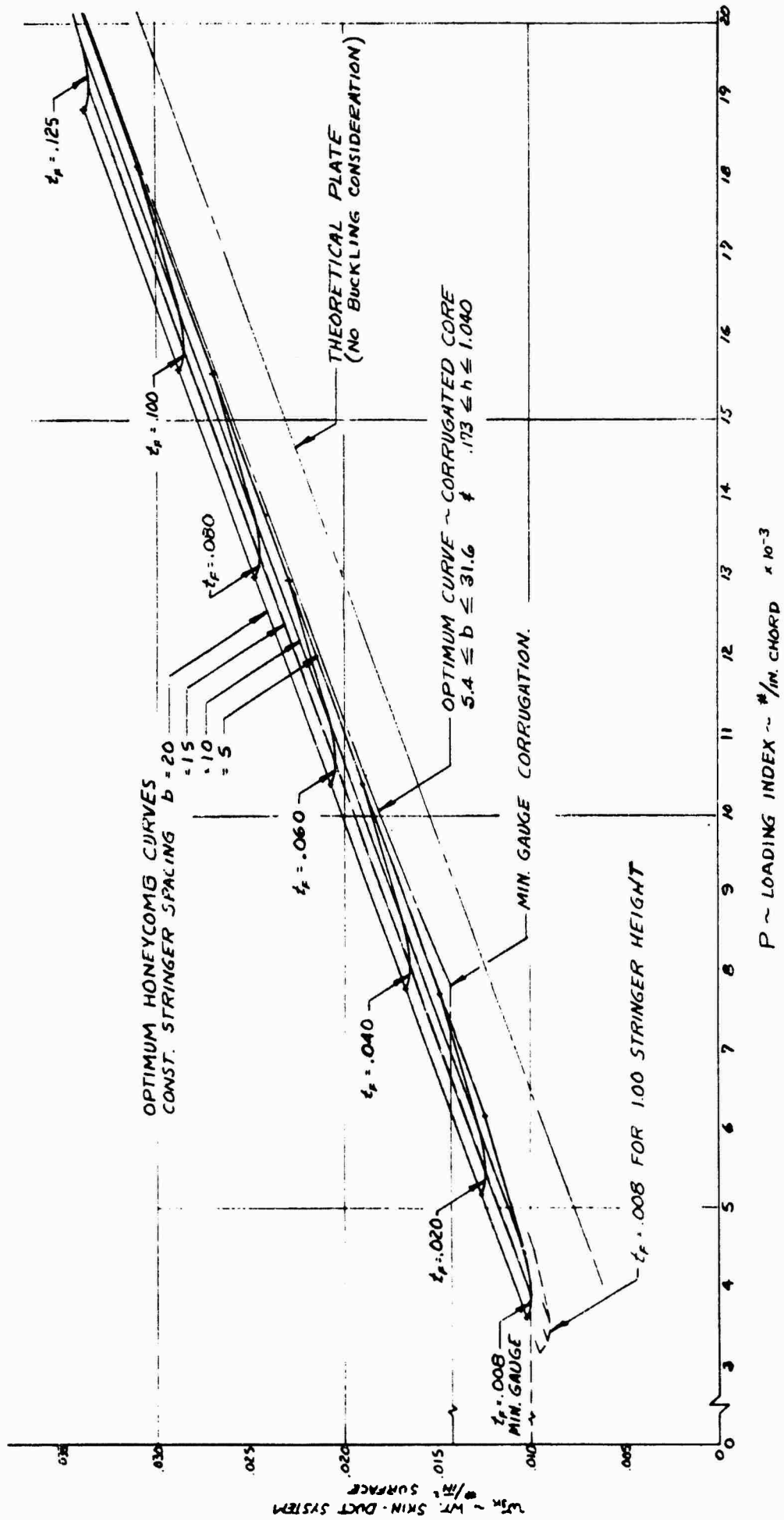


FIGURE 22

DESIGN-WEIGHT SKIN-DUCT CONFIGURATION

$F_{ALL} = 65,000$  psi

2.00 Stringer Height

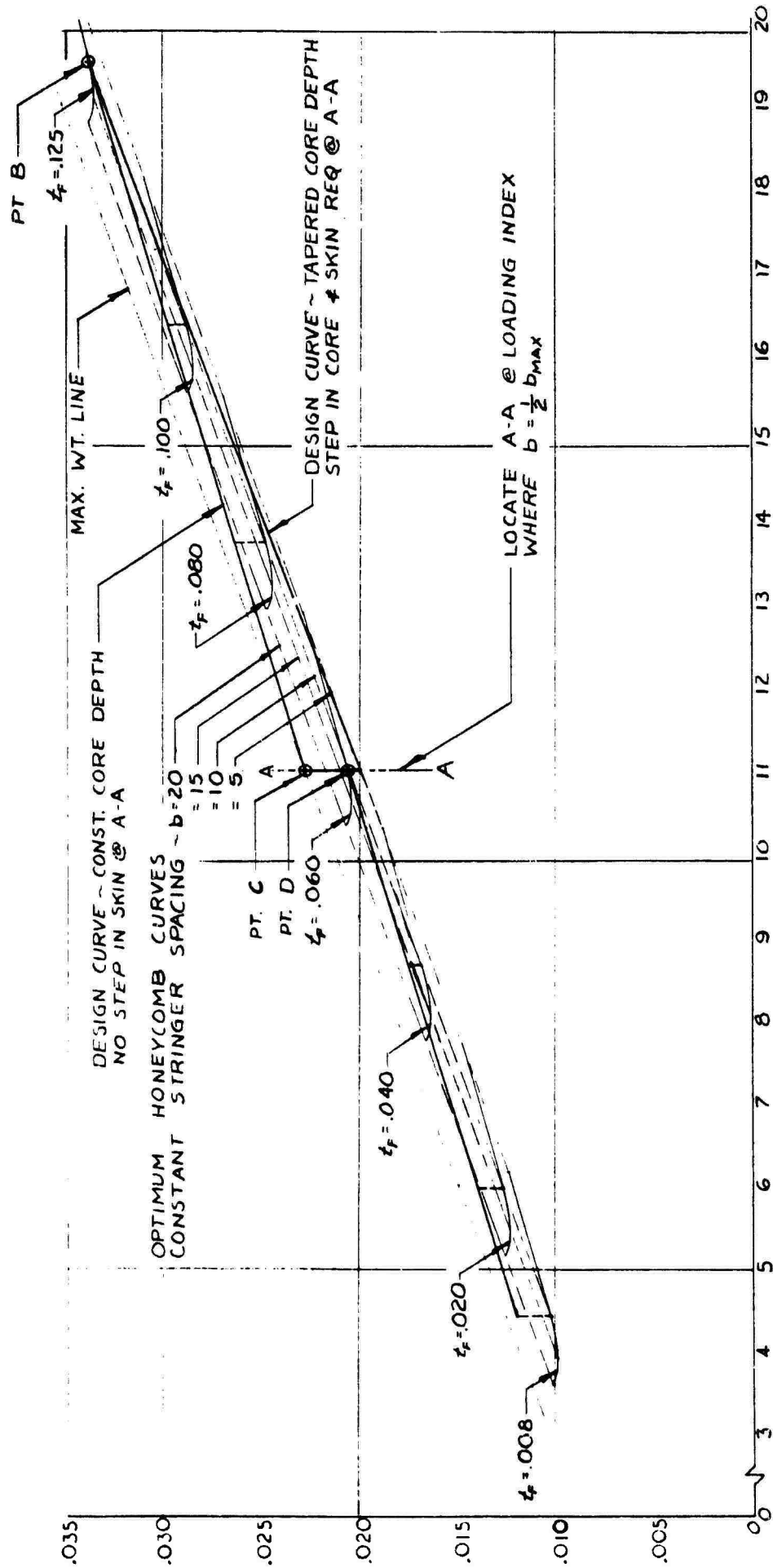


FIGURE 23  
DESIGN-WEIGHT SKIN-DUCT CONFIGURATION

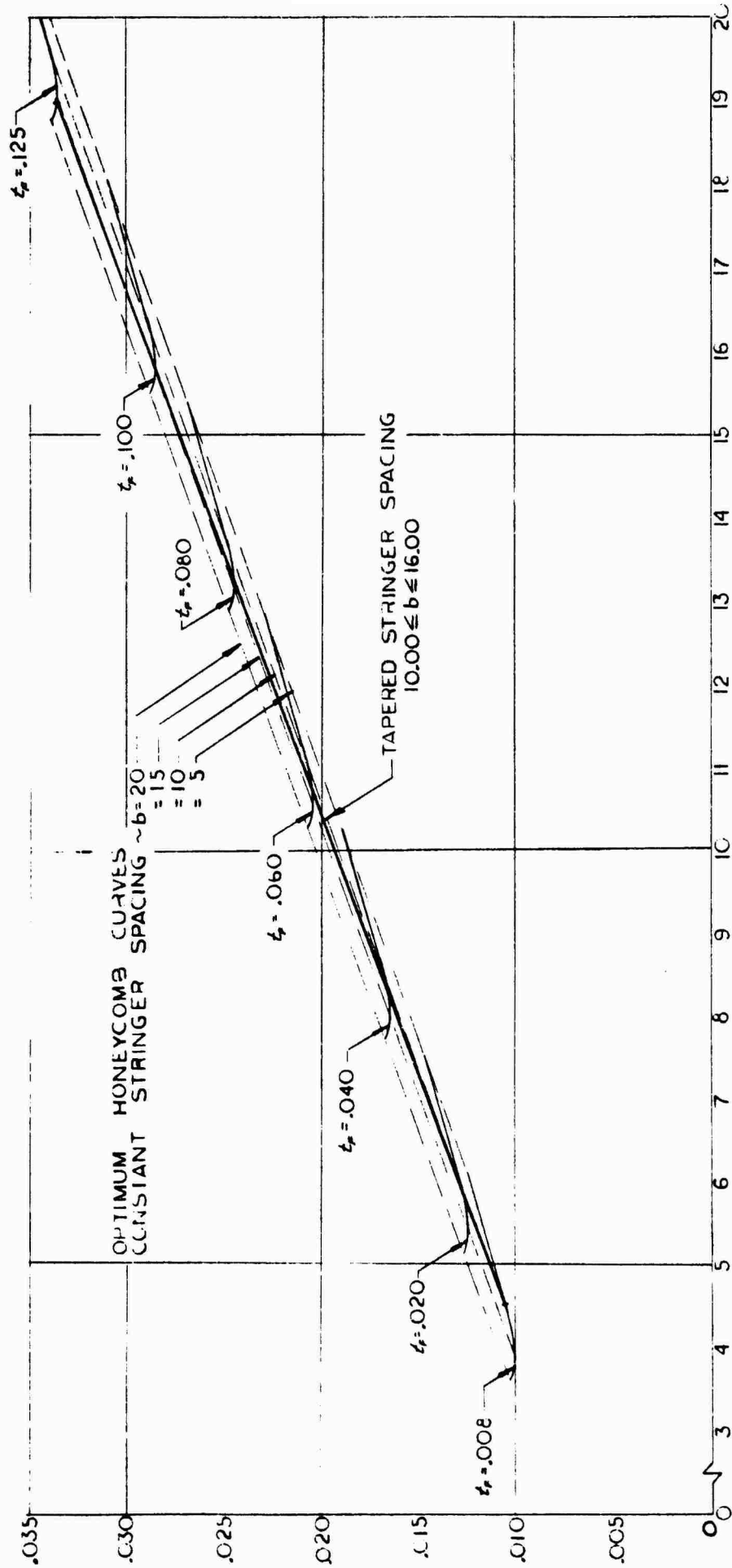


FIGURE 24  
DESIGN-WEIGHT SKIN-DUCT CONFIGURATION

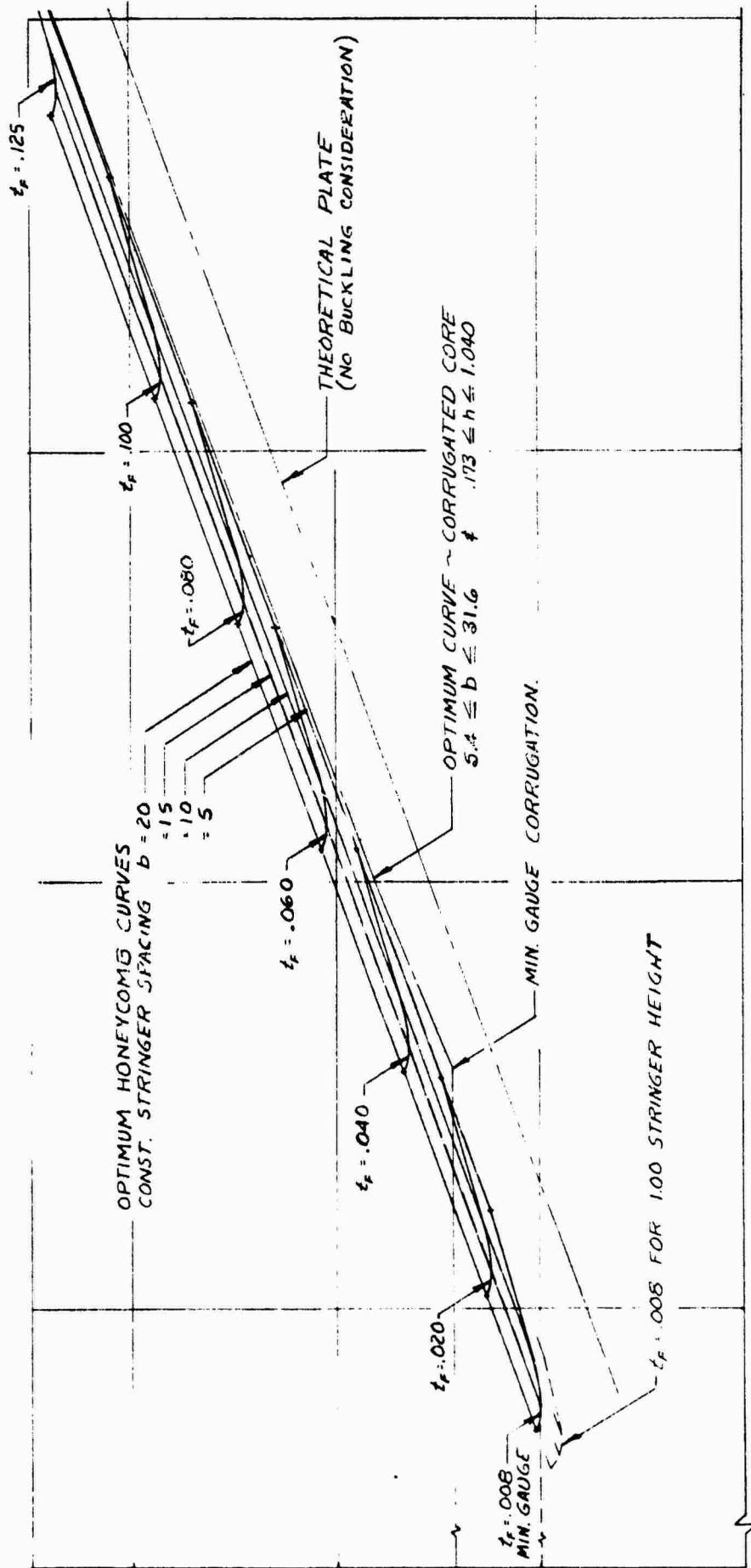


FIGURE 25  
DESIGN-WEIGHT SKIN-DUCT CONFIGURATION

Test Panel - Sealed in Suction Chamber with Tape

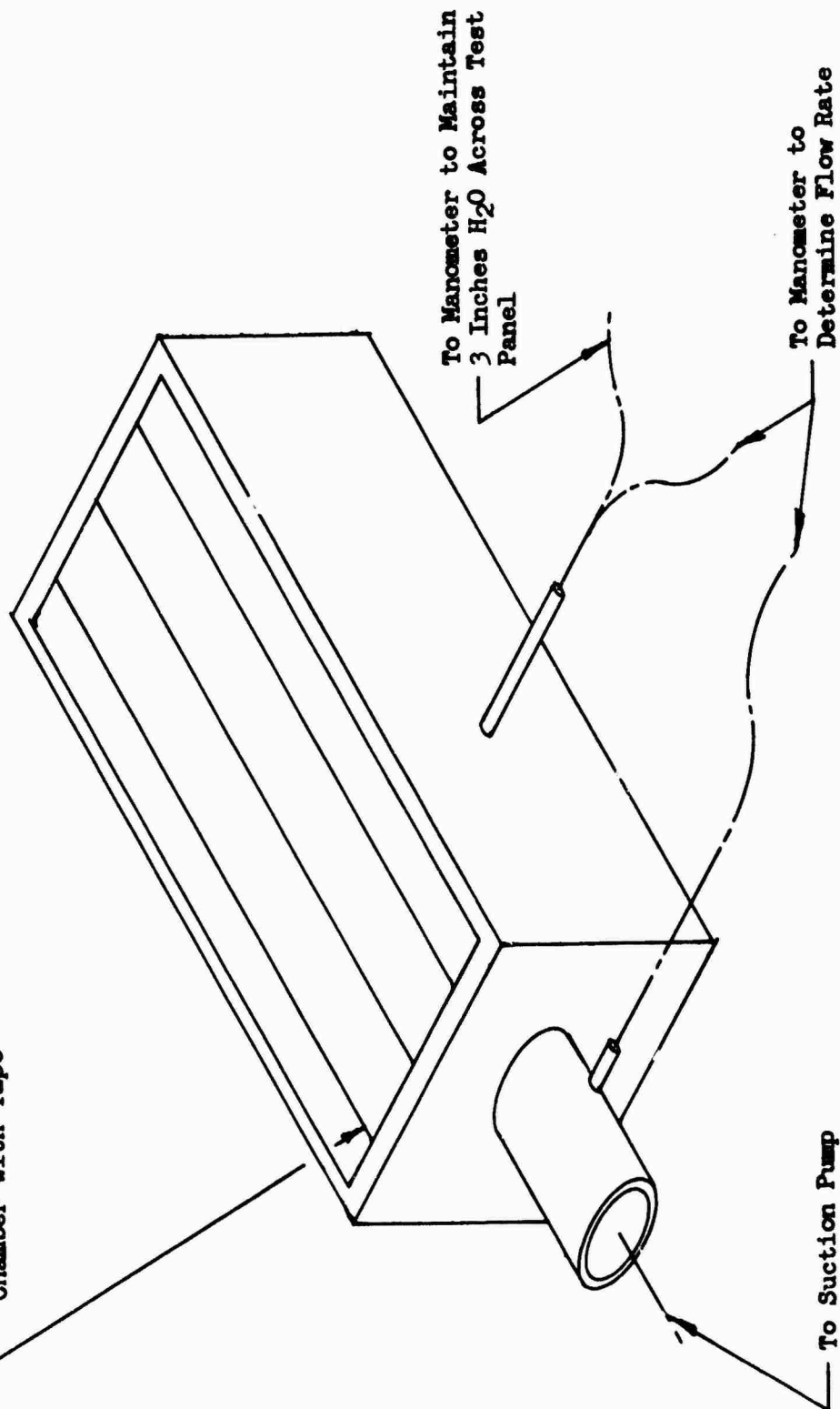


FIGURE 26  
FLOW RATE TEST SETUP



A1 - 7075-T6 Alclad  
 A2 - 2024-T4 Alclad  
 A3 - 6061-T6 Nonclad Anodized

6061-T6 Anodized

.006 Slots - Brush Iridite Surface  
 After Slotting

B1 - 7075-T6  
 B2 - 2024-T4  
 Anodized After  
 Chem-milling

B1 - 7075-T6  
 B2 - 2024-T4  
 Alclad

.035 Dia. Holes  
 .250 o.c.

7075-T6 Anodized

Dwg 4209647

Dwg 4209646

FIGURE 27

BOUNDARY LAYER CONTROL PANELS

**SECTION IV**  
**REFERENCES**

## REFERENCES

1. Raetz, G. S.: A NEW THEORY OF THE CAUSE OF TRANSITION IN FLUID FLOWS, Northrop Corporation, Norair Division Report NOR-59-383 (BLC-121), June 1959.
2. Brown, W. Byron: EXACT NUMERICAL SOLUTION OF THE COMPLETE LINEARIZED EQUATIONS FOR THE STABILITY OF COMPRESSIBLE BOUNDARY LAYERS, Northrop Corporation, Norair Division Report NOR-62-15 (BLC-137), January 1962.
3. Brown, W. Byron: CROSSFLOW STABILITY CALCULATIONS ON HIGHLY SWEEP (65-DEGREE SWEEP) SUPERSONIC LOW DRAG BLC WING (MACH NUMBER 1.8) WITH AND WITHOUT COOLING, Northrop Corporation, Norair Division Report NOR-61-263 (BLC-138), February 1962.
4. Gregory, N. J.; Stuart, T. and Walker, W. S.: "On the Stability of a Three-dimensional Boundary Layer with Application to the Flow due to a Rotating Disc," PHILOSOPHICAL TRANSACTIONS OF THE ROYAL SOCIETY, Series A, No. 943, Vol. 248, pp. 155-199, 1955.
5. Brown, W. Byron: INCOMPRESSIBLE CROSSFLOW STABILITY CALCULATIONS WITH VARIOUS ANGLES OF THE WAVE FRONTS TO THE POTENTIAL FLOW DIRECTION, Northrop Corporation, Norair Division Report NOR-61-262 (BLC-136), November 1961.
6. Brown, W. B.: NUMERICAL CALCULATION OF THE STABILITY OF CROSSFLOW PROFILES IN LAMINAR BOUNDARY LAYERS ON A ROTATING DISC AND ON A SWEEPBACK WING AND AN EXACT CALCULATION OF THE STABILITY OF THE BLASIUS VELOCITY PROFILE, Northrop Corporation, Norair Division Report NAI-59-5 (BLC-117), January 1959.
7. Brown, W. Byron: "Exact Solution of the Stability Equations for Laminar Boundary Layers in Compressible Flow," BOUNDARY LAYER AND FLOW CONTROL, Vol. 2, pp. 1033-1048, Pergamon Press, 1961.
8. Pfenninger, W.; Gross, L. W.; Bacon, J. W., Jr.; and Tucker, V. L.: EXPERIMENTS ON A 30° SWEEP, 12-PERCENT-THICK SYMMETRICAL LAMINAR SUCTION WING IN THE NASA AMES 12-FOOT PRESSURE WIND TUNNEL, Northrop Corporation, Norair Division Report NOR-60-108 (BLC-129), November 1961.
9. Pfenninger, W. and Bacon, J. W., Jr.: ABOUT THE DEVELOPMENT OF SWEEP LAMINAR SUCTION WINGS WITH FULL CHORD LAMINAR FLOW, Northrop Corporation, Norair Division Report NOR-60-299 (BLC-130), September 1960.
10. Pfenninger, W. and Bacon, J. W., Jr.: "About the Development of Swept Laminar Suction Wings with Full Chord Laminar Flow," BOUNDARY LAYER AND FLOW CONTROL, Vol. 2, pp. 1007-1032, Pergamon Press, 1961.

## REFERENCES

11. Gross, L. W.: ANALYSIS OF THE BOUNDARY LAYER DEVELOPMENT ON A  $30^\circ$  SWEPT LAMINAR SUCTION WING, Northrop Corporation, Norair Division Report NOR-61-244 (BLC-134), June 1962.
12. Bacon, J. W., Jr. and Pfenninger, W.: INFLUENCE OF ACOUSTICAL DISTURBANCES ON THE BEHAVIOR OF A SWEPT LAMINAR SUCTION WING, Northrop Corporation, Norair Division Report NOR-62-124 (BLC-141), October 1962.
13. Bacon, J. W., Jr.: INFLUENCE OF ACOUSTICAL DISTURBANCES ON THE BEHAVIOR OF A STRAIGHT LAMINAR SUCTION WING, Northrop Corporation, Norair Division Report NOR-63-53 (BLC-149) (UNPUBLISHED).
14. Gross, Lloyd W.: EXPERIMENTAL INVESTIGATION OF A 4-PERCENT-THICK STRAIGHT LAMINAR SUCTION WING OF 17-FOOT CHORD IN THE NORAIR 7- BY 10-FOOT WIND TUNNEL, Northrop Corporation, Norair Division Report NOR-62-45 (BLC-139), May 1962.
15. Gross, L. W.: INVESTIGATION OF A MODIFIED SEARS-HAACK LAMINAR SUCTION BODY OF REVOLUTION IN THE NORAIR 7- BY 10-FOOT WIND TUNNEL, Northrop Corporation, Norair Division Report NOR-62-125 (BLC-142) (UNPUBLISHED).
16. Groth, Eric E.: LOW DRAG BOUNDARY LAYER SUCTION EXPERIMENTS ON A FLAT PLATE AT MACH NUMBERS 3.0 AND 3.5, Northrop Corporation, Norair Division Report NOR-61-251 (BLC-135), October 1961.
17. Groth, Eric E.: BOUNDARY LAYER SUCTION EXPERIMENTS ON A SLOTTED FLAT PLATE MODEL WITH INTERFERING SHOCK WAVES, Northrop Corporation, Norair Division Report NOR-63-19 (BLC-147) (UNPUBLISHED).
18. Greber, Isaac: INTERACTION OF OBLIQUE SHOCK WAVES WITH LAMINAR BOUNDARY LAYERS, Fluid Dynamics Research Group, Massachusetts Institute of Technology, Technical Report 59-2, April 28, 1959.
19. Pearcey, H. H.: "Shock-induced Separation and Its Prevention by Design and Boundary Layer Control," BOUNDARY LAYER AND FLOW CONTROL, Vol. 2, pp. 1204-1206, Pergamon Press, 1961.
20. Groth, Eric E.: LOW DRAG BOUNDARY LAYER SUCTION EXPERIMENTS AT SUPERSONIC SPEEDS ON AN AGIVE CYLINDER WITH 29 CLOSELY SPACED SLOTS, Northrop Corporation, Norair Division Report NOR-61-162 (BLC-131), August 1961.
21. Groth, Eric E.: LOW DRAG BOUNDARY LAYER SUCTION EXPERIMENTS ON A  $36^\circ$  SWEPT WING AT MACH NUMBERS 2.5, 3.0 AND 3.5, Northrop Corporation, Norair Division Report NOR-63-54 (BLC-150) (UNPUBLISHED).
22. Groth, Eric E.: BOUNDARY LAYER TRANSITION MEASUREMENTS ON SWEPT WINGS AT SUPERSONIC SPEEDS, Northrop Corporation, Norair Division Report NOR-63-55 (BLC-151) (UNPUBLISHED).

## REFERENCES

23. Goldsmith, John: INVESTIGATION OF LAMINAR FLOW CONTROL AIRFOILS SWEEP BEHIND THE MACH ANGLE, Northrop Corporation, Norair Division Report NOR-63-56 (BLC-152) (UNPUBLISHED).
24. Pfenninger, W. and Rogers, K. H.: PRESSURE DROP IN LAMINAR FLOW TUBES WITH COMPRESSIBLE FLOW, Northrop Corporation, Norair Division Report NOR-63-57 (BLC-153) (UNPUBLISHED).
25. Aris, R.: VECTORS, TENSORS, AND THE BASIC EQUATIONS OF FLUID MECHANICS, Prentice-Hall, Inc., 1962.
26. Benjamin, T. B.: "Effects of a Flexible Boundary on Hydrodynamic Stability," JOURNAL OF FLUID MECHANICS, Vol. 9, pp. 513-532, 1960.
27. Benney, D. J. and Lin, C. C.: NONLINEAR OSCILLATIONS IN SHEAR FLOWS, Presented to the American Physical Society, Fluid Dynamics Division, 1961.
28. Benney, D. J. and Niel, A. M.: "Apparent Resonances of Weakly Nonlinear Standing Waves," JOURNAL OF MATHEMATICS AND PHYSICS, Vol. 41, pp. 254-263, 1962.
29. Chandrasekhar, S.: "Adjoint Differential Systems in the Theory of Hydrodynamic Stability," JOURNAL OF MATHEMATICS AND MECHANICS, Vol. 10, pp. 683-690, 1961.
30. Corcos, G. M. and Sellars, J. R.: "On the Stability of Fully Developed Flow in a Pipe," JOURNAL OF FLUID MECHANICS, Vol. 5, pp. 97-112, 1959.
31. Criminale, W. O., Jr.: THREE-DIMENSIONAL LAMINAR INSTABILITY, AGARD Report 266, 1960.
32. Dutton, R. A.: THE EFFECTS OF DISTRIBUTED SUCTION ON THE DEVELOPMENT OF TURBULENT BOUNDARY LAYERS, ARC R&M 3155, 1960.
33. Gregory, N. and Walker, W. S.: THE EFFECT ON TRANSITION OF ISOLATED SURFACE EXCRESCENCES IN THE BOUNDARY LAYER, ARC Report 13,436, 1950.
34. Grohne, D.: ON THE SPECTRUM OF NATURAL OSCILLATIONS OF TWO-DIMENSIONAL LAMINAR FLOWS, NACA TM 1417, 1957.
35. Hardy, G. H.: DIVERGENT SERIES, Oxford University Press, 1956.
36. Hille, E.: ANALYTIC FUNCTION THEORY, Vol. II, Ginn and Company, 1962.
37. Klebanoff, P. S. and Tidstrom, K. D.: EVOLUTION OF AMPLIFIED WAVES LEADING TO TRANSITION IN A BOUNDARY LAYER WITH ZERO PRESSURE GRADIENT, NASA TN D-195, 1959.

## REFERENCES

38. Klebanoff, P. S., Tidstrom, K. D. and Sargent, L. M., "The Three-dimensional Nature of Boundary Layer Instability," JOURNAL OF FLUID MECHANICS, Vol. 12, Part 1, 1962.
39. Kovasznag, L. S. G.: "A New Look at Transition," AERONAUTICS AND ASTRONAUTICS (Proceedings of the Durand Centennial Conference), pp. 161-172, Pergamon Press, 1960.
40. Kurtz, E. F. and Crandall, S. H.: "Computer-aided Analysis of Hydrodynamic Stability," JOURNAL OF MATHEMATICS AND PHYSICS, Vol. 41, pp. 264-279, 1962.
41. Lin, C. C.: THE THEORY OF HYDRODYNAMIC STABILITY, Cambridge University Press, 1955.
42. Lin, C. C. and Benney, D. J.: "On the Instability of Shear Flows," HYDRODYNAMIC INSTABILITY (Proceedings of Symposia in Applied Mathematics, Vol. XIII), pp. 1-24, American Mathematical Society, 1962.
43. Meksyn, D. and Stuart, J. T.: "Stability of Viscous Motion between Parallel Planes for Finite Disturbances," PROCEEDINGS OF THE ROYAL SOCIETY, Series A, No. 208, pp. 517-526, 1951.
44. Meksyn, D.: NEW METHODS IN LAMINAR BOUNDARY LAYER THEORY, Pergamon Press, 1961.
45. Raetz, G. S.: A METHOD OF CALCULATING THREE-DIMENSIONAL LAMINAR BOUNDARY LAYERS OF STEADY COMPRESSIBLE FLOWS, Northrop Corporation, Norair Division Report NAI-58-73 (BLC-114), December 1957.
46. Roberts, P. H.: "Characteristic Value Problems Posed by Differential Equations Arising in Hydrodynamics and Hydromagnetics," JOURNAL OF MATHEMATICAL ANALYSIS AND APPLICATIONS, Vol. 1, pp. 195-214, 1960.
47. Schlichting, H.: BOUNDARY LAYER THEORY, McGraw-Hill Book Company, Inc., 1955.
48. Schubauer, G. B. and Skramstad, H. K.: LAMINAR BOUNDARY LAYER OSCILLATIONS AND TRANSITION ON A FLAT PLATE, NACA Report 909, 1948.
49. Segel, L. A. and Stuart, J. T.: "On the Question of the Preferred Mode in Cellular Thermal Convection, JOURNAL OF FLUID MECHANICS, Vol. 13, pp. 289-306, 1962.
50. Sewell, K. G.: "A New Analytical Model for Boundary Layer Transition," PROCEEDINGS OF HEAT TRANSFER AND FLUID MECHANICS INSTITUTE, pp. 106-119, Stanford University Press, 1960.
51. Stuart, J. T.: "On the Nonlinear Mechanics of Hydrodynamic Stability," JOURNAL OF FLUID MECHANICS, Vol. 4, pp. 1-21, 1958.

## REFERENCES

52. Stuart, J. T.: "On Three-dimensional Nonlinear Effects in the Stability of Parallel Flows," ADVANCES IN AERONAUTICAL SCIENCES, Vol. 3-4, Pergamon Press, 1961.
53. Stuart, J. T.: "Nonlinear Effects in Hydrodynamic Stability," APPLIED MECHANICS (Proceedings of the Tenth International Congress of Applied Mechanics), pp. 63-97, Elsevier Publishing Company, 1962.
54. Theodorsen, T.: THE STRUCTURE OF TURBULENCE, Air Research and Development Command, Office of Scientific Research, Report OSR-TN-54-131, 1954.
55. Tollmien, W. and Grohne, D.: "The Nature of Transition," BOUNDARY LAYER AND FLOW CONTROL, Vol. 2, pp. 602-636, Pergamon Press, 1961.
56. Watson, J.: "On Spacially-Growing Finite Disturbances in Plane Poiseuille Flow," JOURNAL OF FLUID MECHANICS, Vol. 14, pp. 211-221, 1962.
57. Lees, Lester and Reshotko, Eli: "Stability of the Compressible Laminar Boundary Layer," PROCEEDINGS OF THE TENTH INTERNATIONAL CONGRESS OF APPLIED MECHANICS, Stresa, Italy, 1960.
58. Lees, Lester and Lin, Chia Chiao: INVESTIGATION OF THE STABILITY OF THE LAMINAR BOUNDARY LAYER IN A COMPRESSIBLE FLUID, NACA TN-1115, September 1946.
59. Mack, L. M.: CALCULATION OF THE LAMINAR BOUNDARY LAYER ON AN INSULATED FLAT PLATE BY THE KLUNKER-McLEAN METHOD, Jet Propulsion Laboratories, California Institute of Technology Progress Report No. 20-352, July 7, 1958.
60. Howarth, L. (editor): MODERN DEVELOPMENTS IN FLUID DYNAMICS HIGH SPEED FLOW, Vol. I, p. 37.
61. Agnew, R. P.: DIFFERENTIAL EQUATIONS, McGraw Hill Book Company, pp. 325-326, 1942.
62. Demetriades, A.: AN EXPERIMENTAL INVESTIGATION OF THE HYPERSONIC LAMINAR BOUNDARY LAYER, GALCIT Hypersonic Research Project, Memorandum No. 43, May 15, 1958.
63. Laufer, J. and Vrebalovich, T.: "Stability and Transition of a Supersonic Laminar Boundary Layer on an Insulated Flat Plate," JOURNAL OF FLUID MECHANICS, Vol. 9, Part 2, pp. 257-299, 1960.
64. Mack, L. M.: THE STABILITY OF THE COMPRESSIBLE LAMINAR BOUNDARY LAYER ACCORDING TO A DIRECT NUMERICAL SOLUTION, Jet Propulsion Laboratories Space Program Summary 37-16, Vol. 4, Section 327.

## REFERENCES

65. Reshotko, E.: STABILITY OF THE COMPRESSIBLE LAMINAR BOUNDARY LAYER, Guggenheim Aeronautical Laboratory, California Institute of Technology, Hypersonic Research Project Memorandum No. 52, 15 January 1960.
66. Dunn, D. W. and Lin, C. C.: "On the Stability of Laminar Boundary Layer in a Compressible Fluid," JOURNAL OF AERONAUTICAL SCIENCES, Vol. 22, No. 7, pp. 455-477, July 1955.
67. Brown, W. Byron: "A Stability Criterion for Three-Dimensional Laminar Boundary Layers," BOUNDARY LAYER AND FLOW CONTROL, Vol. 2, pp. 913-924, Pergamon Press, 1961.
68. Gregory, N.: THE PRESENT POSITION OF RESEARCH ON LAMINAR FLOW OVER SWEEPED WINGS, British ARC Report, Perp. 1526.
69. Pfenninger, W., Gross, L. W. and Bacon, J. W., Jr.: EXPERIMENTS ON A 30° SWEEPED 12%-THICK SYMMETRICAL LAMINAR SUCTION WING IN THE 5- BY 7-FOOT MICHIGAN TUNNEL, Northrop Corporation, Norair Division Report NAI-57-317 (BLC-93), February 1957; including Appendix by G. S. Raetz, EVALUATION OF THE PROFILE DRAG COEFFICIENT OF AN UNTAPERED SWEEPED SUCTION WING.
70. Bacon, J. W., Jr., Tucker, V. L. and Pfenninger, W.: EXPERIMENTS ON A 30° SWEEPED 12%-THICK SYMMETRICAL LAMINAR SUCTION WING IN THE 5- BY 7-FOOT UNIVERSITY OF MICHIGAN TUNNEL, Northrop Corporation, Norair Division Report NOR-59-328 (BLC-119), August 1959.
71. Boltz, Frederick W., Kenyon, George C. and Allen, Clyde Q.: THE BOUNDARY LAYER TRANSITION CHARACTERISTICS OF TWO BODIES OF REVOLUTION, A FLAT PLATE, AND AN UNSWEEPED WING IN A LOW TURBULENCE WIND TUNNEL, NASA TN D-309.
72. Gault, Donald E.: AN EXPERIMENTAL INVESTIGATION OF BOUNDARY LAYER CONTROL FOR DRAG REDUCTION OF A SWEEPED WING SECTION AT LOW SPEED AND HIGH REYNOLDS NUMBERS, NASA TN D-320.
73. Goldstein, S. (Editor): MODERN DEVELOPMENTS IN FLUID DYNAMICS, Vol. 1, Oxford University Press, 1938.
74. Schiller, L.: HANDBUCH DER EXPERIMENTALPHYSIK, Vol. 4, Part 4, 1932.
75. Rogers, K. H.: EXPERIMENTAL AND THEORETICAL INVESTIGATIONS OF THE PRESSURE DROP THROUGH HOLES AND SLOTS IN INCOMPRESSIBLE VISCOUS FLOW, Northrop Corporation, Norair Division Report NAI-58-19 (BLC-104), December 1957.
76. Raetz, G. S.: A METHOD OF CALCULATING THE INCOMPRESSIBLE LAMINAR BOUNDARY LAYER ON INFINITELY LONG SWEEPED SUCTION WINGS, ADAPTABLE TO SMALL-CAPACITY AUTOMATIC DIGITAL COMPUTERS, Northrop Corporation, Norair Division Report BLC-11, September 1953.



## REFERENCES

77. Pfenninger, W.: EXPERIMENTS WITH A 15%-THICK SLOTTED LAMINAR SUCTION WING MODEL IN THE LOW TURBULENCE TUNNEL (TDT) AT THE NACA, LANGLEY FIELD, VIRGINIA, Northrop Corporation, Norair Division Report A-158, October 1951.
78. Pfenninger, W.: EXPERIMENTS WITH A 15%-THICK SLOTTED LAMINAR SUCTION WING MODEL IN THE NACA LANGLEY FIELD LOW TURBULENCE WIND TUNNEL, AFTR 5982, April 1953.
79. Squire, H. B. and Young, A. D.: THE CALCULATION OF THE PROFILE DRAG OF AIRFOILS, British R&M 1838, November 1937.
80. Theodorsen, T.: THEORY OF WING SECTIONS OF ARBITRARY SHAPE, NACA TR-411, 1931.
81. Herriot, J. G.: BLOCKAGE CORRECTIONS FOR THREE-DIMENSIONAL FLOW IN CLOSED THROAT WIND TUNNELS, WITH CONSIDERATIONS OF THE EFFECT OF COMPRESSIBILITY, NACA TR-995, 1950.
82. Batchelor, G. K. and Shaw, F. G.: A CONSIDERATION OF THE DESIGN OF WIND TUNNEL CONTRACTIONS, Australian Council for Aeronautics Report No. 4, 1944.
83. Carmichael, B. H. and Raspet, A.: LOW DRAG SUCTION EXPERIMENTS ON A GLIDER WING IN THE PRESENCE OF SOUND, Presented at Mississippi State College, October 1954.
84. Bergh, H. and Berg, B. van den: "On the Visualization of Laminar Boundary Layer Oscillations and the Transition to Turbulent Flow," ZEITSCHRIFT FUR ANGEWANDTE MATHEMATIK UND PHYSIK (FESTSCHRIFT JAKOB ACKERET), 1958, pp. 97-104.
85. (a) Pfenninger, W., Groth, E. E., Carmichael, B. H. and Whites, R. C.: LOW DRAG BOUNDARY LAYER SUCTION EXPERIMENTS IN FLIGHT ON THE WING GLOVE OF AN F-94A AIRPLANE. PHASE I - SUCTION THROUGH TWELVE SLOTS, Northrop Corporation, Norair Division Report NAI-55-458, (BLC-77), April 1955.  
  
(b) Groth, E. E., Carmichael, B. H., Whites, R. C. and Pfenninger, W.: LOW DRAG BOUNDARY LAYER SUCTION EXPERIMENTS IN FLIGHT ON THE WING GLOVE OF AN F-94A AIRPLANE. PHASE II - SUCTION THROUGH 69 SLOTS, Northrop Corporation, Norair Division Report NAI-57-318 (BLC-94), February 1957.
86. Pfenninger, W.: EXPERIMENTS WITH LAMINAR FLOW IN THE INLET LENGTH OF A TUBE AT HIGH REYNOLDS NUMBERS WITH AND WITHOUT BOUNDARY LAYER SUCTION, Northrop Corporation, Norair Division Report, May 1952.
87. Gray, W. E.: THE EFFECT OF WING SWEEP ON LAMINAR FLOW, RAE TM Aero 255, February 1952.

## REFERENCES

88. Corrsin, Stanley: EXTENDED APPLICATIONS OF THE HOT WIRE ANEMOMETER, NACA TN-1864
89. Owen, P. R. and Randall, D. J.: BOUNDARY LAYER TRANSITION ON THE SWEPTBACK WING, RAE TM Aero 277, May 1952.
90. Dryden, H. L.: AIR FLOW IN THE BOUNDARY LAYER NEAR A PLATE, NACA TR-562, 1936.
91. Pate, S. R. and Brillhart, R. E.: INVESTIGATION OF BOUNDARY LAYER TRANSITION ON SWEPT WINGS AT MACH NUMBERS 2.5 TO 5.0, AEDC-TDR-63-109, May 1963.
92. Groth, E. E.: BOUNDARY LAYER TRANSITION ON BODIES OF REVOLUTION, Northrop Corporation, Norair Division Report NAI-57-1162 (BLC-100), July 1957.
93. Kuethe, A. M.: ON THE STABILITY OF FLOW IN THE BOUNDARY LAYER NEAR THE NOSE OF A BLUNT BODY, Rand Corporation Report RM-1972, August 1957.
94. Groth, E. E.: LOW SPEED WIND TUNNEL EXPERIMENTS ON A BODY OF REVOLUTION WITH LOW DRAG BOUNDARY LAYER SUCTION, Northrop Corporation, Norair Division Report NAI-58-335 (BLC-107), May 1958.
95. Pankhurst & Holder: WIND TUNNEL TECHNIQUE, Sir Isaac Pitman & Sons, Ltd., London, 1952.
96. Raetz, G. S.: RESONANCE THEORY OF TRANSITION, Northrop Corporation, Norair Division Report NOR-63-52 (BLC-146).
97. SUMMARY OF LAMINAR BOUNDARY LAYER CONTROL RESEARCH, Summary of Contract AF33(616)-3168, WADC Technical Report 56-111, April 1957.
98. Groth, E. E.: LOW DRAG BOUNDARY LAYER SUCTION EXPERIMENTS ON A 5% THICK BICONVEX AIRFOIL SECTION AT  $M = 2.23$  AND  $2.77$ , Northrop Corporation, Norair Division Report NAI-58-195 (BLC-105), March 1958.
99. Jones, J. H. and Pate, S. R.: INVESTIGATION OF BOUNDARY LAYER SUCTION ON A FLAT PLATE AT  $M = 3.0$ , AEDC Report TN-61-128, September 1961.
100. Van Driest, E. R.: "Convective Heat Transfer of Gases," HIGH SPEED AERODYNAMIC AND JET PROPULSION, Section F, Vol. V, Princeton University Press, 1959.
101. Bradfield, W. S., et. al.: THE EFFECT OF LEADING EDGE BLUNTNESS ON A LAMINAR SUPERSONIC BOUNDARY LAYER, Institute of the Aeronautical Sciences, June 1954.

## REFERENCES

102. Moeckel, W. E.: SOME EFFECTS OF BLUNTNES ON BOUNDARY LAYER TRANSITION AND HEAT TRANSFER AT SUPERSONIC SPEEDS, NACA Report 1312, 1957.
103. Belotserkovskii, O. M.: "Flow with a Detached Shock Wave about a Symmetrical Profile," JOURNAL APPL. MATH. AND MECH., Vol. 22, No. 2, 1958.
104. Munk, M. M. and Crown, J. C.: "The Head Shock Wave," PROCEEDINGS OF THE JOURNAL OF INTERNATIONAL CONGRESS FOR APPLIED MECHANICS, Vol. 2, Part II, 1948.
105. Greber, I.: INTERACTION OF OBLIQUE SHOCK WAVES WITH LAMINAR BOUNDARY LAYERS, MIT, Technical Report 59-2, 1959.
106. Pate, S. R. and Deitering, J. S.: INVESTIGATION OF DRAG REDUCTION OF BOUNDARY LAYER SUCTION ON A FLAT PLATE AND A 36° SWEEP WING AT SUPERSONIC SPEEDS, AEDC-TDR-62-144, August 1962.
107. Groth, E. E.: INVESTIGATION OF THE FLOW FIELD AROUND A SUCTION SLOT AT SUPERSONIC SPEEDS, Northrop Corporation, Norair Division Report NAI-59-4 (BLC-116), January 1959.
108. Smith, A. M. O. and Clutter, D. W.: "The Smallest Height of Roughness Capable of Affecting Boundary-Layer Transition," JOURNAL OF THE AERO/SPACE SCIENCES, Vol. 26, No. 4, April 1959, pp. 229-245, 256.
109. Pate, S. R. and Deitering, J. S.: INVESTIGATION OF DRAG REDUCTION BY BOUNDARY LAYER SUCTION ON A 36° SWEEP WING AT  $M = 2.5$  TO 4.0, AEDC-TDR-63-23, February 1963.
110. Groth, E. E.: NOTE ON THE LOW DRAG BOUNDARY LAYER SUCTION EXPERIMENTS ON A 36° SWEEP WING AT MACH NUMBERS 2.5 AND 3.0, Conducted at AEDC Tunnel A during March 1962. Appendix to Report NOR-62-188, Progress Report for period July and August 1962.
111. Northrop Corporation, Norair Division Report NOR-63-8, Progress Report for Period November and December 1962.
112. Cooke, J. C. and Hall, M. G.: BOUNDARY LAYERS IN THREE DIMENSIONS, AGARD Report No. 273, April 1960.
113. Dunning, R. W. and Ulmann, E. F.: EFFECTS OF SWEEP AND ANGLE OF ATTACK ON BOUNDARY LAYER TRANSITION ON WINGS AT  $M = 4.04$ , NACA TN 3473, 1955.
114. Tillie, D. W. and Hopkins, E. J.: EFFECTS OF MACH NUMBER, LEADING EDGE BLUNTNES AND SWEEP ON BOUNDARY LAYER TRANSITION ON A FLAT PLATE, NASA TN D-1071, September 1961.

## REFERENCES

115. Chapman, G. T.: SOME EFFECTS OF LEADING EDGE SWEEP ON BOUNDARY LAYER TRANSITION AT SUPERSONIC SPEEDS, NASA TN D-1075, September 1961.
116. Potter, J. I. and Whitfield, J. D.: EFFECTS OF UNIT REYNOLDS NUMBER, NOSE BLUNTNESS AND ROUGHNESS ON BOUNDARY LAYER TRANSITION, Arnold Engineering Development Center Report AEDC-TR-60-5, March 1960. (Also published in JOURNAL OF FLUID MECHANICS, Vol. 12, Part 4, 1962.)
117. Staff of the Ames 1- by 3-foot Supersonic Wind Tunnel Section: NOTES AND TABLES FOR USE IN THE ANALYSIS OF SUPERSONIC FLOW, NACA Technical Note 1428, December 1947.
118. Goldsmith, J.: IBM COMPUTER PROGRAMS FOR CALCULATING THE VELOCITY AND PRESSURE ON OR NEAR TWO-DIMENSIONAL AIRFOILS, Northrop Corporation, Norair Division Report NOR-61-214 (BLC-132), September 1961.
119. Spreiter, J. R. and Alksne, A. Y.: THIN AIRFOIL THEORY BASED ON APPROXIMATE SOLUTION OF THE TRANSONIC FLOW EQUATION, NACA Technical Note 3970, May 1957.
120. Goethert, B.: PLANE AND THREE-DIMENSIONAL FLOW AT HIGH SUBSONIC SPEEDS, NACA Technical Memorandum 1105, October 1946.
121. Pfenninger, W.: DESIGN CONSIDERATIONS OF LARGE SUBSONIC LONG RANGE TRANSPORT AIRPLANES WITH LOW DRAG BOUNDARY LAYER SUCTION, Northrop Corporation, Norair Division Report NAI-58-529 (BLC-111), October 1959.
122. Pate, S. R. and Deitering, J. S.: INVESTIGATION OF DRAG REDUCTION BY BOUNDARY LAYER SUCTION ON A  $72.5^\circ$  SWEEP WING AT  $M_\infty = 2$  AND  $2.25$ , AEDC-TDR-63-87, May 1963.
123. Groth, E. E.: LOW DRAG BOUNDARY LAYER SUCTION EXPERIMENTS ON AN OGIVE CYLINDER BODY OF REVOLUTION AT SUPERSONIC SPEEDS, Northrop Corporation, Norair Division Report NAI-58-851 (BLC-115), November 1958.
124. Stein, M. and Mayers, J.: COMPRESSIBLE BUCKLING OF SIMPLY SUPPORTED, CURVED PLATED CYLINDERS OF SANDWICH CONSTRUCTION, NACA TN 2601, Jan. 1952.
125. Cliett, C. B.: STRUCTURAL COMPARISON OF PERFORATED SKIN SURFACES WITH OTHER MEANS OF EFFECTING BOUNDARY LAYER CONTROL BY SUCTION, Aeronautical Engineering Review, September 1953.
126. Wieder, J.: BLC UNTAPERED RECTANGULAR BOX TORSION TEST, Northrop Corporation, Norair Division Report (Unpublished).
127. Pfenninger, W.: SOME GENERAL CONSIDERATIONS OF LOSSES IN BOUNDARY LAYER SUCTION DUCTING SYSTEMS, Northrop Corporation, Norair Division Report (BLC-29), February 1954.

#### REFERENCES

128. Rogers, K. H. and Pfenninger, W.: FURTHER INVESTIGATIONS OF AN IMPROVED SUCTION DUCT, Northrop Corporation, Norair Division Report NAI-55-547 (BLC-70), May 1955.
129. Worth, R.: EFFECT OF WEATHERING ON TYPICAL BONDED BOUNDARY LAYER CONTROL STRUCTURE, Northrop Corporation, Norair Division Report NOR-59-608 (BLC-128), January 1960.
130. Hill, W. L.: PRELIMINARY INVESTIGATION ON THE EFFECT OF WEATHERING AND SULFURIC ACID ANODIZING ON SELECTED METAL-TO-METAL ADHESIVE SYSTEMS, Northrop Corporation, Norair Division Report NOR-61-35, March 1961.
131. PROCEEDINGS OF THE SYMPOSIUM ON FATIGUE OF AIRCRAFT STRUCTURES, Wright Air Development Center, USAF, Wright Patterson Air Force Base, Ohio, WADC TR 59-507, August 1959, p. 290.
132. Dally, J. W. and Durelli, A. J.: STRESSES IN PERFORATED PANELS, Product Engineering, March 1956, pp. 188ff.

Aeronautical Systems Division, AF Flight Dynamics Laboratory, Wright-Patterson AFB, Ohio.

Rpt Nr ASD-TDR-63-554. SUMMARY OF LAMINAR BOUNDARY LAYER CONTROL RESEARCH. Final report, March 1964, 868 p. incl illus, tables, refs.

Unclassified Report

At subsonic speeds, full length laminar flow and low drags were obtained up to high length Reynolds numbers on a thin straight, on a swept laminar suction wing and on a suction body of revolution. Moderately increased suction rates in the most critical region of a straight and a swept laminar suction wing enabled full chord laminar flow in the presence of external sound. Theoretical investigations are concerned with nonlinear boundary layer oscillations and stability boundary layer on a flat plate up to high supersonic speeds as well as on a highly swept supersonic low drag suction wing of low wave drag. On a supersonic flat laminar suction plate with and without weak incident shock waves, extensive laminar flow and low

(over)

equivalent drags were obtained at  $M = 3$  up to length Reynolds numbers of  $26 \cdot 10^6$ . Further supersonic low drag suction experiments on a suction body of revolution, on a  $36^\circ$  supersonic yawing wing, as well as on a  $72^\circ$  supersonic yawing wing (swept behind the Mach cone) of low wave drag, are described. The latter wing showed full chord laminar flow with a subsonic type pressure distribution at  $M = 2$  and  $R_c \approx 9 \cdot 10^6$ .

UNCLASSIFIED

1. Boundary layer
2. Laminar boundary layer
3. Aerodynamics
4. Boundary layer control
5. Boundary layer stabilization

- I. AFSC Project 1366, Task 136612
- II. Contract AF33(616)-7564
- III. Northrop Norair, a Division of Northrop Corporation, Hawthorne, Calif.
- IV. Dr. W. Pfenninger, et al
- V. Avail fr OTS
- VI. In ASTIA Collection

UNCLASSIFIED

UNCLASSIFIED

UNCLASSIFIED